NONLINEAR FINITE ELEMENT MODELLING OF REINFORCED CONCRETE FRAMES RETROFITTED WITH SHAPE MEMORY ALLOY BUCKLING RESTRAINED BRACES

PEDRO ALEXANDRE GUIMARAES ROCHA

A THESIS SUBMITTED TO THE FACULTY OF GRADUATE STUDIES IN PARTIAL FULFILLMENT OF THE REQUIREMENTS FOR THE DEGREE OF MASTER OF APPLIED SCIENCE

GRADUATE PROGRAMM IN CIVIL ENGINEERING

YORK UNIVERSITY

TORONTO, ONTARIO

August 2020

ABSTRACT

Reinforced concrete buildings built prior to the enactment of modern seismic provisions are vulnerable when subjected to high-magnitude earthquakes since they lack the capacity to properly dissipate the energy associated with the ground excitation. Therefore, this research aims to investigate the benefits of Buckling-Restrained Braces (BRBs) as a retrofit technique for accommodating seismic demands in seismically deficient reinforced concrete frames, the dominant structural system of pre-1970s construction. The efficiency of Superelastic-Shape Memory Alloys (SE-SMA) as the core material of the BRB is also evaluated. Improvements in lateral strength capacity and residual displacements of the SMA-BRB retrofitted frames are assessed against a previously tested bare concrete frame and frames retrofitted with BRBs incorporating stainless steel and chrome-molybdenum steel core bars. Reverse cyclic finite-element modelling of the frames was conducted with VecTor2, and the numerical models were validated through experimental results present in the literature. The validated numerical models were further modified to address deficiencies in the original BRB design by including improvements in restraining of the buckling. The SMA-BRB provided lateral strength comparable to the modified steel BRB models with enhancements in ductility capacity. Notably, the SMA-BRB system did not accumulate additional residual displacements beyond those experienced by the bare frame alone. Therefore, the reduction in residual displacements, in comparison to conventional steel core BRB materials, illustrates one of the main benefits of SMA bars, leading to a viable and efficient alternative to increase the seismic performance and reduce damage in structural elements located in high seismic zones. Furthermore, nonlinear time-history analyses are conducted. Earthquake records that simulate design earthquakes for the cities of Montreal and Vancouver were selected for the dynamic loading. At the end of the thesis, an optimized BRB design is provided in which the full capacity of the core bars is achieved since localized buckling is minimized.

Keywords: Reinforced concrete structures, moment-resisting frames, buckling-restrained braces, superelastic shape-memory alloys.

ACKNOWLEDGEMENTS

First, the author would like to acknowledge the endless support provided by his supervisor Dr. Dan Palermo. Over the course of two years, Dr. Palermo has been offering valuable insights over the research topic, confidence over the author's ability to conduct the research, and encouragement in the face of challenges. The author is sincerely grateful for his support.

The author is also extremely thankful for the assistance given by the administrative staff of York University. They have been fundamental in providing the necessary tools for the completion of this research. Special thanks are directed to Sindy Mahal for the patience in providing information, and for always answering my long e-mails. Still in the university community, the author would like to thank his colleagues for their patience and support during these two years, including Danelle, Everett, and Daniela.

To my friends, including Jaime, Luiza, Carol, and Marina, my sincere gratitude for always being there when needed, for listening to my complaints, and for giving me good advices. Special thanks are also extended to Jamie and Larry for the friendship developed in the first year of my masters. To my love Richard, thank you for facing all the excitements and hardships of this phase of my life, and for not measuring efforts to help me.

To my parents, Anderson and Neide, I would like to thank for always being accepting of who I am, respectful of my decisions, and for prioritizing my education since I was a kid. I am honoured to be your son. Special thanks are also offered to my little, but not so little, brother, for promptly answering my desperate messages after a long day of working. To my family that has moved mountains to invest in my education, I would like to express my sincere gratitude. Special thanks to my grandparents for educating me. Without their support, I would not be here. I love all of you.

To God, I would like to express my genuine gratitude for giving me the opportunity of living in this amazing world, for always being by my side, and for always listening to my prayers.

TABLE OF CONTENTS

LIST OF TABLES

LIST OF FIGURES

Chapter 1

Introduction

1.1 General

Advancements in seismological knowledge, related to the impact ground motions have on structural elements, have led to significant changes in seismic provisions. Structures built prior to the enactment of these modern seismic standards may be vulnerable when subjected to high-magnitude earthquakes. In Canada, particularly, seismic force design requirements have increased approximately 100% since the 1970s (Cheung et al. 2000). Likely deficiencies arising from vulnerable structures consist of insufficient: ductility, base shear strength, and capacity to properly dissipate the energy associated with strong ground excitations. Therefore, design requirements prescribed in current building codes are not implemented in a large number of old structures, which presents a considerable threat to life safety and economic losses.

Non-ductile or limited ductility reinforced concrete moment-resisting frames were the dominant structural system of pre-1970's construction; its application ranged from residential to hospital and school facilities, which are required to maintain structural integrity post-disaster by current building codes. Moment-resisting frames were designed based on the strong beam and weak column theory; thus, the bottom of the columns and beam-column joints are highly susceptible to damage. Under a seismic event, it has been observed that RC frames are damaged due to widely spaced and/or poorly anchored transverse reinforcement (Yavari, 2011). Hence, columns are highly vulnerable to shear failure that may lead to reduction in axial load resistance and building collapse.

As a result, there has been an increasing interest to perform seismic risk mitigation by retrofitting older structures designed according to deficient/outdated seismic provisions. This risk mitigation can be effectively achieved by conducting a vulnerability assessment to select an appropriate seismic retrofit. The retrofitting objectives range from controlling lateral drift and seismic deformation demands to preventing collapse. Steel bracing is a widely used technique that improves the seismic performance of reinforced concrete moment-resisting frames by increasing lateral strength and stiffness of the structural element. Buckling Restrained Braces (BRBs) are an enhanced form of steel braces where the brace yields in both tension and compression. However, as BRBs induce a considerable permanent deformation and may reduce ductility of the system due to concentration of stresses within the brace components, it will be further explored in this thesis and modifications to address its deficiencies will be assessed.

Seismic risk should be understood as a product of seismic hazard and vulnerability of structures. For instance, although the Canadian West Coast is highly influenced by the Pacific Ring of Fire, other regions (Eastern Canada) susceptible to moderate earthquakes also under significant seismic risk as their building stock comprises older, poorly designed structures. In Canada, there are two well defined seismic zones: Western and Eastern. Western Canada is characterized by high magnitude earthquakes with low frequency and long return periods; while Eastern Canada is characterized by high frequency and short periods. These two seismic zones represent higher seismic risk as a result of the population density. Therefore, these two regions are typically studied to capture different earthquake characteristics. This will be further discussed in Chapter 6, Section 6.3.

1.2 Research significance

Following major earthquakes and advancements in assessing the seismic performance of structural systems, seismic provisions in the National Building Code of Canada (NBCC) have significantly changed. Improvements in provisions include addition of site and importance factors, description of the effects of ductility and overstrength, and implementation of the higher mode effects for the equivalent static force procedure; in addition, dynamic analysis requirements have been added to the NBCC (Al-Sadoon, 2017). These improvements directly affect the design base shear forces of non-ductile reinforced concrete frame buildings located in high and moderate seismic zones.

As moment-resisting frames were the dominant reinforced concrete structural system of pre-1970s construction, a large number of older structures are vulnerable to strong ground excitations due to the lack of seismic provisions of that era. Considering a prototype, six-storey RC frame building located in Vancouver as an example, the design base shear force has increased by more than four times from the 1970 to the 2010 NBCC (National Research Council of Canada, 1965 and 2010). Thus, lateral strength, energy dissipation and displacement ductility capacities of these construction types must be improved by an appropriate retrofitting technique.

This thesis, therefore, investigates the seismic response of a reinforced concrete frame designed according to the pre-1970s edition of the NBCC and the benefits of retrofitting with Buckling-Restrained Braces (BRBs). However, the steel core component of BRBs induce an increase in permanent displacement due to the post-yield plastic properties of steel bars, which can be observed in the stress-strain relationship of the material in Figure 1-1 (a). This permanent displacement leads to considerable economic loss due to repair costs of the structure if possible or demolition in many cases. To mitigate the accumulation of plastic deformation in RC frames, the implementation of Superelastic-Shape Memory Alloy (SE-SMA) bars as the core material of the brace will be investigated through nonlinear static and dynamic analyses. The self-centering capability of SE-SMAs, which is evident in the stress-strain relationship illustrated in Figure 1-1 (b), is expected to reduce the permanent displacements.

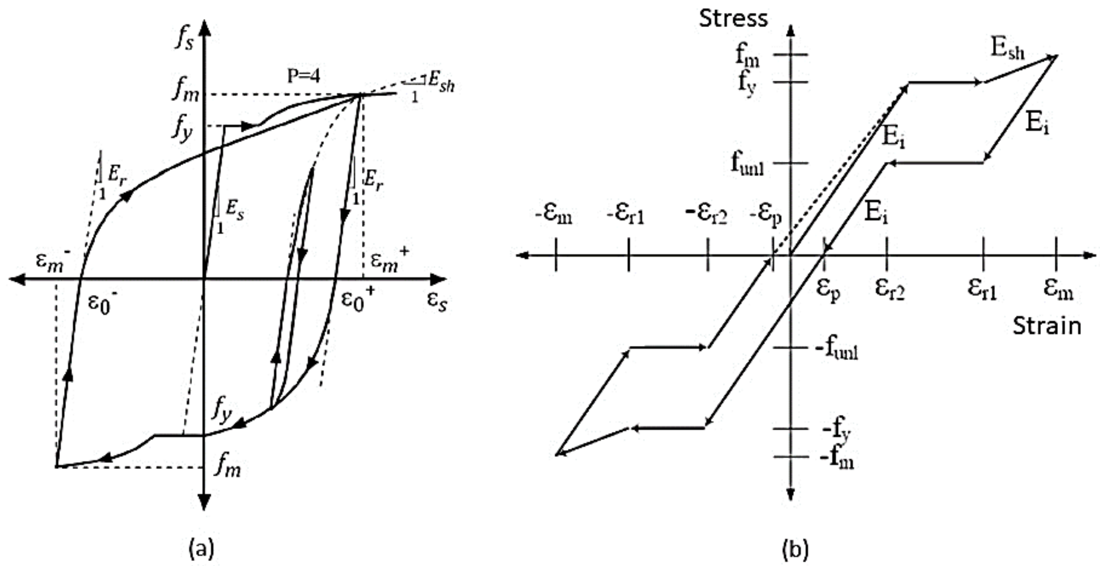

Figure 1-1: Stress-strain relationship of: (a) steel bars (Seckin, 1981); and (b) SE-SMA bars (Abdulridha et al., 2013)

Conventional steel core BRBs often fail due to localized buckling of the core bar at internal and external reserve gaps, which are intended to eliminate direct bearing of the outer steel casing, or due to concentration of stresses inside the brace. In both cases, the ductility of the structural system is affected and, frequently, unpredictable. Therefore, even though BRBs increase the lateral strength capacity of the system, it restricts the frame from sustaining large deformations to an uncertain level. The uncertainty also complicates the BRB efficiency analysis since analytical approaches assume the full capacity of the core bar, which is commonly not attained.

In order to avoid the localized buckling at the edges of the steel core bar, Al-Sadoon (2016) designed steel end elements that eliminates internal and external reverse gaps and avoids direct bearing. Thus, the proposed brace design will be numerically analyzed through a finite element software. However, as this BRB system presents localized concentration of stresses within the brace, a new system will be idealized and proposed in which the core bar does not experience this phenomenon. Therefore, the mechanical behaviour of the retrofitted system is expected to be controlled by the core bar material. Furthermore, the introduction of a BRB without concentration of stresses allows uncertainties to be mitigated, the full capacity of the core bar to be utilized, and the behaviour of the retrofitted reinforced concrete frame to be numerically predictable.

As a result, in addition to presenting a buckling-restrained brace without concentration of stresses and localized buckling, this research will evaluate the benefits and efficiency of superelastic shape-memory alloys, as the bracing core bar, to improve the seismic performance of a common 1970s frame structure. The novelty of this thesis also includes nonlinear time-history analysis of the BRB retrofitted frames, where the full-scale finite element model permits an explicit evaluation of damage, crushing of concrete, strain in the BRB core bar, and overall mechanical behaviour of the structural system. It is important to highlight that understanding the full performance of a BRB retrofitted frame is critical to comprehend the interaction of this emerging material (SE-SMA) with the other materials as part of an efficient design.

1.3 Research objectives

The primary objective of this thesis is to develop a cost-effective, buckling-restrained bracing system to retrofit seismically deficient reinforced concrete frames. The structural superiority of this idealized BRB relies on improving the restraining of the buckling by eliminating concentration of stresses, which will allow the core bar to reach its full capacity. The objective also includes nonlinear finite element time-history analysis of a pre-1970s reinforced concrete frame to evaluate its seismic performance once retrofitted by the idealized BRB. Furthermore, the efficiency of superelastic-shape memory alloy bars as the core material of the BRB is evaluated under nonlinear static reverse-cyclic and dynamic analyses.

1.4 Scope

To achieve the proposed objectives, the tasks presented bellow were completed.

- Thorough investigation on buckling restrained bracing systems as a retrofit for seismically deficient reinforced concrete moment-resisting frames. The focus was on evaluating the concept, different types and applications of the BRBs.

- Review of superelastic shape-memory alloy (SE-SMA) bars focusing on their ability to sustain large deformations and recover to a pre-determined shape when loading is removed. Therefore, assess the potential benefits once a SE-SMA bar is used as the bracing core bar of a BRB.
- Select a prototype moment-resisting frame building that represents common pre-1970s reinforced concrete construction and develop a finite element model of a frame, with and without a BRB retrofit, in VecTor2 (Vecchio et al., 2013). Conduct nonlinear static reverse cyclic analysis and validate the numerical model against experimental results available in the literature.
- Evaluate the seismic performance of the frame retrofitted with the BRB proposed by Al-Sadoon (2016) with respect to increasing lateral strength and displacement ductility. Assess the deficiencies of the retrofitting system by analysing the mechanical behaviour of both the brace and frame.
- Modify the BRB to increase the buckling restraining. Therefore, idealize an improved buckling-restrained brace able to address the deficiencies in the original testing program. Furthermore, model SE-SMA bars as the core of the improved BRB.
- Conduct nonlinear static and dynamic analyses of the modified BRB retrofitted system. The static analysis was performed under reverse cyclic incrementally increasing lateral displacements, while the dynamic study considered time-history analysis through scaled earthquake records based on the NBCC 2015 recommendations.
- Analysis of the seismic performance of the reinforced concrete frame retrofitted by the idealized BRB. Evaluate of the lateral strength capacity, displacement ductility and failure mode of the system.

Figure 1-2 presents a flowchart of the research approach.

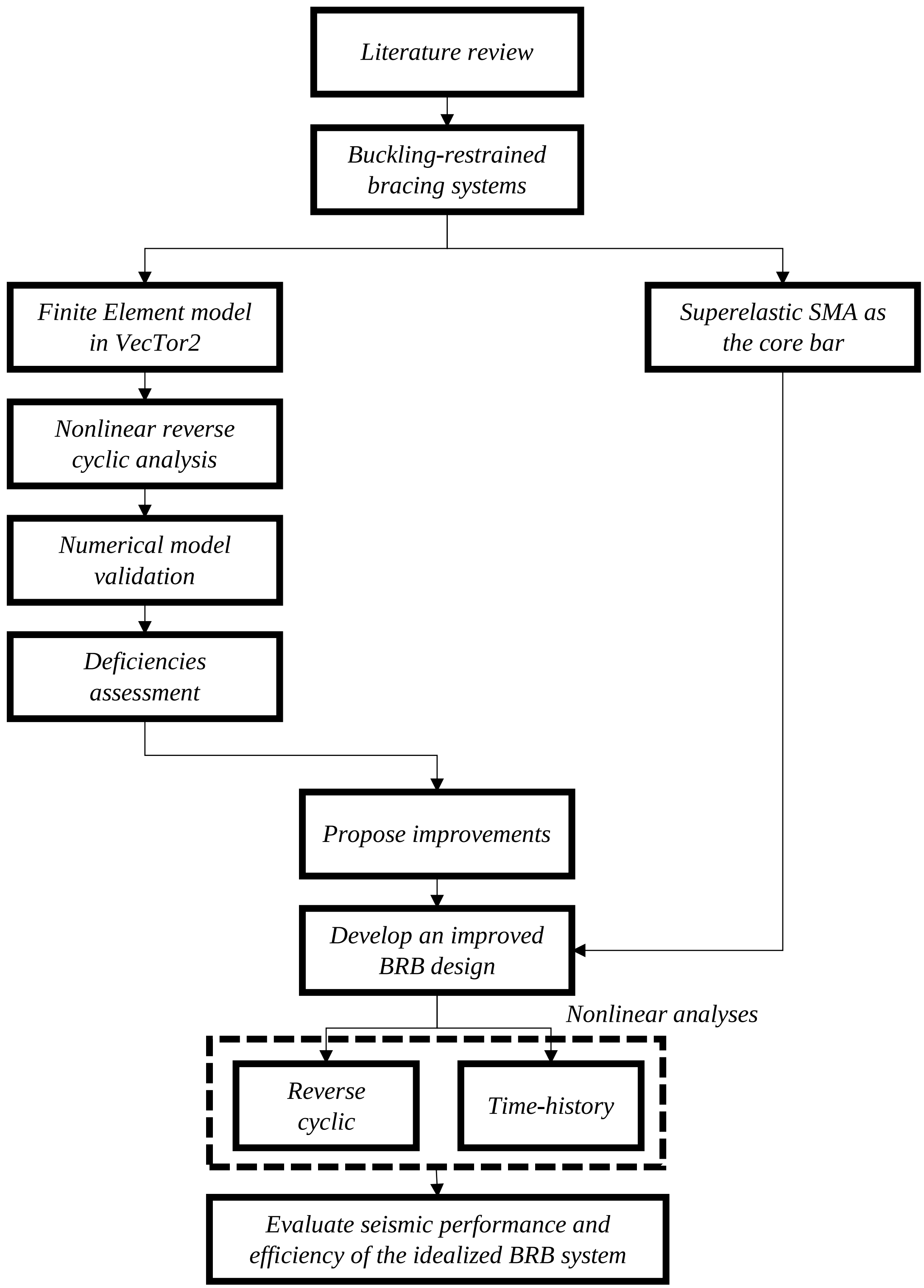

Figure 1-2: Research approach

1.5 Thesis organization

This thesis is organized in eight chapters. Chapter 1 contains the background, objectives and scope of the present research. Chapter 2 highlights significant experimental research conducted in the past to assess the efficiency of buckling-restrained braces as a seismic retrofit technique for moment-resisting frames. The application of superelastic shape-memory alloy bars is addressed as an alternative to increase ductility and to control residual deformations of concrete structures in Chapter 3.

Chapter 4 includes important features of the finite element program VecTor2 (Vechio et al., 2013) and an overview of the finite element model developed for the prototype reinforced concrete frame. The parameters adopted for the nonlinear static and dynamic analyses are presented. Furthermore, the model development and validation process are briefly discussed, and the constitutive models, element types and contact parameters are highlighted.

Chapters 5 and 6 present details of the static and dynamic analyses, respectively. The performance of the BRB retrofitted frame under incrementally increasing lateral displacements in terms of ductility and residual deformations is highlighted. The drift cycles are discussed, and details of the failure mode are presented. In addition, the response of the idealized BRB is also presented and discussed with the SE-SMA bar as the bracing core. Furthermore, in Chapter 5, a sensitivity analysis highlights the impact the above parameters have on the mechanical behaviour of the investigated structural element. Chapter 6 includes the dynamic time-history analyses of the frames in two different seismic zones and the improvements in behaviour of the retrofitted system with the SMA core material.

Chapter 7 provides a summary of the static and dynamic analyses; the results are discussed and the verified improvements of the modified BRB are addressed. In Chapter 8, conclusions are drawn on the applicability of the software to capture the response of the structural element under cyclic loading. The contributions of the shape memory alloy core bar brace and its efficiency in increasing ductility and controlling permanent deformation are also discussed. Furthermore, design recommendations for the buckling-restrained brace will be presented.

Chapter 2

Literature review

2.1 Introduction

Seismic retrofit is utilized to assure life safety by improving the performance of structural systems to satisfy current seismic provisions. However, an increase in strength capacity is not the only target performance point. The challenge resides in selecting a seismic retrofit technique capable of mitigating the damage inflicted by an earthquake to the serviceability state of a structure. To reduce recovery time and repair costs, this research aims to evaluate the seismic response of reinforced concrete moment-resisting frames retrofitted with a Buckling-Restrained Brace (BRB) incorporating a Shape-Memory Alloy (SMA) core bar. Therefore, this chapter aims to introduce pertinent previous research to an adequate understanding of this thesis including the concept and applications of BRBs in reinforced concrete structures. In addition, available retrofit techniques for moment-resisting frames will be introduced and their deficiencies presented to corroborate the benefits of BRBs. Further discussion is conducted regarding the different types and deficiencies of traditional BRBs.

2.2 Seismic retrofit of reinforced concrete moment-resisting frames

Existing Moment-Resisting Frame (MRF) buildings were typically constructed without the seismic detailing that are prescribed in current building codes. As this structural system composes part of the backbone of the world's infrastructure (Al-Sadoon, 2016), seismic retrofit of existing buildings should be considered. Two approaches can be taken to seismically improve frames: local element and global system retrofitting. Research regarding the former will be presented as it relates to beam-column joint retrofitting. In discussing the latter, diagonal braces will be presented. Among retrofitting strategies, diagonal bracing is the most used methodology for MRFs. Based on previous research, the BRBs has been utilized to accommodate compression, tension or both types of demands, and the objective is to increase the lateral strength capacity and stiffness of the system.

2.2.1 Local element retrofitting

During recent earthquakes, shear failure of beam-column joints has been identified as the primary cause of collapse of reinforced concrete moment-resisting frame buildings (Ghobarah et al., 2002). The strong-beam, weak-column design concept added to poorly spaced transverse reinforcement in the joints and is the main reason for this element to fail due in shear during earthquakes. Thus, there has been scientific motivation to explore retrofitting alternatives to improve the behaviour of the joints and prevent local failure of these elements (Said et al., 2008). Rehabilitation strategies that can be easily implemented include: providing effective element confinement with glass-fibre reinforced polymer sheets, local implementation of steel bracing, and the addition of internal reinforcement (Al-Sadoon, 2016).

To provide effective confinement, Ghobarah et al. (2002) designed four reinforced concrete beam-column joints following pre-1970's code provisions. Both column and beam cross-sections had dimensions of 250 mm x 400 mm; the column was 3000 mm high, while the beam was 1750 mm long from the face of the column to the free end. Six, No. 20 and two, No. 15 bars formed the longitudinal reinforcement in the column, while No. 10 rectangular ties composed the transverse reinforcement. For the beam, both top and bottom principal reinforcements were composed by four No. 20 bars, while No. 10 rectangular ties composed the transverse reinforcement. As per code requirements of that era, no reinforcement was required in the beam-column joint. Figure 2-1 illustrates the test set up.

The joints were tested under a constant axial load applied through the column and a reverse, quasi-static cyclic load applied at the beam tip. Two of the joints were tested as a control; T1 was tested with a constant axial load equivalent to 20% of the column capacity and T2 under 10% of the column axial capacity. After failure during the control test, the joints were repaired and retested as T1R and T2R, respectively. The joints were repaired with Glass-Fibre Reinforced Polymer (GFRP) "U" shaped sheets. Figures 2-2 (a) and (b) present the response of T1 and T1R, respectively. The retrofitted joint T1R was able to undergo larger deformations, and both the shear resistance and ductile behaviour were enhanced. Therefore, failure was no longer controlled by shear, but by flexural hinging of the beam. In addition, the energy dissipation of the rehabilitated joints was substantially increased in comparison to the control joints. As a result, this study demonstrated that the repair technique increased the confinement of the joint.

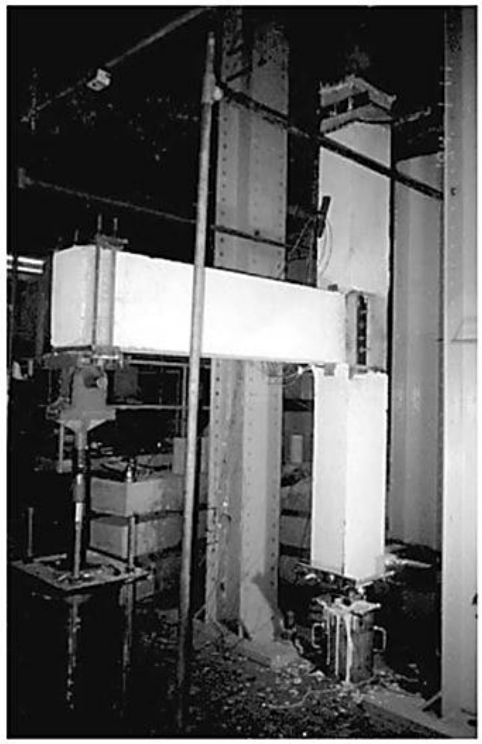

Figure 2-1: Test set up with specimen from Ghobarah et al. (2002)

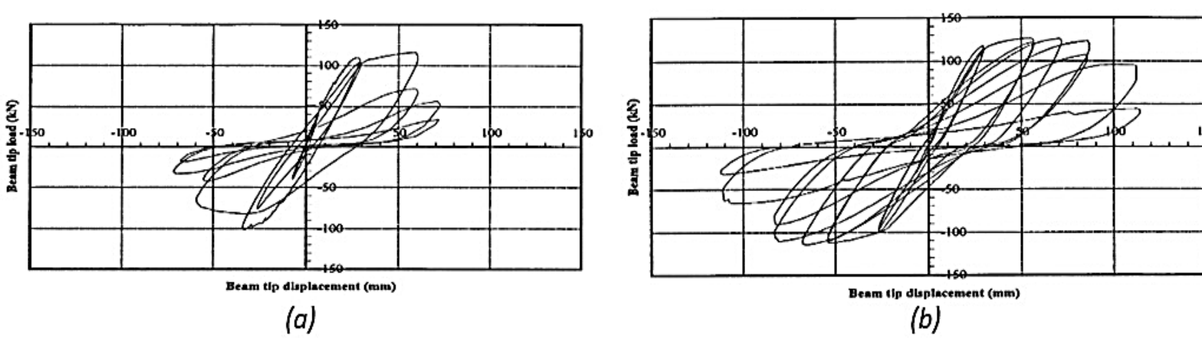

Figure 2-2: Beam tip load-displacement response:(a) Joint T1; and (b) Joint T1R adapted from Ghobarah et al. (2002)

The rehabilitation through steel braces was assessed by Said et al. (2008). Given that beam-column joints can be isolated from the frame at the points of contraflexure in the experimental joint specimen, the beam was taken from the midspan of the bay, while the column from the mid-height of one storey to the mid-height of the adjacent storey. Two joints were built and tested under reverse cyclic loading. The results were then compared to a similar un-retrofitted joint (*T0*) reported in the literature by El-Amoury et al. (2002). The three joints were similar in dimension, Joint *J1* was not retrofitted, representing a standard joint designed based on modern seismic provisions; and Joint *J2* was retrofitted by a steel brace. Joints *J2* and *T0* were designed based on pre-1970s code provisions. The bracing system is illustrated in Figure 2-3.

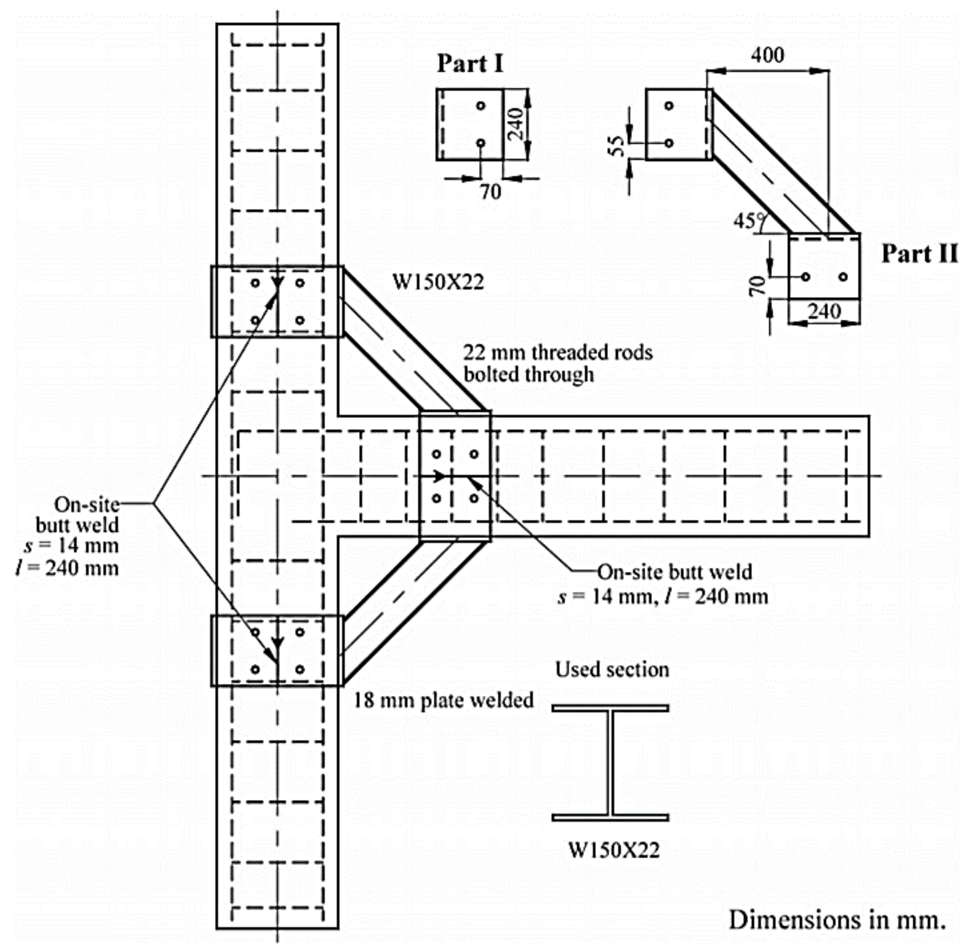

Figure 2-3: Local steel bracing retrofitting scheme (Said et al., 2008)

In Figure 2-4, the response of Joint *J1* represents the desired performance of the structural element. *T0* showcases the deficiencies of structures designed according to a pre-1970s arising during an earthquake, such as insufficient drift and strength capacities. The results demonstrate that the rehabilitation technique can improve the performance of beam-column joints to achieve the performance expected by current standards. This can be observed by evaluating the response of *J2* and its differences to the response provided by Joint *T0*, and the similarity of Joint *J2* with *J1*. As a result, the retrofitting technique enhanced the maximum drift, load carrying capacity, and energy dissipation by approximately 3, 1.7, and 12.6, respectively. Joint *J1* failed at the beam plastic hinge due to buckling of the reinforcement under compression at a displacement ductility of 6. Joint *J2* failed at a displacement ductility of 2.5 since, according to the researchers, the cantilever beam length was reduced due to the implementation of the steel braces in the frame. In Joint *J2*, an increased beam tip yield capacity was experienced, and the elements remained elastic until failure of the system. As few joints were tested, a global analysis was recommended by the researchers to validate the study.

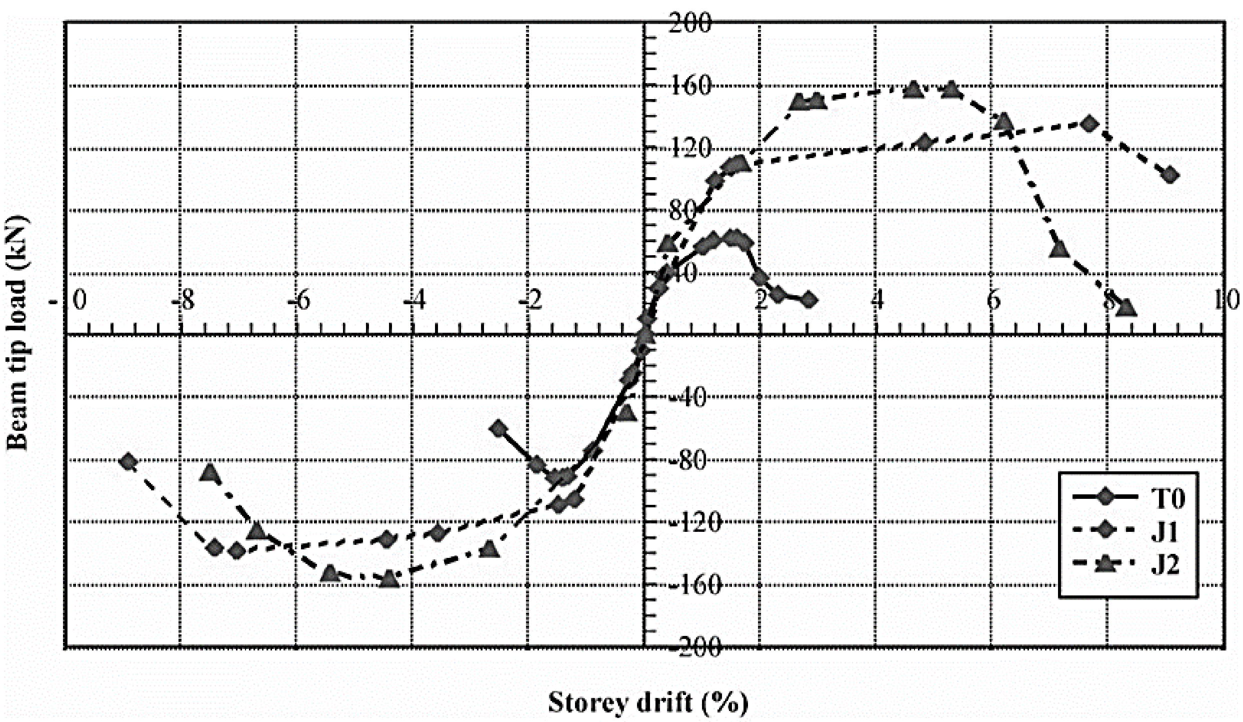

Figure 2-4: Load-storey drift envelopes for the tested joints (adapted from Said et al., 2008)

Beam-column joints can also be retrofitted by adding internal steel reinforcement. This was one of the first retrofit techniques proposed by researchers, and its effectiveness has been demonstrated by Abdel-Fattah et al. (1987). The objective of this retrofit is to move the location of the plastic hinge from the face of the column to prevent stiffness and strength degradation at original location at the beam-column joint. Figure 2-5 illustrates the proposed components. Top and bottom reinforcement are added over a specific length (Al-Sadoon, 2016). The strategy was found to be successful in improving the seismic performance of reinforced concrete frames; flexural-shear cracks were distributed along the beam length rather than at the joint.

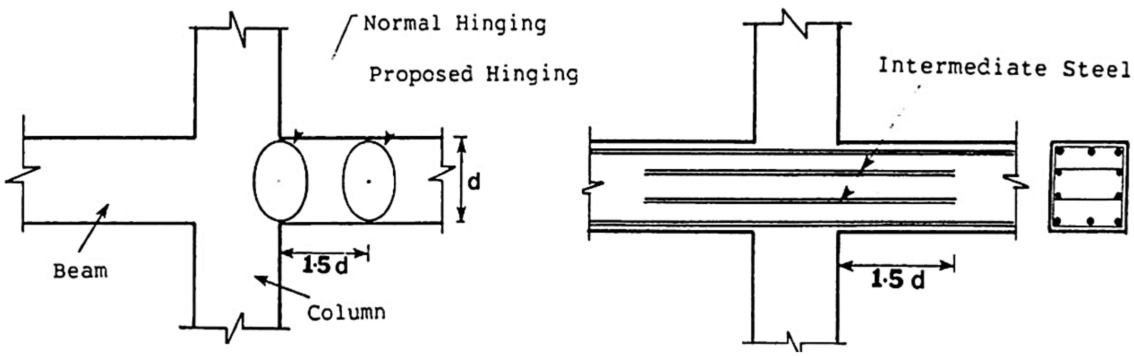

Figure 2-5: Proposed methodology (Abdel-Fattah et al., 1987)

2.2.2 Global system retrofitting

Among past studies, diagonal braces have been used in compression, tension, or both as a global seismic retrofit for reinforced concrete moment-resisting frames. Different types of braces have been investigated such as conventional steel braces, composite braces, braces with self-centering capabilities, braces that incorporates damping devices, and buckling-restrained braces.

2.2.2.1 Steel braces

A nonductile reinforced concrete frame was experimentally investigated by Bush et al. (1991). The building consisted of three storeys and two bays, and a two-third-scale model was constructed in the laboratory. The bracing consisted of continuous X-braces across two stories with an effective slenderness ratio of 100; this ratio was proven to exhibit better energy-absorbing characteristics (Black et al., 1980). A static cyclic lateral load was applied at the third level of the prototype frame producing constant shear over the height of the frame. The bare frame was designed to be deficient in lateral strength and displacement ductility to represent code requirements of the 1990s; the maximum applied loading was below the shear capacity of the columns. After testing the control frame, the brace was implemented and the static cyclic displacement-controlled lateral load was reapplied at the third floor.

The braced frame lateral load capacity increased 2.24 times relative to its expected design capacity, and the ultimate lateral capacity was approximately six times the failure capacity of the control frame. In addition, failure of the system was controlled by buckling of the braces, followed by failure of the bracing welded connections and shear in the columns. Due to buckling at the upper-level stories, inter-storey drifts were not uniform over the frame height. Furthermore, the axial load carried by the braces were directly affected by the upper-level buckling; once the upper-level brace buckled, the force carried by the lower-level was reduced. Before failure, the braces were responsible for carrying approximately 70% of the lateral shear, and the lateral capacity of the columns were increased by approximately 50% due to the steel plates applied to the side of the columns composing the brace-frame connection. As a result, the researchers highlighted the that the connection detailing between the brace and the frame impacts the response of the system; the brace welds were found to play an important role in the ultimate capacity of the frame. Therefore, it was recommend to examine the quality of the welds to ensure proper and stable connection between the brace and the original reinforced concrete frame.

Maheri et al. (1997) tested four scaled frames aiming to evaluate the effectiveness of different diagonal bracing arrangements to increase the shear capacity and to assess the compressive and tensile behaviour of the system under an earthquake. The researchers separately evaluated the frames in compression and tension to create a detailed profile of how the system behaves. A common diagonal X-brace was evaluated, and four scaled reinforced concrete frames were tested: un-braced, X-braced, diagonal tension-only brace, and diagonal compression-only brace. The bracing systems were designed to carry 75% of the total earthquake load. Regarding the brace-frame connection, the braces were welded to the sides of an in-plane steel plate (Figure 2-6 (a)). In addition, to minimize buckling effects in the X-braced frame, the two diagonal braces were connected to each other at mid-length through steel plates as illustrated in Figure 2-6 (b).

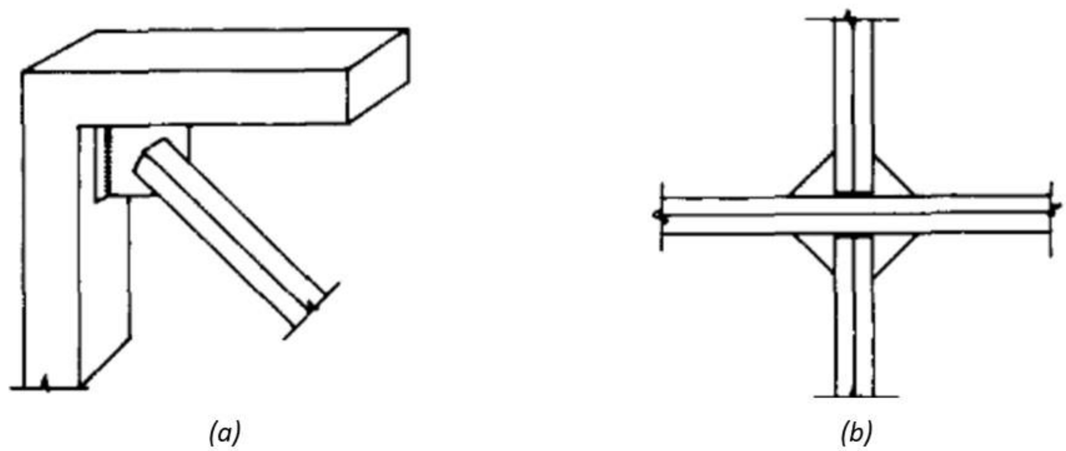

Figure 2-6: Bracing details: (a) frame to brace connection; and (b) diagonal brace to brace connection (Maheri et al., 1997)

A significant increase in the shear strength of the system was achieved during testing. Aa diagonal single-braced frame, either in tension or compression, was able to increase the shear capacity by a factor of 2.5. For those single-braced frames, the mechanical behaviour of the system was dominated by the frame given that it carried the majority of the in-plane loading in bending. The shear capacity of the X-braced frames, however, was increased by a factor of 4 relative to the un-braced frame. In the X-braced frame system, the mechanical behaviour was dominated by the brace, and failure was due to the tension capacity of the tensile brace followed by buckling of the compressive brace. Another important characteristic in a X-braced frame is that the tensile brace carried 15% more load than the compression brace.

The study by Maheri et al. (1997) also highlighted the importance of an effective connection between the braces and the frame. An insufficiently fixed connection may lead to an ineffective utilization of the full capacity of the brace. Therefore, a series of tests on full-scale connections was performed by Maheri et al. (1997) and illustrated in Figure 2-7. Connections (a) and (b) are for frames in new construction, while (c) and (d) are for existing structures. The results indicated how the connections influence the behaviour of the system and indicated it can control the failure if poorly anchored. Given the relatively small-scale specimens, the testing was found to be inconclusive for both the connections and bracing systems. Thus, further investigation was recommended by the researchers.

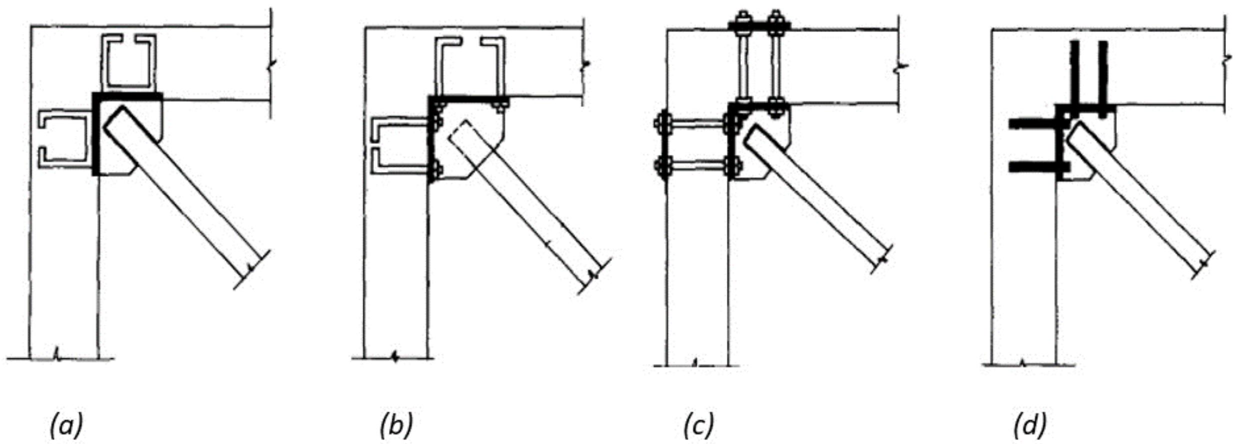

Figure 2-7: Brace-frame connection details (Maheri et al., 1997)

According to Youssef et al. (2007), steel bracing has been proven to be effective in improving the lateral capacity of moment-resisting frames, but guidelines for its use in newly constructed buildings still lack development. The advantage of using braces for newly built frames is a decrease of the building weight, thus reduction of seismic demands, and an increase in ductility performance. Their research considered two frames that were designed and tested. The first was a bare moderately-ductile moment-resisting frame designed according to the American Concrete Institute (ACI) 318-2 requirements; the reinforcement detailing followed the ACI special seismic provisions. The second frame was designed based on the ACI 318-2 (American Concrete Institute, 2002), but no special seismic detailing was followed. Concentric internal braces were also designed for the second frame following a design methodology proposed by the researchers. The frames were two-fifth scale models (Figure 2-8) of an ordinary, four-storey building.

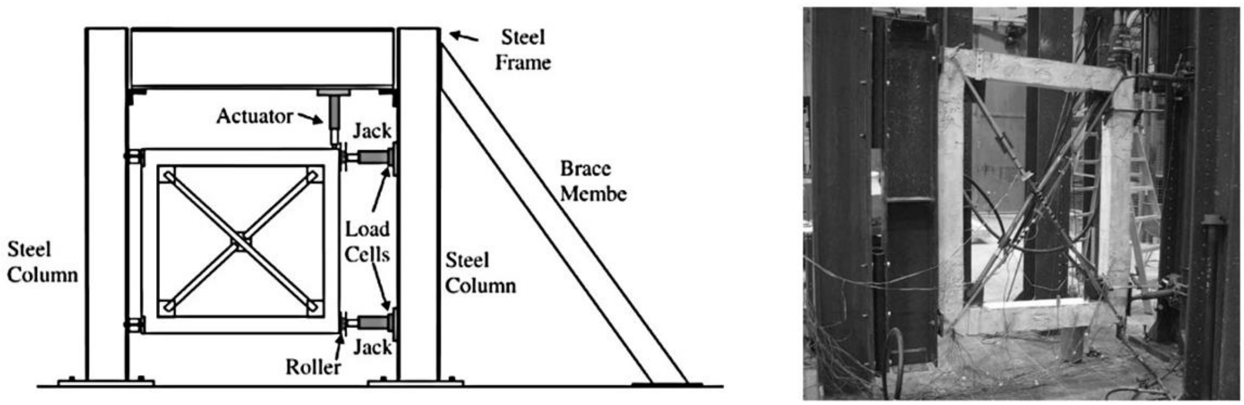

Figure 2-8: Test set up and components (Youssef et al., 2007)

The initial stiffness of the braced frame was 2.5 times greater than the bare frame. The displacement ductility of the braced frame, however, decreased in relation to the bare frame; while the ductility of the braced frame corresponded to 1.9, while the bare frame presented a ductility of 3. This reduction in ductility was due to the over-strength provided by the brace. The lateral capacity of the braced system was approximately three times the un-braced structural element. Furthermore, from the hysteretic behaviour of the tested frames (Figure 2-9), it is clear the braced frame has a superior seismic performance including a reduction in pinching. Regarding energy dissipation, at low drift ratios, the amount dissipated by the braced frame was lower than the original frame. However, at high drift ratios, the dissipated energy from the braced system was greater, corroborating that the implementation of internal steel braces increases the seismic performance of RC frames.

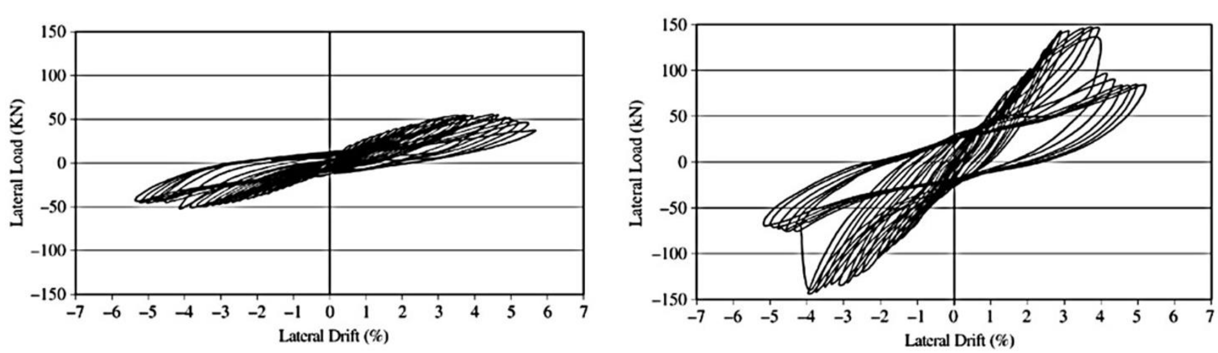

(a) *(b)*

Figure 2-9: Hysteretic response of: (a) un-braced; and (b) braced RC frame (Youssef et al., 2007)

Maheri et al. (2008) extended the previous work with the intention to further investigate the strength interaction between RC frames and the bracing system. Thus, a third frame was developed, and different brace sections were evaluated under reverse cyclic loading. The three frames were designed according to the ACI 318-2 (American Concrete Institute, 2002) guidelines; F1 was designed as a control frame, i.e., without a bracing system. The other two frames, FX1 and FX2, were braced with different sections; FX1 was braced with a non-slender channel cross section (C3 mm x 3.5 mm), while FX2 was braced with a slender double angle cross-section (L25 mm x 25 mm x 3.2 mm). To determine the forces in the braces and establish the force carried by the brace and the frame, the researchers used the displacements recorded along the diagonal brace. From the results, it was evident that the capacity of the braced frame was greater than the capacity of the bare frame combined with the capacity of the brace. The researchers attributed this phenomenon to the overstrength due to the stiffening effects generated by the brace-frame connections. It has also been highlighted that the parameters that affect the capacity interaction are the number of braced bays, frame storeys, and the stiffness ratio added by the brace-frame connection.

Caron (2010) investigated the advantages of using compression-only X-braces for repaired reinforced concrete frames. Two, half-scale damaged frames were tested after repair. The frames were designed according to the ACI 1963 (American Concrete Institute, 1965), representing construction prior to the enactment of modern seismic provisions. Both frames were repaired before testing, with one frame further retrofitted with a steel bracing system. The testing consisted of reverse cyclic loading applied at the beam mid-height. The results demonstrated that the repaired un-braced frame provided limited ductility and the damage was concentrated at the base of the columns. In the repaired braced frame, the behaviour was dominated by the braces. The braces did not achieve their full capacity due to tension failure at the base of the columns. The lateral strength capacity, however, increased five times greater than the un-braced frame, demonstrating that the bracing system was efficient in improving the seismic performance of the structure.

2.2.2.2 Buckling-restrained braces

2.2.2.2.1 Concept and components

Buckling-restrained braces (BRBs) were originally introduced in Japan by Atsushi Watanabe et al. in 1988 and were initially applied as a hysteretic damper for seismic behavioural improvement of moment-resisting frames after the 1995 Kobe Earthquake. By that time, damage tolerant structures - in which the primary structural element was designed to undergo elastic deformations only, while energy was dissipated through stable tension-compression yield cycles in special components - were receiving increased attention from researchers (Clark et al., 1999, and Wada et al., 1992). Since then, more than 250 buildings have been constructed incorporating BRBs in Japan, and 350 in the United States (Uang et al., 2004, and Kimberley et al., 2011). As the BRB was found to significantly improve the seismic performance of buildings, design guidelines for BRB retrofitted frames were included in the Seismic Provisions for Structural Steel Buildings in 2002 (ANSI/AISC 341-05).

Buckling-restrained braces can be defined by five main components according to Uang et al. (2004). The steel core is the axial force-resisting element of BRBs and can be divided into three segments: (1) a restrained yielding segment - usually with reduced cross-sectional area to induce yielding at this specific segment; (2) a restrained-nonyielding segment – encased by the restraining walls, but with a larger cross-sectional area than the yielding segment; (3) and an extended, non-yielding unrestrained zone that connects brace and frame where in steel structures this connection is in the form of bolting, welding or a true pin (Lopez et al., 2004). Figure 2-10 illustrates the segments of a BRB element. The two remaining components to characterize a BRB are: an un-bonding insulator to provide a gap and minimize frictional force between the restrained yielding core and mortar or concrete, which could be vinyl sheets, asphalt paint, rubber sheets, among others; and a restraining system for overall buckling such as steel casing and fill materials to restrain the core, usually mortar or concrete.

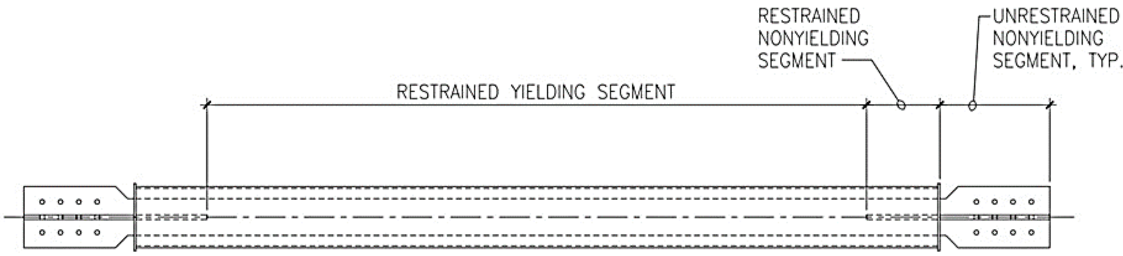

Figure 2-10: BRB segments (Wada et al., 1998)

The fundamental principle of a buckling-restrained brace is to avoid Euler buckling of a central steel core. Hence, the brace is composed of a core bar/element, which is designed to yield under both tension and compression to allow for dissipation of energy under inelastic deformations. To avoid global buckling, the core is encased in a steel tube, usually a steel hollow section, filled with either concrete or mortar (Figure 2-11 (a) and (b)). The steel core should be unbonded from the surrounding material to allow the core to slip during an imposed stress without transferring axial load to the mortar or to the hollow structural section (Uang et al., 2004).

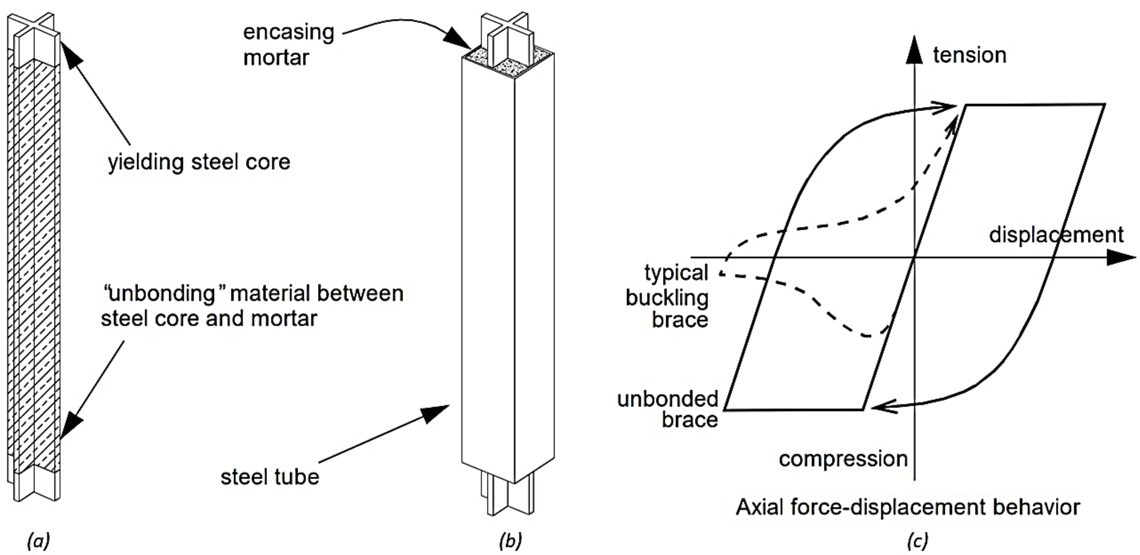

Figure 2-11: Components of a common buckling-restrained brace: (a) steel core; (b) buckling restraining system; and (c) axial force – displacement curve of an unbonded and typical buckling brace (Clark et al., 1999)

The slip should be carefully designed to allow relative movement between the core and mortar due to shearing and Poisson's effect (Clark et al., 1999). When properly designed, the core can undergo full reverse cycles without losing stiffness or strength due to global and local buckling. Due to a stable hysteretic response, since buckling is prevented/minimized, the behaviour of a buckling-restrained brace significantly opposes that exhibited by steel braces during the response under compression (Figure 2-11 (c)). Figure 2-11 (c) also demonstrates that BRBs act as a damper that dissipates energy under tension and compression stress conditions. Even though detailing for conventional Concentrically Braced Frames (CBFs) have improved, the behaviour mode in compression remains global buckling, which reduces strength and stiffness of the brace.

Buckling of braces is intrinsically related to the slenderness ratio of the element, which is defined as the ratio of effective length to the least radius of gyration of the cross section (Al-Sadoon, 2016). Thus, large cross-sectional areas are commonly utilized to prevent buckling of the element under compression. Several steel core cross-sections have been proposed in the literature as illustrated in Figure 2-12 (Corte et al., 2005).

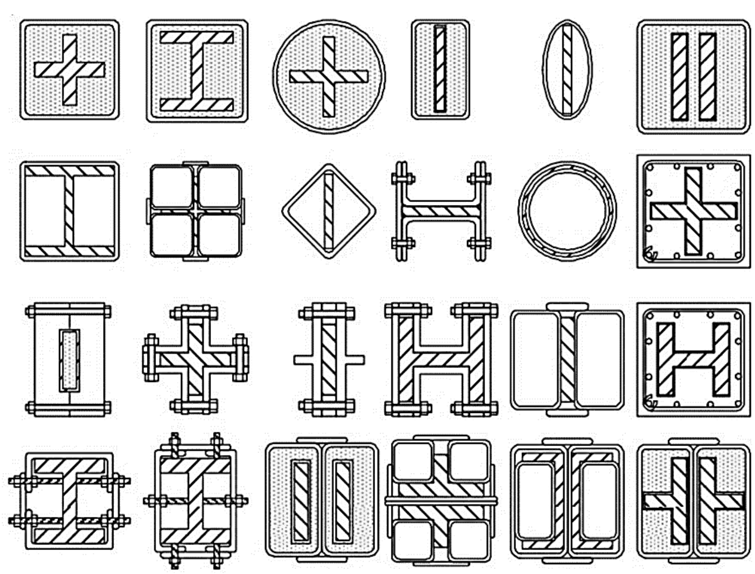

Figure 2-12: Typical BRB cross-sections (Corte et al., 2005)

According to Takeuchi (2018), to achieve hysteretic stability, not only should global buckling be avoided, but a series of local and global behaviours must be taken into consideration (Figure 2-13): (1) the restrainer between the brace and frame must successfully avoid first-mode flexural buckling of the core; (2) global out-of-plane stability must be guaranteed specially for connections; (3) the restraining mortar, concrete, or steel should overcome higher mode buckling; (4) the fatigue capacity of the core must be sufficient for the expected loading cycles; and (5) the connection should be carefully designed to remain elastic and resist the design loads.

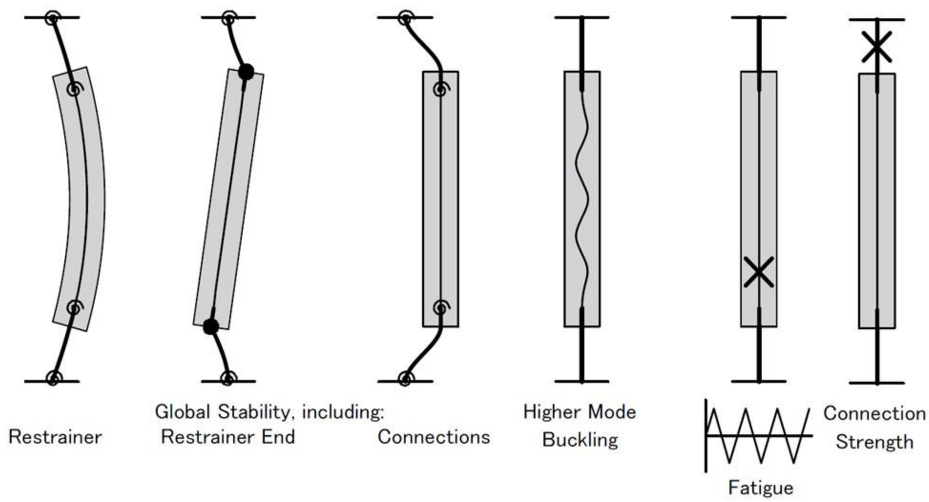

Figure 2-13: Failure modes to avoid guaranteeing stability and strength of a BRB (Takeuchi, 2018)

As the brace is connected to the frame directly through the unrestrained nonyielding segment, there is no contact between the supporting restraining system, the mortar or concrete, and the brace. The steel core, restrained yielding segment, is the load carrying element of the brace and is shortened or elongated during loading (Al-Sadoon, 2016). The surrounding casing remains at a constant length since no longitudinal stresses are applied to it. To avoid transfer of load to the restraining support element, internal and external gaps are utilized in the bracing system as shown in Figure 2-14. The absence of gaps may induce premature buckling at the mid-length of the brace since the load will bear on the supporting restraining system. However, the presence of the gap exposes a portion of the yielding section unrestrained allowing buckling effects to be developed (Al-Sadoon, 2016). The steel-core-end buckling was reported by Tremblay et al. (2006) and Aiken et al. (2002).

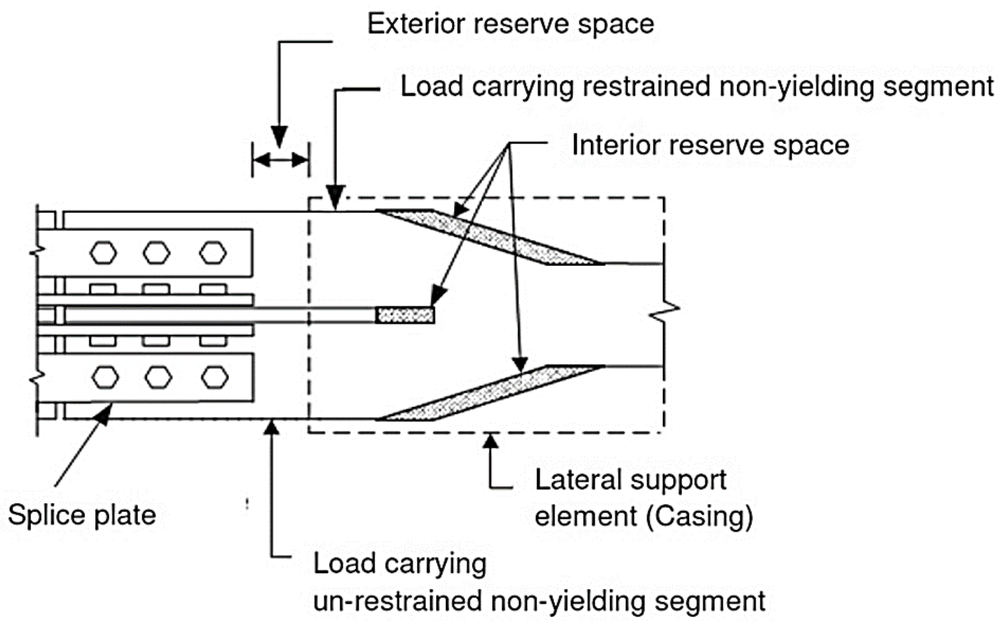

Figure 2-14: External and internal gaps to prevent load bearing (Al-Sadoon (2016) and Chen et al. (2001))

Since a proper restraint and stiffness of the end yielding segments should be provided, a novel BRB system was introduced by Al-Sadoon (2016), where internal and external gaps are eliminated. In the proposed BRB design by Al-Sadoon (2016), the end zones are also restrained from buckling and load bearing is prevented through a sliding system. Detailing of the restraining mechanism utilized at the edges is illustrated in Figure 2-15. The end elements have essentially two components (Part 1 and 2) consisting of a cored end section that allows relative longitudinal movement between the two parts. Part 2 is 60 mm thick and is placed inside the HSS casing, while Part 1 is 170 mm thick and is connected to a 57 mm-thick joint steel plate. Parts 1 and 2 each contain 140 mm-long wedge elements that are offset between Part 1 and 2 such that they can slide between each other to form a closed hollow section. The hollow section has a diameter of 46.5 mm and was designed to accommodate a 44.5 mm diameter core bar. The BRB proposed by Al-Sadoon (2016) was able to avoid local buckling at the end segments of the core bar and load bearing.

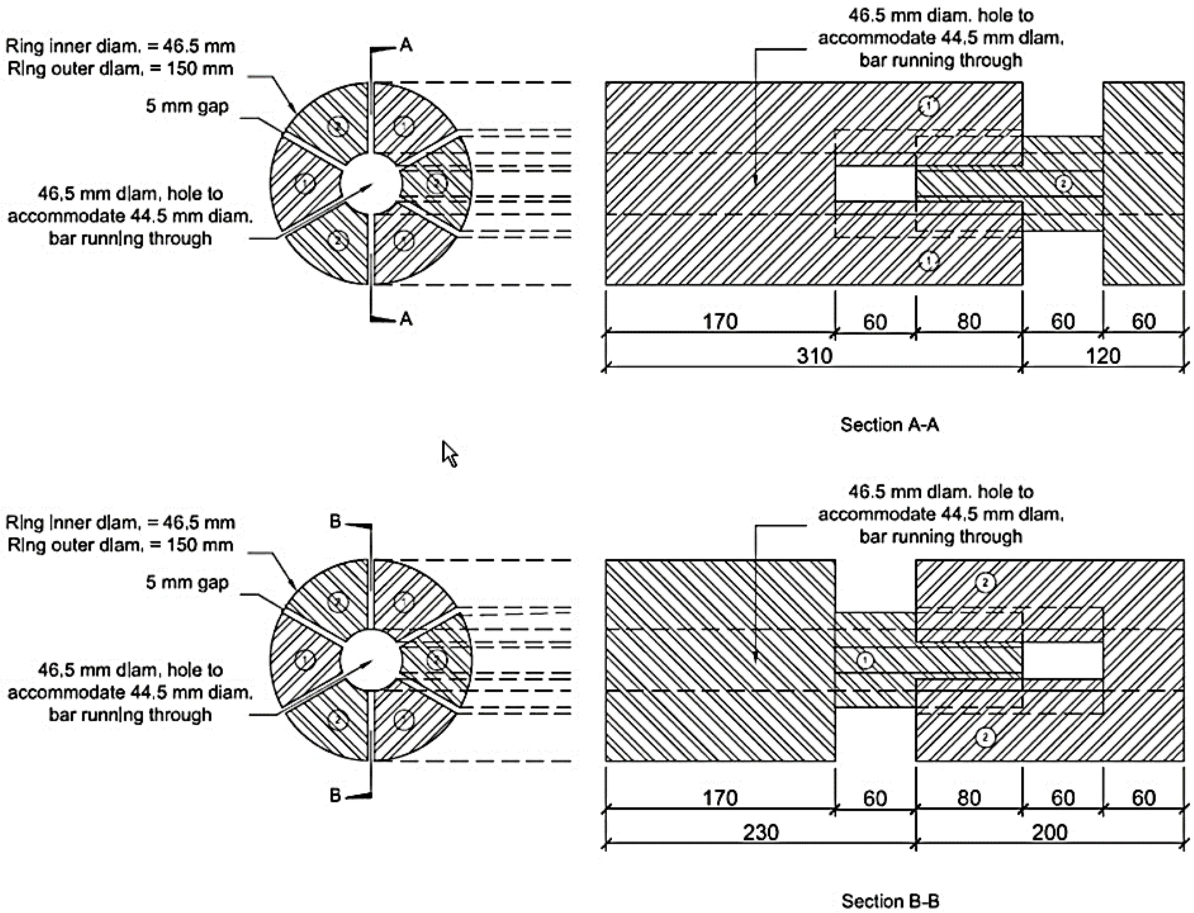

Figure 2-15: Cross sections of steel core restraining end elements (Al-Sadoon, 2016)

When comparing the performance of conventional and buckling-restrained braces, it has been largely proven that BRBs are structurally superior in improving the seismic performance of moment-resisting frames. Conventional braces reduce the fundamental vibration period of buildings, which may lead to an amplification of the seismic loading (Mahrenholtz et al., 2015). Furthermore, once the force in the brace exceeds a predefined critical limit, conventional braces buckle losing their compressive capacity (Figure 2-16). Conversely, BRBs possesses a stable hysteretic response and can undergo large strain cycle reversals dissipating significant energy without strength degradation. In addition, BRBs are more cost-effective in comparison to conventional braces (Della Corte et al., 2011). Figure 2-16 illustrates the performance of BRBs with a symmetric hysteretic response under reverse cycles, while conventional braces behave poorly under compression.

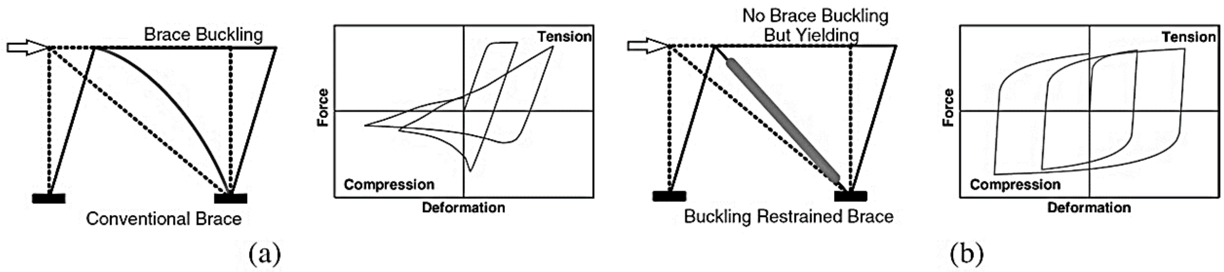

Figure 2-16: Seismic behavior: (a) conventional braces: and (b) BRB systems (Mahrenholtz et al., 2015)

2.2.2.2.2 Previous research on BRBs

According to Della Corte et al. (2011), experimental studies on BRBs have been conducted in four major areas: investigation of the casing stiffness and the transfer of forces; deformation capacity and low cycle fatigue for different loading scenarios; connections between the frame and brace focusing on failure and effectiveness to allow brace to reach full capacity; and the influence of the un-bonding layer between the core and the restraining system on the response of the BRB system. Thus, relevant studies are presented in the following sections.

As previously discussed, the casing should prevent the steel core from buckling allowing it to develop a stable axial configuration. This stable axial stress can be achieved by selecting an adequate stiffness for the casing. The required stiffness is selected based on the ratio between the casing Euler buckling axial load (P_e) and the steel core yield force (P_y). A pioneering study on the influence of the P_e/P_y ratio on the behaviour of BRBs was conducted by Watanabe et al. (1988). The researchers developed a systematic study of the ratio suggesting a stable configuration is achieved if the ratio is at least 1.5.

Iwata et al. (2006) conducted an experimental study focusing on several specimens with different P_e/P_y ratios ranging from 1.5 to 5.2. The specimen configuration is illustrated in Figure 2-17. The core material yielding load (P_y) was established by multiplying the yield stress by the cross-sectional area. The total length of the specimen was 2351 mm, which was used as the buckling length. The loading was applied horizontally in increasingly incremental reverse cycles to a rate such that the plastic strain of the core plate was close to the drift angle. The results concluded that the higher the P_e/P_y ratio, the more stable the axial stress distribution over the steel brace length, i.e., the strain is constant over the brace core. Furthermore, for approximately similar P_e/P_y ratios, the larger the clearance, the larger the number of buckling modes on the steel core. Therefore, the magnitude of P_e/P_y determines the magnitude of the restraining force that directly contributes to the number of buckling modes. In addition, stress concentrates at the end of the steel core plastic region leading to local deformations. The concentration of deformation and stresses at the end of the steel core is, according to the researchers, due to the absence of restraining in that region (Figure 2-17).

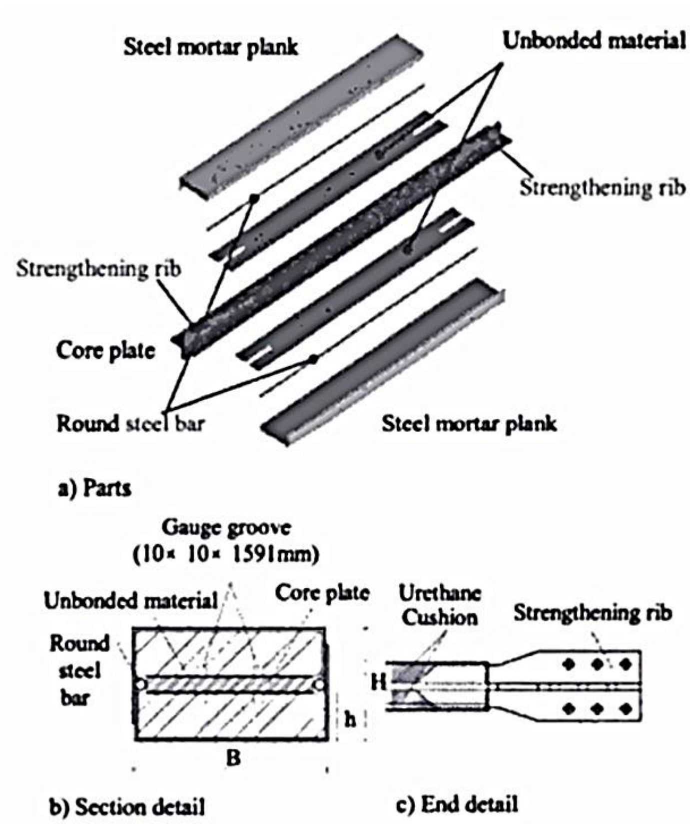

Figure 2-17: Specimen configurations (Iwata et al., 2006)

Experimental studies have also been conducted to evaluate the increase in displacement ductility for frames equipped with a BRB. Those studies have shown that cumulative ductility capacity of unbonded buckling-restrained braced frames have an average value of 1000 when the maximum ductility demand – peak total deformation divided by the yielding deformation - does not exceed 15 (Della Corte et al., 2011). Ductility and energy dissipation capacity are closely related to the P_e/P_y ratio and the casing detailing. Black et al. (2004) conducted an experimental study to evaluate the effects of BRB detailing on the deformation, strength, and energy dissipation capacities of the system. The testing was conducted in displacement control mode, and the set up and detailing of the braces are presented in Figure 2-18.

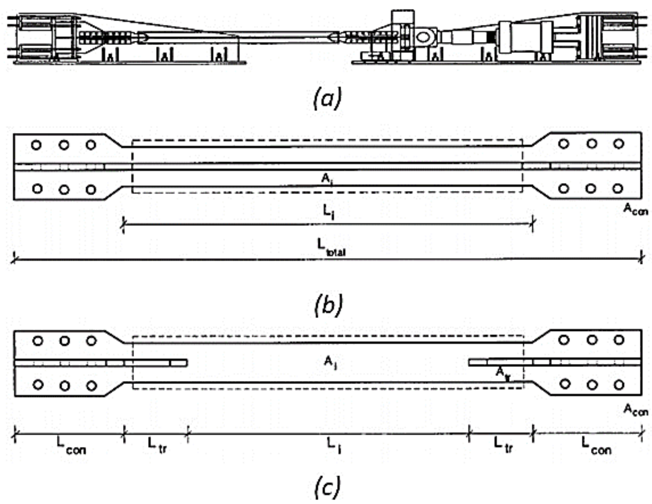

Figure 2-18: Bracing details: (a) test setup side view; (b) first possible configuration of inner core; and (c) second possible configuration of inner core (Black et al., 2004)

The results demonstrated that the brace exhibited stable hysteretic response with low cycle fatigue. The expected number of cycles to develop failure of the brace was 20. However, the brace was able to undergo 31 cycles without failing. At the thirty-first cycle, the researchers terminated testing to avoid damage of the instrumentation. Furthermore, Cumulative Plastic Ductility (CPD) is a measure of the cumulative total deformation of the brace divided by the corresponding yielding deformation. For the braces tested, the CPD ranged from 278.7 to 1045. As a result, the unbonded braces exhibited ductile, stable, and repeatable hysteretic behaviour (Black et al., 2004); the ductility exceeded the specified design requirements in terms of maximum deformation and CPD.

The connection between the brace and the frame has been largely investigated and evident in the literature. Aiken et al. (2002) conducted tests on one-bay, one-storey, 0.7 scaled BRB frames with bolted connections between the brace and gusset plate; the plate was fixed to the frame. Reverse cyclic loading was applied at the system and the results indicated out-of-plane buckling of the gusset plate. The results also demonstrated that significant in- and out-of-plane bending moments can develop at the connections if the brace possesses rigid end connections, in this case, bolted connections. Furthermore, Tsai et al. (2008) demonstrated through testing that the BRB retrofitted frame performance may be lower than the BRB alone due to degrading rotational effects imposed at the gusset plate connection.

Fahnestock et al. (2007) investigated the performance of a large-scale BRB frame with an improved connection (Figure 2-19). The frame was subjected to multiple earthquake records through a hybrid pseudo-dynamic testing method. The results illustrated the novel BRB was able to withstand significant drifts with no severe damage to the structure. In addition to four hybrid pseudo-dynamic earthquake records, the frames were also subjected to a quasi-static cyclic test, which demonstrated the novel connection minimized bending moment at the beam-column-brace joint by allowing rotation; this resulted in minor yielding at an imposed storey drift of 0.048 rads. At the end of testing, the BRB system was able to undergo a ductility of 26 and a CPD ranging from 372 to 453 under quasi-static cyclic loading. The researchers concluded that the excellent performance of the connection was attributed to a combination of pinned connections and stocky gusset plates.

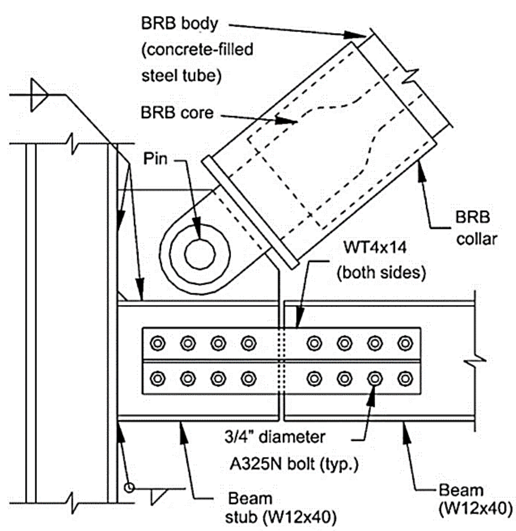

Figure 2-19: Beam-column-brace connection from Fahnestock et al. (2007)

With regards to the un-bonding layer between the steel core and restraining component, a wide range of materials have been studied, such as epoxy, resin, silicon resin, vinyl tapes, etc. (Della Corte et al., 2011). The thickness of this layer commonly varies between 0.15 mm and 2 mm and should allow the steel core to deform in the transverse direction due to Poisson's effect. Tsai et al. (2004) conducted testing on ten, nearly identical BRBs, where the difference resided on the un-bonding material, aiming to evaluate the effect on the seismic performance of the BRB system. The un-bonding material layers varied from asphalt painting to silicon rubber sheets of different thicknesses. An incrementally increasing reverse cyclic displacement-controlled loading was applied to the system. In Figure 2-20, the difference in axial load over cycle numbers for the ten studied specimens in which a 2 mm-thick silicon rubber sheet is illustrated, showing the least difference between the compressive and tensile axial load capacity (10% at an axial strain of 2%) under the imposed displacement-controlled loading. The difference is related to the compression and tension resistance since an ideal un-bonding layer would allow a symmetrical hysteretic response.

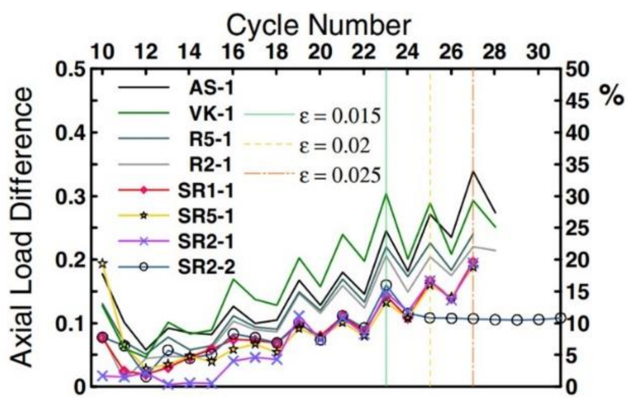

Figure 2-20: Axial load difference under cyclic loading (Tsai et al., 2004)

In "all-steel" devices, a void is placed between the steel core and the restraining system to avoid transverse distribution of stresses. Iwata et al. (2000) tested both "all-steel" BRBs and those with an unbonded layer. The tests demonstrated that BRBs without un-bonding material experienced local buckling and core fracture due to plastic strain concentration. By placing an un-bonding material into the "all-steel" BRBs, the response of the system significantly increased given that strain concentration was avoided. The concentration of stresses on the core was also emphasized by Tremblay et al. (2006). The researchers highlighted that friction forces should be minimized to avoid core buckling and allow uniform strain over the core length. Studies have shown, however, that even without an un-bonding layer leading to a localized strain and core buckling, BRBs exhibit a CPD equal to 235, which may be sufficient to satisfy current seismic provisions (D'Aniello et al. (2009), and Della Corte et al. (2010)).

2.3 Implementation of self-centering devices in Moment-Resisting Frames (MRFs)

A buckling-restrained brace has two crucial components: a core bar responsible for carrying the axial load, and an exterior restraining element responsible for preventing buckling of the core. Although steel core BRBs offer advantages over conventional steel braces, it lacks self-centering capacity which is a shortcoming in controlling repair costs and downtime. Therefore, by implementing an NiTi SE-SMA core in the BRB, the energy dissipation will increase with controlled accumulated residual displacements and minor impacts on serviceability. Self-Centering (SC) structural systems able to dissipate energy and return to their original position are a relatively new concept for seismic design and are not limited to shape-memory alloys. Demonstrating SC systems is crucial to better understand the superiority of shape-memory alloy BRBs. For moment-resisting frames, self-centering systems can be categorized in three groups: systems with horizontal post-tensioned steel elements, rocking systems, and braced frame systems.

2.3.1 Systems with horizontal post-tensioned connections

The development of Post-Tensioned Energy Dissipating (PTED) connections followed the unexpected failure of beam-to-column connections in moment-resisting frames during the 1994 Northridge California Earthquake. Horizontal Post-Tensioned (PT) steel elements provide self-centering through a flexural gap opening between the beam and the column when the frame is subjected to lateral loading. In 1999, Priestley et al. proposed a series of beam-to-column connections that combined self-centering characteristics with energy dissipation. Testing demonstrated that the connection improved the seismic performance of the element, ensuring small permanent drifts when inelastic transient deformations were experienced during the cyclic response. Christopoulos et al. (2002) proposed a steel moment-resisting frame connection that incorporated high strength post-tensioned steel with energy dissipating bars. Figure 2-21 (a) illustrates the geometric configuration of a frame incorporating the post-tensioned energy dissipating steel connection, while Figure 2-21 (b) shows the connection details.

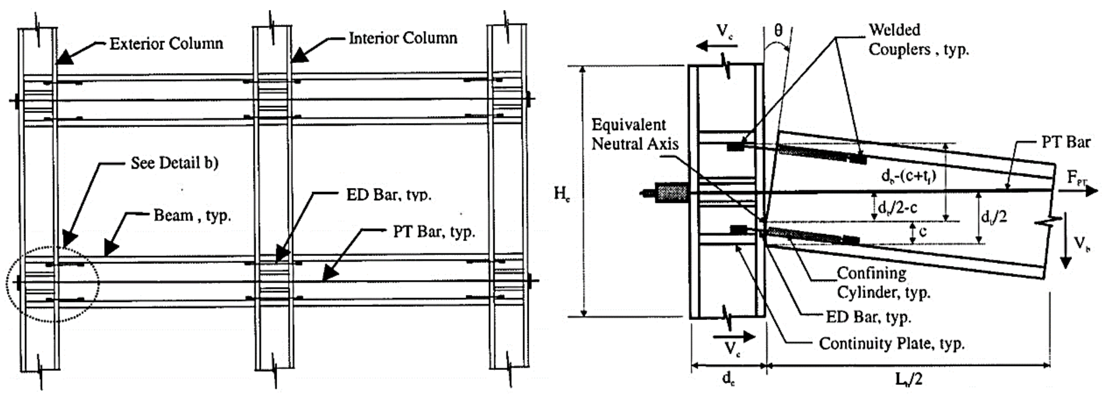

Figure 2-21: Schematic illustration: (a) moment-resisting frame with post-tension energy dissipating connections; and (b) geometric representation of the connection (Christopoulos et al., 2002)

The PT force is provided by two high-strength bars placed at the mid-height of the beam, one at each side of the web. Four Energy Dissipating (ED) bars are placed in the connection to provide dissipation under seismic loading and are inserted into steel cylinders to prevent buckling during compression. The four ED bars dissipate energy by yielding in axial tension and compression. The drift-controlled loading protocol and the corresponding force-inter-storey drift response are presented in Figure 2-22. The response illustrates that the connection undergoes large deformations with significant energy dissipation, while the beam and column remain undamaged due to small residual deformations (Christopoulos et al., 2002).

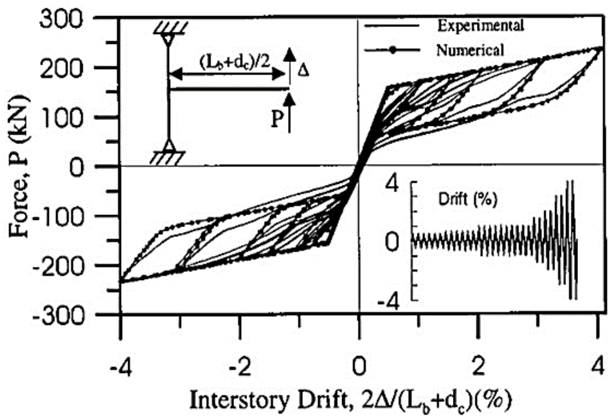

Figure 2-22: Force-inter-storey drift response of steel moment-resisting frames with PTED connections (Christopoulos et al., 2002)

Another self-centering, post-tensioned seismic-resistant connection was proposed by Ricles et al. (2001). The advantages include the absence of field welding and negligible residual drift after an earthquake. In addition, damage is localized in the connection and repairs are easily conducted. Figure 2-23 (a) illustrates the post-tensioned steel connection. Under cyclic loading, the flexural behaviour of this PT connection is characterized by a gap opening and closing, which ensures self-centering. Under time-history analysis, this connection exceeded the seismic performance of an MRF with conventional welded connections. The energy dissipation is provided by the inelastic deformation and damage experienced by the connection. Furthermore, the study indicated the impact of the size and gauge length of the angles on the energy dissipated by the connection; the bigger the size and length, the more energy dissipated by the system. Figure 2-23 (b) depicts the lateral load - lateral displacement response of three of the connections. PT connection 5 presents the larger angle dimensions.

For reinforced concrete moment-resisting frames, an unbonded post-tensioned connection was proposed by El-Sheiklh et al. (1999). It was found that the mechanical behaviour of unbonded post-tensioned precast frames is adequate for severe earthquake loading. Figure 2-24 is a representation of this connection. The post-tensioned precast concrete frame is designed as a ductile frame, and nonlinear/inelastic deformations are solely expected at the connection (El-Sheiklh et al., 1999). Thus, the unbonded length of the post-tensioning steel should be designed to allow the design-level earthquake displacement to be reached without yielding of the post-tensioning steel. The study also demonstrated that the energy dissipated by the system is inversely proportional to its self-centering capacity, i.e., a system that dissipates more energy will generate a greater residual deformation.

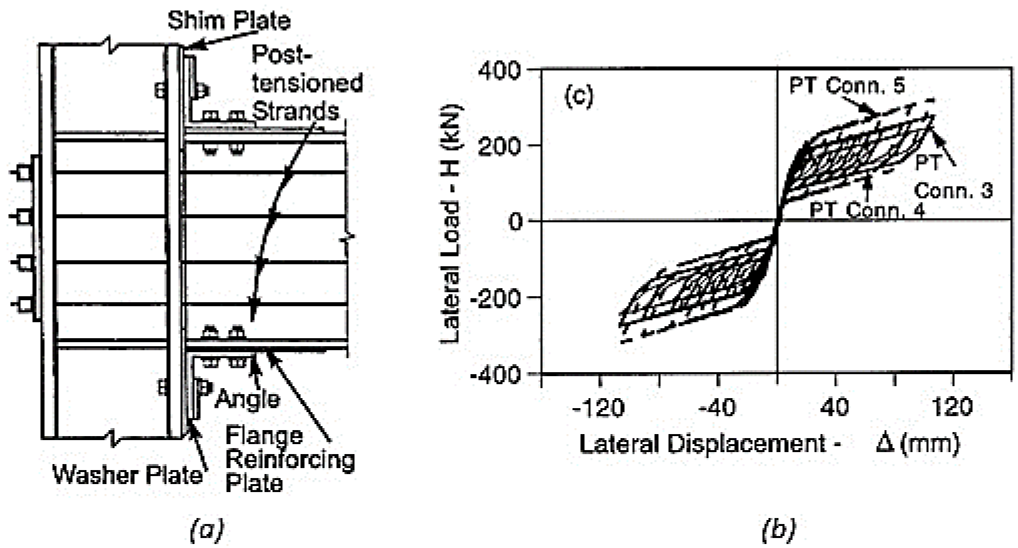

Figure 2-23: Post-tensioned system: (a) connection in moment-resisting frames; and (b) hysteretic response of PT connections 3, 4 and 5 (Ricles et al., 2001)

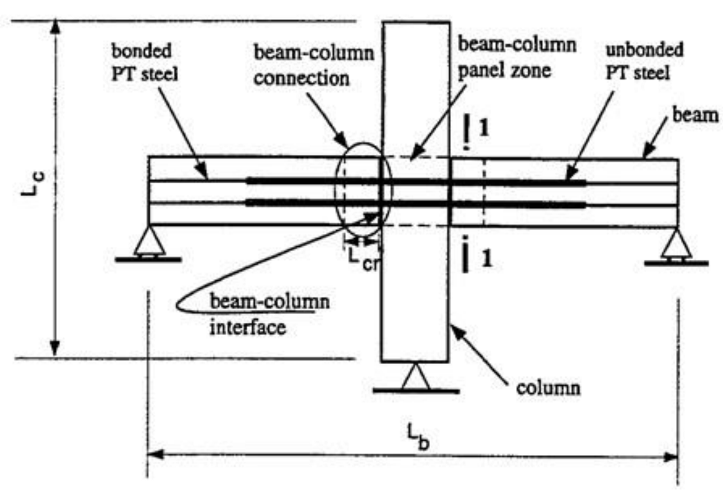

Figure 2-24: Unbonded post-tensioned pre-cast beam-to-column connection assemblage (El-Sheikh et al., 1999)

2.3.2 Rocking systems

The self-centering capability of rocking RC frames is provided by an uplift at the base of the column during lateral loading. Hence, when subjected to a lateral load, a downward vertical force (restoring force) is applied to the rocking system by the post-tensioning to close the gap. According to Eatherton et al. (2014), the rocking system virtually eliminates residual deformations and concentrates damage in easily replaceable elements. In addition, the system consists of a post-tensioning strand anchored between the foundation and the roof level of the braced frame. Given that rocking systems are primarily governed by first mode rigid body rotation, the seismic response is controlled by overturning moment rather than base shear. The rocking system, however, needs to be combined with an external brace or friction dampers; Figure 2-25 illustrates alternatives for braced frame rocking systems. Eatherton et al. (2014) evaluated the response of a Concentrically Braced Frame (CBF) combined with the rocking retrofit. Figure 2-26 illustrates the overturning moment - roof drift response of the proposed three-storey building with a rocking system (Figure 2-26) under the JMA Kobe ground motion scaled by 1.10. The response demonstrates the self-centering capacity of the system since the residual drift is close to zero.

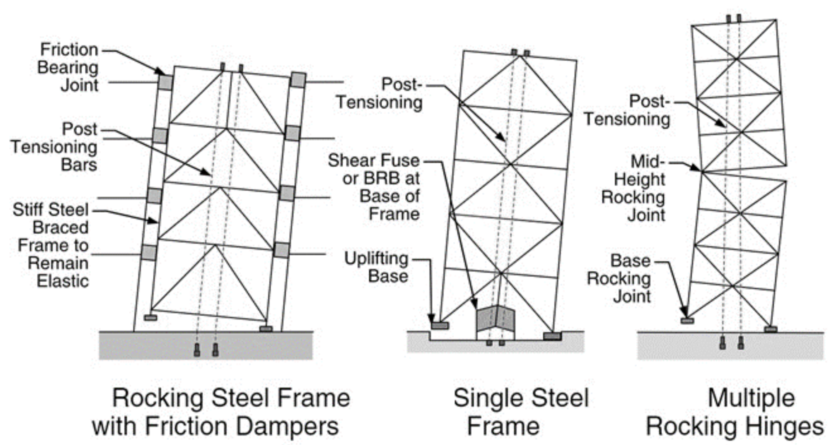

Figure 2-25: Common rocking structural systems (Eatherton et al., 2014)

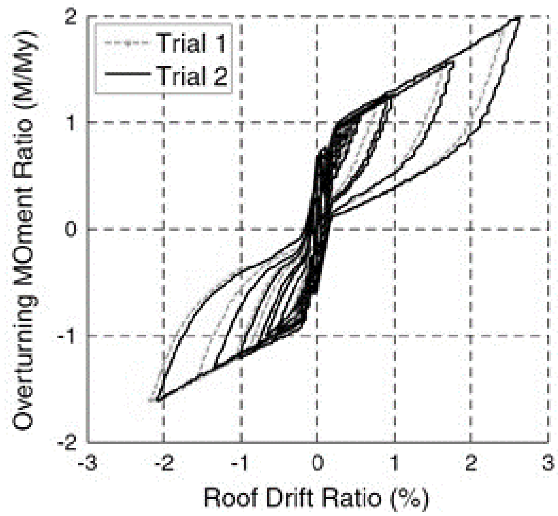

Figure 2-26: Load deformation response of the building under the scaled JMA Kobe ground motion (Eatherton et al., 2014)

Concentrically braced rocking frame systems are superior than conventional CBFs; it possesses a greater drift capacity before damage and small permanent drift under seismic loading. Ricles et al. (2010) developed a performance-based seismic design procedure for SC-CBF that can satisfactorily predict the response of the structural element. Throughout testing, the self-centering capacity of the rocking system was demonstrated by the cost of a lower energy dissipation.

2.3.3 Braced frame systems

Self-centering braces offer a significant advantage over the SC system since they do not interfere with the gravity load resistance nor with the transfer of inertia forces (Garlock et al., 2008). Buildings designed according to modern seismic provisions are expected to behave under a controlled inelastic response during earthquakes. This means the structure will experience significant structural damage and substantial residual deformations after a design-level earthquake. To minimize those effects, a Self-Centering Energy Dissipative (SCED) bracing system has been proposed by Christopoulos et al. (2008). Figure 2-27 presents this SCED brace concept.

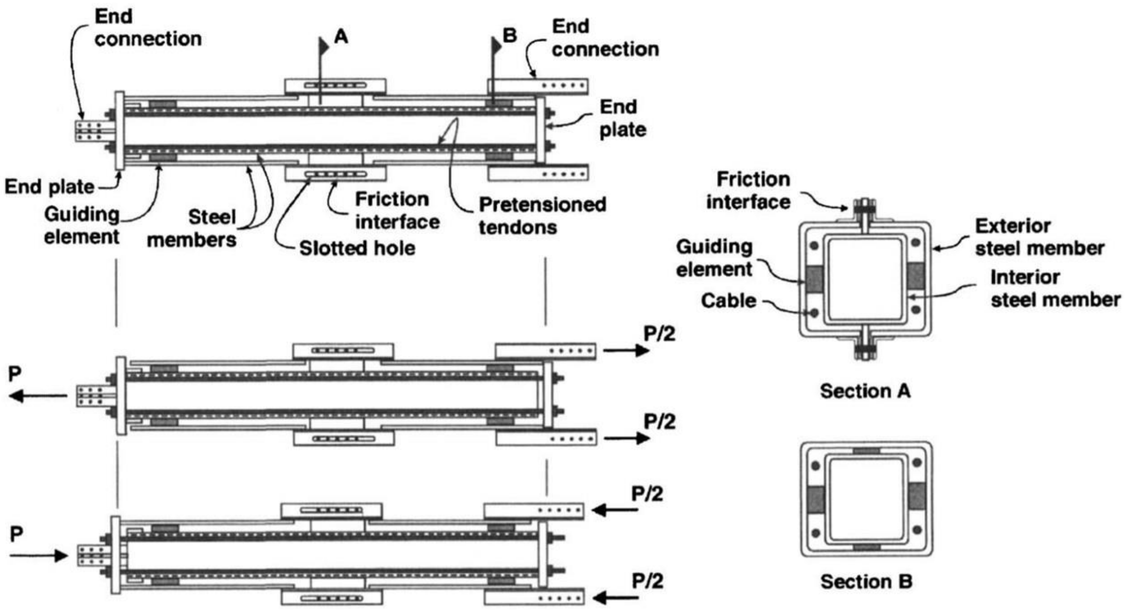

Figure 2-27: SCED brace system with tubes, tendons, and friction dissipative mechanism (Christopoulos et al., 2008)

Through quasi-static and dynamic inter-storey drift time-histories, the system proposed by Christopoulos et al. (2008) could repeatably self-center. However, the self-centering capacity was lost once the tendon elongation capacity was exceeded, triggering the system to respond as a conventional friction brace. For instance, in the hysteretic response presented in Figure 2-28 for a single braced frame, the tendon elongation capacity was exceeded at a top drift of 3%; thus, significant permanent structural damage was induced. As a result, even though the proposed bracing system possessed self-centering capacity, it was limited by the tendon strain capacity. An alternative to accommodate large deformations and avoid development of residual displacements include the utilization of a frictional fuse.

The research also corroborates the superiority of SCED braced frames over the SC frames. That is based on the ability of the SCED braces to return to its original position, if the strain capacity of the tendon is not reached, and energy dissipation is guaranteed through the inelastic deformations of the braces. The SCED prototype illustrated in Figure 2-27, and a self-centering post-tensioning system were also tested under quasi-static axial loading. The responses are presented in Figure 2-29. It is evident that the SCED can undergo larger deformations while dissipating energy. However, the drawback of the SCED retrofit proposed by the researchers consists of unexpected failure of the tendon elements due to concentration of stresses under compression, an indication of local buckling.

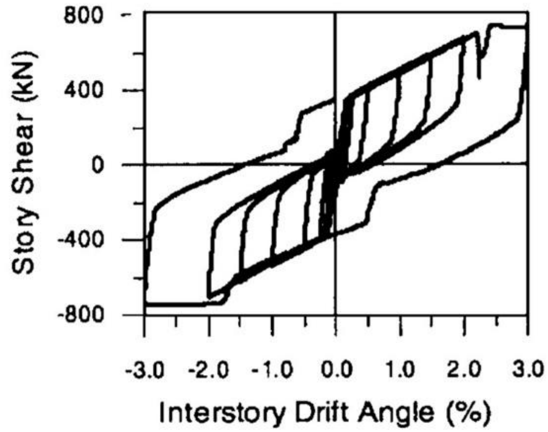

Figure 2-28: SCED braced frame under a time-history analysis (Christopoulos et al., 2008)

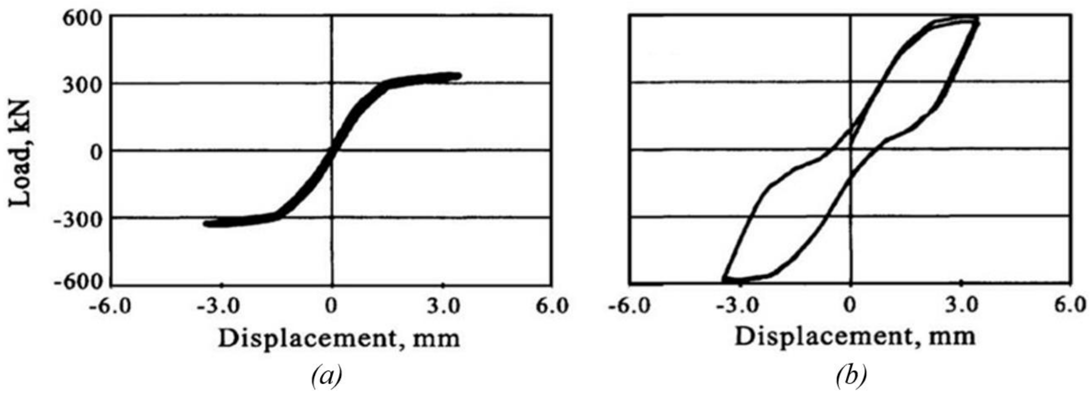

Figure 2-29: Displacement – Load response under quasi-static axial loading of: (a) post-tensioning; and (b) SCED braced system (Christopoulos et al., 2008)

The seismic performance of a frame can also be improved by a BRB equipped with a shape-memory alloy (SMA) core material. As SMA-BRB retrofitted frames are the focus of this current research, the mechanical properties of shape-memory alloys and its application in BRB systems will be presented in Chapter 3.

Chapter 3

SMA BRBs for retrofitting moment-resisting frames

3.1 Introduction

Shape Memory Alloys (SMAs) are a class of material capable of recovering deformations due to superelastic (SE) and shape memory properties (Figure 3-1). The former recovers deformations when the applied stresses are released at a given temperature. The latter, on the other hand, recovers deformations due to an increase of temperature that allows the polycrystalline structure of the material to transform from its martensite to its austenite phase. According to DesRoches et al. (2004), Nickel-Titanium (NiTi) superelastic SMAs are an attractive alternative for seismic retrofitting of reinforced concrete structures due to its excellent strain capacity, hysteretic damping, and deformation recovery. In addition, NiTi SMAs exhibit low temperature sensitivity (Duerig 1990), which allows the material to recover deformations at ambient temperatures.

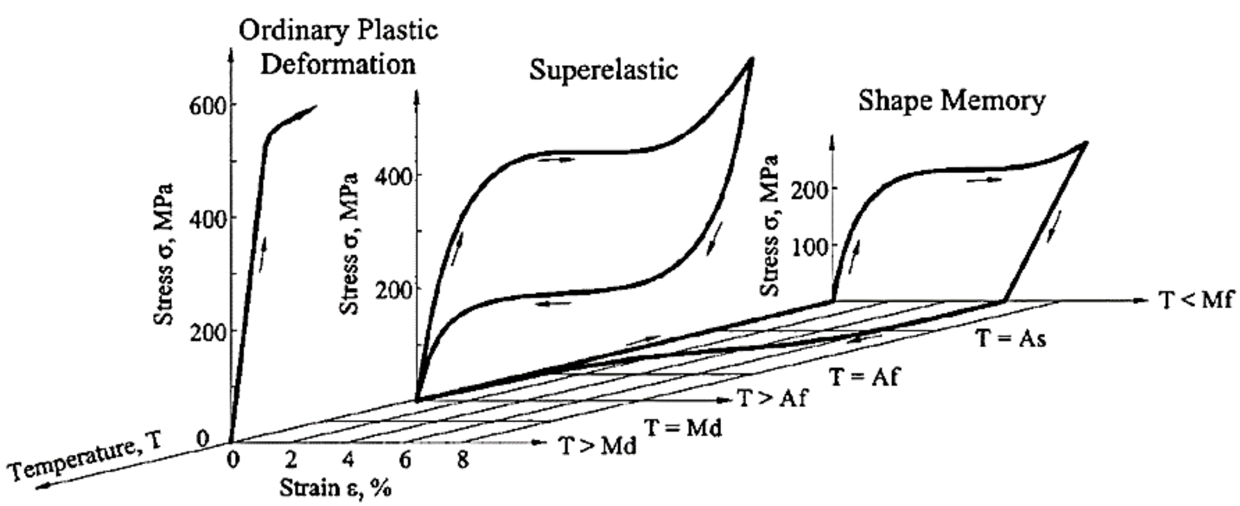

Figure 3-1: Three-dimensional stress-strain-temperature diagram of NiTi SMAs (DesRoches et al., 2004)

3.2 Properties of Superelastic NiTi SMA

Shape Memory Alloys are an exceptional class of materials that recover their shape once the temperature is increased. Within the typical operating temperature range of the SMA, it has two phases with different crystal structures and properties. The high temperature phase is known as austenite and the low phase as martensite. Austenite has a generally cubic crystal structure, while martensite can be structured in tetragonal, orthorhombic, or monoclinic (Figure 3-2). The transformation from one phase to the other occurs by shear lattice distortion rather than diffusion of atoms (Lagoudas, 2008). In Figure 3-2, A_s is the temperature in which the austenite phase initiates, while A_f is the temperature when the transformation is completed. Similarly, M_s is the martensitic start temperature and M_f is the finish temperature.

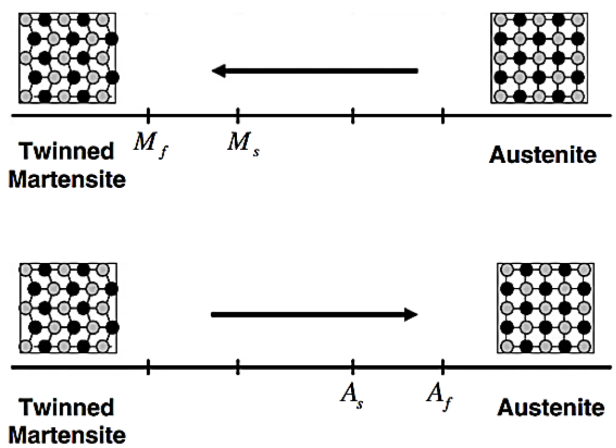

Figure 3-2: Temperature-induced phase transformation without mechanical loading (Lagoudas, 2008)

The engineering application of SMAs had a breakthrough in the 1960's when Buehler and coworkers discovered the Nickel-Titanium equiatomic combination (Buehler et al., 1963). Few years later, it was discovered that small increments of Nickel (Ni) largely attenuated A_f to temperatures around 40^{o}C below zero. Therefore, upon release of stresses at ambient temperatures (23^{o}C), the alloy would transform from the martensite to the austenite phase. Furthermore, controlled variations in the composition of NiTi SMAs provides a pseudoelasticity; i.e., pseudoelastic-behaving SMAs possess a stress-induced crystal structure transformation. Figure 3-3 illustrates the two pseudoelastic loading paths. Path a-b-c-d-e is for an SMA under a thermomechanical loading. Figure 3-3 also demonstrates the phase diagram of an SMA represented by loading path A-B-C-D-E-F. This path starts at a temperature greater than A_f and zero stress.

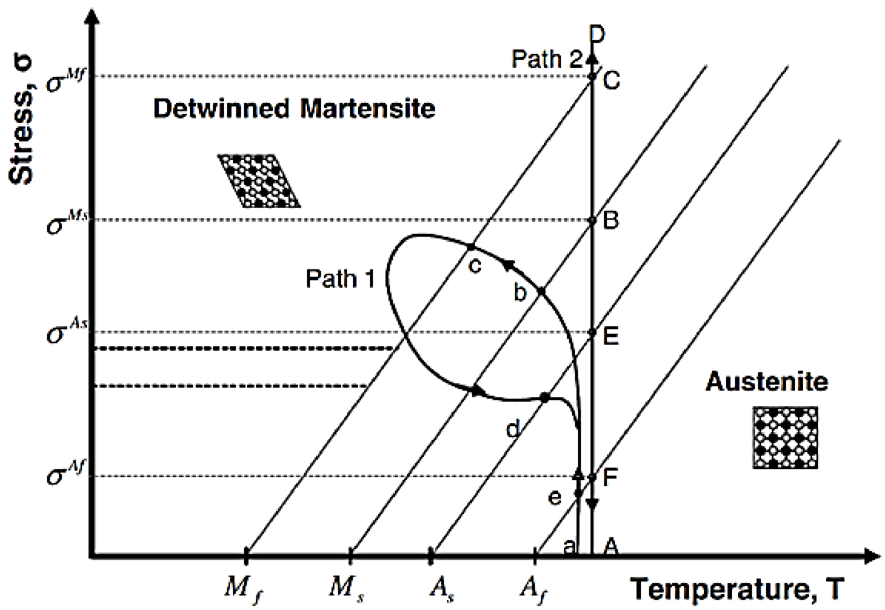

Figure 3-3: Phase diagram of two pseudoelastic thermomechanical loading paths (Lagoudas, 2008)

Figure 3-4 illustrates a detailed representation of the loading cycle of a typical SMA (Lagoudas, 2008). When stress is induced, the austenite phase undergoes elastic loading until it reaches the initiation of martensitic transformation phase (A-B). At point C, the martensitic phase has been completed and a significant change of slope is experienced in the stress-strain curve given that only the deformation of the martensite phase occurs. At point D, the stress is gradually released until it reaches point E where the unloading path intersects A_s and the austenite transformation phase is initiated. The E-F path is characterized by recovery of strain due to transformation of phase. At point F the austenite phase has been completed, and the curve elastically unloads to A. Figure 3-4 also illustrates an attractive characteristic of SMAs, the hysteresis resulting from a pseudoelastic complete cycle. The area within the curve represents the energy dissipated in the transformation cycle, which can vary with the different compositions of SMA. Therefore, this is another appealing characteristic when seismically retrofitting a structure in addition to the shape memory effect.

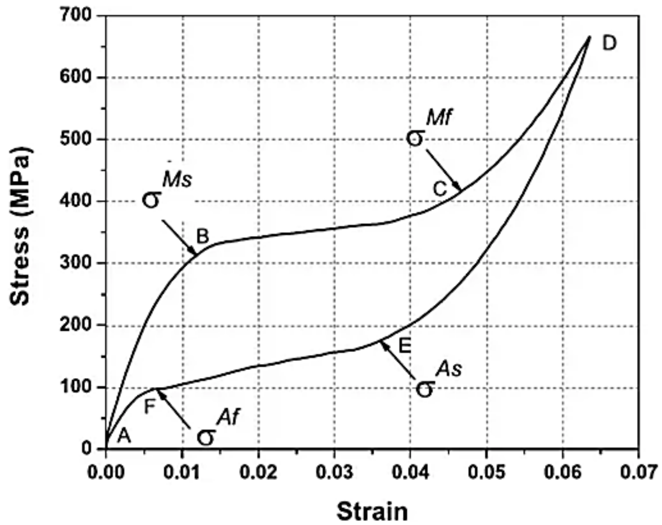

Figure 3-4: Stress-strain relationship of a common SMA pseudoelastic loading cycle (Lagoudas, 2008)

Mechanical properties of a superelastic NiTi SMA are slightly unique due to its pseudo-yielding (Figure 3-5). The superelastic SMA stress-strain response is characterized by an upper (*UPS*) and lower (*LPS*) plateau stresses; initial elastic modulus (E_i); residual (El_r) and ultimate (El_u) elongations; and equivalent viscous damping (ξ_{eq}), based on the area within the hysteretic loop. For the NiTi SMA represented in Figure 3-5, 6% strain is assumed to be the strain recover limit. For strains beyond 6%, permanent strains accumulate with further loading. However, if the temperature is increased, the shape memory effect is induced, and the strains can be recovered. Note that Figure 3-5 is based on the characterization of superelastic SMA according to ASTM (2014). The UPS is determined at 3% strain, while the LPS at 2.5% strain.

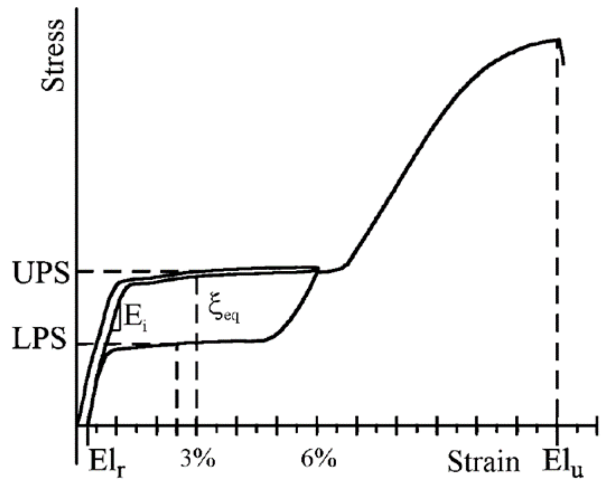

Figure 3-5: Stress-strain response of NiTi SMA bars (ASTM, 2014)

It is important to highlight that yielding implies large permanent deformations; however, superelastic SMAs can sustain and recover large deformations from approximately 1% to 6% due to its phase transformation. Therefore, for superelastic SMAs, the term pseudo-yielding is utilized and is more appropriate. A conservative strain of 6% is adopted as the recoverable deformation ratio to avoid the SMA reaching the stiffening phase to maintain the self-centering capability of the system (Yang et al., 2008). If the SMA stiffening phase is reached, the strength of the member can increase up to 5 times that of its pseudo-yielding strength which may result in significant damage to adjacent structural elements.

Table 3-1 lists the mechanical properties of typical SE NiTi SMA large diameter bars at room temperatures according to Yin et al. (2015). Even though SMAs present an asymmetrical stress-strain compressive and tensile behaviour, it is sufficiently accurate to assume the tensile-based models to represent the entire behaviour of this material according to Tarzav and Saiidi (2015) after investigating different NiTi commercial samples. Therefore, the properties provided in Table 3-1 were utilized to model the tensile and compressive behaviour of the SE-SMA bars in this thesis.

Table 3-1: Mechanical properties of large diameter SMA bars at ambient temperatures (Yin et al., 2015)

Mechanical Property	***Value***
Upper plateau stress	*400-500 MPa*
Elastic modulus	*40-75 GPa*
Ultimate tensile stress	*1100-1400 MPa*
Ultimate elongation	*15-20%*

3.3 SMA braced frames

Bracing a reinforced concrete frame has been demonstrated to improve the seismic performance of the system. Large residual deformations, however, are expected to arise as the most significant deficiency of common braces. To address the challenge of controlling residual deformations, researchers have focused on evaluating the implementation of novel materials/systems that are capable of re-centering structures during a seismic event. Due to the superior shape-memory effect of SE-SMA, the material is expected to improve the seismic performance of a given structure while maintaining low levels of residual displacements provided the seismic loading does not exceed the recoverable strain capacity of the alloy. The literature on this topic is scarce and relevant studies that implement SMAs in braced frames are herein discussed.

A braced frame system that implements Nitinol was developed by Zhu and Zhang (2007). The intention was to create a bracing system able to outperform conventional BRBs by preventing the accumulation of residual deformation. A Reusable Hysteretic Damping Brace (RHDB) was developed relying on Superelastic Nitinol wires as the energy dissipating component (Figure 3-6). These wires exhibit self-centering hysteresis and excellent fatigue properties with a maximum recoverable strain of 8%. The study also demonstrated Nitinol wires with diameter of 0.58 mm can sustain 2000 load cycles under the maximum strain capacity without performance deterioration.

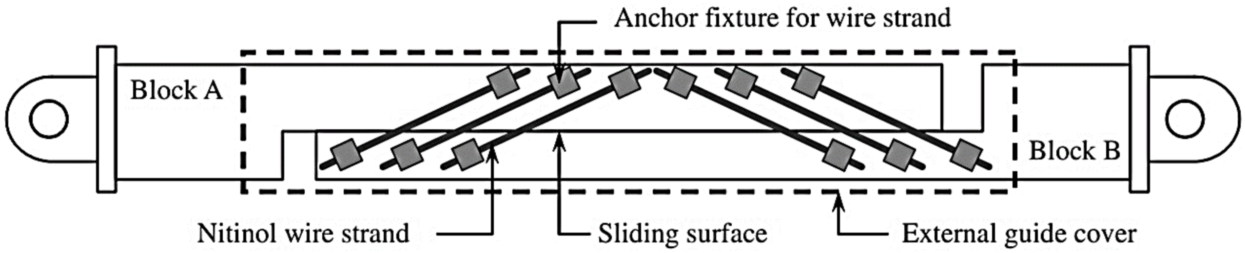

Figure 3-6: Residual hysteretic damping brace proposed by Zhu and Zhang (2007)

Zhu and Zhang (2007) also demonstrated that pre-tensioned Nitinol wires can effectively enhance energy dissipation capacity and post-yield stiffness of the RHDB system. Furthermore, a nonlinear time-history analysis study was conducted on three-storey moment-resisting frame buildings. The modelled frames were retrofitted with a BRB; a RHDB-C, where no pretension was applied on the Nitinol wires; and with a RHDB-D, where the Superelastic wires were pretensioned. The frames were then subjected to different scaled earthquake records according to the FEMA (FEMA, 2012) guidelines. The results illustrated that the RHDB frames were able to significantly reduce the residual deformation (Figure 3-7 (a)) and increase the drift capacity (Figure 3-7 (b)) when compared to the BRB retrofitted model. It was also proven that RHDB-C frames presented a higher maximum drift capacity than the brace with pretensioned wires.

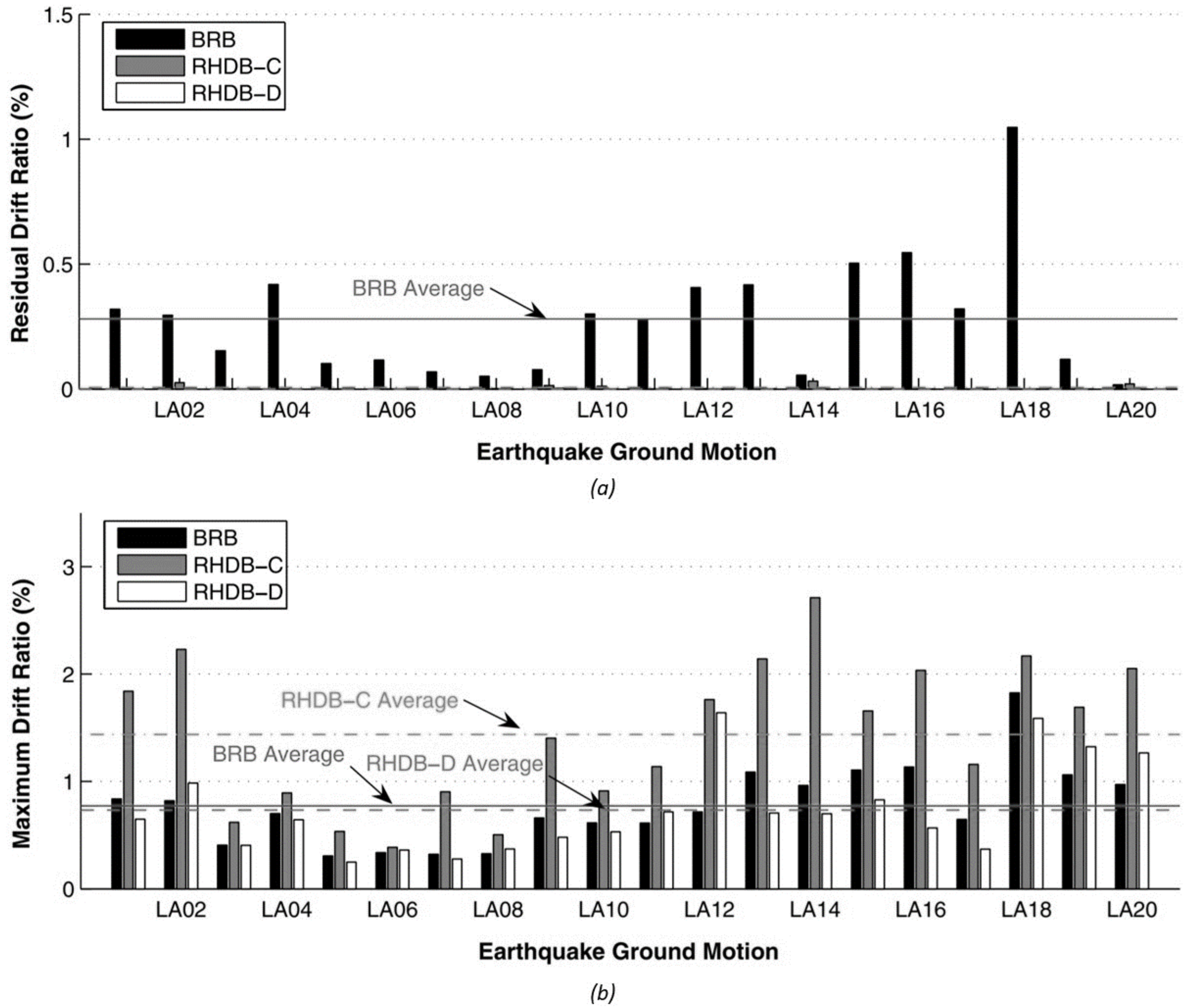

Figure 3-7: Performance of 3-storey frame buildings: a) residual drifts; and (b) maximum drifts (Zhu and Zhang, 2007)

In another study, Auricchio and Desroches (2006) evaluated the seismic performance of steel frames with Nitinol braces through nonlinear numerical analyses assisted finite element modelling. A three-storey steel frame building with BRBs implementing SMA bars at the connections, as illustrated in Figure 3-8. For comparison purposes, a control building with conventional BRBs with steel connections was also assessed. The SMA braces were designed to yield at the same force and axial stiffness as the steel braces. Hence, the structure with the innovative elements had the same natural period as the steel braces, and both braces were expected to yield at the same force level (Auricchio and Desroches, 2006).

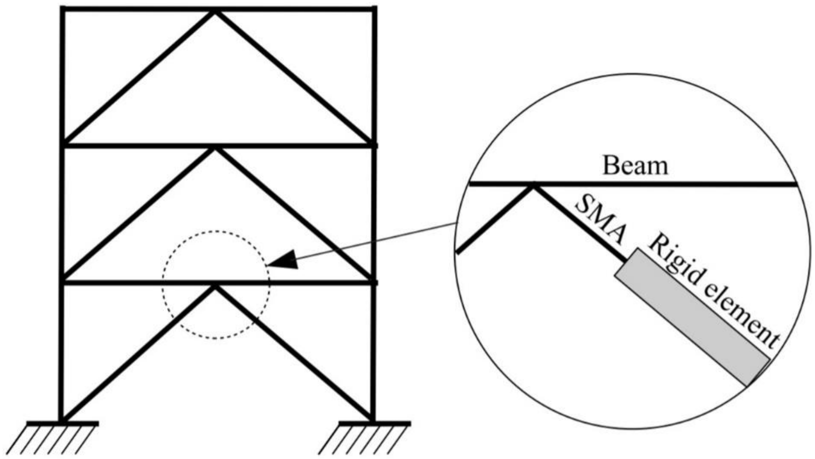

Figure 3-8: Superelastic SMA brace installed in the steel frame building (Auricchio and Desroches, 2006)

The 1979 Imperial Valley earthquake scaled to a PGA value of 0.67g provided the strongest effects on the structure with the steel BRB. The record is illustrated in Figure 3-9 (a), while the maximum displacement experienced by the top floor of the two braces is presented in Figure 3-9 (b). The SMA braced frame building reduced the top floor displacement by 45% in comparison to the steel braced building. In addition, it was observed that the Nitinol SMA braced frame significantly decreased the residual displacement to 2.5mm, while the steel BRB frame presented a residual displacement of approximately 192mm.

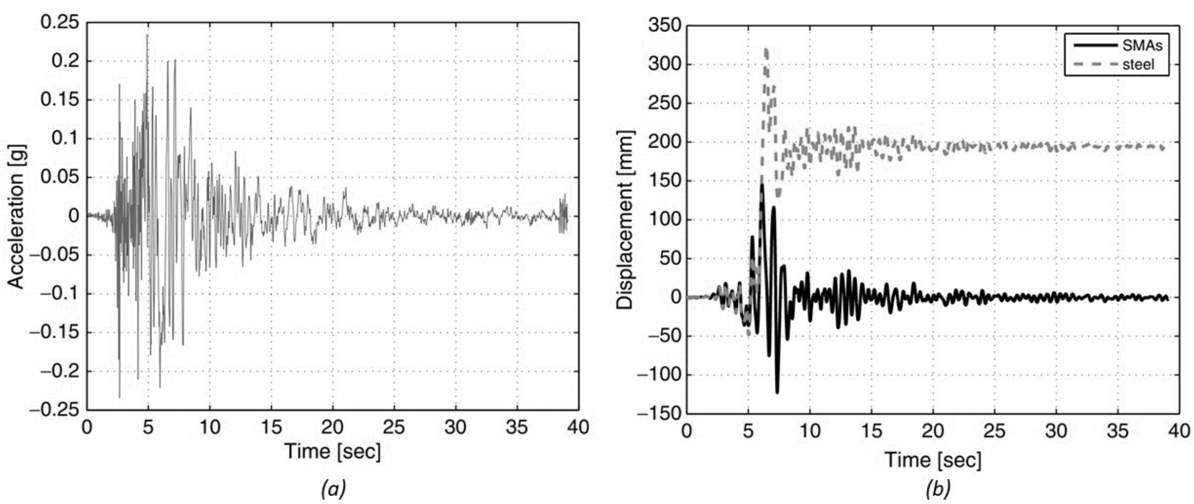

Figure 3-9: Time histories: (a) applied ground motion; and (b) displacement time-histories (Auricchio and Desroches, 2006)

The study from Auricchio and Desroches (2006) also demonstrated that even though the energy dissipation of steel BRBs was significantly higher, the re-centering characteristic of the frame with SMA was fundamental in reducing structural oscillations and permanent damage. Figure 3-10 illustrates the residual drift of the top floor of the building under different ground records (Auricchio and Desroches 2006). The superiority of the innovative brace in reducing the residual drift is evident. However, an interesting observed aspect is that for record Number 8 and 14, the SMA brace presented a higher residual displacement than the traditional steel brace. According to Auricchio and Desroches (2006), that was due to the post-inelastic behaviour of the Nitinol braces that was not properly captured by the SMA model utilized in the finite element program.

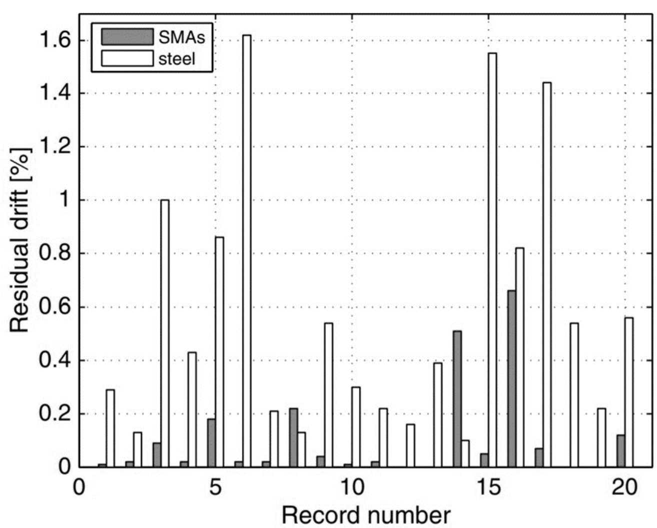

Figure 3-10: Residual displacement for different ground motion records (Auricchio and Desroches, 2006)

The same bracing system from Auricchio and Desroches (2006) was evaluated by Youssef et al. (2010) as an alternative to improve the seismic performance of reinforced concrete frames. At peak ground acceleration values near the design PGA, the use of SMAs in the bracing of reinforced concrete frames led to significant reduction of residual deformations; a decrease of 83% in comparison to the traditional steel BRB RC frame (Figure 3-11). In addition, for PGA values close to failure, the residual deformation was similar for the SMA and traditional BRB given that the residual deformation resulted from the concrete frame (Youssef et al., 2010).

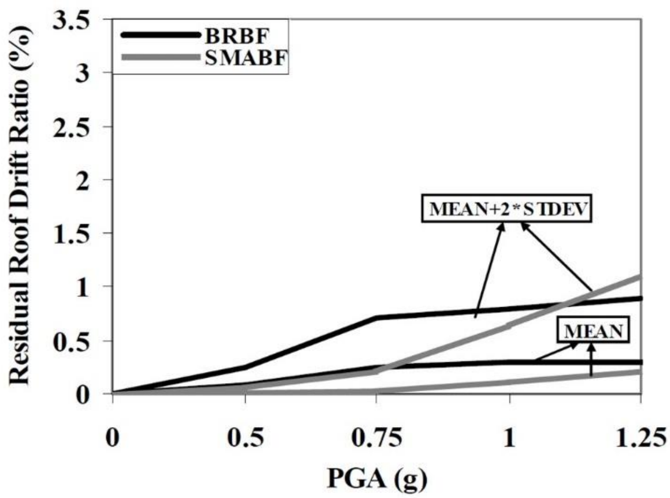

Figure 3-11: Variation of the mean of the residual roof drift ratio for frames with steel and SMA BRBs (Youssef et al., 2010)

Miller et al. (2011) implemented SMA rods acting alongside a BRB (Figure 3-12). The BRB core was a continuous steel plate element, responsible for providing the majority of the energy dissipation. An inner tube was placed to avoid local buckling and the region between the tube and steel core was filled with concrete to prevent transverse movements of the core. In addition to restraining for buckling, the middle tube was part of the axial load transfer since it carried compression forces during shortening of the system. The SE-SMA rods are pretensioned to create an initial compressive stress; the self-centering ability arises primarily from the pretension of the SMA rods.

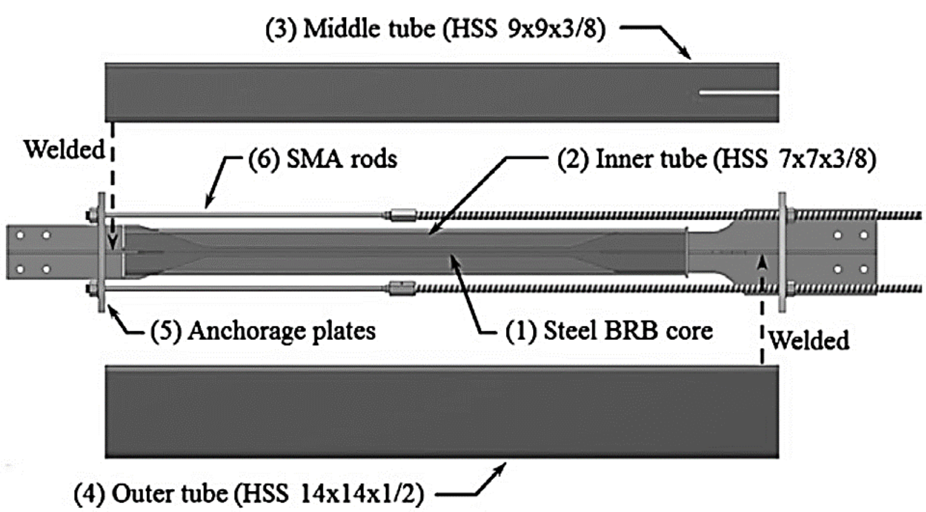

Figure 3-12: Self-centering BRB components from Miller et al. (2011)

In this study, two SC-BRB systems were developed and subjected to different displacement-controlled loading protocols (Figure 3-13). The SC-BRB systems had similar components. However, the cross-sectional area of SC-BRB 1 was 484 mm^2 and the core yield stress corresponded to 365 MPa, while SC-BRB 2 had a 452mm^2 area and a 305MPa yield stress. The SMA pretension stress and area were similar in both braces. The self-centering behaviour of SC-BRB 2 was superior to the SC-BRB 1, exhibiting a small residual displacement after the load was released (Figure 3-14). The residual displacements of both frames was half of what would be experienced by a BRB alone.

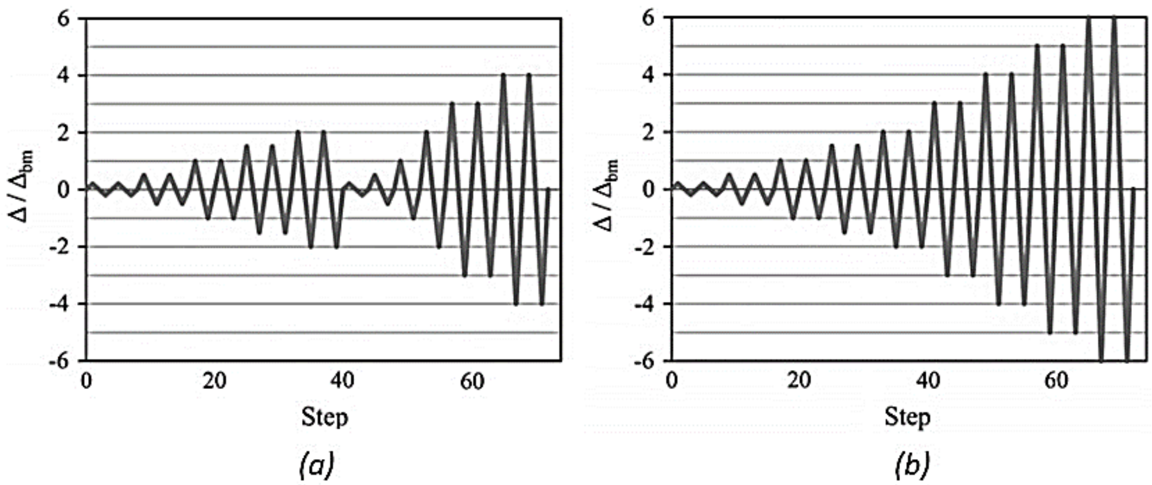

Figure 3-13: Testing protocol: (a) SC-BRB 1; and (b) SC-BRB 2 (Miller et al., 2011)

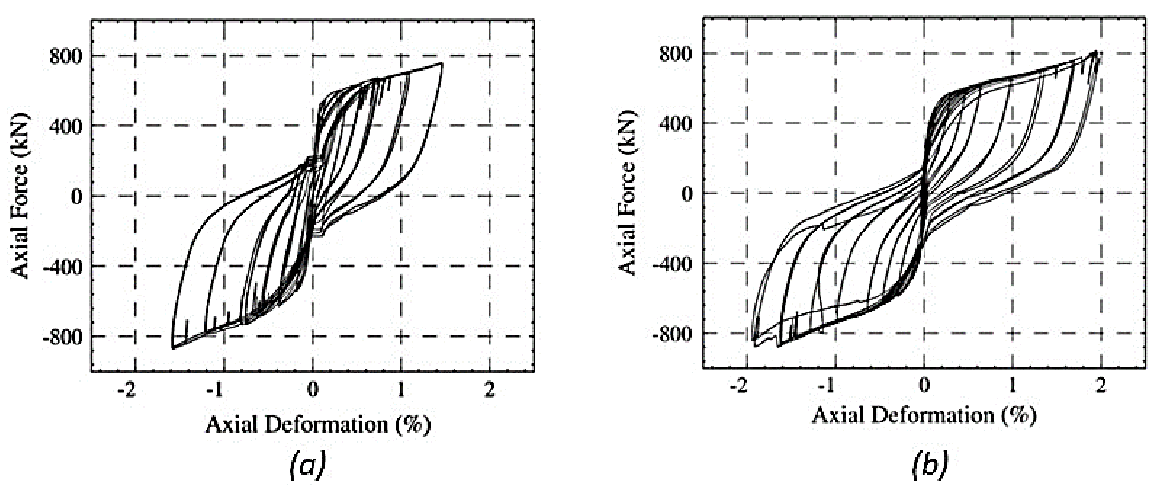

Figure 3-14: Axial deformation – axial force response: (a) SC-BRB 1; and (b) SC-BRB 2 (Miller et al., 2011)

Another group of researchers conducted a comparative study between steel and Nitinol buckling-restrained braced frames (Hu et al., 2013). It was demonstrated that when Nitinol is used at the edges of BRBs, the hysteresis response is flag-shaped with reduced residual deformation due to the re-centering capabilities of the material. However, as it has been previously stated that the combination of a steel core BRB with Nitinol bars at the edges does not provide full permanent deformation recovery. The literature is still lacking studies on implementing SMAs as the axial load carrying core bar, reaffirming the novelty of this thesis, where the main focus is to evaluate the response of a SE-SMA core bar in a BRB system.

Chapter 4

Finite element modelling of reinforced concrete moment-resisting frames

4.1 Introduction

When facing problems with complex geometries, complicated loadings, and different material parameters, a numerical method is desired since an analytical mathematical solution may not be capable to precisely capture the behaviour of the structural member/system in question. The advantage of a numerical method also relies on the possibility of implementing it into a programming language. Therefore, the Finite Element (FE) method, which is a numerical method widely used by the engineering community, has been chosen to assist the numerical analysis of this thesis. This method is a reliable tool in evaluating the behaviour of structural members, specially after a model is validated.

The FE method consists in dividing a certain member into a finite number of elements. Each element has different behaviour governed by its stiffness matrix, which is a function of the material properties of the member. Hence, when a local force is applied at a certain element, the displacement will be a function of the stiffness matrix and the magnitude of the applied stress. For this thesis, the numerical analyses were conducted using VecTor2 (Vecchio et al., 2013), a two-dimensional nonlinear finite element program that is applicable to membrane structures under static and dynamic loading. The program has been selected since it is capable of successfully capturing the behaviour of numerous reinforced concrete structural elements without requiring extended computational time in comparison to other commercial programs. Relevant parameters for an accurate numerical analysis are discussed in this chapter.

4.2 Finite element analysis program

VecTor2 (Vecchio et al., 2013) is a nonlinear finite element analysis program suitable for static and dynamic analysis of two-dimensional membrane structures. The Modified Compression Field Theory and the Distributed Stress Field Model (Vecchio et al., 1986 and 2000) are the theoretical formulations that form the basis of the analysis. When a reinforced concrete membrane is subjected to shear and normal stresses (Figure 4-1), the Modified Compression Field Theory (MCFT) determines average and local strains and stresses in both the concrete and reinforcement. In addition, the MCFT calculates crack width and orientation from the load-deformation response of the RC membrane element. The failure mechanism of the element is determined based on those principles.

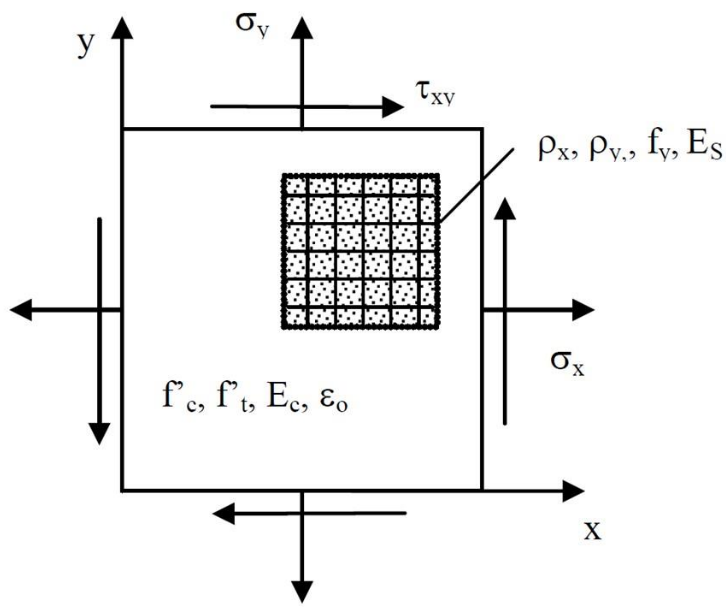

Figure 4-1: RC membrane element subjected to in-plane stresses (Vecchio et al., 2013)

The MCFT allows complex analysis to be performed under a reduced computational time. This is attributed to the fact that cracked concrete is modelled as an orthotropic material through a smeared rotating crack approach in VecTor2. In this approach, cracking is distributed over the membrane element, which is treated as a solid continuum, instead of a solid element interrupted by discrete physical discontinuities (Vecchio et al., 2013). Thus, the smeared cracks reorient with the principal concrete compressive stress field and this behaviour has been observed in several reinforced concrete elements. Some of the basic original assumptions of the MCFT formulation at element-level are: uniformly distributed reinforcement and rotating cracks, applied shear and normal stresses are uniform, orientation of principal strain and principal stresses are equal, bond between concrete and reinforcement is perfect, and constitutive relationships of concrete and reinforcement are independent (Vecchio et al., 2013).

Three categories of elements can be found in the VecTor2 library and the categories are defined based on the type of material the element is used for. The first element category is utilized to model solid materials such as concrete; constant strain triangular, plane stress rectangular and quadrilateral elements can be used to model such materials (Figure 4-2). These are low powered elements as the minimum number of nodes are defined, the boundaries of the elements are straight lines, and a linear function defines the deformation of the edges. When modelling reinforcements, it can either be defined as smeared within the solid elements or as discrete truss bars, which defines the second category of elements.

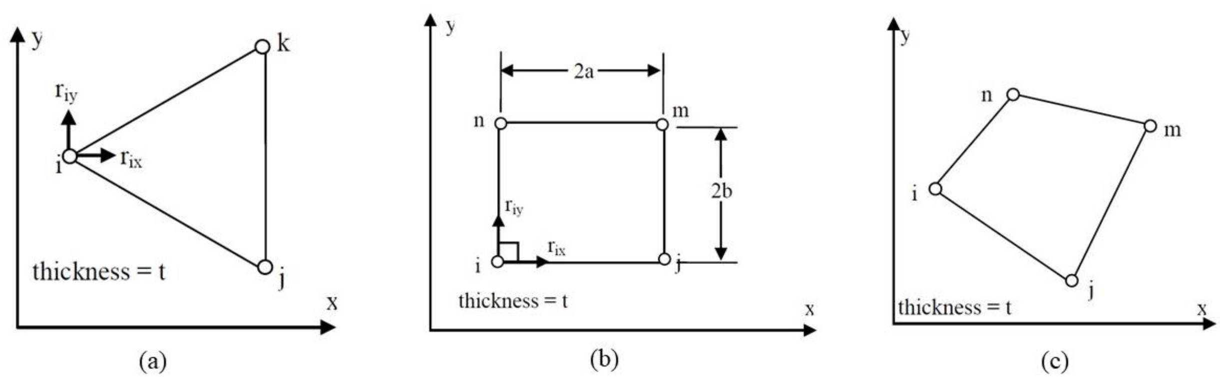

Figure 4-2: Solid elements: (a) constant strain triangle; (b) plane stress rectangle; and (c) quadrilateral (Vecchio et al., 2013)

When reinforcement is not smeared within elements, they are defined by discrete two-noded elements with constant cross-sectional area (Figure 4-3). This element possesses four degrees of freedom, where each node can deform in the x and y directions, and no bending is present. Once loaded, these elements offer resistance along its axis. The third category of elements in the VecTor2 library are the bond-slip elements that are defined by common nodes between solid concrete and discrete reinforcement elements. The bond elements can be specified as 2-node, 4-degress of freedom link elements (Figure 4-4) with a constant and exact bond slip or as a 4-node, 8-degrees of freedom interface elements (Figure 4-5) with linear displacement function, which can yield constant or linearly variable exact solutions. The latter are extremely useful for bond slip with nonlinear variations (Vecchio et al., 2013).

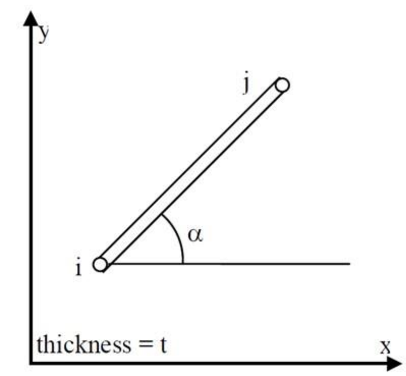

Figure 4-3: Truss bar element (Vecchio et al., 2013)

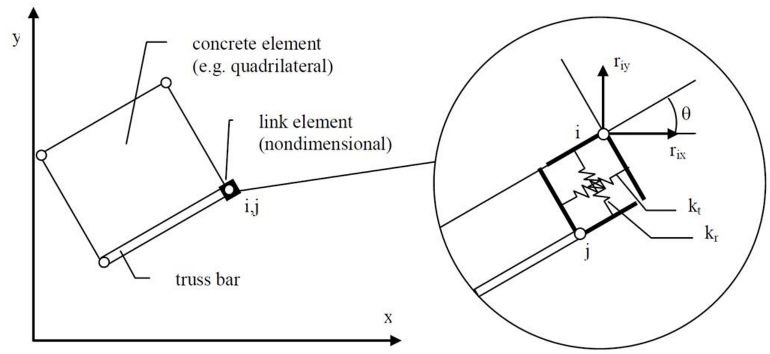

Figure 4-4: Link elements for bond-slip (Vecchio et al., 2013)

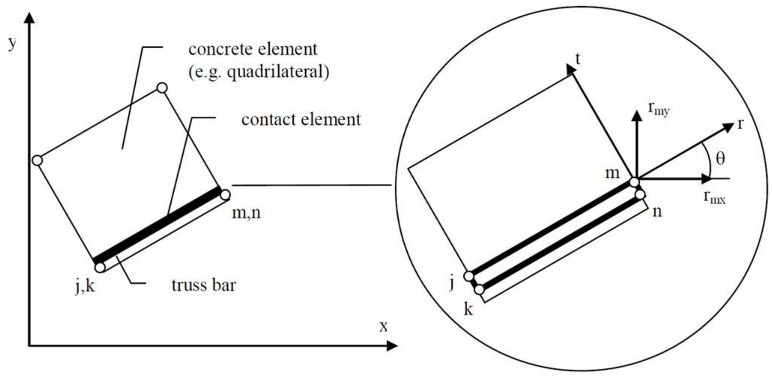

Figure 4-5: Interface elements for bond-slip (Vecchio et al., 2013)

Dynamic analysis in VecTor2 employed the Raleigh's viscous damping model. The program offers two types of structural damping, the Alternative and the Rayleigh Damping. In the former, the damping ratio for several modes is specified and zero viscous damping is assumed for the remaining modes. In the latter, two damping ratios define the damping frequency for all modes. Thus, the selected modes should be able to represent the behaviour of the structure. As the Rayleigh Damping was selected in this study to model viscous damping, the first mode should be the fundamental mode as the vibration at this mode dominates the seismic response of the concrete frame investigated. For the second mode, it is common to select that which corresponds to 90% of the accumulated modal mass participation (Maciel, 2019).

As previously discussed, the constitutive response of concrete and reinforcement are independent. To model the material behaviour, constitutive models that can simulate the expected response of the material must be selected. The compression pre-peak, compression post-peak, compression softening, tension stiffening , tension softening, lateral expansion, confinement strength, crack criterion, and crack width check represent several phenomena that must be defined to predict the behaviour of concrete materials. For the reinforcement material, the hysteretic response, dowel action, and reinforcement buckling must be specified. To evaluate whether the specified constitutive models are representative of the behaviour of the structure, the model must be validated either through previous experimental data present in the literature or throughout analytical calculations. However, it is common practice to select the default constitutive models, which have been proven to provide satisfactory simulations of behaviour, are well tested, and are the simpler models in VecTor2.

4.3 Object of study

4.3.1 Prototype frame

As the process of validation of the finite element model is crucial to ensure that the numerical response of the structure provides a satisfactory representation of the real behaviour, the prototype building investigated in this study was based on the study and frame tested by Al-Sadoon (2016). Subsequent to the validation of the FE model of the bare frame structure, the evaluation of the behaviour of the BRB system using the validated FE model as the basis is assumed to provide reasonable and satisfactory results.

In this thesis, the prototype structure is based on a 6-storey reinforced concrete moment-resisting frame structure. The structure represents a seismically deficient, limited ductility frame construction that represents a medium-rise office built during the 1960's. The building in question was initially described in the Concrete Design Handbook (Cement Association of Canada, 2006), but modifications included the floor plan dimensions and storey heights (Al-Sadoon, 2016). Figure 4-6 illustrates the prototype building. The design of the structural elements, in the study by Al-Sadoon (2016), was based on the 1965 NBCC load combinations for dead, live, wind and earthquake. In regards to the dimensions, the first storey is 4.5 m high, while the remaining storeys are 3.5 m; with 3 bays in the E-W direction and 7 bays in the N-S. The slab thickness is 110mm, and the interior and exterior columns are of 500 x 500 mm and 450 x 450 mm, respectively. The principal beams are of 400 mm wide and 600 mm deep, while the secondary beams are 300 mm wide and 350 mm deep.

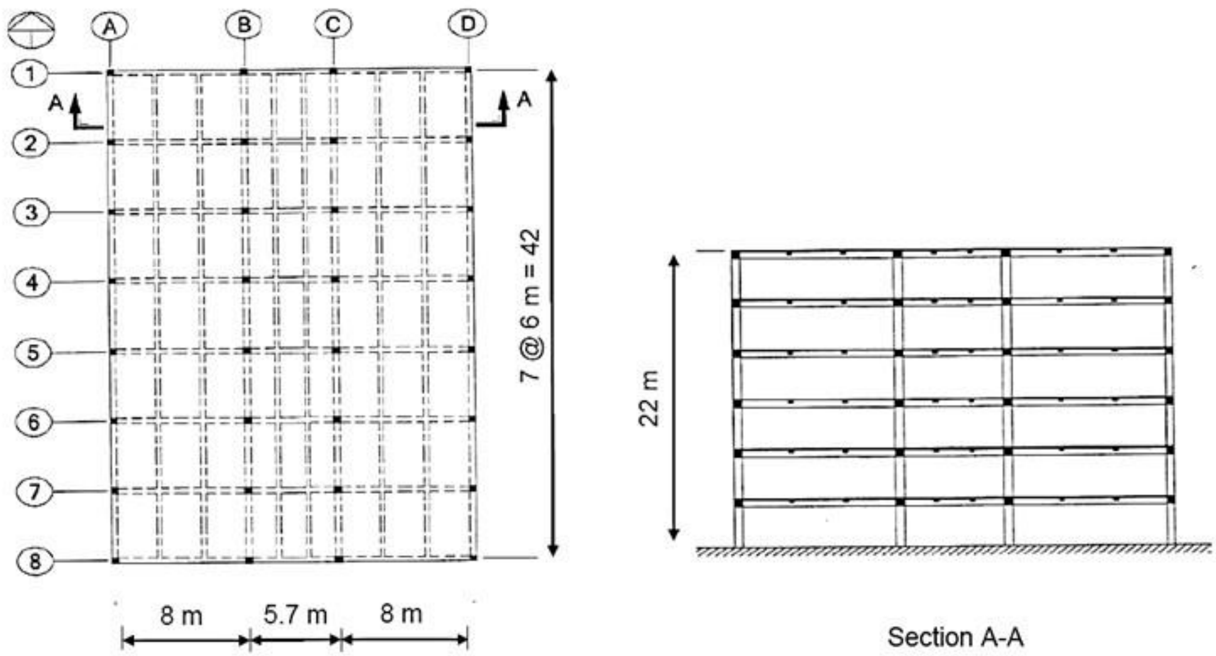

Figure 4-6: Plan and elevation views of the prototype frame structure (Al-Sadoon, 2016)

The numerical model was developed to simulate the two-third scale, single bay single height frame from the prototype structure in Figure 4-6. Therefore, all dimensions were scaled by two-thirds and applied loadings by $(2/3)^2$. The first-storey, mid-bay frame was selected for the study and based on the work of Al-Sadoon (2016); its two-third scale is illustrated in Figure 4-7. The frame was constructed on 500 mm-thick foundation, which was designed to remain elastic during testing. Plan and sectional views of the frame are presented in Figure 4-8. The beam reinforcement layout was composed of 4-20M bars at the top and 2-20M at the bottom; at the supports, additional 2-15M bars were added at the top, and at mid-span, additional 2-15M bars were added at the bottom. Along the length of the beam, 10M stirrups were spaced at 150 mm. As per the 1965 NBCC, no ties were placed in the beam-column joint. For the columns, 8-20M bars were placed longitudinally and 10M ties were allocated every 200 mm. Regarding the splices at the bottom of the column, the 1965 NBCC specified a minimum requirement of 24 times the bar diameter; thus, a bar splice of 480 mm was implemented. Additional details of the longitudinal and transverse steel reinforcement is illustrated in Figures 4-7 and 4-8.

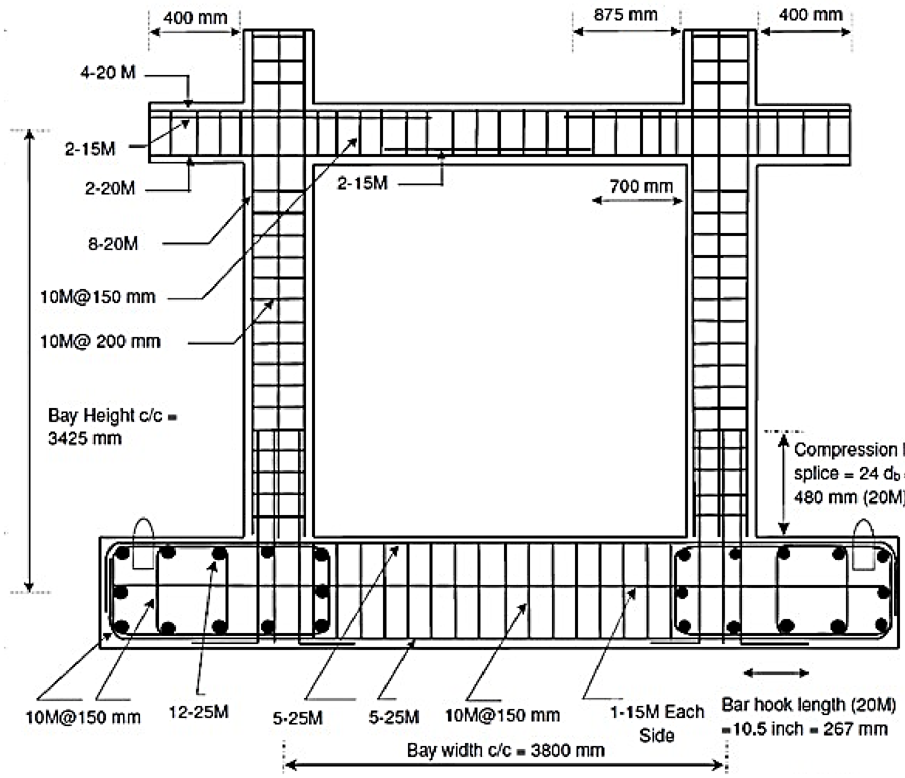

Figure 4-7: Reinforced concrete frame details (Al-Sadoon, 2016)

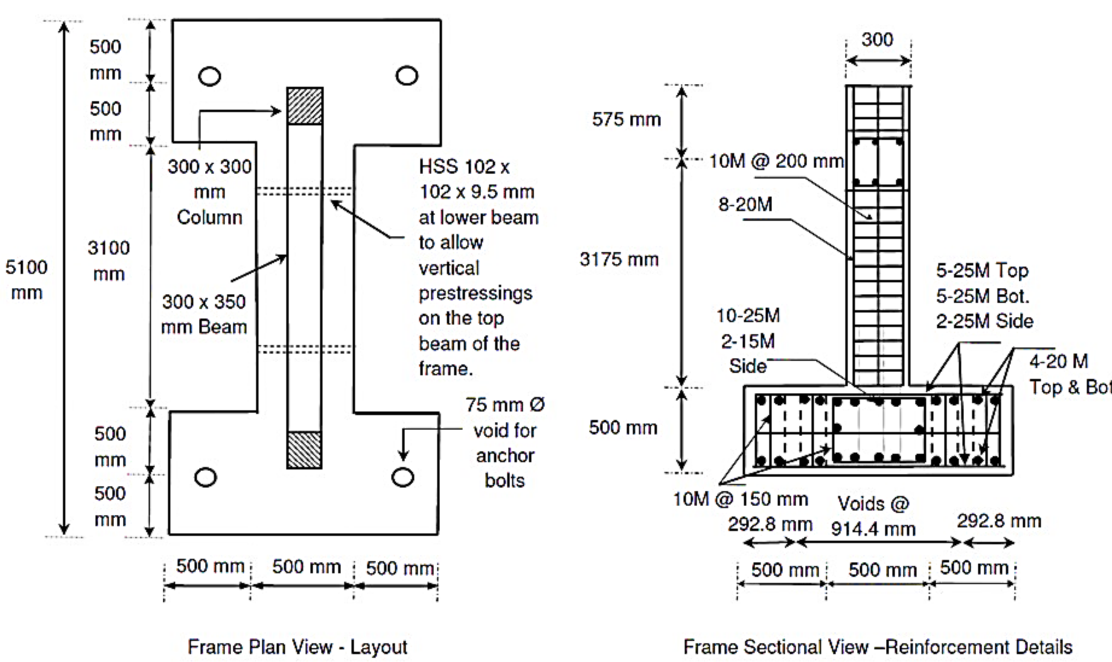

Figure 4-8: Frame plan and sectional views (Al-Sadoon, 2016)

The frame was analyzed under constant axial load applied on the columns and transverse load applied to the beam. The reverse cyclic load was applied at the top beam mid-height. The lateral loading protocol used during testing and replicated in the analysis was selected to induce forces that simulate high levels of inelastic deformations that may be experienced by RC frames under severe earthquakes. In addition, the loading consisted of three cycles of incrementally increasing lateral displacements reversals as per ACI-374.1-05 (2006) loading protocol. Further details regarding the loading protocol are provided in Chapters 5 and 6.

4.3.2 Buckling-restrained brace

The BRB proposed by Al-Sadoon (2016) was selected as the structural component of this research. In the previous research, the BRB was proven to seismically increase the strength and stiffness capacities of the frame system, but the full capacity of the core bars were not realized due to concentration of stresses that developed within the brace. Even without achieving the full capacity of the BRB system, the retrofit was able to eliminate BRB-frame connection challenges by allowing the brace to freely rotate due to a pin connection; thus, no rotation was imposed at the bottom of the columns nor at the beam-column joints. Furthermore, the reserve gaps at the edges of the BRB (Section 2.2.2.2) were eliminated and the probability of buckling at these locations was reduced. Therefore, the BRB proposed by Al-Sadoon (2016) is able to successfully address common issues with BRBs. However, given that abrupt failures of the brace were experienced, a thorough investigation can evaluate the causes of failure, lead to improvements in the BRB system by developing a modified buckling-restrained brace, and provide an evaluation of the impact of the BRB in the original structure, which are the main proposed objectives of this current research.

The retrofit methodology consisted of a diagonal BRB that utilizes the full compressive and tensile capacity of the retrofit system. Figure 4.9 illustrates the BRB, which was proposed and designed by Al-Sadoon (2016). This bracing system was designed to eliminate internal and external reserve gaps along the brace by restraining deformations in the transverse direction at the edges of the core bar. The BRB is composed of a circular rigid steel element that prevents the core from buckling over its entire length. The total length of the streel core bar is 2700mm with a diameter of 44.5mm. To promote yielding away from the threaded ends of the core bar, the bar diameter is reduced to 31.8mm near the mid-length. Four, 12.7mm bar spacers were placed along the core bar to accommodate the strain gauges and wiring for the experimental testing and to prevent buckling of the core bar (Figure 4-10). An epoxy-sand mixture is utilized to fill the area between spacers and principal bracing core. This internal core bar is then encased into a 59mm-diameter steel pipe surrounded by mortar (Sikacrete-08), which, in turn, is encased in a 168mmx8mm HSS.

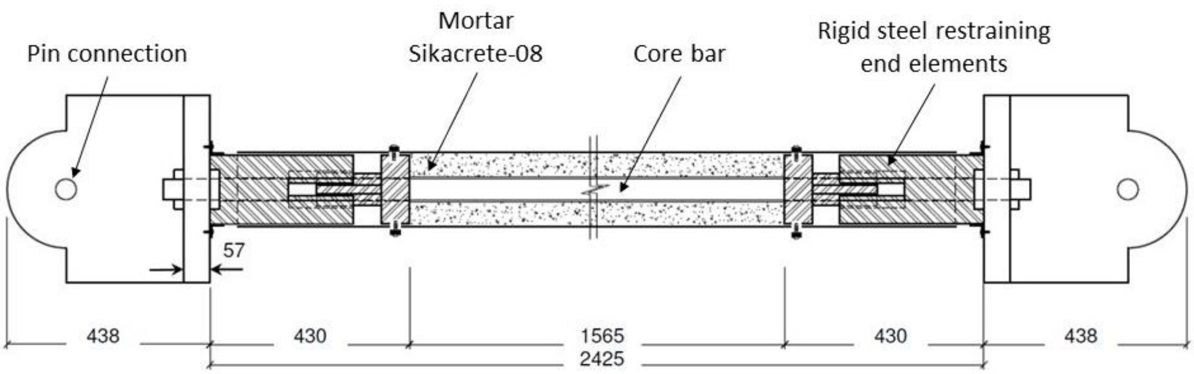

Figure 4-9: BRB proposed by Al-Sadoon (2016)

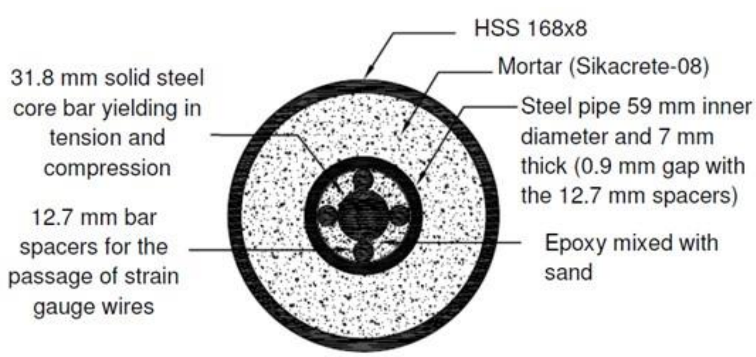

Figure 4-10: Cross-section of the BRB system configuration (Al-Sadoon, 2016)

It is important to highlight that in the study conducted by Al-Sadoon (2016), three different steel core bars were investigated. For each core bar implementation, the researcher improved the cross-section of the BRB to implement changes and minimize the deficiencies evaluated after every test. The cross-sectional view presented in Figure 4-10 is the last proposed BRB system; hence, the superior results recorded during testing. For this current thesis, two of the researcher's proposed BRBs will be modeled: the BRB with AISI 4140 chrome-molybdenum high tensile steel core bar, in which the same cross-section from Figure 4-10 was used; and one BRB with AISI Type 304 stainless steel core bar, in which the epoxy mixed with sand that fills the void between the core bar and the 59 mm-pipe was absent (refer to Figure 4-10). Figure 4-11 illustrates the BRB retrofitted concrete frame with details of the brace-frame connection. When modelling this structure through the finite element program, assumptions to model the connection were necessary and numerically analyzed to verify applicability and satisfaction of the results in comparison to the experimental behaviour.

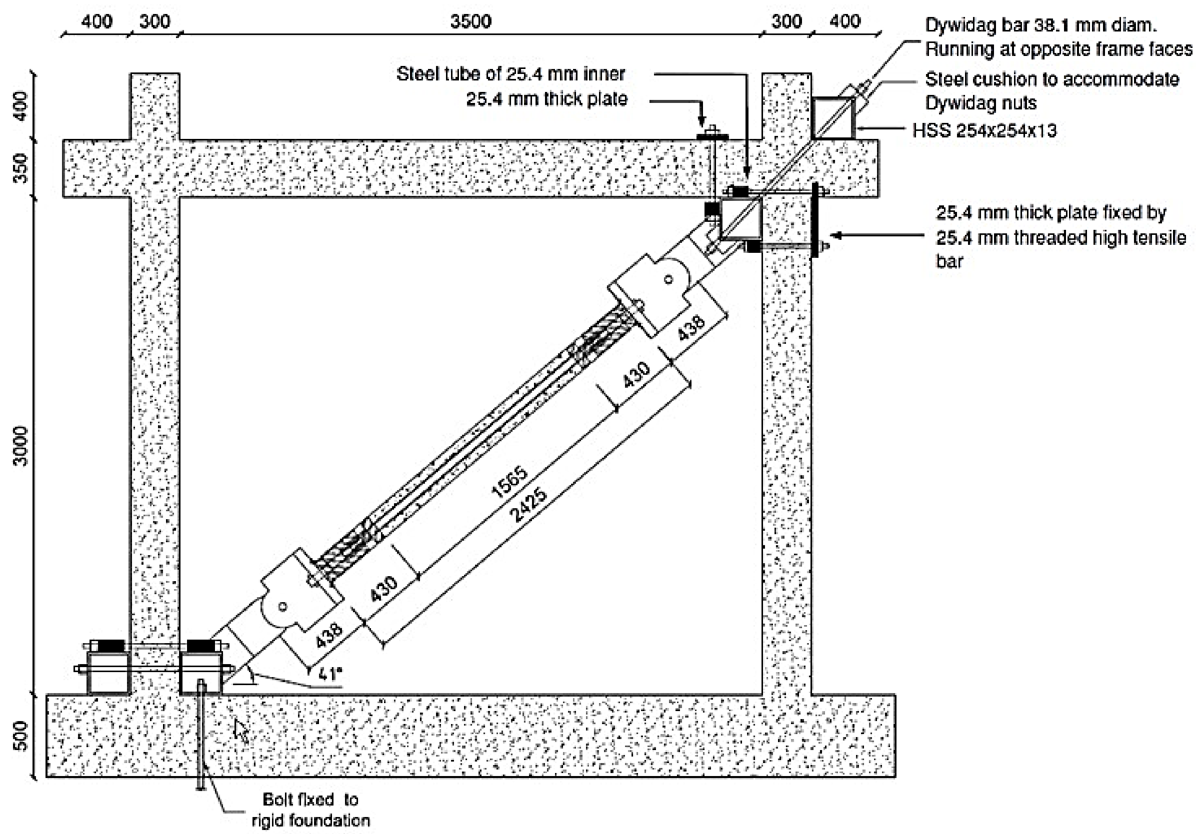

Figure 4-11: BRB configuration in the test frame (Al-Sadoon, 2016)

4.3.3 Proposed buckling-restrained brace

The main contributions of this current thesis include proposing an idealized BRB system able to improve the buckling restraining of the core bar and address deficiencies of BRBs proposed in the literature; and evaluating the seismic superiority of utilizing a SE-SMA core bar BRB system to implement self-centering capabilities to the BRB to reduce permanent deformation. For the modified BRB system, the BRB proposed by Al-Sadoon (2016) was utilized as a basis. Deficiencies in the original brace design were assessed and an improved design is suggested herein to improve the response (Chapter 5). For the improved BRB design, local buckling effects have been mitigated by omitting the bar spacers and decreasing the steel pipe radius from 59mm to 46.5mm for core bars sizes of 44.5mm and to 34mm for core bar sizes of 31.8mm (Figure 4-12). The void between the bar and the steel pipe will be filled with 2 mm-thick silicon rubber sheet as it was found to be the most effective material to minimize concentration of stresses according to Tsai et al. (2004).

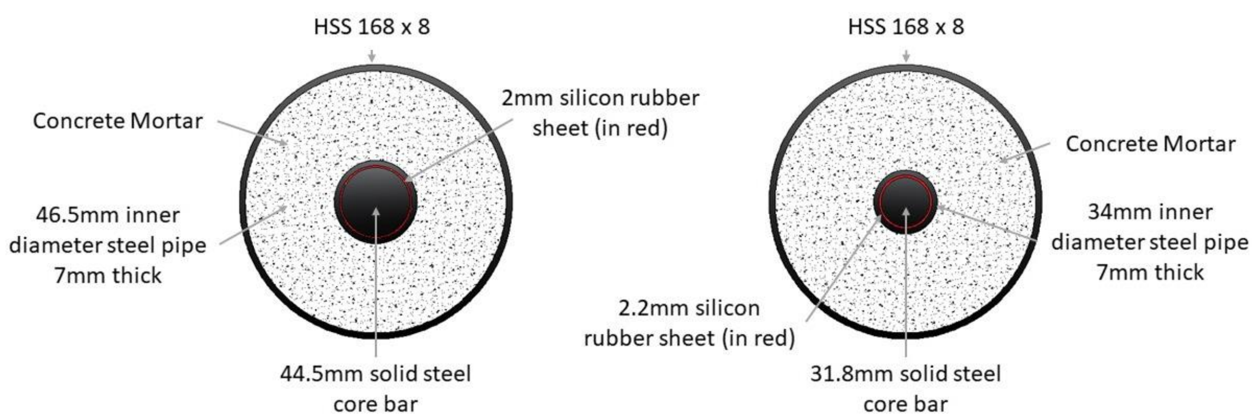

Figure 4-12: Modified BRB cross-sectional view

In the proposed design illustrated in Figure 4-12, the HSS 168mmx8mm remained from the BRB design of Al-Sadoon (2016) to fulfill the stiffness requirement the section must provide to avoid buckling of the core bar once the hollow section is filled with a concrete mortar. Between the concrete mortar and the core bar, no loading should be transferred. Through the literature review presented in Chapter 2, silicon rubber sheets can successfully mitigate this load transfer more efficiently than other materials. Furthermore, a supporting steel pipe is placed between the rubber sheet and concrete mortar as a tool to avoid friction forces between the concrete and the rubber.

To implement the self-centering component in the brace, Superleastic Shape Memory Alloy bars were used as the core of the BRB system. The SE-SMA material properties are based on those reported by Yin et al. (2015) that are listed in Table 3-1. The bar diameter was selected to provide the same yielding strength (F_y) and same axial stiffness (K) as the other steel cores. This was intended to ensure that the retrofitted frames with the same BRB concept but difference internal core exhibit the same natural period and yield at the same lateral force. To achieve this, the SE-SMA bar diameter was approximated 44.5mm. However, to evaluate the efficiency of utilizing a SE-SMA core bar with the same size and diameter as the chrome-molybdenum and stainless steel core BRBs, which were tested by Al-Sadoon (2016), additional models were investigated where the SE-SMA diameter was reduced at the mid-length to localize yielding.

4.4 Finite element model

4.4.1 Bare concrete frame

Figure 4-13 illustrates the finite element model of the Bare Concrete Frame (BCF). Six main concrete regions have been defined and modelled with plane stress, four-noded, eight-degrees of freedom rectangular elements. Region 1 and 2 includes the rigid foundation - 5100mm long x 500mm high x 500mm wide at the centre of the bay and 1500mm wide at the edges (Figure 4-8), where all the transverse reinforcement was considered smeared in the concrete elements, while the longitudinal bars were model as discrete reinforcement in the form of two-noded truss bar elements. Support conditions were assigned to the nodes at the base of the foundation and applied through vertical and horizontal restraints. Note that the restraints were only considered over the wider section of the foundation, which corresponds to the location of the anchoring bolts used during testing. The remaining regions are all 300 mm wide. Region 3 defines the column zone where the transverse reinforcement was defined as smeared within the concrete elements, while the longitudinal reinforcement was represented by discrete truss bar elements. Region 4 applied to both columns and beam and corresponded to the concrete cover where no transverse horizontal nor longitudinal reinforcement was defined, but a confinement reinforcement was included to account for the out-of-plane legs of the ties/stirrups. Region 5 is similar to Region 3 and defined the beam, but the steel reinforcement was smeared in the vertical direction. Region 6 defined the beam column joint where no transverse reinforcement was defined following the NBCC 1965 provisions.

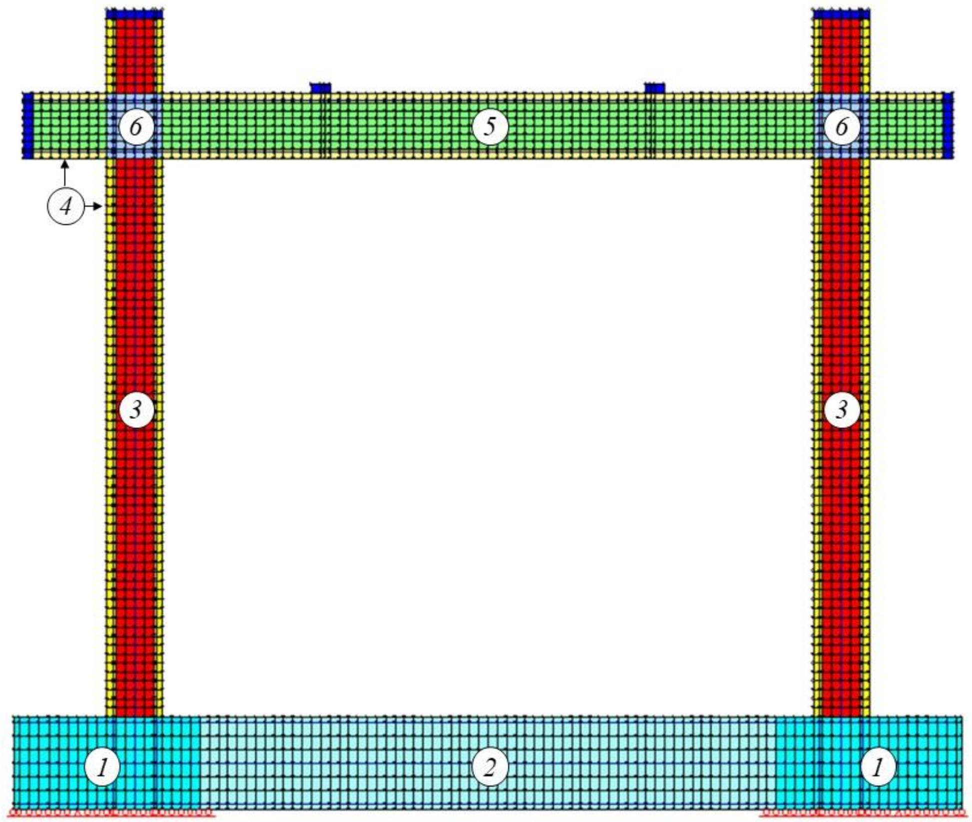

Figure 4-13: Finite element model in FormWorks (Vecchio et al., 2013) of the bare concrete moment-resisting frame

In Regions 1 and 2, the mesh aspect ratio was kept at 1.4 with elements of approximately 50 mm x 70 mm, while in Regions 3, 4, 5, and 6, the aspect ratio was kept at 1 with elements of 50 mm x 50 mm. The 50 mm-length is used for the truss elements such that the nodes coincided with the rectangular concrete elements. It is important to note that a 7th region was created to represent the steel plates that were utilized during the testing conducted by Al-Sadoon (2016). Those plates were placed where the loads were applied: at the top of the columns, edges of the beam, and along the beam where the transverse beams would transfer load to the main beam. The plates were 50 mm thick and 300 mm wide rigid structural steel. In total, 3018 rectangular and 1202 truss elements were created, and 50 nodes were restrained by support conditions.

Ductile longitudinal steel reinforcement in the columns, beam, and foundation were modeled as discrete truss bars perfectly bonded to the concrete. However, steel bars are not necessarily perfectly bonded to the surrounding concrete and for the bars to achieve their yield capacity, a development length should be provided. Considering the columns, the longitudinal bars initiating at the base of the column, or the termination of the starter bars into the column should not be considered full bonded, given that the development length has not been provided to achieve the proper transfer of stresses. Once the length of these bar segments is at least equal to the development length, the bar is assumed to be fully bonded or able to achieve the full yield force. Therefore, the capacity of the bar is not fully utilized over the length that is less than the development length; but the force that can be developed increases linearly reaching its yield capacity at the development length. This phenomenon has a direct and significant impact on the stiffness at the base of the columns and in the beam-column joints, thus the bar splice must be greater than the development length of the bar.

As the investigated frame was designed based on the 1965 NBCC, the splices provided at the base of the columns were 480 mm for a 20 mm-diameter ductile steel bar. According to the CSA A23.3-14 provisions, however, the required splice length for the same column should be 734.5mm since the required development length for the longitudinal bars in the columns equals 565 mm. For the longitudinal bars in the beam, the splice length should be 546 mm as the required development length equals 420 mm. Thus, structural systems designed based on previous building codes also present deficiencies in their bar splicing details. To account for the development length of the longitudinal bars in the FE model based on the CSA A23.3-14, the effects of un-bonding or accounting for a more accurate representation of the development of the stresses along the bar, the longitudinal bars were scaled based on their cross-sectional areas and not their strength capacity since a change in the diameter (area) also affects the stiffness of the bar. Figure 4-14 illustrates the concept for scaling the bars; from the beginning point of the longitudinal bars and their development length, scaled diameters were defined so that at length 0, the diameter was equal to 0 mm; at length equal to the development length, the diameter was 20 mm. As a result, between 0 and 565 mm, each 50 mm-truss bar element was assigned a different cross-sectional area that varied linearly from 0 to πr^2 depending on their length. The same scaling process was followed for the longitudinal bars in the beam.

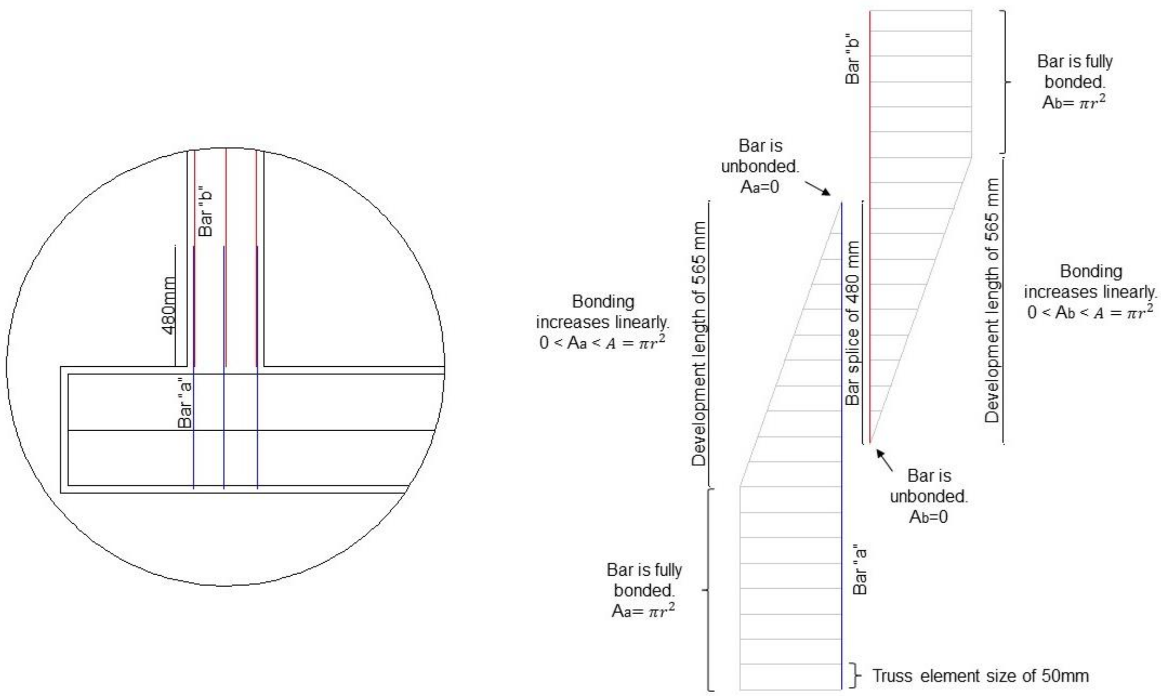

Figure 4-14: Accounting for the development of longitudinal reinforcement at the bottom of the columns

4.4.2 BRB retrofitted frame

The FE model for the BRB retrofitted frame was composed of the FE model for the bare reinforced concrete frame presented in the previous section with the addition of the retrofitting element. Therefore, in addition to the seven regions necessary to model the BCF, the retrofitted frame incorporated five additional regions modelled with constant strain 3-noded, 6-degrees of freedom triangular elements (Figure 4-15). Region 8 defined the rigid structural steel connection between the BRB and the reinforced concrete frame. Region 9 modeled the gap between the core bar and the steel pipe; this was created to avoid load transfer between the core bar and the restraining material based on the design from Al-Sadoon (2016). Region 10 included the portion of the BRB that provides restraining of the core bar, i.e., the area between the steel pipe and the hollow section that was filled by a concrete mortar (Sikacrete-08). Region 11 included the 168 mm x 8 mm rigid steel hollow section that provides an external restraining to the system. Finally, Region 12 modeled the connection between the steel casing (HSS 168 mm x 8 mm) and the steel end elements, where no load transfer was permitted to avoid load bearing.

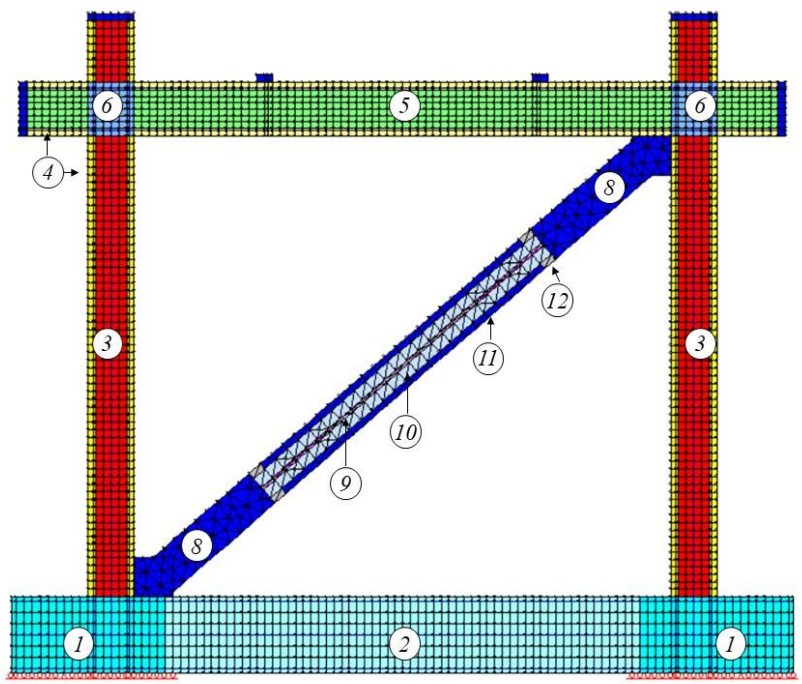

Figure 4-15: Finite element model in FormWorks (Vecchio et al., 2013) of the BRB retrofitted frame

In addition to the constant strain triangular elements, 100 mm-long truss bar elements were utilized to model the core bar of the buckling-restrained brace. As in the original BRB design, the core bar had a reduced diameter section at its mid-length, thus two different discrete reinforcements were created with different cross-sectional areas. In Regions 8 to 12, the constant strain triangular elements complexity factor was maintained at 0.5, and at least one of the edges of the element was maintained as 100 mm. In total, the retrofitted frame model was composed of 3018 rectangular, 504 triangular, and 1228 truss elements. In addition, 50 nodes were restrained by support conditions.

In modelling the BRB retrofitted frame, a number of assumptions were implemented and their impact to the response of the frame was evaluated before defining a final FE model. In the BRB design (Figure 4-11), rotation in the brace-frame connection was permitted to avoid transfer of moment by the BRB to the frame, and vice-versa. The free rotation was provided by allocating a pin joint between the connection and the brace. The FE program does not allow for the user to implement a pin joint connection between structural elements. Therefore, Figure 4-16 illustrates an attempt to model relative rotation between the elements in question. In that model, a ductile steel truss bar was placed where the pin joint was designed. The bar has a cross-sectional area sufficiently large to ensure elastic behaviour throughout loading. Furthermore, the truss bar is surrounded by a void, where no load can be carried. As the truss bar nodes can displace in the x and y directions only, the moment transfer between brace and frame is minimized. After conducting reverse cyclic analysis on the retrofitted frame with and without the alternative pin joint, it became evident that the rotation of the brace was negligible between the two models. In addition, in the FE model with no pin joint, the effects of the moment transfer to the RC frame was not present, and both the lateral strength capacity and overall behaviour of the structural system were unaffected. Therefore, it was decided to omit the alternative pin-joint from the final FE model.

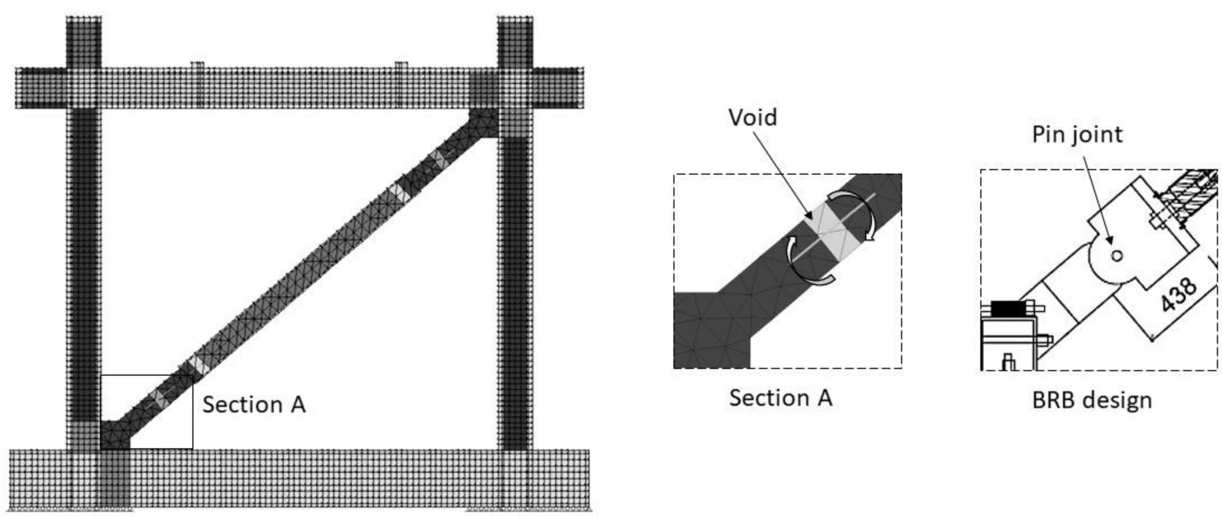

Figure 4-16: FE model that implements an alternative pin joint

In the BRB design from Al-Sadoon (2016), to guarantee a rigid brace-frame connection, external 38.1 mm-diameter rods were utilized. The connection was incorporated 25.4 mm-thick steel plates and 13 mm-thick square hollow sections with 254 mm side dimensions. The effects of the external rods and HSS were evaluated separately in the FE model. The rigid HSS was designed to remain elastic during loading. Therefore, Figures 4-17 to 4-20 illustrate attempts to model the hollow sections. The analysis results from pushover static analysis demonstrated that the capacity of the frame did not exceed more than 2% across the models illustrated in Figures 4-17, 4-18, and 4-19. The FE model in Figure 4-17 had convergence issues in the brace-frame connection, where a single element distorted significantly in comparison to the others. The thickness of the section in contact with the frame was increased in the model illustrated in Figure 4-18. However, convergence issues were still present resulting in premature failure of the structure.

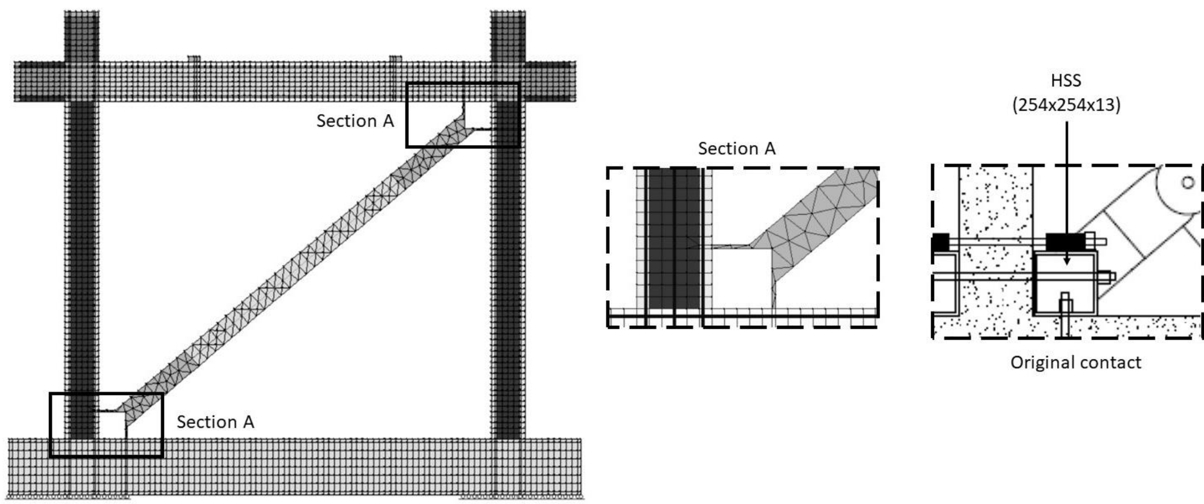

Figure 4-17: FE model that incorporated the brace-frame contact through a 13 mm-thick steel plate

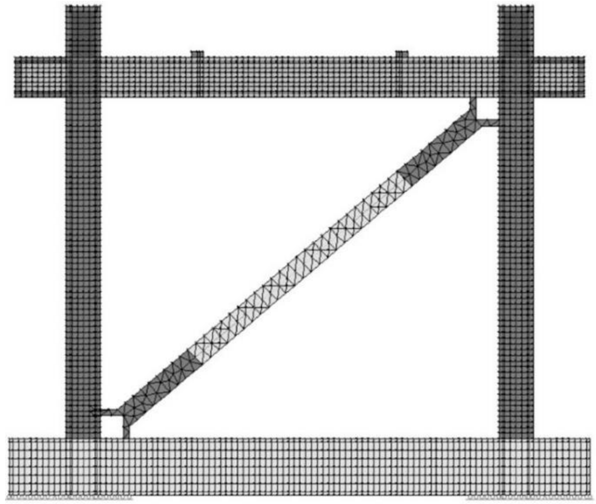

Figure 4-18: Brace-frame contact implemented through a 50 mm-thick steel plate

The model shown in Figure 4-19 provided a more stable behaviour than the previous models. In this model, all sides of the hollow section were implemented in the FE model. However, as the aspect ratio of the elements could not be maintained over the acceptable range, the model was discarded. That is due to the fact that a non-uniform mesh may lead to superficial stiffening of a region, which will affect the behaviour of the structure. An addition model was developed based on the same contact in Figure 4-17, but to minimize element distortion, the external rods were implemented by modelling them as external steel skin plates (Figure 4-20). The intention by modelling the plates was to increase the strength of the elements in contact with the rigid steel connection. The element distortion was minimized, but the capacity of the frame increased as the skin plates are assumed to be perfectly bonded to the concrete elements, which improved the stiffness of the column leading to unrealistic behaviour. In modelling a solid steel connection, where the void within the HSS was neglected, and comparing the results with the model illustrated in Figure 4-19, there was no change in capacity and behaviour between the two models. Therefore, the solid steel section was implemented in the final FE model given that there was no superficial increase in stiffness of the concrete elements as an evenly distributed mesh was applied.

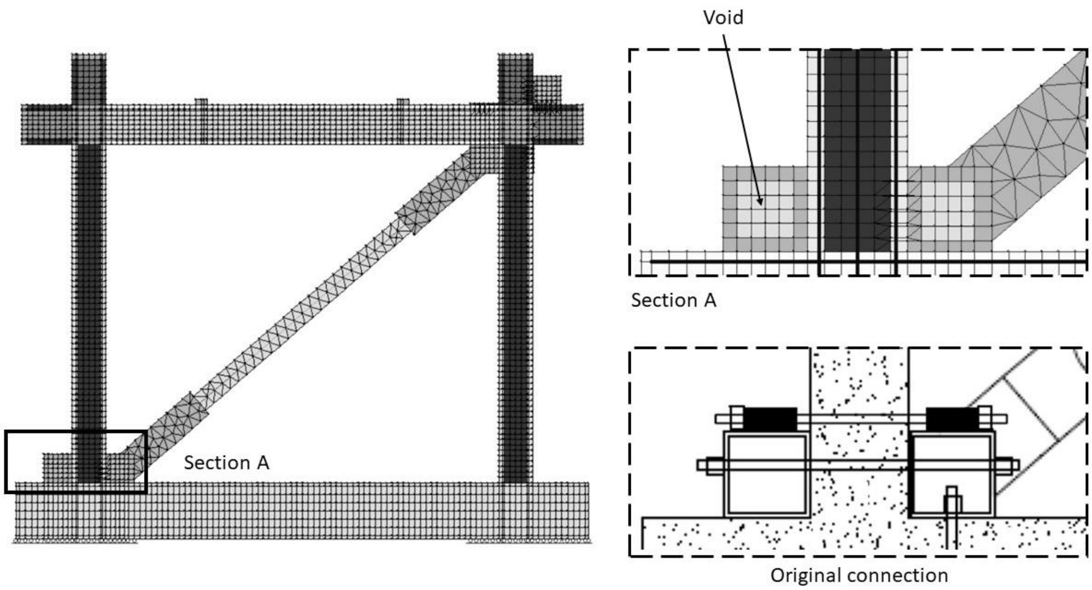

Figure 4-19: FE model that defines the brace-frame contact throughout a steel hollow section

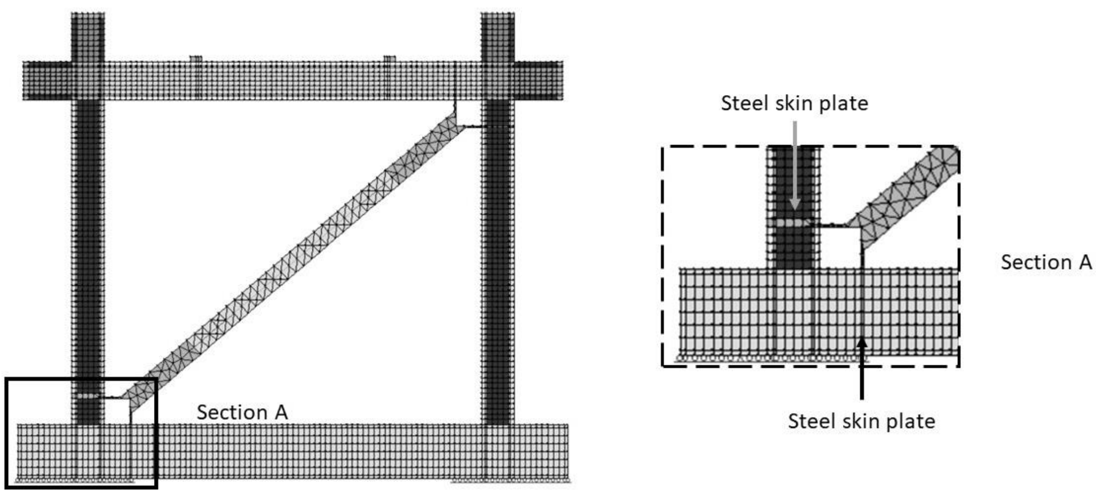

Figure 4-20: FE model that incorporates the brace-frame contact through a 13 mm-thick steel plate and incorporates the steel rods through steel skin plates

A further challenge in creating the FE model was to implement the contact between the buckling restraining material (concrete mortar) and the steel end elements (Figure 4-9). The challenge arises when, in the brace, the axial load can only be carried through the core bar. This particular contact could only be achieved by incorporating void elements between the concrete mortar and the steel end elements, which was implemented in the model presented in Figure 4-21 (a). Figure 4-21 (b) illustrates the results of the structure under pushover loading. As the model did not converge and the frame failed prematurely, this model was discarded.

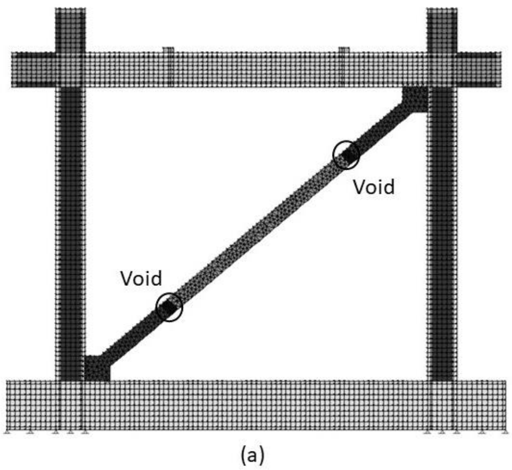

Figure 4-21: Implementation of void elements between the concrete mortar and the steel end elements: a) model; and b) deformed shape at failure

In the model in Figure 4-22, the external circular steel hollow section (HSS 168x8) was implemented to provide restraining to the void elements and avoid the non convergence verified in the previous model. The outcome was not as expected as the node shared between the HSS and the steel end connections allowed part of the axial load to be carried by the HSS. As a result, the capacity of the system increased 10 times, which was deemed unrealistic. Furthermore, the failure mode did not coincide with the test results in the literature (Al-Sadoon, 2016). The problem with the contact between the restraining material and steel end elements was only solved when the concrete mortar was modelled.

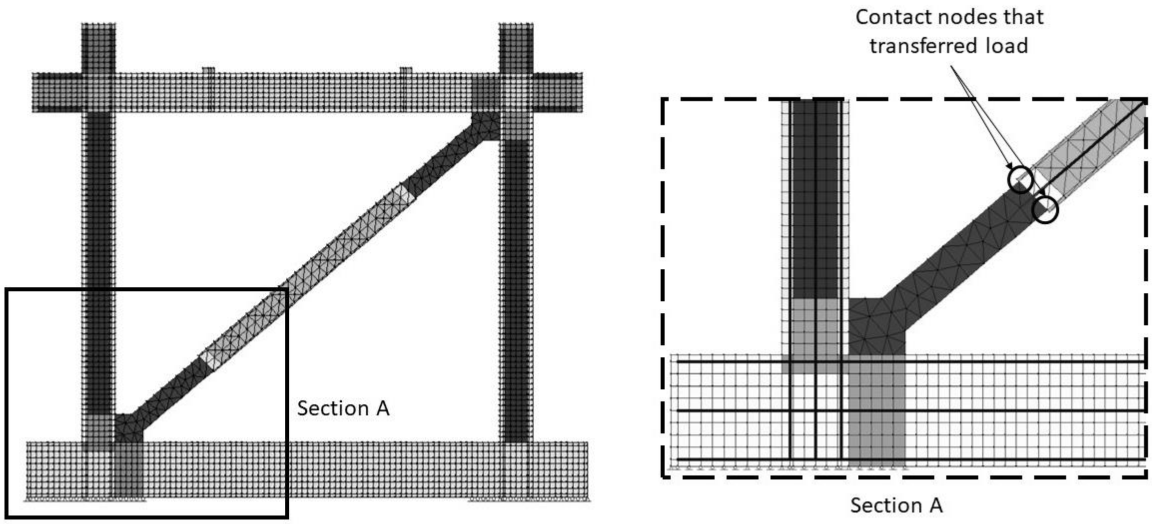

Figure 4-22: Attempt to model the HSS (168mm x 8mm)

The first attempt to model the restraining material (concrete mortar) was through concrete elements, but the load was carried through contact with the steel end elements which affected the performance of the core bar. Hence, it was decided to create a “fixed orthotropic” material, where only transverse compressive and tensile strength was implemented to the material. The longitudinal axis of the material was selected as 41 degrees from the horizontal axis, where a strength resistance of 0 MPa was specified. The strength capacity of the material in the direction perpendicular to the axis of the core bar was then modelled as 45MPa as to simulate the strength of the concrete mortar selected in the original design. By applying the fixed orthotropic material, the problem of contact between the concrete mortar and the steel end elements was resolved and no axial load could be carried by the fixed orthotropic material. To model the contact between the steel HSS and the steel end elements, void elements were applied to avoid load transfer (Figure 4-23). As a result, the axial load can only be carried throughout the core bar in contact with the steel end element; and the orthotropic material provided sufficient restraining to the bar.

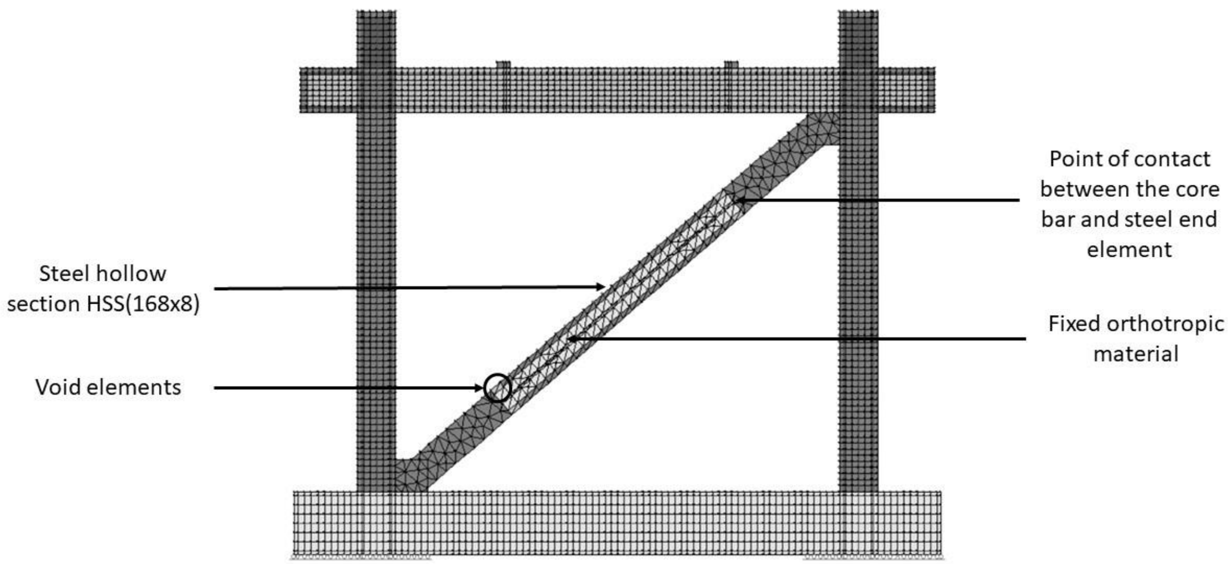

Figure 4-23: FE model that defines crucial regions of the BRB

After analysis of the model in Figure 4-23, the capacity of the retrofitted frame was in agreement with the experimental results presented by Al-Sadoon (2016). To capture the behaviour of the core bar, the gap between this bar and the steel pipe was modelled. In the original design from Al-Sadoon (2016), the gap was provided by spacers to allow strain gauges to be attached to the core bar. As the FE program does not allow penalty contact – nonlinear boundary condition, where contact is induced once a loading is applied - between elements, two alternatives were considered, either to model the gap through void elements or by calculating and implementing the unsupported length (b/t) of the core bar. The latter is used to evaluate the buckling capacity. In the first model that implemented void elements between the core bar and the 59 mm-diameter steel pipe, the core bar was immersed in a 2 mm thick void surrounding the bar. The capacity of the retrofitted frame was comparable to the experimental results, but a brittle failure occurred due to non-convergence of the model. A further model was created to evaluate the effects of void elements within the hollow section. A void was placed at the mid-length of the brace (Figure 4-25) in order to evaluate how the core bar surrounded by a void would behave. It was verified that the response of the frame was similar to the previous model where the void was placed across the core bar. Therefore, as the system was failing prematurely, the next attempt was to model the void by implementing the unsupported length (b/t) of the core bar calculated based on the VecTor2 User's Manual (Vecchio et al., 2013). After implementing the unsupported length, the lateral strength capacity and behaviour of the frame was similar to the experimental response from Al-Sadoon (2016), thus this approach was incorporated in the final FE model.

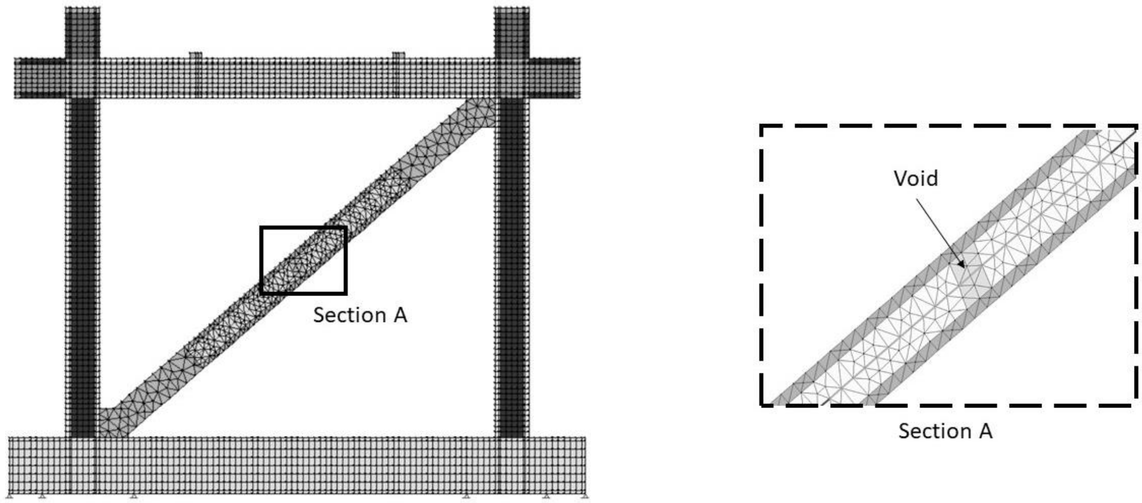

Figure 4-24: FE model implementing a void region to simulate unrestrained section inside the BRB

4.5 Material models and properties

4.5.1 Bare concrete frame

Among the constitutive material models available in the VecTor2 library, the selected models for the analyses in this thesis are summarized in Table 4-1. Detailed information of the models can be found elsewhere (Vecchio et al., 2013). According to Abdulridha (2013), default material models are preferred, unless a different constitutive model is proven to better represent the behaviour of the material. For this thesis, the behaviour of the materials was defined through the default constitutive models in VecTor2.

In the analyses, geometric nonlinearity was considered since large deformations can alter the material behaviour, the deformations, and resistance to the applied loads. For the concrete stress-strain response characterization, the compression pre-peak curve was defined by the Hognestad Parabola as it is suited for normal strength concrete. The descending portion of the curve was defined by the Modified Park-Kent model. This post-peak model accounts for the enhancement of concrete strength and ductility when the material is confined. In both the column and beam sections, even though poorly spaced stirrups were provided (following the 1965 NBCC provisions), the concrete was partly confined by the out-of-plane legs of the ties and stirrups. The selected post-peak curve is characterized by a linearly descending branch.

Table 4-1: Adopted material models in the FE analysis

Material Property	***Constitutive Model***
Concrete compression base curve (pre-peak)	*Hognestad Parabola*
Concrete compression post-peak	*Modified Park-Kent*
Concrete compression softening	*Vecchio 1992-A (E1/E2-Form)*
Concrete tension stiffening	*Modified Bentz 2003*
Concrete tension softening	*Bilinear*
Concrete confinement strength	*Kupfer/Richart*
Concrete dilatation	*Variable – Isotropic*
Concrete cracking criterion	*Mohr-Coulomb (Stress) Model*
Concrete crack stress calculation	*Basic (DSFM/MCFT)*
Concrete crack width	*Agg/2.5 Max Crack Width*
Concrete crack slip	*Walraven*
Concrete hysteretic response	*Non-Linear with Plastic Offsets*
Concrete bond	*Eligehausen*
Reinforcement hysteretic response	*Bauschinger Effect – Seckin*
Reinforcement Dowel action	*Tassios – Crack Slip*
Reinforcement buckling	*Akkaya – 2012*
Crack spacing	*CEB-FIP 1978 Deformed Bars*

Compression softening models the reduction of the concrete compressive strength once the concrete cracks and due to the tensile straining in the transverse direction, this effect was considered through the model proposed by Vecchio 1992-A (e1/e2-Form). The tension stiffening in the concrete after cracking and caused by the bond action between the reinforcement and the concrete was considered through the Modified Bentz 2003 model. The tension softening defines the post-cracking tensile stress generated in plain concrete, and its effects are significant in lightly reinforced regions. As the beam-column joint was designed based on the

1965 NBCC, it was not reinforced with transverse reinforcement, which makes this region vulnerable to the effects of tension softening. This phenomenon was then modelled by a bilinear descending response provided by the 1990 CEB-FIP model. Furthermore, the confined strength due to out-of-plane reinforcement (stirrups/ties) was modelled based on the Kupfer/Richart model.

As cracking of concrete, specially at the bottom of the columns and beam-column joints, has a significant impact in the behaviour of moment-resisting frames, a crack width check was considered. Essentially, a reduction in the concrete compressive strength is applied when the crack surpasses a defined limit. For this model, the limit was based on the aggregate size utilized in the concrete mix. The concrete hysteretic response was considered through the nonlinear plastic offsets model proposed by Vecchio et al. (2013). It is important to highlight creep and relaxation were not considered in the FE model.

The ductile steel reinforcement model characterized the reinforcement stress-strain response. For the hysteretic response, the Seckin Model with Bauschinger Effect was selected. In this model, the steel reinforcement exhibits premature yielding once load reversal takes place due to stress changes at microscopic level. In addition, to model the shear resistance generated from reinforcing bars crossing a crack slip transverse to its longitudinal axis (dowel action), the Tassios model was selected. This phenomenon is particularly important as dowel action contributes significantly to the shear strength of reinforced concrete members. Furthermore, the Modified Akkaya (2012) model was selected to characterize the buckling of discrete reinforcement, and the bond between concrete and reinforcement was considered perfect given that the development length was explicitly modelled.

VecTor2 requires several mechanical properties to be specified by the user, while others are implicitly determined. For concrete, the compressive strength is the only required property. For the reinforcement, the user must provide bar diameter, cross-sectional area (discrete reinforcement), reinforcement ratio (smeared reinforcement), yielding strength, ultimate strength, modulus of elasticity, and strain hardening and ultimate strains. To consider buckling, an unsupported length (b/t) can be defined. For the BCF model, no unsupported length was defined, but for the retrofitted system model, this parameter was important to capture the response of the core bar within the BRB (Section 4.5.2). The concrete and reinforcement properties for the BCF model are defined in Table 4-2.

Table 4-2: Mechanical properties for concrete and steel from Al-Sadoon (2016)

Property	***Value***
Concrete compressive strength	*30 MPa*
Modulus of elasticity of concrete	*24647.5 MPa*
Yielding strength for 10M steel bars	*481 MPa*
Ultimate Strength for 10M steel bars	*650 MPa*
Modulus of elasticity for 10M steel bars	*200000 MPa*
Strain hardening for 10M steel bars	*1.8%*
Ultimate strain for 10M steel bars	*12%*
Yielding strength for 15M steel bars	*450 MPa*
Ultimate Strength for 15M steel bars	*600 MPa*
Modulus of elasticity for 15M steel bars	*200000 MPa*
Strain hardening for 15M steel bars	*2%*
Ultimate strain for 15M steel bars	*14%*
Yielding strength for 20M steel bars	*430 MPa*
Ultimate Strength for 20M steel bars	*700 MPa*
Modulus of elasticity for 20M steel bars	*200000 MPa*
Strain hardening for 20M steel bars	*1%*
Ultimate strain for 20M steel bars	*12%*

4.5.2 BRB retrofitted frame

The same constitutive models listed in Table 4-1 were defined for the retrofitted frame. The only difference between the two FE models resides on defining the behaviour of the reinforcing material; in the BCF model only deformed steel bars were used. While the ductile steel reinforcement was used for the discrete steel bars and characterized by a linear-elastic region, yielding plateau, and strain-hardening until rupture (Seckin, 1981) as depicted in Figure 4-25 (a); the SE-SMA core bar followed the constitutive model proposed by Abdulridha et al. (2013) as illustrated in Figure 4-25 (b). The SE-SMA constitutive model can capture the pseudo-yielding characteristic of superelastic shape memory alloys and can be employed for the material under both tensile and compressive stress states. The mechanical properties of the SE-SMA are listed in Table 3-1.

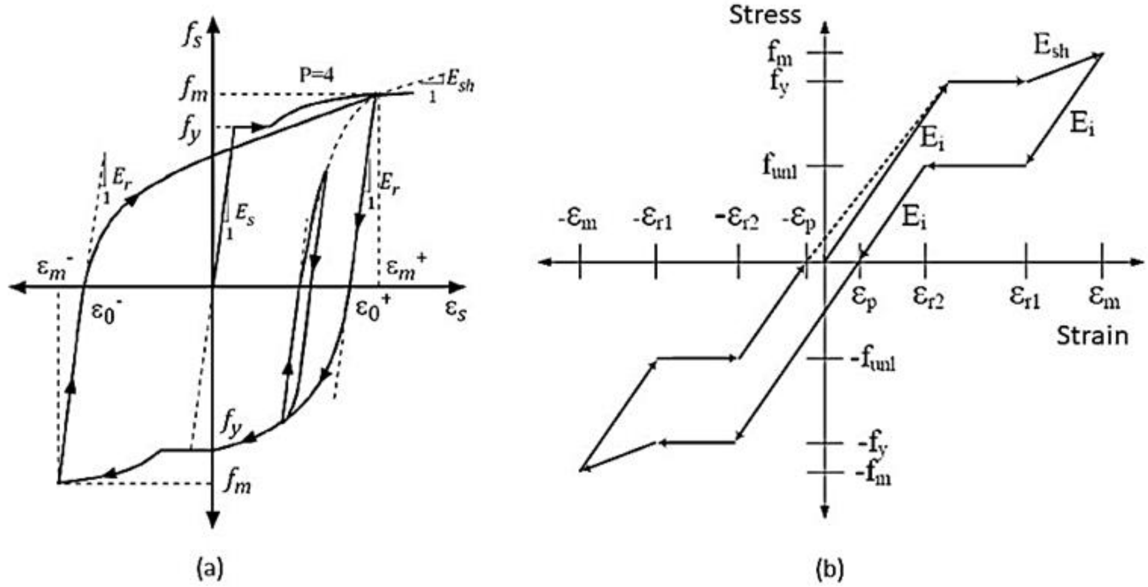

Figure 4-25: Stress-strain response: (a) steel bars (Seckin, 1981); and (b) SE-SMA bars (Abdulridha et al., 2013)

In addition to defining the stress-strain response for the SE-SMA core bar, all core bars evaluated in this study - chrome-molybdenum, stainless steel, and SE-SMA - were also modelled considering an unsupported length (b/t). To determine the unsupported length ratio (b/t), the Dhakal and Maekawa (2002c) method was utilized, where the ratio is calculated as a function of the reduced flexural rigidity, normalized stiffness of the bar, and tie spacing (not applicable for the core bar of the brace). Regarding the concrete compressive strength of the retrofitted frame, it was set to 31 MPa to simulate the properties of the frames tested by Al-Sadoon (2016). Furthermore, the mechanical properties of the core bars are presented in Table 4-3, which were taken from from Al-Sadoon (2016).

Table 4-3: Chrome-molybdenum high tensile steel and Stainless steel mechanical properties (Al-Sadoon, 2016)

Property	***Stainless Steel***	***Chrome-Molybdenum***
Yield stress	*303 MPa*	*390 MPa*
Yield strain	*0.16%*	*0.38%*
Ultimate tensile stress	*505 MPa*	*740 MPa*
Ultimate elongation	*50%*	*10.8%*
Young's modulus	*199.2 GPa*	*190.5 GPa*

A perfect bond between the core bars of the BRB and the surrounding material (fixed orthotropic) was considered since the unsupported length was defined separately. The fixed orthotropic model is characterized by a material in which the mechanical properties vary significantly in two or more directions. No relationship between the two directions is assumed in VecTor2, thus this provides an alternative to model a novel material or to eliminate load transfer in a specified direction. The fixed orthotropic material was defined with a longitudinal axis oriented 41 degrees from the horizontal axis, the same angle as the BRB (Figure 4-11). The longitudinal compressive and tensile strength was set to 0 as no loading should be carried by the restraining region. However, as the restraining material, which surrounds the core bar, is present to provide buckling restraining to the bar, a 45 MPa transverse compressive and tensile strength was assigned to the orthotropic material. The 45 MPa is the average strength of the concrete mortar assumed in the BRB design.

4.6 Finite element model validation

Results from the experimental testing of the bare concrete and BRB retrofitted moment-resisting frames conducted by Al-Sadoon (2016) were used to validate the results from the static analyses in this thesis. The capacity of the bare concrete frame from the numerical analysis deviated less than 2% in relation to the experimental response from Al-Sadoon (2016), as it is illustrated in Figure 4-26. For the BRB retrofitted frame incorporating a Stainless Steel core, a margin of error was expected given that the system tested by

Al-Sadoon (2016) could not completely avoid load bearing in the brace. As a result, the difference in lateral strength capacity from the numerical model to the tested frame was approximately 7% on average. In addition, the models satisfactorily captured the overall behaviours and failure modes. The similarities were an indication that the reverse cyclic nonlinear analyses conducted in this thesis could adequately predict the response of the bare concrete and BRB retrofitted frames. The FE model validation is thoroughly discussed in Chapter 7, Section 7.3.

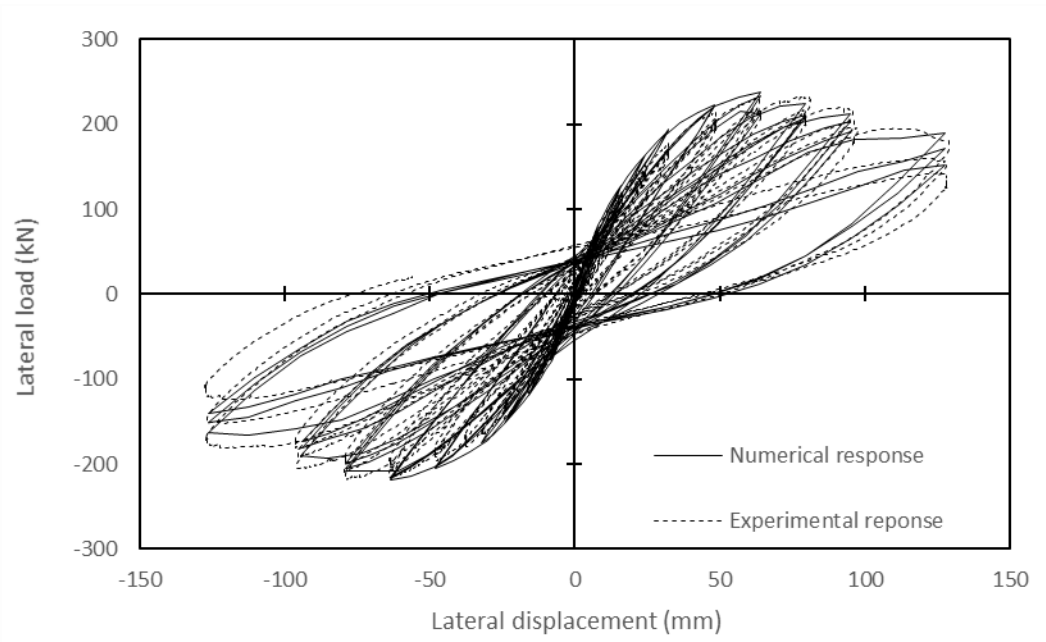

Figure 4-26: Hysteretic numerical and experimental (Al-Sadoon, 2017) response

Chapter 5

Nonlinear static numerical analyses and results

5.1 Introduction

This chapter presents the methodology and results of the numerical analysis conducted in this thesis. For the analyses, the RC frames were modelled as 2-D, two-third scale of the prototype frame. The results were obtained through the program Augustus, a post-processor of VecTor2 (Vecchio et al., 2013). The frames were subjected to pushover and reverse cyclic analyses to evaluate strength capacity, failure mechanism, residual displacements, crack patterns, and for the validation process of the model.

The finite element model was validated against the experimental results in the literature (Al-Sadoon, 2016), where reinforced concrete frames were subjected to incrementally increasing reverse cyclic lateral displacements. The numerical results for both the bare concrete and BRB retrofitted frames are compared to the experimental results from Al-Sadoon (2016). Furthermore, this chapter provides the results obtained from static analysis of the frame retrofitted with a modified BRB, which addresses the deficiencies of the buckling-restrained brace from Al-Sadoon (2016). When modelling the SE-SMA bars, the study by Abdulridha and Palermo (2017) was essential to model the constitutive response of the material in the finite element program. The chapter ends with sensitivity analyses on the impact of the different constitutive models on the response of the frame under static loading.

5.2 Loading application

Two types of nonlinear static analysis were conducted: pushover and reverse cyclic. Independent of the analysis type, gravity loads were applied on both columns and the beam as depicted in Figure 5-1. A load that corresponds to 25% of the column axial compressive resistance was applied on the columns and scaled gravity loads were applied on the beams. An axial load placed on top of the columns influences the stiffness and lateral strength of the frame; hence, the applied value was based on scaled dead and live load combinations for the frame. For the static nonlinear analyses, the lateral load simulating earthquake actions was displacement-controlled, and incremental displacements were applied at the mid-height of the beam in the horizontal direction. For the pushover analysis, the lateral load was applied as shown Figure 5-1; while for the reverse cyclic analysis, the location of the lateral load varied for the positive and negative cycles as shown in Figure 5-2. The load was applied in a pushing manner to avoid local distortions that are associated when pulling on an element.

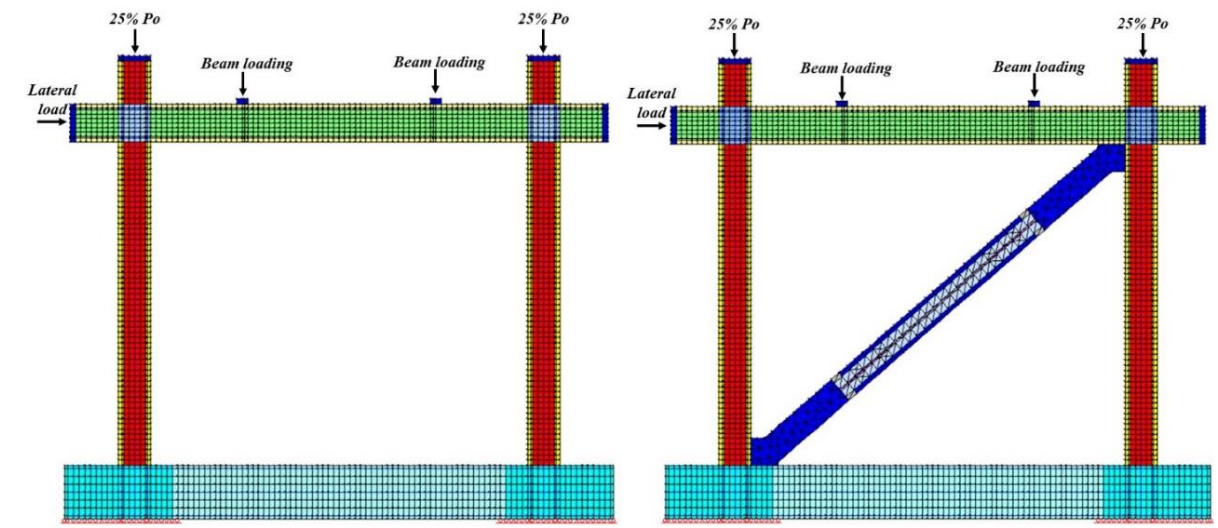

Figure 5-1: Loading scheme for the control and BRB retrofitted RC frames under pushover loading

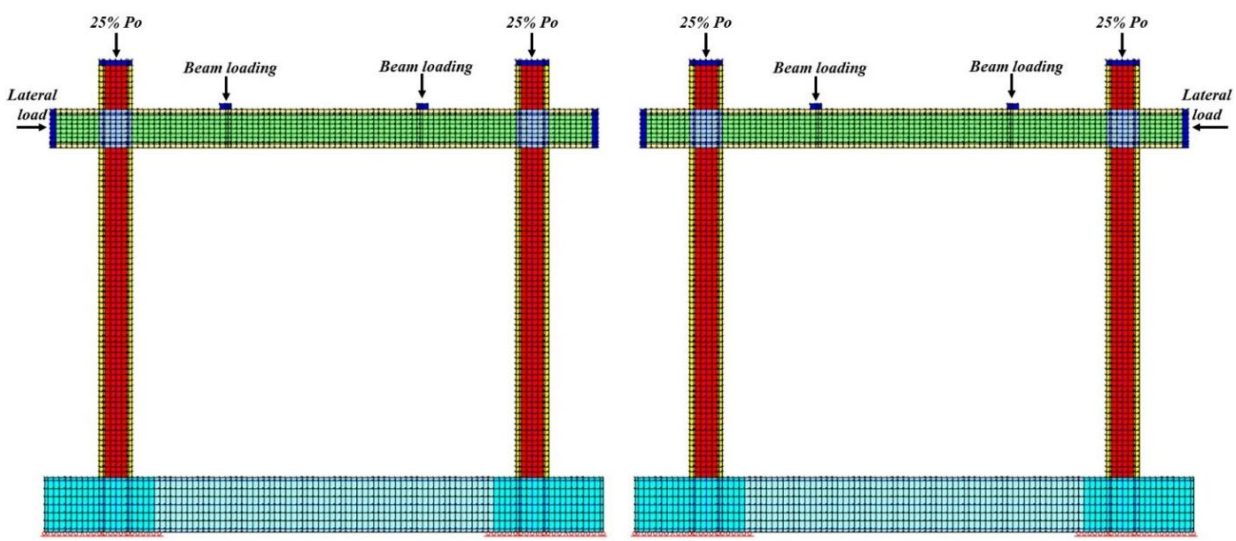

Figure 5-2: Loading scheme for the frames under reverse cyclic loading

5.3 Pushover analysis

The pushover analysis was conducted by applying at the beam mid-height incremental lateral displacements of 1 mm. From the pushover response, the lateral strength, effective stiffness, yield point, ultimate displacement, and displacement ductility were established. For the BRB retrofitted frames, the pushover analysis was conducted twice to compute the results with the brace under tension and compressions stress states separately.

The lateral strength was approximated as the maximum strength capacity of the frame under pushover loading. To determine the yield point, the Reduced Stiffness Elasto-Plastic Yield Method by Park (1988) was utilized (Figure 5-3). The method captures a reduction in the stiffness of the structure due to cracking near the end of the elastic range, which accurately determines the yield deformation of reinforced concrete structures (Maciel, 2019). In this method, the yield displacement (Δ_y) is approximated from the intersection between the secant stiffness and the maximum strength (F_{max}). The yield strength (F_y) is the lateral load corresponding to that displacement. The secant stiffness was determined at 75% of the maximum lateral strength. Furthermore, the effective stiffness was calculated as the slope of the secant stiffness branch intercepting the yielding point.

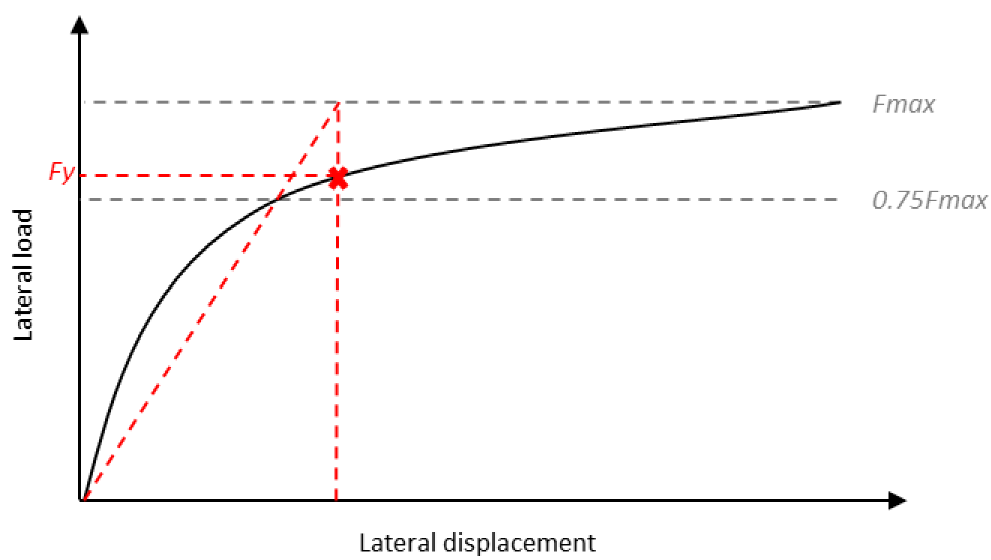

Figure 5-3: Reduced Stiffness Elasto-Plastic Yield Method (Adapted from Park, 1988)

The lateral displacement capacity (Δ_u) of the frames was defined, in the post-peak branch, as the displacement corresponding to 80% of the peak lateral load, the displacement corresponding to the peak lateral load, or the displacement prior to fracturing of the reinforcement. The displacement ductility (μ) was defined as the ratio between the ultimate (Δ_u) and yield (Δ_y) displacements. In discussing yielding in BRBs that incorporate SE-SMA core bars, it is important to note that yielding does not imply permanent inelastic deformations. Therefore, the pseudo-yielding point was calculated as the equivalent yielding point of the steel core BRB retrofitted frames.

Under pushover loading, nine frames were analyzed: a bare concrete frame to serve as a control frame; four frames retrofitted with the BRB proposed by Al-Sadoon (2016) incorporating stainless steel, chrome-molybdenum, SE-SMA, and SE-SMA with constant 44.5 mm diameter as the core bars; and four retrofitted frames with the improved BRB incorporating stainless steel, chrome-molybdenum, SE-SMA, and SE-SMA with constant 44.5 mm diameter as the core bars. The frames were analyzed twice to induce compression and tensile stresses on the brace separately.

5.3.1 Bare Concrete Frame (BCF)

Figure 5-4 illustrates the pushover response of the Bare Concrete Frame (BCF). The yield point of BCF was determined at a displacement of 38 mm and a lateral strength of 207 kN. A maximum lateral strength of 235 kN and a 5.4 kN/mm effective stiffness was experienced by the bare frame. As the ultimate displacement was evaluated at a drop of 20% of the peak lateral strength, the ultimate displacement was 150 mm. Therefore, the displacement ductility was equal to 3.9. Figure 5-5 illustrates the response of the BCF under pushover loading in the opposite direction. The differences in response were negligible.

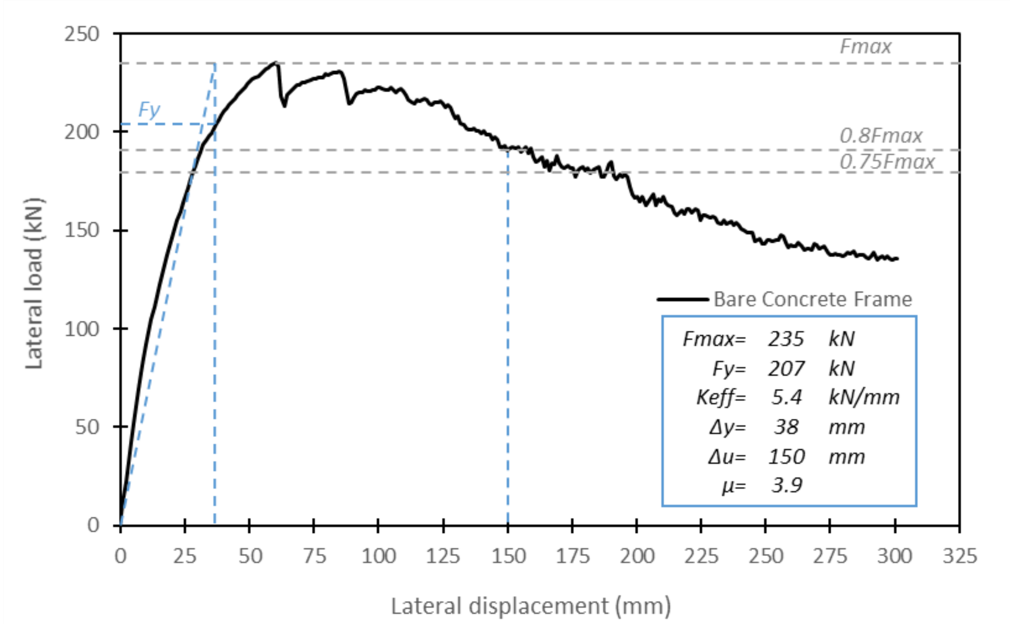

Figure 5-4: Pushover response of Bare Concrete Frame with lateral displacements applied on the left side

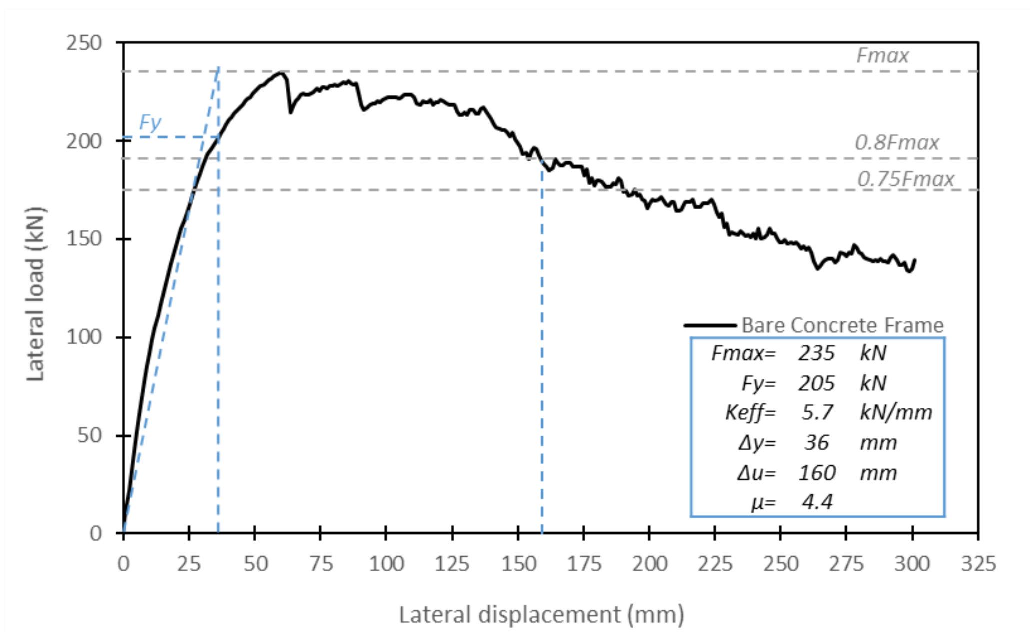

Figure 5-5: Pushover response of BCF with lateral displacements applied on the right side

5.3.2 Stainless Steel core BRB retrofitted frames

Figure 5-6 illustrates the pushover response of the Stainless Steel core BRB frame when the brace is under tension; while Figure 5-7 illustrates the response under compression. From Figure 5-6, the yield point was approximated through the Reduced Stiffness Elasto-Plastic Yield Method (Park, 1988) at a displacement of 67 mm and a strength of 557 kN. The lateral capacity of the frame was of 696 kN, and the ultimate displacement was of 229 mm. Furthermore, the displacement ductility was 3.4 and the effective stiffness was 8.3 kN/mm.

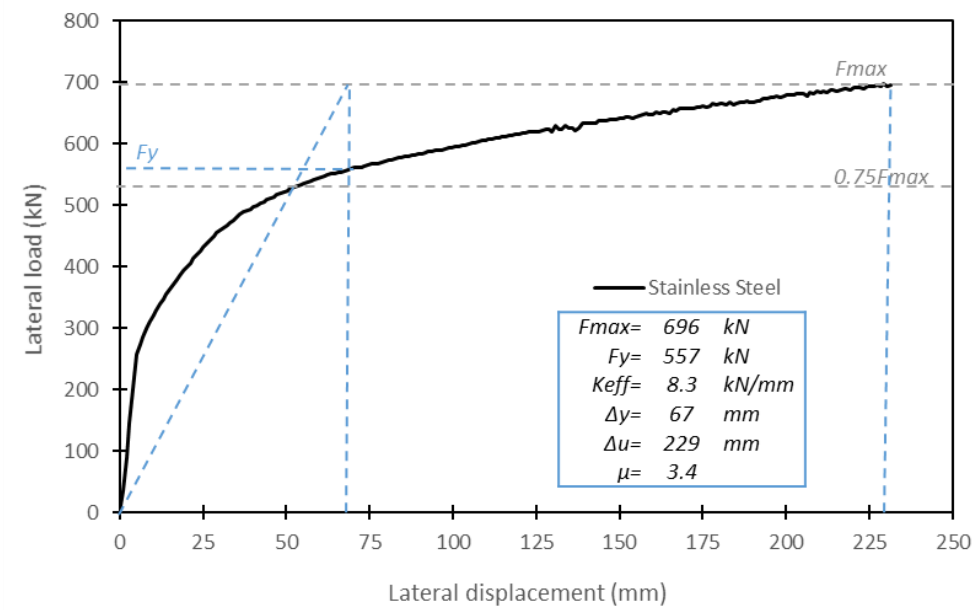

Figure 5-6: Pushover response of the Stainless Steel core BRB retrofitted frame with brace under tension

Figure 5-7 presents the behaviour of the frame with the brace core under compression. The maximum lateral strength was 514 kN, while the yield strength corresponded to 426 kN. The frame was able to sustain a maximum displacement of 90 mm, and yielding initiated at a displacement of 35 mm. This resulted in a displacement ductility equal to 2.6, which is lower than what the frame experienced when the brace was under tension. The effective stiffness was calculated as equal to 12.2 kN/mm.

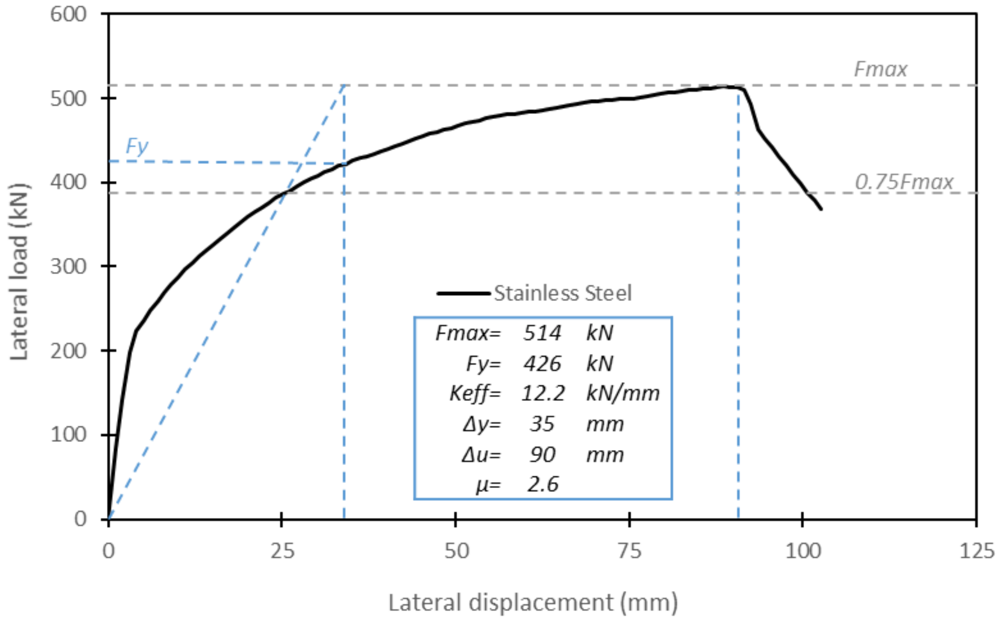

Figure 5-7: Pushover response of the Stainless Steel core BRB retrofitted frame with brace under compression

The lateral load–lateral displacement responses under pushover loading of the frame retrofitted with the improved BRB that incorporates a stainless steel core are represented in Figures 5-8 and 5-9. Under tension loading of the brace (Figure 5-8), the lateral capacity was 698 kN and the ultimate displacement corresponded to 231 mm. The yield point was established at a displacement of 68 mm and a corresponding lateral strength of 558 kN. The resulting displacement ductility was 3.4 and effective stiffness was 8.2 kN/mm.

Figure 5-9 illustrates the response of the frame with the improved BRB system under compression. In this case, the yield point corresponded to a displacement of 52 mm, and the ultimate displacement at 178 mm. This resulted in a displacement ductility of 3.4. The frame experienced a peak lateral strength of 584 kN. The effective stiffness, based on the yield point, was equal to 9.1 kN/mm.

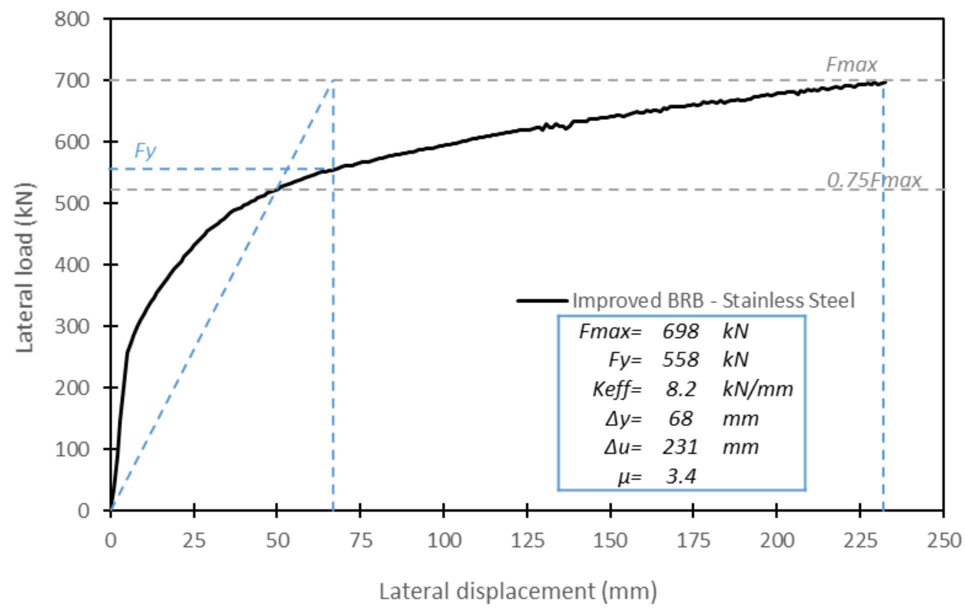

Figure 5-8: Pushover response from the improved BRB with Stainless Steel core under tension

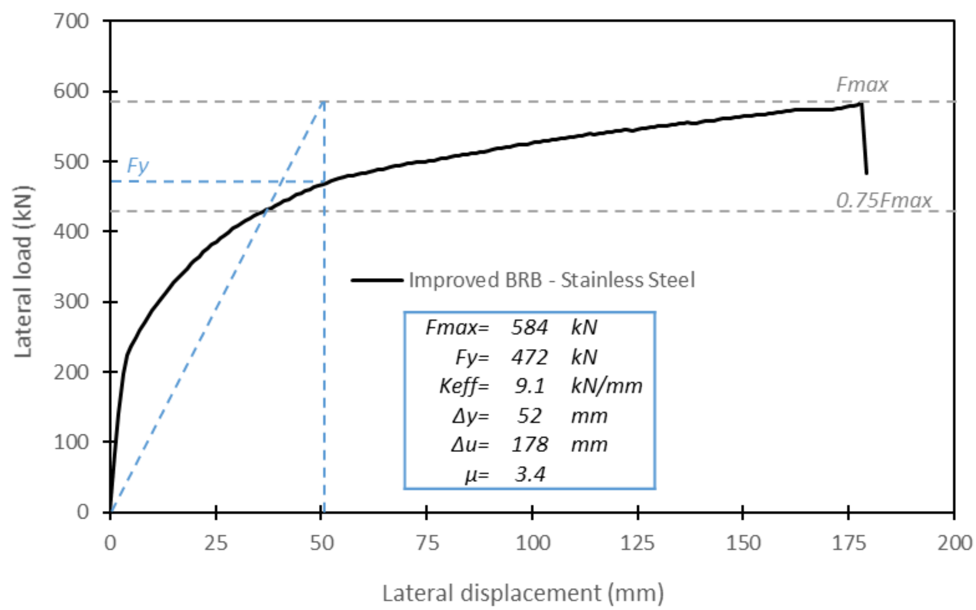

Figure 5-9: Pushover response from the improved BRB with Stainless Steel core under compression

5.3.3 Chrome-Molybdenum core BRB retrofitted frames

Figure 5-10 illustrates the pushover response of the frame retrofitted with the BRB from Al-Sadoon (2016) incorporating a Chrome-Molybdenum core. The frame sustained a peak lateral strength of 813 kN and an ultimate displacement of 171 mm. The structure yielded at a displacement of 49 mm and with a 668 kN lateral strength; the effective stiffness was then calculated as 13.6 kN/mm. The ratio between the ultimate and yield displacements was 3.5.

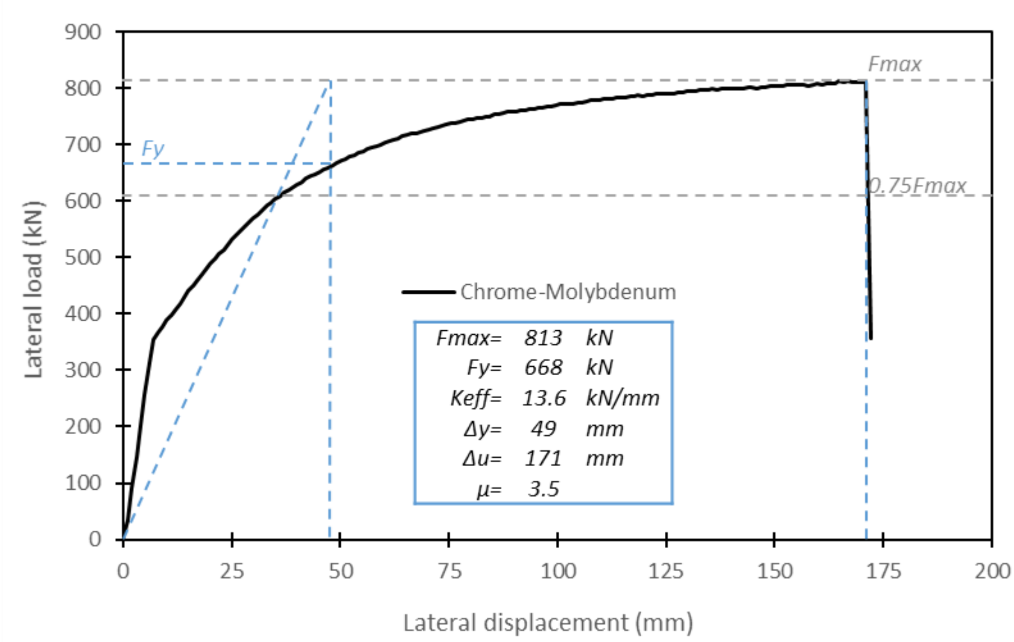

Figure 5-10: Pushover response of the Chrome-Molybdenum core BRB retrofitted frame with brace under tension

Figure 5-11 provides the response of the same retrofitted frame with the brace under compression. The retrofitted system was able to experience a maximum lateral displacement of 61 mm. The peak strength experienced by the frame corresponded to 550 kN. Yielding was established at a displacement of 24 mm and a lateral strength of 448 kN resulting in an effective stiffness of 18.7 kN/mm. Hence, the displacement ductility was of 2.5.

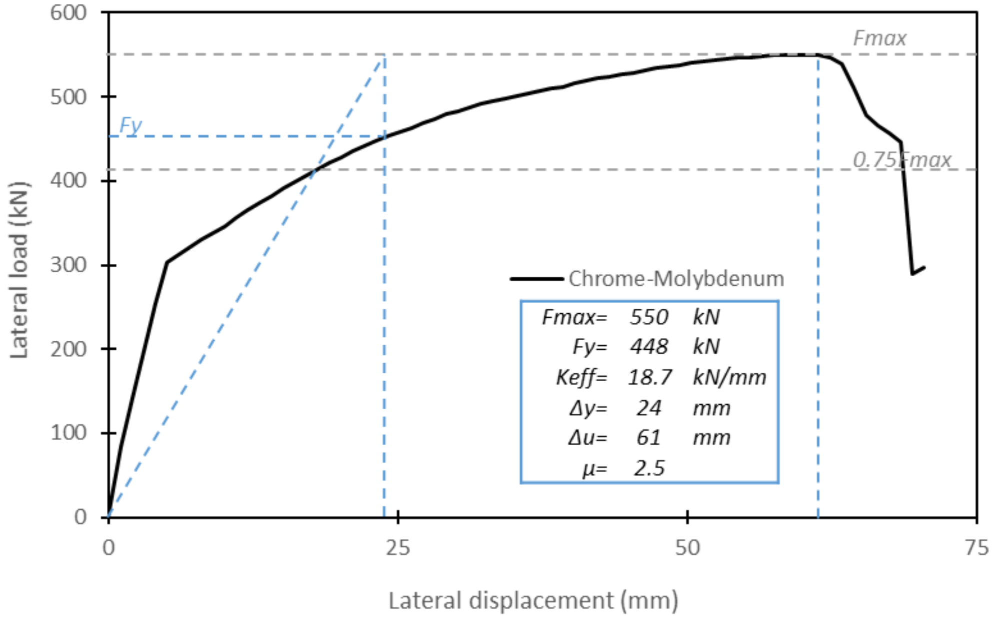

Figure 5-11: Pushover response of the Chrome-Molybdenum core BRB retrofitted frame with brace under compression

In addition, the frame was numerically evaluated with the improved BRB incorporating a Chrome-Molybdenum core. For this frame, with the brace under tension (Figure 5-12), the lateral capacity was 879 kN with an ultimate displacement of 168 mm. The frame experienced yielding at a displacement of 49 mm corresponding to a lateral strength of 716 kN. The effective stiffness was calculated as 14.6 kN/mm and the displacement ductility was 3.4.

For the same system with the brace under compression (Figure 5-13), the frame experienced a peak lateral strength of 774 kN and an ultimate displacement of 181 mm. The yield point was located at a displacement of 51 mm, which resulted in a ductility ratio of 3.6. The effective stiffness of the frame was slightly lower related to the brace under tension equating to a value of 12.5 kN/mm.

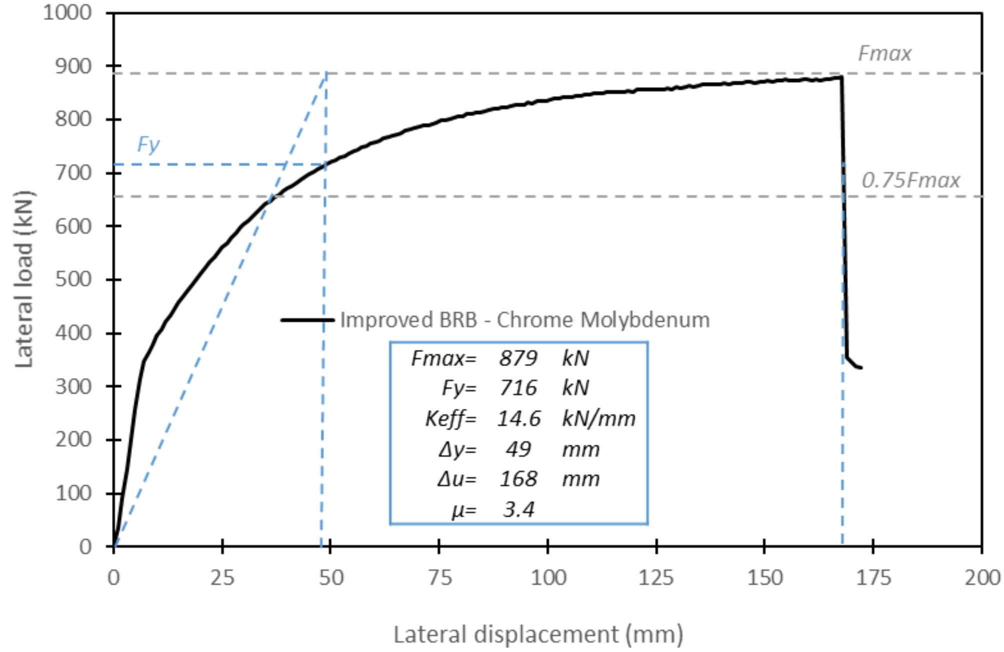

Figure 5-12: Pushover response from the modified BRB with Chrome-Molybdenum core under tension

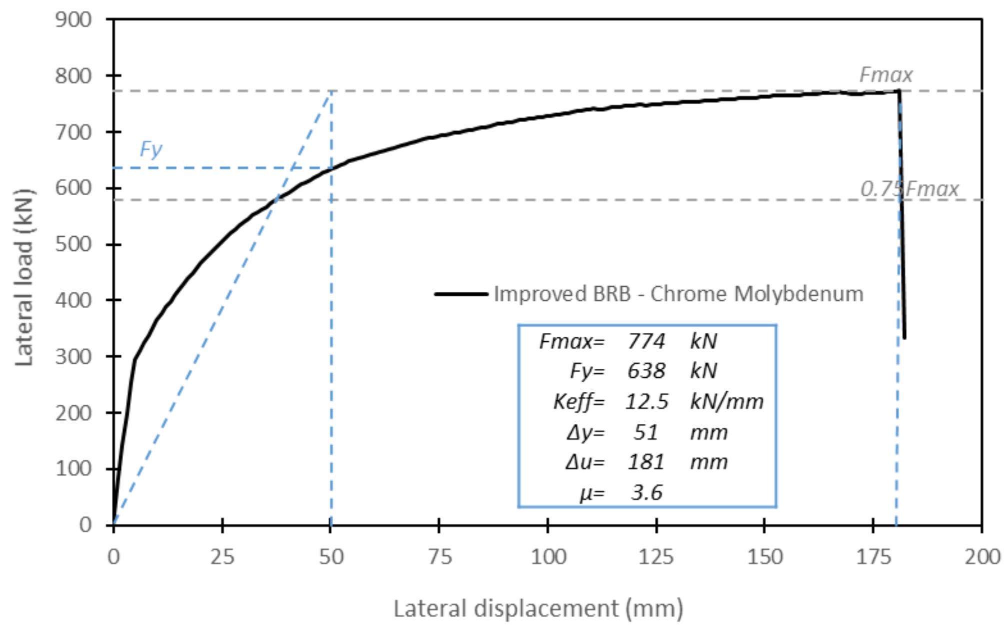

Figure 5-13: Pushover response from the modified BRB with Chrome-Molybdenum core under compression

5.3.4 BRB retrofitted frames incorporating SE-SMA

The frame retrofitted with the original BRB was also evaluated in VecTor2 (Vecchio et. Al, 2013) incorporating a SE-SMA core bar. As discussed in Chapter 3, SE-SMA bars have two defined responses: pseudo-yielding and followed by stiffening. To efficiently incorporate SMAs in a structure, the material should be limited to the pseudo-yielding phase, which refers to the phase the material is able to fully recover its original length. Figure 5-14 illustrates the pushover response of the SE-SMA core BRB system under tension; while Figure 5-15 illustrates the system response with the brace under compression.

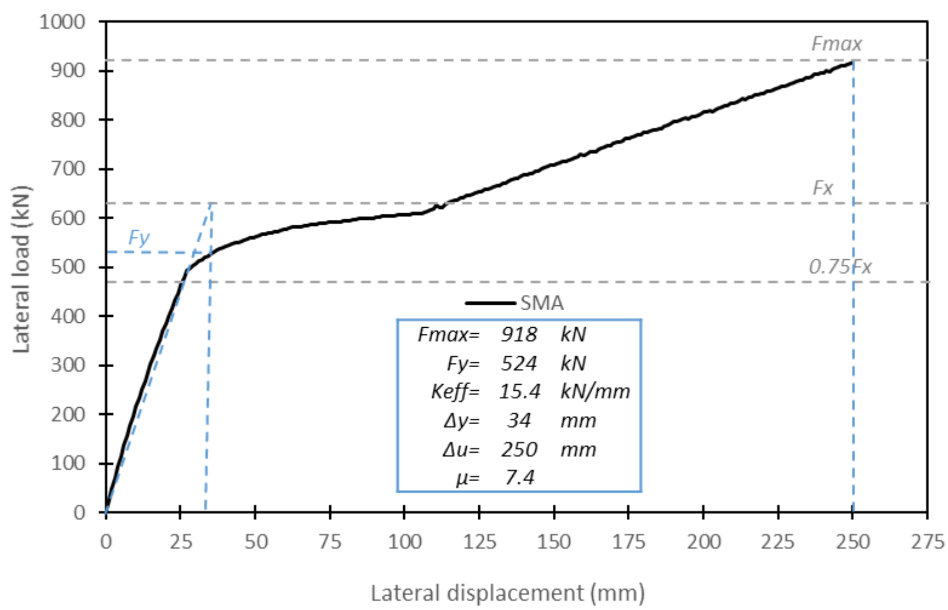

Figure 5-14: Pushover response of the BRB retrofitted frame with SE-SMA core under tension

Since the maximum lateral strength of the BRB retrofitted system differed from the maximum capacity for the system to be efficient, the pseudo-yielding was calculated based on the force F_x rather than the peak strength. The force F_x can be understood as the maximum design force for the SE-SMA bar to be efficiently utilized, given that beyond this force level the SMA bar exhibits the stiffening phase and is not able to recover its original length jeopardizing its self-centering capability. Therefore, Figure 5-14 illustrates the behaviour of the improved BRB incorporating the SE-SMA core under tension. The reduced stiffness equivalent elasto-plastic yield method resulted in a pseudo-yield displacement of 34 mm and corresponding for of 524 kN. The frame experienced an effective stiffness of 15.4 kN/mm and sustained loads up to an ultimate displacement of 250 mm. Hence, a displacement ductility of 7.4 was calculated.

Figure 5-15 illustrates the same retrofitted system with the brace under compression. This frame experienced a maximum lateral strength of 660 kN and an ultimate displacement of 187 mm. The pseudo-yielding point was determined at a displacement of 34 mm and lateral strength of 464 kN. Based on the pseudo-yielding point, the effective stiffness was calculated as 13.6 kN/mm. The displacement ductility ratio was approximated as 5.5.

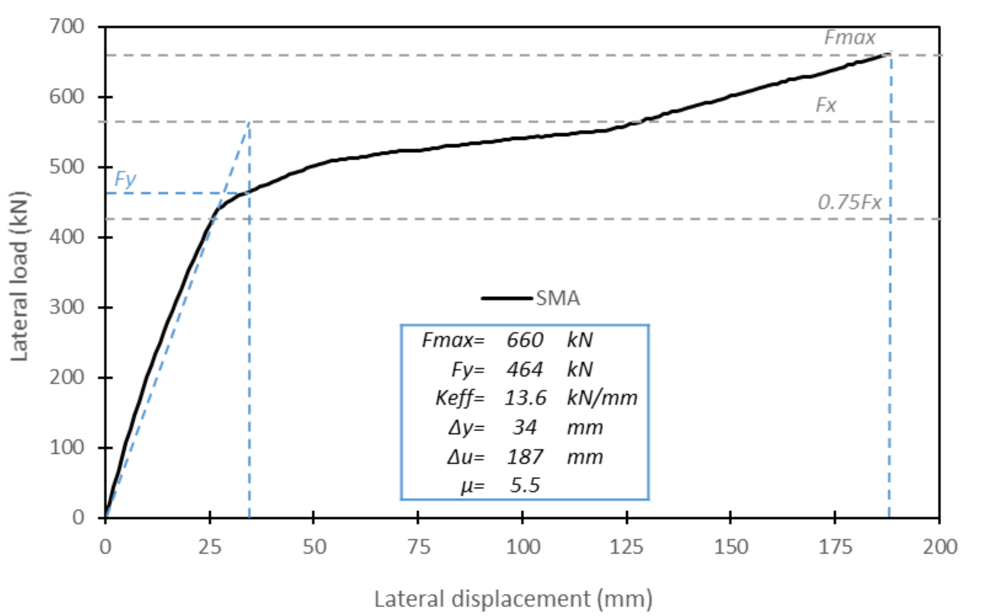

Figure 5-15: Pushover response of the BRB retrofitted frame with SE-SMA core under compression

The frame retrofitted with the modified BRB system that incorporates a SE-SMA core was also investigated. Figure 5-16 illustrates the pushover response of the system. The frame was able to sustain a displacement of 250 mm with a peak strength of 916 kN. The pseudo-yield strength was defined as 527 kN at a displacement of 35 mm. Hence, the ductility displacement and effective stiffness were calculated as 7.1 and 15.1 kN/mm, respectively.

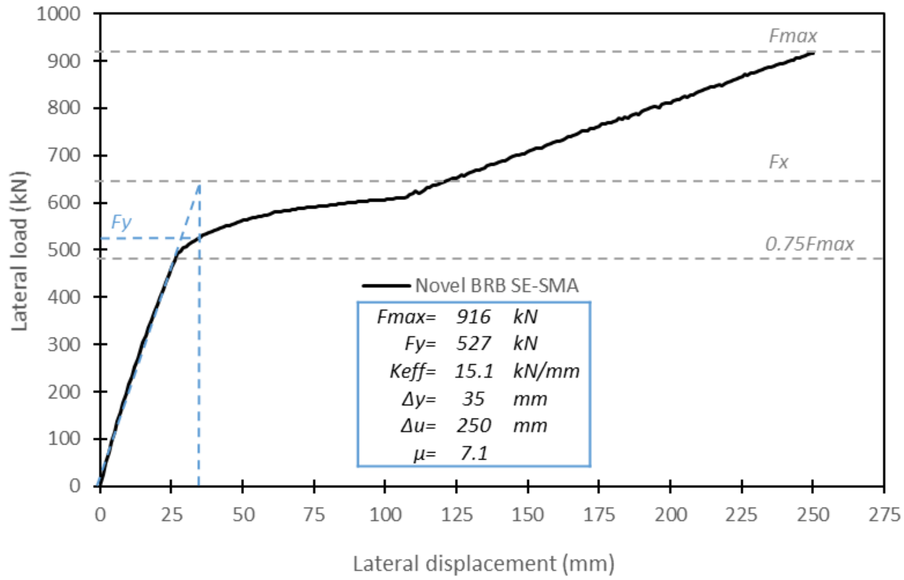

Figure 5-16: Pushover response of the modified BRB with SE-SMA core under tension

For the same system with the brace under compression, the pushover response is presented in Figure 5-17. The maximum load capacity corresponded to 700.7 kN. The pseudo-yielding point corresponded to 34 mm and 464 kN. The effective stiffness was then calculated as 13.6 kN/mm. The frame was able to experience a maximum displacement of 216 mm, which resulted in a displacement ductility of 6.4.

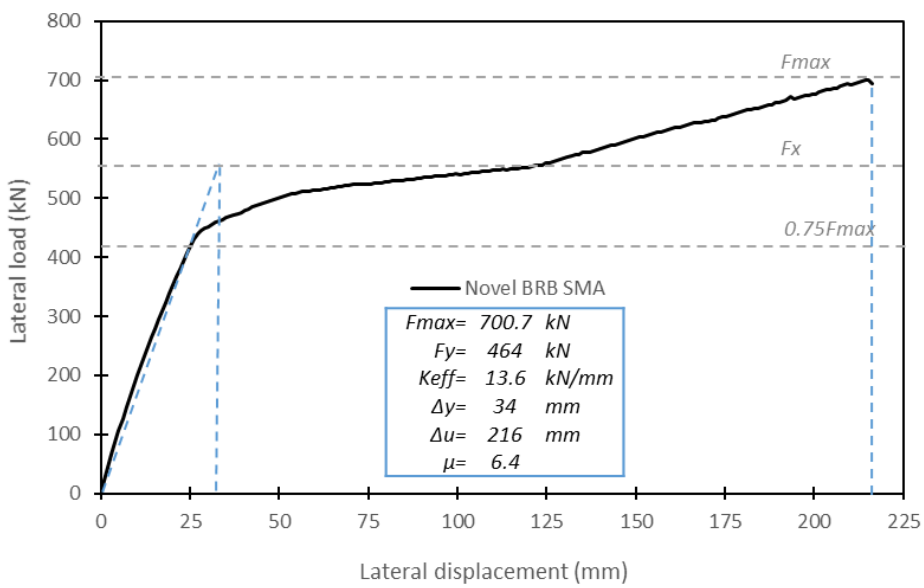

Figure 5-17: Pushover response of the modified BRB with SE-SMA core under compression

5.3.5 BRB retrofitted frames with constant 44.5 mm SE-SMA core

In addition to BRB that incorporated the same SE-SMA core bar size as the other conventional steel cores designed by Al-Sadoon (2016) and previously presented in this chapter, a SE-SMA bar with uniform 44.5 mm diameter was evaluated. Figure 5-18 illustrates this retrofitted frame system with the brace under tension. The pseudo-yielding point occurred at a displacement of 41 mm and lateral strength of 796 kN. The frame experienced a maximum lateral strength of 1300 kN and an ultimate displacement of 366 mm. Therefore, the effective stiffness and displacement ductility were equal to 19.4 kN/mm and 8.9, respectively.

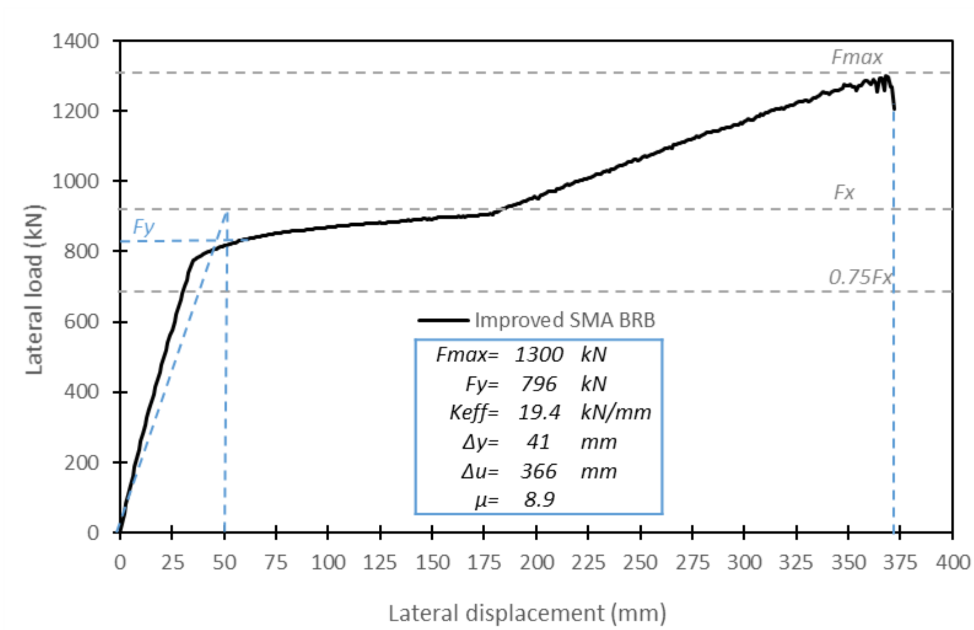

Figure 5-18: Pushover response of the SE-SMA BRB with 45.5 mm diameter core under tension

In Figure 5-19, the same frame was evaluated with the brace subject to compression. The frame experienced an ultimate lateral displacement of 342 mm and a peak lateral strength of 1023 kN. The pseudo-yielding point was determined at a displacement of 42 mm and a corresponding strength of 706 kN. As a result, the effective stiffness was determined as 16.8 kN/mm and the displacement ductility as 8.1.

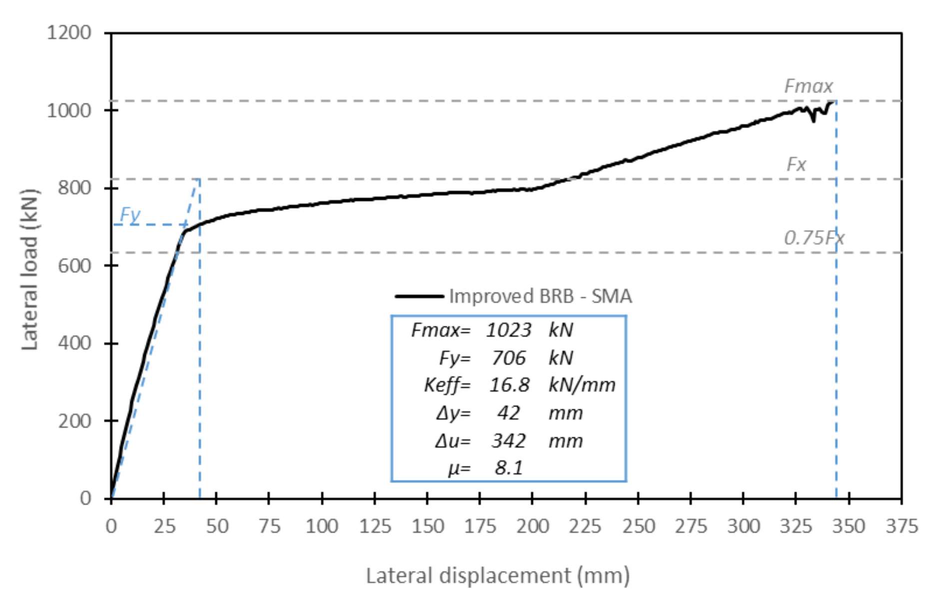

Figure 5-19: Pushover response of the SE-SMA BRB with 45.5 mm diameter core under compression

The 44.5 mm-diameter SE-SMA core bar was also incorporated in the modified BRB (Figure 5-20). For the brace under tension, the frame could sustain a lateral displacement of 375 mm and a force of 1302 kN. The pseudo-yielding point occurred at 39 mm and 790 kN. Therefore, the effective stiffness and displacement ductility were determined as 20.3 kN/mm and 9.6, respectively.

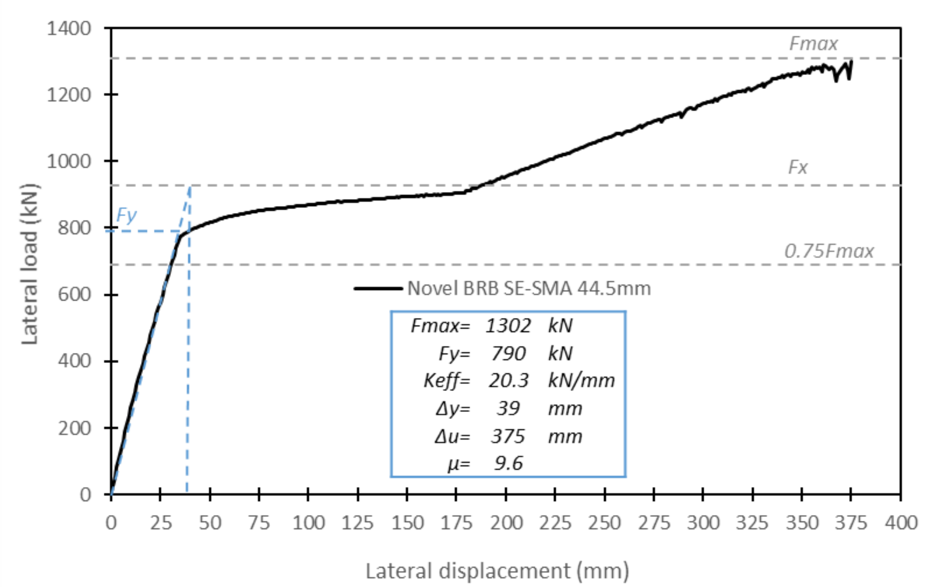

Figure 5-20: Pushover response of the modified BRB with 45.5 mm-diameter SE-SMA core under tension

For the same frame with the modified brace under compression (Figure 5-21), the displacement ductility was calculated as 8.8 since the pseudo-yielding displacement was equal to 39 mm and the maximum displacement was 345 mm. The system provided a peak lateral capacity of 1034 kN and pseudo-yielding strength of 698 kN.

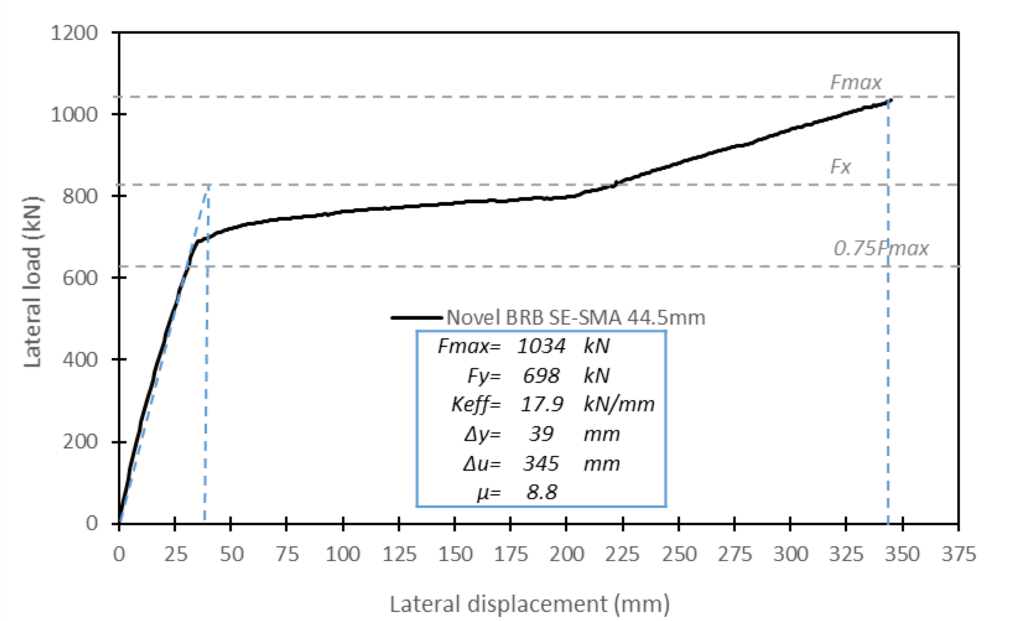

Figure 5-21: Pushover response of the modified BRB with 45.5 mm diameter SE-SMA core under compression

The pushover analyses of the frame provided insights over the behaviour of the retrofitted system once the brace is under tension and compression. It was verified higher loads and displacements were obtained when the brace was in tension as concentration of stresses were avoided, so once the brace is under compression lower strength and displacement capacity were experienced by the system, Furthermore, modified braces provided enhancements in both strength and displacement capacity.

5.4 Reverse cyclic analysis

The frames were also subjected to reverse cyclic analysis. In addition to the gravity loads applied on the models – 800 kN on each column and the two point loads (62 kN each) applied on the beam at a distance of 0.85 m from the beam-column joints, each of 62 kN - the seismic load was simulated with incrementally increasing displacement reversals applied at the mid-height of the beam. Furthermore, three repetitions were applied at each lateral displacement level. The displacement cycles were based on suggestions by existing loading protocols (ACI-374.1-05, 2006).

Two different loading programs were utilized. The loading protocol illustrated in Figure 5-22 was applied to the bare concrete frame; while the protocol illustrated in Figure 5-23 was used for the retrofitted frames. The loading program for the retrofitted frames consisted of additional cycles to closely evaluate the performance of the BRB during the analysis given that these retrofitted frames present a higher stiffness. Furthermore, the loading protocols were consistent with those used during testing of the frames by Al-Sadoon (REF HERE). The BCF was loaded in drift increments of 0.25% until a drift of 1%. From a drift of 1% to a drift of 3%, the increments were 0.5%. Thereafter, a drift of 4% was applied. For the BRB retrofitted frames, lateral loaded was in increments of 0.175% until a drift of 0.75%. Between drifts of 1% and 3%, the same 0.5% drift increments were applied. Beyond a 3% ratio, the increments were 1%.

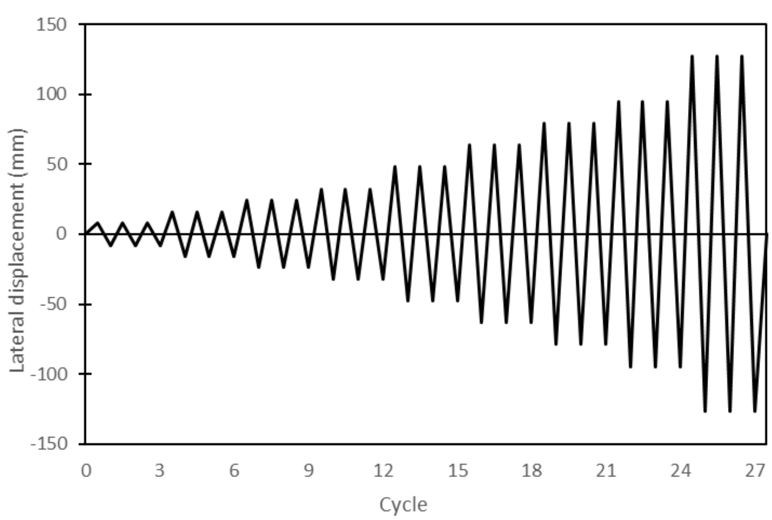

Figure 5-22: Load protocol for reverse cyclic analysis of the bare concrete frame

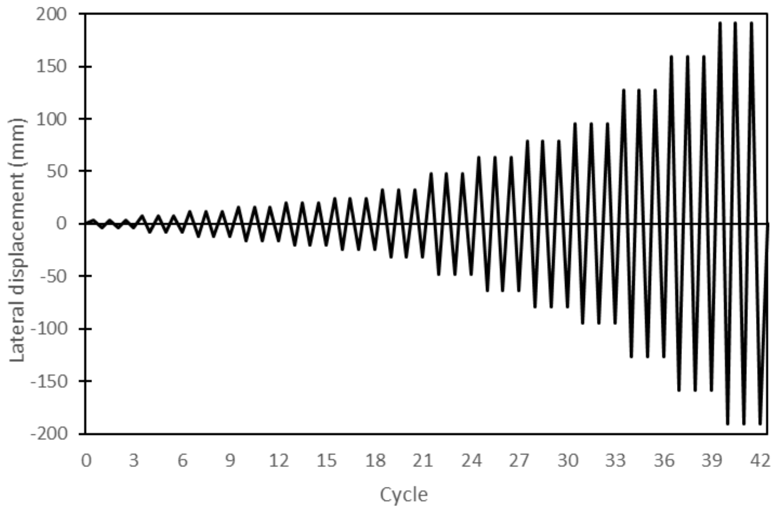

Figure 5-23: Load protocol of reverse cyclic analysis of BRB retrofitted frames

The drift was calculated as the ratio of the lateral displacement applied at the mid-height of the beam to the height of the frame – taken as the height from the bottom of the column to where lateral displacements were applied. The hysteretic responses from the nonlinear reverse cyclic analysis of the frames are presented in this section. The lateral load–lateral displacement responses illustrate the nonlinear response of the frames under displacement reversals. Furthermore, information regarding failure mode and crack patterns are presented. The failure mode was assessed based on the stresses and strains in the reinforcing steel bars, concrete elements, and bracing core. The reverse cyclic analysis was conducted on six different frames. Three of those frames were previously tested by Al-Sadoon (2017): a Bare Concrete Brame (BCF), and Chrome-Molybdenum core (CM-BRB) and Stainless Steel core (SS-BRB) BRB retrofitted frames. The three remaining frames were retrofitted with the modified BRB; those BRB systems incorporated a Chrome-Molybdenum (CM-NBRB), a Stainless Steel (SS-NBRB), and a Superelastic Shape-Memory Alloy (SMA-NBRB) core bar. It is important to note that all the bracing cores incorporated the same dimensions as discussed in Section 4.3.2.

5.4.1 Bare Concrete Frame (BCF)

The hysteretic response of the BCF is presented in Figure 5-24. The frame sustained a peak strength (F_{max}) of 238 kN in the positive direction. The effective stiffness (k_{eff}) was approximated as 5.6 kN/mm. This stiffness was determined based on the Reduced Stiffness Equivalent Elasto-Plastic Yield Method by Park (1988), which approximates k_{eff} as the slope of the loading branch that goes through the yield point. Yielding initiated at a displacement (Δ_y) of 36 mm with a corresponding lateral strength of 202 kN. The frame sustained deformations up to a lateral displacement of 127 mm at which point the lateral capacity dropped more than 20% from the peak strength of the frame ($0.8F_{max}$). Therefore, the ultimate drift capacity of the frame was 3%.

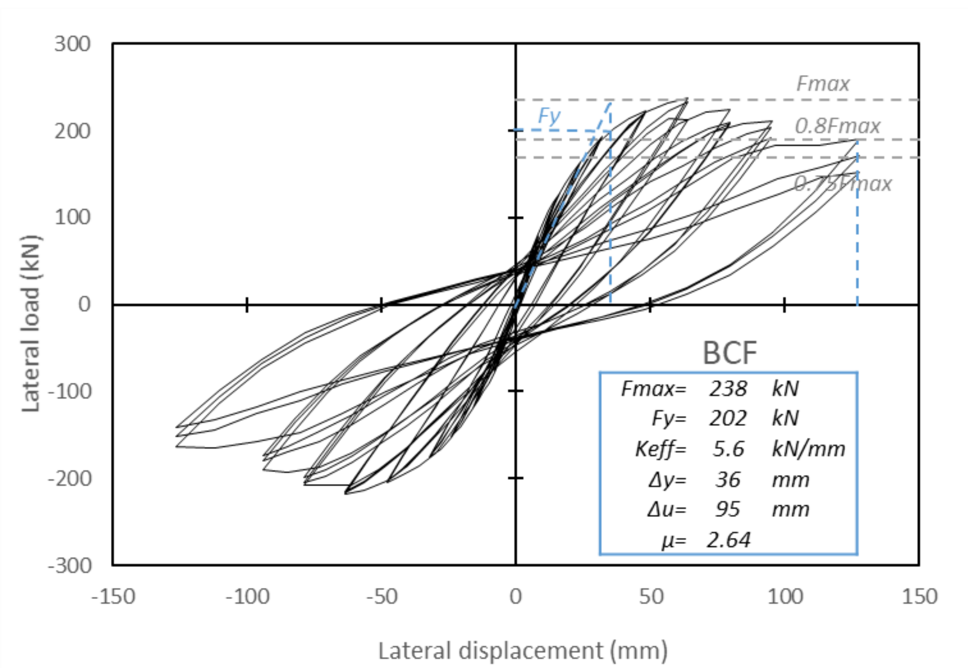

Figure 5-24: Lateral load – lateral displacement hysteretic response of the bare concrete frame

Figures 5-25 and 5-26 illustrate the displaced shape and crack patterns of the bare concrete frame at different drifts. Figure 5-25 provides an overview of the frame subjected to a drift of 2%. The 2% drift corresponds to the peak lateral strength of the frame. At this drift, 3.180 mm-wide cracks were formed at the bottom of the columns, while 2.350 mm-wide cracks were recorded in the beam-column joints. At 4% drift (Figure

5-26), the cracking expanded and the base of the columns experienced cracks up to 5.150 mm wide in the left column, and 6.120 mm wide in the right column. At the same drift, concrete spalling was evident in the beam-column joints, where cracks 10.810 mm wide were captured.

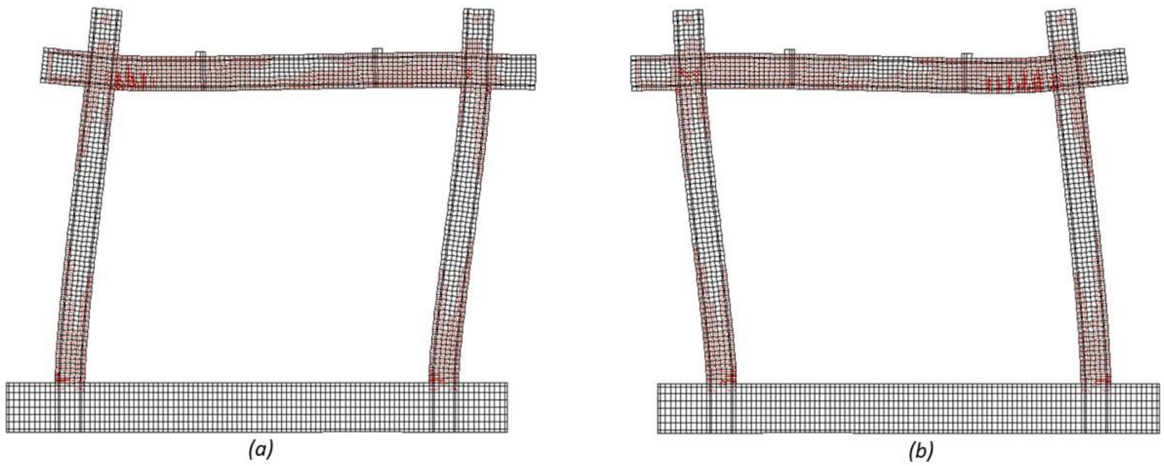

Figure 5-25: Displaced shape and crack patterns of BCF at peak strength (drift of 2%): (a) positive direction; (b) and negative direction

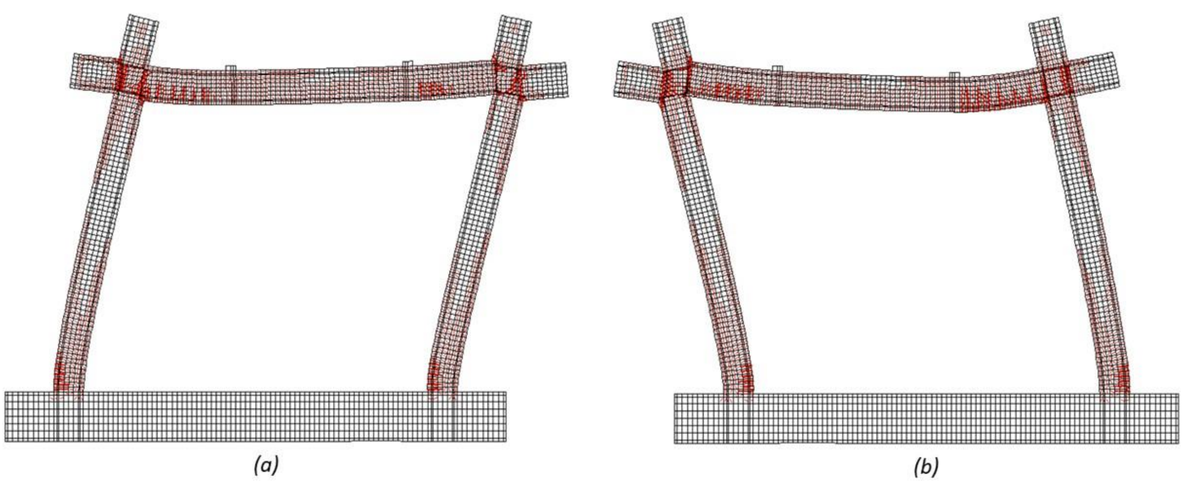

Figure 5-26: Displaced shape and crack patterns of BCF at peak drift (drift of 4%): (a) positive direction; (b) and negative direction

Figure 5-27 (a) illustrates the displaced shape and crack patterns of BCF at zero-load following the 4% drift cycle. A top permanent displacement of 52 mm was observed, and concrete spalling was evident at the base of the columns and in the beam-column joints. In Figure 5-27 (b), the longitudinal steel reinforcement stress profile is presented at the last drift (4%). It was verified that the longitudinal bars experienced yielding where concrete spalling was evident. The BCF deteriorated at a drift level of 4% and concrete spalling surfaced in the columns and in the beam near the joints. As a result, the frame lost part of its lateral capacity resulting in a drop of 20% of its peak strength.

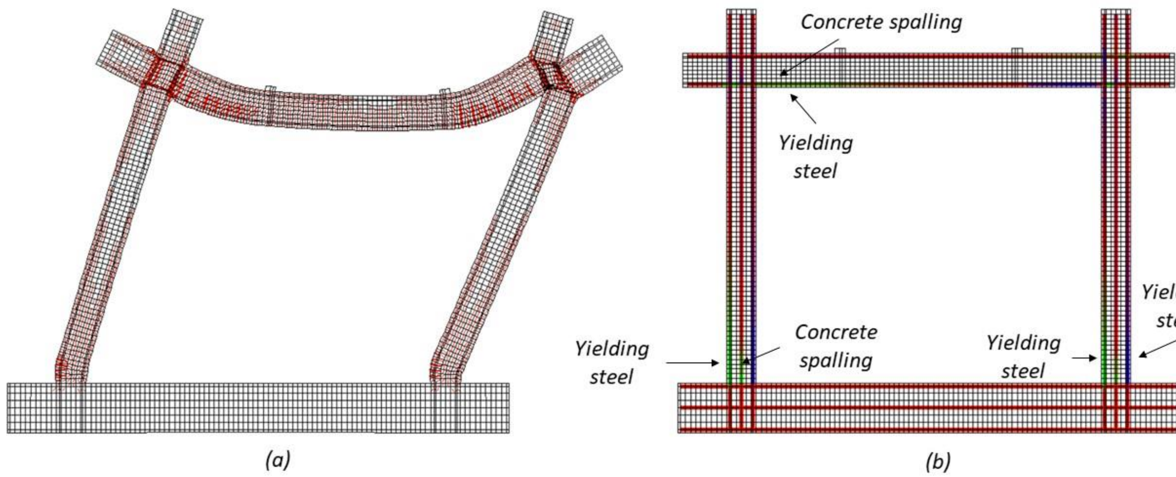

Figure 5-27: BCF response: (a) displaced shape and crack patterns at zero load; and (b) steel reinforcement stress profile at peak drift (4%)

5.4.2 Chrome-Molybdenum BRB retrofitted frame (CM-BRB)

Figure 5-28 illustrates the hysteretic response of the original BRB with a Chrome Molybdenum core. The retrofitted frame experienced a maximum top displacement of 49 mm and a peak lateral strength of 488 kN during the positive direction of loading. For this frame, the ultimate displacement was determined as that corresponding to the peak strength. Yielding initiated at a displacement of 18 mm and a lateral strength of 353 kN. This resulted in an effective stifssfness of 19.6 kN/mm and a displacement ductility of 2.7. Note that higher lateral strength (672.4 kN) was captured in the negative direction of loading given that the core failed in the positive direction.

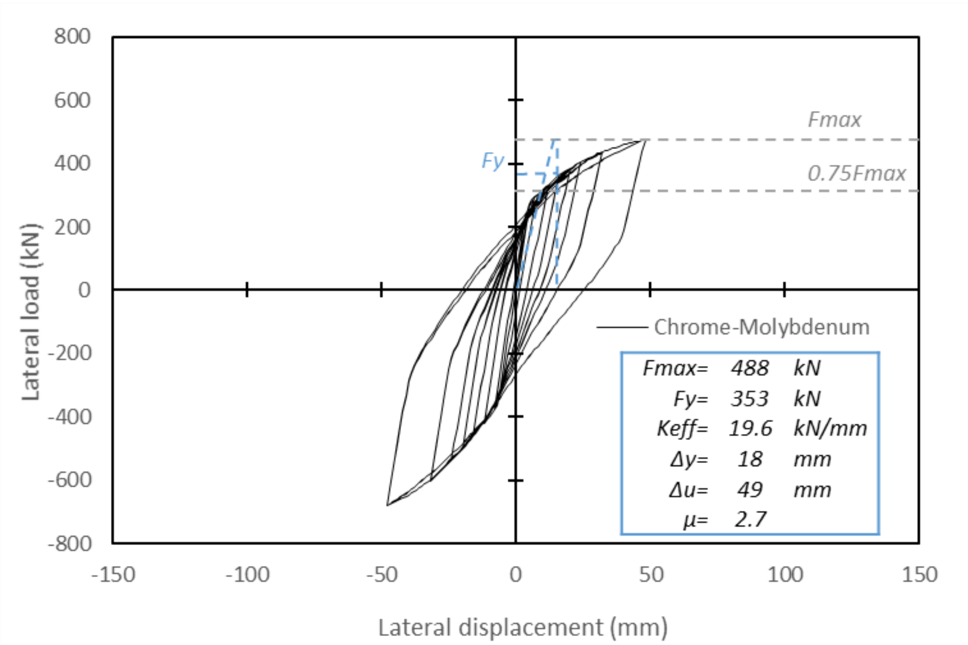

Figure 5-28: Lateral load – lateral displacement hysteretic response of the BRB frame with Chrome-Molybdenum core

Displaced shape and crack patterns of the retrofitted frame are presented in Figures 5-29 to 5-31. Figure 5-29 illustrates the response of the frame at yielding. The cracks are mostly concentrated along the beam with small crack openings at the base of the columns. In the beam-column joints, the cracks that were initially observed at the bottom of the beam shifted to the top when the retrofit was applied. During this drift stage of 1% drift, the crack width was of 0.1 mm.

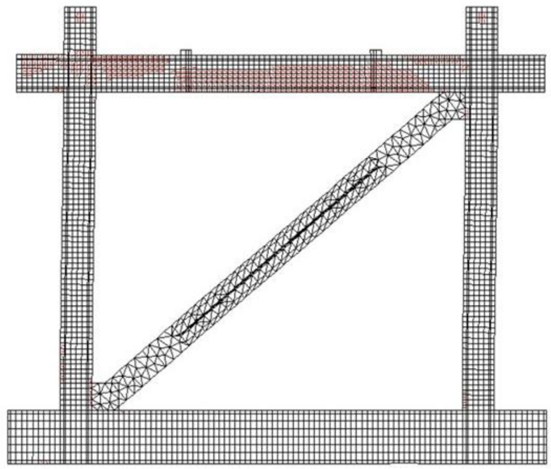

Figure 5-29: Displaced shape and crack patterns of Chrome-Molybdenum core BRB retrofitted frame at 1% drift

Figure 5-30 illustrates the displaced shape and crack patterns of the frame at the peak drift (1.5%). At this stage, the frame experienced cracking in both columns and beam. In the beam, cracks of 0.150 mm width were observed, while at the column base, 0.400 mm wide cracks were distributed from the base of the columns to mid-height.

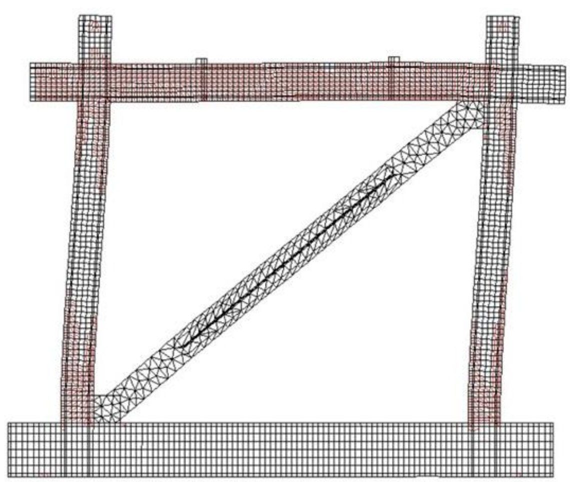

Figure 5-30: Crack pattern of Chrome-Molybdenum core BRB retrofitted frame at maximum drift

In Figure 5-31, the steel reinforcement stress profile at peak drift (1.5%) is presented. The longitudinal reinforcement yielded at the column base, while remaining in the elastic range in the beam. The Chrome-Molybdenum bar yielded at a drift of 0.375%. The frame failed due to fracture of the core bar during the third positive cycle. The failure occurred in the reduced diameter portion of the core.

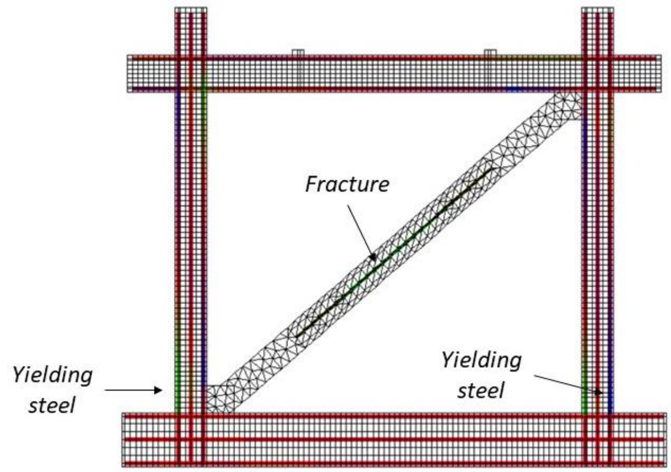

Figure 5-31: Longitudinal reinforcement stress profile at peak drift

5.4.3 Stainless Steel BRB retrofitted frame (SS-BRB)

The numerical hysteretic response of the BRB designed by Al-Sadoon (2017) with a stainless steel core is illustrated in Figure 5-32. The frame experienced a peak lateral strength of 549 kN and a top ultimate displacement of 94.5 mm (drift of 3%), where the BRB core failed due to concentration of stresses during the second positive cycle. According to the method developed by Park (1988) to evaluate the yield point of reinforced concrete structures, the frame yielded at a displacement of 45 mm and a lateral strength of 456 kN. This resulted in an effective stiffness of 10.1 kN/mm and a displacement ductility of 2.1.

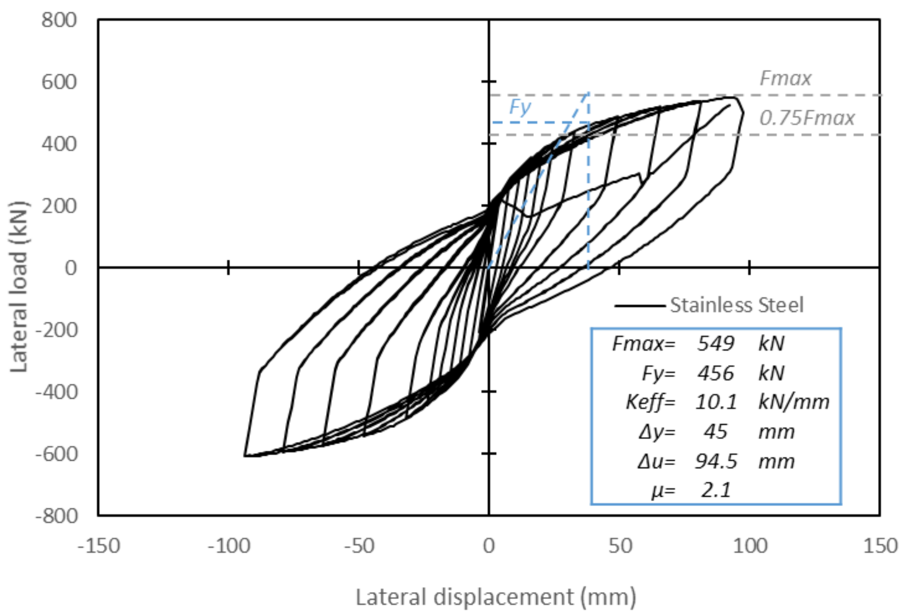

Figure 5-32: Lateral displacement – lateral load hysteretic response of SS-BRB

Figure 5-33 portrays the damage in the during the peak drift cycles in both directions of loading. The cracks were distributed in both columns and beam. However, at the base of the columns and in the beam near the joint wider crack openings were detected. At the base of the columns, 7 mm-wide cracks were predicted during the positive cycle, while 5.990 mm-wide cracks surfaced during the negative cycle. In the beam, the cracks were limited to an opening of 1 mm. Furthermore, concrete spalling was evident at the base of the left column during the peak drift in the positive cycle. The first 1 mm-wide flexural crack appeared after the 1.5% drift cycle at the base of the columns, which corresponds to the yield point.

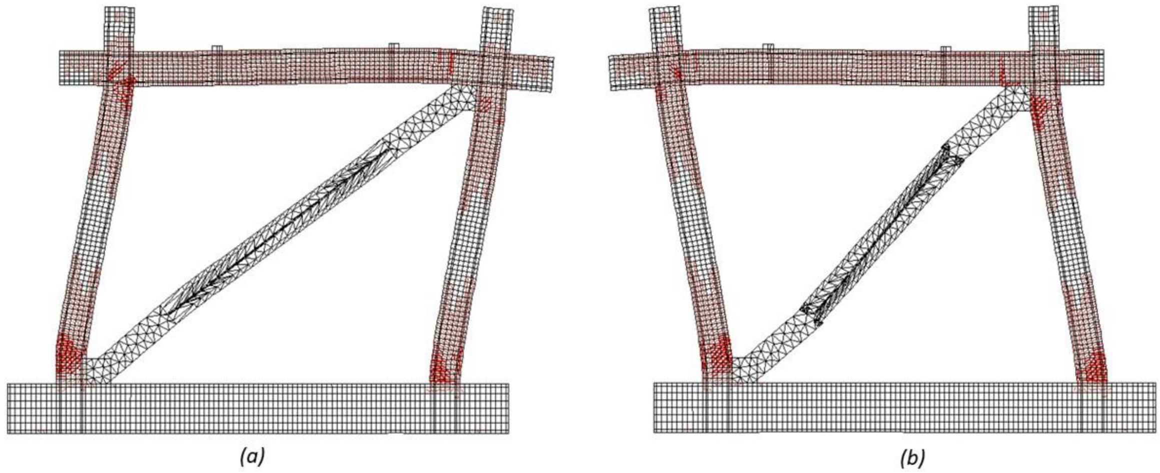

Figure 5-33: Displaced shape and crack pattern of SS-BRB at a 3% drift: a) positive direction; and b) negative direction

At the ultimate drift, the longitudinal bars at the column near the base and the joint experienced yielding. In addition, the beam top longitudinal reinforcement was yielding (Figure 5-34). The longitudinal reinforcement in the beam-column joint also experienced yielding during the peak drift. Furthermore, the stainless steel core bar yielded during the 1.5% drift cycle. The retrofitted system failed due to fracture of the core bar during the second positive cycle at 3% drift.

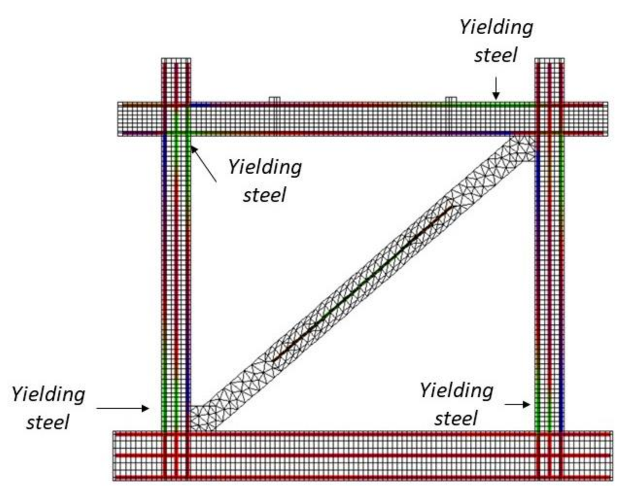

Figure 5-34: Longitudinal reinforcement stress profile of SS-BRB at peak drift

5.4.4 Modified BRB incorporating Chrome Molybdenum core (CM-MBRB)

The modified BRB discussed in Chapter 4 was evaluated under reverse cyclic loading. Figure 5-35 illustrates the lateral displacement–lateral load hysteretic response of the RC frame retrofitted with the modified BRB incorporating a Chrome-Molybdenum core. The frame was able to sustain a maximum top displacement of 158 mm with a lateral strength of 891 kN. The frame yielded at a displacement of 48 mm and a corresponding lateral strength of 725 kN. The displacement ductility of the frame increased, relative to the original BRB, being equal to 3.3; while the effective stiffness was calculated as 15.1 kN/mm.

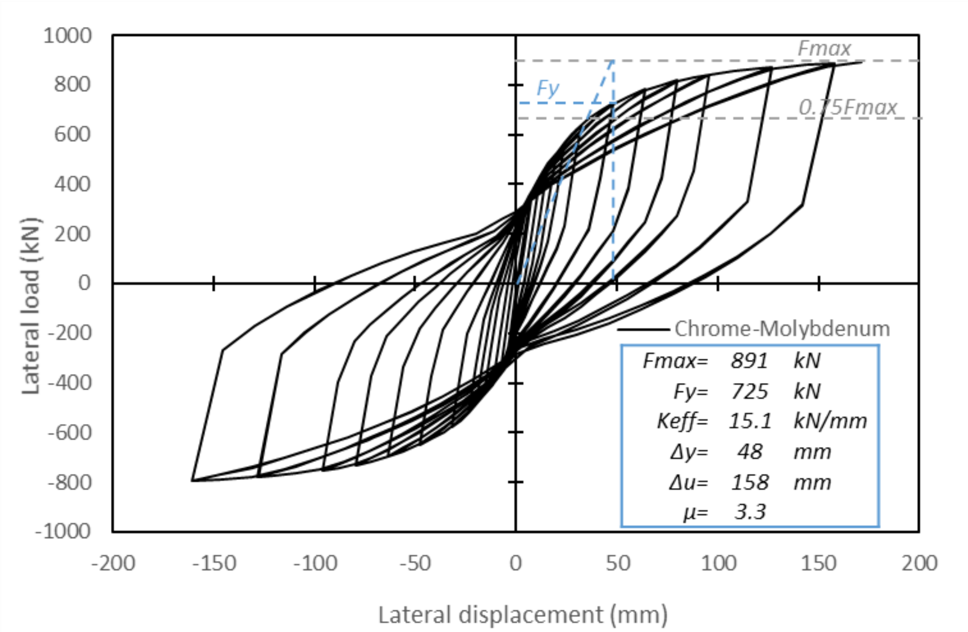

Figure 5-35: Hysteretic response of CM-MBRB

Figure 5-36 illustrates the cracking patterns of the frame at the yield drift. At this stage, the cracks were distributed across the beam and in the columns near the base and the joints. Regarding their width, the cracks were up to 1 mm wide. There were no significant differences between the two loading directions other than the width of cracks, where in the negative cycle the cracks are more concentrated near the frame-brace connection.

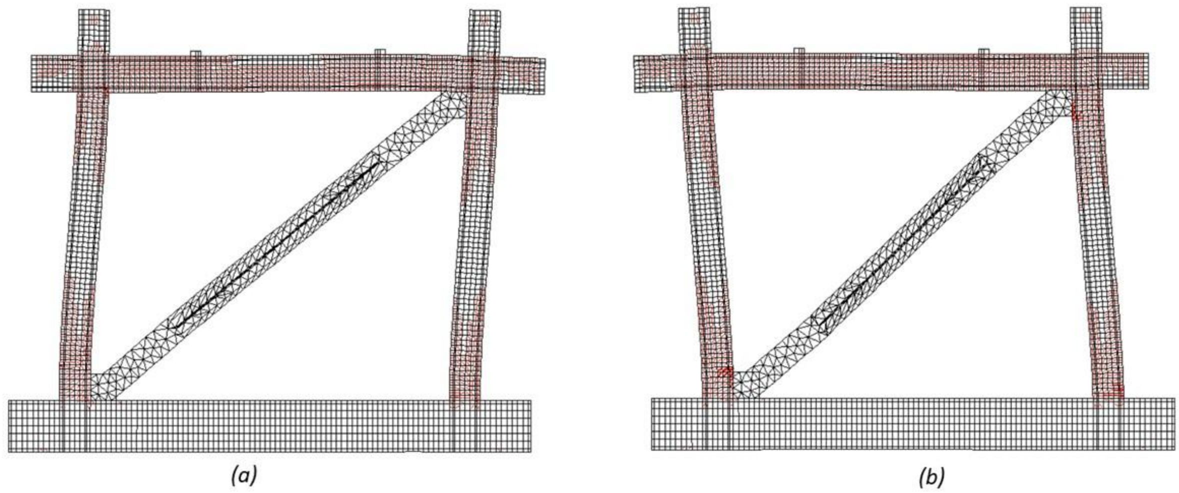

Figure 5-36: Displaced shape and crack patterns of CM-MBRB at a 1.5% drift: (a) positive cycle; and(b) negative cycle

Figure 5-37 presents two profiles of the mechanical behaviour of the frame at failure. The displaced shape of the frame at the ultimate displacement is presented in Figure 5-37 (a), where wide cracks are observed at the column base and near the joints. The cracks were 8.390 mm wide at the column base and 10.190 mm wide at the beam-column joint. It is evident that the frame deteriorated, and concrete spalling was observed near the wide cracks. The data presented in the reinforcement stress profile in Figure 5-37 (b) indicated that the BRB core bar failed at a drift of 6%, in the first positive cycle, followed by fracture of the longitudinal steel reinforcement at the base of the column. At failure, the steel reinforcement in both columns and beam near the joints were yielding.

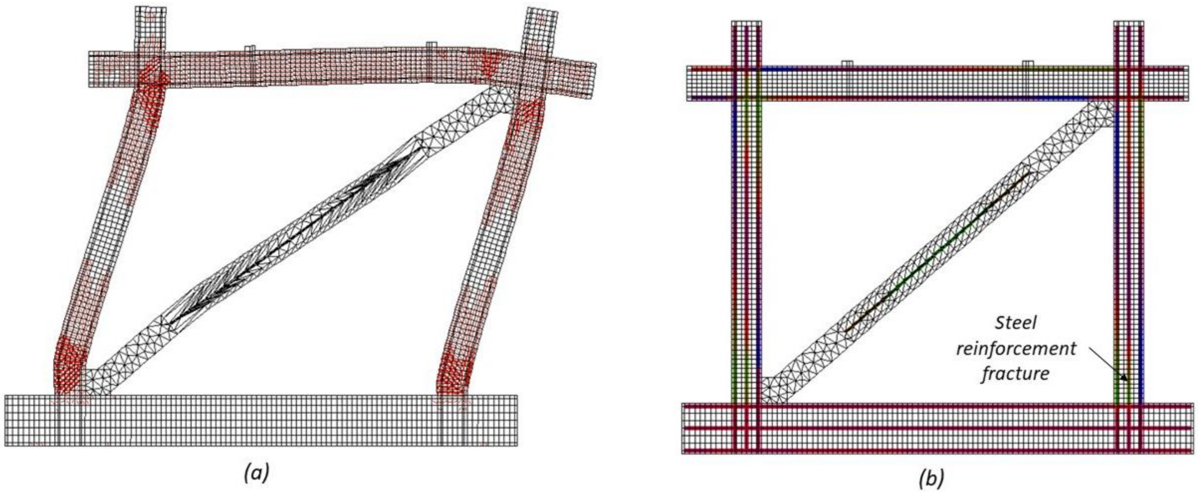

Figure 5-37: At peak drift: (a) displaced shape and crack pattern; and (b) discrete reinforcement stress profile

5.4.5 Modified BRB incorporating Stainless Steel core (SS-MBRB)

The modified BRB was also evaluated with a Stainless Steel core bar. The hysteretic response of the frame is presented in Figure 5-38, where the frame sustained an ultimate top displacement of 191 mm. Furthermore, the frame yielded at a displacement of 48 mm. This resulted in a displacement ductility of 4. The retrofitted system sustained a peak lateral strength of 690 kN. The frame yielded at a lateral load of 540 kN, and the effective stiffness was approximately 11.3 kN/mm.

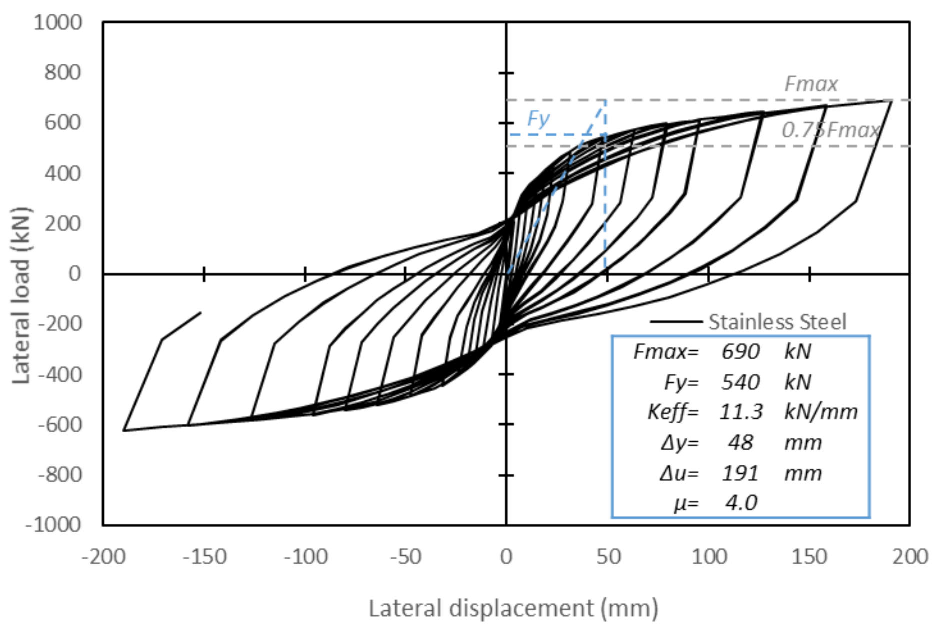

Figure 5-38: Lateral displacement–lateral load hysteretic response of SS-MBRB

Figure 5-39 illustrates the cracking pattern of the frame at yielding and peak drift. At the yielding point (Figure 5-39 (a)), the cracks are evenly distributed along the beam, but concentrated at the base of the columns and near the beam-column joints. During yielding, the cracks were 1 mm wide and similar in both directions of loading. At the maximum drift (Figure 5-39 b), however, the cracks at the base of the right column achieved a width of 14.390 mm, which was assumed to represent concrete spalling. in the beam, the cracks were limited by an opening of 12.870 mm. As a result, spalling was observed at the column base and beam-column joints.

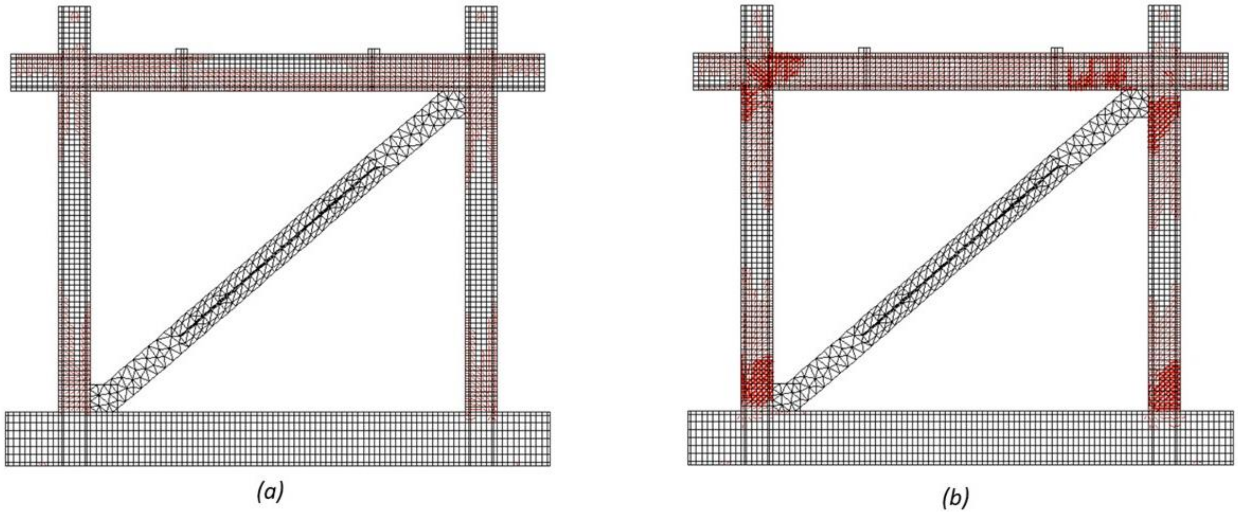

Figure 5-39: Crack patterns of SS-MBRB frame during positive cycle: (a) yielding: and (b) peak drift

In the discrete reinforcement stress profile (Figure 5-40), the longitudinal bar at the base of the left column failed due to buckling. The other longitudinal reinforcing bars at the base of the column and in the beam near the joints were yielding. The retrofitted system failed due to deterioration of the original reinforced concrete frame.

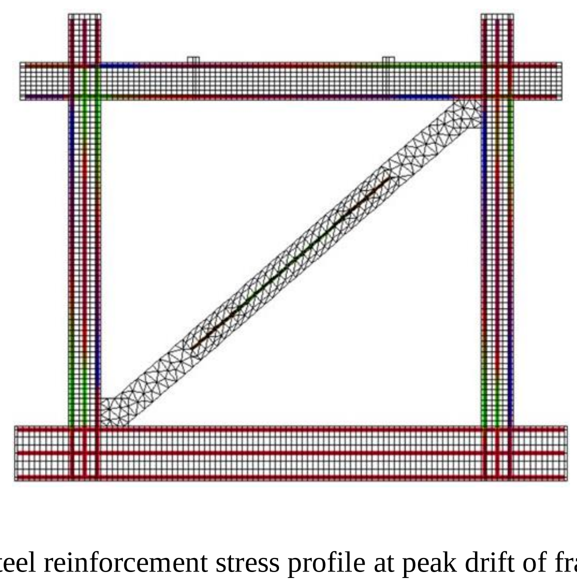

Figure 5-40: Steel reinforcement stress profile at peak drift of frame SS-MBRB

5.4.6 Modified BRB incorporating SE-SMA core bar (SMA-MBRB)

Figure 5-41 illustrates the lateral displacement–lateral load hysteretic response of the frame retrofitted with the modified BRB and with the SE-SMA core with reduced cross section to induce yielding at in the mid-length. Based on the numerical hysteretic response, the frame sustained a lateral displacement of 158 mm without accumulating permanent displacement. The frame sustained a last cycle of 220 mm in the stiffening phase of the SE-SMA. During the stiffening phase, the frame accumulated a permanent displacement of 25 mm, which was two times smaller than what was experienced by the bare concrete frame under a top displacement of 127 mm. The peak strength of the frame corresponded to 858 kN. The pseudo-yield point was evaluated at a displacement of 45 mm, which resulted in a displacement ductility of 4.8. The effective stiffness was calculated as 11.7 kN/mm.

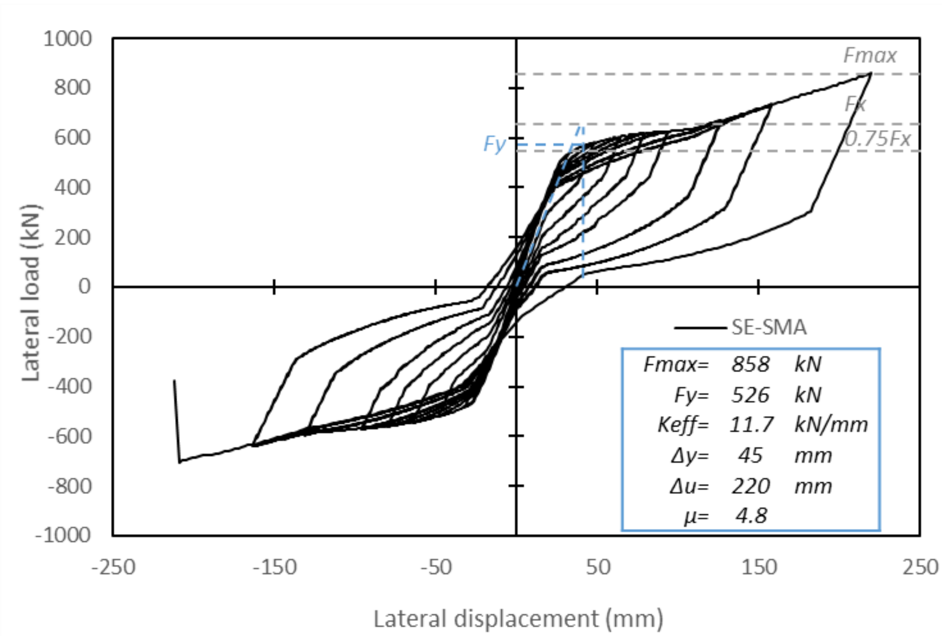

Figure 5-41: Hysteretic response of modified BRB retrofitted frame with SE-SMA core bar

Figure 5-42 illustrates the crack patterns of the frame during the last positive cycle. At this drift, the cracks were concentrated at the base of the column, and near the brace-frame connection. The cracks were 3 mm wide at the base of the columns and 2.8 mm wide at the beam near the joints. When evaluating the displaced shape at load zero after the last cycle (Figure 5-43), the cracks were limited to a width of 0.1 mm, which demonstrates the efficiency of the SMA in restoring the frame to its initial position without accumulating permanent displacements.

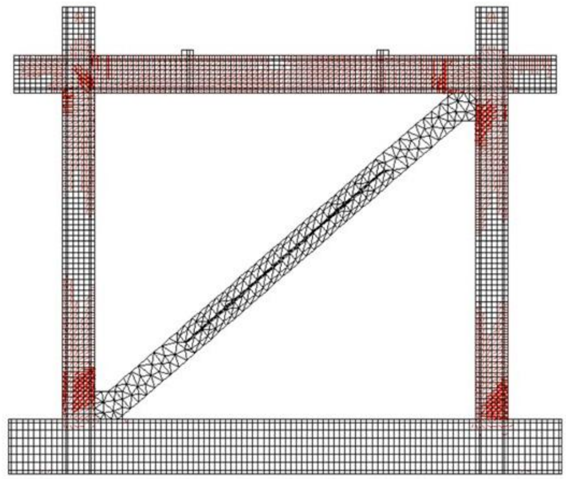

Figure 5-42: Crack patterns of the frame at maximum drift under positive cycle

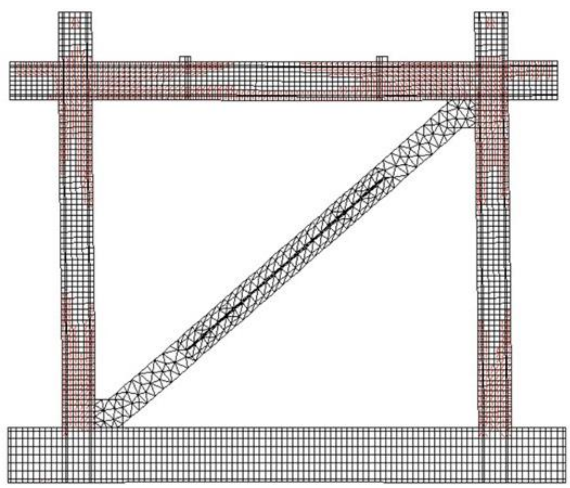

Figure 5-43: Displaced shape of the frame at load zero after the last positive cycle

The frame yielded at a displacement of 45 mm, where the cracks were limited to a width of 0.1 mm. The SE-SMA core was able to provide its full capacity and provide damage control to the system. Failure was controlled by the core bar that achieved its full capacity in both tension and compression. During the last cycle, the SE-SMA core was under a strain of 20%. As this was the maximum strain considered for the analysis, it was evident the failure was controlled by the core. Figure 5-44 illustrates the steel reinforcement stresses profile for the last drift cycle, where the longitudinal reinforcement at the base of the left column buckled prior to the brace core capacity limit.

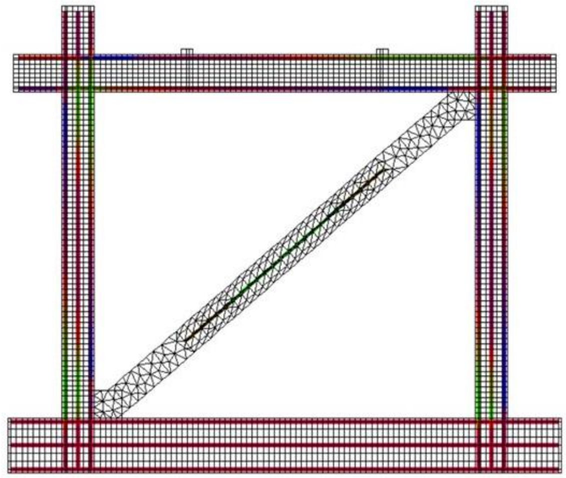

Figure 5-44: Discrete reinforcement stress profile for SMA-MBRB

5.5 Sensitivity analysis

Sensitivity analyses were conducted to evaluate the impact of the constitutive models for the concrete and reinforcing steel on the hysteretic response of the bare concrete frame. The analyses were only conducted for BCF, which served as the basis for the retrofitted models. Three phenomena were evaluated: concrete compression pre-peak; concrete compression post-peak; and hysteretic response of the reinforcement. These three behavioural characteristics are crucial when evaluating the reverse cyclic response of the frames, the energy dissipated, and the shape of the lateral load – lateral displacement curve. The frames were subjected to the loading protocol presented in Figure 5-18, but only one repetition was conducted per cycle to minimize computational time.

5.5.1 Pre-Peak constitutive models for concrete

Figures 5-45 to 5-53 illustrate the hysteretic response of the frame for the various compression pre-peak constitutive model. The default constitutive model is presented in Figure 5-45 and its selection resulted in a strength capacity of 231.1 kN and 207.5 kN in the positive and negative cycle, respectively. The frame reached its peak lateral strength at a drift of 1.89% in the positive and 1.51% in the negative cycles. The Hognestad parabola constitutive model (Vecchio et al., 2013) is a simple model that has been proven to accurately simulate the behaviour of normal strength concrete (up to 40MPa).

The constitutive models proposed by Attard and Setunge (1994) and Samani and Setunge (2012) were not accurate in simulating the response of BCF (Figures 5-46 and 4-47); the frames failed unexpectedly at a 1% drift in both simulations. Figure 5-48 illustrates the response of the frame with the Elastic-Plastic (Vecchio et al., 2013) constitutive model, where the frame was able to sustain displacement beyond its capacity based on analytical calculations, and the model did not accurately predict the behaviour of the frame. Furthermore, for the Smith-Yong (1956) and Linear (Vecchio et al., 2013) models (Figures 5-49 and 5-50), the frame sustained displacements up to 200 mm and 250.6, respectively, and was in not in good agreement with the actual response of the frame. Recall that in addition to the analytical and previous calculations, previous large-scale testing was conducted on the frame (Al-Sadoon, 2016), thus the validation of the constitutive models was conducted against both the analytical and experimental investigations.

In addition to the default Hognestad parabola (Vecchio et al., 2013) model, both Popovics (1973) and Lee et al. (2012) models were accurate in predicting the behaviour of the frame. The Popovics constitutive model is commonly utilized for high-strength concrete, which simulates a steep descending branch in the stress-strain curve. By utilizing the Popovic (HSC) constitutive model, the area enclosed inside the loop is smaller than what was experienced by BCF during the testing conducted by Al-Sadoon (2016), which directly affects the energy dissipated by the system (Figure 5-51). Therefore, this model was not used to simulate the response of the frame. The Popovics (NSC) accurately reflected the hysteretic response and lateral strength capacity of BCF, but it overestimated the displacement capacity of the frame. The lateral strength capacity of the frame at the 4% drift cycle was more than 80% of the lateral capacity of the actual frame (Figure 5-52), so the frame did not fail at a 4% lateral drift. Figure 5-53 illustrates the response of the frame with the Lee et al. (2012) compression pre-peak model. The model was able to closely capture the lateral strength capacity and ultimate drift of the frame. However, for simplicity, it was decided to select the default constitutive model for all analyses since it presented accurate capacities and shape of the cycle loops.

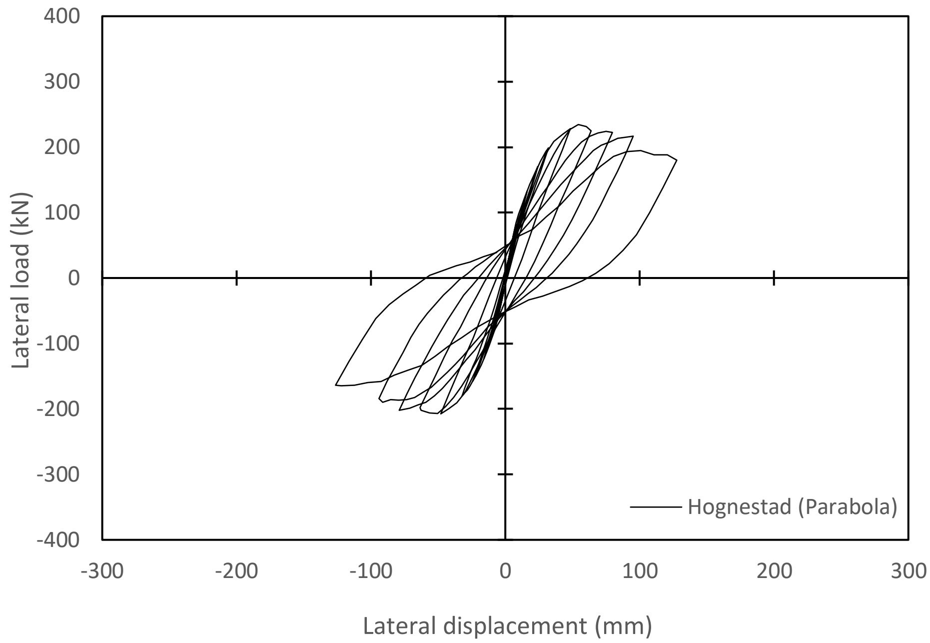

Figure 5-45: BCF hysteretic response utilizing the Hognestad Parabola (Vecchio et al., 2013) as the pre-peak constitutive model

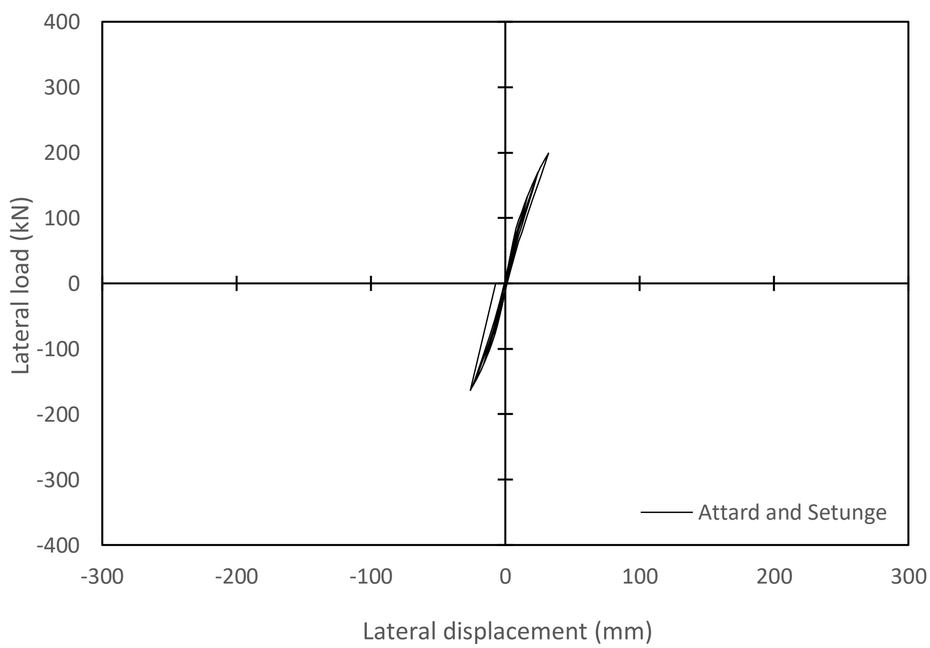

Figure 5-46: BCF hysteretic response utilizing the Attard and Setunge (1994) as the pre-peak constitutive model

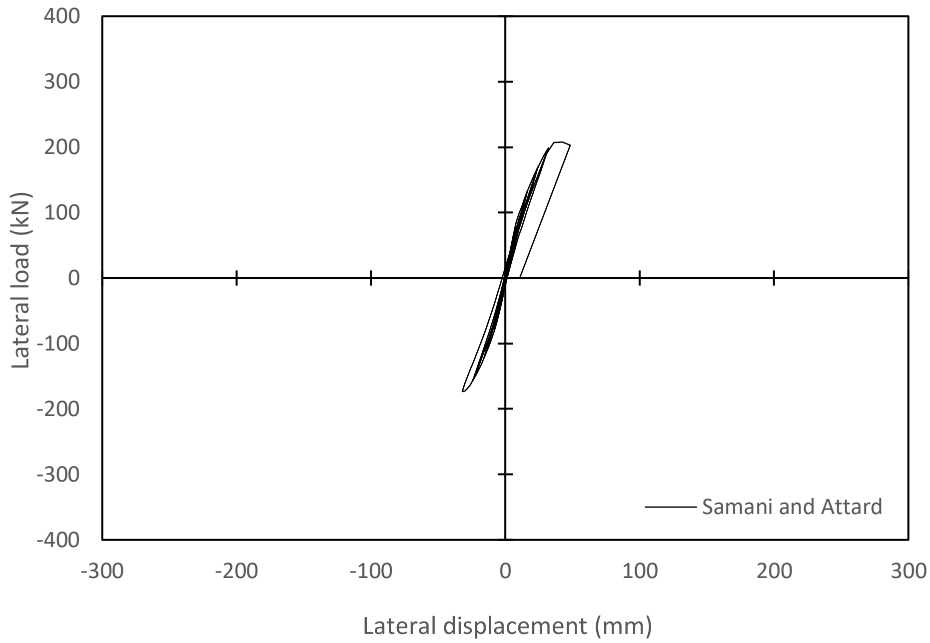

Figure 5-47: BCF hysteretic response utilizing the Samani and Attard (2012) as the pre-peak constitutive model

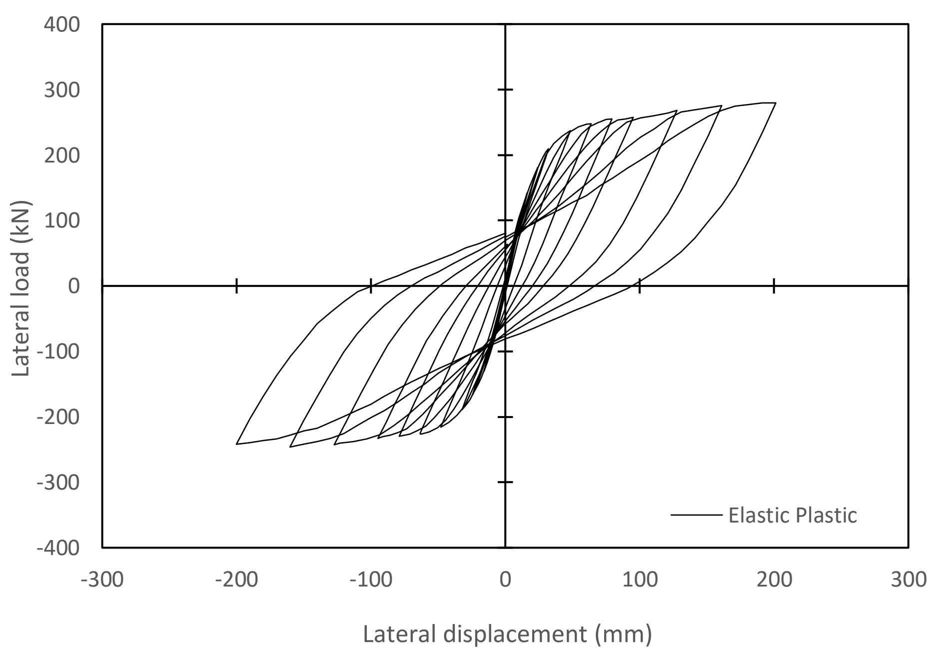

Figure 5-48: BCF hysteretic response utilizing the Elastic Plastic (Vecchio et al., 2013) as the pre-peak constitutive model

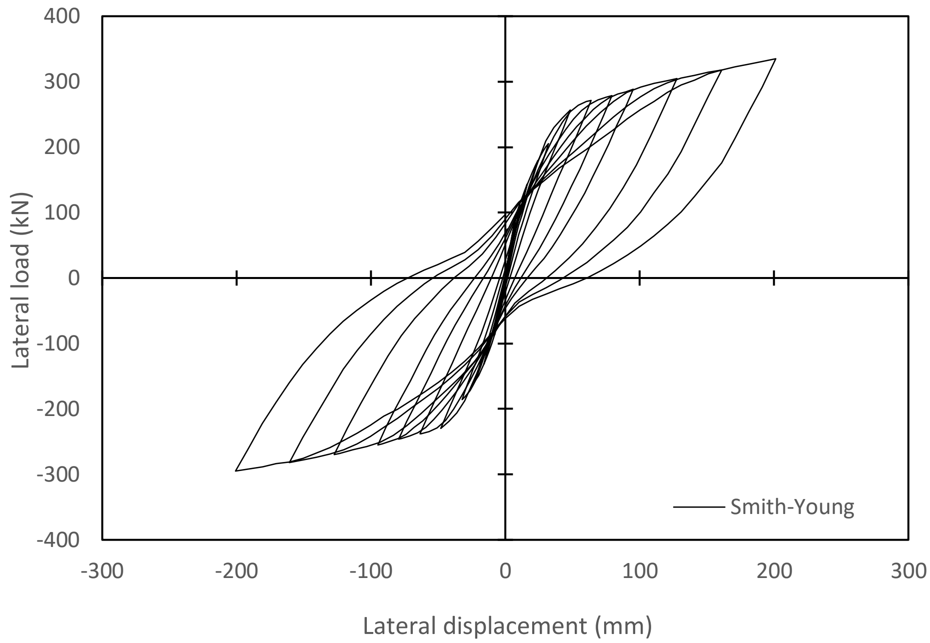

Figure 5-49: BCF hysteretic response utilizing the Smith-Young (1956) as the pre-peak constitutive model

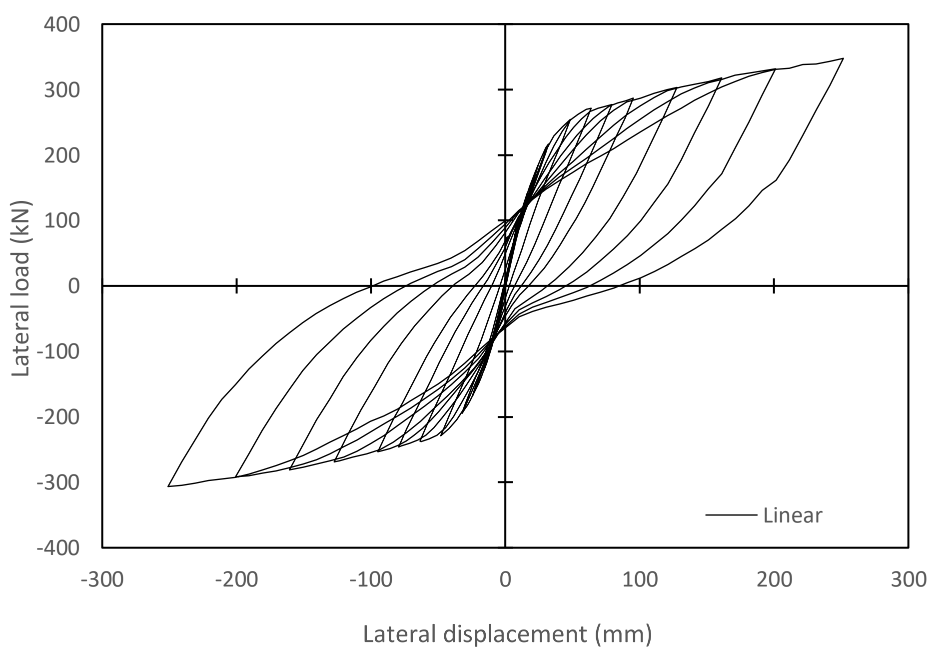

Figure 5-50: BCF hysteretic response utilizing the Linear (Vecchio et al., 2013) as the pre-peak constitutive model

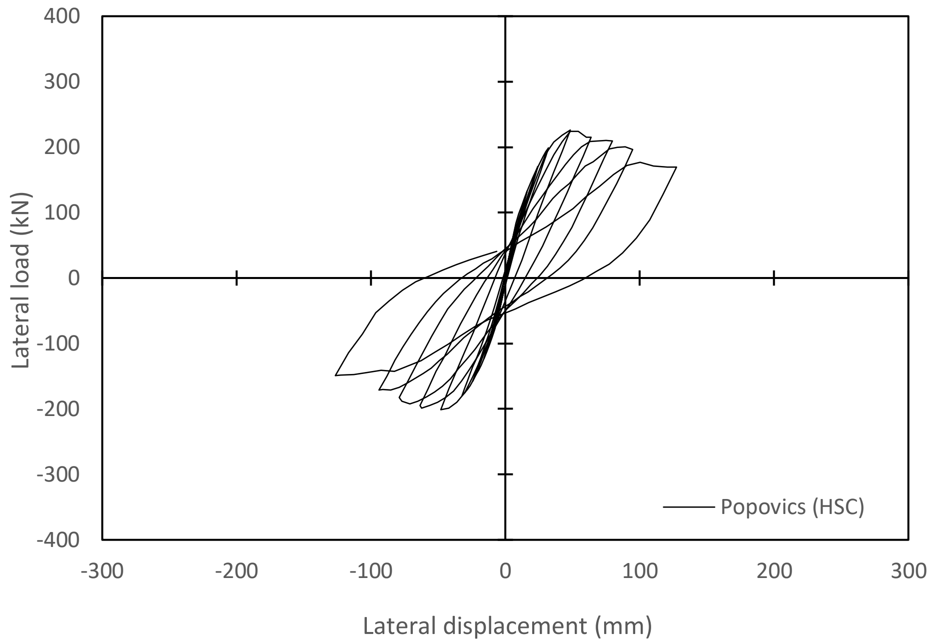

Figure 5-51: BCF hysteretic response utilizing the Popovics HSC (1973) as the pre-peak constitutive model

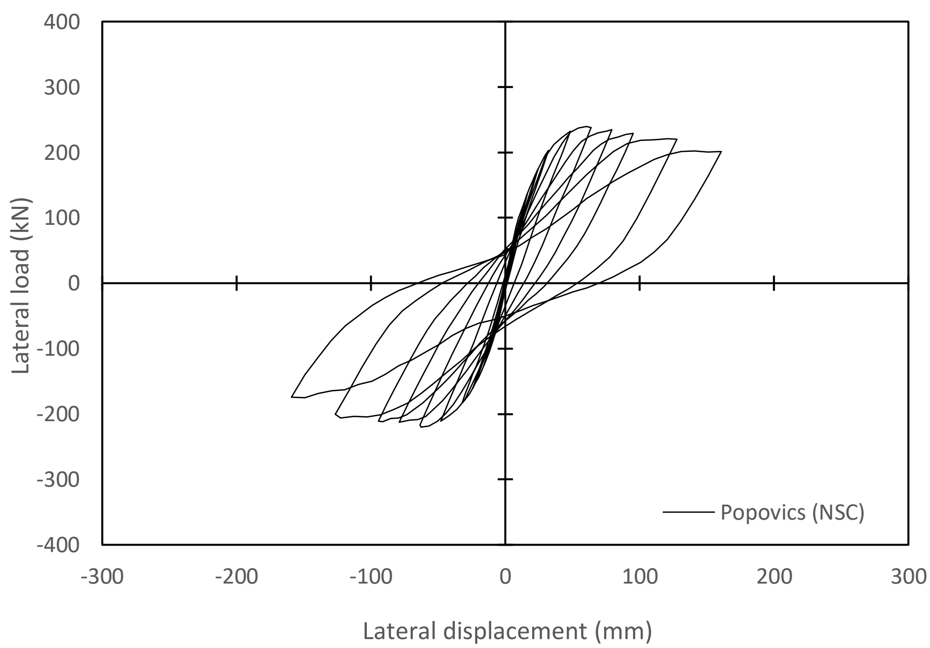

Figure 5-52: BCF hysteretic response utilizing the Popovics NSC (1973) as the pre-peak constitutive model

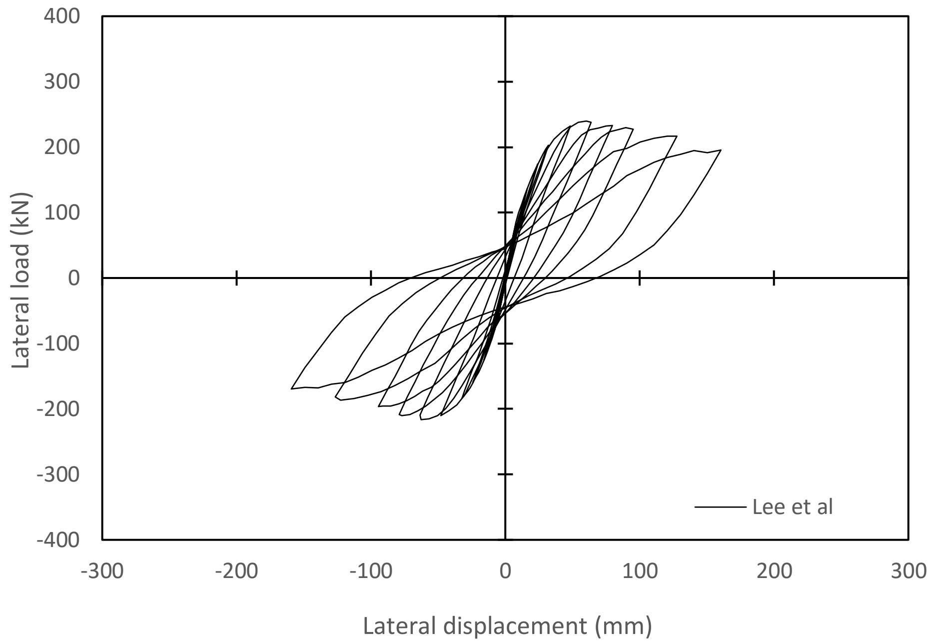

Figure 5-53: BCF hysteretic response utilizing the Lee et al. (2012) as the pre-peak constitutive model

5.5.2 Post-Peak constitutive models for concrete

The concrete compression post-peak response was also evaluated by simulating the frame with different constitutive models; their response under reverse cyclic loading are presented in Figures 5-54 to 5-63. The compressive post-peak response models change the failure mode – from brittle to ductile - with the inclusion of confinement in the concrete. Figure 5-54 presents the response of the frame with the default constitutive model, the Modified Park-Kent (Park et al., 1982). It is important to highlight that the response in Figure 5-54 was includes 3 repetitions per drift cycle.

Using the Attard and Setung (1994) and Samani and Attard (2012) models, the frames fail prematurely (Figures 5-55 and 5-56), which is similar to the results with the same models used to simulate the compression pre-peak response. Following the Elastic-Plastic (Vecchio et al., 2013) model represented in Figure 5-57, the remaining post-peak models were able to simulate the behaviour of the frame. That is a result of the fact that the compressive post-peak response of the concrete significantly impacts the hysteretic response when the structure is highly reinforced (Vecchio et al., 2013); as the investigated frame is designed based on the pre-1970s building code, the transverse reinforcement is widely spaced and poorly anchored, which minimizes the influence of the compressive post-peak models.

The post-peak Base Curve (Vecchio et al., 2013) constitutive model utilizes the constitutive model selected for the pre-peak response as a basis for the post-peak response. This model, thus, presents accurate results when either the Popovics (HSC and NSC), Hognestad (Parabola), or Linear models are selected for the compression pre-peak response model. Given that the Hognestad (Parabola) constitutive model was utilized in the pre-peak response, the Base Curve was a good alternative to model the post-peak response (Figure 5-59). The Modified Park Kent model (Park et al., 1982) was developed to account for an increase in ductility and strength due to confinement provided by transverse hoop reinforcement, which aligns with the reinforcement provided in the columns of the frames. As a result, the default constitutive model was selected for simplicity and accurately predicts the response of the bare concrete frame (Figure 5-54).

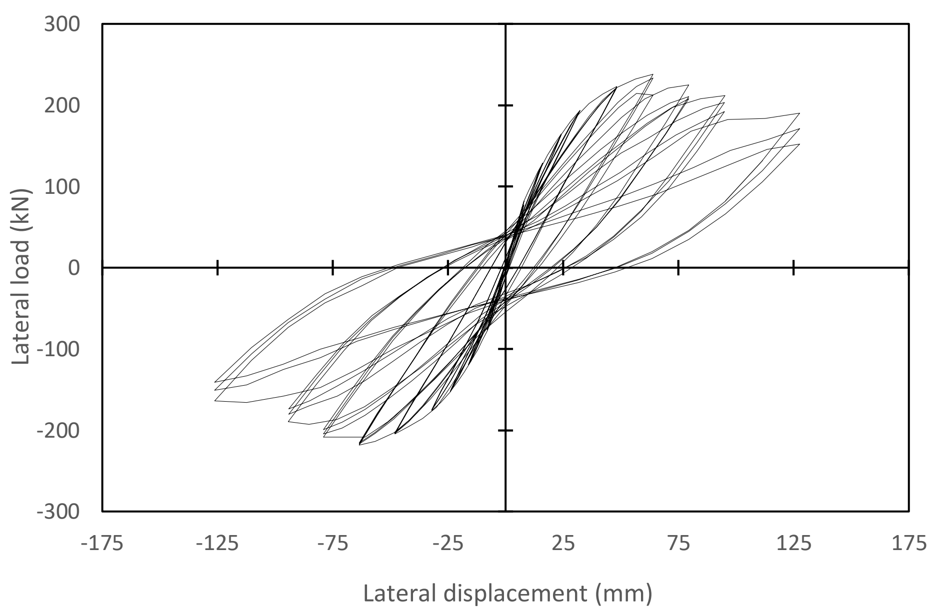

Figure 5-54: BCF hysteretic response utilizing the Modified Park-Kent (Park et al., 1982) model to simulate the post-peak response

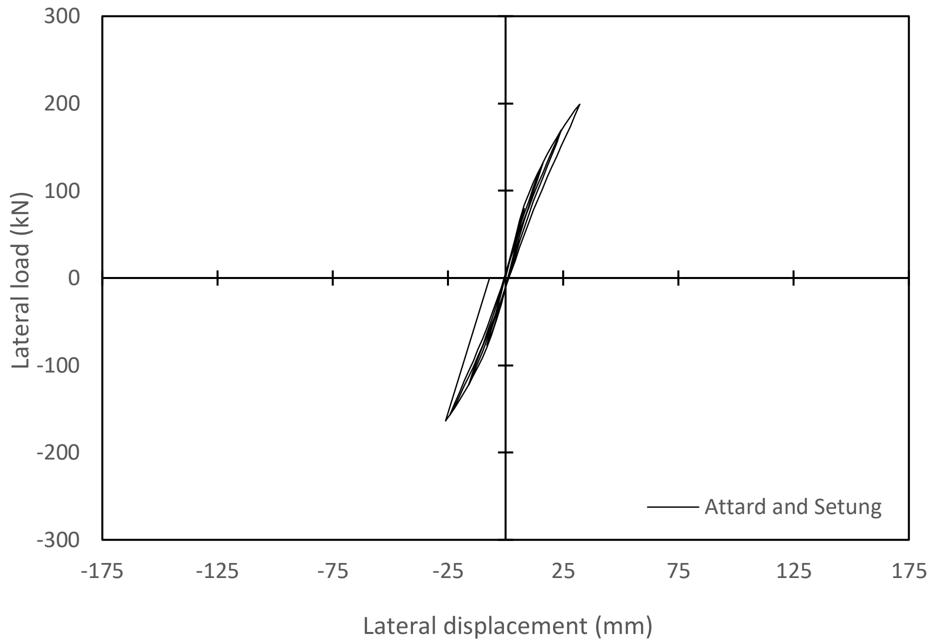

Figure 5-55: BCF hysteretic response utilizing the Attard and Setung (1994) model to simulate the post-peak response

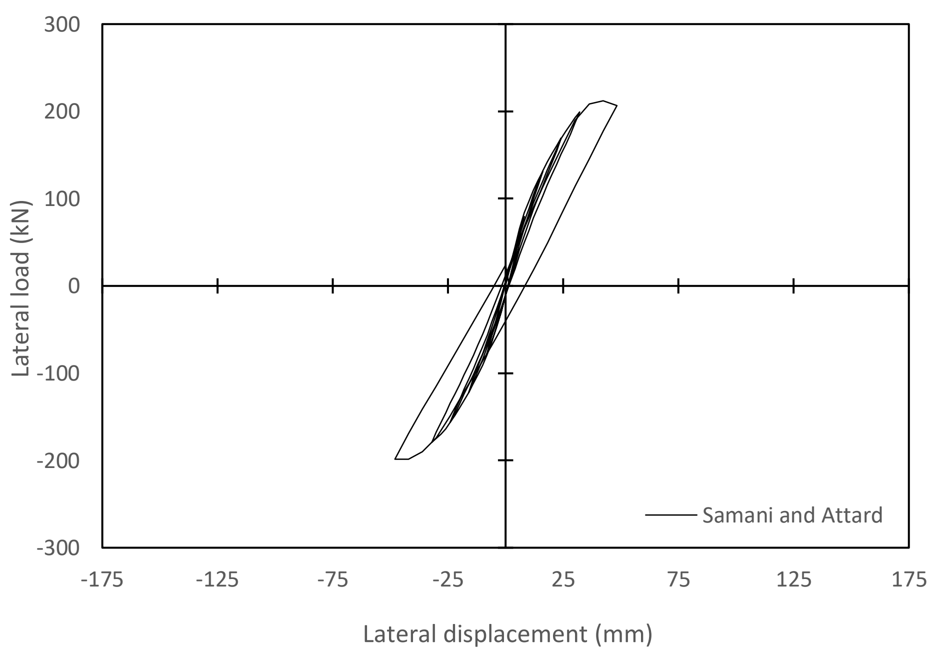

Figure 5-56: BCF hysteretic response utilizing the Samani and Attard (2012) model to simulate the post-peak response

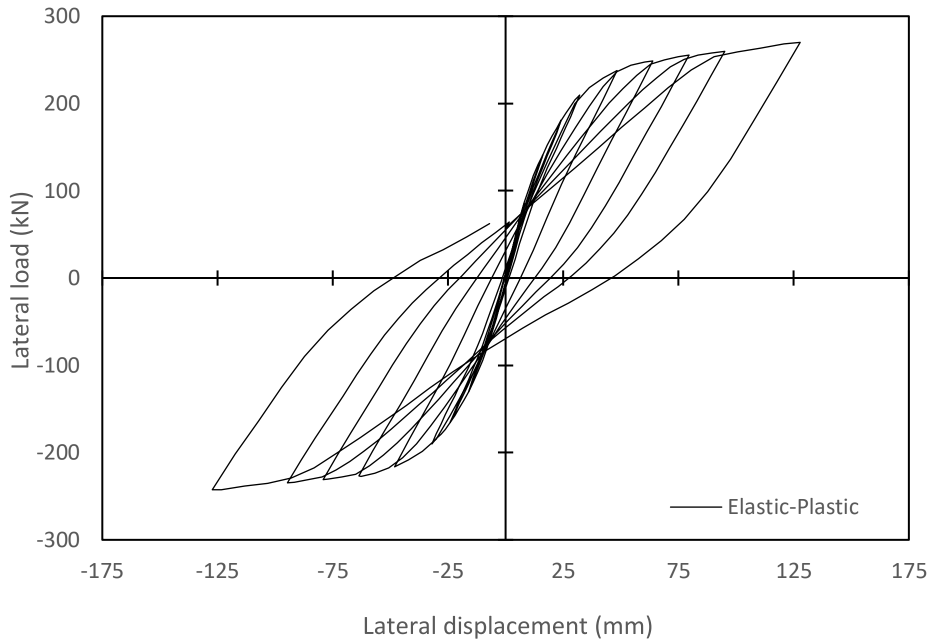

Figure 5-57: BCF hysteretic response utilizing the Elastic-Plastic (Vecchio et al., 2013) model to simulate the post-peak response

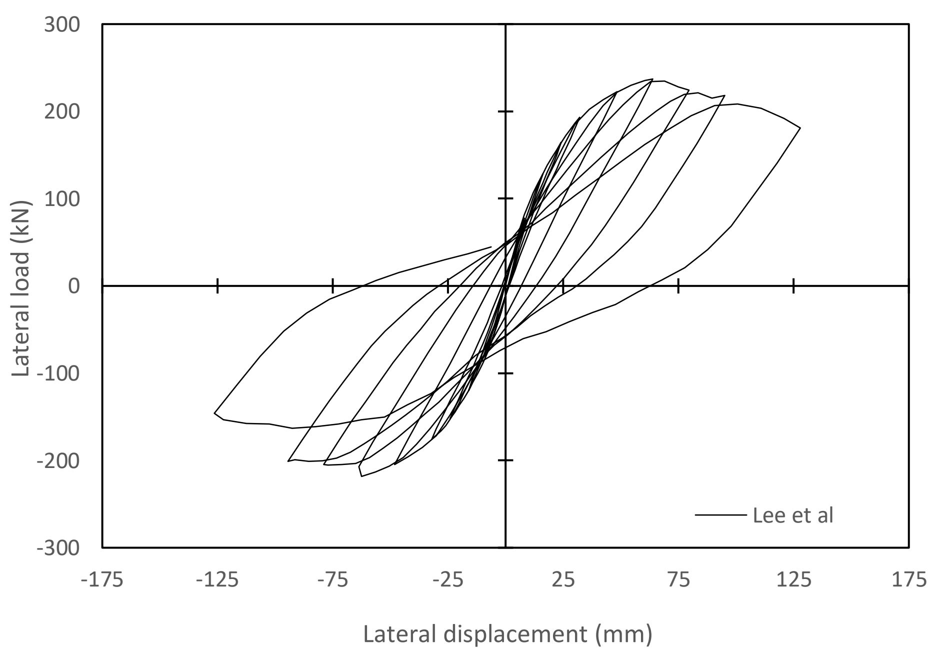

Figure 5-58: BCF hysteretic response utilizing the Lee et al. (2012) model to simulate the post-peak response

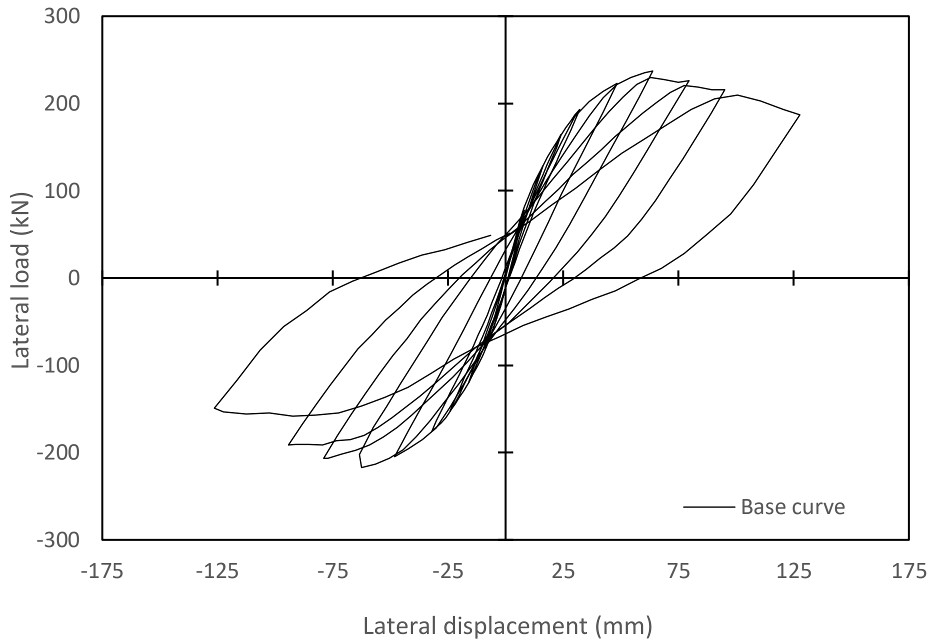

Figure 5-59: BCF hysteretic response utilizing the Base curve (Vecchio et al., 2013) model to simulate the post-peak response

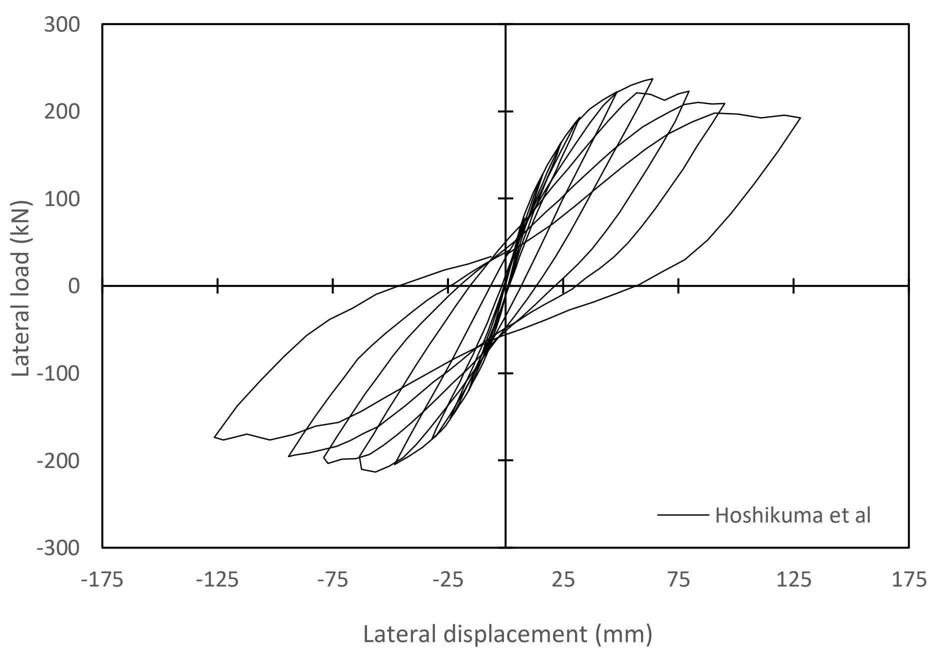

Figure 5-60: BCF hysteretic response utilizing the Hoshikuma et al. (1997) model to simulate the compression post-peak response

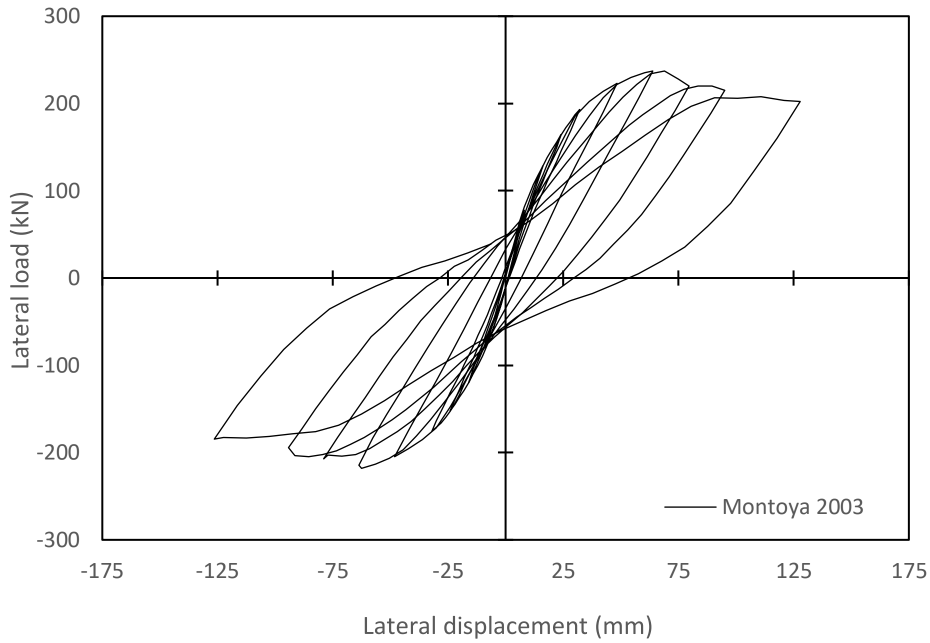

Figure 5-61: BCF hysteretic response utilizing the Montoya 2003 (2004) model to simulate the compression post-peak response

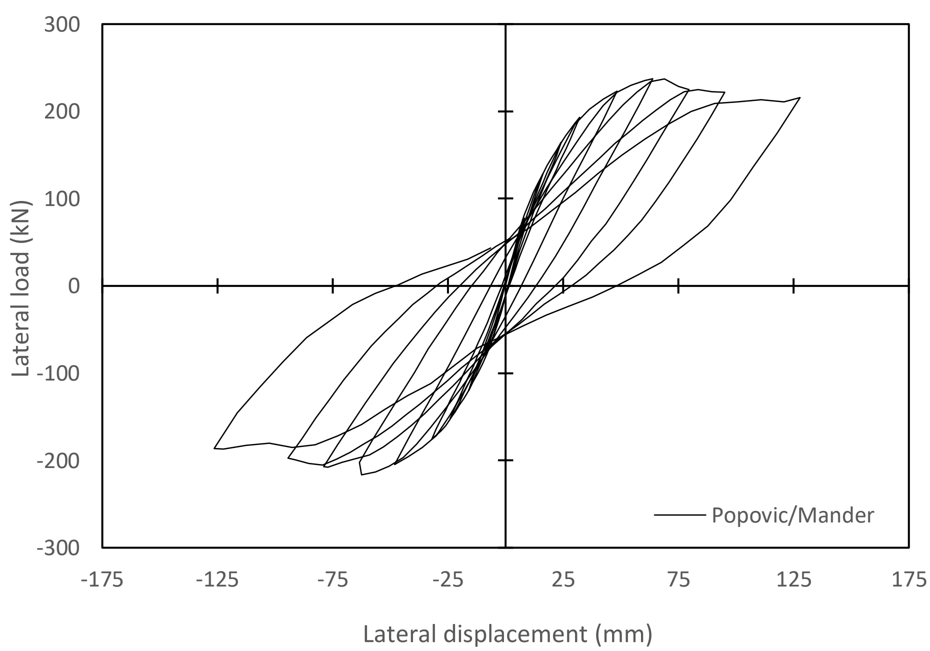

Figure 5-62: BCF hysteretic response utilizing the Popovic/Mander (Mander et al., 1988) model to simulate the compression post-peak response

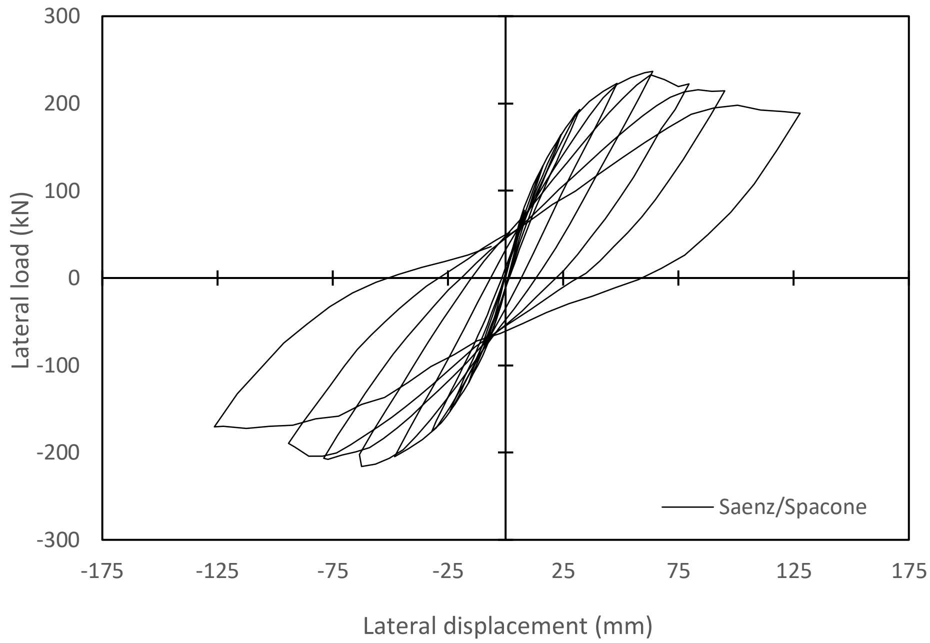

Figure 5-63: BCF hysteretic response utilizing the Saenz/Spacone (Saenz, 1964) model to simulate the compression post-peak response

5.5.3 Hysteretic response constitutive models for reinforcement

Figures 5-64 to 5-71 illustrates the results of the different constitutive models for the hysteretic response of the reinforcement. This constitutive model simulates the loading, unloading and reloading response of the reinforcement using the monotonic stress-strain relationship as the envelope. The default constitutive model for the hysteretic response is the Bauschinger Effect (Seckin, 1981; Figure 5-64). The default model was able to accurately simulate the shape of the BCF hysteretic response in comparison to the tested frame; similar energy dissipation and permanent displacements were predicted. Among the models available in VecTor2, the only model that presented discrepancy with the experimental results from Al-Sadoon (2016) was the linear constitutive model (Figure 5-65). Using this constitutive model, the hysteretic response of the frame did not converge, which affected both the strength and displacement capacities as the reinforcement unloads and reloads linearly to and from the point of zero strain and stress. Furthermore, it is important to note that the hysteretic response of the frame was not significantly affected by the other constitutive models for the hysteretic response of the reinforcement.

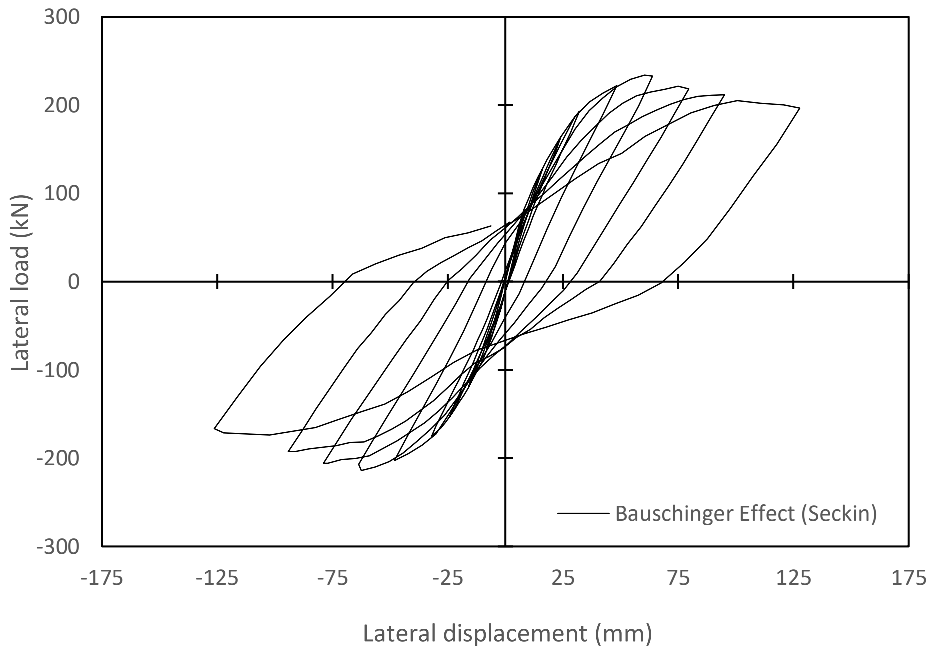

Figure 5-64: BCF hysteretic response utilizing the Bauschinger Effect (Seckin, 1981) model to simulate the hysteretic behaviour of the reinforcement

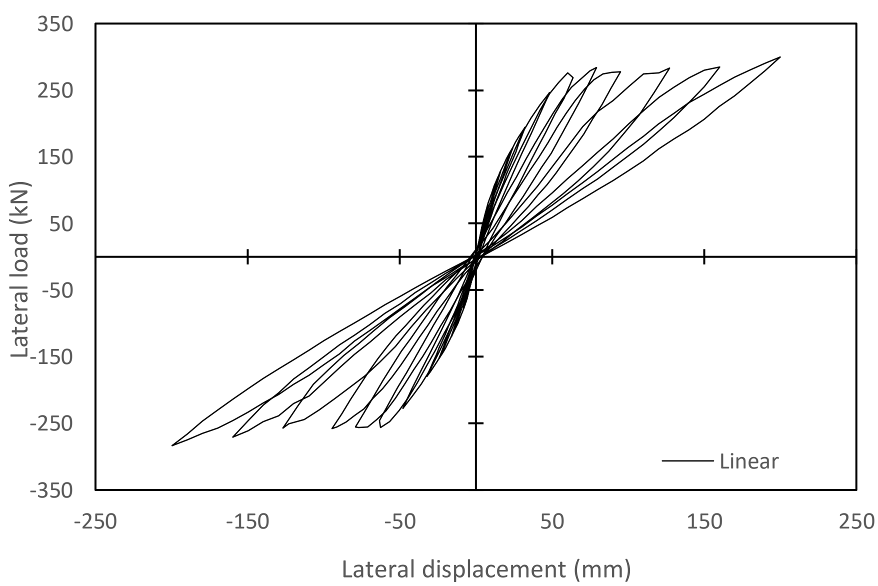

Figure 5-65: BCF hysteretic response utilizing the Linear (Vecchio et al., 2013) model to simulate the hysteretic behaviour of the reinforcement

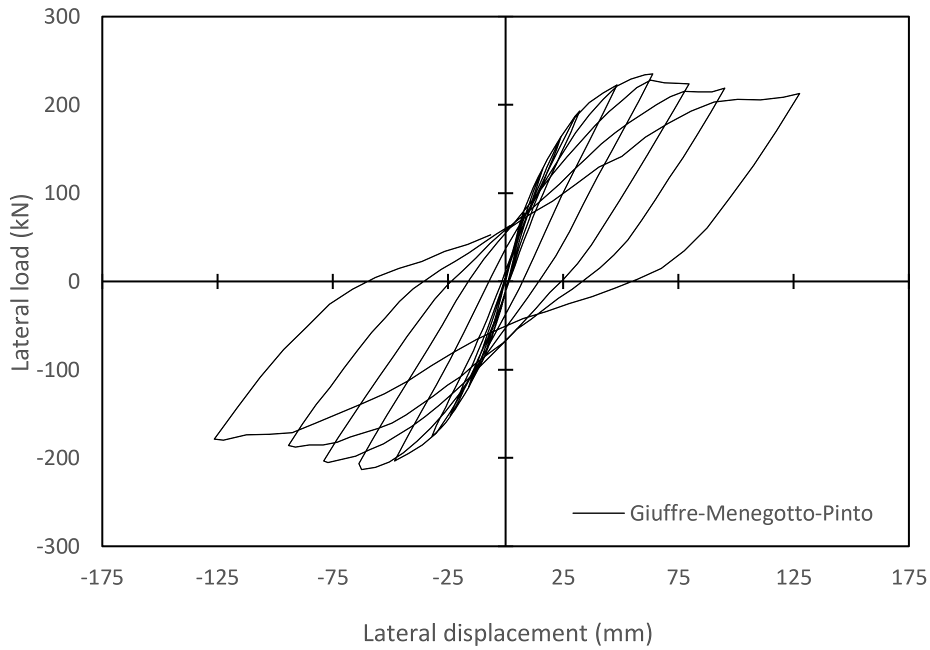

Figure 5-66: BCF hysteretic response utilizing the Giuffre-Menegotto-Pinto (Manegotto et al., 1973) model to simulate the hysteretic behaviour of the reinforcement

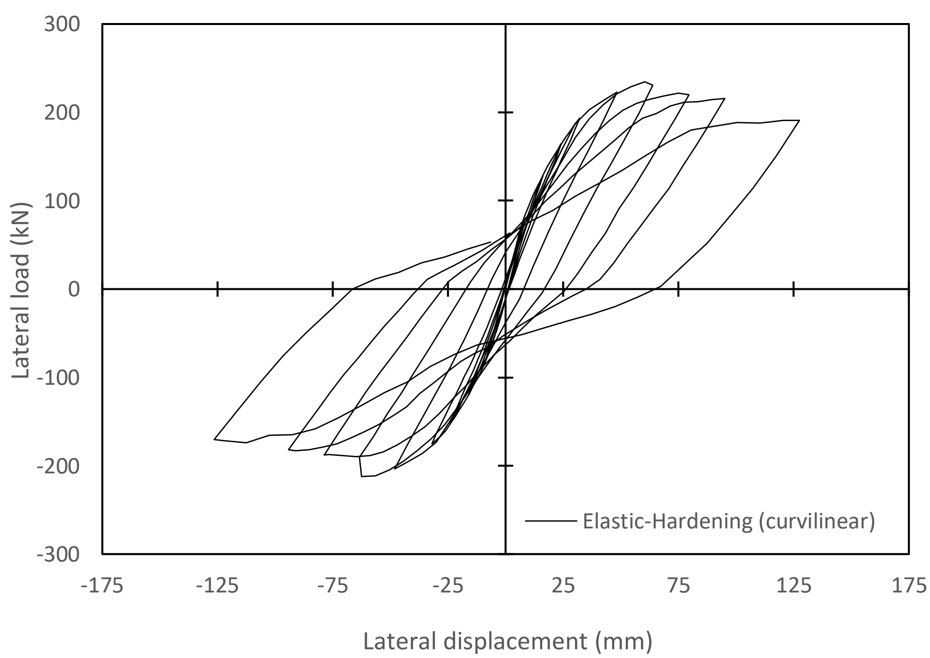

Figure 5-67: BCF hysteretic response utilizing the Elastic-Hardening (curvilinear) model to simulate the hysteretic behaviour of the reinforcement

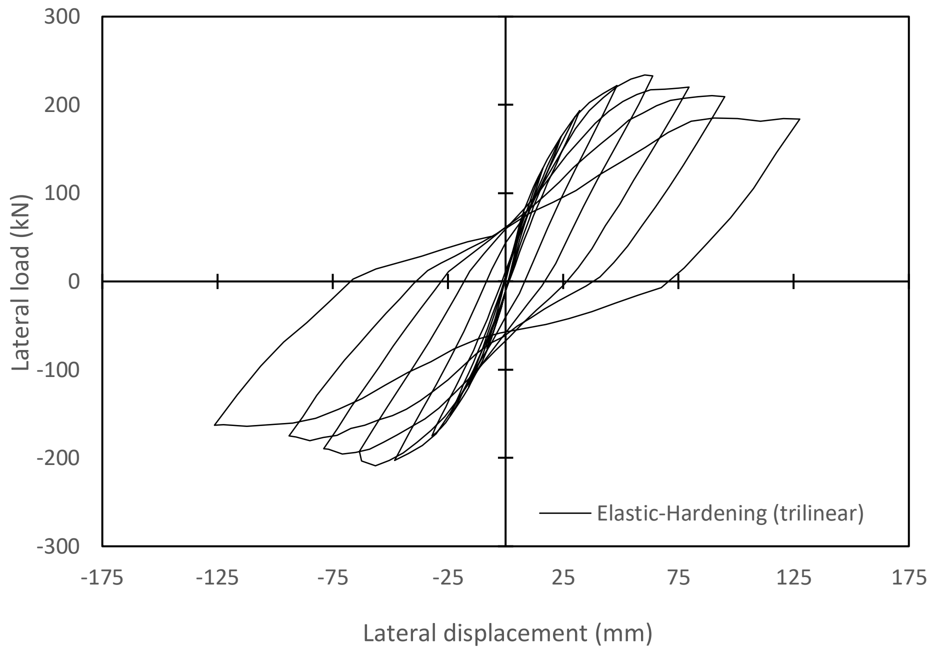

Figure 5-68: BCF hysteretic response utilizing the Elastic-Hardening (trilinear) model to simulate the hysteretic behaviour of the reinforcement

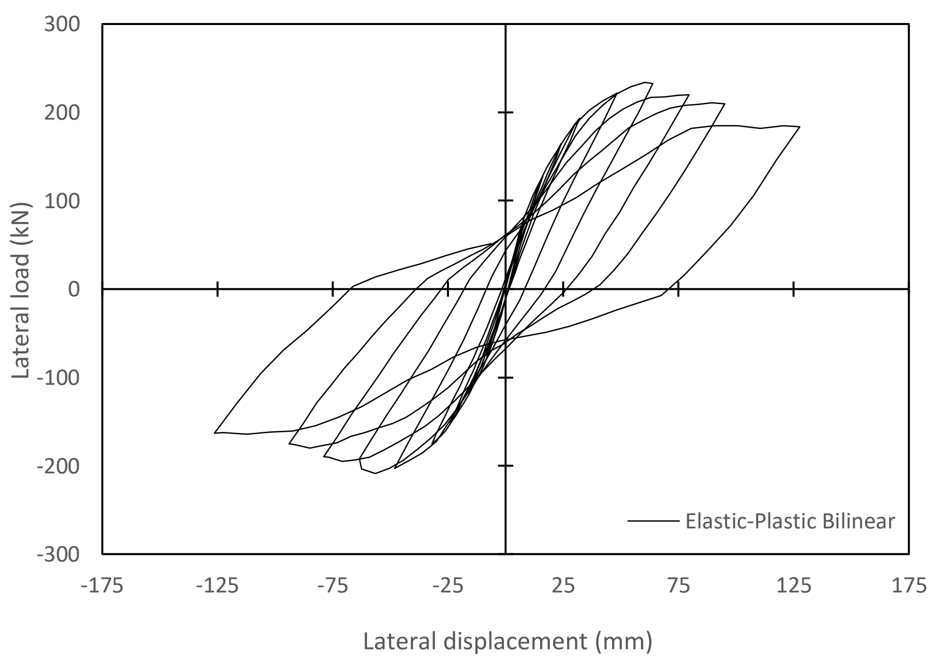

Figure 5-69: BCF hysteretic response utilizing the Elastic-Plastic Bilinear model to simulate the hysteretic behaviour of the reinforcement

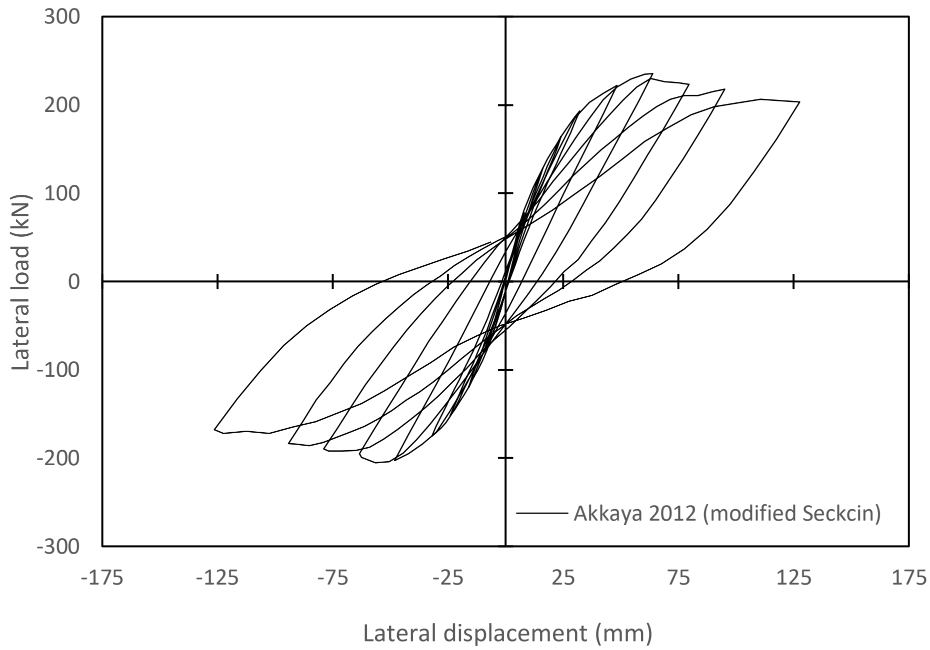

Figure 5-70: BCF hysteretic response utilizing the Akkaya 2012 (modified Seckin) model to simulate the hysteretic behaviour of the reinforcement

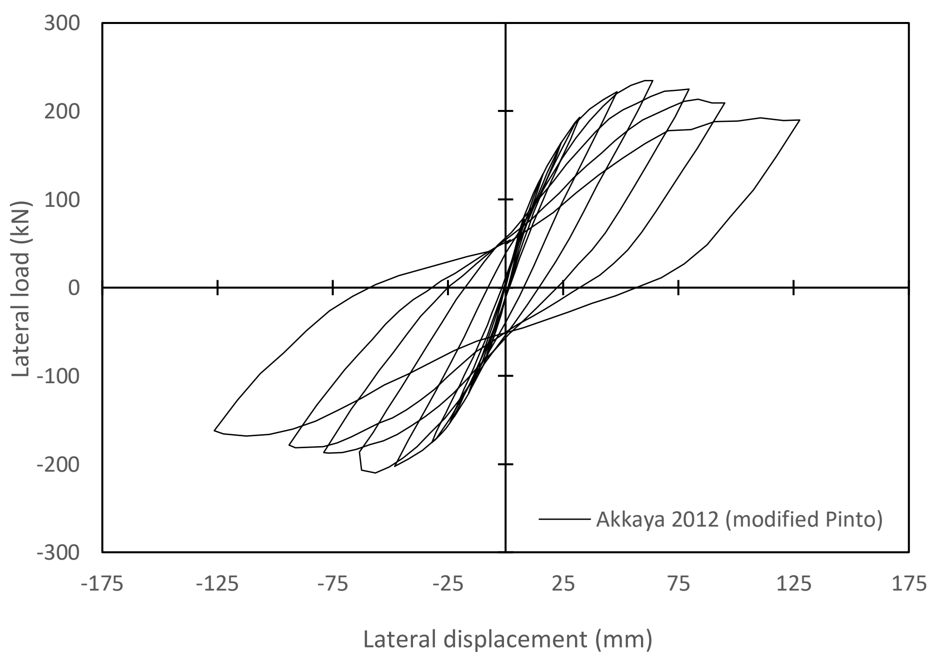

Figure 5-71: BCF hysteretic response utilizing the Akkaya 2012 (modified Pinto) model to simulate the hysteretic behaviour of the reinforcement

Chapter 6

Nonlinear dynamic numerical analyses and results

6.1 Introduction

Two frames were subjected to earthquake records scaled to match the Uniform Hazard Spectra of Montreal and Vancouver to properly evaluate the seismic performance of the frames in terms of transient and permanent lateral displacements. From both the static pushover and hysteretic responses, the frame retrofitted with the modified BRB incorporating an SE-SMA core - with reduced cross sectional area to induce yielding at its mid-length - presented an increase in displacement ductility, strength, and structural resilience related to the conventional steel core BRBs and the bare concrete frame. Therefore, the dynamic analysis was conducted on the frame retrofitted with the modified BRB incorporating an SE-SMA core and on the bare concrete frame.

To conduct the dynamic analyses, the seismic weight was converted into mass and distributed along the beam. Furthermore, the analyses were conducted for two site locations in Canada, the cities of Montreal and Vancouver, to capture the behaviour of the frames in different seismic zones. Due to limitations imposed by the VecTor2 for dynamic analysis, simplified finite element models were necessary and, hence, developed. The limitations are due to the size and complexity of the stiffness matrix; thus, when prior to conducting the dynamic analysis, the initial mesh size of the finite element model developed in Chapter 4 was reviewed to accommodate the limitations.

This chapter provides an overview of the nonlinear dynamic analysis including the modified finite element model and the procedures followed to approximate the seismic weight. Furthermore, as the dynamic analyses were carried out by subjecting the frames to earthquake records, the selection of ground motions is discussed. Seismic response indexes that will be used to evaluate the performance of the frames will also be outlined. Finally, the dynamic response of the two frames will be provided under the selected scaled ground motions.

6.2 Finite element model

To perform dynamic analyses, simplifications in the finite element model were necessary to satisfy limitations in the program. To reduce the stiffness matrix, the number of degrees of freedom were reduced by increasing the mesh size. The new models employed in the dynamic analyses are illustrated in Figure 6-1. As previously stated, the seismic weight was converted into mass and applied along the beam.

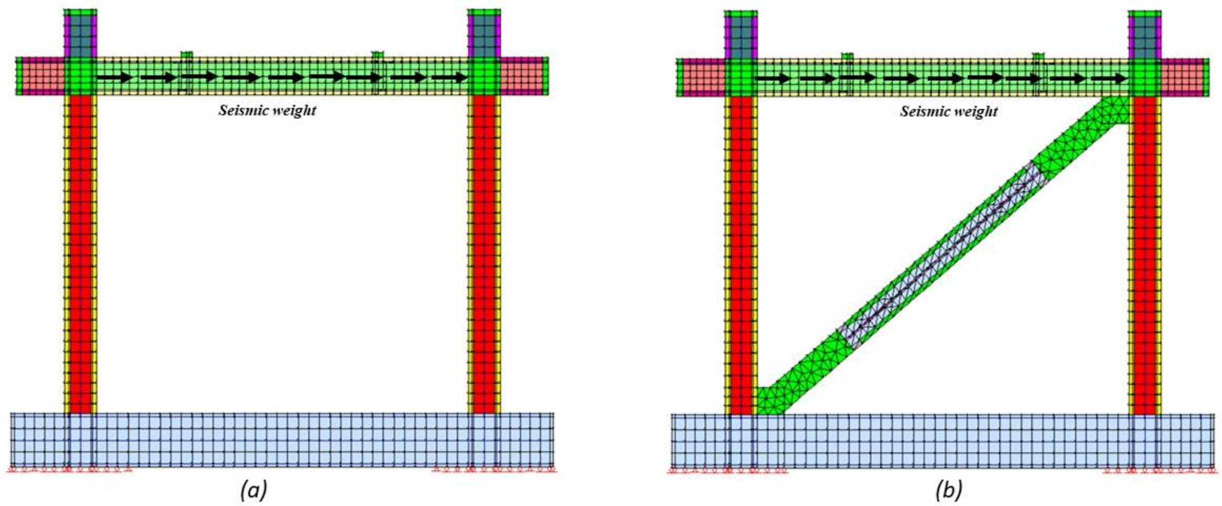

Figure 6-1: Modified finite element models in FormWorks (Vecchio et. Al, 2013) for dynamic analysis: (a) bare concrete frame; and (b) retrofitted frame

The mesh size was increased while maintaining the accuracy to a specified level of 5% relative to the original finite element model presented in Chapter 4. Figure 6-2 illustrates the pushover responses of the modified finite element model of the retrofitted frame in comparison to the original model with the brace under tension loading; while Figure 6-3 illustrates the response with brace under compression. The modified FE model resulted in a difference in lateral strength capacity of 2.94% compared to the original model. Therefore, the increase in mesh size did not affect the accuracy of the model in terms of lateral stiffness and strength capacity. The dynamic analyses were conducted with the modified mesh given that the FE new model satisfied the limitations imposed by VecTor2 while maintaining satisfactory results.

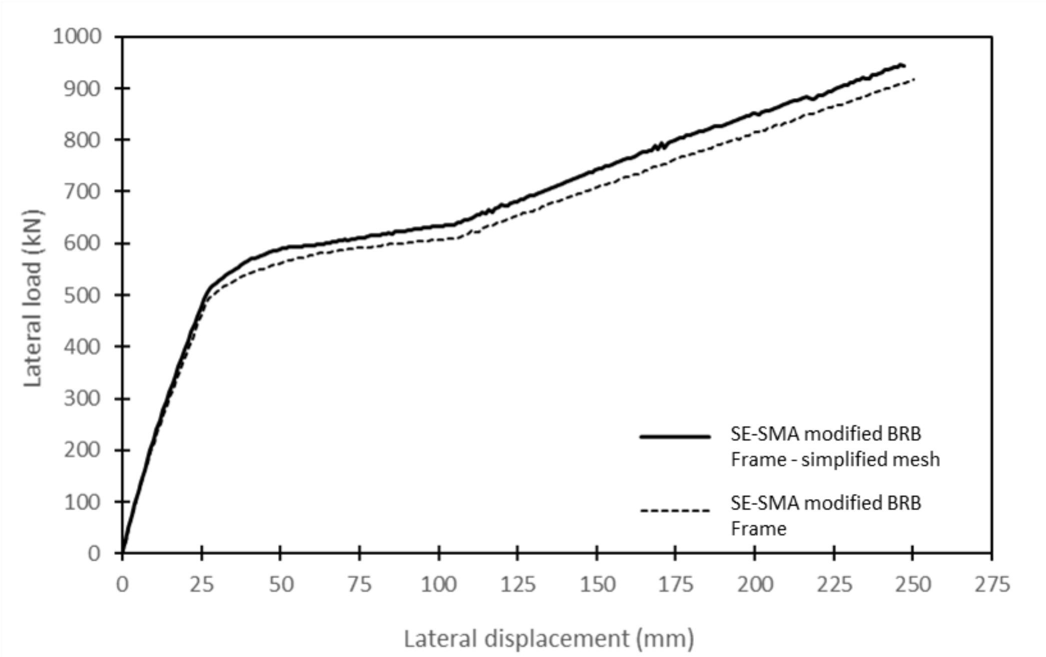

Figure 6-2: Pushover response of the original and modified finite element models of the retrofitted frame with brace under tension

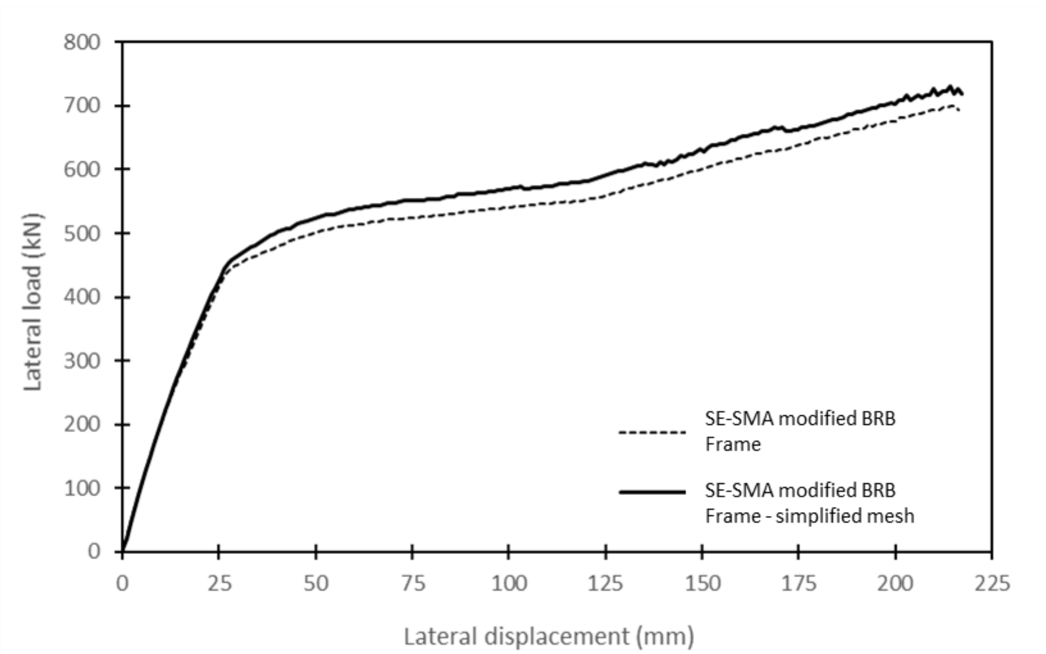

Figure 6-3: Pushover response of the original and modified finite element models of the retrofitted frame with the brace under compression

The material properties incorporated in the dynamic analyses were similar to the static analyses. Furthermore, the ground motion acceleration records were only considered in the horizontal direction. For the investigated frame, the first mode of vibration accumulates more than 90% of the structural mass, thus viscous damping of 1.0% was assigned to this mode. To accurately evaluate residual displacements, the analyses were conducted for an additional 20 seconds beyond the earthquake record duration to allow the frame to decay from free vibration (Maciel, 2019).

6.3 Site location of dynamic analyses

Figure 6-4 illustrates the seismic hazard of Canada based on 2015 and provided by the Natural Resources Canada. According to Filiatrault et al. (2013), in the provinces of British Columbia and Quebec, the population is highly concentrated in urban centres, and as those provinces are susceptible to significant earthquakes, they constitute high seismic risk zones. In assessing seismic risk in Canada, it should be understood as a product of the seismic hazard and the structural vulnerability. Therefore; the probability of occurrence of a high magnitude earthquake, which is higher in Western Canada, should not be the only concern for earthquake engineers. Cities located in Eastern Canada are also at risk due to seismically deficient structures that behave poorly during medium- and high- magnitude earthquakes. As a result, both the West and East should be carefully assessed for seismic risk.

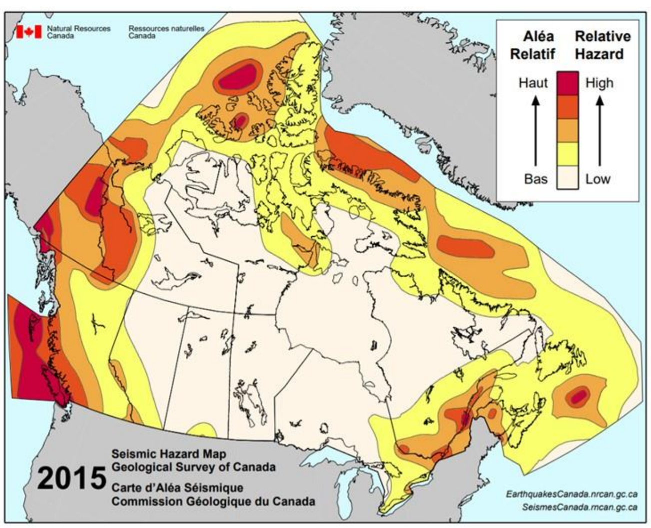

Figure 6-4: Seismic hazard map of Canada (NRC, 2017)

The movements of three tectonic plates – the Juan de Fuca, and the Pacific and the North American – are responsible for most of the earthquakes in Western Canada. Figure 6-5 illustrated the seismic hazard map of British Columbia. According to Filiatrault et al. (2013), this region is part of the Pacific Ring of Fire and is characterized by high magnitude earthquakes with low frequency and long return periods. In this region, earthquakes are commonly associated with fault systems that has also been the cause for the largest historic earthquake in Canada with a Magnitude of 8.1 in 1949. Furthermore, the subduction mechanisms of the Juan de Fuca plate beneath the North American Plate can produce focal points beyond 15 km. According to the NRC (2017), the seismic hazard in British Columbia may be caused by three sources: shallow crustal, instraslab subduction, and subduction interface.

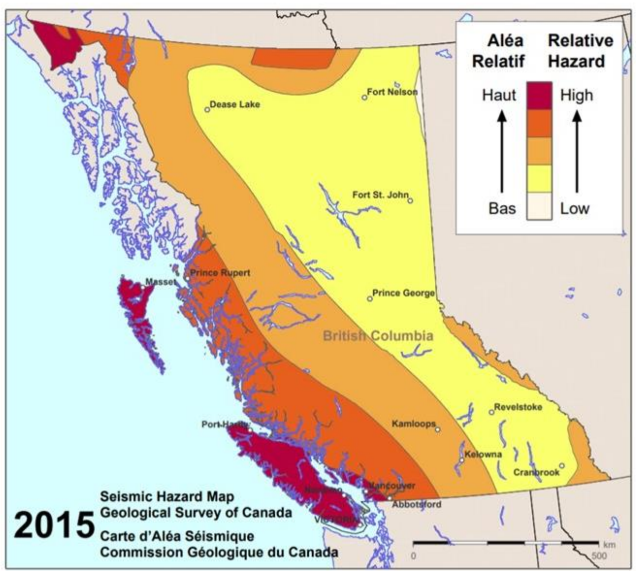

Figure 6-5: Seismic hazard map of the province of British Columbia (NRC, 2017)

In Eastern Canada, ground motions are commonly caused by a reactivation of an old system of rift faults oriented from northeast to east. Figure 6-6 illustrates the seismic hazard map of the province of Quebec. The ground motions in Eastern Canada are characterized by high frequency and short periods. When assessing attenuation, the seismic waves propagate farther than what is experienced in Western Canada. The largest earthquake observed in this zone corresponds to a 7.2 magnitude earthquake in 1929 in southeast of Newfoundland. As a result, to represent characteristic sites from both eastern and western parts of

Canada, the cities of Montreal and Vancouver have been selected as the site location for the nonlinear dynamic analyses, respectively.

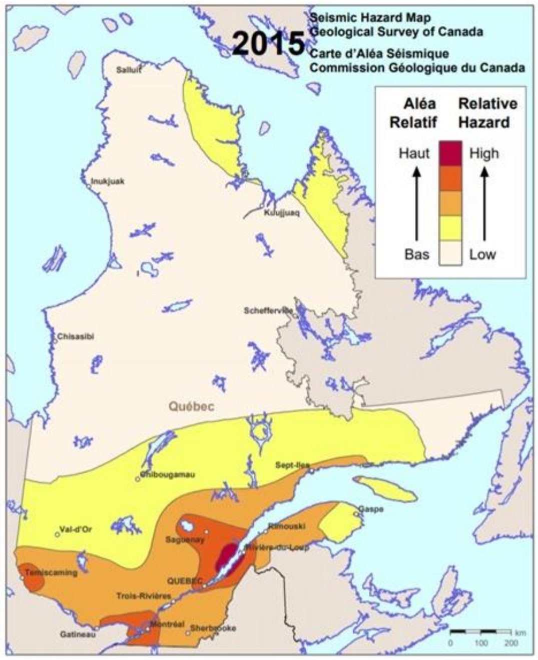

Figure 6-6: Seismic hazard map of the province of Quebec (NRC, 2017)

6.4 Seismic weight

The seismic weight of the frame was approximated utilizing the Uniform Hazard Spectra (UHS), the capacity of the bare concrete frame from the reverse cyclic analysis (F_{max}) and the natural period of the structure (T_a). The intent was to back calculate a seismic weight that would result in the bare concrete frame reach it peak lateral strength capacity under the dynamic analyses. The natural period of the structure was determined based on Clause 4.1.8.1 of the National Building Code of Canada (NRC 2015), where T_a is approximated as stated in Equation 6-1. In that equation, h_n is the frame height above the foundation in meters, which was taken as 3.175 m resulting in a fundamental period of 0.1784 seconds.

$$T_a = 0.075{h_n}^{3/4} \qquad \text{Equation 6-1}$$

The UHS is provided by the NBCC to determine the seismic demands of a specific geographic location in Canada for a probability of exceedance of 2% in 50 years. Having the fundamental period and the Uniform

Hazard Spectra, the horizontal peak ground acceleration (PGA) can be determined. The UHS is approximated for fundamental periods ranging from 0 s to 10 s, and it considers the site seismicity and soil type. The cities of Montreal and Vancouver were selected due to their high seismic risk and difference in ground motions. The building was assumed to be placed in a firm ground, which is defined as Class C by the NBCC 2015. Therefore, the spectra illustrated in Figure 6-7 was generated for the selected locations. It is important to highlight that the NBCC 2015 recommends a more detailed UHS for selecting ground motions records at short periods, which will be elaborated in Section 6.5.

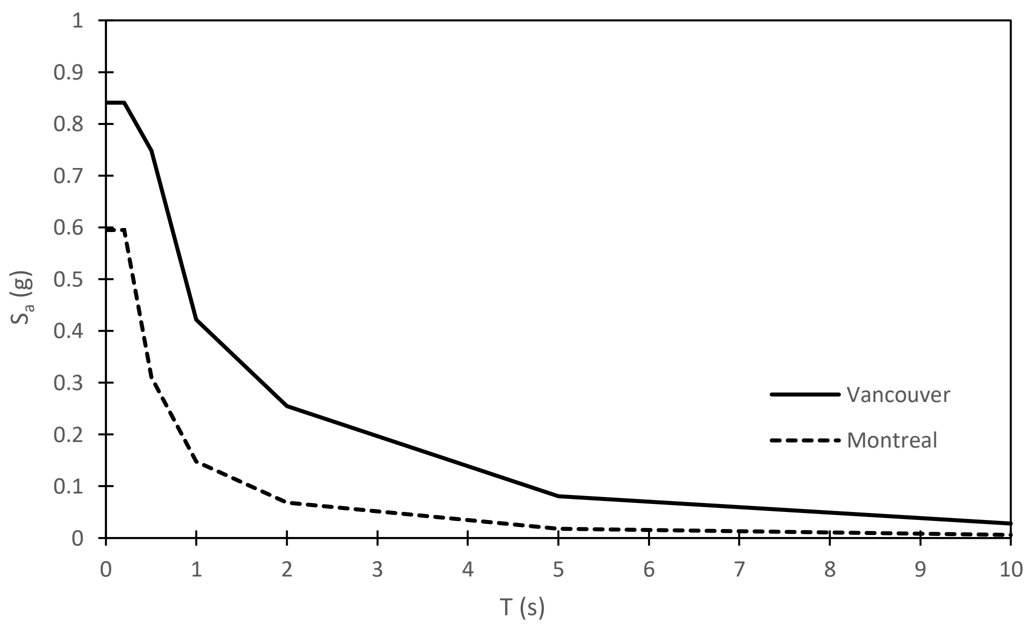

Figure 6-7: Pseudo-acceleration spectra for Montreal and Vancouver considering firm ground

For the bare concrete frame, the peak ground acceleration for the city of Montreal and Vancouver corresponded to 0.6224 g and 0.8062 g, respectively. The seismic demand of a structure can be approximated through the Equivalent Static Force Procedure. In this method, the structure should resist a base shear per Equation 6-2. $S(T_a)$ is the peak ground acceleration for a given site that was determined through the UHS. M_v is the higher mode factor being equal to 1.0 for the bare concrete frame. I_E is the importance factor of the structure and equal to 1.0 since the building was taken as normal importance. W is the seismic weight of the building. R_d is the ductility related modification factor and R_o is the overstrength related factor.

$$V = (S(T_a)M_v I_E W/(R_d R_o) \qquad \text{Equation 6-2}$$

If the structure responds predominantly in the first mode, the code specifies a method of determining the elastic base shear (V_e) presented in Equation 6-3. Given that the frame can be represented as a single degree of freedom with more than 90% of its mass accumulated in the first mode of vibration, M_v equals 1.0. To evaluate the frame as an independent portion of the building, the seismic weight has been approximated based on the reverse cyclic response capacity. Therefore, with the pseudo-acceleration determined from the natural period and UHS, and a frame capacity of 233 kN from the static analysis, the seismic weight was approximated to be 38160 kg for the city of Montreal and 29460 kg for the city of Vancouver.

$$V_e = S(T_a)M_v W \qquad \text{Equation 6-3}$$

6.5 Selection of ground motion records

To select a proper ground motion for a given site, the record must be selected based on the geotechnical conditions of the site, and magnitude and distance that control the seismic hazard. The earthquake records are then selected, from previous records, to match the target acceleration response spectra ($S_T(T)$) over the period range (T_R), which is defined based on the structure in question. This period range should be carefully determined to capture the periods of vibration that significantly contributes to the dynamic response of the structure. T_R can be determined based on the seismic provisions provided by the 2015 NBCC (NBR, 2015b).

The formulations to define the minimum and maximum values of the period range are presented in Equation 6-4 and 6-5 taken from Structural Commentary J of the NBCC 2015. The upper period (T_{max}) is equal to the greater of the value between two times the first mode period and 1.5 seconds. The minimum period (T_{min}) is determined as equal to the period of the highest mode of vibration necessary to accumulate 90% of the total mass of the structure ($T_{90\%}$), but it should not exceed 15% of the first mode period. It is important to highlight that the upper and lower limit of the period range should be determined using the periods obtained in the direction the structure is analyzed; for this study, the horizontal direction.

$$T_{min} = min\begin{cases} 0.15T_1 \\ T_{90\%} \end{cases} \quad \text{Equation 6-4}$$

$$T_{max} = max\begin{cases} 2T_1 \\ 1.5s \end{cases} \quad \text{Equation 6-5}$$

The NBCC 2015 provides two methods of selecting the ground motion records that match the target acceleration response spectra ($S_T(T)$). Method A considers a single target response spectrum for the entire period range. That method was adopted to match the ground motion records for the cities of Montreal and Vancouver in this study. According to Tremblay (2015), Method A accurately provides a selection of scaled earthquakes to reflect M-R scenarios of a given location. When using Method A to match the target spectrum, a minimum number of five ground motion records should be selected to suit each scenario-specific range (T_{RS}), but the total number of earthquake records should not be less than 11 (NRC, 2015b). For Montreal two scenario-specific ranges (T_{RS}) were defined, while for Vancouver three T_{RS} were determined; this will be further discussed in Sections 6.5.1 and 6.5.2.

The spectral matching technique developed by Atkinson (2009) was utilized in this research since it provides an accurate fit between the target spectrum and historical records over a determined period range. The recommended procedures to select and scale ground motion records are as follows:

1- Determine the target Uniform Hazard Spectra (SA_{targ}) for the locality and site conditions based on the NBCC 2015 (NRC, 2015). Carefully assess substituting the plateau between the periods of 0 s and 0.5 s by discrete Peak Ground Acceleration for periods of 0 s, 0.05 s, 0.1 s and 0.3 s as per Commentary J of the National Building Code.

2- Specify the period range of interest for matching SA_{targ} based on the Equations 6-4 and 6-5 from the 2015 NBCC.

3- Select appropriate records (SA_{sim}) based on the specific situation, period range, and magnitude. This will depend on the location of the ground motion in question. The PEER records database is a great source.

4- For each selected record, calculate the ratio SA_{targ}/SA_{sim} for the specified period range. Then, calculate the mean and standard deviation of the SA_{targ}/SA_{sim} ratio.

5- Select the ground motions with lowest standard deviation, which will have the best matching shape to the target, and with a mean raging between 0.5 and 2.0 when possible (Atkinson, 2009).

6- For the selected ground motions, scale the accelerogram by multiplying each point with the SA_{targ}/SA_{sim} mean. According to Commentary J of the NBCC 2015 (NRC, 2015b), the ground motions should be scaled so that on average the response spectrum should equal or exceed the target spectrum.

7- For a scenario-specific time history (T_{RS}) all records must be scaled by a second common factor. After applying the second scaling factor, the mean response spectrum of the records should not fall bellow 10% of the target spectrum (SA_{targ}) at any point of the period range.

The Pacific Earthquake Engineering Research (PEER) database was selected as a source of ground motion records. In the PEER database, the records are separated in two different zones that accurately simulates Western and Eastern Canada.

To ease the matching process between the target response spectra and the ground motion records present in the literature, the NBCC 2015 (NRC, 2015b) advises to substitute the plateau present in the uniform hazard spectra between periods of 0 s and 0.5 s with discrete Peak Ground Acceleration (PGA) values corresponding to periods of 0 s, 0.05 s, 0.1 s and 0.3 s. Therefore, the Uniform Hazard Spectra previously developed and illustrated in Figure 6-7 was modified for selecting earthquake records. Figure 6-8 illustrates the modified UHS for the city of Montreal; while Figure 6-9 depicts for the city of Vancouver.

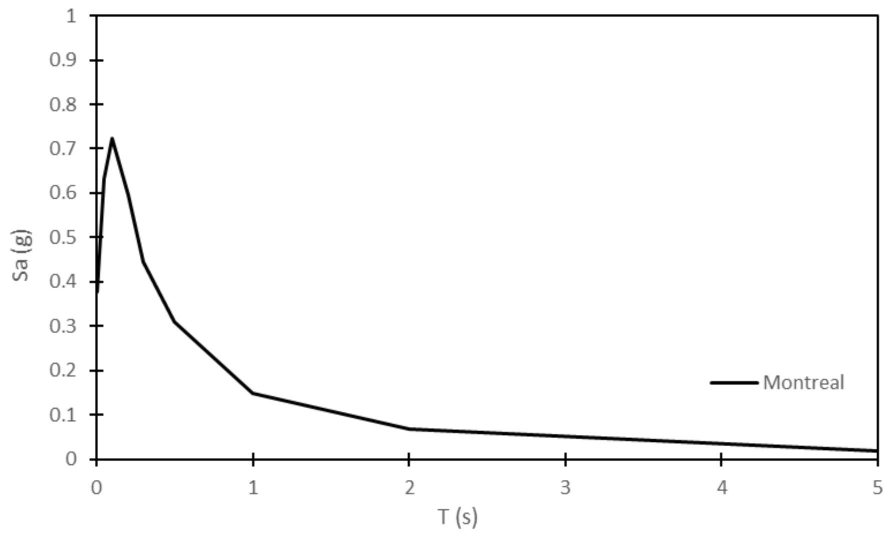

Figure 6-8: Target acceleration spectrum for Montreal

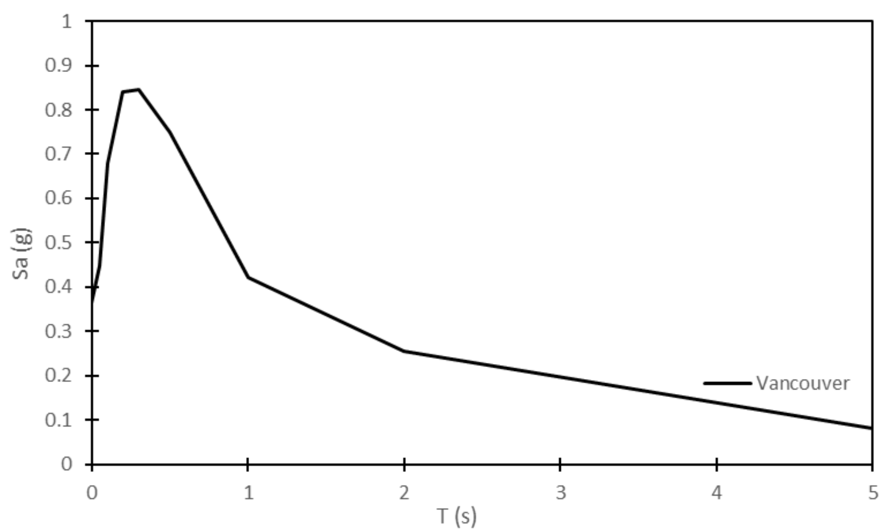

Figure 6-9: Target acceleration spectrum for Vancouver

6.5.1 Ground motions for Montreal – Quebec

The ground motions were selected to accurately simulate the M-R scenarios that significantly contributes to the seismic hazard of the selected zone. For the city of Montreal, the period to match the ground motion to the target spectrum ranged from 0.0268 s to 1.5 s. According to Atkinson (2009), the seismic hazard of Eastern Canada (M-R) is characterized by two different scenarios. The first scenario is defined by earthquakes with magnitude of 6.5 in a 10 km – 30 km distance range. This scenario significantly affects the period range between 0.0268 s to 1.0 s, which will be designated as T_{RS1}. The second scenario is characterized by 7.0 magnitude earthquakes occurring 20 km to 70 km away from the city; this scenario affects the period range between 1.0 s and 1.5 s, herein designated T_{RS2}.

For each M-R scenario, T_{RS} period ranges, a single target response spectrum was determined based on the UHS corresponding to a 2% probability of exceedance in 50 years. Therefore, six ground motion records were selected for the M-R scenario 1 that ranges from a period of 0.0268 s to 1.0s; while five records were chosen for the scenario 2. Table 6-1 lists important characteristics of the 11 ground motion records, including magnitude, PGA and duration of the earthquake. Furthermore, Figure 6-10 illustrates the unscaled ground motion records selected for the city of Montreal. In this figure, the target spectrum determined from the NBCC 2015 is also presented.

Table 6-1: Relevant characteristics of ground motion records utilized for the dynamic analysis in Montreal

Scenario	***Reference code***	***Magnitude***	***Duration (sec)***	***PGA (g)***	***Mean (SA_{targ}/SA_{sim})***
1	***TR1-1***	*6*	*26.2*	*0.79*	*1.46*
	TR1-2	*6*	*36.9*	*0.57*	*1.91*
	TR1-3	*6*	*45.7*	*1.72*	*1.07*
	TR1-4	*6*	*51.6*	*0.81*	*1.88*
	TR1-5	*6*	*40.0*	*1.03*	*1.44*
	TR1-6	*6*	*37.6*	*1.42*	*0.95*
2	***TR2-1***	*7*	*54.3*	*0.59*	*0.88*
	TR2-2	*7*	*21.0*	*0.63*	*1.28*
	TR2-3	*7*	*54.6*	*0.28*	*1.66*
	TR2-4	*7*	*33.0*	*0.47*	*1.17*
	TR2-5	*7*	*44.0*	*0.20*	*1.48*

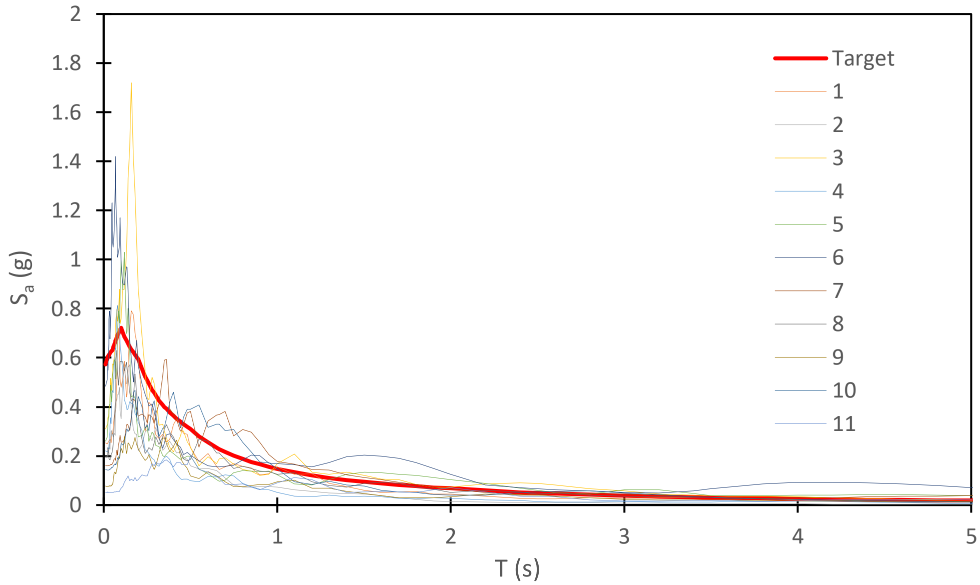

Figure 6-10: Spectral acceleration of unscaled ground motions for dynamic analysis in Montreal

Figure 6-11 illustrates the scaled ground motion records for T_{RS1}, while Figure 6-12 depicts the scaled ground motions that simulate the seismic hazard of the M-R scenario dominant on T_{RS2}. As per the recommendations from Atkinson (2009), the eleven selected ground motions, illustrated in Figures 6-8 and 6-9, were also scaled by a second common factor of 1.3.

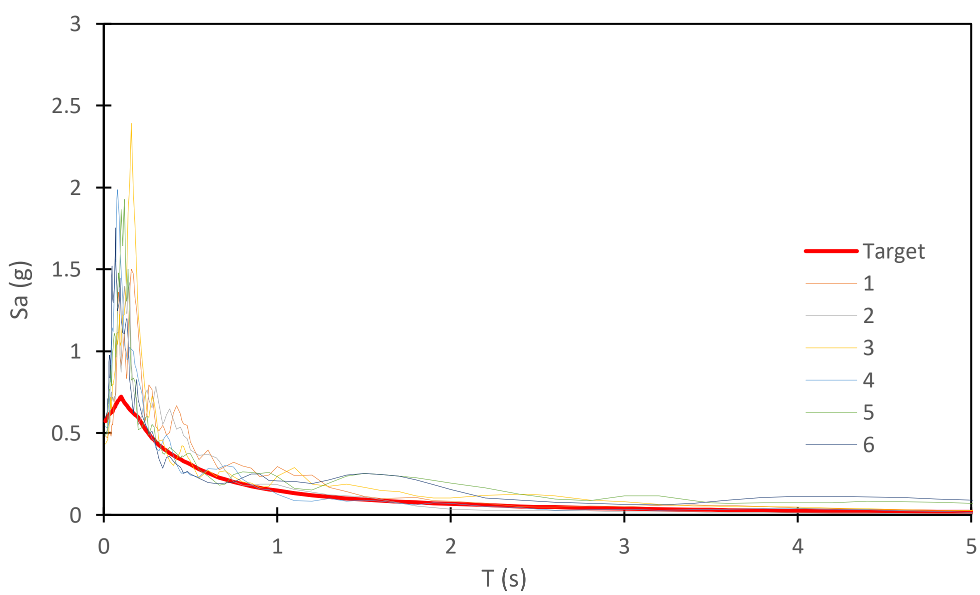

Figure 6-11: Spectral acceleration of scaled ground motions for dynamic analysis in Montreal in the T_{RS1}

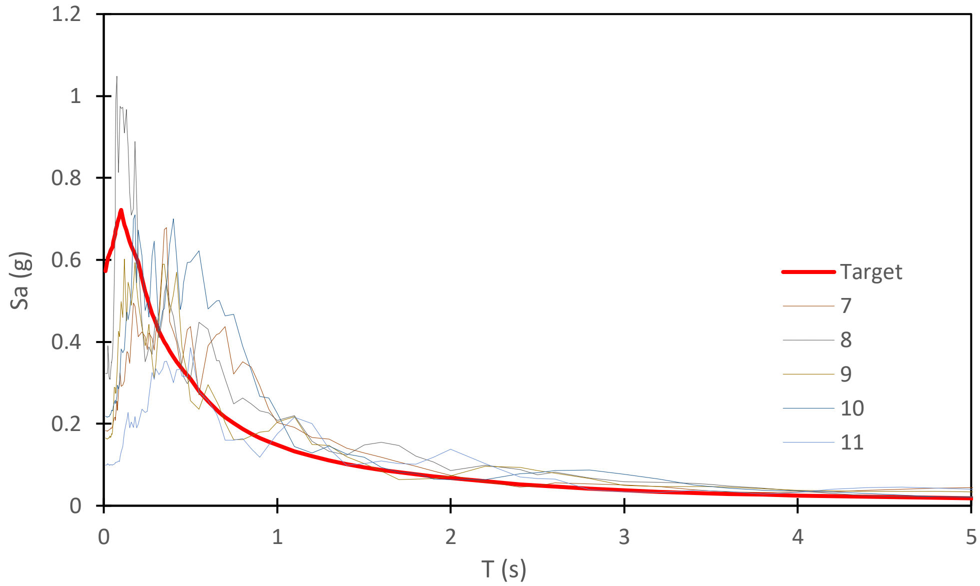

Figure 6-12: Spectral acceleration of scaled ground motions for dynamic analysis in Montreal in the T_{RS2}

Figure 6-13 illustrates the mean of the spectral acceleration of the selected ground motions. The mean response of the different M-R scenarios is plotted to corroborate that their acceleration spectrum do not fall bellow 10% of the target spectrum (SA_{targ}) at any point of the period between 0.0268 and 1.5 seconds as it is recommended by Commentary J in the 2015 NBCC.

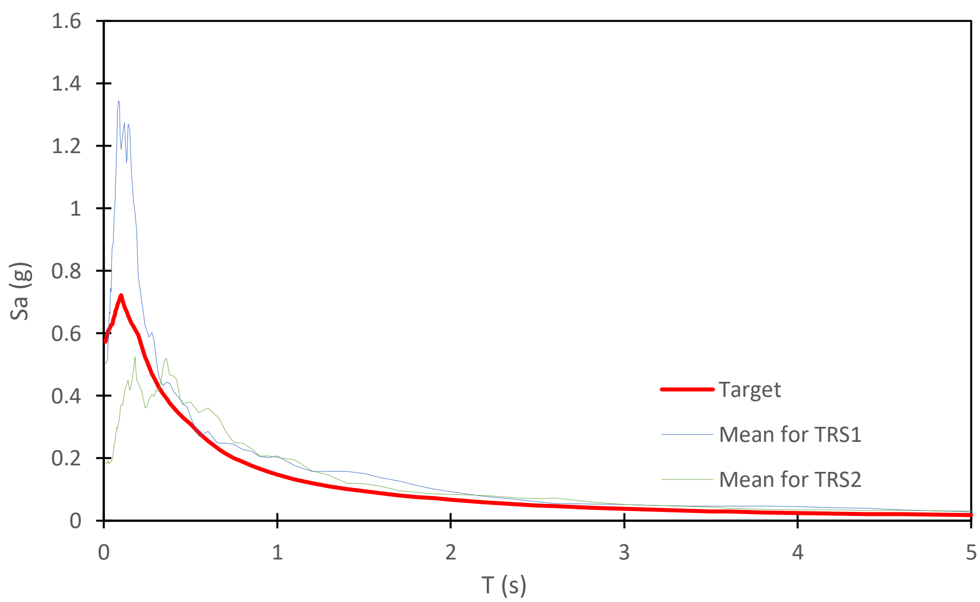

Figure 6-13: Mean of the records selected and scaled for Scenarios 1 and 2 in comparison to the target spectrum for the city of Montreal

Since the ground motions were applied as time-histories in VecTor2 (Vecchio et al., 2013), the scaling factors applied to each acceleration spectrum were also applied to their acceleration time-histories. As previously noted, to allow for the free vibration to decay after the ground excitation, the earthquake records were extended for an additional 20 seconds with acceleration equal to zero.

6.5.2 Ground motions for Vancouver – British Columbia

For the dynamic analysis for Vancouver, the period range of interest is the same as Montreal, from 0.0268 s to 1.5 s. For the complex seismic hazard scenarios of Vancouver, three different M-R scenarios are required to match the ground motion records. According to Tremblay et al. (2015) and Maciel (2019), Scenario 1 (T_{RS1}) is characterized by earthquakes with low magnitudes of 6 and at a distance of approxinately14 km; Scenario 2 (T_{RS2}) is defined by ground motions with magnitude 7 and a distance of 54 km; and Scenario 3 (T_{RS3}) is characterized by magnitudes between 8 and 9 and distance of 141 km. Each scenario is represents a different seismic hazard that arises from the tectonic movements: scenario 1 is characterized by shallow earthquakes, scenario 2 by deep sub-crustal events, and scenario 3 by interface or subduction earthquakes occurring at the boundary of two plates.

According to Tremblay et al. (2015), T_{RS1} ranges from 0.2 to 0.8 seconds, T_{RS2} from 0.3 to 1.5 seconds, and T_{RS3} from 1 to 1.5 seconds. Initially T_{RS3} was bounded by an upper limit of 3 s, but as the period range of interest for the moment-resisting frame in question is limited by 1.5 s, so will T_{RS3}. Tremblay et al. (2015) also suggested an acceptable distance range for each scenario. Therefore, the acceptable range of magnitude, distance, and the quantity of records per scenario are listed in Table 6-2. Table 6-3 presents important characteristics of the eleven ground motion records, including magnitude, PGA and duration of the earthquake.

Table 6-2: Information for selection of the ground motion records for dynamic analysis in Vancouver adapted from Tremblay et al. (2015) and Maciel (2019)

Event type	***Magnitude***	***Distance***	***Scenario 1***	***Scenario 2***	***Scenario 3***
Shallow	*5.7-7.7*	*0-54 km*	*4 records*		
Sub-crustal	*6.0-8.0*	*0-112 km*		*3 records*	
Subduction	*7.6-9.6*	*81-201 km*			*4 records*

Table 6-3: Relevant characteristics of the selected ground motion records for dynamic analysis in Vancouver

Scenario	***Reference code***	***Magnitude***	***Duration (sec)***	***PGA (g)***
1	***TR1-1***	*6*	*40.00*	*0.33*
	TR1-2	*6*	*50.00*	*0.13*
	TR1-3	*6*	*54.37*	*0.60*
	TR1-4	*5*	*40.00*	*0.18*
2	***TR2-1***	*6*	*40.48*	*0.36*
	TR2-1	*7*	*70.19*	*0.12*
	TR2-3	*7*	*54.37*	*0.60*
3	***TR3-1***	*7*	*33.00*	*0.11*
	TR3-2	*7*	*33.00*	*3.35*
	TR3-3	*7*	*50.00*	*0.42*
	TR3-4	*7*	*52.43*	*0.18*

Figure 6-14 illustrates the eleven selected unscaled ground motion records from the PEER database against the target acceleration spectrum. As three scenarios were utilized to characterize the seismic hazard in Vancouver, Figures 6-15 to 6-17 provide the scaled selected ground motions for each scenario. After scaling with the mean SA_{targ}/SA_{sim}, a secondary common scaling factor equal to 1.3 was applied to all the records.

This scaling factor intends to guarantee that the mean response of the selected ground motions do not fall bellow 10% of the target spectrum at any period within the M-R scenario period range they correspond to. The target spectrum is then plotted with the mean target for each period range in Figure 6-18.

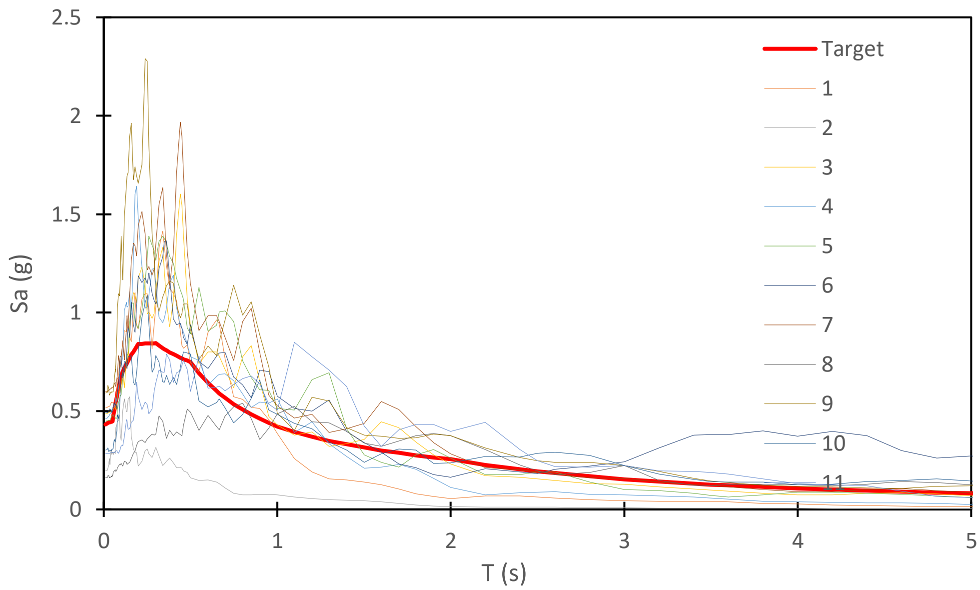

Figure 6-14: Unscaled ground motion records for dynamic analysis in Vancouver

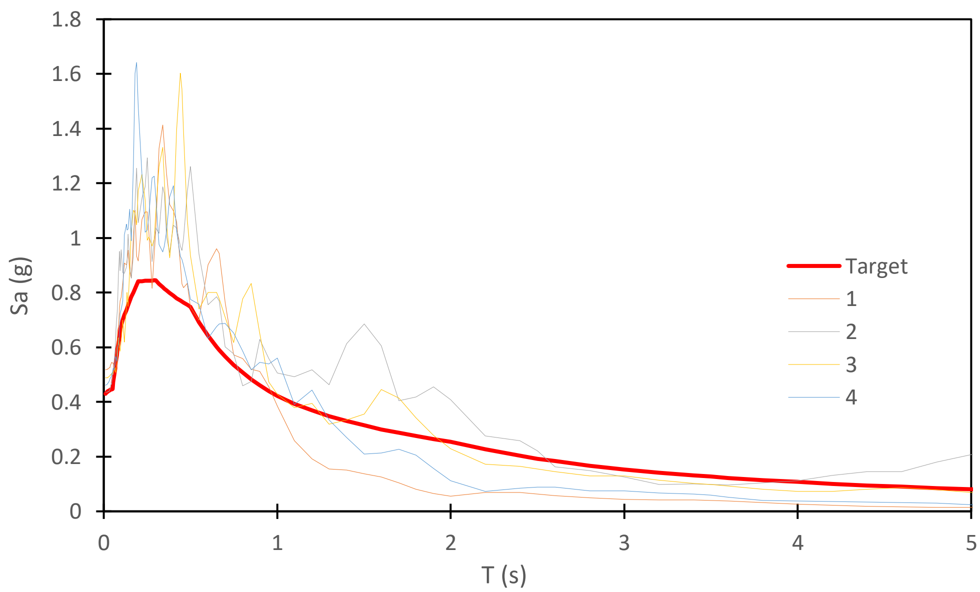

Figure 6-15: Scaled ground motion records for T_{RS1}

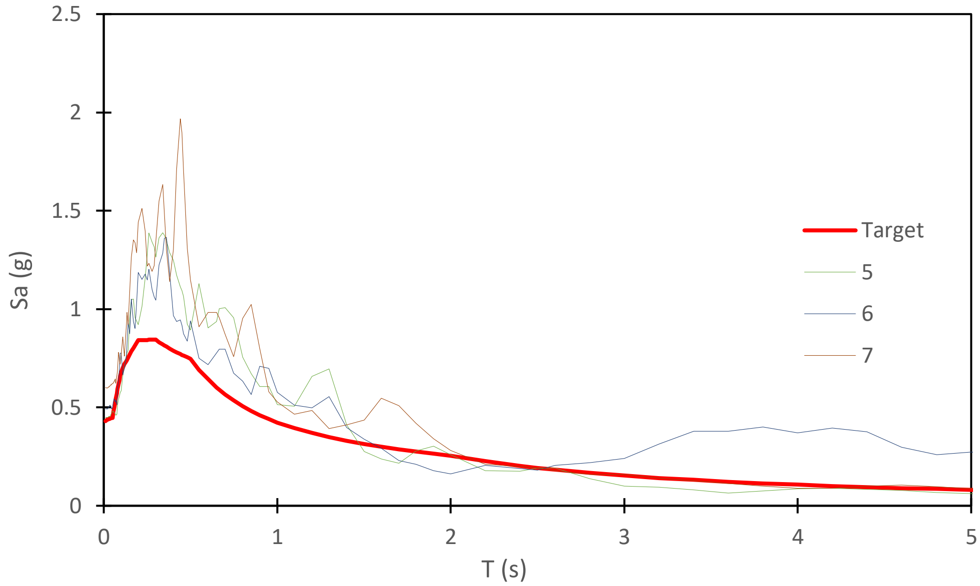

Figure 6-16: Scaled ground motion records for T_{RS2}

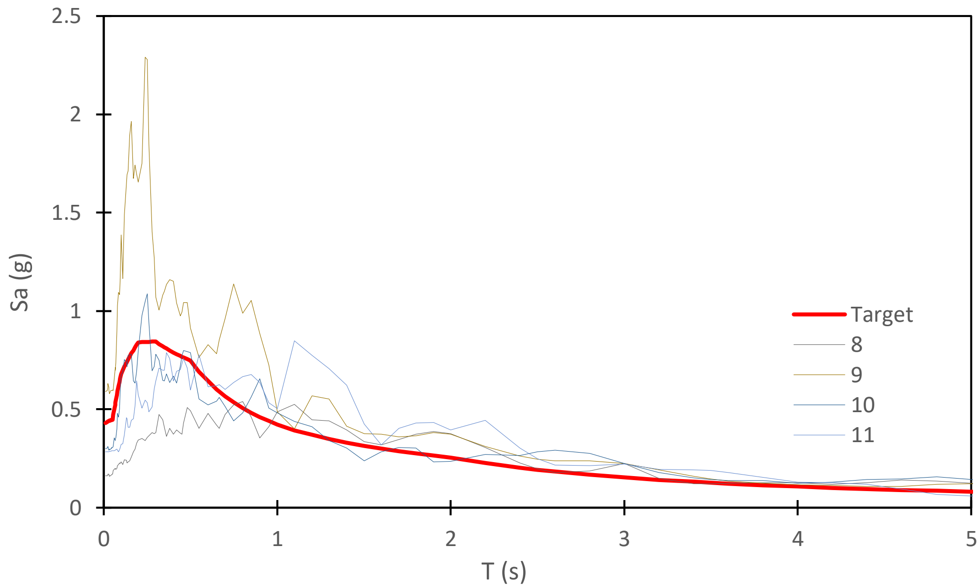

Figure 6-17: Scaled ground motion records for T_{RS3}

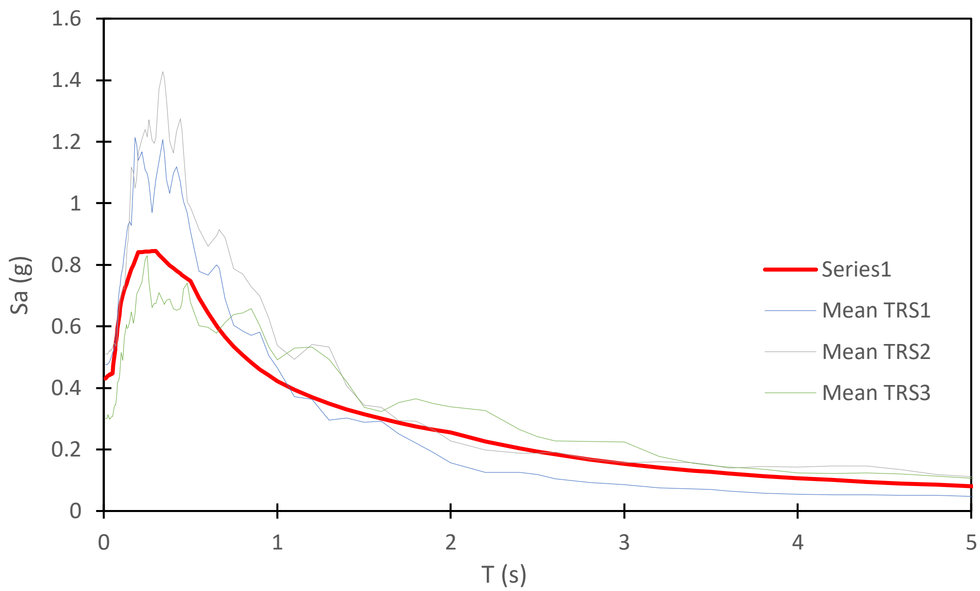

Figure 6-18: Mean of the records selected and scaled for Scenarios 1, 2 and 3 in comparison to the target spectrum for the city of Vancouver

6.6 Dynamic response

The dynamic response of the frames was developed after employing the ground motion records to perform nonlinear time history analysis. Therefore, the response of both the control frame and the frame retrofitted with modified BRB incorporating an SE-SMA core bar are herein presented, where the response of the frames located in Montreal (QC) and Vancouver (BC) are separately demonstrated. All frames were subjected to the ground motion records obtained from the PEER database with the additional 20 s to allow for complete decay of the response. For each M-R scenario, the response of the frames under two different ground motion records will be presented in this section, the remaining responses from the earthquake records of each M-R scenario are presented in the Appendix. From the dynamic analysis, the hysteretic, lateral strength time history, and top displacement time history responses are presented. For the top displacement time history response, the blue line identifies the yielding displacement of the frame based on the static reverse cyclic behaviour, while the red line illustrates the ultimate displacement. Furthermore, the displaced and cracked shapes are illustrated, and the permanent displacement of the frames subjected to the ground motion records are noted. To evaluate the performance of the retrofitted frame against the control frame, both frames were also subjected to a ground motion record from Vancouver and increased by 100%, 300%, and 500%. The results will be assessed in terms of lateral permanent and transient drifts, and failure mechanism.

6.6.1 Bare concrete frame

6.6.1.1 Earthquake records Montreal – QC

6.6.1.1.1 TR1-5

Figure 6-19 illustrates the lateral displacement–lateral load, lateral load time-history, and lateral top displacement time-history responses from the bare concrete frame under the ground motion record TR1-5. This earthquake record represents the seismic hazard of Eastern Canada, where yielding of the frame was not induced. As the frame did not experience plastic deformations, residual displacements were negligible as shown in Figures 6-19 (a) and (c). Figure 6-19 (a) also demonstrates the absence of inelastic displacement and relatively low dissipated energy from the hysteretic response. A top displacement of 30.915 mm was imposed on the system corresponding to a lateral strength of 145.4 kN (Figure 6-19 (b)).

Figure 6-20 illustrates the displaced shape and crack patterns of the frame after applying the ground motion record. Although cracks were distributed in both the columns and beam, they were concentrated near the base of the columns and near the beam-column joint. Given that the frame was in the elastic range, the cracks were limited to 1 mm width and concrete spalling was not present. The structural integrity of the frame was confirmed after the applied earthquake record.

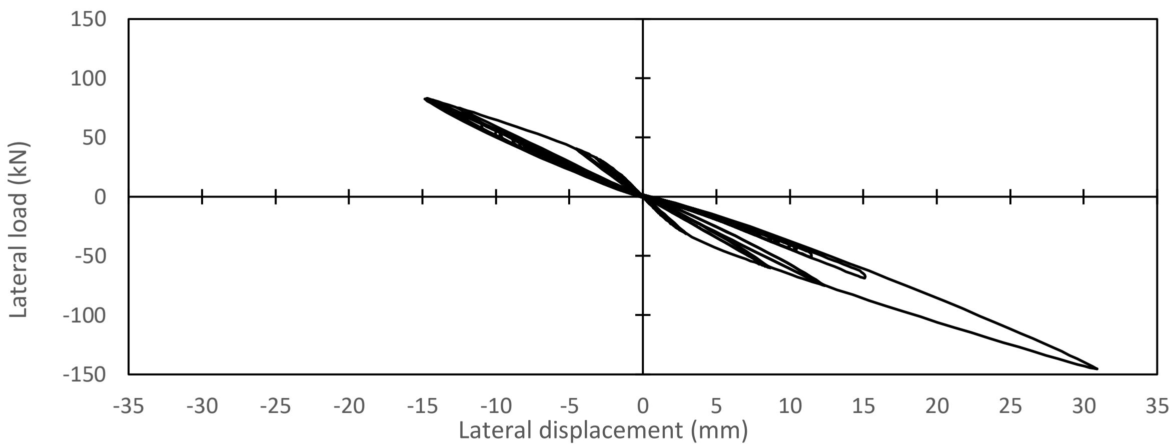

(a)

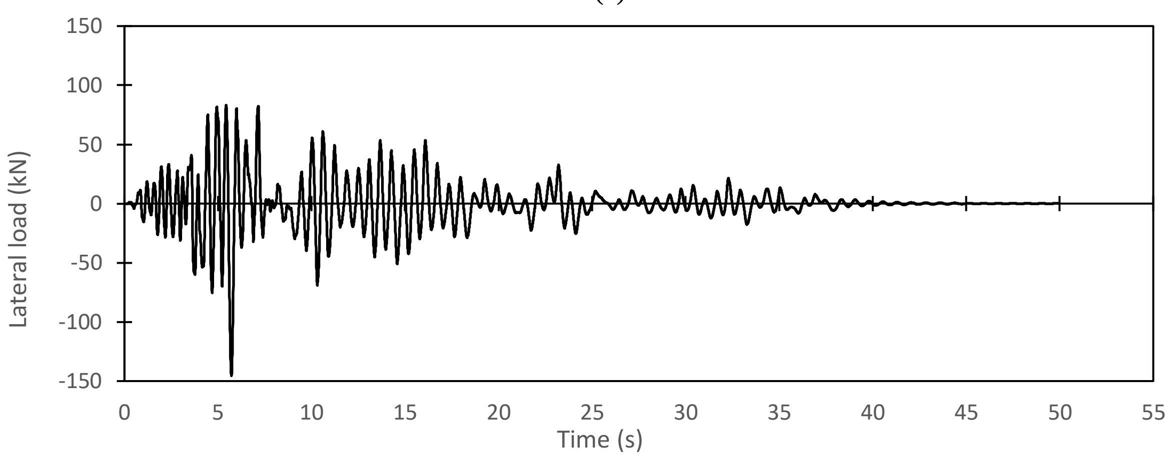

(b)

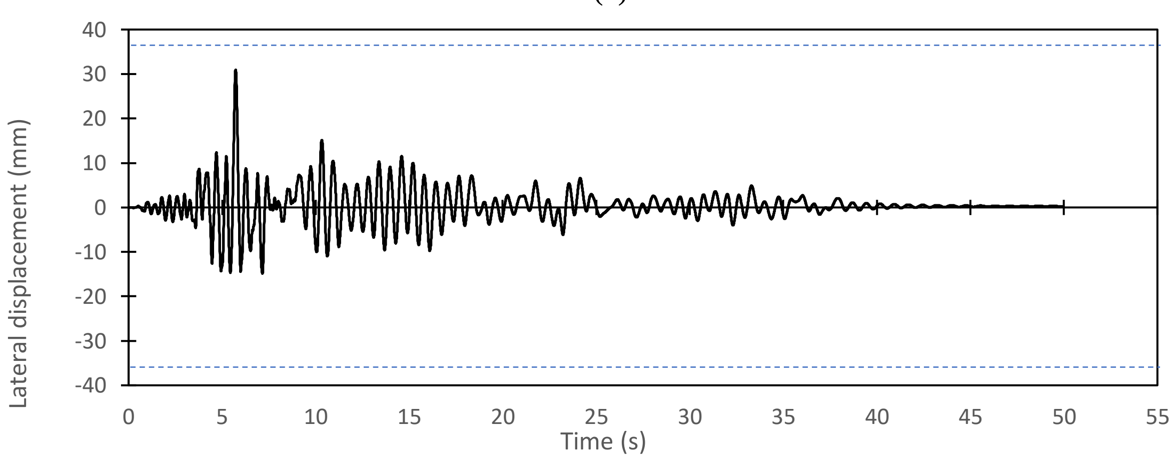

(c)

Figure 6-19: Bare concrete frame under earthquake record TR1-5: (a) lateral displacement-lateral load response; (b) lateral load time history; and (c) lateral displacement time history

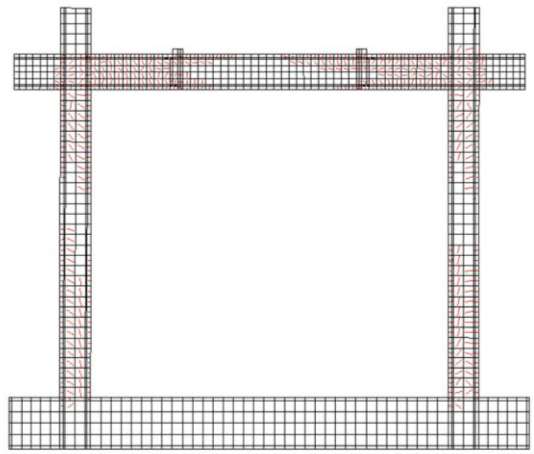

Figure 6-20: Displaced shape and crack patterns of BCF at the end of the analysis for earthquake record TR1-5

6.6.1.1.2 TR1-6

The only ground motion record from the first M-R scenario (TR1) for the city of Montreal that induced inelastic deformations in the system was TR1-6. The inelastic deformations in the lateral displacement–lateral load response illustrates an increase in energy dissipation relative to the response from TR1-5 (Figure 6-21 (a)). The maximum lateral strength exhibited by the frame corresponded to 185.2 kN and 178.8 kN, in the negative and positive directions, respectively (Figure 6-21 (b)). The ground motion record induced displacements up to 78.29 mm, and a permanent displacement of 5.347 mm was accumulated at the end of the analysis (Figure 6-21 (c)). Ratcheting was identified in the frame, which corresponds to accumulation of damage in one direction resulting in permanent displacements at the end of the analysis.

Figure 6-22 illustrates the displaced shape and crack pattern of the control frame under the current ground motion record. The crack pattern shows shear cracks are concentrated near the beam-column joints. Flexural cracks were also evident at bottom of the beam at the midspan. Wider cracks were observed at the base of the column, achieving openings of 2 mm.

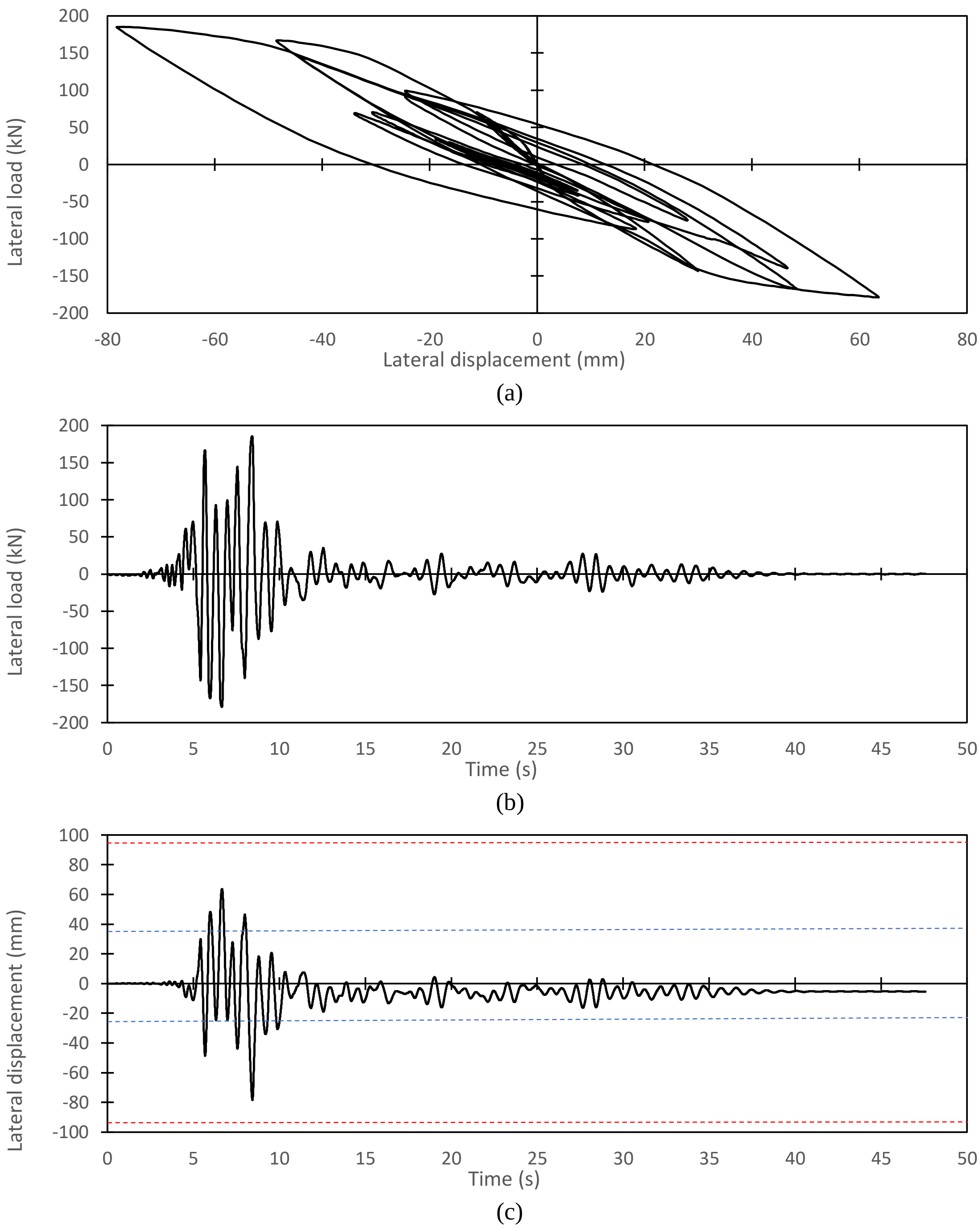

Figure 6-21: Bare concrete frame under earthquake record TR1-6: (a) lateral displacement-lateral load response; (b) lateral load time history; and (c) lateral displacement time history

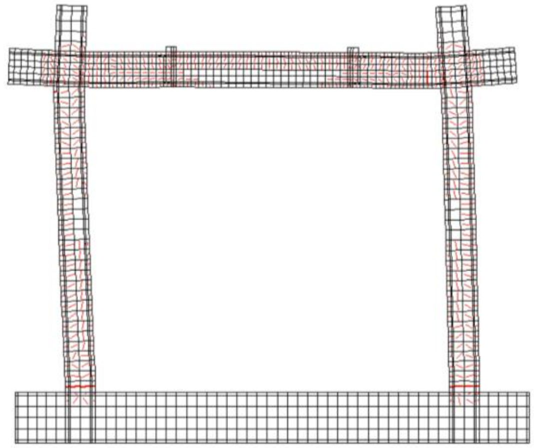

Figure 6-22: Displaced shape and crack pattern of BCF at the end of the analysis for earthquake record TR1-6

6.6.1.1.3 TR2-2

Figure 6-23 illustrates the response of the frame for the second M-R scenario (TR2), where the frame yielded, and ratcheting is evident. The ground motion record induced a maximum displacement of 47.656 mm and the frame sustained a peak lateral strength of 167.4 kN. Furthermore, since the frame yielded, a permanent displacement of 1.279 mm accumulated at the end of the ground shaking.

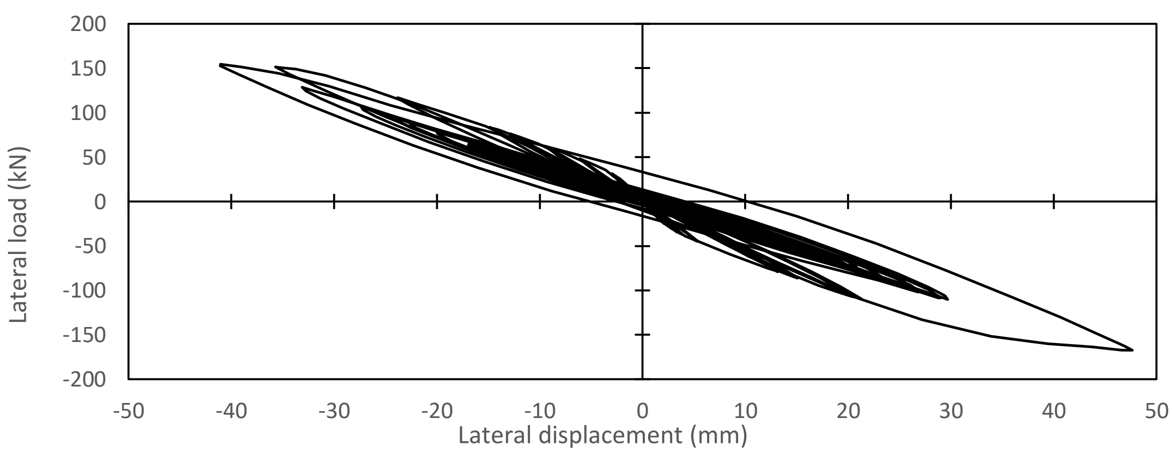

(a)

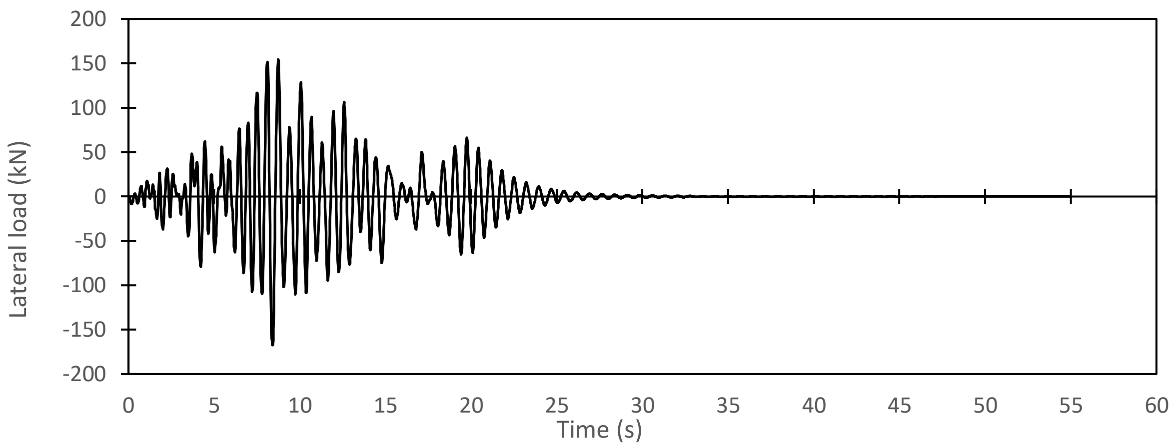

(b)

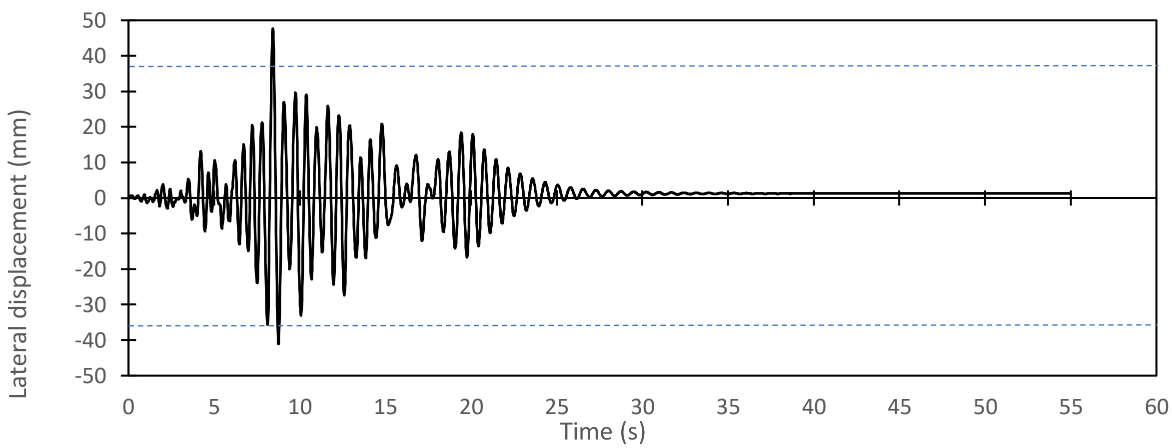

(c)

Figure 6-23: Bare concrete frame under earthquake record TR2-2: (a) lateral displacement-lateral load response; (b) lateral load time history; and (c) lateral displacement time history

The displaced shape and crack patterns at the end of the dynamic analysis, including both flexural and shear cracks are illustrated in Figure 6-24. Cracks were distributed over the beam and columns. Flexural cracks were observed in the beam at mid-span and column base, while shear cracks were observed near the beam-column joints.

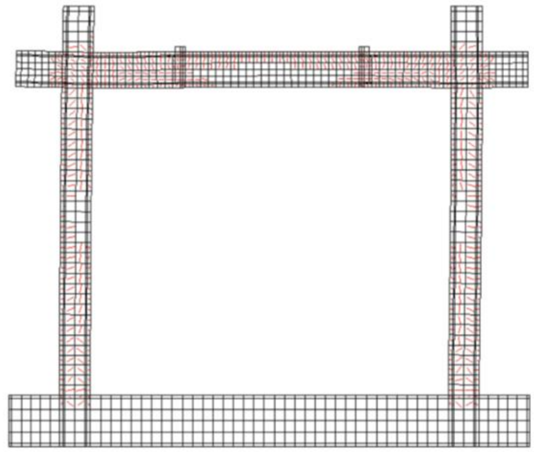

Figure 6-24: Displaced shape and crack pattern of BCF at the end of the analysis for earthquake record TR2-2

6.6.1.1.4 TR2-3

Figure 6-25 illustrates the response of the bare concrete frame under an earthquake record (TR2-3) that simulates the second period range target acceleration spectrum. From the lateral displacement–lateral load response in Figure 6-25 (a), the frame experienced inelastic deformations, which resulted in permanent displacements corroborated in Figure 6-25 (c). It is evident the frame yielded and reached both the yielding and ultimate displacements from the nonlinear static analysis. The frame sustained a peak lateral strength of 200.9 kN, and a peak lateral displacement of 113.8 mm, corresponding to a drift of 3.58%. Ratcheting was also evident in the response as damage accumulated in one direction and a permanent displacement of 5.257 mm was observed at the end of the analysis.

Figure 6-26 shows the displaced shape and crack patterns of the frame, where cracks were distributed over the beam and columns. Given that the ultimate displacement was achieved, larger cracks were observed at the base of the columns and near the beam-column joints. At the end of the ground motion record, the frame had deteriorated, and permanent displacement was evident.

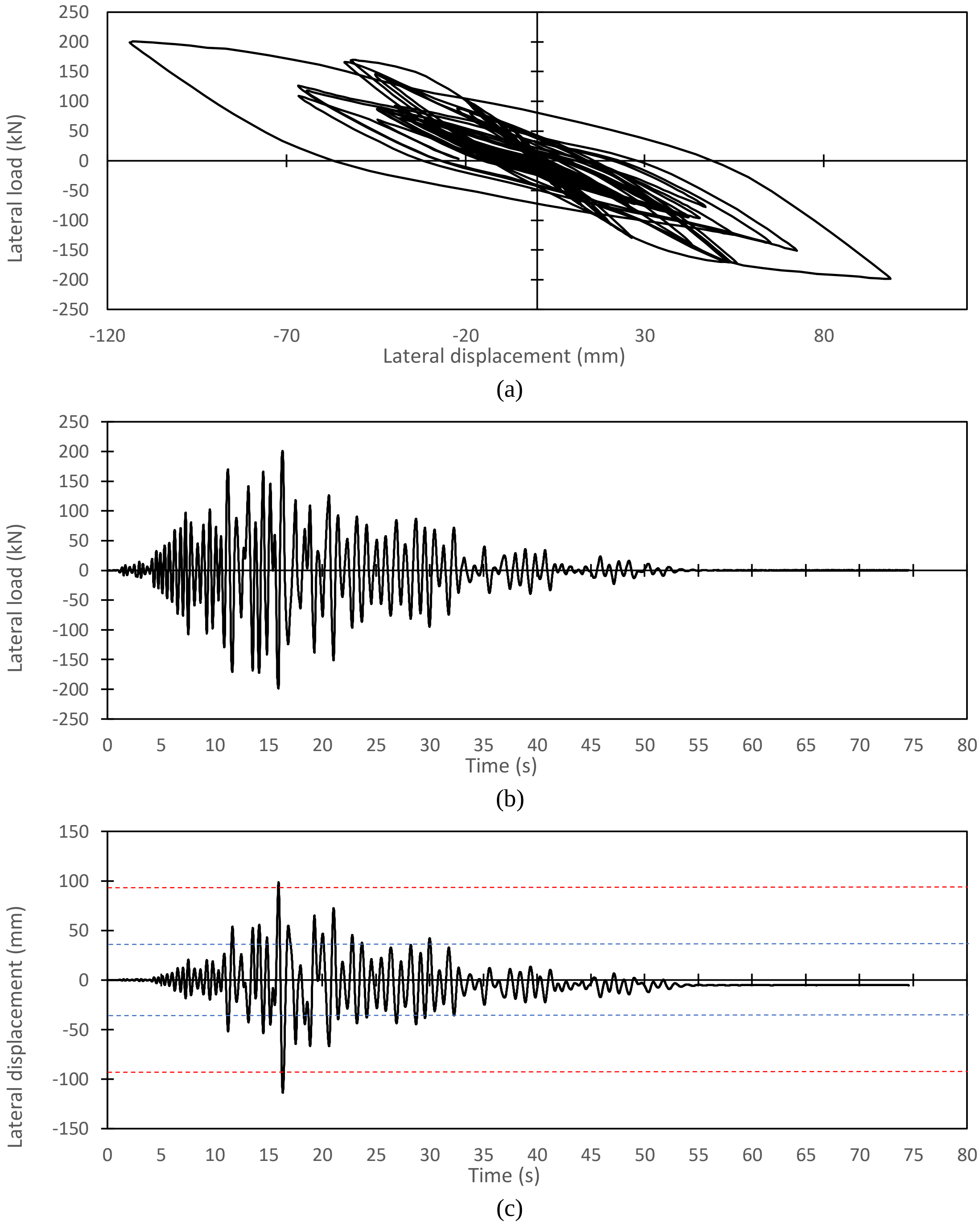

Figure 6-25: Bare concrete frame under earthquake record TR2-3: (a) lateral displacement-lateral load response; (b) lateral load time history; and (c) lateral displacement time history

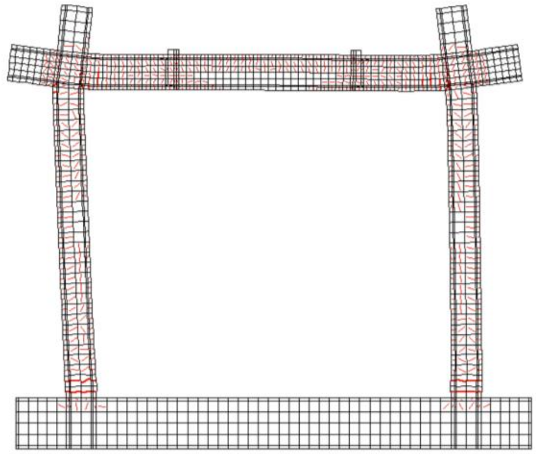

Figure 6-26: Displaced shape and crack pattern of BCF at the end of the analysis for earthquake record TR2-3

Table 6-4 summarizes the results of the bare concrete frame under the ground motion records that simulates the seismic hazard of the city of Montreal. The maximum transient displacement experienced by the frame was under TR2-3 and equal to 113.8 mm corresponding to a drift of 3.58%. In terms of permanent displacements, the peak was reached under the earthquake record TR1-6 corresponding to a residual displacement of 5.347 mm (0.17%). Top displacements that exceed yielding and ultimate displacements are highlighted in Table 6-4. The earthquake records presented significant variability, therefore, based on the NBC 2015 (NRC, 2015), the dynamic response of the structure is to be evaluated with the mean of all the records. Therefore, the mean transient displacement was 27.39 mm, corresponding to a mean drift of 0.863%, which is below the yielding displacement of the frame. The top lateral displacement time history, lateral strength time history, and hysteretic response of the remaining earthquake records are presented in the Appendix.

Table 6-4: Summary of results from time history analyses of the BCF located in Montreal

		Transient displacement		***Permanent displacement***	
Scenario	***Reference code***	***Displacement (mm)***	***Drift (%)***	***Displacement (mm)***	***Drift (%)***
1	*TR1-1*	*10.342*	*0.32573*	*0.012*	*0.00038*
	TR1-2	*10.599*	*0.33383*	*0.077*	*0.00243*
	TR1-3	*20.692*	*0.65172*	*0.036*	*0.00113*
	TR1-4	*24.921*	*0.78491*	*0.005*	*0.00016*
	TR1-5	*30.915*	*0.97370*	*0.266*	*0.00838*
	TR1-6	***78.291***	*2.46586*	*5.347*	*0.16841*
2	*TR2-1*	***52.316***	*1.64775*	*0.491*	*0.01546*
	TR2-2	***47.656***	*1.50098*	*1.279*	*0.04028*
	TR2-3	***113.80***	*3.58425*	*5.257*	*0.16557*
	TR2-4	*34.389*	*1.08312*	*0.485*	*0.01528*
	TR2-5	*4.8780*	*0.15364*	*0.025*	*0.00079*

6.6.1.2 Earthquake records Vancouver – BC

The bare concrete frame subjected to the earthquake records that simulate the Vancouver seismic hazard experienced yielding for all eleven earthquake records, and the ultimate displacement under three of the records.

6.6.1.2.1 TR1-3

Figure 6-27 illustrates the response of the frame under the ground motion record TR1-3. From the hysteretic response illustrated in Figure 6-27 (a), the frame was able to dissipate energy corroborating it sustained inelastic deformations. The frame experienced a peak lateral strength of 194.5 kN (Figure 6-27(b)). The frame yielded in both directions, reaching a maximum displacement of 95.518 mm (drift of 3.01%), which is greater than the maximum displacement experienced by the same frame under nonlinear static reverse cyclic analysis. The frame also experienced ratcheting, where accumulation of displacements was more evident in one direction with a permanent displacement of 6.05 mm (Figure 6-27 (c)). Figure 6-28 illustrates the displaced shape and crack pattern of the frame under this ground motion record, where cracks up to 1.5 mm wide were observed, and the deterioration of the frame was evident based on the deformed shape after the ground shaking.

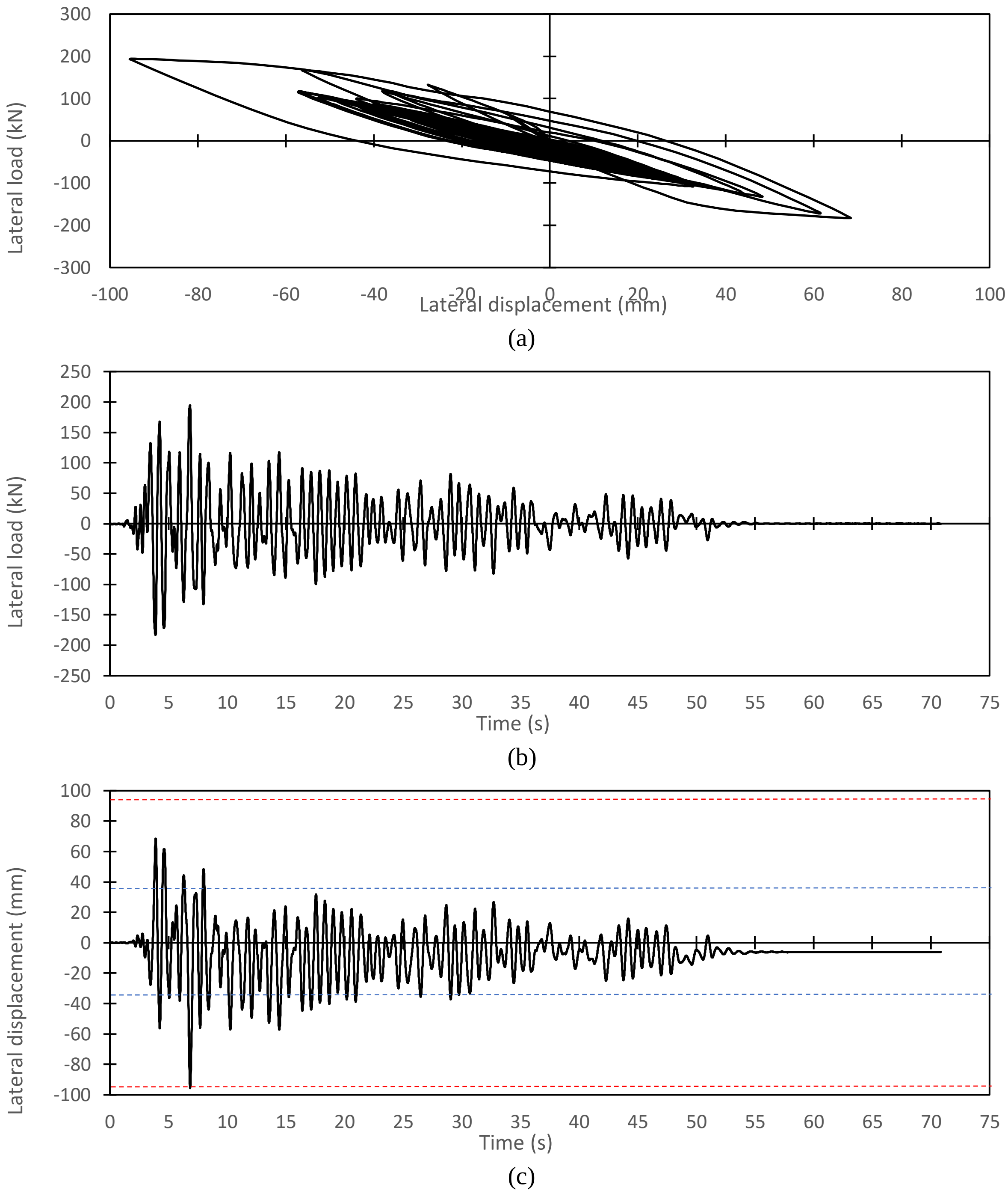

Figure 6-27: Bare concrete frame under earthquake record TR1-3: (a) lateral displacement-lateral load response; (b) lateral load time history; and (c) lateral displacement time history

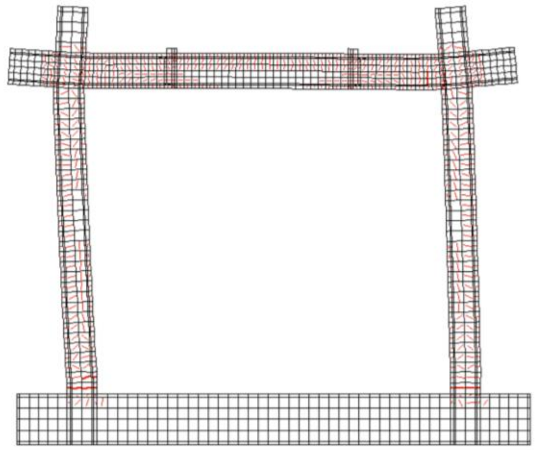

Figure 6-28: Displaced shape and crack pattern of BCF at the end of the analysis for earthquake record TR1-3

6.6.1.2.2 TR1-4

By closely evaluating the hysteretic response in Figure 6-29 (a), the frame experienced a peak top displacement of 78.55 mm (drift of 2.47%), which is above the yielding point for the frame. Therefore, the frame sustained plastic deformations that resulted in accumulation of damage. This residual displacement was equal to 10.303 mm, and the presence of ratcheting is notable (Figure 6-29 (c)). In addition, a peak lateral strength of 187 kN was experienced by the frame.

Figure 6-30 illustrates the displaced shape and crack pattern of the control frame after the application of the ground motion. The cracks are distributed in both columns and beam; shear and flexural cracks are observed, where wider cracks formed at the base of the columns, and near the beam-column joints.

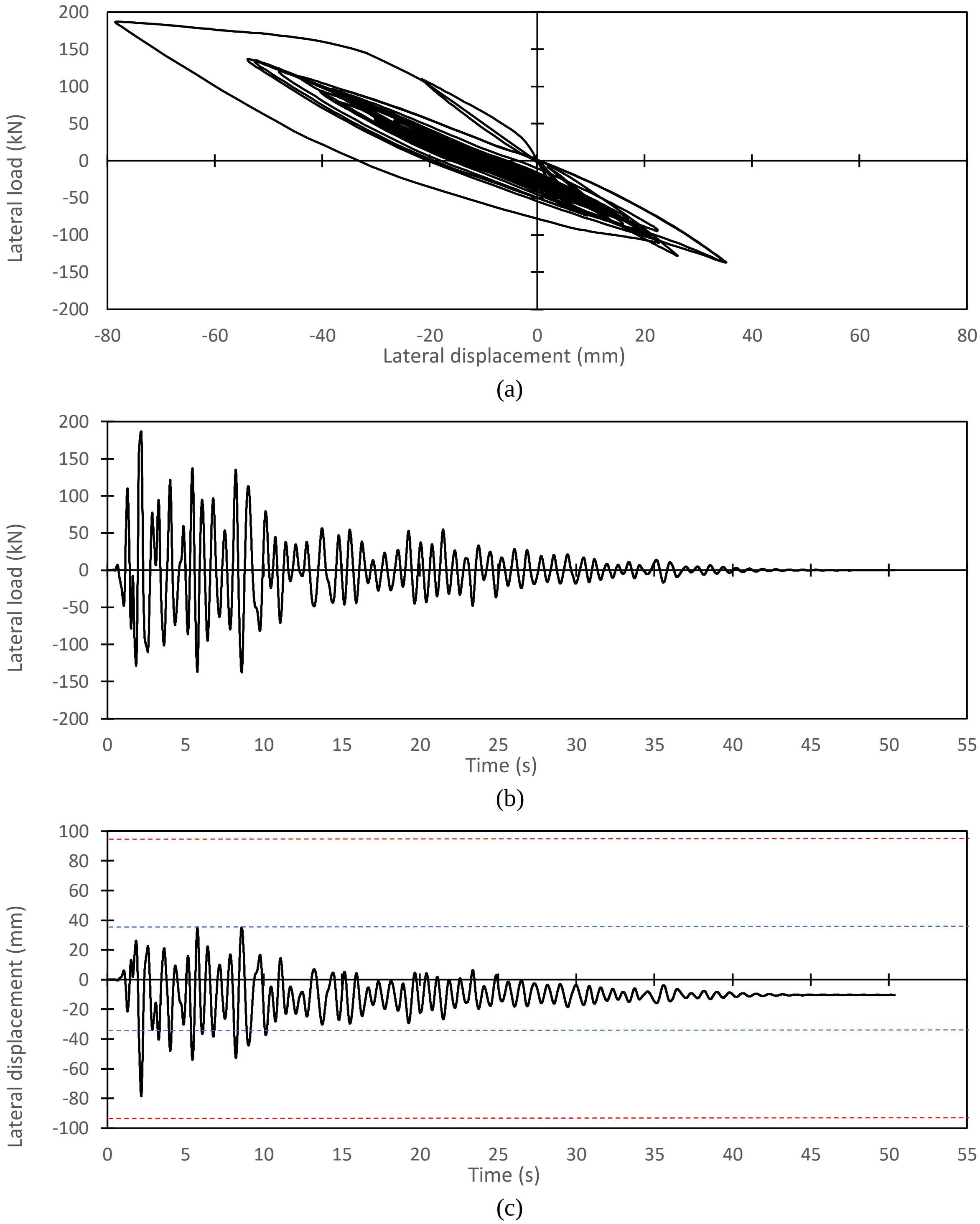

Figure 6-29: Bare concrete frame under earthquake record TR1-4: (a) lateral displacement-lateral load response; (b) lateral load time history; and (c) lateral displacement time history

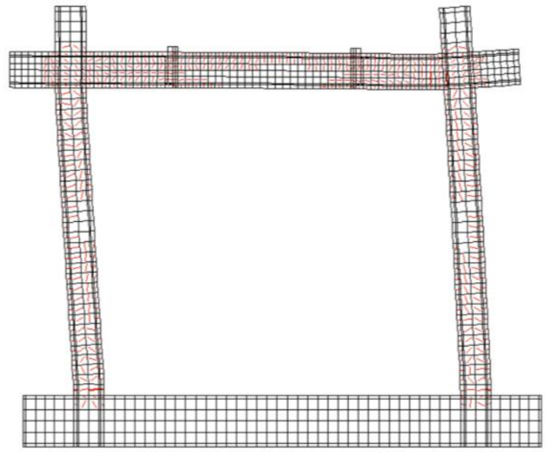

Figure 6-30: Displaced shape and crack pattern of BCF at the end of the analysis for earthquake record TR1-4

6.6.1.2.3 TR2-1

For the second M-R scenario to simulate the seismic hazard of Western Canada, the frame reached its maximum lateral displacement capacity. From the lateral displacement–lateral load response (Figure 6-31 (a)), it is evident the frame exceeded yielding and sustained plastic deformations. The frame sustained a peak lateral strength of 193.9 kN (Figure 6-31 (b)). Furthermore, in Figure 6-31 (c), two characteristics of the dynamic response of the frame are present: ratcheting and permanent displacements. Due to the ratcheting, the residual displacement in the frame was 2.94 mm. Figure 6-32 illustrates the displaced shape of the frame and the cracking pattern.

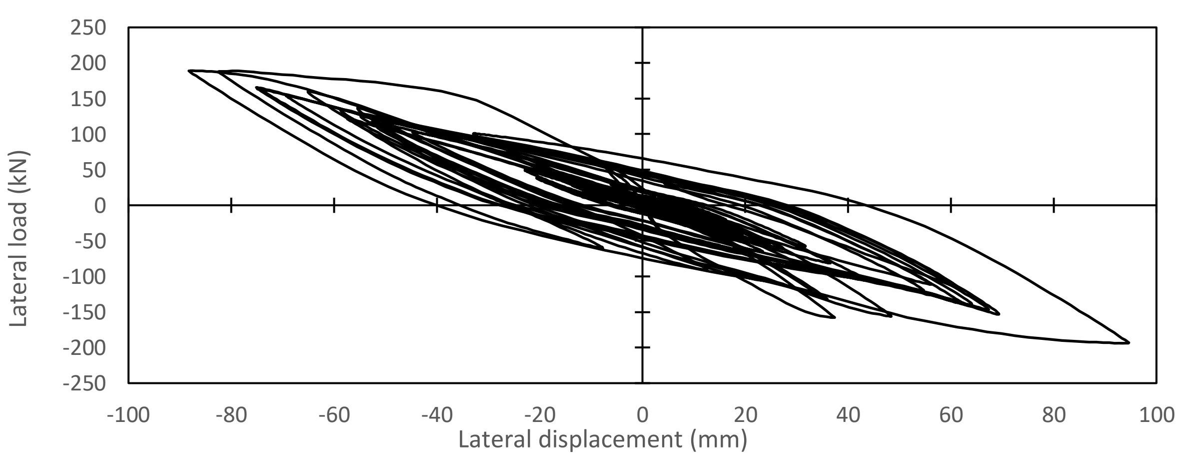

(a)

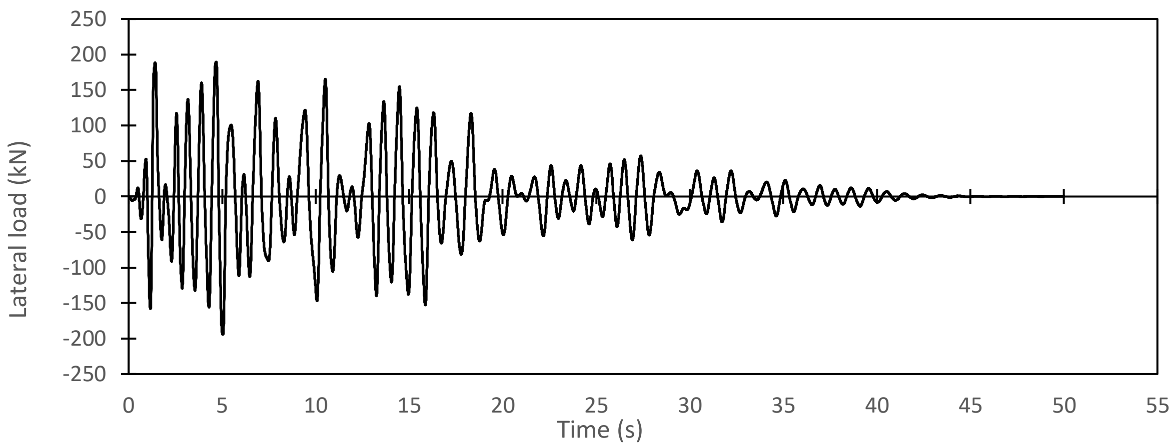

(b)

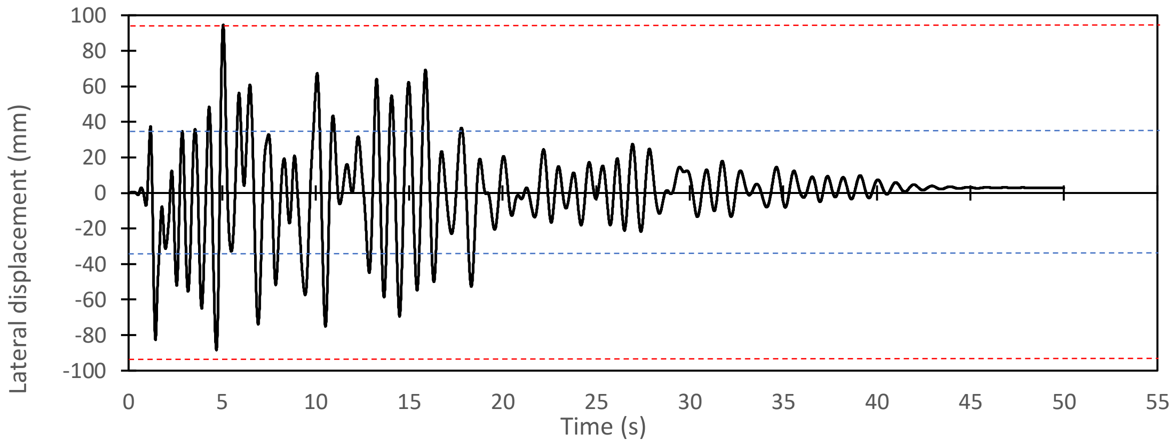

(c)

Figure 6-31: Bare concrete frame under earthquake record TR2-1: (a) lateral displacement-lateral load response; (b) lateral load time history; and (c) lateral displacement time history

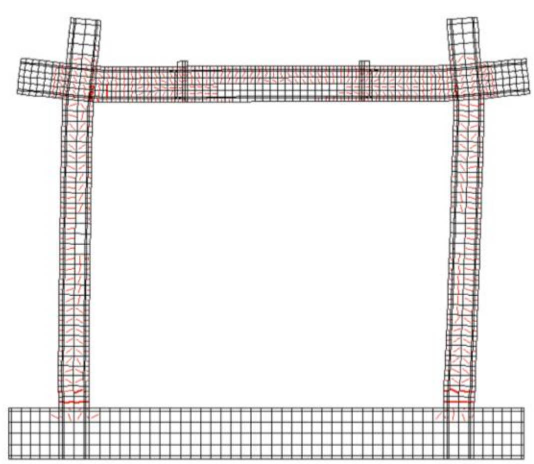

Figure 6-32: Displaced shape and crack pattern of BCF at the end of the analysis for earthquake record TR2-1

6.6.1.2.4 TR2-2

When under the earthquake recorded TR2-2, the frame exceeded its ultimate displacement of 95 mm (Figure 6-33 (a)). The lateral displacement-lateral load response also demonstrates that the frame experienced plastic deformation. A peak lateral strength of 211.2 kN was observed in Figure 6-33 (b). By evaluating the top displacement time history, the bare concrete frame experienced a peak lateral displacement of 144.75 mm corresponding to a drift of 4.56% (Figure 6-33 (c)). This significant lateral displacement resulted in ratcheting of the frame and an accumulation of residual displacement of 19.55 mm. In Figure 6-34, the displaced shape of the frame after the dynamic analysis illustrates the deterioration of the frame and the significant residual displacement after exceeding the ultimate displacement of the frame. Furthermore, the crack pattern demonstrates wider cracks are concentrated at the column base and in the beam adjacent to the beam-column joints.

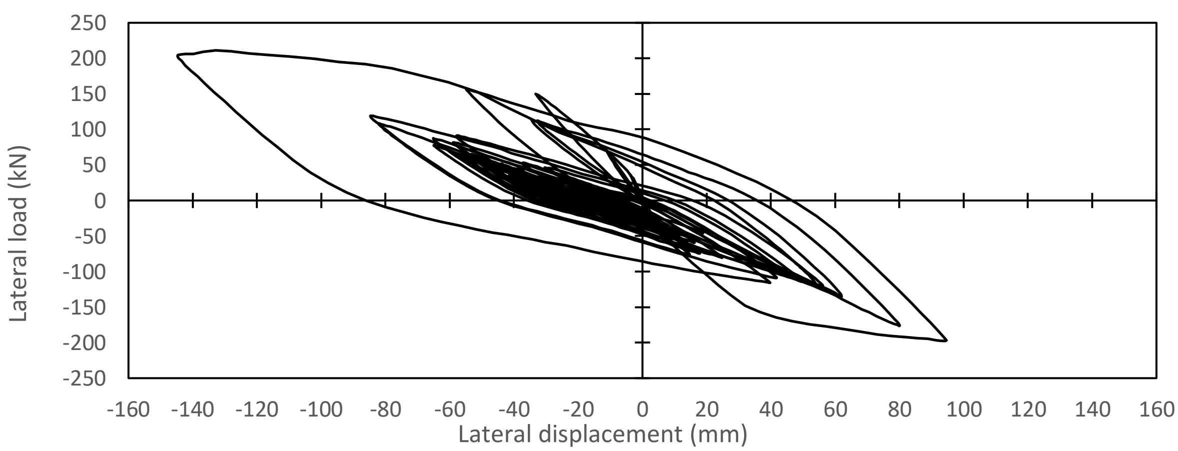

(a)

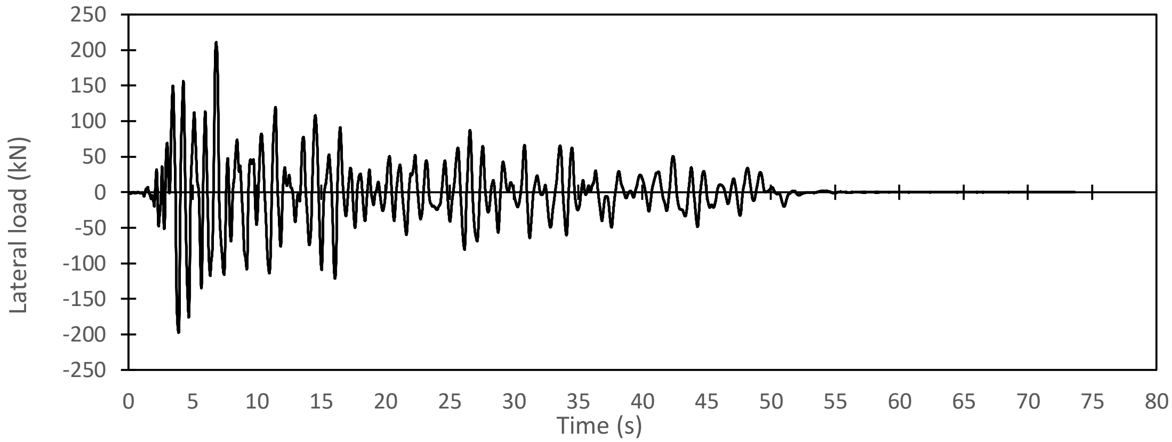

(b)

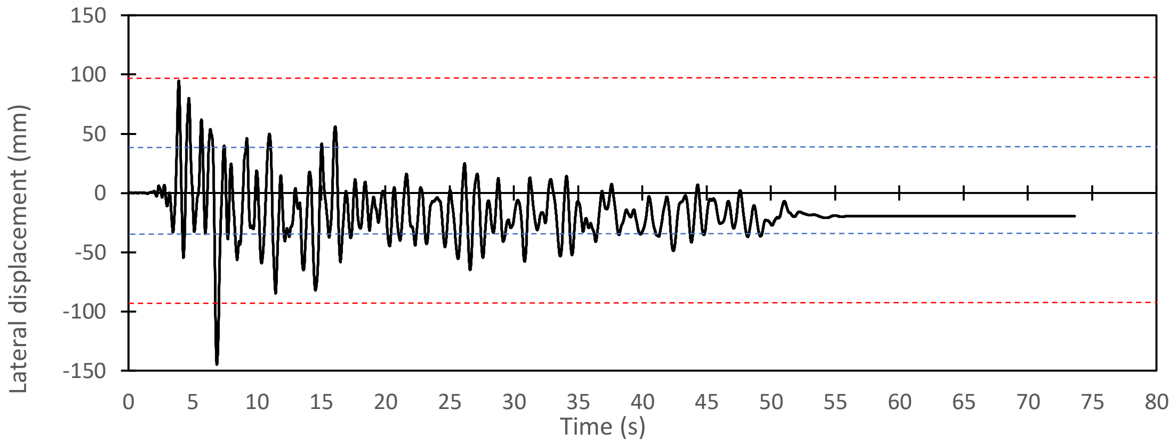

(c)

Figure 6-33: Bare concrete frame under earthquake record TR2-2: (a) lateral displacement-lateral load response; (b) lateral load time history; and (c) lateral displacement time history

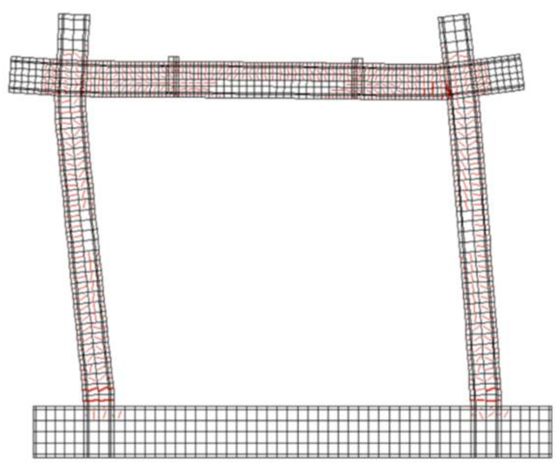

Figure 6-34: Displaced shape and crack pattern of BCF at the end of the analysis for earthquake record TR2-2

6.6.1.2.5 TR3-1

The third M-R seismic hazard scenario of the city of Vancouver is presented in Figure 6-35 for the ground motion record TR3-1. In Figure 6-35 (a), it is evident that the system dissipated considerable energy. As energy is dissipated when the frame experiences inelastic deformation, it follows that the frame exceeded its yielding point. In Figure 6-35 (b), the lateral load time history response is presented, where a peak lateral strength of 208.7 kN was experienced by the frame. The ultimate displacement of the frame was exceeded. By analysing the top displacement time history response (Figure 6-35 (c)), the displacement experienced by the frame corresponded to 134.72 mm (drift of 4.243 %). Ratcheting was evident in one direction, and a permanent displacement of 22.4 mm accumulated after the ground motion record was applied. Figure 6-36 illustrates the displaced shape and crack pattern of the frame after decay of the vibration.

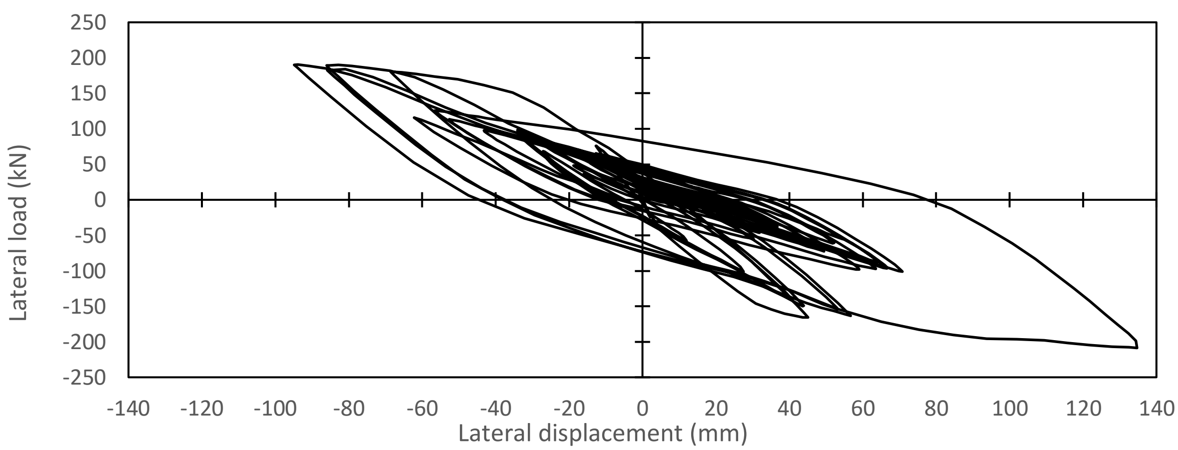

(a)

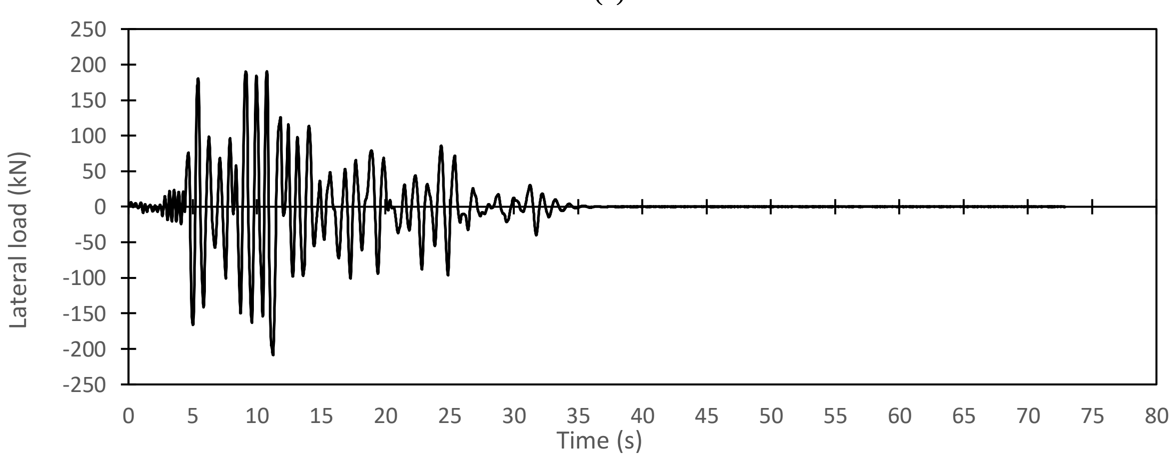

(b)

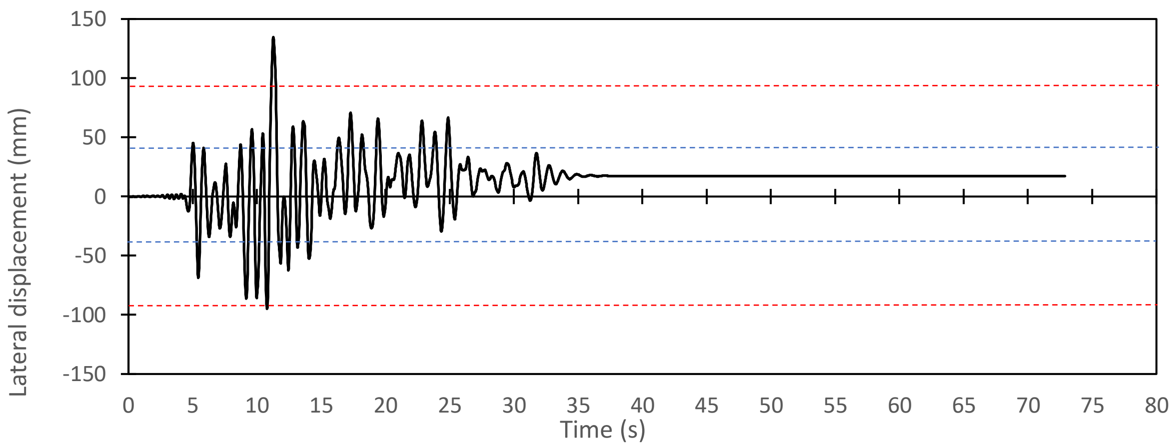

(c)

Figure 6-35: Bare concrete frame under earthquake record TR3-1: (a) lateral displacement-lateral load response; (b) lateral load time history; and (c) lateral displacement time history

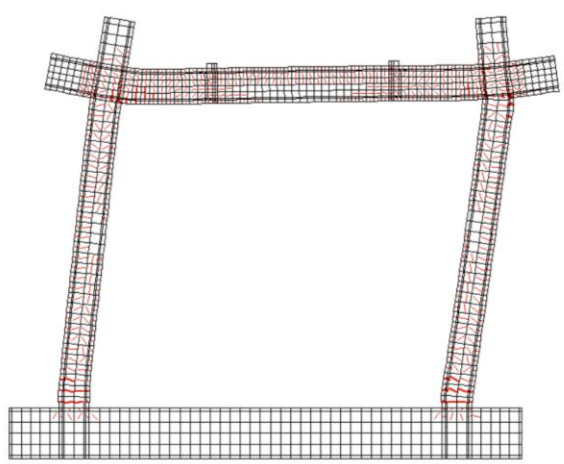

Figure 6-36: Displaced shape and crack pattern of BCF at the end of the analysis for earthquake record TR3-1

6.6.1.2.6 TR3-2

For the earthquake record TR3-2, the ultimate displacement was not reached, but the hysteretic response presented in Figure 6-37 (a) illustrated that yielding was achieved as significant energy was dissipated during the earthquake. A peak lateral strength of 184 kN was observed in both directions of loading (Figure 6-37 (b)). From the top displacement time-history response, the ultimate displacement was not reached, ratcheting was evident, and the frame accumulated approximately 3 mm of residual displacement. Figure

6-38 illustrates the displaced shape and crack pattern of the frame, where wider cracks were concentrated near the column base and the beam-column joint.

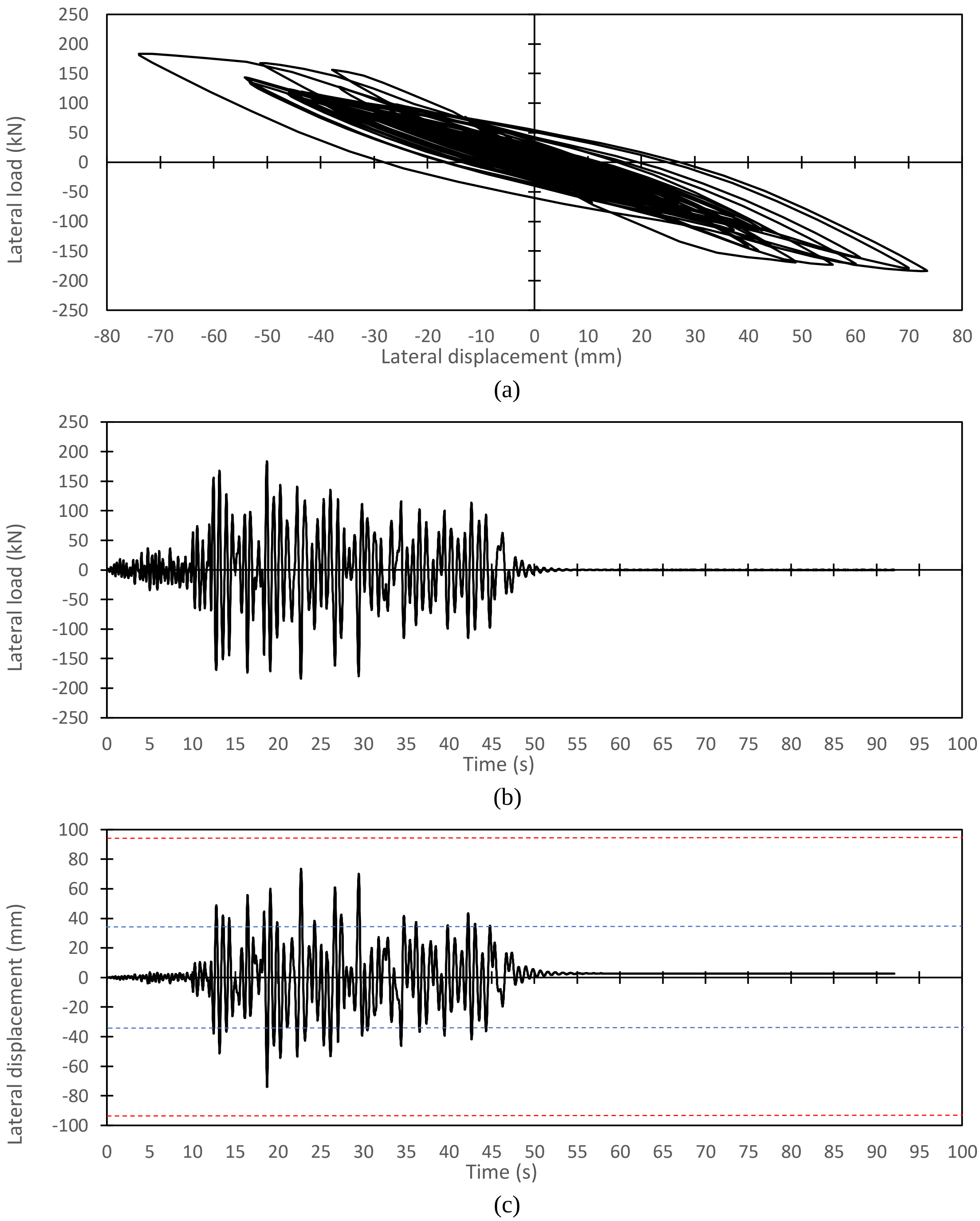

Figure 6-37: Bare concrete frame under earthquake record TR3-2: (a) lateral displacement-lateral load response; (b) lateral load time history; and (c) lateral displacement time history

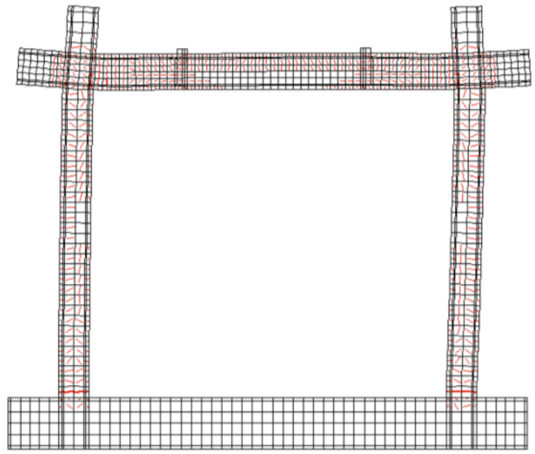

Figure 6-38: Displaced shape and crack pattern of BCF at the end of the analysis for earthquake record TR3-2

Table 6-5 summarizes the results from the eleven earthquake records applied to the bare concrete frame. All the records induced yielding of the frame, and the transient displacements that exceed the maximum displacement of the frame from nonlinear static analysis are highlighted. The mean transient top displacement was 82.77 mm corresponding to a drift of 2.6%, which exceeded the yielding displacement and is slightly lower than the maximum ultimate of 95 mm. The top transient displacement experienced by the frame was equal to 144.75 mm, accumulating a permanent displacement of 19.548 mm.

Table 6-5: Summary of results from time history analyses of the BCF located in Vancouver

		Transient displacement		*Permanent displacement*	
Scenario	***Reference code***	***Displacement (mm)***	***Drift (%)***	***Displacement (mm)***	***Drift (%)***
1	*TR1-1*	*70.227*	*2.21187*	*3.9580*	*0.12466*
	TR1-2	*74.263*	*2.33899*	*4.5020*	*0.14180*
	TR1-3	***95.518***	*3.00844*	*6.0480*	*0.19049*
	TR1-4	*78.548*	*2.47395*	*10.303*	*0.32450*
2	*TR2-1*	*94.640*	*2.98079*	*2.9420*	*0.09266*
	TR2-2	***144.75***	*4.55906*	*19.548*	*0.61569*
	TR2-3	*50.547*	*1.59203*	*1.7930*	*0.05647*
3	*TR3-1*	***134.72***	*4.24315*	*22.400*	*0.70551*
	TR3-2	*74.009*	*2.33099*	*2.7070*	*0.08526*
	TR3-3	*69.785*	*2.19795*	*0.6220*	*0.01959*
	TR3-4	*66.291*	*2.08791*	*1.5690*	*0.04942*

6.6.2 Frame retrofitted with modified BRB incorporating SE-SMA core

The frame retrofitted with the modified BRB with an SE-SMA core bar was evaluated under the same earthquake records as the bare concrete frame to illustrate the differences in response after retrofit.

6.6.2.1 Earthquake records Montreal – QC

The results of the retrofitted frame under the earthquake records are summarized in Table 6-6. Under the earthquake records to simulate the seismic hazard of the city of Montreal, the frame did not yield. The maximum displacement experienced by the retrofitted frame was 0.983 mm corresponding to a top transient drift of 0.031%, which presents an improvement relative to the bare concrete frame. Regarding the permanent displacement, a negligible mean value of 0.003 mm was observed, which was associated to the deformation of the concrete frame. The response of the retrofitted frame was significantly low in terms of transient and permanent displacements, and the lateral strength experienced by the frame was negligible relative to its capacity; the frame experienced lateral loading and displacements that were approximately

10% of its capacity. As a result, the hysteretic response, top displacement and lateral load time histories are presented, but not discussed in detail. Furthermore, to evaluate the behaviour of the retrofitted frame, the frame was subjected to amplified earthquake records in Section 6.6.3.

Table 6-6: Summary of results from time history analyses of the retrofitted frame located in Montreal

		Transient displacement		***Permanent displacement***	
Scenario	***Reference code***	***Displacement (mm)***	***Drift (%)***	***Displacement (mm)***	***Drift (%)***
1	*TR1-1*	*0.175*	*0.00551*	*0.002*	*6.3E-05*
	TR1-2	*0.554*	*0.01745*	*0.000*	*0.00000*
	TR1-3	*0.539*	*0.01698*	*0.003*	*0.00100*
	TR1-4	*0.408*	*0.01285*	*0.003*	*9.4E-05*
	TR1-5	*0.461*	*0.01452*	*0.003*	*9.4E-05*
	TR1-6	*0.983*	*0.03096*	*0.003*	*9.4E-05*
2	*TR2-1*	*0.349*	*0.01099*	*0.003*	*9.4E-05*
	TR2-2	*0.362*	*0.01140*	*0.003*	*9.4E-05*
	TR2-3	*0.620*	*0.01953*	*0.003*	*9.4E-05*
	TR2-4	*0.335*	*0.01055*	*0.003*	*9.4E-05*
	TR2-5	*0.101*	*0.00318*	*0.003*	*9.4E-05*

6.6.2.1.1 TR1-5

The response of the retrofitted frame is presented in Figure 6-39. The frame behaved solely in the elastic range, and an accumulation of residual displacement equivalent to 0.002 mm was present. Slight ratcheting was observed accumulating in a displacement of 0.002 mm. A peak top displacement of 0.175 mm was recorded corresponding to a peak lateral load of 4.2 kN. No cracks were observed in the frame after the earthquake record was applied.

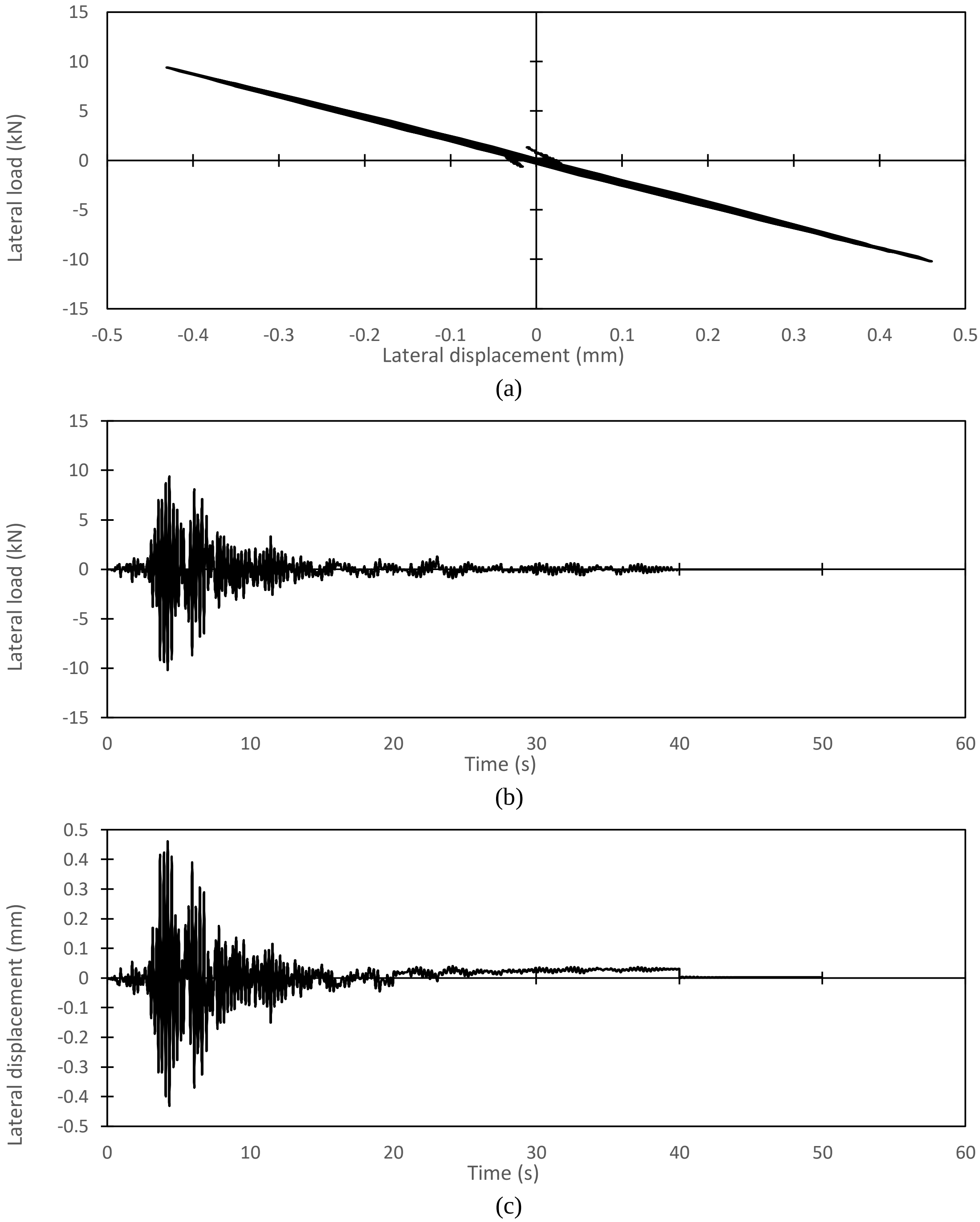

Figure 6-39: Retrofitted frame under earthquake record TR1-5: (a) lateral displacement-lateral load response; (b) lateral load time history; and (c) lateral displacement time history

6.6.2.1.2 TR1-6

The response of the retrofitted frame under the earthquake record TR1-6 is presented in Figure 6-40. The frame responded below the yield point, and a residual displacement equivalent to 0.003 accumulated. A peak top displacement of 0.983 mm was predicted corresponding to a peak lateral load of 23.8 kN. Cracks were absent in the response of the retrofitted frame under the earthquake record.

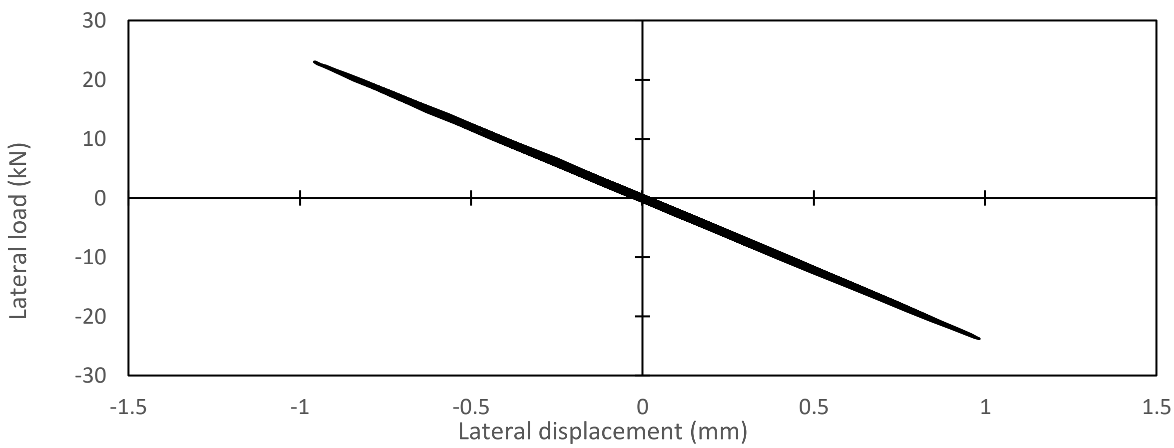

(a)

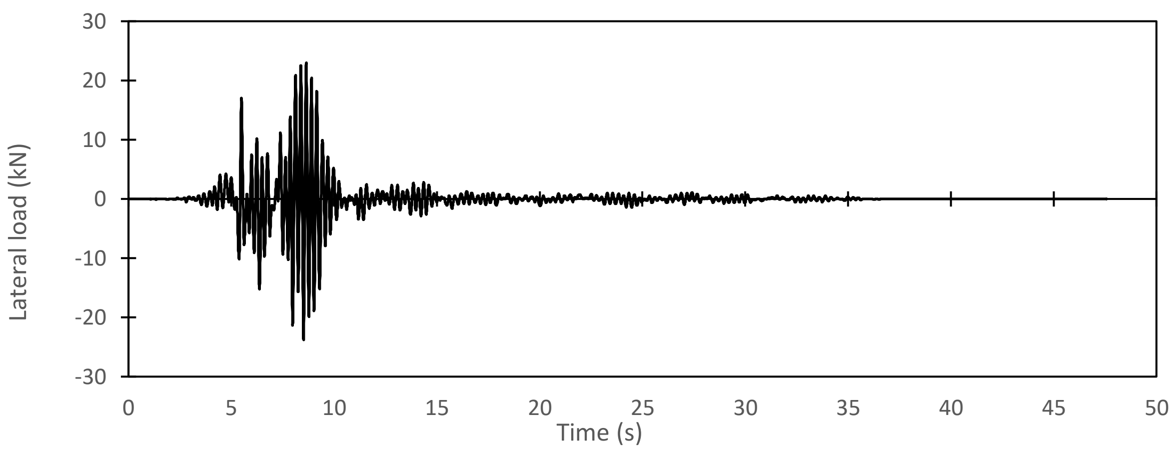

(b)

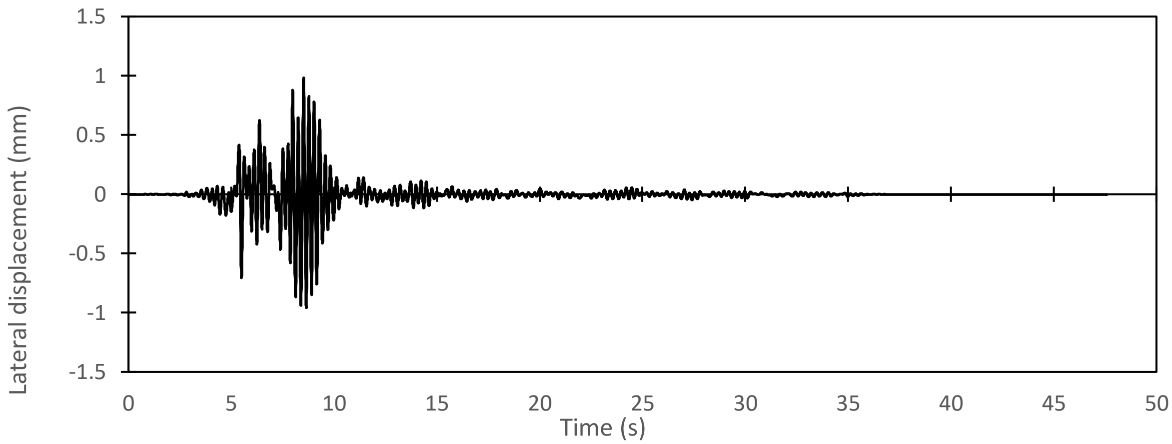

(c)

Figure 6-40: Retrofitted frame under earthquake record TR1-6: (a) lateral displacement-lateral load response; (b) lateral load time history; and (c) lateral displacement time history

6.6.2.1.3 TR2-2

The response of the retrofitted frame is presented in Figure 6-41. A residual displacement of 0.003 mm was captured. A peak top displacement of 0.362 mm was experienced by the frame, which corresponded to a peak lateral strength of 8.7 kN. No cracks were evident in the frame.

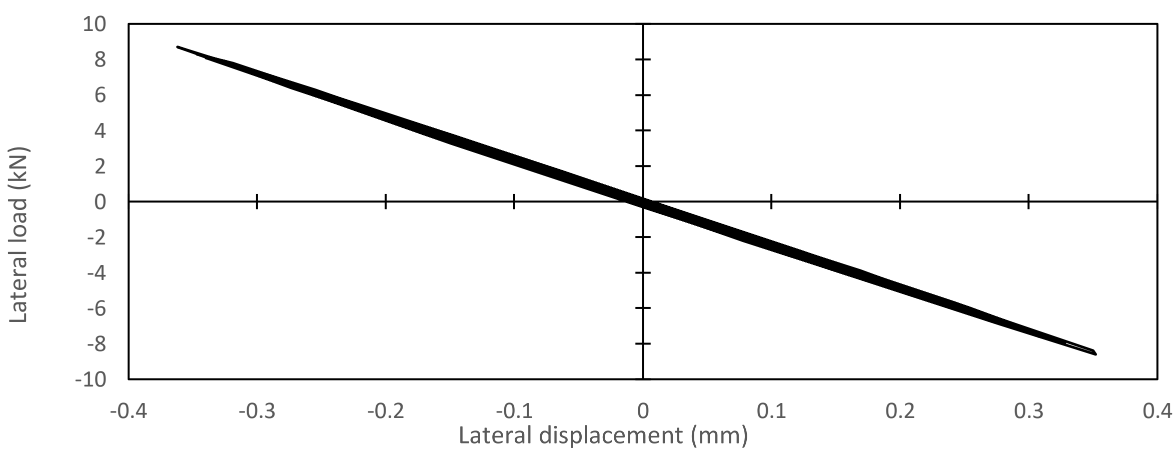

(a)

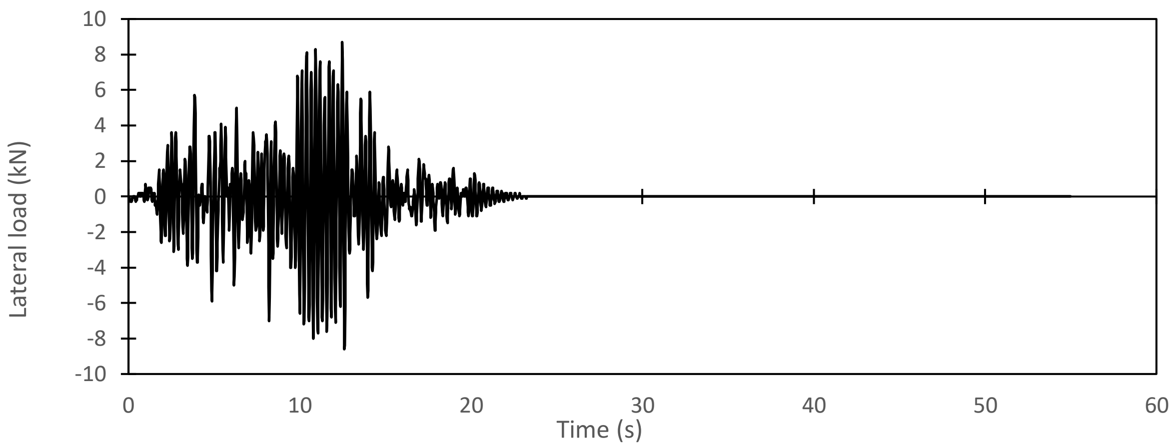

(b)

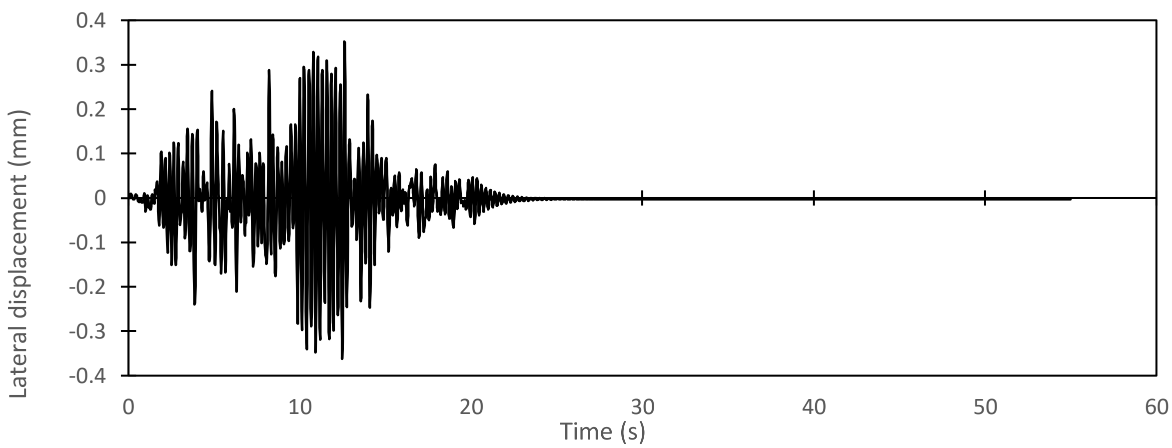

(c)

Figure 6-41: Retrofitted frame under earthquake record TR2-2: (a) lateral displacement-lateral load response; (b) lateral load time history; and (c) lateral displacement time history

6.6.2.1.4 TR2-3

Figure 6-42 illustrates the response of the retrofitted frame under the earthquake record corresponding to TR2-3. The retrofitted frame did not yield. A residual displacement equal to 0.003 mm was observed at the end of the ground motion. The peak top displacement was equivalent to 0.62 mm corresponding to a peak lateral load of 15 kN. No cracks were observed in the frame after the earthquake record was applied.

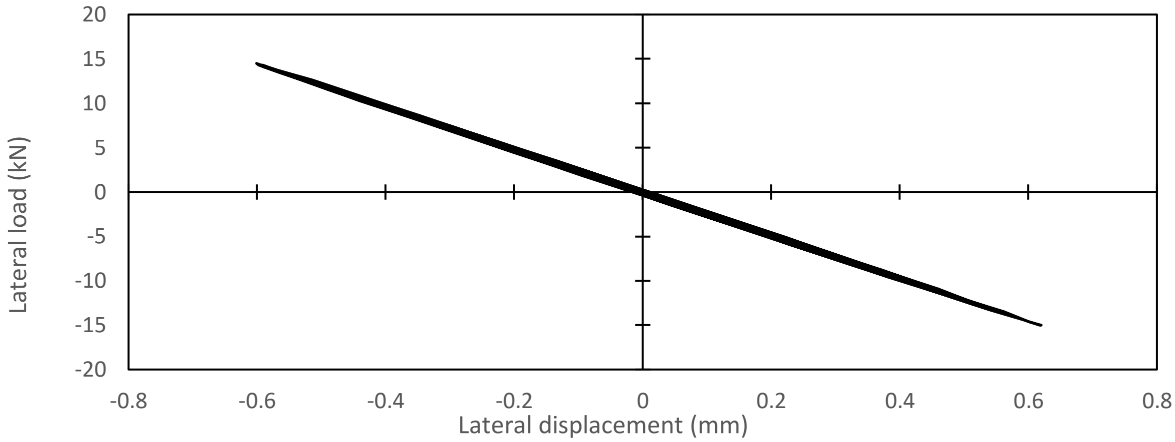

(a)

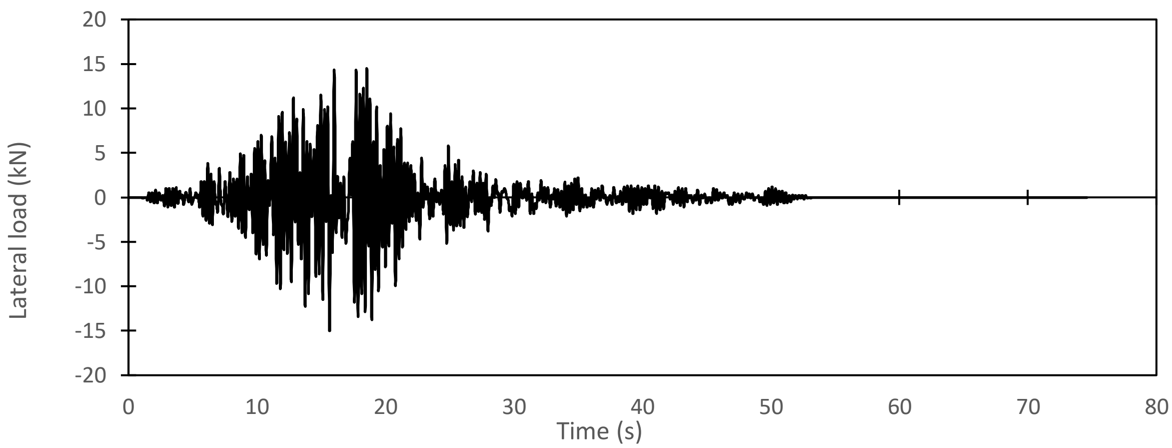

(b)

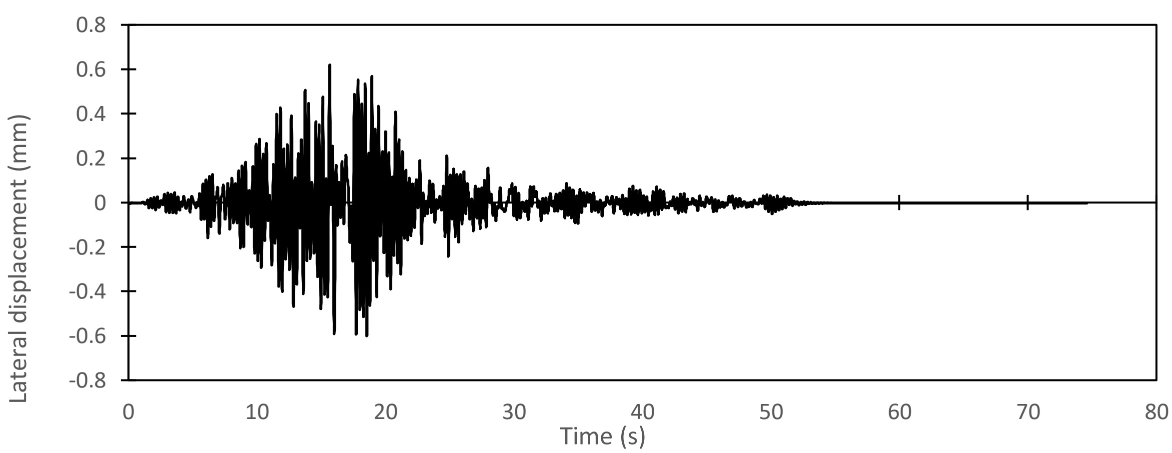

(c)

Figure 6-42: Retrofitted frame under earthquake record TR2-3: (a) lateral displacement-lateral load response; (b) lateral load time history; and (c) lateral displacement time history

6.6.2.2 Earthquake records Vancouver – BC

The dynamic response of the retrofitted frame located in the city of Vancouver was similar to the responses in Montreal. The frame did not yield and responded well below the yielding point. The largest top transient displacement experienced by the frame was under the ground motion TR3-1. The permanent displacement was limited to 0.003 mm under this earthquake record. The results of the retrofitted frame under the earthquake records are summarized in Table 6-7.

Table 6-7: Summary of results from time history analyses of the retrofitted frame located in Vancouver

		Transient displacement		***Permanent displacement***	
Scenario	***Reference code***	***Displacement (mm)***	***Drift (%)***	***Displacement (mm)***	***Drift (%)***
1	*TR1-1*	*0.873*	*0.02750*	*0.003*	*9.4E-05*
	TR1-2	*1.095*	*0.03449*	*0.003*	*9.4E-05*
	TR1-3	*0.900*	*0.02835*	*0.003*	*9.4E-05*
	TR1-4	*0.955*	*0.03008*	*0.002*	*6.3E-05*
2	*TR2-1*	*1.301*	*0.04098*	*0.003*	*9.4E-05*
	TR2-2	*1.106*	*0.03483*	*0.003*	*9.4E-05*
	TR2-3	*0.337*	*0.01061*	*0.003*	*9.4E-05*
3	*TR3-1*	*1.611*	*0.05074*	*0.003*	*9.4E-05*
	TR3-2	*0.985*	*0.03102*	*0.003*	*9.4E-05*
	TR3-3	*0.465*	*0.01465*	*0.037*	*0.00117*
	TR3-4	*0.567*	*0.01786*	*0.003*	*9.4E-05*

6.6.2.2.1 TR1-3

The response of the retrofitted frame presented in Figure 6-43 corresponds to the earthquake record TR1-3. The frame behaved in the elastic range, and an accumulation of residual displacement equivalent to 0.003 mm was observed. A peak top displacement of 0.9 mm was captured corresponding to a peak lateral load of 21.7 kN. No cracks were observed in the frame at the end of the earthquake record.

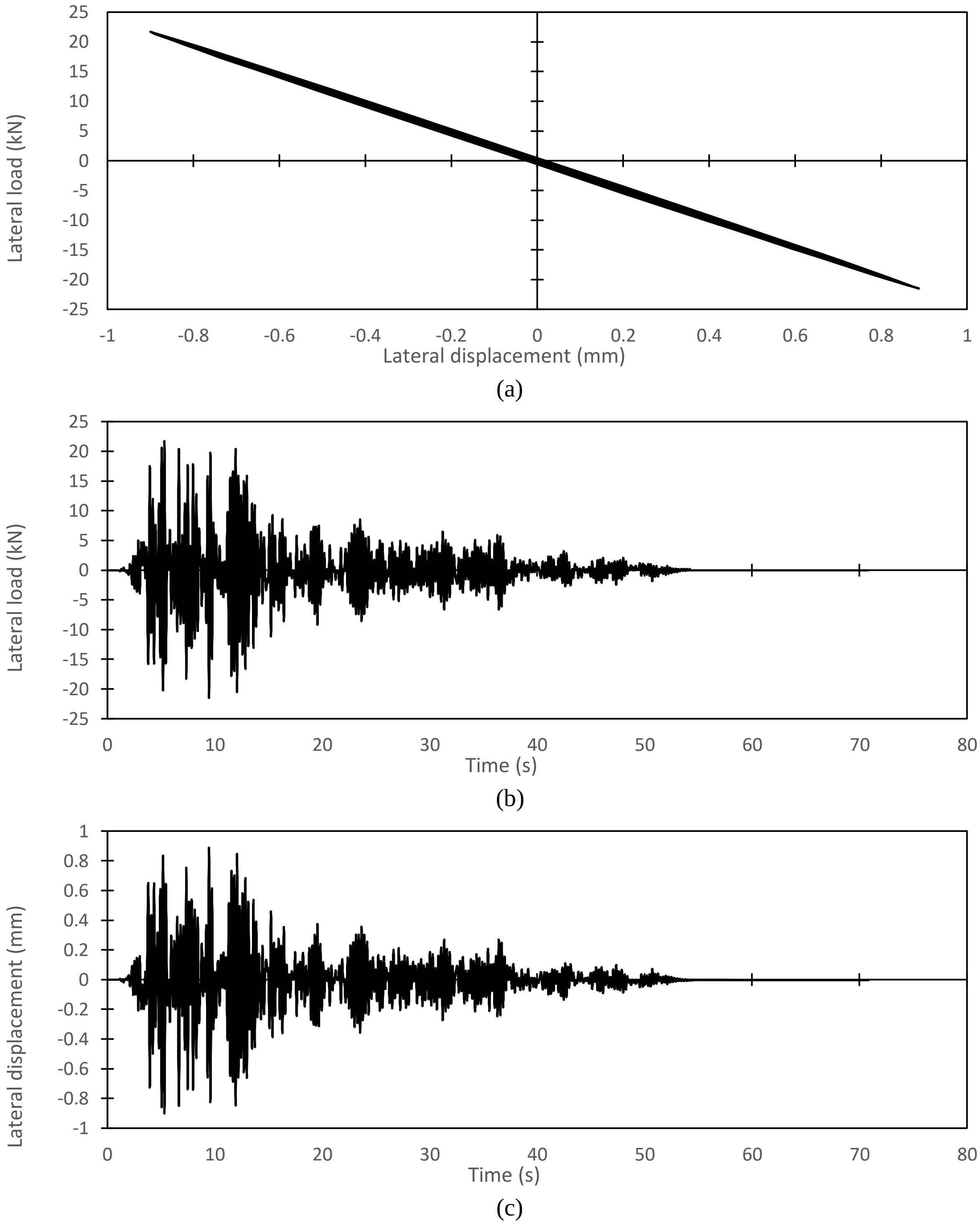

Figure 6-43: Retrofitted frame under earthquake record TR1-3: (a) lateral displacement-lateral load response; (b) lateral load time history; and (c) lateral displacement time history

6.6.2.2.2 TR1-4

Figure 6-44 illustrates the response of the retrofitted frame under the earthquake record TR1-4. The structure behaved in the elastic range, thus the advantages of the shape-memory alloy were not exploited. An accumulation of residual displacement equivalent to 0.002 mm was verified. A peak top displacement of 0.955 mm and a peak lateral strength of 23 kN were predicted. Cracks were absent in the frame during and after the ground motion record.

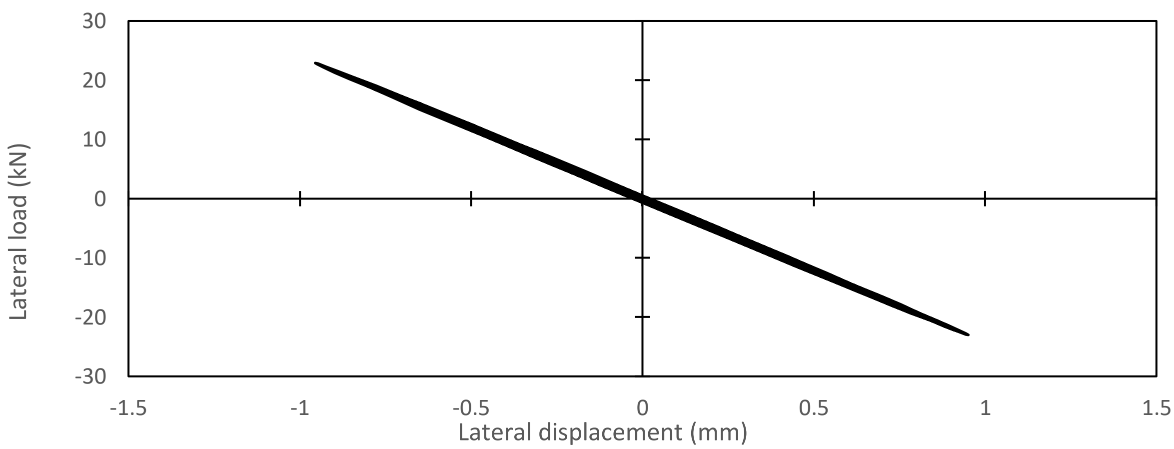

(a)

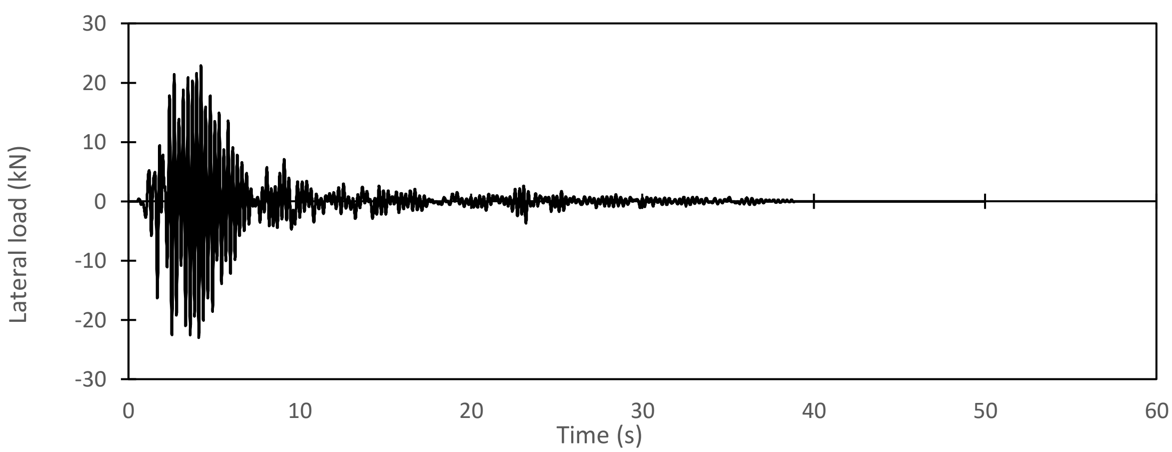

(b)

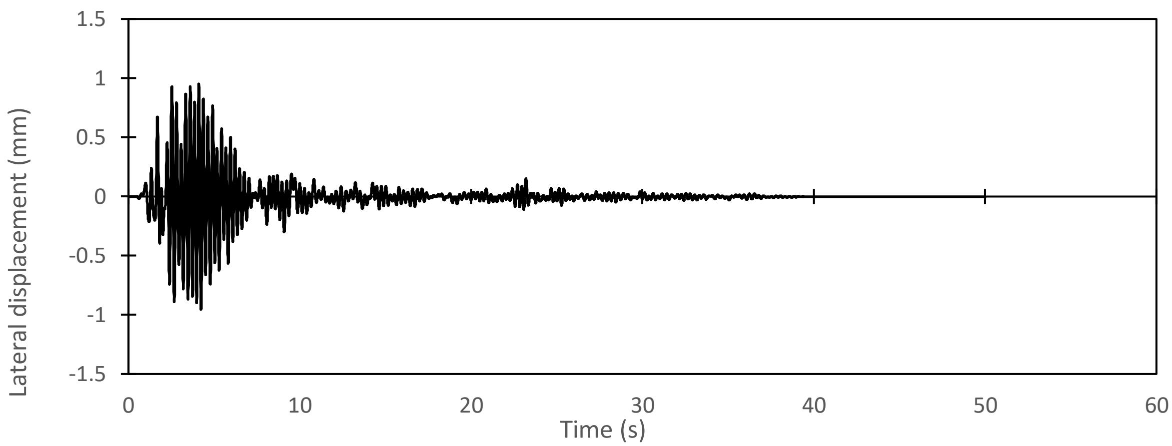

(c)

Figure 6-44: Retrofitted frame under earthquake record TR1-4: (a) lateral displacement-lateral load response; (b) lateral load time history; and (c) lateral displacement time history

6.6.2.2.3 TR2-1

Figure 6-45 illustrates the response of the retrofitted frame under the ground motion scaled to simulate the seismic hazard for the second M-R scenario of the city of Vancouver. The frame performed in the elastic range experiencing a top transient displacement of 1.301 mm and a lateral strength of 30.6 kN. Furthermore, the frame accumulated a residual displacement of 0.003 mm. Cracks were not observed in the frame during and after the ground motion record was applied.

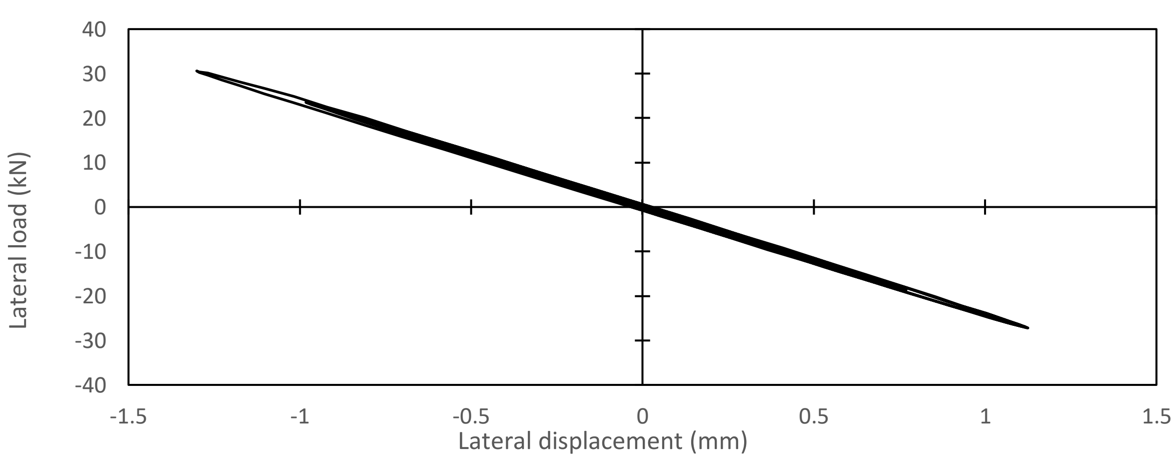

(a)

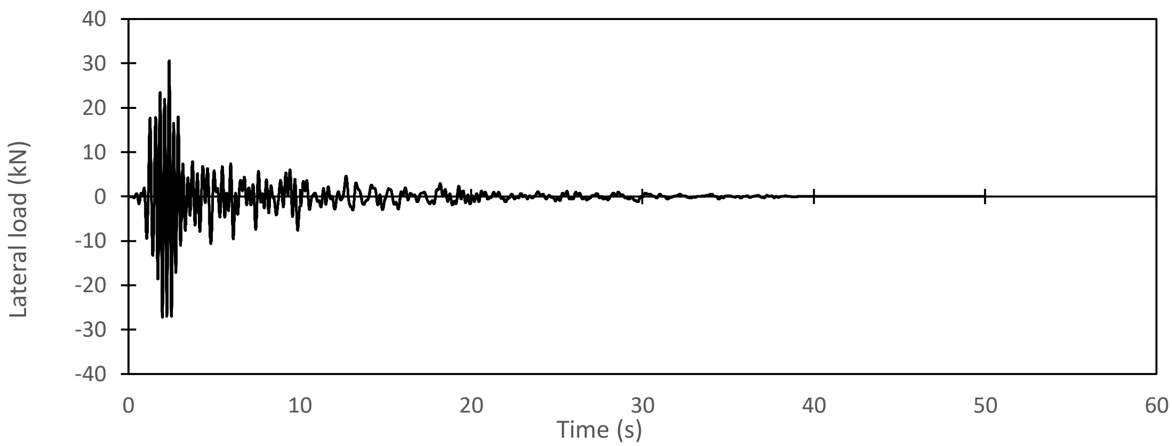

(b)

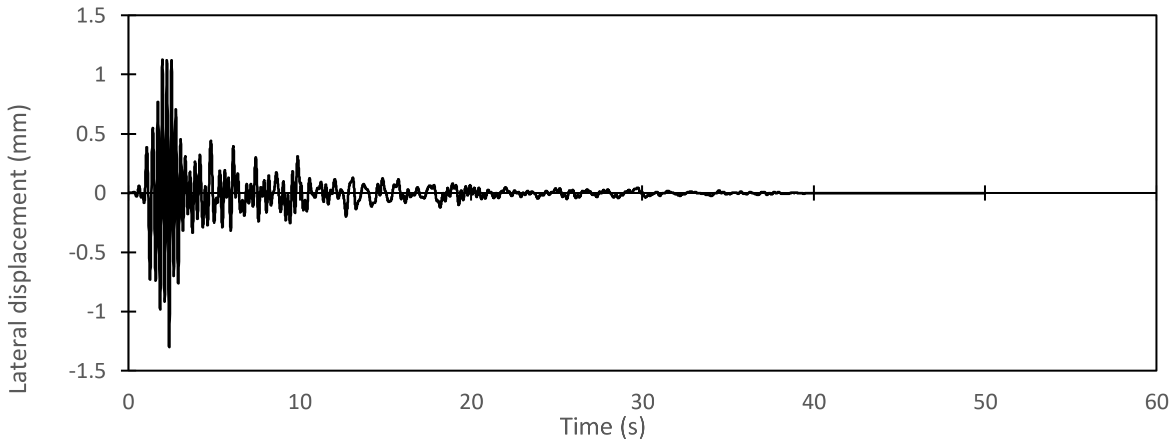

(c)

Figure 6-45: Retrofitted frame under earthquake record TR2-1: (a) lateral displacement-lateral load response; (b) lateral load time history; and (c) lateral displacement time history

6.6.2.2.4 TR2-2

The response presented in Figure 6-46 is from the retrofitted frame under the earthquake record to TR2-2. The frame behaved in the elastic range, and a residual displacement equal to 0.003 mm was observed at the end of the earthquake record. The frame experienced a peak top displacement of 1.106 mm and a peak lateral strength of 26.6 kN. No cracks were observed in the frame.

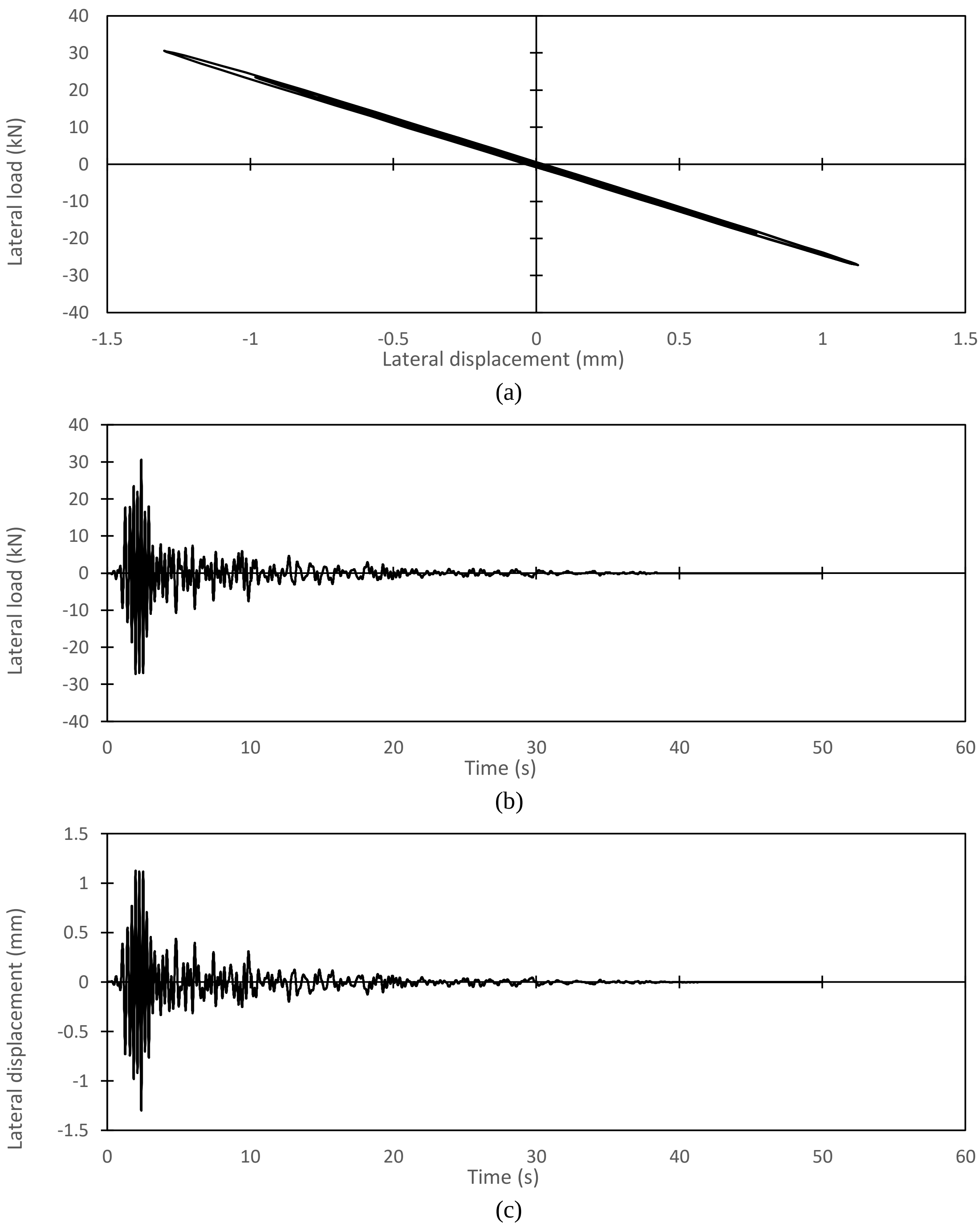

Figure 6-46: Retrofitted frame under earthquake record TR2-2: (a) lateral displacement-lateral load response; (b) lateral load time history; and (c) lateral displacement time history

6.6.2.2.5 TR3-1

Figure 6-47 (a) illustrates the lateral displacement–lateral load response of the retrofitted frame under the earthquake record corresponding to TR3-1, where the frame behaved in the elastic range. A residual displacement equivalent to 0.003 mm was recorded. A peak transient displacement of 1.611 mm and a peak lateral load of 38.1 kN were predicted. No cracks were observed in the frame.

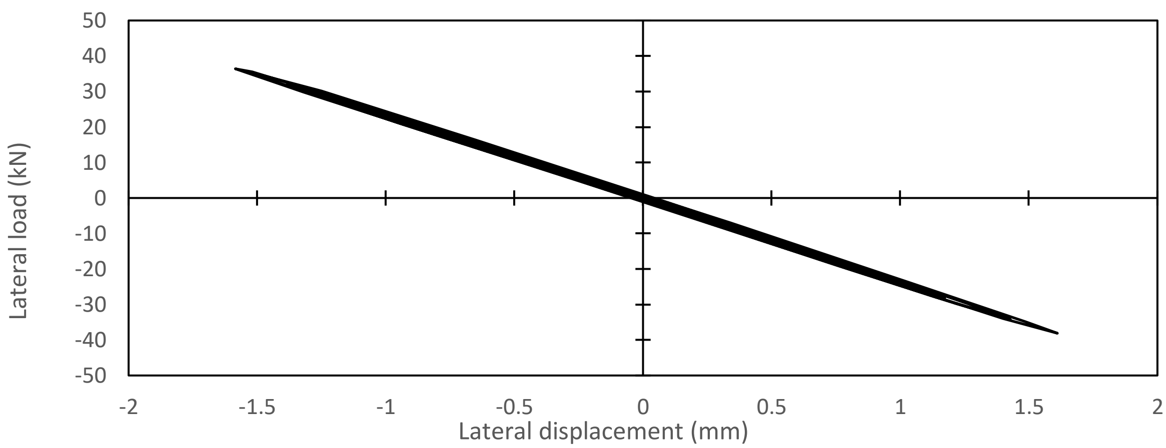

(a)

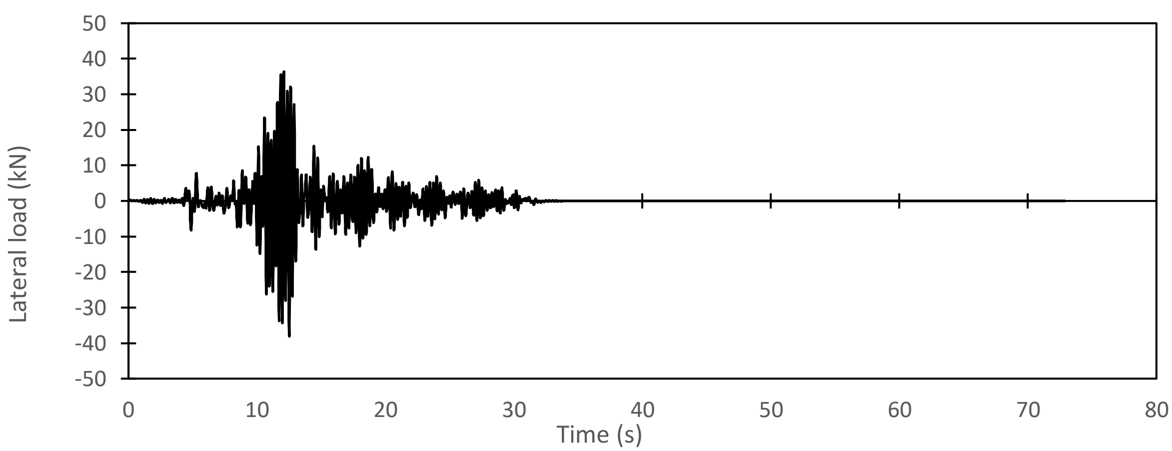

(b)

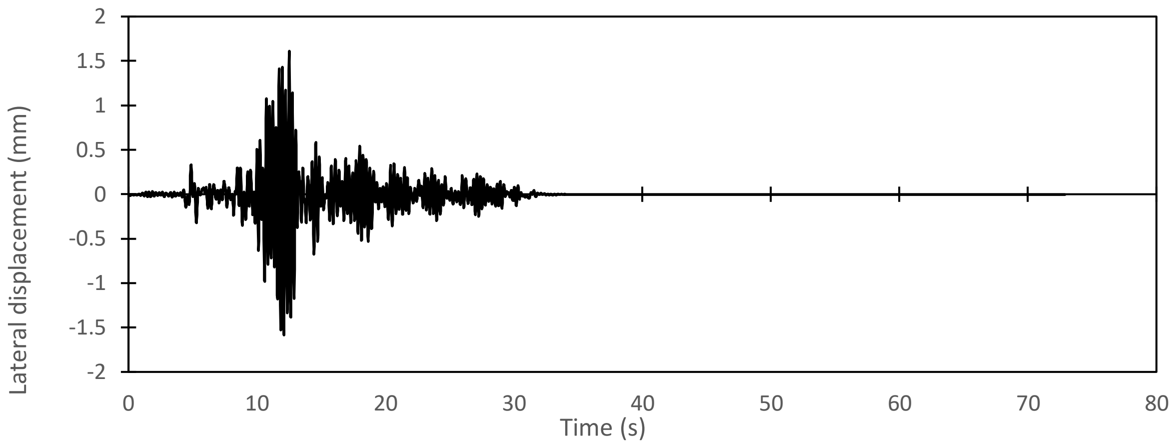

(c)

Figure 6-47: Retrofitted frame under earthquake record TR3-1: (a) lateral displacement-lateral load response; (b) lateral load time history; and (c) lateral displacement time history

6.6.2.2.6 TR3-2

Figure 6-48 illustrates the response of the retrofitted frame subjected to the ground motion TR3-2. The retrofitted frame did not experience inelastic deformations. An accumulation of residual displacement 0.003 mm was noted. The frame experienced a top transient displacement of 0.985 mm, and a peak lateral strength of 23.8 kN. As the frame behaved below the yielding point and the induced displacement was negligible in comparison to the capacity of the system, no cracks were verified.

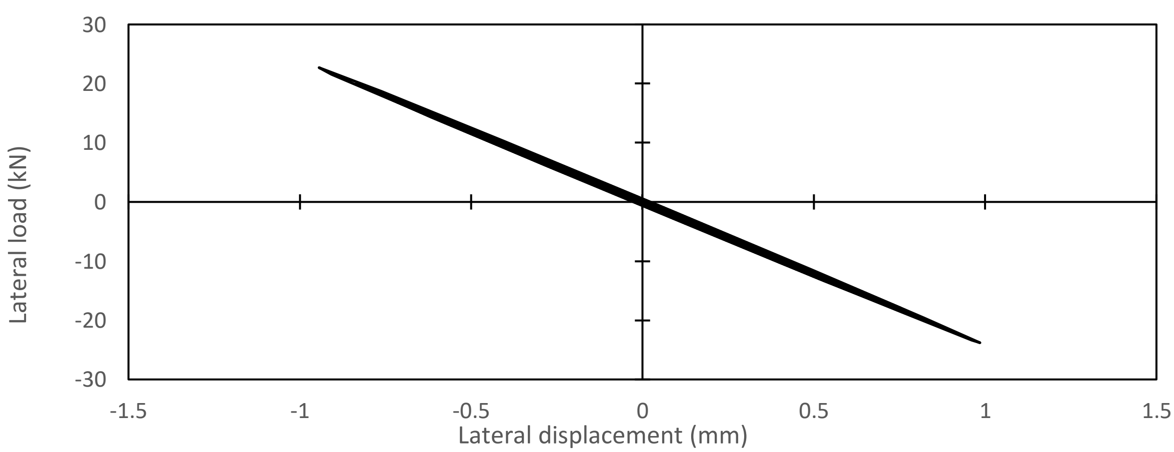

(a)

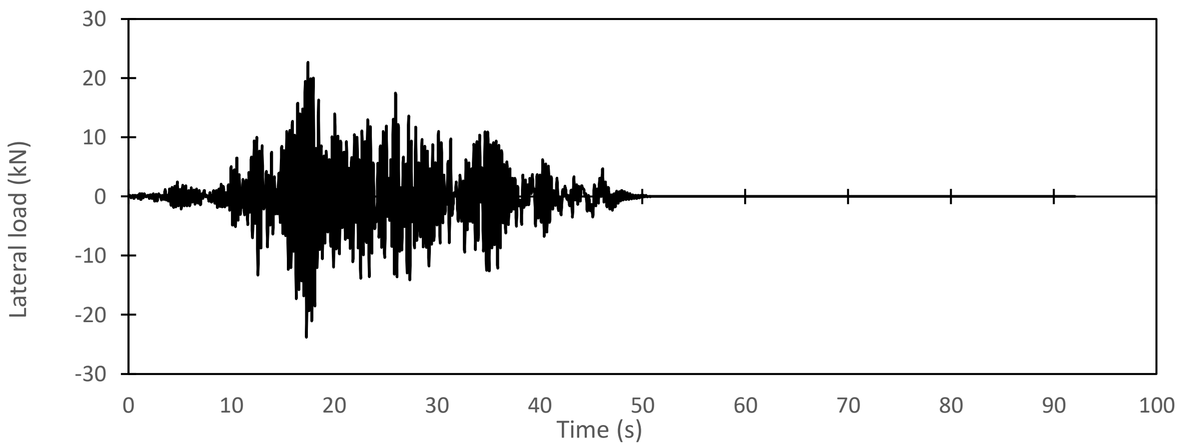

(b)

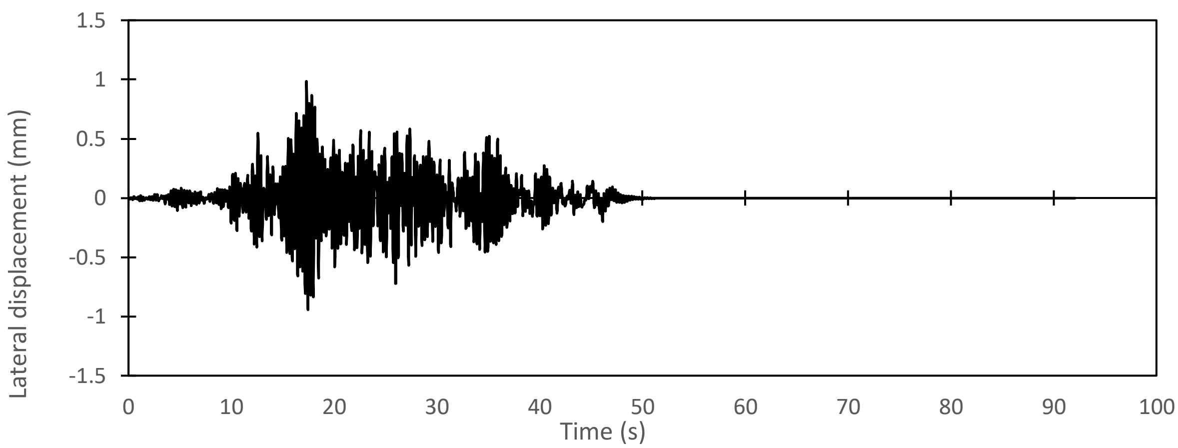

(c)

Figure 6-48: Retrofitted frame under earthquake record TR3-2: (a) lateral displacement-lateral load response; (b) lateral load time history; and (c) lateral displacement time history

6.6.3 Dynamic response to amplified earthquake records

The bare concrete and retrofitted frames were subjected to amplified ground motion records to further investigate the benefits of utilizing a SE-SMA core and understand the response well into the inelastic range. The earthquake record that induces the largest transient displacement, TR2-2, was selected and amplified to 100%, 300%, and 500%. Figure 6-48 depicts the top displacement time-history and the lateral displacement–lateral load hysteretic response for the bare concrete frame under the 100% amplified earthquake record, where the frame experienced displacements beyond its capacity according to the static analysis. As a result of ratcheting, residual displacements accumulated in one direction with a maximum of

26.5 mm of permanent displacement (0.835% drift). Furthermore, the frame experienced a maximum transient displacement of 260 mm (8.18% drift). After the top displacement was reached, the capacity of the frame decreased significantly indicating failure of the frame as observed in Figure 6-49 (b). After the transient displacement of 8.18%, the longitudinal steel reinforcing bars fractured at the base of the columns and near the beam-column joint.

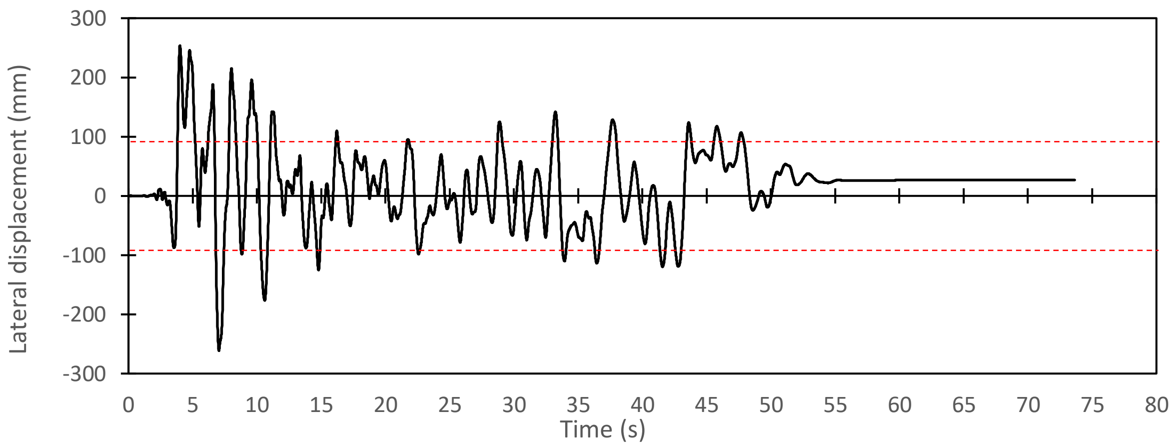

(a)

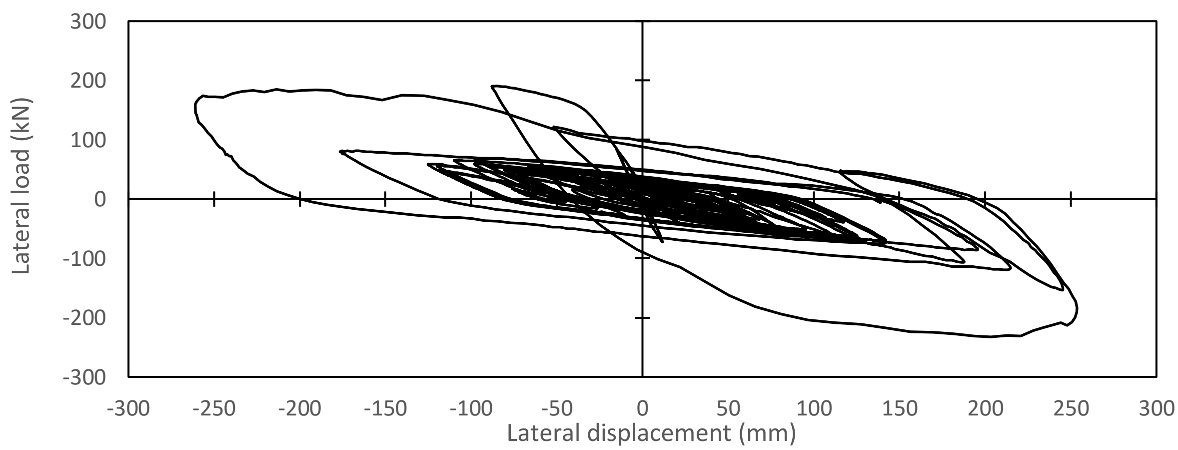

(b)

Figure 6-49: Bare concrete frame subjected to 100% of TR2-2: (a) Lateral displacement time history; and (b) hysteretic response

By evaluating the displaced shape and crack pattern at the end of the dynamic analysis, concrete spalling was evident at the base of the columns and near the beam-column joint (Figure 6-50). In addition to concrete spalling, cracks up to 5 mm wide were predicted by the model. The displaced shape after application of the amplified earthquake record showcases the effects of the residual deformation and structural degradation.

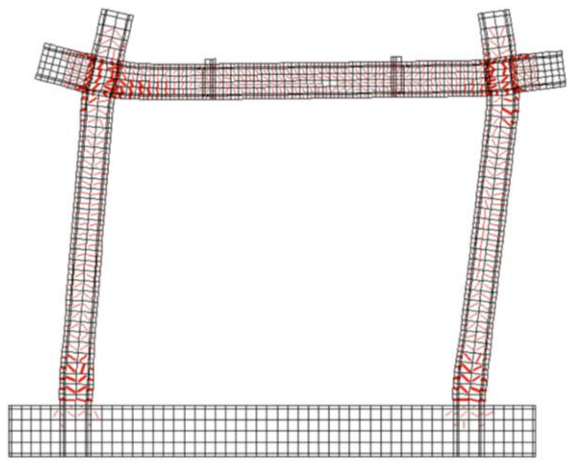

Figure 6-50: Displaced shape and crack patterns of the control frame under the 100% amplified earthquake record TR2-2

Subjected to the same amplified ground motion, the retrofitted frame only experienced forces below the yielding point. The hysteretic response presented in Figure 6-51 illustrates that the retrofitted frame behaved below pseudo-yielding. Furthermore, Figure 6-52 illustrates the displaced shape and crack pattern, where small cracks developed, and no residual displacement had accumulated. As the desirable characteristics of the SE-SMA were not evident, the frame was subjected to a 300% increase in the earthquake record.

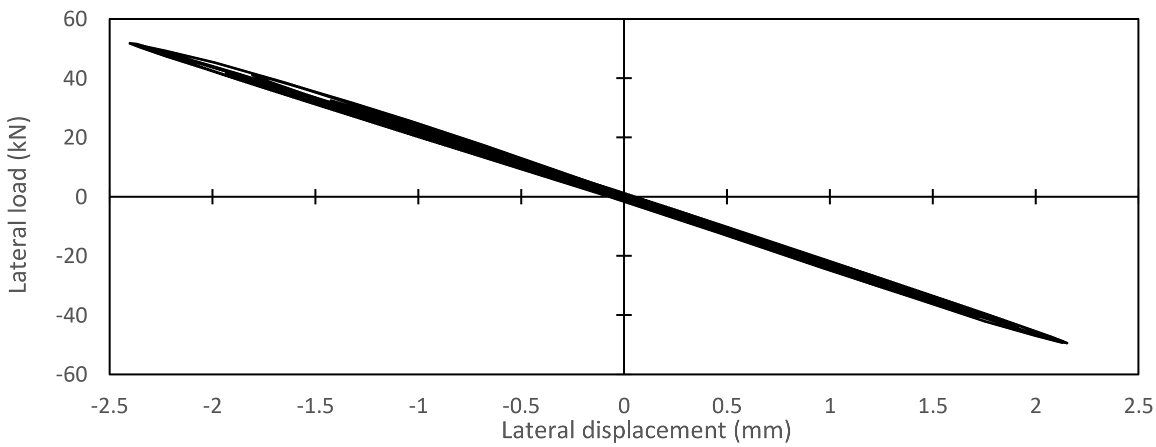

Figure 6-51: Hysteretic response of the BRB retrofitted frame under the earthquake record TR2-2 amplified by 100%

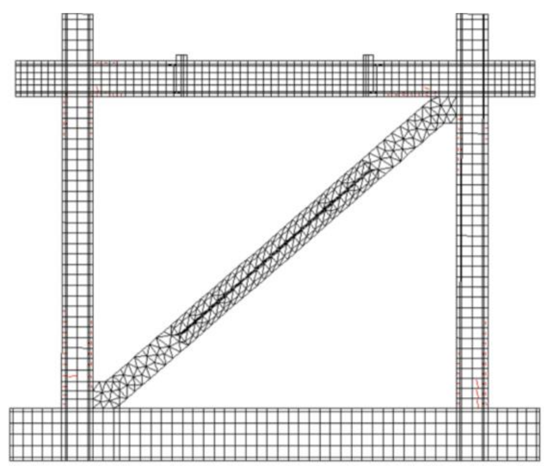

Figure 6-52: Displaced shape and crack pattern of the retrofitted frame under the 100% increased earthquake record TR2-2

The bare concrete frame was subjected to a 300% amplified earthquake record, and the transient time history displacement is provided in Figure 6-53. The frame exceeded its transient displacement capacity 3.8s after the beginning of the earthquake. By exceeding the yielding point, the frame experienced significant inelastic deformations and accumulating residual displacements. In addition, failure of the longitudinal reinforcing bars at the base of the columns were observed. Figure 6-53 (b) illustrates that after the peak displacement was experienced, the capacity of the frame decreased more than 20%, which is indicative of structural degradation of the structure in this thesis (Chapter 5). It is also important to highlight that the strength capacity of the frame is 233 kN and once this was achieved, as depicted in Figure 6-53 (b), the frame diminished its strength resistance under larger displacements. Figure 6-54 illustrates the cracking pattern after the ground motion; it is evident that both shear and flexural cracks surfaced. In addition, concrete spalling was observed near the beam-column joints, as expected, since this region was poorly reinforced following pre-1970s code provisions.

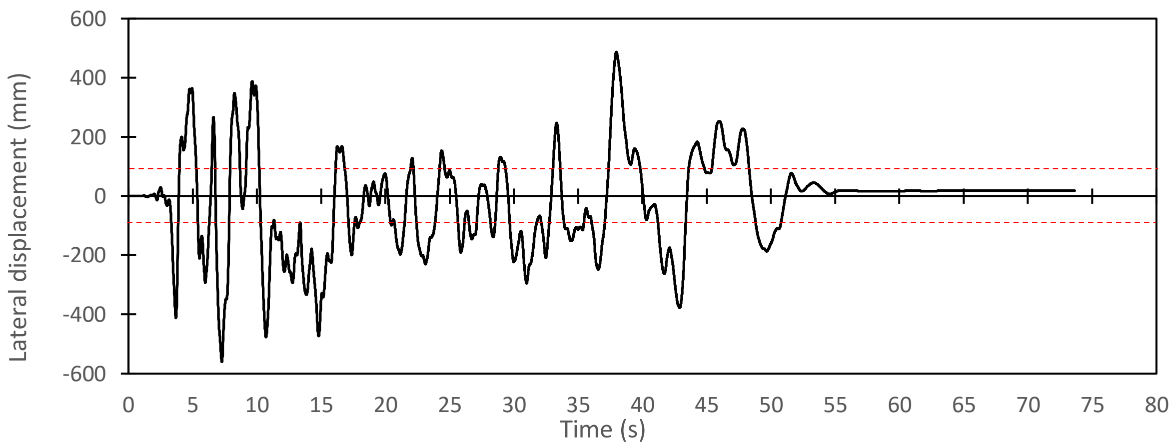

(a)

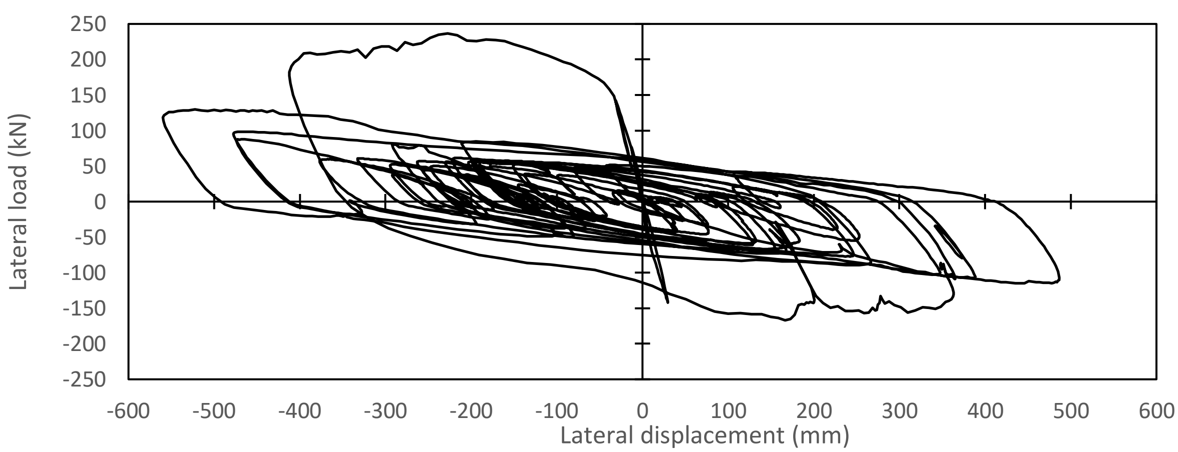

(b)

Figure 6-53: Bare concrete frame subjected to 300% of TR2-2: (a) Lateral displacement time history; and (b) hysteretic response

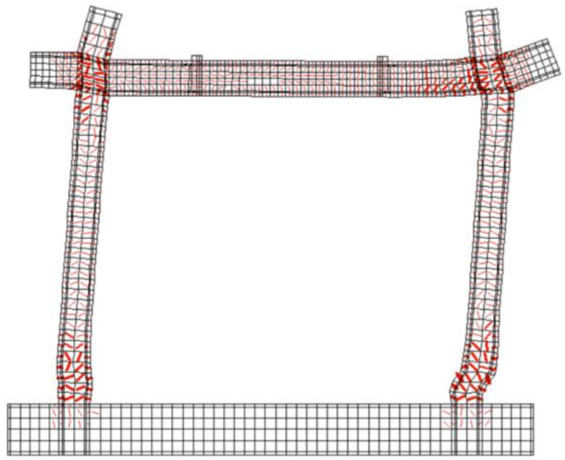

Figure 6-54: Displaced shape and crack pattern of the retrofitted frame under the 300% increased earthquake record TR2-2

When evaluating the performance of the retrofitted frame under the 300% amplified earthquake record TR2-2, pseudo-yielding was not reached as illustrated in the hysteretic response in Figure 6-55 (a). The retrofitted frame experienced a top transient displacement of 5.5 mm corresponding to a peak lateral strength of 103 kN. No residual displacements were predicted, and the crack pattern and displaced shape are demonstrated in Figure 6-55 (b), where only small cracks were evident.

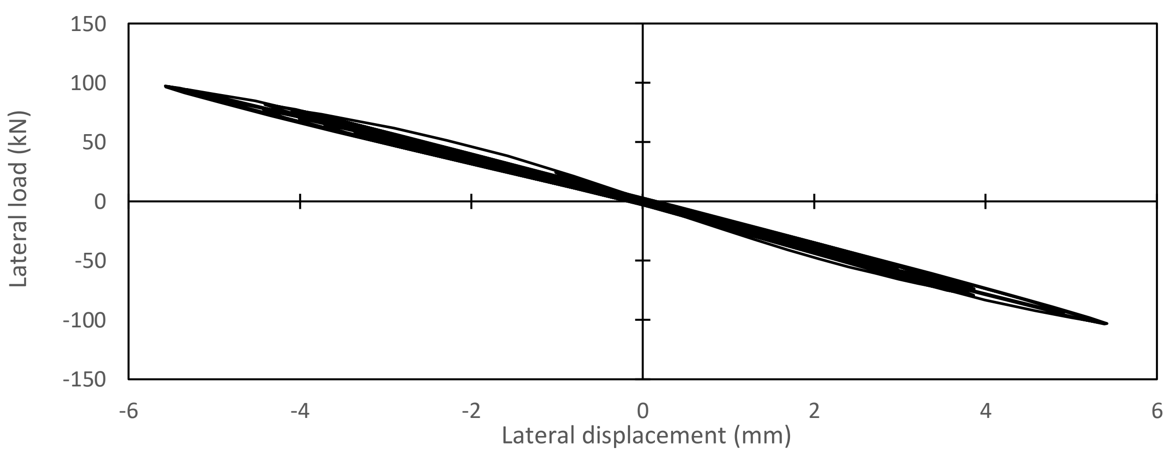

(a)

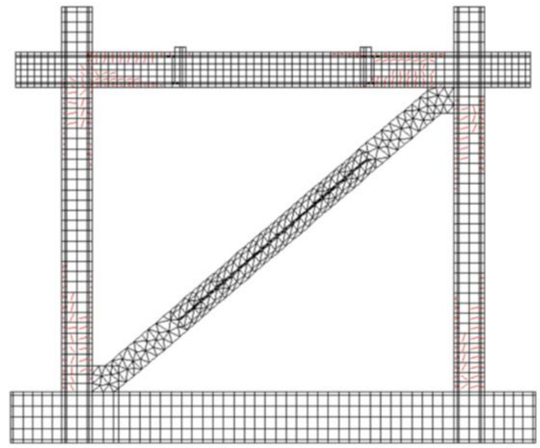

(b)

Figure 6-55: (a) transient displacement time history and (b) crack patterns of the retrofitted frame subjected to the earthquake record amplified to 300%

The final attempt to reach the pseudo-yielding response of the retrofitted frame was included subjecting the frame to the earthquake record amplified by 500%. Although the bare concrete frame failed 4.46 s after the beginning of the earthquake record (Figure 6-56 (a)), the retrofitted frame behaved below the pseudo-yielding point (Figure 6-56 (b)). This highlights two points regarding the retrofitted frame that will be further discussed in Chapter 7: the retrofitted frame presents a high stiffness, and the lumped mass are not sufficient to push the frame into the inelastic range.

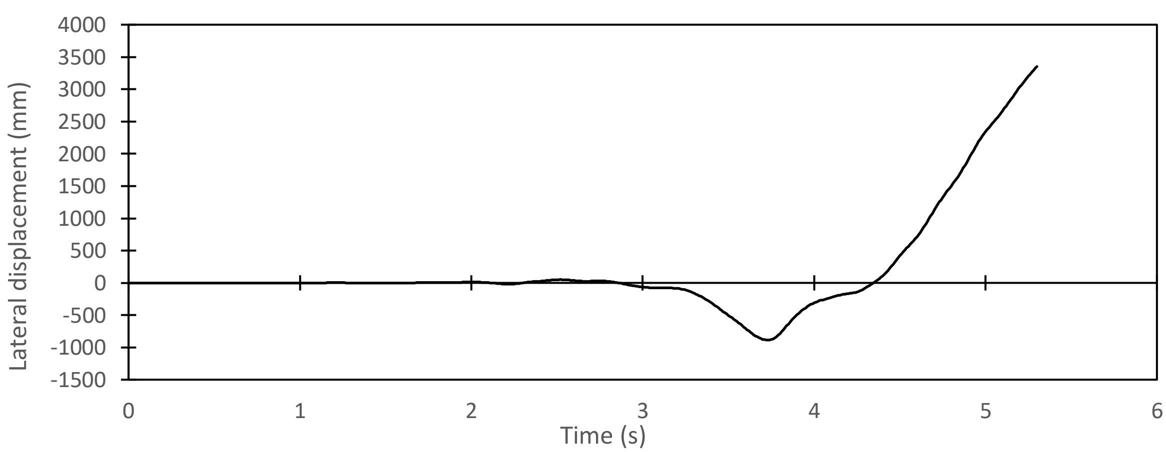

(a)

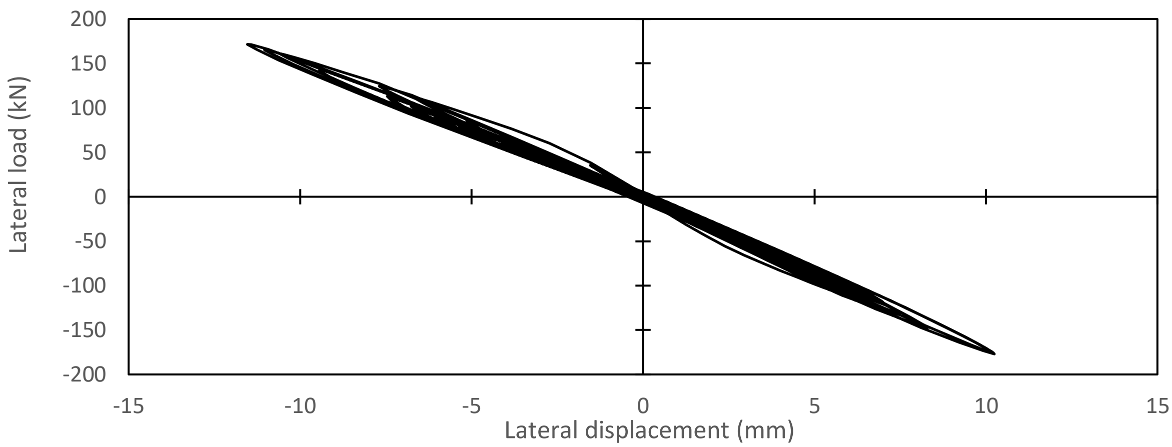

(b)

Figure 6-56: Response under 500% increased earthquake record TR2-2: (a) transient displacement time history of the bare concrete frame; and (b) lateral displacement–lateral load of the retrofitted frame

Chapter 7

Discussion of numerical results

7.1 Introduction

This chapter provides a brief overview of the seismic indexes utilized to evaluate the seismic performance of the numerically modelled reinforced concrete frame; the validation process of the finite element model for the bare and retrofitted frames; and a discussion of the results of the numerical nonlinear static and dynamic analyses presented in Chapters 5 and 6. The response of the frame retrofitted with the modified BRB incorporating the SE-SMA core will be assessed against the results of the bare concrete frame and the frames retrofitted with the original BRB incorporating conventional steel cores. From the monotonic and hysteretic responses, the discussion focuses on the lateral strength capacity, failure mode, ultimate drift, residual displacements, displacement ductility, and energy dissipation. The time-history response of the retrofitted frame with modified BRB and SE-SMA core will be assessed against the dynamic response of the control frame in terms of permanent and transient displacements. At the end of the chapter, further improvements to the brace will be presented.

7.2 Seismic response indexes

To assess the seismic response of the frames, seismic indexes present in the literature and building codes were used. These indexes are briefly discussed in this section and applied to provide an assessment of the nonlinear static and dynamic results. The first index relates to residual deformations, which can be understood as the permanent deformation of the structural members after the imposed load ceases. Depending on the level of residual displacement, repair is costly and non-viable. Studies present in the literature demonstrate the acceptable level of permanent displacement is measured based on the structural type. According to Erochko et. al (2011), structures with a residual drift ratio between 0.5% and 1% are highly susceptible to P-delta effects, which significantly shifts the behaviour of the structure beyond the original design capacity. Therefore, the 0.5% residual drift limit proposed by McCormick in 2008 will be used as the drift limit of the frames studied herein. Beyond that drift ratio, the structure is expected to be inhabitable. Furthermore, transient storey drift ratio limits have been defined by the ASCE/SEI 41-17 (ASCE, 2017) with an upper limit of 2.5% for two and four-storey buildings, and a limit of 2% for other vertical constructions.

The American Society of Civil Engineers (ASCE, 2017) provides guidelines for evaluating the seismic performance and for retrofitting existing buildings. The Federal Emergency Management Agency (FEMA, 2012) defines performance levels the building must satisfy depending on the acceptable overall damage after a seismic event. The damage can be characterized as very light (1-A), light (1-B), moderate (3-C) and severe (5-D).

The operational performance level (1-A) represents structures with very low risk of life-threatening injuries from structural failure. After an earthquake, a structure designed for a performance level 1-A can be easily repaired and immediately re-occupied. For an immediate occupancy performance level (1-B) more damage compared to 1-A is expected, and both structural and non-structural elements may require repair. In the life safety performance level (3-C) significant damage to the structure is expected, but structural collapse is avoided due to a margin of safety. In this performance level, injuries to the occupants may occur, but no life-threatening risks are expected due to the structural damage; and extensive repair is needed, which may require considerable time and investment. The structural stability performance level (5-D) is characterized by severe damage in which the structure is on the verge of experiencing partial or total collapse. Although substantial damage occurs at this level, the gravity load resisting system should carry their demands. The stability of the building is guaranteed, but there is a significant risk of injury. For concrete buildings in this level of damage, repair is technically and economically unfeasible. Table 7-1 provides the correlation between the performance levels and the storey drift limits prescribed by the FEMA P-58-1 (FEMA, 2012) and NBCC 2015 (NRC, 2015).

Table 7-1: Building performance levels and storey drifts for reinforced concrete frames from FEMA P-58-1 (FEMA, 2012) and 2015 NBCC (NRC, 2015)

	Performance level			
	1-A	***1-B***	***3-C***	***5-D***
Residual storey drift	*0.2%*	*0.5%*	*1.0%*	*1% (low-ductility buildings)*
Transient storey drift	*1.0%*	*1.5%*	*2.0%*	*2.5%*

7.3 Analyses validation

The validation of the numerical models used in the static and dynamic analyses was conducted in two phases. The bare concrete frame model was validated through previous tests present in the literature by comparing the numerical response with the testing conducted by Al-Sadoon (2016) of the frame under the same reverse cyclic displacement-controlled loading. After corroboration, the model was used to also simulate the retrofitted frame in the second phase. In this phase, the numerical hysteretic response was compared to the experimental results from Al-Sadoon (2017) for the frame retrofitted with a BRB incorporating a Stainless Steel and Chrome-Molybdenum core bar. The validation focused on the strength capacity, ultimate displacement, failure mode, and crack patterns.

Figure 7-1 (a) illustrates the experimental, from Al-Sadoon (2017), and numerical lateral displacement–lateral load responses for the Bare Concrete Frame (BCF), where the FE model satisfactorily simulated the response. The maximum lateral load capacity recorded during testing was 233 kN and 219 kN in the positive and negative directions, respectively; while for the numerical model, it was 238 kN and 219 kN, respectively. In both numerical and experimental responses, the frame was considered to have reached its maximum drift capacity at a displacement of 95 mm (3% drift) given that the lateral strength decreased by more than 20% from the peak beyond that drift. At the end of the FE analysis, significant cracks were captured at the base of the columns and at the beam-column joints. This was consistent with that observed behaviour during testing. Furthermore, a residual drift of 1.6% was experienced by the frame in the numerical model, which is similar to the permanent drift observed at the end testing. Therefore, the numerical model was considered representative of the behaviour of the bare concrete frame.

To assess the numerical response of the retrofitted frame, the BRB retrofitted frame incorporating a Stainless Steel core bar was utilized. The hysteretic response of the numerical model was presented in Figure 5-30. In the positive direction of loading, the capacity of the retrofitted frame was 549 kN, and the frame was able to sustain a maximum displacement of 94.5 mm (3% drift). The system failed due to fracture of the core bar during the second repetition in the positive direction to 3% drift. At the end of unloading, the cracks were concentrated from the base of the columns up to a height of 300 mm, and a residual drift of 1.6% was captured. The experimental results from Al-Sadoon (2016) for same frame provided a lateral strength capacity of 577 kN, which differed by less than 5% in comparison to the numerical response. The drift capacity of the retrofitted frame corresponded to 3%, and failure occurred due to fracturing of the bracing core bar. In addition, a residual drift of 1.89% was observed at the end of testing. The results corroborate that the responses of the numerical model of the retrofitted system comply with the experimental observations. Figure 7-1 (b) provides the lateral load-lateral displacement responses for the numerical model and experimental testing.

The validation of the BRB model was also assessed for the Chrome-Molybdenum core bar. The numerical hysteretic response of the retrofitted frame (Figure 5-26) indicated the frame failed at a lateral drift of 1.5% due to fracture of the core bar during the third repetition in the positive direction at the mid-length of the bracing core. In the experimental results from Al-Sadoon (2016), the frame failed at the same drift ratio, but during the second repetition in the positive direction. Furthermore, at the ultimate drift, the frame was able to sustain a lateral force of 488 kN in the numerical analysis, which is slightly lesser than what was recorded during testing (510 kN). As the difference in lateral strength capacity was only 4.3% and corresponded to the same lateral drift capacity, the numerical model was assessed to be representative of the response of the frame. Figure 7-1 © provides the lateral load-lateral displacement responses for the numerical model and experimental testing.

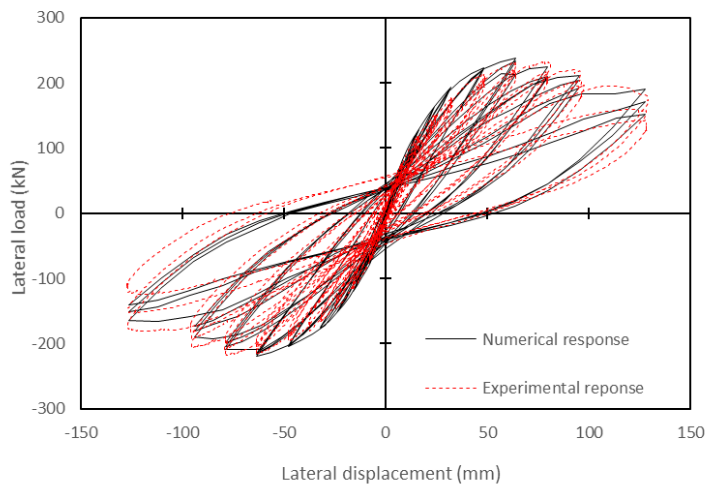

(a)

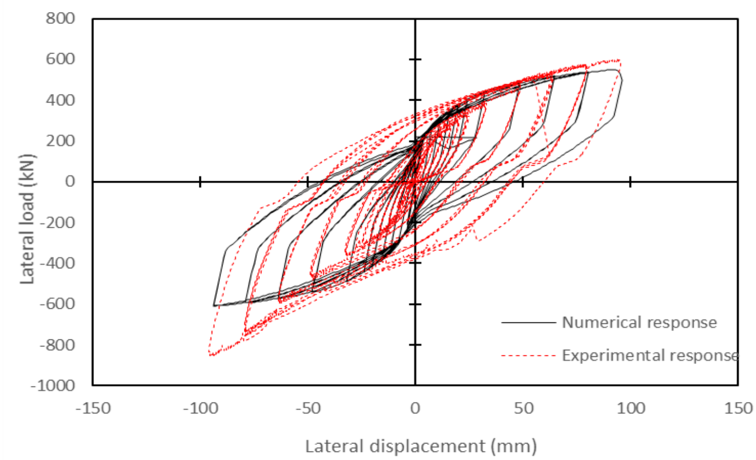

(b)

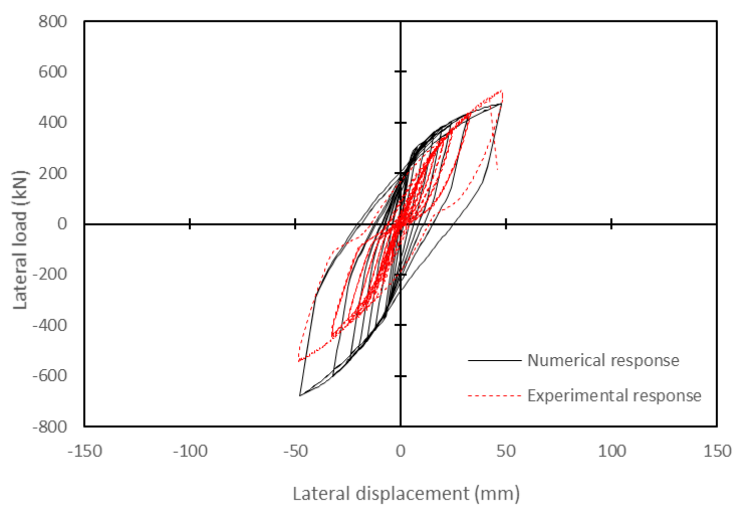

(c)

Figure 7-1: Hysteretic numerical and experimental response (Al-Sadoon, 2016): (a) bare concrete frame, (b) original BRB retrofitted frame incorporating SS core, (c) original BRB retrofitted frame incorporating CM core

7.4 Assessment of monotonic response

Figure 7-2 illustrates the monotonic response of the bare concrete frame against the response of the frames retrofitted with the original BRB incorporating the conventional steel cores under tension. Two different steel cores are presented in the responses, a Chrome-Molybdenum (C-M) and a Stainless Steel (S-S). By retrofitting the frame with a BRB, the lateral strength capacity of the system increases at a ratio of 3.5 and 3.0, relative to the control frame, for the C-M and S-S core, respectively. Furthermore, with the C-M core incorporated into the system, the frame is able to sustain an ultimate displacement of 170.9 mm, which is 6% higher than the bare concrete frame under pushover loading. With the Stainless-Steel core, the ultimate displacement increases 18% relative to the BCF. While the BCF failed due to fracture of longitudinal steel at the base of the columns, fracture of the BRB steel core was verified in the retrofitted systems. Failure in the bracing core is desirable such that repair may be restricted to the retrofitting system. In this regard, the core serves as a sacrificial element. Furthermore, regarding the effective stiffness (k_{eff}) of the C-M BRB, it is approximately twice the bare concrete frame, while the k_{eff} of the S-S BRB is 50% greater than the BCF. The stiffness of the system has an impact on the seismic forces transferred to the foundations during a seismic event. Therefore, a thorough analysis of such parameter is fundamental when selecting an appropriate retrofit technique.

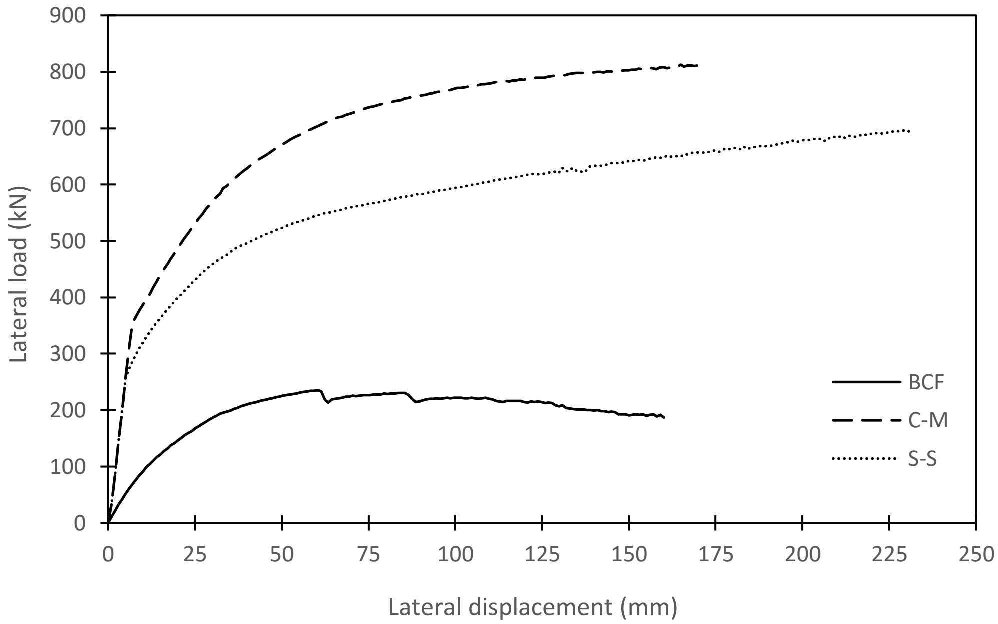

Figure 7-2: Pushover responses of the bare concrete frame and conventional-BRB retrofitted frames with the brace under tension

The capacity of the retrofitted system is controlled by the brace when subjected to compressive stresses. With the brace in compression, the capacity of the frame significantly diminished as localized stresses accumulated in the core bar. In Figure 7-3, the pushover responses of the BCF, C-M BRB, and S-S BRB are illustrated with the braces under compression loading. Although the retrofitted frames possess lateral strength capacities two times greater than the BCF, the ultimate displacements were significant reduced. For the C-M BRB frame, the ultimate displacement was 56% smaller than the BCF; and when the S-S core is used, the frame provided only 64% of the drift capacity of the BCF.

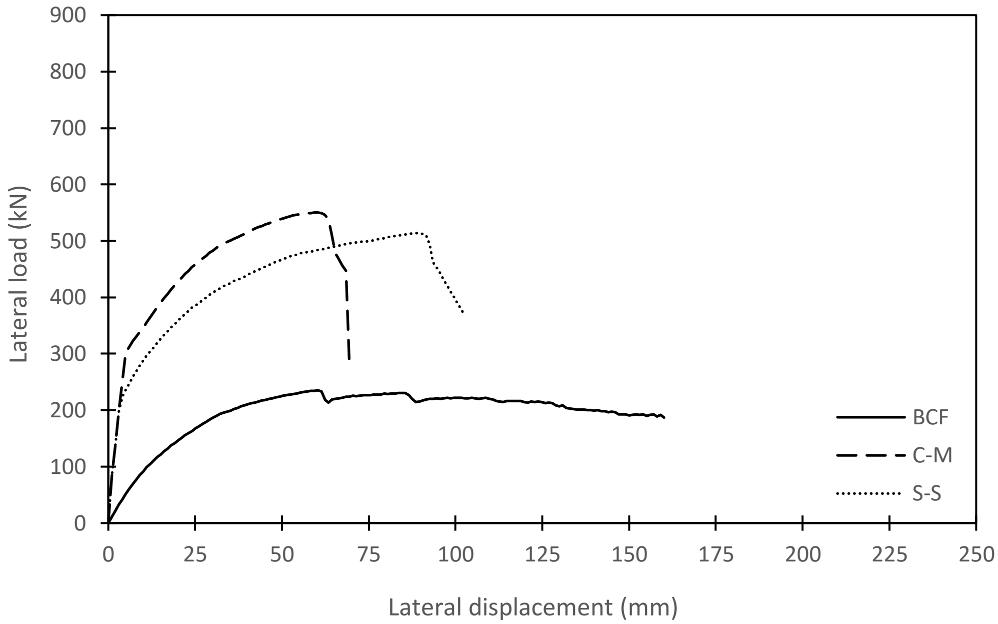

Figure 7-3: Pushover responses of the bare concrete frame and conventional BRB retrofitted frames with the brace under compression

The concentration of stresses and buckling of the bracing core can be attributed to insufficient buckling restraining and/or inappropriate un-bonding layer between the steel core and restraining component. In the BRB design proposed by Al-Sadoon (2016), there was no un-bonding layer for the stainless steel core bar, thus a void separated the core from the surrounding restraining system. The absence of an un-bonding layer allows frictional forces between the core bar and the surrounding restraining component that permit transfer of axial load between the elements to occur, which may induce concentration of strains and stresses. When strains are localized at a single point, the structure of the material becomes vulnerable to fracture and buckling at that specific point. This phenomenon intensifies when the bar experiences cyclic loading alternating the stress on the brace between tension and compression, which may cause premature failure of the bar. Furthermore, when the Chrome-Molybdenum core was used during testing, the void was partially filled by epoxy mixed with sand, but a 0.9 mm gap remained between the bar spacers and the steel pipe (Figure 4-10). The study conducted by Tsai et al. (2004) demonstrated that when a gap is used as an un-bonding layer, concentration of stresses is generated and this manifests in the asymmetric hysteretic response due to altering of tensile and compressive actions on the brace.

By modifying the BRB to increase buckling restraining, an improved system was developed (Figure 4-12). The pushover responses of the frame retrofitted with the modified BRB incorporating either a C-M or a S-S core are represented in Figures 7-4 and 7-5, respectively. The figures depict the response of the system retrofitted with the modified BRB under compression loading against the numerical response of the system equipped with the conventional BRB proposed by Al-Sadoon (2016). The modified BRB improved both lateral strength capacity and displacement ductility of the frames relative to the same frame with the original BRB. For the C-M core BRB, the displacement ductility increased from 2.9 to 3.6, and the strength capacity from 550 kN to 774 kN. This represents an increase in the ultimate displacement of 40% and a strength capacity improvement of 150%, by increasing the buckling restraining and adding a 2 mm-thick silicon rubber sheet as an un-bonding layer in the brace.

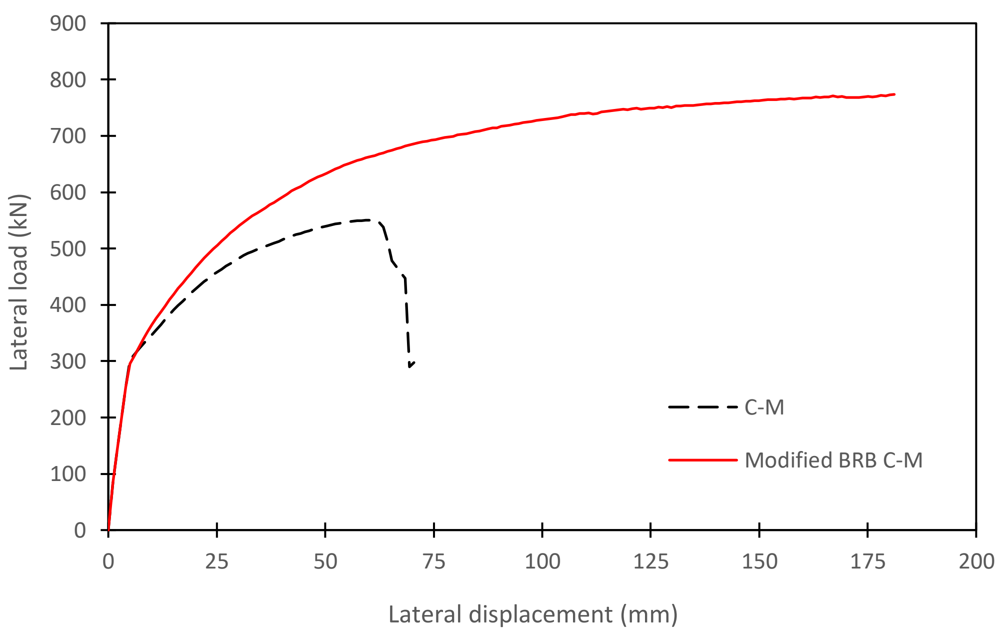

Figure 7-4: Pushover responses of the frame retrofitted with the original and modified BRB incorporating a C-M core bar under compression

For the braced system incorporating a stainless steel core bar, the increase in lateral strength with the modified BRB corresponded to 13% relative to the conventional BRB, while the ultimate displacement increased 73%. When evaluating the response of the modified BRB under tension against the original BRB, no significant changes were evident in the strength capacity of the system since the core bar was subjected to tensile stresses and buckling related issues are not applicable. The increase in lateral strength capacity and ductility displacement corroborates the improvements of the modified BRB and highlights the importance of a stable un-bonding layer.

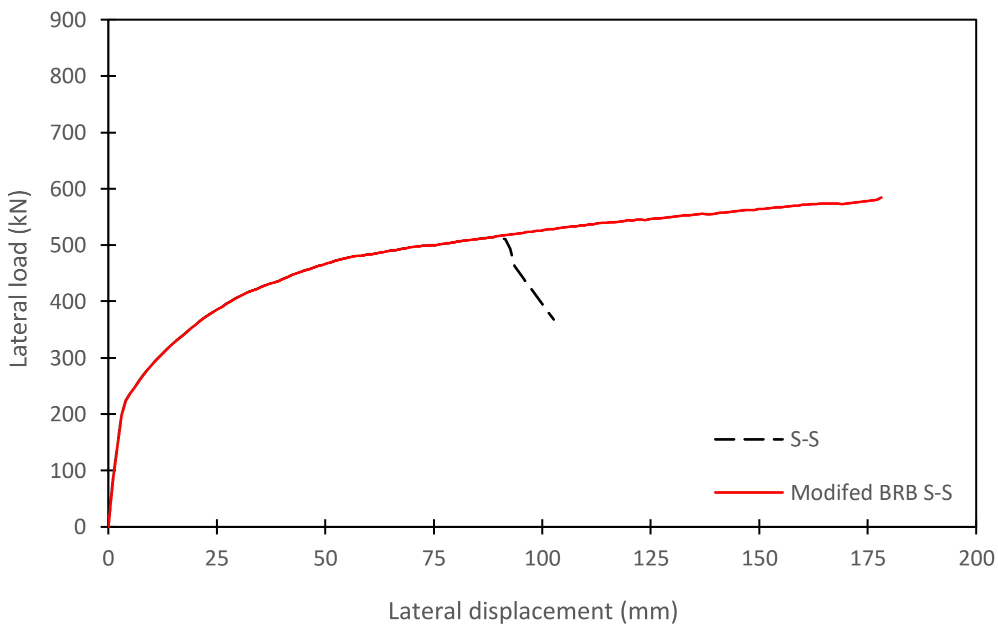

Figure 7-5: Pushover responses of the frame retrofitted with original and modified BRB incorporating a S-S core bar under compression

For the SE-SMA BRB with core diameter similar to the conventional steel core bars – reduction of diameter at mid-length to induce yielding, the lateral strength capacity of the frame with the brace under tension is 2.7 times the capacity of the BCF; while the BRB that incorporates a SE-SMA core bar with constant diameter of 44.5 mm, the lateral strength capacity increased approximately 4.1 times that of the bare frame. Regarding the ultimate displacement, the constant diameter SE-SMA core bar BRB was able to sustain larger lateral deformations in the pseudo-yielding range reaching a magnitude of 200 mm, which is 25.6% greater than the displacement experienced by the BCF.

Improvements in both strength and displacement capacities are evident when a SE-SMA bar is utilized (Figure 7-6). The effects of buckling were identified in the reduction in lateral strength capacity; however, as SE-SMAs can recover their initial shape once the imposed stresses are removed, the effects of strain concentration are minimized. For the SE-SMA BRB with a reduction in the cross-sectional area under compression, a drop of 8% of the strength capacity of the system was experienced. For the core bar with constant 44.5 mm diameter, the drop in the capacity corresponded to approximately 11%. As the response of the reduced diameter SE-SMA was more stable and symmetric, it was decided to conduct the hysteretic response only on this model. The modified BRB was able to increase the strength capacity of both retrofitted systems that incorporate SE-SMA, but at smaller rates. For the system retrofitted with modified BRB incorporating a constant 44.5 mm-diameter SE-SMA core bar, at a displacement of 150 mm, the concrete frame experienced large cracks at the bottom of the column. This does not imply residual deformation to the structure, but damage on the frame should be avoided.

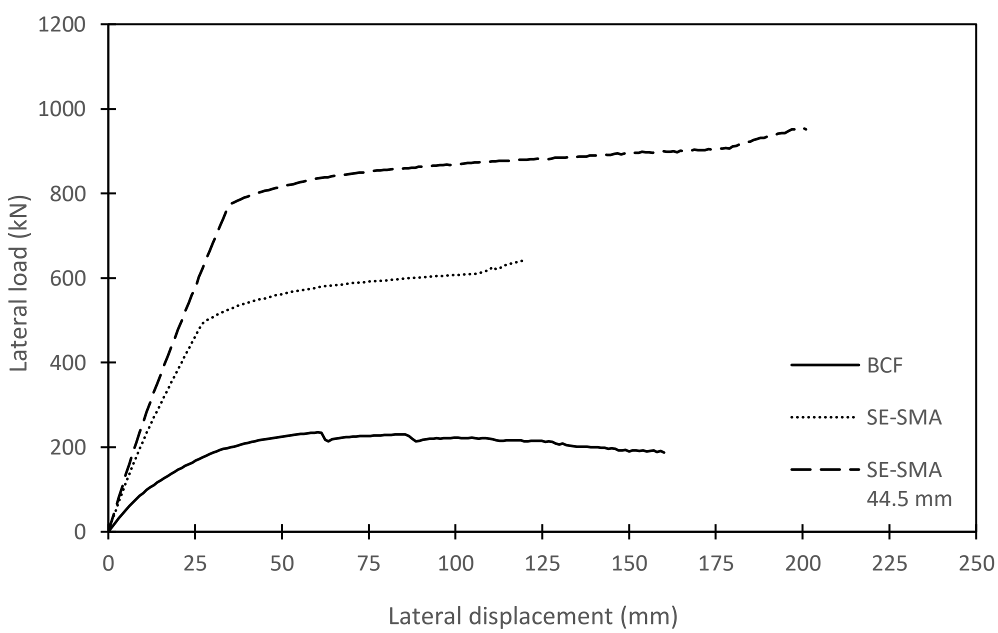

Figure 7-6: Conventional BRB incorporating SE-SMA core bar under tension

Independent of the BRB design, the retrofitting technique was able to increase the lateral strength capacity of the system. When utilizing the original BRB with the conventional steel cores, however, the displacement capacity decreased relative to the bare control frame due to concentration of stresses in the bracing core. Therefore, it became evident that the modified BRB design provided improvements due enhanced buckling restraining, which allows the system to experience larger deformations and the core bar to reach its full capacity. It is important to note the desirable characteristic of SE-SMA bars cannot be measured under pushover analysis. The self-centering ability of SMA bars is crucial to reduce residual displacements, which can only be evaluated under reverse cyclic and time-history analyses.

7.5 Assessment of hysteretic response

7.5.1 Bare concrete frame

For the reverse cyclic analysis, six frames were studied. The bare concrete frame was analyzed to corroborate the numerical model against the actual behaviour of the structure in terms of strength capacity, failure mode, residual displacements, and crack patterns. Likewise, the reverse cyclic analysis was conducted on the BRB designed by Al-Sadoon (2016) with a Stainless Steel and a Chrome Molybdenum core to validate the numerical response with the results from previous testing. The remaining frames were retrofitted with the modified BRB incorporating either a Chrome-Molybdenum, Stainless Steel, or Superelastic SMA core. Based on the pushover response, the proposed retrofitting system of this thesis included the modified BRB incorporating a SE-SMA core bar with reduced cross-sectional area at mid-length. Therefore, analysis was conducted to determine the efficiency of the SE-SMA bar only on the modified BRB system.

Figure 7-7 illustrates the lateral load–lateral displacement response of the bare concrete frame against the pushover response. The strength capacity of both responses was similar with a difference of 2%. The drift capacity of the frame under reverse cyclic analysis corresponded to 3%, while under pushover it corresponded to 4.7%. This can be attributed to repetition of cycles in the reverse cyclic analysis; thus, the frame accumulates more damage. Furthermore, as the pushover response produces cracking in only one direction, it delays failure. When evaluating the effective stiffness, in both analyses similar values were verified with the hysteretic response presenting a slight increase of 3.6% relative to the pushover response.

Flexural cracks initiated at a 0.25% drift in the hysteretic response - the drift was calculated as the imposed lateral displacement divided by the height from the base of the column to the center of the beam. At a drift of 0.756%, shear cracks were evident at the beam-column joint. The frame was able to sustain a maximum drift of 3%, and as yielding initiated at a lateral displacement of 36 mm, the displacement ductility was approximated as 2.64, which is approximately 70% of the ductility experienced by the frame under pushover loading. Comparing the yielding drift of the reverse cyclic numerical response to the experimental response by Al-Sadoon (2016), both yielded at similar drift ratios (1.13%).

Concrete spalling at the base of the column and at the beam-column joint was observed and this resulted in strength degradation. At these locations, the longitudinal steel reinforcement was yielding with strains close to the ultimate. At the drift cycle of 4%, the frame failed as lateral strength capacity decreased more than 20% from the peak lateral strength. At this drift, flexural cracks were distributed from the base of the column to its mid-height. Furthermore, cracks 6.12mm wide were also predicted at the base of the columns. The beam-column joint, however, had wider cracks, up to 10.81 mm, and this is an indication of the deficient reinforcement design since no transverse reinforcement was specified in this region when following pre-1970s building code provisions.

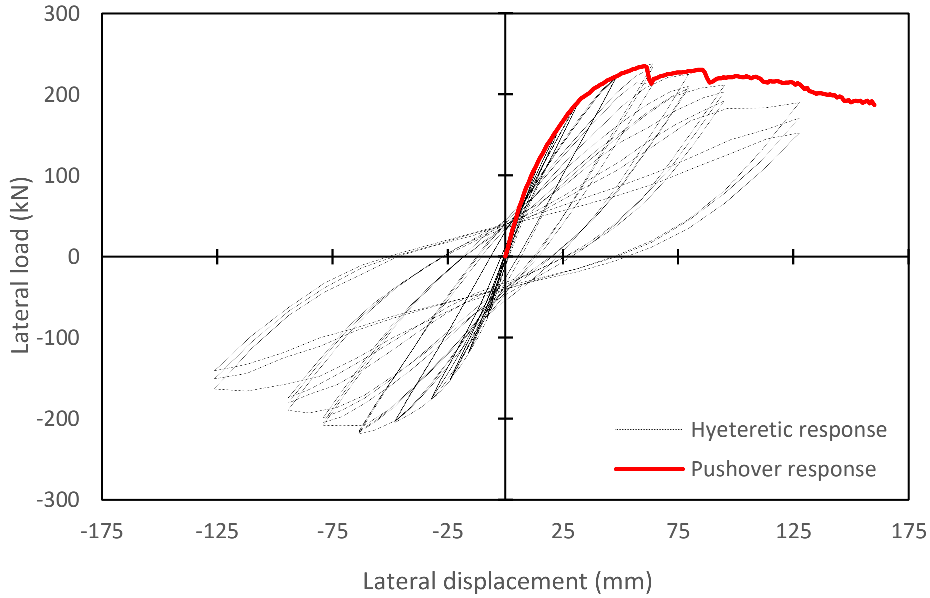

Figure 7-7: Hysteretic and pushover responses of the bare concrete frame

7.5.2 Original BRB incorporating Stainless Steel core retrofitted frame

The differences between the reverse cyclic and pushover responses become more apparent when evaluating the performance of the retrofitted frames with the BRB proposed by Al-Sadoon (2016). This is attributed to the concentration of stresses present on the core bar leading to a reduction of stiffness and decrease in strength capacity. In addition, the retrofitted frames incorporating the conventional steel cores accumulate significant residual displacement, which increases the P-delta phenomenon and increases the risk of spalling at the base of the columns. Figure 7-8 illustrates the behaviour of the BRB incorporating a Stainless Steel core under reverse cyclic and pushover analyses. The capacity of the frame under pushover and reverse cyclic analyses correspond to 696 kN and 549 kN, respectively. Therefore, the lateral strength capacity of the frame under reverse cyclic loading is more than 20% lower than the system under pushover loading.

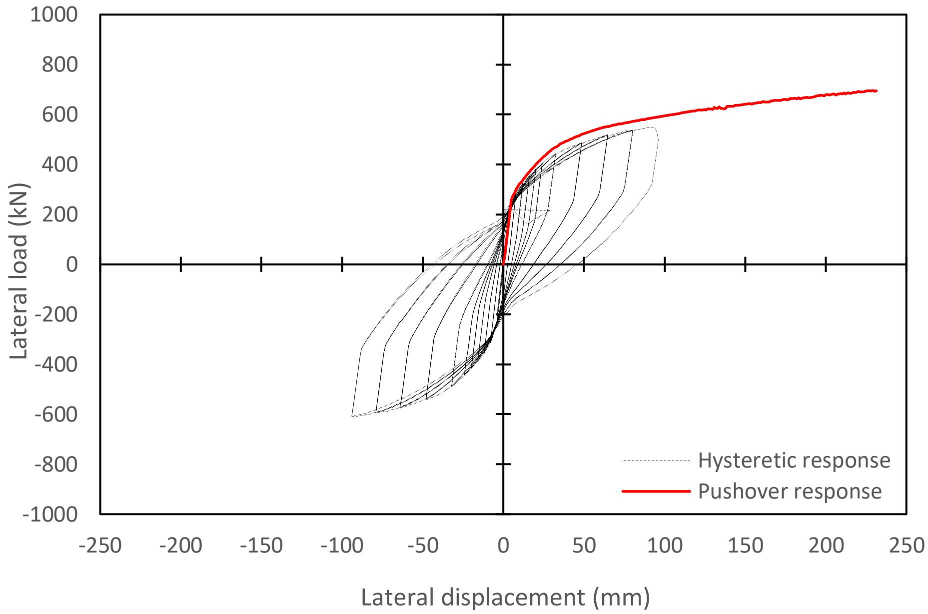

Figure 7-8: Hysteretic and pushover responses of the BRB retrofitted frame with Stainless Steel core

The drift capacity decreased significantly from the pushover to the reverse cyclic analysis, from 7% to 3%, respectively. The system failed due to fracture of the core bar during the second repetition in the positive direction. At the ultimate drift, the column longitudinal reinforcement exceeded the yield strain at the base and near the beam-column joint. It was observed that when the material surrounding the core bar does not provide sufficient stiffness against buckling, stresses and deformations accumulate on the core bar within the brace. The accumulation of stresses and strains in the core modifies the cross-sectional area and diminishes the capacity of the bar. As a result, that point of concentration becomes a zone of vulnerability that results in premature failure.

The core bar did not reach its full capacity, and this was assessed by evaluating the strains of the core at the maximum drift. Figure 7-9 illustrates the lateral displacement – reinforcement strain of a section of the core bar at its mid-length, which is characterized by a reduced cross-sectional area. The elongation capacity of a Stainless Steel core bar corresponds to 50%. The maximum strain experienced by the truss element provided a stable response to failure, where a significant increase in strain (44.8%) was experienced.

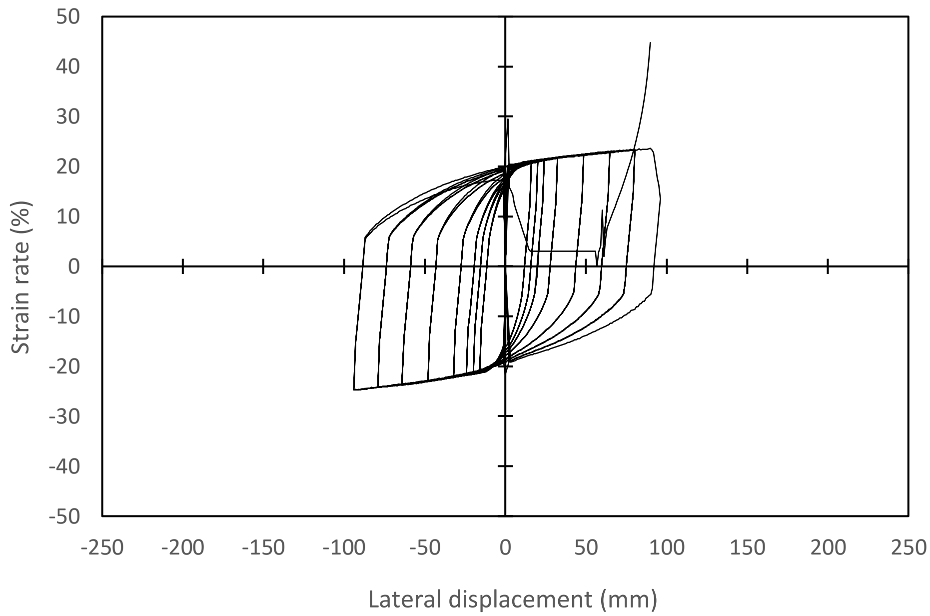

Figure 7-9: Strain-lateral displacement response of the Stainless Steel core in the BRB retrofitted frame

By evaluating the cracking patterns from the reverse cyclic response, flexural cracks at the beam mid-span were observed on the first drift cycle (0.125%). Approaching a drift equal to 1.42%, shear cracks were verified at the beam near the joint, and flexural cracks were observed distributed at the base of the column. At 2% lateral drift, concrete spalling was observed at the base of the columns, which contributed to the deterioration of the frame and an increase in permanent deformation. At the ultimate drift ratio (3%), the cracks were distributed from the base of the column to a height of 1.1 m for both directions of loading, and wider cracks of 7 mm were observed at the column base.

The numerical hysteretic response of the Stainless Steel BRB retrofitted frame was similar to the experimental results reported by Al-Sadoon in 2016; the responses are in agreement with the drift capacity of 3%, the flexural capacity of the beam and columns not being achieved, the longitudinal reinforcement indicating yielding during the last drift cycle, and the concrete spalling that surfaced at 2% drift. Furthermore, the difference in capacity between the numerical and experimental responses corresponded to 8.5%.

7.5.3 Original BRB incorporating Chrome-Molybdenum core retrofitted frame

Figure 7-10 illustrates the hysteretic and pushover responses of the frame retrofitted with a BRB incorporating a Chrome-Molybdenum core. The discrepancy in strength and displacement capacities are significant between the two responses attributed to the high initial stiffness of the frame, which is directly influenced by the bracing core material. The strength and displacement capacities of the frame under reverse cyclic loading was approximately 60% and 28% of the pushover analysis results, respectively. The reduction in capacity in the reverse cyclic results is attributed to the high stiffness of the core material; the core bar attracts most of the imposed deformation, and given the lack of an un-bonding layer, frictional forces are present, which leads to concentration of stresses and strains. Due to the high initial stiffness of the frame, the effects of concentration of strains are observed during early loading stages, which contributed to the capacity softening in the hysteretic response in comparison the pushover response.

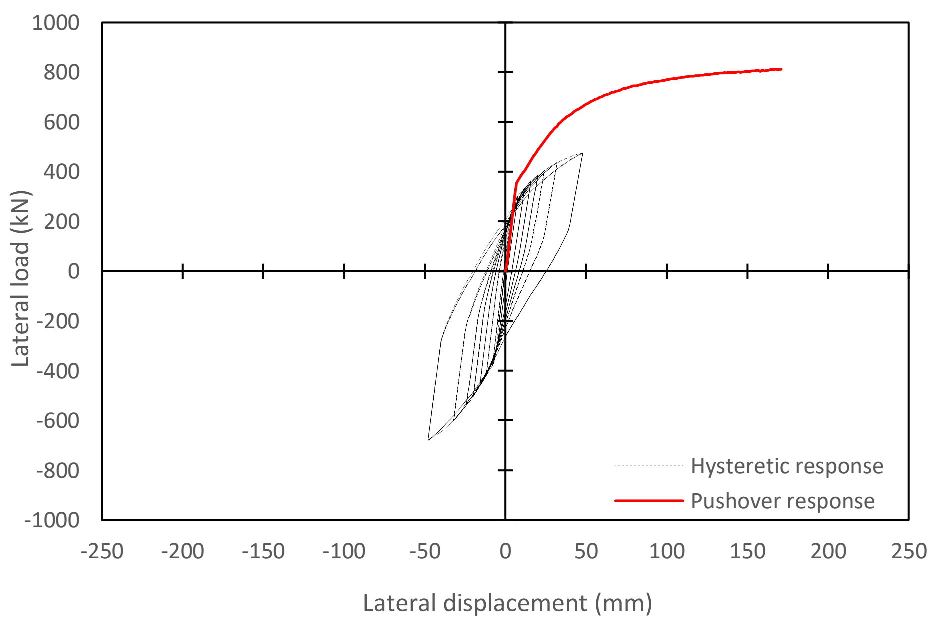

Figure 7-10: Hysteretic and pushover responses of the frame retrofitted with the original BRB incorporating a Chrome-Molybdenum steel core

In the hysteretic response, the frame failed at an imposed lateral displacement of 48 mm due to fracture of the core bar during the third repetition in the positive direction. The fracture occurred in the middle section of the core bar, where the cross-sectional area was reduced to induce yielding. The lateral displacement – strain response of a truss element located at the mid-section of the bracing core was examined and the maximum elongation of 10% was not reached (Figure 7-11). It was concluded, therefore, that during the negative cycles, the strain was concentrated at the mid-section and upon reloading to the positive direction, the core bar fractured at the centre. This phenomenon could be easily addressed by a proper restraining element.

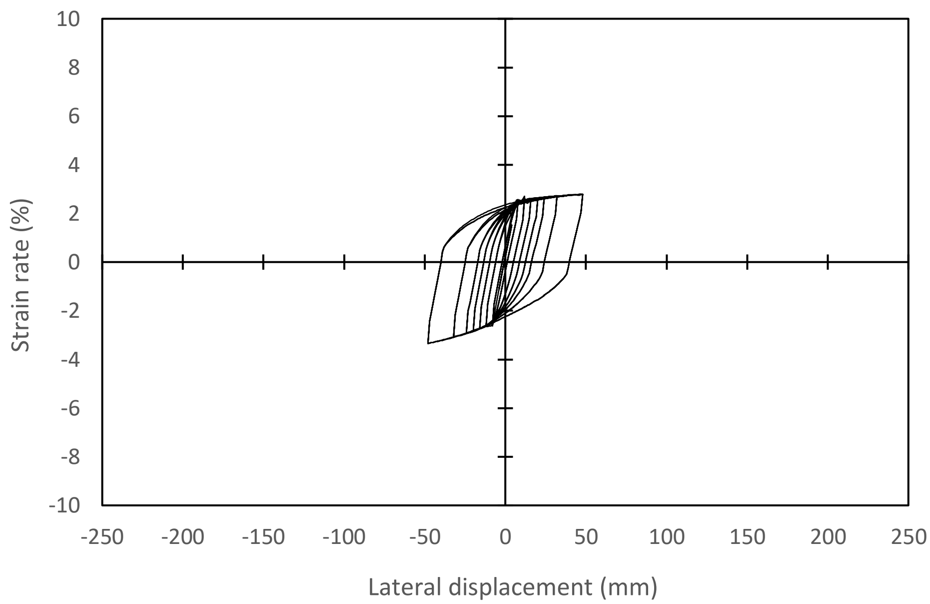

Figure 7-11: Strain-lateral displacement response of the Chrome-Molybdenum core in the BRB retrofitted frame

The frame first yielded at a drift of 0.56%. At this lateral drift, cracks were distributed from the base of the column to a height of 900 mm. At the ultimate lateral displacement, the cracks propagated from the base of the column to a height of 1.1 m. These cracks were concentrated at the column base and near the beam-column joint. In the beam, flexural cracks were observed at the mid-span, while shear cracks were evident near the joint and the brace-frame connection. When comparing the numerical response to the experimental data (2016), the same ultimate drift ratio was achieved, failure occurred during the second repetition in the positive direction, and the experimental strength capacity differed from the numerical response by approximately 5%.

Another important aspect from the numerical response is that it illustrates the transfer of axial load between the restraining element (concrete mortar and hollow section) and the brace end elements. This load bearing allows part of the load to be transferred by the brace casing (hollow section in which the core bar is immersed), and results in an increase in stiffness and lateral strength when the brace is subjected to compression. This behaviour contributes to the asymmetric shape of the hysteretic response. The disadvantage related to load bearing is that it contributes to concentration of stresses and the core bar is not fully utilized in compression, which points to the fact that improvements in this BRB design would improve the overall behaviour.

The BRB design proposed by Al-Sadoon in 2016 is able to eliminate local buckling at the end elements and provide restraining along the length of the core bar. However, the un-bonding layer between the core bar and the restraining supporting element has been proven to be inefficient for three main reasons. First, the hysteretic response does not provide symmetry between the two directions of loading; thus, stresses are concentrated, which diminishes the capacity of the frame with the brace under compression. Although the concrete mortar provides sufficient restraining for the core, the absence of an appropriate un-bonding layer allows frictional forces and axial load transfer to occur. An appropriate layer is a 2 mm-thick silicon rubber sheet. Second, load bearing is present between the brace casing and the connection, which allows the casing to transfer part of the axial loading. This has been demonstrated by an increase in the lateral capacity of the retrofitted frame with the brace under compression loading. Finally, the concrete mortar is a material with considerable specific weight making the brace heavy and difficult to move and allocate when retrofitting a structure. The concrete mortar can be substituted by a steel pipe of significantly reduced thickness (25 mm), which will reduce the weight of the brace while still providing enough stiffness, this will be discussed in Section 7.7.

7.5.4 Modified BRB incorporating Stainless Steel core retrofitted frame

Figure 7-12 illustrates the response of the frame retrofitted with the modified BRB design incorporating a Stainless Steel core, which addresses deficiencies assessed in previous braces. The modifications include improvement in buckling restraining and addition of an un-bonding layer between the core bar and the restraining system (Figure 4-12). By observing the hysteretic response in Figure 7-12, it is evident the frame is able to exhibit higher lateral displacements in comparison to the original BRB, in which the reverse cyclic loading resulted in a maximum drift of 3% and the pushover a drift of 7%. Furthermore, since the concentration of stresses have been reduced by utilizing a silicon rubber sheet, and the buckling restraining improved by removing the gap between the core bar and surrounding pipe, the ultimate drift for the reverse cyclic response is equal to 6%. When evaluating the strength capacity of both responses in Figure 7-12, the pushover analysis yielded a lateral capacity of 698 kN, while the capacity from the hysteretic response was equivalent to 690 kN.

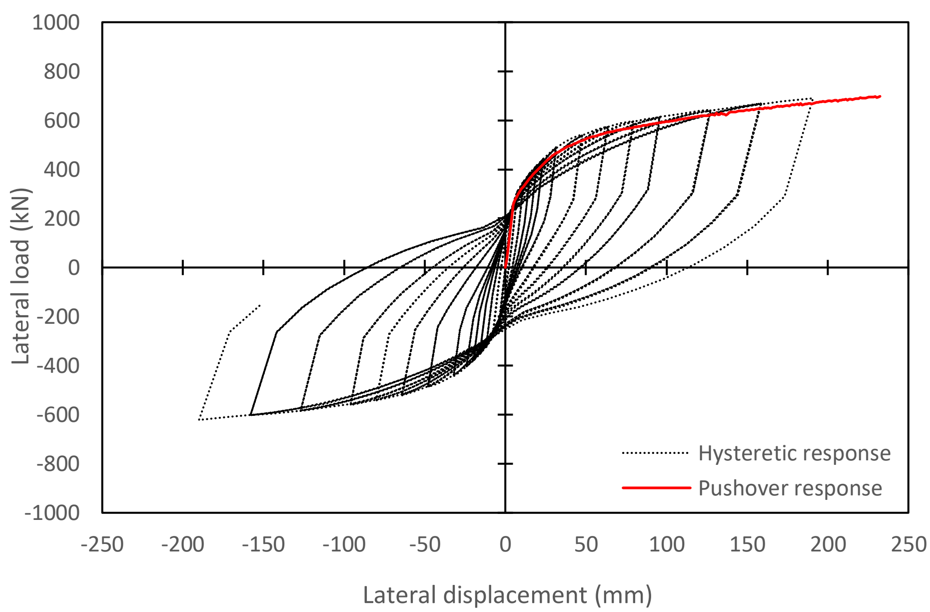

Figure 7-12: Hysteretic and pushover responses of the frame retrofitted with the modified BRB incorporating a Stainless Steel core

The cracking pattern from the reverse cyclic response illustrates cracking initiated at the initial drift of 0.125%. Yielding of the frame first surfaced at a drift of 1.5%, where flexural cracks were distributed up to a height of 1.2 m from the base of the columns. Cracks were also observed in the beam during this drift ratio and were distributed at the mid-span (flexural cracks) and near the joint (shear cracks). At the ultimate drift of 6%, concrete spalling was evident at the base of the columns and near the beam-column joint. At the base of the columns, cracks 14.39 mm wide were observed, while 12.87 mm wide cracks surfaced at the beam-column joints; this considerable opening contributed to concrete spalling. It is important to note that although near the brace-frame connection cracks were distributed, they were not as wide as in other regions and that is attributed to the connection stiffening this region.

Concrete spalling at the column base indicated buckling of the longitudinal reinforcement during the negative cycle at 6% drift. An accumulation of permanent deformation contributed to the deterioration of the frame near the base of the columns, adding to the P-delta effect. The deteriorated capacity of the concrete at the base of column lead to buckling of the longitudinal reinforcement due to an insufficient buckling restraining reinforcement and confinement in the concrete. The system, therefore, failed at the base of the frame during the first repetition in the negative direction to 6% drift.

The frame retrofitted with the modified BRB was able to sustain a positive cycle of 6% and a negative cycle of 5% with lateral strength capacity of 690 kN and 620 kN, respectively. Hence, the modified BRB increased the lateral strength capacity of the system by 15% in comparison to the original BRB. In terms of drift capacity, the increase corresponded to approximately 100% relative to the original BRB retrofitted frame. The failure mechanism of the frame also corroborates the improvement due to the modifications. As there was no concentration of stresses, fracture of the core bar did not happen manifest. The failure mode was controlled by the frame capacity. However, failure is more desirable in the core bar; repair of this device is easier than of the concrete frame. Therefore, either the length or size of Stainless Steel core in the modified BRB can be reduced to ensure the bar reaches its elongation capacity prior to the frame failing.

7.5.5 Modified BRB incorporating Chrome-Molybdenum core retrofitted frame

The pushover and hysteretic responses of the frame retrofitted with the modified BRB with a Chrome-Molybdenum core bar is presented in Figure 7-13. Lateral strength and displacement capacities were similar among the two nonlinear static responses. This illustrates two main characteristics: the length of the bar is ideal for the Chrome-Molybdenum material to be fully utilized, and localized buckling and concentration of stresses were mitigated with the modified BRB. In addition, the absence of concentration of stresses led to a stable and symmetric hysteretic response.

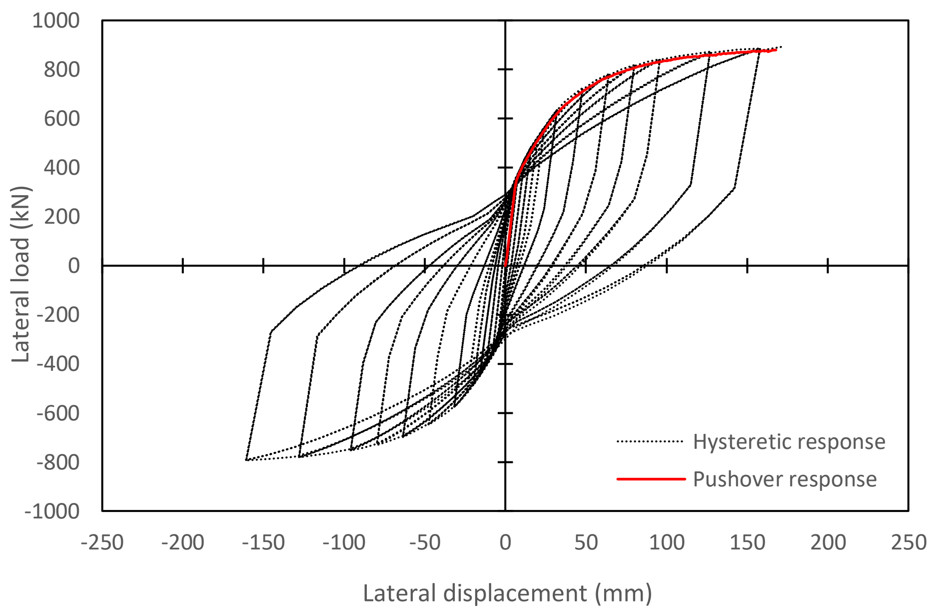

Figure 7-13: Hysteretic and pushover responses of the frame retrofitted with modified BRB incorporating a Chrome-Molybdenum core

The frame failed due to fracture of the bracing core during the first repetition in the positive direction to a drift of 6%. The fracture occurred in the middle of the bar where it reached its maximum elongation capacity, this was assessed by verifying the strains and stresses of the truss elements that modelled the core bar in the numerical model. Subsequent to failure of the core, the longitudinal reinforcement at the bottom of the columns fractured. A 890 kN and 800 kN peak lateral strengths in the positive and negative cycles, respectively, were developed; this is approximately an increase of 75% of the strength capacity when compared to the capacity of the retrofitted frame tested by Al-Sadoon (2016) with a Chrome-Molybdenum core. Furthermore, the frame retrofitted with the modified BRB was able to sustain a lateral displacement of 158 mm, which is 3.29 times more of what the original BRB retrofitted frame experienced.

When evaluating the crack patterns from the hysteretic response, the first crack appeared during the initial stages of loading (0.125% drift). At the yielding drift of 1.5%, both flexural and shear cracks were observed and distributed in the frame, but wider cracks were concentrated near the beam-column joints. At the ultimate drift, wider cracks were established at the base of the column near the brace-frame connection, which could soften the preconceived idea that the connection controls the cracking. Therefore, the brace-frame connection has been verified to control the cracks only when it is connected to the beam. At the base of the columns, concrete spalling was evident and cracks up to 7 mm wide were also observed. Furthermore, it was evident that the residual displacement exceeded the allowable limit according to the NBCC 2015. Significant permanent displacements at this level may also make repair economically unfeasible.

7.5.6 Modified BRB incorporating SE-SMA core retrofitted frame

Figure 7-14 illustrates the response of the frame retrofitted with the modified BRB design incorporating a SE-SMA bracing core under pushover and reverse cyclic analyses. By studying the cyclic response, the modified BRB utilized the full capacity of the core bar. In the hysteretic response, the frame sustained deformations up to a drift of 7% in the positive cycle, and a drift of approximately 6% in the negative cycle. Under pushover loading, the frame sustained a lateral displacement of 250 mm equivalent to a drift of 7.87%. In terms of strength capacity, the pushover analysis predicted a lateral strength of 918 kN, while the reverse cyclic loading resulted in a capacity of 858 kN.

As previously discussed in Chapter 3, the stress-strain relationship of an SE-SMA is characterized by two phases, the pseudo-yielding and the stiffening phases. As the response of the retrofitted frame is significantly influenced by the behaviour of the core bar material, which attracts most of the imposed deformations, the global behaviour of the retrofitted frame follows those two well-defined phases of a shape-memory alloy material. The first phase is characterized as a pseudo-yielding, where the self-centering ability of SMAs are efficiently utilized. In this strain range, the material fully recovers its initial shape. In the hysteretic response, the pseudo-yielding phase initiates at a lateral displacement of 45 mm and finishes at approximately 107 mm. Thereafter, the core bar exhibits the stiffening phase and the deformations imposed on the frame cannot be fully recovered resulting in permanent displacements, but significantly lower in comparison to the bare concrete frame and conventional steel core BRBs. The stiffening phase initiates at the lateral displacement of 107 mm and until failure of the system at 220 mm.

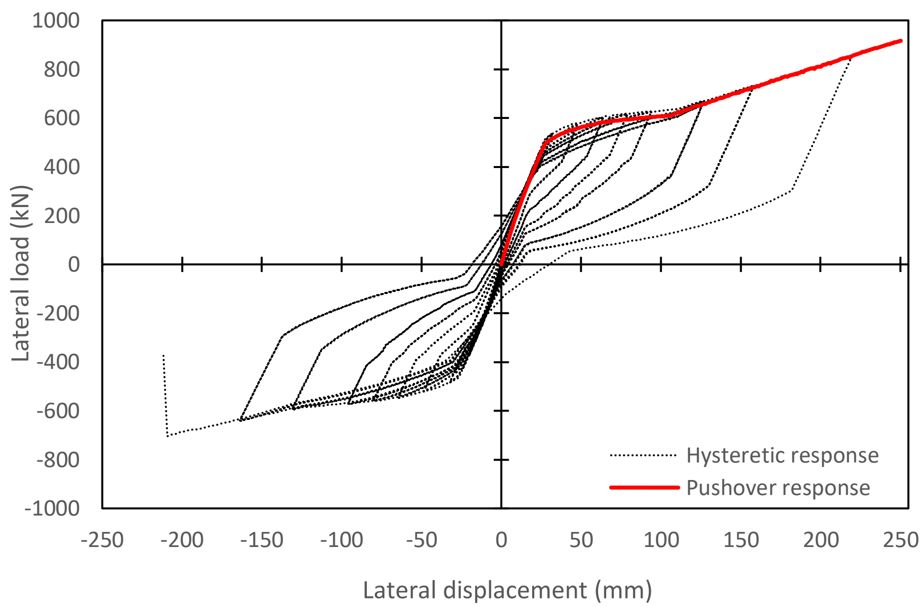

Figure 7-14: Hysteretic and pushover responses of the frame retrofitted with modified BRB incorporating a SE-SMA core bar

When utilizing the modified BRB with the self-centering material as the core, the frame failed when the ultimate elongation of the SE-SMA bar was reached under compression. This was corroborated by the strain response of the core bar in Figure 7-15. The maximum elongation of the SE-SMA core bar was defined as 20% as per Yin et al. (2015) and this strain level was attained at a lateral displacement of 207 mm. In the SE-SMA bracing core, the pseudo-yielding phase initiated at a lateral displacement of 28 mm and ended at

110 mm, which is similar to what was observed in the global behaviour of the structure. Therefore, at a drift cycle of 4% (127 mm), permanent displacement started to be accumulate.

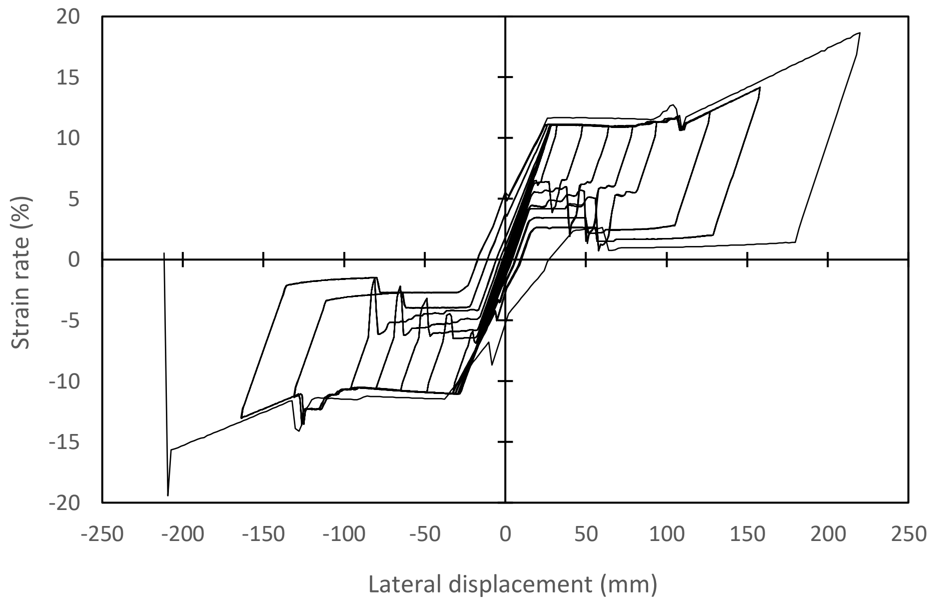

Figure 7-15: SMA strain-lateral displacement response of the frame retrofitted with modified BRB incorporating a SE-SMA core bar

The retrofitted frame failed when the strain capacity of the core bar was achieved under compression. After the core failed, buckling of the longitudinal reinforcement at the base of the left column was observed. The cracking was significantly reduced in comparison to conventional steel core BRBs due to the self-centering ability of the SE-SMA. Thus, it was evident the SE-SMA BRB does improve the recentring of the system once the imposed load is retrieved. Regarding the cracking pattern, the cracks first developed at the initial stages (drift of 0.125%). The cracks surfaced at the base of the columns and near the brace-frame connection. During the last positive cycle, the cracks were limited to a width of 3 mm. At load zero, the SE-SMA was successful at controlling the crack width when re-centering the frame, which resulted in cracks with a maximum residual opening of 0.1 mm.

7.5.7 Energy dissipation

Energy is dissipated when concrete structures move from the elastic to plastic response. In this thesis, the dissipated energy was approximated from the area within the closed loop for each drift cycle. As three repetitions were imposed at each drift cycle, the energy dissipated in the first repetition was solely considered to compare the frames. Figure 7-16 illustrates the strain energy as a function of the lateral drift from the numerical models of the frames previously tested by Al-Sadoon (2016) - the bare concrete frame and the retrofitted frames incorporating either a Chrome-Molybdenum or Stainless Steel core. From the numerical analysis, the retrofitted frames were able to dissipate more energy than the bare concrete frame. The retrofitted frame incorporating a Chrome-Molybdenum core dissipated 38 116 kN.mm of energy at the lateral drift of 1.5%, which represents an increase of 5.4 relative to the bare concrete frame (7109 kN.mm) at the same drift. Furthermore, the Stainless Steel core BRB retrofitted frame dissipated approximately 3.8 times more energy than the BCF at a drift ratio of 3%.

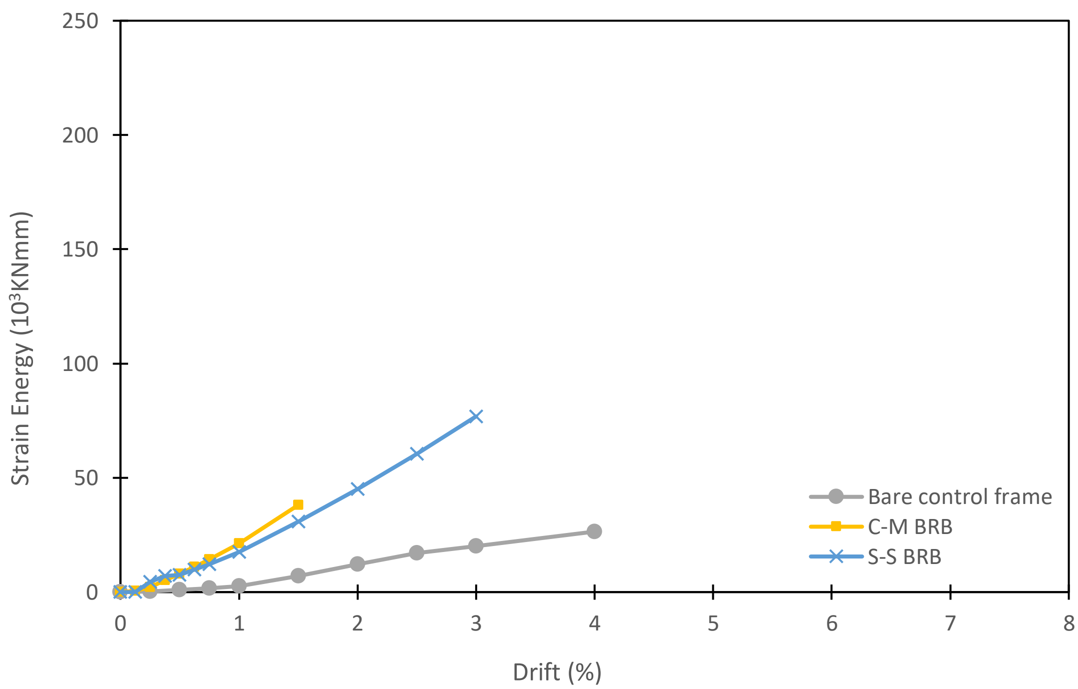

Figure 7-16: Energy dissipation-lateral drift responses from the numerical models of the frames previously tested by Al-Sadoon (2016)

The difference in energy dissipated by the frames retrofitted with conventional and modified BRB (Figure 7-17) was not notable for similar drift levels. At a drift of 1.5%, for the two BRBs that incorporate a Chrome-Molybdenum core, the energy dissipated by system with the modified BRB was 26% higher than what was dissipated by the conventional BRB. In the system incorporating the Stainless Steel core for a drift of 3%, the system with the modified BRB dissipated an additional 8967 kN.mm of energy relative to the conventional BRB retrofitted frame. However, it should be noted that as the systems retrofitted with the modified BRB sustained larger deformations, their cumulative dissipated energy is significantly higher in comparison to the frames retrofitted with conventional BRBs.

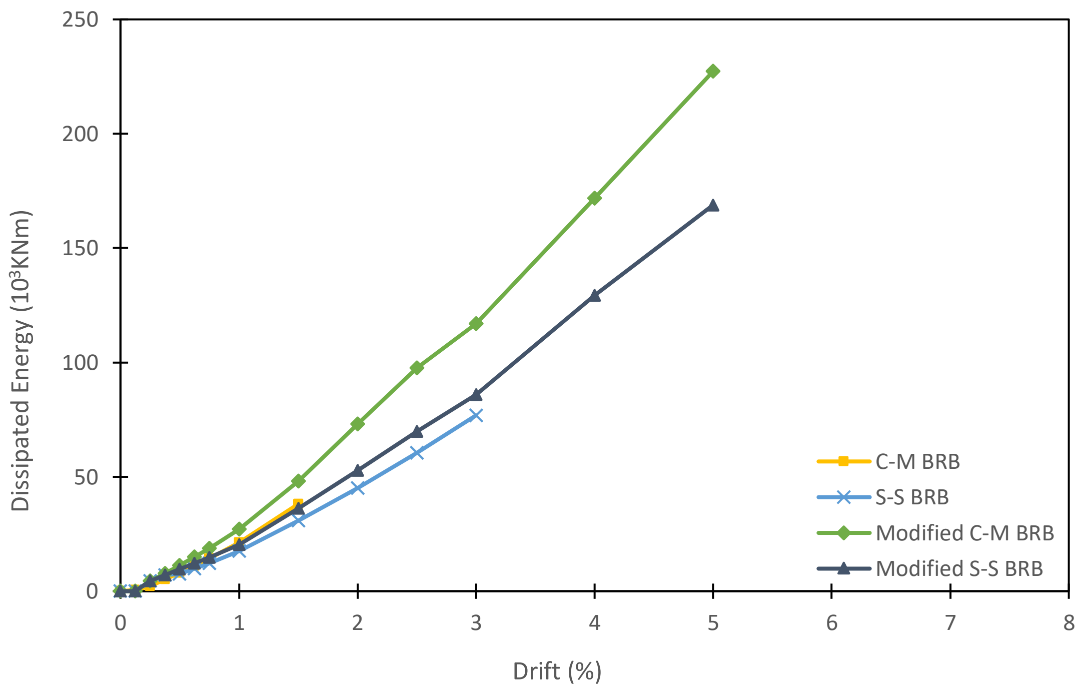

Figure 7-17: Comparison of the energy dissipated between the frames retrofitted with original and modified BRB incorporating different conventional steel cores

The proposed retrofit from this research includes the modified BRB incorporating a SE-SMA core bar. When comparing the energy dissipated by this system with the BCF, the retrofitted system dissipates approximately three times more energy than the bare frame at a drift of 4%. However, when evaluating the ability of dissipating energy in comparison to the other retrofitted frames, the SE-SMA retrofitted system dissipates less energy any given drift. The advantage of utilizing the SE-SMA retrofit is that it sustained larger lateral displacements, and its cumulative dissipated energy was greater than what was experienced by the control frame. The other main advantage is related to the shape-memory effect of SMAs, which controls damage and reduces permanent deformations of the structure. Solely from the fact the SE-SMA retrofitted frame dissipated more energy than the BCF, demonstrates improved seismic performance over the control frame.

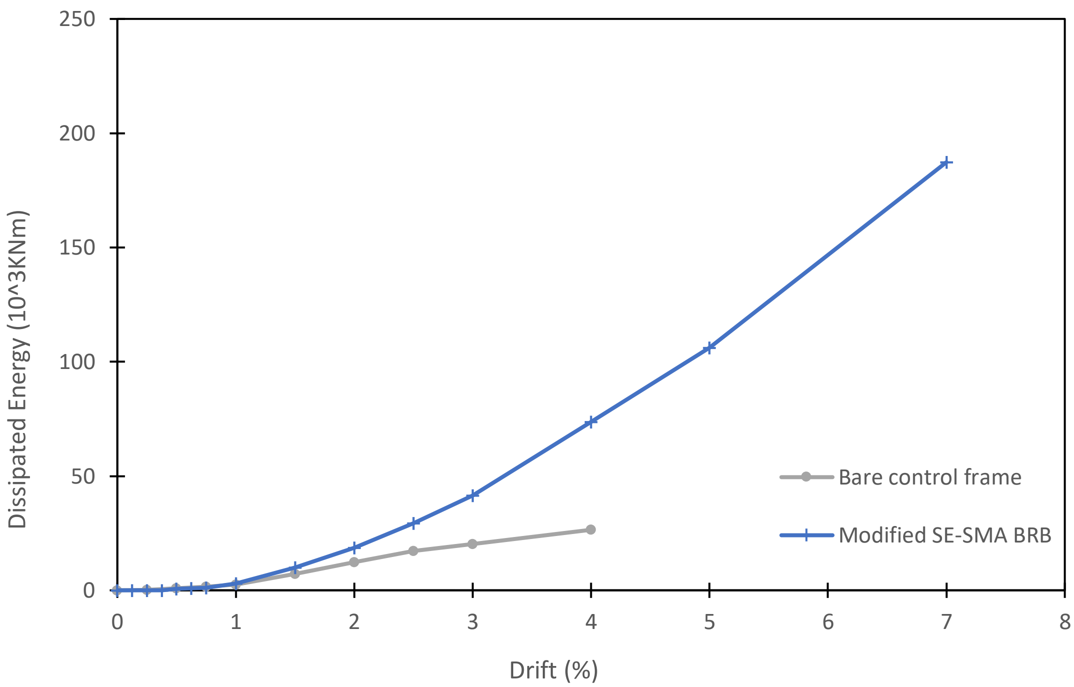

Figure 7-18: Energy dissipated by the bare concrete frame and SE-SMA modified BRB retrofitted frame

7.5.8 Residual displacements

Residual deformation is a measure of damage in structures. The damage can be experienced by the main or secondary structural elements. As per Table 7-1, the permanent drift can be directly related to damage in the structural elements. For example, the residual drift limit for the life safety performance level (3-C) corresponds to 1%, which is approximately 31.75 mm for the frames in this study. At this performance level, extensive repair is required before re-occupancy of the building. For the immediate occupancy performance level (1-B), the structure must limit its transient storey drift to 1.5% to limit permanent drifts to a maximum of 0.5%. Figures 7-19 and 7-20 illustrate the residual drift for the frames. Figure 7-19 specifically provides the permanent displacement accumulated during the positive cycles; while Figure 7-20 illustrates the residual displacement in the negative cycle, in which both the transient drifts and permanent displacements are presented in the negative quadrant to differentiate from the positive direction of loading. The accumulation of displacements between the two directions of loading are similar. Therefore, the discussions to follow are based on the residual displacements from the positive cycles.

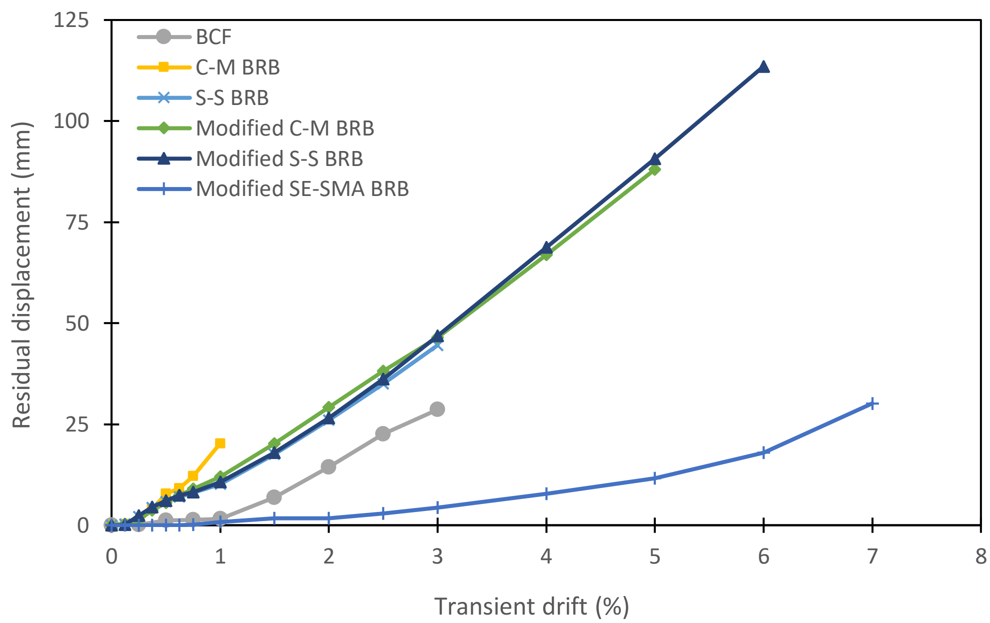

Figure 7-19: Residual displacement-transient drift response during positive cycles

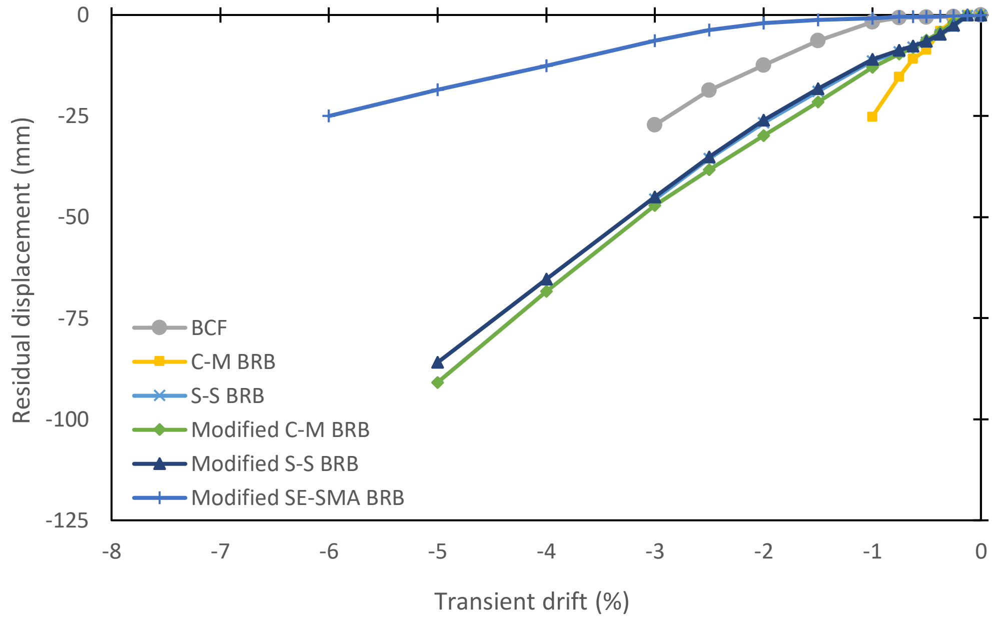

Figure 7-20: Residual displacement-transient drift response during negative cycles

Figure 7-21 illustrates the residual displacement of the control frame against the frames retrofitted with the original BRB with Chrome-Molybdenum or Stainless Steel core. The retrofitted frames exhibit higher residual displacements than the bare concrete frame. At a transient drift of 1%, the Chrome-Molybdenum retrofitted frame accumulated approximately 13 times more residual displacement than the control frame, while the Stainless Steel retrofitted frame accumulated 6.7 more damage than the BCF. At 3% transient drift, when utilizing a Stainless Steel BRB, the structural system accumulated 55% more damage than the control frame. By assuming a life safety performance level, the S-S BRB accumulated approximately 39% more damage than what is prescribed by seismic provisions.

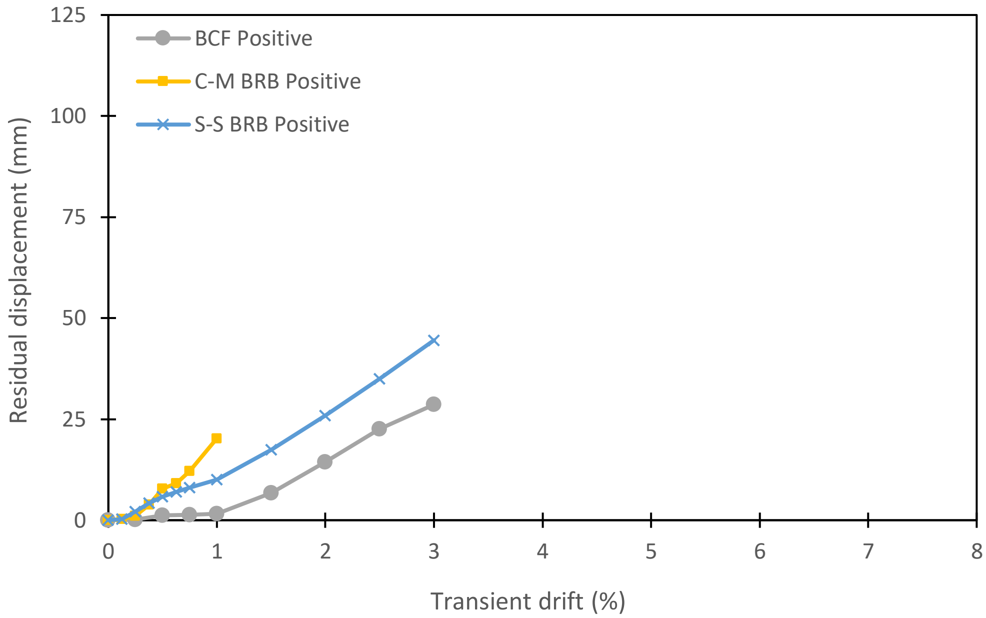

Figure 7-21: Residual displacement of the bare concrete frame and retrofitted frames incorporating a C-M or S-S core bar

The residual displacement of the frames retrofitted with the modified BRB (Figure 7-22) accumulated the same level of permanent displacements as the BRB proposed by Al-Sadoon (2016). However, as the frames with the modified BRB sustained larger lateral displacements, the accumulated damage increased significantly at the last transient drift for the BRBs incorporating conventional steel cores. At a drift of 3%, the control frame accumulated a residual displacement of 28.6 mm, while the frame retrofitted with the modified BRB with C-M, S-S, and SE-SMA core accumulated, 46.8 mm, 44.5 mm, and 4.34 mm, respectively. That indicates that the conventional steel core bars experienced an increase in the permanent displacement of the frame, which can be translated as extensive structural damage and costly repair. Conversely, the frame retrofitted with the modified BRB and a SE-SMA core bar accumulated only 15% of what was accumulated by the control frame.

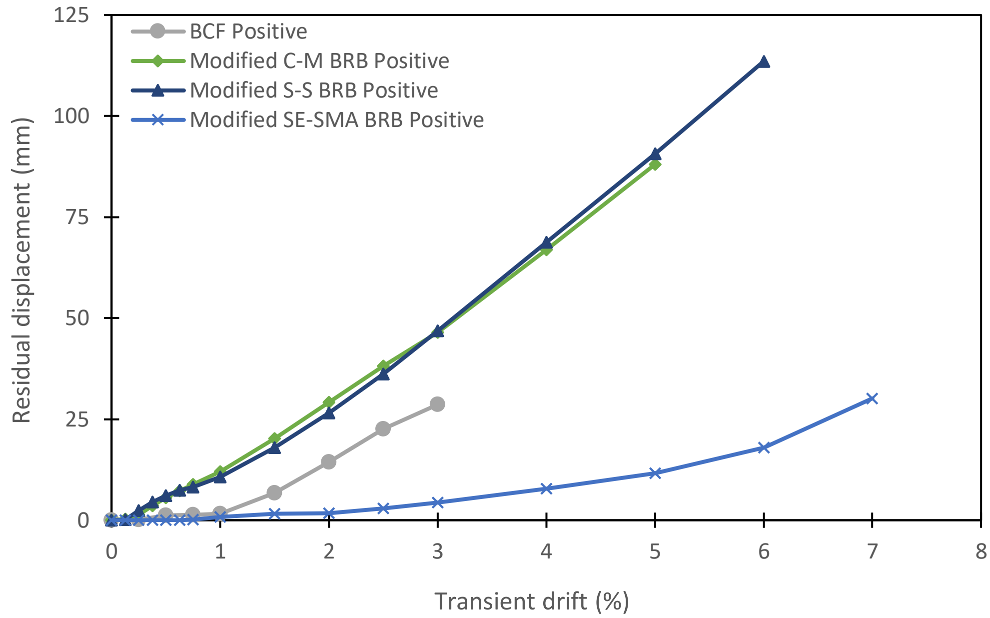

Figure 7-22: Residual displacement of the frames retrofitted with the modified BRB

At a transient drift of 5%, the modified BRB retrofitted frames with the S-S steel core accumulated approximately 90 mm of residual displacement, while the SE-SMA retrofitted frame accumulated 11.6 mm. Furthermore, at the ultimate drift of the SE-SMA BRB, the residual drift is 0.95%, which is lower than the limits imposed by the NBCC 2015 and the life-safety seismic performance level from NRC (2015) and FEMA (2012).

Figure 7-23 depicts a comparison between the bare concrete frame and the frame retrofitted with the modified BRB incorporating a SE-SMA core. Although the retrofitted frame experiences two times the lateral displacement capacity of the BCF, the residual displacement at the last drift cycle (7%) is 57% of the residual displacement of the BCF at 4% drift. Therefore, the modified BRB with SE-SMA core proposed by this research can increase the strength capacity, sustain large deformations, and guarantee structural resilience by controlling damage.

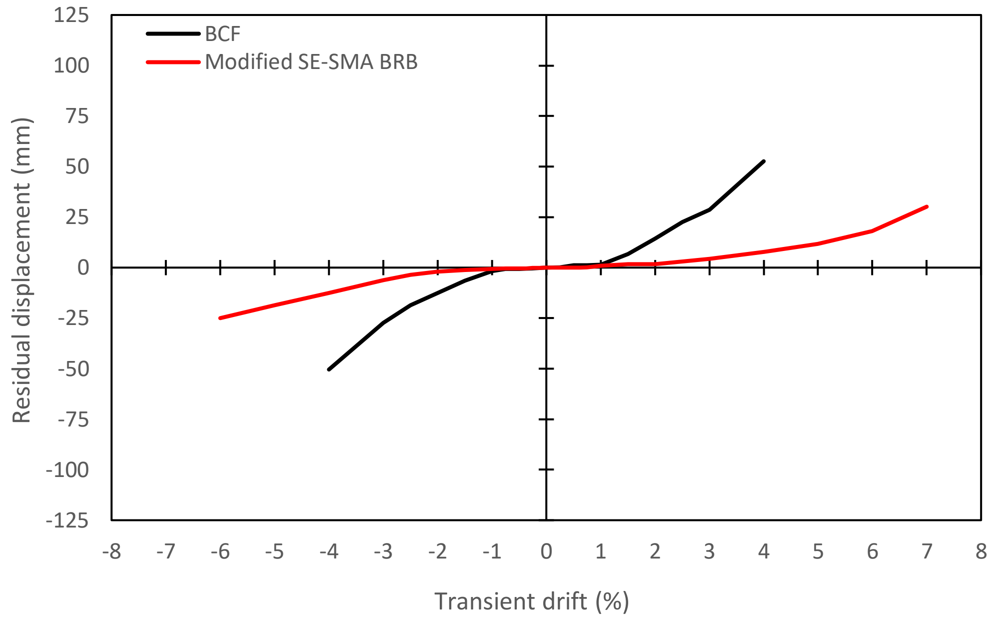

Figure 7-23: Residual displacement- transient drift response of the bare concrete and SE-SMA modifed BRB retrofitted frames

7.6 Assessment of time-history responses

In this section, the performance of the frame retrofitted with the modified BRB incorporating an SE-SMA core is assessed against the response of the control bare concrete frame under the same eleven earthquake records for both locations (Montreal and Vancouver). The discussion focuses on transient and permanent drifts, and the seismic demands imposed by the earthquake records, which were previously presented in Section 6.6. To conclude, the response of the two frames to the amplified earthquake record will be assessed and discussed.

For the building located in Montreal, the ground motion records representative of the M-R Scenario 2 induced the highest displacement demands for the bare concrete frame, while the displacement demands for the retrofitted frame from Scenario 1 were approximately 47% higher than what was imposed by Scenario 2. Although the fundamental period of the bare concrete frame was evaluated as 0.17 s by the NBCC 2015 (NRC, 2015) and 0.36 s by an eigenvalue analysis of the frame in VecTor2 (Vecchio et al., 2013), the response of the frame was highly influenced by Scenario 2 in which the period ranges from 1.0 s to 1.5 s. For the bare concrete frame in Vancouver, Scenario 2 induced the highest displacements in the structure, while for the retrofitted frame, Scenario 1 induced slightly higher displacements relative to Scenario 2.

For the frame located in Montreal, the seismic demands anticipated by the NBCC 2015 (NRC, 2015) did not match the seismic response, so the frame was not pushed to its capacity. The mean top transient displacement of the eleven earthquake records for the bare concrete frame was 27.39 mm, which is 24% below the yielding displacement defined from nonlinear static analysis. This indicates that the selected ground motion records for Eastern Canada induced demands on the frame lower than expected. Furthermore, this could also be an indication of an inappropriate approximation of the applied lumped masses.

Significant differences arose in assessing the displacement experienced by the frames retrofitted with the BRB relative to the control frame. Due to the increased stiffness of retrofitted frames as a result of the buckling-restrained brace, the effects of the ground motion records were negligible. The mean transient displacement of the bare concrete frame located in Montreal for the eleven ground motion records was 27.39 mm. This falls below the yielding displacement for the frame evaluated in the static analysis. From the period range of the first M-R scenario in Montreal, the earthquake record corresponding to TR1-6 induced the largest transient displacement corresponding to 78.291 mm, which exceeded the yielding point causing the frame to experience inelastic deformations. This is corroborated by ratcheting and accumulation of damage in the structure in the form of a permanent displacement of 5.347 mm. In the Scenario 2 for the city of Montreal, the control frame experienced a maximum transient displacement of 113.8 mm, which exceeded both the yielding and ultimate displacements. The frame experienced ratcheting, and damage accumulated in one direction. As a result, a maximum permanent top displacement of 5.257 mm was observed.

The BRB retrofitted frame under the same earthquake records as the bare control frame for the city of Montreal and with the same lumped masses experienced a mean top transient displacement of 0.38 mm. This displacement is insignificant and less than the capacity of the retrofitted frame. The pseudo-yielding plateau of the BRB retrofitted frame incorporating a SE-SMA core was not reached. This negligible displacement level induced by the earthquake records is attributed to the lateral stiffness added by the brace to the system. In addition, it is probable that the lumped masses also were not sufficient to induce larger demands on the retrofitted frame. The maximum transient displacement experienced by the retrofitted frame in the first M-R scenario was 0.983 mm, while for the second M-R scenario it corresponded to 0.620 mm. A constant permanent displacement of 0.003 mm was observed in this frame, which does not pose any risk to the structural integrity of the structural and non-structural elements.

The transient displacement induced to the bare concrete frame by the ground motion records that simulate the seismic hazard of Vancouver was higher than Montreal. The mean transient displacement was 82.774 mm, which is above the yielding point where the frame experiences inelastic displacements and potential ratcheting. The frame exceeded the yielding point in all eleven ground motion records and exceeded the ultimate displacement for three records. For the first M-R scenario, the maximum transient displacement was 95.52 mm (drift of 3.01%), where the frame experienced ratcheting, and a residual displacement of 6.05 mm was observed at the end of the earthquake record. As provided in Table 7-1, for a transient drift above 2.5%, the structure falls under the structural stability performance level, where extensive structural damage is observed, but the principal load carrying elements are able to transfer the load to the foundation avoiding building collapse. In terms of residual storey drift, the frame meets the operational performance level, which is limited by 0.2% residual drift.

For the second M-R scenario, one of the ground motions induced transient displacements up to 144.75 mm to the control frame, which is equivalent to a drift of 4.56%. This displacement exceeds the maximum displacement the frame can sustain according to the static analysis. The frame experienced ratcheting, and the damage accumulated in one direction, which is corroborated by the presence of a residual displacement at the end of the analysis corresponding to 19.55 mm (drift of 0.61%). The transient drift demonstrates that the frame performed beyond the structural stability level and risk of partial or total collapse of the structure being imminent. The permanent drift, in addition, illustrates the frame performed within the life safety performance level of not exceeding 1% drift.

The third M-R scenario for the city of Vancouver induced a transient displacement of 134.72 mm (drift of 4.24%) to the BCF, and a permanent displacement of 22.4 mm was observed equating to a 0.7% drift. The peak drift is higher than the displacement capacity of the frame. Therefore, regarding transient drift, the frame is performed beyond the structural stability level, while it performed within the life safety performance level when evaluating the permanent drift. By observing the crack patterns of the frame located in Vancouver, both flexural and shear cracks were observed in all eleven earthquake records. Flexural cracks were noted at the beam mid-span and at the base of the columns, while shear cracks were verified adjacent to the beam-column joints given that the joint was poorly transversely reinforced.

Independent of the M-R scenarios simulating the Vancouver seismic hazard, the retrofitted frame performed within the operational performance level. The mean transient displacement experienced by the retrofitted frame was 0.85 mm corresponding to a drift of 0.026%, while the mean permanent displacement corresponded to 0.003 mm. When comparing the performance of the retrofitted frame against the control frame, the improvement is evident. The stiffness added by the brace diminished both the transient and permanent drifts improving the seismic performance of the frame. Figure 7-24 illustrates the improvement in seismic performance by retrofitting the frame with the modified BRB; it is evident that the transient and residual drifts of the retrofitted frame are negligible. The advantages of utilizing the SE-SMA core in place of steel core is better evaluated under higher seismic loads. Therefore, the frames were also subjected to amplified ground motions to evaluate the response of the BRB retrofitted frame incorporating an SE-SMA core. The earthquake record TR2-2 for the Vancouver location was selected as it induced the highest transient displacements on the control frame.

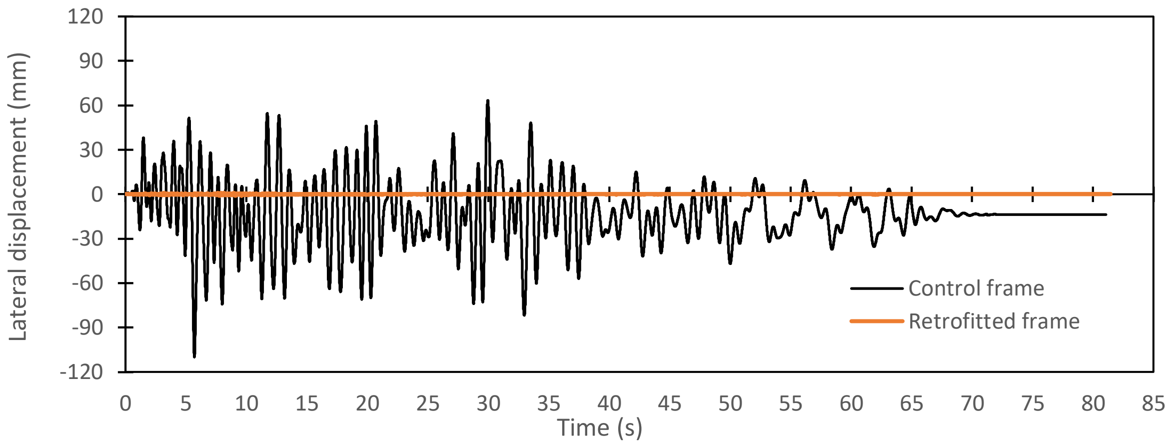

Figure 7-24: Lateral displacement-time-history of the bare concrete frame and retrofitted frame under the earthquake record TR2-2

The earthquake records increased by 100%, 300% and 500% were applied to both the bare concrete and retrofitted frames to investigate the advantages of utilizing a self-centering material during dynamic loading. Figure 7-25 illustrates the response of both frames under the earthquake record amplified by 100%, where the red lines define the ultimate displacement for the control frame evaluated from the nonlinear static analysis. The small displacements experienced by the retrofitted frame can be attributed to its large stiffness. When evaluating the response of the bare concrete frame, ratcheting is evident, and an accumulation of damage is clear. The residual displacement recorded for the control frame at the end of the earthquake record corresponded to 26.534 mm (drift of 0.84 %), which falls into the life safety performance level. However, as the transient drift is above 2.5%, the frame falls within the severe risk of collapse. Regarding the BRB retrofitted frame, the maximum transient displacement was approximately 2.5 mm, which does not induce yielding nor inelastic displacements in the structure.

An assessment of the crack patterns suggests concrete spalling in the control frame, which contributed to deterioration of the structure and degradation of its lateral strength. For the retrofitted frame, small cracks were evident, due to shear, in the column and near the beam-column joint. The control frame failed due to structural deterioration after concrete spalling was observed. After the peak displacement was experienced, the maximum lateral capacity of the frame was achieved and the longitudinal steel reinforcement at the base of the column fractured; thus, the capacity of the frame decreased more than 20% in the succeeding imposed displacements. The retrofitted frame, however, did not fail during the earthquake record.

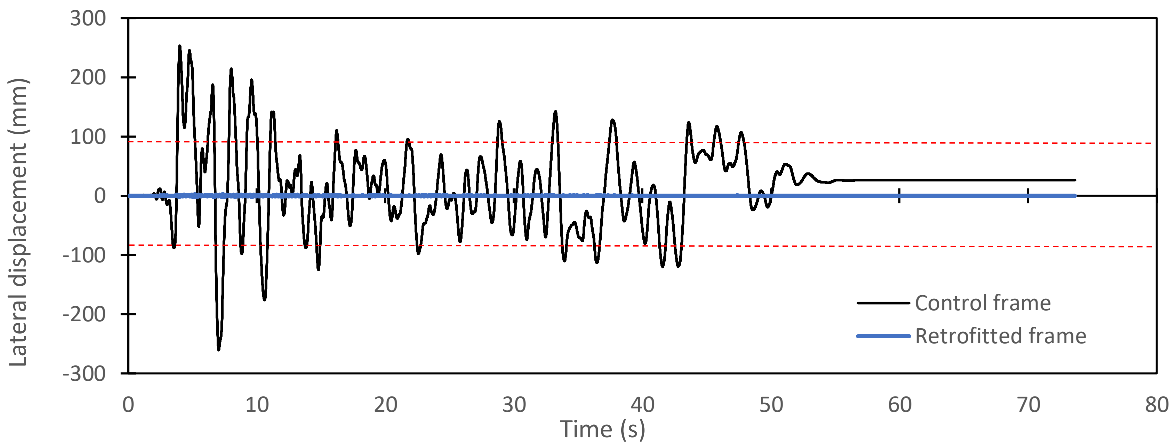

Figure7-25: Displacement-time history of the bare and retrofitted frames under a 100% amplified earthquake record TR2-2

Subjected to the 300% amplified earthquake record, the bare concrete frame experienced displacements beyond its maximum capacity resulting in significant structural deterioration, concrete spalling, and fracture of the steel reinforcement at the base of the columns and near the beam-column joint. The structural degradation can be observed from the lateral load-lateral displacement response provided in Figure 7-26, where the lateral strength capacity evaluated from the static analysis is indicated by the red lines. Beyond it's the point that the strength capacity is achieved in the response, the frames deteriorates, and the lateral strength falls below 20% of its peak strength for the remaining cycles of induced displacements, which is an indication of degradation. Severe concrete spalling was observed at the end of the analysis in the beam-column joint, and cracks 6 mm wide were verified in the columns.

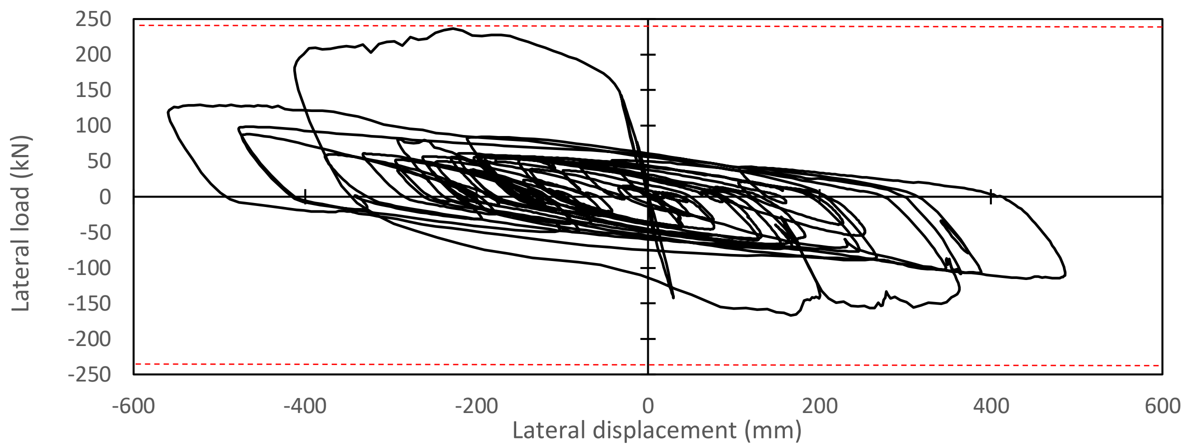

Figure 7-26: Lateral load-lateral displacement response of the bare concrete frame under the earthquake record TR2-2 amplified by 300%

The displacement-time history response of the retrofitted and control frames (Figure 7-27) illustrates the increase in seismic performance by adding the brace, but the advantages of the SE-SMA have not been fully utilized. Furthermore, Figure 7-28 illustrates the displacement-time history response of the control frame under a 100% and 300% amplified earthquake record TR2-2, where it is evident the amplification of the earthquake record has a direct impact on the induced transient displacements. In addition, the frame under the 300% amplified ground motion exceeded the maximum displacement in 1236 of the record data points, which is equivalent to 16% of the total ground motion record, while the frame subjected to the 100% increased earthquake only exceeded the maximum displacement for 628 of the record data points equivalent to 8.53% of the earthquake record.

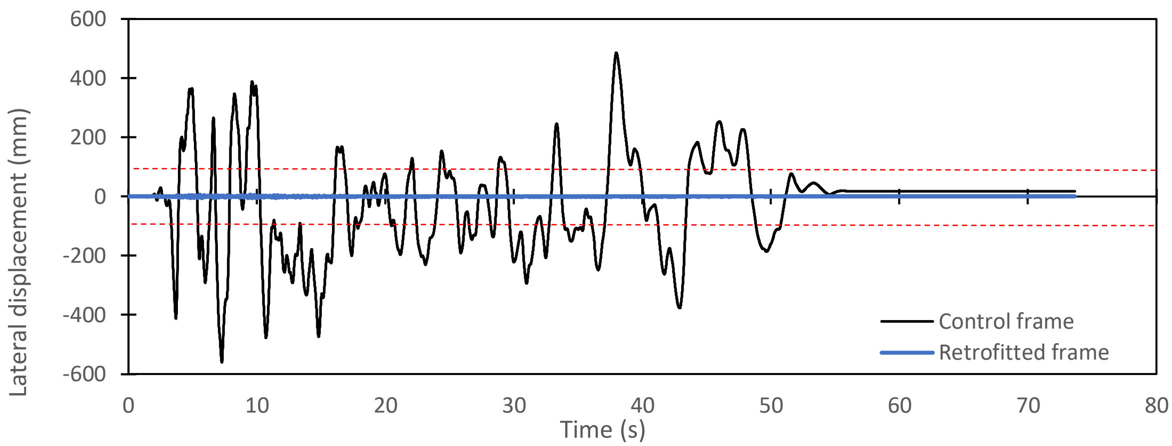

Figure 7-27: Displacement-time history responses of the bare concrete and retrofitted frame under the 300% amplified earthquake record TR2-2

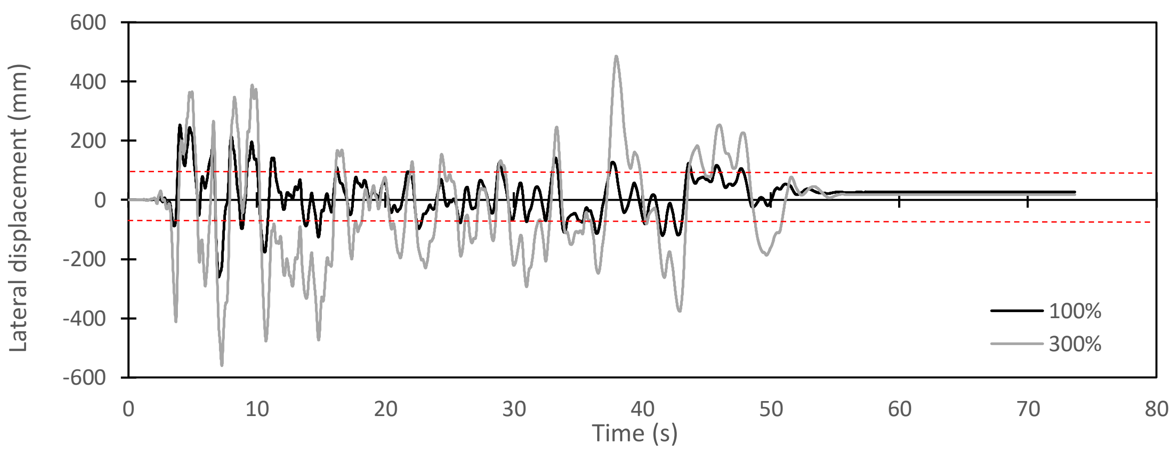

Figure 7-28: Displacement-time history responses of the bare concrete frame for the 100% and 300% amplified earthquake record TR2-2

The frames were further subjected to the TR2-2 ground motion amplified by 500%. Under this earthquake record, the control frame failed 4.46 s after the ground motion was applies (Figure 7-29). In contrast, the retrofitted frame did not reach its pseudo-yielding as depicted in Figure 7-29. Following fracture of main longitudinal steel, the bare concrete frame offered no resistance to the lateral displacements induced by the amplified earthquake record. This is verified in Figure 7-30 that illustrates the lateral load-time history response of the bare concrete frame, where beyond the lateral capacity was attained, the frame experienced degradation of its strength capacity by more than 20%, an indication of failure. Furthermore, the longitudinal reinforcement of the beam that extended through the beam-column joint also fractured as the concrete in that region deteriorated.

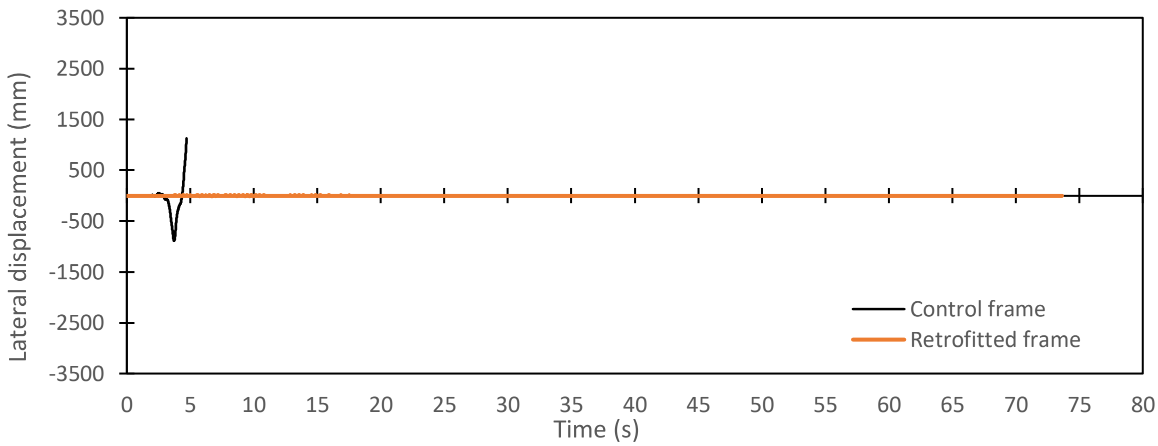

Figure 7-29: Displacement-time history responses of the bare concrete and retrofitted frames subjected to the earthquake record TR2-2 amplified by 500%

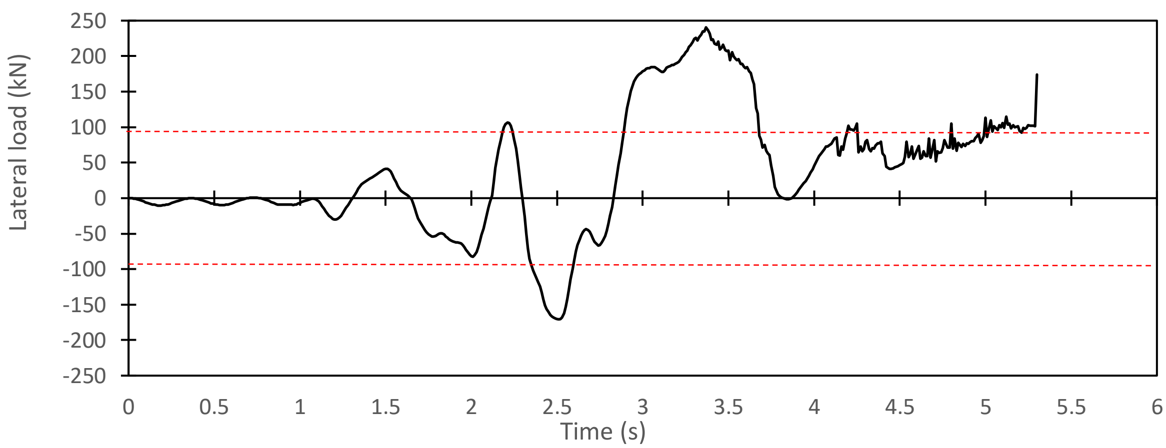

Figure 7-30: Lateral strength-time history response of the control frame subjected to the 500% amplified earthquake record TR2-2

The hysteretic response of the bare and retrofitted frames (Figure 7-31) point to the marked improvement in the seismic performance with the implementing of the BRB; the retrofitted system does not fail, nor is there accumulation of residual damage. In addition, the strength capacity of the retrofitted system is approximately 4 times the capacity of the control frame.

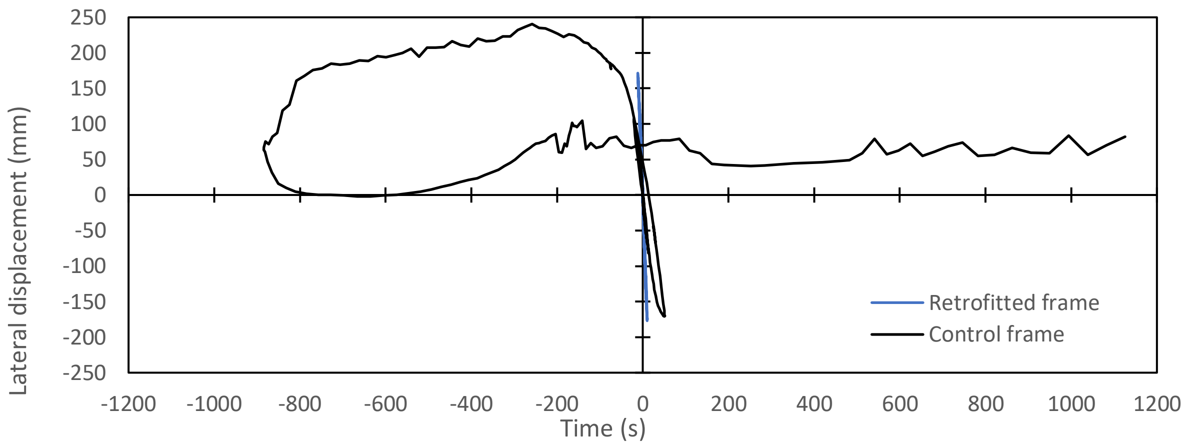

Figure 7-31: Hysteretic responses of the control and retrofitted frames subjected to a 500% increased TR2-2 earthquake record

The results of the retrofitted frames subjected to the same earthquake recorded as the bare concrete frame illustrate that the demands imposed on the BRB strengthened frames were negligible. This is attributed to the significantly increased strength and stiffness. This suggests that the retrofitting system has excess capacity and can be redesigned to be more efficient. This would involve parametric studies on the length and size of the core bar. Furthermore, the main advantages of the SE-SMA core bar would be better utilized with a redesign of its length and size.

7.7 Further improvements to the BRB

The only drawback of the modified BRB design is the size of the brace. The restraining supporting system is composed of a 34 mm inner diameter pipe with 7 mm thickness and a hollow section with 168 mm inner diameter and 8 mm thickness; the void between the two pipes is filled with a concrete mortar. Thus, the restraining system is heavy, which increases the structural weight. Furthermore, the concrete mortar must be cast on site to avoid heavy lifting off site and minimize transportation related costs; hence, quality control might be affected, and the process of retrofitting becomes time consuming.

To accommodate these challenges regarding the weight of the brace, a new design is herein recommended and presented in Figure 7-32. The system is composed of a 31.8 mm-diameter SE-SMA core bar surrounded by a 2 mm-thick silicon rubber sheet restrained by a steel pipe of inner diameter of 34 mm and thickness of 25 mm. The proposed system possesses the same transverse stiffness and the same un-bonding layer as the previous proposed system, which aims to restrain buckling and mitigation of concentration of stresses.

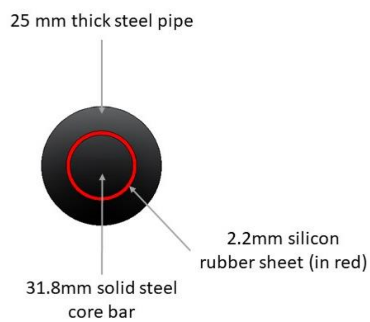

Figure 7-32: Cross-sectional view and details of the BRB system recommended for future investigation

Chapter 8

Conclusions and recommendations

8.1 Summary

Over the last two decades, advancements in seismological knowledge lead to the significant changes in seismic provisions. For medium-rise buildings, for example, the seismic force demand has doubled in magnitude since the 1965 NBCC (NRC, 1965). Prior to the enactment of modern seismic provisions, buildings were built to resist gravity and wind loads only. In Canada, structures built according to pre-1970s building codes present a significant seismic risk, which is a relation of the seismic hazard of the site and the structural vulnerability of the construction.

Reinforced concrete structures designed based on the 1965 NBCC (NRC, 1965) are highly susceptible to damage when subjected to design ground excitations. During that era, the dominant RC structural system is characterized by non-ductile or limited ductility moment-resisting frames. These structures pose a threat under seismic events since they were designed based on the strong beam – weak column concept, which underestimates the required transverse reinforcement resulting in poorly spaced and anchored stirrups and ties. Thus, beam-column joints and the base of the columns are highly susceptible to damage under a seismic event; these structural elements are vulnerable to shear failure that may lead to a reduction in axial load resistance of the columns and, subsequently, increasing the collapse potential.

When evaluating possible retrofit techniques for this type of structural system, steel bracing is a viable alternative that has been proven to enhance the seismic performance of reinforced concrete moment-resisting frames by improving lateral strength and stiffness. However, conventional diagonal steel braces behave poorly under compression due to buckling. BRBs are a specific form of steel bracing that provides an improvement in the compressive capacity of the brace by restraining the effects of buckling. However, it should be highlighted that conventional steel core BRBs increase permanent deformation in the system owing to the yielding of the steel core. Furthermore, BRBs often fail due to localized buckling of the core or due to concentration of stresses within the brace, which reduces the displacement ductility of the frame and increases uncertainty in the capacity. This uncertainty complicates the efficiency in predicting the behavior of BRB retrofitted systems as analytical and numerical approaches are based on the full capacity of the bracing core bar.

The objective of this research, therefore, was to develop a finite element model of a seismically deficient reinforced concrete frame designed in accordance with the 1965 NBCC, evaluate the seismic response improvement of this prototype frame due to retrofitting with a BRB design from the literature, assess deficiencies of steel core BRBs in terms of residual deformation and reduction in displacement ductility, propose modifications to the original BRB design to increase the buckling restraining, and assess the implementation of a self-centering material (superelastic shape memory alloys (SE-SMA)) as the bracing core bar. Therefore, the main objective of this research is to retrofit seismically deficient frame structures to meet current design code requirements based on seismic demands without inducing an increase in permanent deformations nor a decrease in ductility relative to that experienced by the bare concrete frame.

The effectiveness of several BRB designs was first evaluated to investigate the BRB components and functions. Local and global retrofitting were evaluated separately to ensure the BRB system did not transfer moment between the frame and the brace, and to address connection challenges. Then, a study in the implementation of self-centering materials in retrofitted system was conducted and relevant properties of SE-SMAs were highlighted. The prototype frame was scaled from a 6-storey reinforced concrete moment-resisting frame structure designed in accordance with the 1965 NBCC. The building was taken from the Concrete Design Handbook (Cement Association of Canada, 2006). This prototype frame was selected as it was previously tested as part of a large-scale experimental program and reported in the literature, and it provided the opportunity to corroborate the numerical models of this study.

Several frames models were numerically evaluated: a control frame, frames retrofitted with conventional steel core BRBs from Al-Sadoon (2016), frames with the modified BRB with steel core bars, and a frame retrofitted with the modified BRB design incorporating a SE-SMA core bar. The numerical analyses considered three types of loading: static pushover, static reverse cyclic, and dynamic time-history. The pushover analysis was conducted to evaluate the lateral strength capacity of the frame, displacement ductility, and effective stiffness. The reverse cyclic analysis aimed to verify the lateral strength and displacement capacities of the frames, energy dissipation, failure mechanism, and residual displacements. The time-history analysis was performed to evaluate lateral transient drifts and residual displacements of two frames under earthquake records.

8.2 Proposed modifications to conventional BRB design

A modified BRB was proposed and investigated in this research. The modifications included improvements in buckling restraining that allow the core bar capacity to be fully utilized. Furthermore, the effects of concentration of stresses were mitigated by utilizing a 2 mm-thick silicon rubber sheet as the un-bonding layer between the core bar and the restraining system. The system was numerically proven to increase the lateral strength, displacement capacity, and, when incorporating a SE-SMA core, to decrease the permanent displacements experienced by the frame. As a result, after analysing the frame with the modified BRB, it was illustrated that the stiffness provided by the restraining system and un-bonding layer was sufficient to mitigate concentration of stresses within the brace.

8.3 Conclusions

Seismic performance and potential benefits of retrofitting a moment-resisting frame with a modified buckling-restrained brace incorporating a SE-SMA core were investigated by comparing the response of the alternative SE-SMA BRB retrofitted frame with: an un-retrofitted control frame, frame retrofitted with the original BRB design incorporating conventional steel cores, and a frame retrofitted with the modified BRB incorporating conventional steel core bars. Static and dynamic nonlinear numerical analyses were performed with the FE software VecTor2. The static analyses were performed under two types of loads, with the frames subjected to pushover and reverse cyclic loadings. Time-history analysis was conducted as part of the dynamic evaluation, and the seismic performance of the modified SE-SMA BRB retrofitted frame was assessed against the response of the control frame under ground motion records that simulate the M-R scenarios for the cities of Montreal and Vancouver. The conclusions are separately presented based on the analysis type.

8.3.1 Pushover behaviour of the frames

1. The pushover response of the frames indicated that buckling-restrained braces are effective in increasing the seismic performance of seismically deficient moment-resisting frames in terms of lateral strength capacity and stiffness.
2. The prototype BRB design from Al-Sadoon (2016) increased the lateral strength capacity of the frame at a rate depending on the core bar material and on the stresses dominating the brace. When a stainless-steel bar was utilized and the brace was under tension, the frame experienced an increase in its maximum strength capacity of approximately 300% when compared to the control frame. For a chrome-molybdenum bar incorporated into the system and for the brace under tensile stresses, the lateral capacity increased approximately 350% compared to the control frame.
3. The behaviour of the retrofitted frames was significantly different for the braces subjected to compressive and tensile stresses. When the brace was under compressive stresses, the lateral strength of the SS-BRB and CM -BRB retrofitted frames corresponded to 73% and 67% of their capacity relative to the brace under tension, respectively. The difference was due to insufficient restraining of the core bar, which permitted the core bar to buckle prematurely.
4. Insufficient buckling restraining of the core bar also affected the displacement ductility of the frame by reducing the ultimate lateral displacement. The frame retrofitted with a SS-BRB sustained 58% of the ultimate displacement of the control frame, while a CM-BRB retrofitted frame captured 39% of that experienced by the concrete bare frame.
5. The modified BRB design increased the lateral strength and displacement capacities of the retrofitted system independent of the core bar material. The increase in lateral strength was sufficient for the frame to satisfy current seismic provisions of shear force demands and drift limits.

6. The modified brace designed to mitigate the buckling of the bracing core increased the restraining, such that the retrofitted system behaved similarly under tension and compression. The SS - Modified BRB frame sustained 12% larger lateral displacement than the control frame, while the CM – Modified BRB frame increased the lateral displacement capacity 13% relative to the bare concrete frame when the brace was subjected to compressive stresses.
7. The lateral strength capacity of the modified BRB retrofitted system increased compared to the conventional BRB from Al-Sadoon (2016) independent of the core bar material. With the brace under compression, the SS – Modified BRB frame's lateral strength increased 13% and the CM – Modified BRB's lateral capacity increased 41% relative to the conventional BRB.
8. When incorporating SE-SMA in the modified BRB design, the frame exhibited similar lateral strength and displacement capacities relative to the conventional steel core bars. However, the capacity was highly influenced by the bar diameter. By incorporating a SE-SMA core bar with constant cross-sectional diameter of 44.5 mm in the modified BRB, an increase of 410% to the lateral strength and 25% to the ultimate displacement relative to the bare frame was achieved. These values were calculated disregarding the additional capacities due to the stiffening phase of the SE-SMA Modified BRB frame.

8.3.2 Reverse Cyclic behaviour of the frames

1. The numerical reverse cyclic response of the control bare concrete frame successfully simulated the behaviour of the frame compared to the same frame tested by Al-Sadoon (2016) under the same loading conditions. The displacement and strength capacities were in excellent agreement and within 2% of each other. Furthermore, it was verified that the two responses developed the same residual displacements and failure mode.
2. Independent of the BRB core bar, the drift capacity, crack patterns, failure mode and strength capacity of the numerical hysteretic response were similar to the experimental response from Al-Sadoon (2016). Minor differences were evident in the strength capacity, when a SS core bar was utilized, the numerical

model predicted lateral strength was 5% smaller than the experimental; for a CM core bar, the lateral strength capacity of the numerical response was 4.3% lower relative to the frame tested by Al-Sadoon (2016).

3. The displacement capacity of the retrofitted frames under reverse cyclic loading significantly decreased relative to their pushover response and to the response of the bare control frame. This phenomenon was attributed to the accumulation of damage due to the effects of reverse cyclic loading.
4. The modified BRB improved the performance of the frames by increasing the buckling restraining and minimizing concentration of stresses on the core bar, thus allowing the bracing core to reach its full capacity. Improved buckling restraining was achieved by replacing the internal gaps between the core bar and the supporting restraining component with a 2 mm-thick silicon rubber sheet as an un-bonding layer. The concentration of stresses was also mitigated due to the presence of the un-bonding layer that prevented load transfer between the bracing core bar and its surrounding.
5. Significant improvements in the displacement capacity were achieved with the modified BRB design used as a retrofit. For the system incorporating a CM core, the displacement capacity of the structural system increased 329% in comparison to the BRB proposed by Al-Sadoon (2016), and 68% when compared to the bare concrete frame. For the system incorporating a SS core bar, the increase in displacement capacity corresponded to 202% relative to both the frame retrofitted with the original brace designed by Al-Sadoon (2016) and the bare concrete frame.
6. Cracking patterns were similar in all the retrofitted frames. The difference in crack widths, however, was dependent on the core bar material. The frame retrofitted with the modified BRB incorporating a SE-SMA as the bracing core presented minimal cracks due to the self-centering ability of the core material. The maximum width of 3 mm was captured at a 7% lateral drift.
7. Given that energy is dissipated by the system once the structure yields, the frame retrofitted with the modified BRB incorporating a CM core provided the highest energy dissipation. At a lateral drift of 4%, the modified CM-BRB dissipated 6.49, 1.33, and 2.33 of the energy dissipated by the BCF, the modified SS-BRB, and the modified SE-SMA BRB, respectively.

8. At low drifts, the energy dissipated by the bare concrete frame was higher than the modified BRB incorporating an SE-SMA. At higher drifts, however, the energy dissipated by the retrofitted frame was higher, which corroborated that the brace increased the seismic performance of the frame. The energy dissipated by the frame retrofitted with the modified SE-SMA BRB was 278% greater than the control frame at a lateral drift cycle of 4%.
9. At a lateral drift of 3%, the frames retrofitted with conventional steel core bars accumulated more permanent damage than the bare concrete frame. The modified CM-BRB and modified SS-BRB accumulated permanent displacements of 46.48 mm and 46.81 mm, respectively, while the bare concrete frame accumulated 28.6 mm.
10. The frame retrofitted with the modified BRB incorporating a SE-SMA core bar accumulated less permanent displacement, which was attributed to the shape-memory effect. At a lateral drift of 3%, the retrofitted frame accumulated 4.34 mm of permanent displacement, which is 15% of that experienced by the control frame.

8.3.3 Dynamic behaviour of the frames

1. Eigenvalue analysis of the frames through VecTor2 resulted in fundamental periods larger than prescribed by the NBCC 2015 (NRC, 2015) for a reinforced concrete moment-resisting frame. The study indicated that the fundamental period of the frame was two times that prescribed by the code seismic provisions.
2. Under the same earthquake records and lumped masses according to Commentary J provisions of the NBCC 2015 (NRC, 2015b), the pseudo-yielding of the modified SMA BRB retrofitted frame was not reached during the dynamic analysis, while the bare concrete frame reached both the yielding and ultimate displacements.
3. The mean peak transient displacement of the bare concrete frame located in Montreal evaluated from the time history analyses was approximately 24% below the yielding displacement of the frame from the nonlinear static analysis.

4. Montreal M-R Scenario 2 induced the highest transient displacements on the bare concrete frame.
5. The lateral stiffness provided by the modified BRB incorporating a shape memory alloy core limited the transient displacements induced by the earthquake records simulating the Montreal seismic hazard. For that location, the peak drift experienced by the retrofitted frame corresponded to 0.02%.
6. For the city of Montreal, with the exception of two ground motion records scaled to match the target UHS, the response of both the bare concrete and retrofitted frames was lower than expected. Thus, following the mean response, the frames did not experience yielding under the dynamic analysis.
7. According to the mean transient displacements of both frames located in Montreal, the frames performed in the operational performance level (1-A), where light damage is expected.
8. For western Canada, the bare concrete frame failed when subjected to four different earthquake records. The failure initiated through fracture of longitudinal bars at the base of the columns, followed by fracture of the beam longitudinal bars that extended through the beam-column joint.
9. Concrete spalling was evident in most of the frame analyses subjected to ground motions simulating the seismic hazard of Vancouver. Concrete spalling was attributed to the poorly spaced and anchored transverse reinforcement of the structural elements. Furthermore, the locations more likely to experience spalling were at the base of the columns and beam-column joints.
10. The bare concrete frame located in Vancouver experienced a mean top transient displacement of 82.77 mm, which exceeded the yielding displacement and is approximately 13% lower than the maximum displacement capacity of the control frame evaluated from the nonlinear static analysis. The mean transient drift of 2.61% indicates the frame performed beyond the structural stability performance level, where severe damage is expected in the structural and non-structural elements and partial or total collapse of the structure is imminent.
11. Both shear and flexural cracks were observed in the control frame subjected to the earthquake records. The shear cracks initiated at early stages near the beam-column joints and expanded through the structural elements as larger transient displacements beyond yielding were induced.

12. The bare concrete frame experienced a maximum permanent displacement of 0.7% when subjected to an earthquake record simulating the third M-R Scenario of the city of Vancouver demonstrating the frame performed within the life safety performance level.
13. The mean transient displacement experienced by the retrofitted frame located in Vancouver corresponded to 0.85 mm (drift of 0.03%) indicating the structure was within the operational performance level and negligible residual drifts were observed (0.0001%).
14. The dynamic analyses indicated the improved seismic performance of the retrofitted frame in comparison to the bare concrete frame. While the control frame experienced transient displacements beyond the structural stability from the FEMA P-58-1 (FEMA, 2012), the retrofitted frame was performed within the operational level in which immediate re-occupancy is allowed after an earthquake.
15. Subjected to a 100% increased ground motion record, the bare concrete frame reached its maximum transient displacement, where longitudinal reinforcing bars at the base of the column and near the beam-column joint fractured. Ratcheting was observed resulting in a residual displacement of 26.5 mm (drift of 0.83%). Under a 300% increased earthquake record, 16% of the transient displacements experienced by the control frame were above its ultimate capacity, which resulted in severe structural damage, deterioration of concrete, and failure of the longitudinal reinforcement in multiple locations. Furthermore, for the 500% increased earthquake record, the bare concrete frame failed 4.46 s after the ground motion initiated.
16. Subjected to amplified earthquake records, the retrofitted frame did not yield. The structure was able to withstand the amplified ground motions without accumulating structural damage nor presenting transient drifts beyond 0.36%, indicating the frame was within the operational performance level.

8.4 Recommendations

The following recommendations are suggested for future research based on the outcomes of this thesis:

1. Conduct nonlinear time-history analysis on the frames retrofitted with the modified BRB incorporating conventional steel cores to evaluate the performance against the modified BRB with SE-SMA core, and to assess the efficiency of utilizing the self-centering SE-SMA material.
2. Cyclic uniaxial testing of the modified buckling-restrained brace incorporating a SE-SMA core under incrementally increasing axial deformation reversals. The tests will provide better understanding of the hysteretic response of the BRB brace, and better inform the constitutive material models used to simulate the BRB in the analysis of the frames.
3. Evaluate a reduction in the core bar size to reduce cost and allow the SE-SMA bar to perform within its pseudo-yielding zone, such that the self-centering characteristics are efficiently utilized.
4. Conduct 3D numerical analyses of prototype buildings under the scaled earthquake records to investigate the interaction between the retrofitted frame and other components of the structure. This will assess the efficiency of the modified BRB, and provide an avenue to assess the distribution of the retrofit technique to other critical floors of locations in the structure.
5. Conduct large-scale testing of a reinforced concrete frame designed based on pre-1970s building codes and retrofitted with the modified BRB incorporating the SE-SMA core bar. Assess the strength and displacement capacities of the system against the numerical analyses.
6. Evaluate the feasibility of the modified BRB for both old and new construction focusing on the reduction of the seismic weight with the implementation of the modified BRB in the system in different seismic regions.
7. Assess the improvement in the seismic performance of reinforced concrete frames retrofitted with the new BRB for seismic regions beyond the Canadian seismic hazard scenarios.

REFERENCES

Abdel-Fattah, B., and Wight, J.K. (1987). Study of moving beam plastic hinging zones for earthquake-resistant design of Reinforced Concrete buildings. ACI Structural Journal, 84(1), 31-39.

Abdulridha, A. (2013). Performance of Superelastic Shape Memory Alloy Reinforced Concrete Elements Subjected to Monotonic and Cyclic Loading. PhD thesis, University of Ottawa, Ottawa, ON, Canada.

Abdulridha, A., Palermo, D., Foo, S., Vecchio, F.J. (2013). Behavior and modeling of superelastic shape memory alloy reinforced concrete beams. Engineering Structures, Elsevier, 49:893-904.

ACI Committee Report (1965). Commentary on Building Code Requirements for Reinforced Concrete – ACI 318-63, American Concrete institute, Detroit Michigan, 91.

ACI Standard 318- 02 (2002). Building Code Requirements for Reinforced Concrete, American Concrete institute, Detroit Michigan.

Aiken, I. D., Mahin, S. A., Uriz, P. (2002). Large-scale testing of buckling-restrained braced frames. Proceedings of Japan Passive Control Symposium, Tokyo Institute of Technology, Japan.

AISC (2002). Seismic provisions for structural steel buildings, (ANSI/AISC 341-05), American Institute of Steel Construction, Chicago, IL.

Akkaya, Y., Guner, S. and Vecchio, F. J., (2013). Modeling inelastic buckling behavior of reinforcing bars in compression. University of Toronto, Toronto, ON, Canada.

Al-Sadoon, Z. (2016). Seismic Retrofitting of Conventional Reinforced Concrete Moment-Resisting Frames Using Buckling Restrained Braces. PhD thesis, University of Ottawa, Ottawa, ON, Canada.

Al-Sadoon, Z., Palermo, D., Saaticioglu, M. (2017). Retrofit of Seismically Deficient Reinforced Concrete Frame with Buckling Restrained Braces. The 11th Canadian Conference on Earthquake Engineering, Victoria, BC, Canada.

Ancheta, T.D., Darragh, R.B., Stewart, J.P., Seyhan, E., Silva, W.J., Chiou, B.S.J., Wooddell, K.E., Graves, R.W., Kottke, A.R., Boore, D.M., Kishida, T., Donahue, J.L. (2013). PEER NGA-West2 Database, PEER Report 2013/03, Pacific Earthquake Engineering Research Center, University of California, Berkeley, CA, USA.

ASTM. (2014). ASTM F2516-14: Standard test method for tension testing of nickel-titanium superelastic materials. ASTM International, West Conshohocken, PA, USA.

Atkinson, G.M. (2009). Earthquake time histories compatible with the 2005 National building code of Canada uniform hazard spectrum. Canadian Journal of Civil Engineering, NRC Research Press, 36:991-1000.

Auricchio, F., Fugazza, D., DesRoches, R. (2006). Earthquake performance of steel frames with Nitinol braces. Journal of Earthquake Engineering. Imperial College Press. Volume 10, 45-66.

Black, C., Makris, N., Aiken, I. (2004). Component Testing, Stability Analysis and Characterization of Buckling-Restrained Unbonded Braces. PEER Report 2002/08. Pacific Earthquake Engineering Research Center, College of Engineering, University of California, Berkeley.

Black, R. G.; Wenger, W. A. B.; Popov, E. P. (1980). Inelastic Buckling of Steel Struts under Cyclic Load Reversals. National Science Foundation, Washington, DC.; American Iron and Steel Inst., Washington, DC., October 1980, 172 p.

Buehler, W.J., Gilfrich, J.V., Wiley, R.C. (1963). Effect of low-temperature phase changes on the mechanical properties of alloys near composition TiNi. Journal of Applied Physics, AIP Publishing, 34:1475-1477.

Bush, T.D., Jones, E.A., Jirsa, J.O. (1991). Behaviour of Reinforced Concrete frame strengthened using structural steel bracing. ASCE Journal Structural Engineering, 117(4):1115-26.

Caron, F. (2010). Repair and retrofit of non-ductile reinforced concrete frames with diagonal steel compression struts, M.Sc. Thesis, University of Ottawa, Ottawa, ON, Canada.

Cement Association of Canada (2006). Concrete Design Handbook, 3rd edition, Ottawa, Ontario, Canada.

Chen, C.C., Chen, S.Y., and Liaw, J.J. (2001). Application of low yield strength steel on controlled plastification ductile concentrically braced frames, Canadian Journal of Civil Engineering, 28, 823–836.

Christopoulos, C., Filiatrault, A., Uang, C., Folz, B. (2002). Posttensioned Energy Dissipating Connections for Moment-Resisting Steel Frames. ASCE Journal of Structural Engineering, 128:9(1111).

Christopoulos, C., Tremblay, R., Kim, H., Lacerte, M. (2008). Self-Centering Energy Dissipative Bracing System for the Seismic Resistance of Structures: Development and Validation. ASCE Journal Structural Engineering, 134(1):96.

Clark, P., Aiken, I., Kasai, K., Ko, E., and Kimura, I. (1999). Design procedures for buildings incorporating hysteretic damping devices. Proceedings of the 68th Annual Convention, Structural Engineers Association of California, Sacramento, 355-371.

D'Aniello, M., Della Corte, G., and Mazzolani, F. M. (2009). All-steel buckling-restrained braces for seismic upgrading of existing reinforced concrete buildings (Book, Chapter 80), Behaviour of Steel Structures in Seismic Areas.

Della Corte, G., D'Aniello, M., Landolfo, R., and Mazzolani, F. M. (2011). Review of steel buckling-restrained braces. Steel Construction, 4: 85–93.

Della Corte, G., D'Aniello, M., Landolfo, R., and Mazzolani, F. M. (2011). Review of steel buckling-restrained braces. Steel Construction, 4: 85–93.

Della Corte, G., D'Aniello, M., Maz-zolani, F. M. (2010). Sperimentazione al verodi controventi BRB "solo acciaio". Costruzioni metalliche, vol. LVII, Milan, Italy, No. 1, 35–44 (in Italian).

Della Corte, G., D'Aniello, M., Mazzolani, F. M. Seismic upgrading of Reinforced Concrete buildings using buckling restrained braces: full-scale experimental tests. Proceedings of the XX Italian Congress on Steel and Composite Structures, Ischia, Italy, Sept 2005, 26–28.

DesRoches, R., McCormick, J., Delemont, M. (2004). Cyclic Properties of Superelastic Shape Memory Alloy Wires and Bars. ASCE Journal Structural Engineering, 130:1(38).

Duerig, T., Melton, K., Stokel, D., and Wayman, C. (1990). Engineering aspects of shape memory alloys, Butterworth–Heinemann, London.

Eatherton, M., Hajjar, J. (2014). Hybrid simulation testing of a self-centering rocking steel braced frame system. The Journal of the International Association for Earthquake Engineering, Earthquake Engineering and Structural Dynamics. 43:1725–1742.

El-Amoury, T. and Ghobarah, A. (2002). Seismic Rehabilitation of Beam-Column Joint using GFRP Sheets. Engineering Structures, 24:1397–1407.

El-Sheikh, M., Sause, R., Pessiki, S., Lu, L. (1999). Seismic Behavior and Design of Unbonded Post-Tensioned Precast Concrete Frames. PCI Journal. 54-88.

Fahnestock, L. A, Ricles, J. M,Sause, R. (2007). Experimental evaluation of a large-scale buckling-restrained braced frame. Journal of Structural Engineering (ASCE), 133:1205–1214.

FEMA. (2012). FEMA P-58-1: Seismic performance assessment of buildings: volume 1 - methodology. Federal Emergency Management Agency, Washington, D.C, USA.

Filiatrault, A., Tremblay, R., Christopoulos, C., Folz, B., Pettinga, D. (2013). Elements of Earthquake Engineering and Structural Dynamics. Presses Internationales Polytechnique, 3rd ed., Quebec, Canada.

Garlock, M, and Li, J. (2008). Steel Self-Centering Moment Frames with Collector Beam Floor Diaphragms, Journal of Constructional Steel Research, Elsevier, Volume 64, n 5, p 526-538.

Ghobarah, A., Said, A. (2002). Shear Strengthening of beam-column joints. Engineering Structures, Elsevier, 27:881-888.

Goulet, C.A., Kishida, T., Ancheta, T.D., Cramer, C.H., Darragh, R.B., Silva, W.J., Hashash, Y.M.A., Harmon, J., Stewart, J.P., Wooddell, K.E., Youngs, R.R. (2014). PEER NGA-East Database, PEER Report 2014/17, Pacific Earthquake Engineering Research Center, University of California, Berkeley, CA, USA.

Hu, J., Choi, D., Kim, D. (2013). Inelastic behavior of smart re-centering buckling-restrained braced frames with superelastic shape memory alloy bracing systems. Journal of Mechanical Engineering Science. 227(4):806-818.

Iwata, M., Kato, T., Wada, A. (2000) Buckling-restrained braces as hysteretic dampers. Proceedings of STESSA 2000, Montreal, Quebec, 21–24.

Iwata, M., Murai, M. (2006). Buckling-restrained brace using steel mortar planks; performance evaluation as a hysteretic damper. Earthquake Engineering Structural Dynamics, 35:1807-1826.

Kimberley, R., and Cameron, M. (2011). Getting the most out of buckling restrained braces, Modern Steel Construction Journal, Vol. 4, April issue.

Lagoudas, D.C. (2008). Shape Memory Alloys: Modelling and Engineering Applications. Springer, 1st ed., New York, London.

López, W. A., and Sabelli, R. (2004). Seismic design of buckling-restrained braced frames, Steel TIPS Report, Structural Steel Education Council, Chicago, IL.

Maciel, M. (2019). Seismic performance analysis of mid-rise concrete shear walls reinforced with superelastic shape memory alloys. Masters thesis, York University, Toronto, ON, Canada.

Maheri, M. R., and Ghaffarzadeh, H. (2008). Connection overstrength in steel-braced Reinforced Concrete frames. Engineering Structures, 30(7), 1938-1948.

Maheri, M. R., and Sahebi, A. (1997). Use of steel bracing in reinforced concrete frames. Engineering Structures, Vol. 19, No. 12, pp. 1018-1024.

Mahrenholtz, C., Lin, P., Wu, A., Tsai, K., Hwang, S., Lin, R., Bhayusukma, M. (2015). Retrofit of reinforced concrete frames with buckling-restrained braces. The Journal of the International Association for Earthquake Engineering, Earthquake Engineering and Structural Dynamics. 44:59–78.

Miller, D. (2011). Development and experimental validation of self-centering buckling-restrained braces with shape memory alloy. M.S. Thesis, University of Illinois at Urbana–Champaign.

NBCC. 1960. 1965. 2005. 2010. National Building Code of Canada Associate Committee on the National Building Code, National Research Council of Canada, Ottawa, ON.

NRC. (2015). Division B, Part4, Structural Design National Building Code of Canada. National Research Council of Canada, Ottawa, ON, Canada.

NRC. (2015b). Structural Commentary J National Building Code of Canada. National Research Council of Canada, Ottawa, ON, Canada.

NRC. (2017). Geological Survey of Canada. Natural Resources Canada, Ottawa, ON, Canada. Retrieved 5 February, 2020, from http://earthquakescanada.nrcan.gc.ca.

Park, R. (1988). Ductility Evaluation from Laboratory and Analytical Testing, Proceeding of Ninth World Conference on Earthquake Engineering, 605-616.

Priestley, M., Sritharan, S., Conley, J., Pampanin, S. (1999). Preliminary Results and Conclusions from the PRESSS Five-Story Precast Concrete Test Building. Special Report. PCI Journal. November-December. 42-67.

Ricles, J. M., Sause, R., Garlock, M. M., and Zhao, C. (2001). Posttensioned seismic-resistant connections for steel frames. Journal Structural Engineering, 127(2), 113–121.

Ricles, J., Sause, R., Karavasilis, T., Chen, C. (2010). Performance-Based Seismic Design and Experimental Evaluation of Steel MRFs with Compressed Elastomer Dampers (Chapter 26). From Advances in Performance-Based Earthquake Engineering (Michael N. Fardis). Editor Springer. Geotechnical, Geological and Earthquake Engineering, Volume 13.

Said, A., and Nehdi, M. (2008). Rehabilitation of Reinforced Concrete frame joints using local steel bracing. Structure and Infrastructure Engineering, 4(6), 431-447.

Takeuchi, T. (2018). Buckling-restrained brace: history, design and applications. 9th International Conference on Behavior of Steel Structures in Seismic Areas Christchurch, Newzealand, Februaly 14-16.

Takeuchi, T., Ida, M., Yamada, S., Suzuki, K. (2008). Estimation of cumulative deformation capacity of buckling restrained braces. Journal of Structural Engineering, vol. 134, No. 5, 822–831.

Tarzav, M., Saiidi, M.S. (2015). Reinforcing NiTi Superelastic SMA for Concrete Structures. Journal of Structural Engineering, ASCE, 141(8):0414197-1-10.

Tremblay, R., Atkinson, G.M., Bouaanani, N., Daneshvar, P., Léger, P., Koboevic, S. (2015). Selection and scaling of ground motion time histories for seismic analysis using NBCC 2015. The 11th Canadian Conference on Earthquake Engineering, Victoria, BC, Canada.

Tremblay, R., Bolduc, P., Neville, R., and Devall, R. (2006). Seismic testing and performance of buckling-restrained bracing systems. Canadian Journal of Civil Engineering. 33: 183–198.

Tsai, K. C., Hsiao, P. C. (2008). Pseudo-dynamic test of a full-scale CFT/BRB frame – Part II: Seismic performance of buckling-restrained braces and connections. Earthquake Engineering and Structural Dynamics, 37: 1099–1115.

Uang, C. M., and Nakashima, M. (2004). Steel buckling-restrained braced frames. Earthquake engineering from Engineering Seismology to Performance-based Engineering (Book, Chapter 16). Bozorgnia Y. and Bertero V. V. (eds.), CRC Press L. L. C., Boca Raton, FL, 16-1-37.

Vecchio, F.J. (2000). Disturbed Stress Field Mode1 for Reinforced Concrete: Formulation. ACI Structural Journal, ACI, 1070-1077.

Vecchio, F.J., Collins, M.P. (1986). The Modified Compression Field Theory for Reinforced Concrete Elements Subject to Shear. ACI Journal, ACI, 83(2):219-231.

Vecchio, F.J., Wong, P., Trommels, H. (2013). VecTor2 and Formworks Manual, 2nd ed., University of Toronto, Toronto, ON, Canada.

Wada, A., Connor, J., Kawai, H., Iwata, M., and Watanabe, A. (1992). Damage tolerant structures, Proceedings of the 5th U.S.–Japan Workshop on the Improvement of Structural Design and Construction Practices, San Diego, CA, Applied Technology Council, ATC-15-4, 27–39.

Wada, A., Saeki, E., Takeuchi, T., and Watanabe, A. (1998). "Development of Unbonded Brace," in Nippon Steel's Unbonded Braces (promotional document), pp. 1-16, Nippon Steel Corporation Building Construction and Urban Development Division, Tokyo.

Watanabe, A., Hitomi, Y., Saeki, E., Wada, A., and Fujimoto, M. (1988). Properties of brace encased in buckling-restraining concrete and steel tube. Proceedings of Ninth World Conference on Earthquake Engineering. Vol. IV. 1988. p. 719–24.

Yang, S., Seelecke, S. (2008). Modeling and analysis of SMA-based adaptive structures. Proc. COMSOL Conf. Boston, MA.

Yin, Q., Wu, X., Huang, C., Wang, X., Wei, Y. (2015). Atomistic study of temperature and strain rate-dependent phase transformation behaviour of NiTi shape memory alloy under uniaxial compression. Phil Mag 95(23):2491–2512.

Youssef, M. A., Ghaffarzadeh, H., and Nehdi, M. (2007). Seismic performance of Reinforced Concrete frames with concentric internal steel bracing. Engineering Structures, 29 (7), 1561-1568.

Youssef, M.A., Elfeki, M.A. (2010). Seismic Performance of Shape Memory Alloy Reinforced Concrete Frames. 10th Canadian Conference on Earthquake Engineering, Toronto, ON, Canada.

Zhang, Y., Zhu, S. (2007). A shape memory alloy-based reusable hysteretic damper for seismic hazard mitigation. Smart Materials and Structures. IOP Publishing Ltd. Volume 16, Number 5.

APPENDIX

Dynamic response to the earthquake records

I. Bare concrete frame

A) Earthquake records Montreal – QC

1. TR1-1

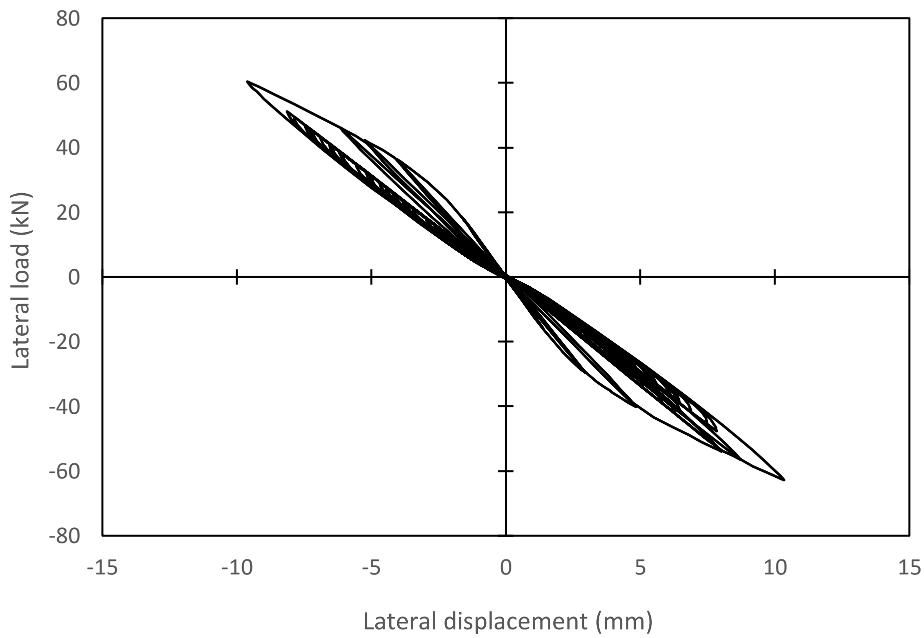

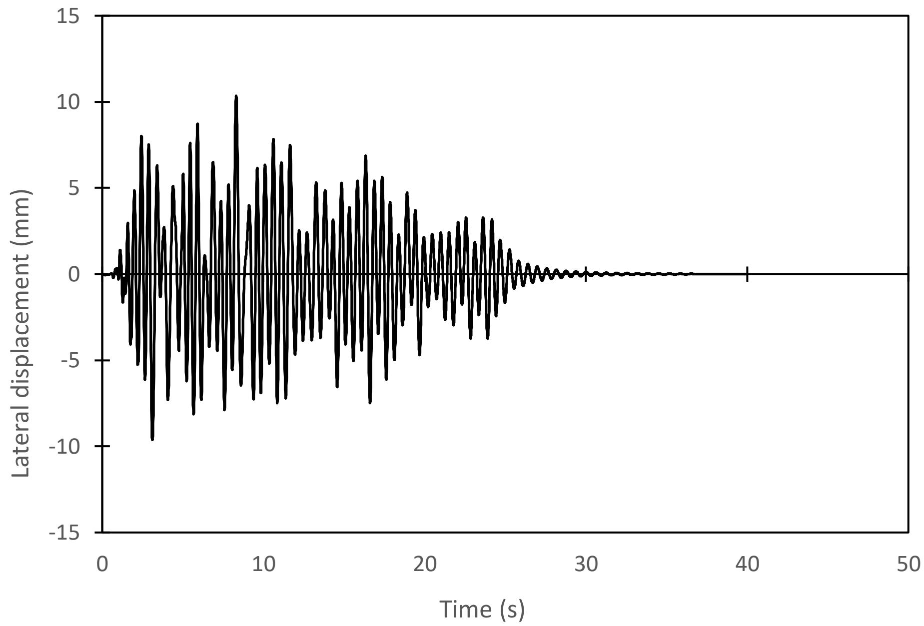
Lateral displacement (mm)
Time (s)

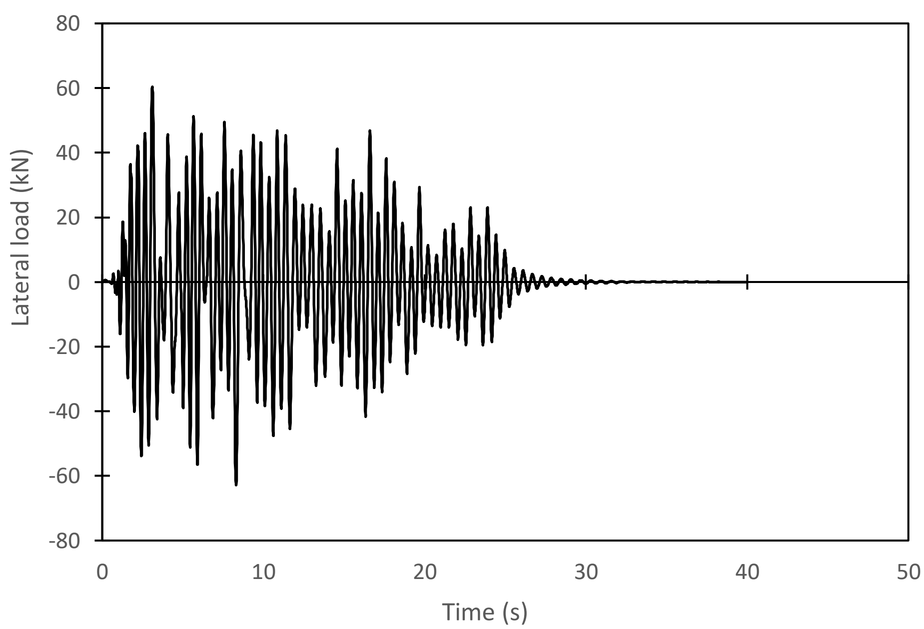
Lateral load (kN)
Time (s)

2. TR1-2

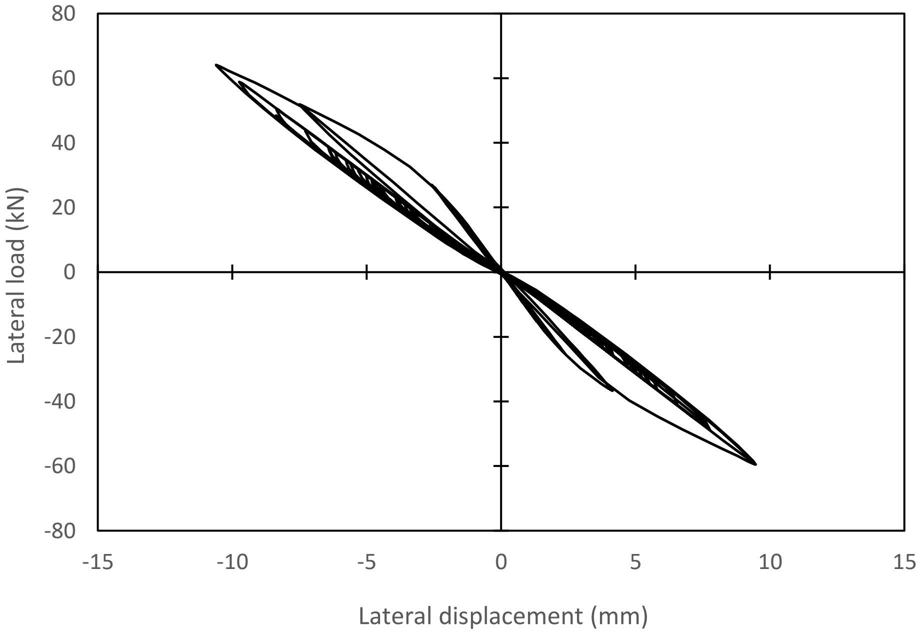
80
60
40
20
0
-20
-40
-60
-80
Lateral load (kN)
-15
-10
-5
0
5
10
15
Lateral displacement (mm)

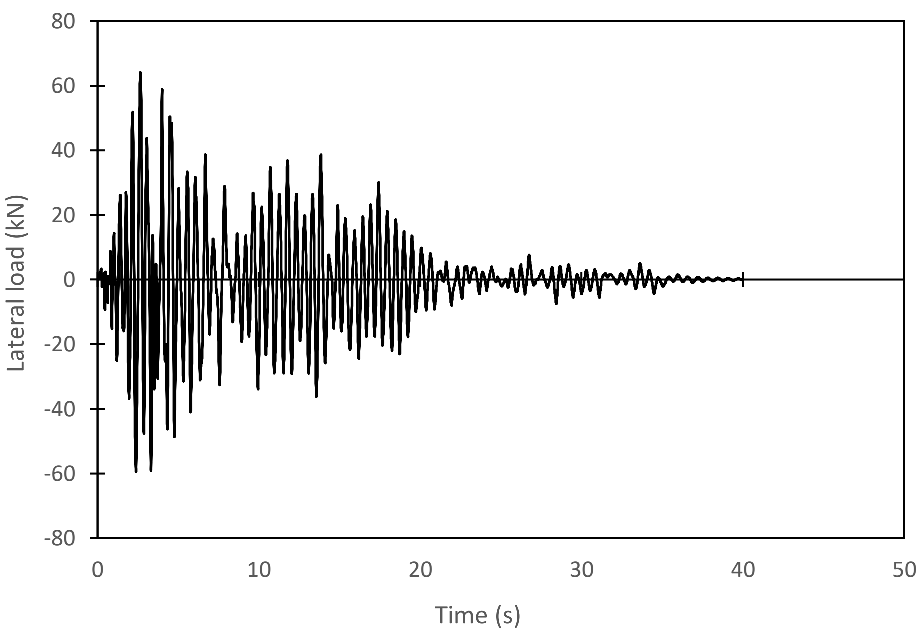
80
60
40
20
0
-20
-40
-60
-80
Lateral load (kN)
0
10
20
30
40
50
Time (s)

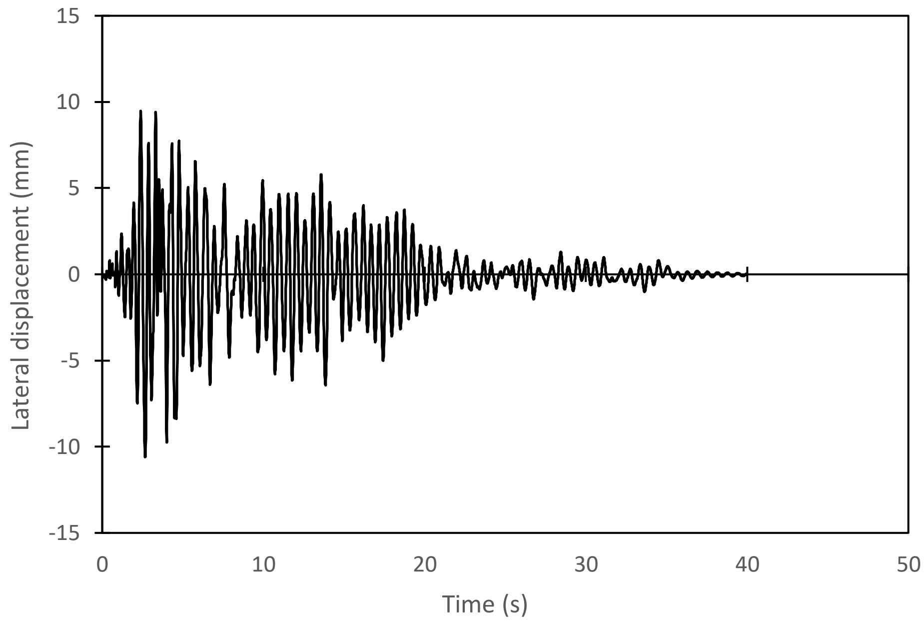

Lateral displacement (mm)
Time (s)
15
10
5
0
-5
-10
-15
0
10
20
30
40
50

3. TR1-3

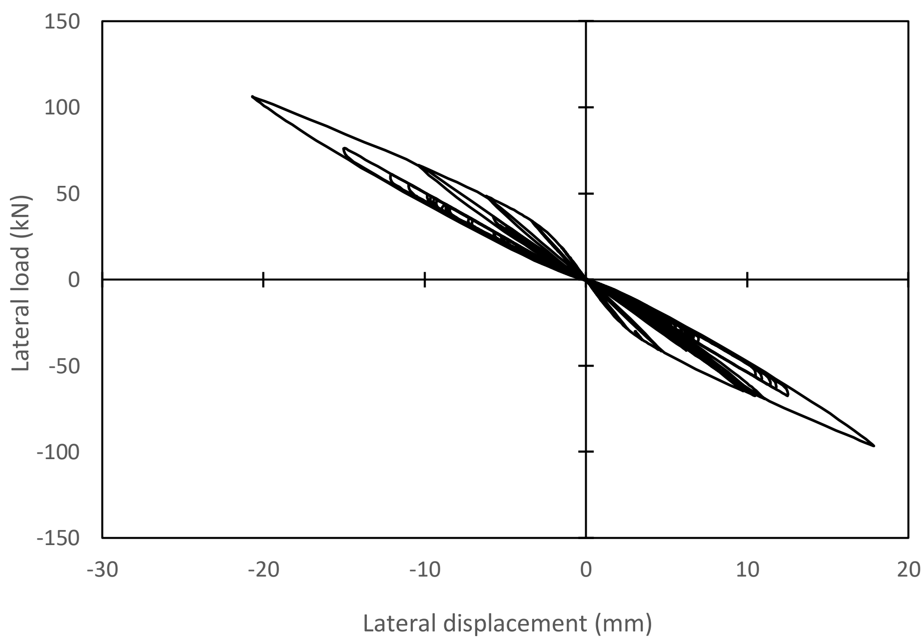

Lateral load (kN)
Lateral displacement (mm)
150
100
50
0
-50
-100
-150
-30
-20
-10
0
10
20

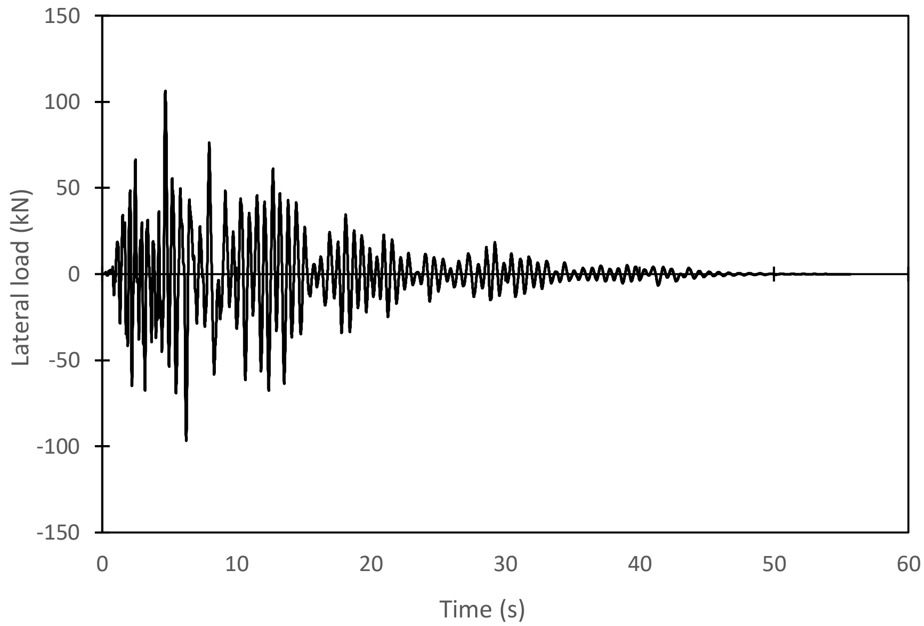
150
100
50
0
-50
-100
-150
Lateral load (kN)
0
10
20
30
40
50
60
Time (s)

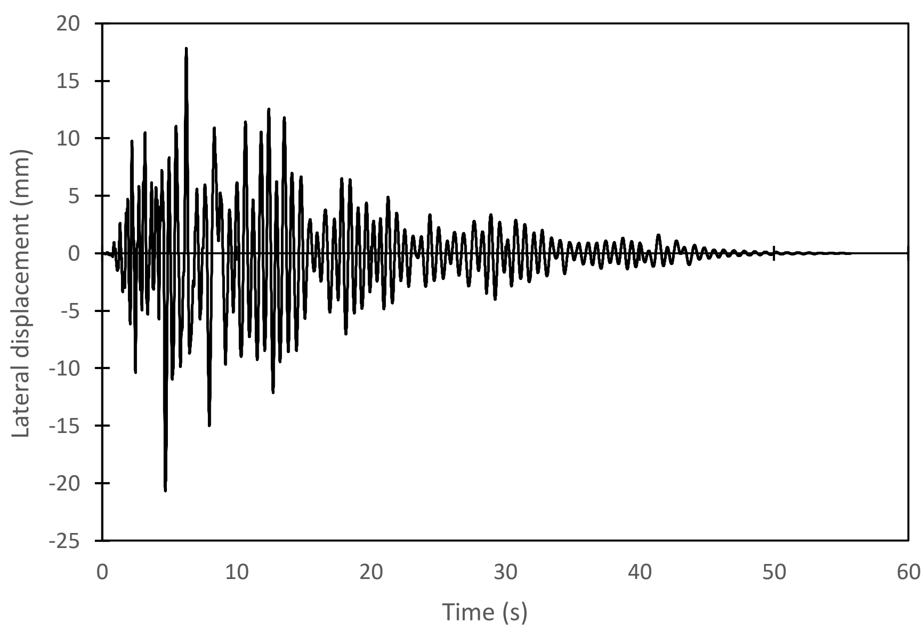
20
15
10
5
0
-5
-10
-15
-20
-25
Lateral displacement (mm)
0
10
20
30
40
50
60
Time (s)

4. TR1-4

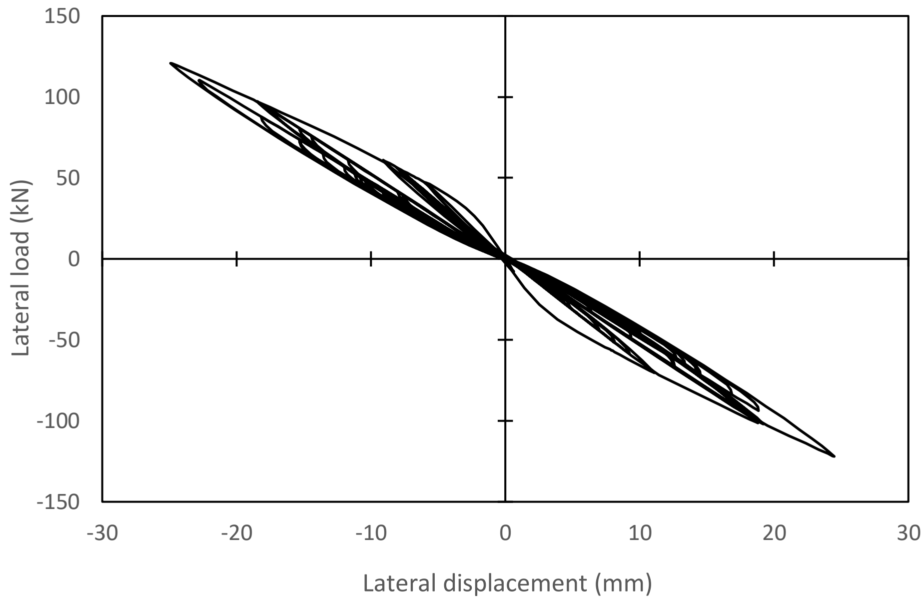

150
100
50
0
-50
-100
-150
-30
-20
-10
0
10
20
30
Lateral load (kN)
Lateral displacement (mm)

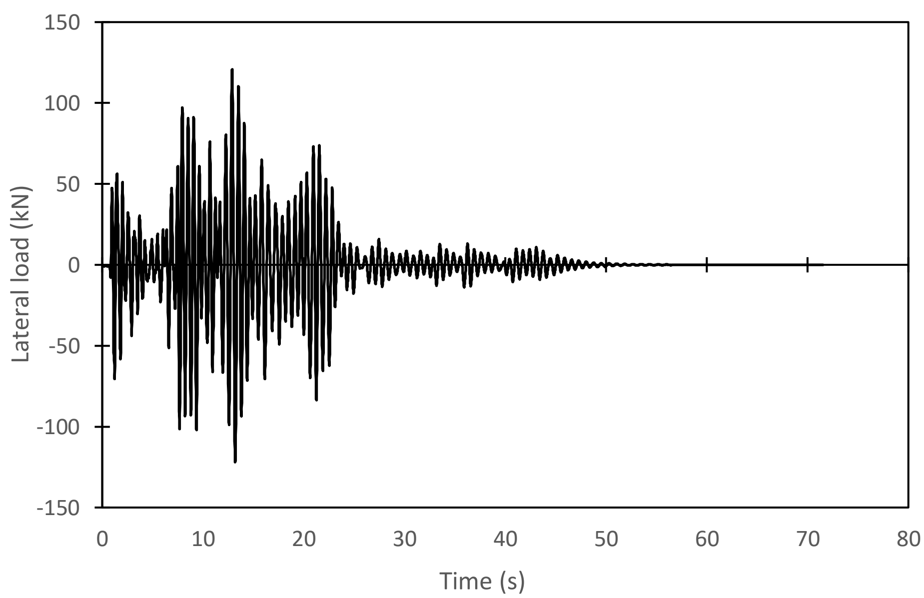

150
100
50
0
-50
-100
-150
0
10
20
30
40
50
60
70
80
Lateral load (kN)
Time (s)

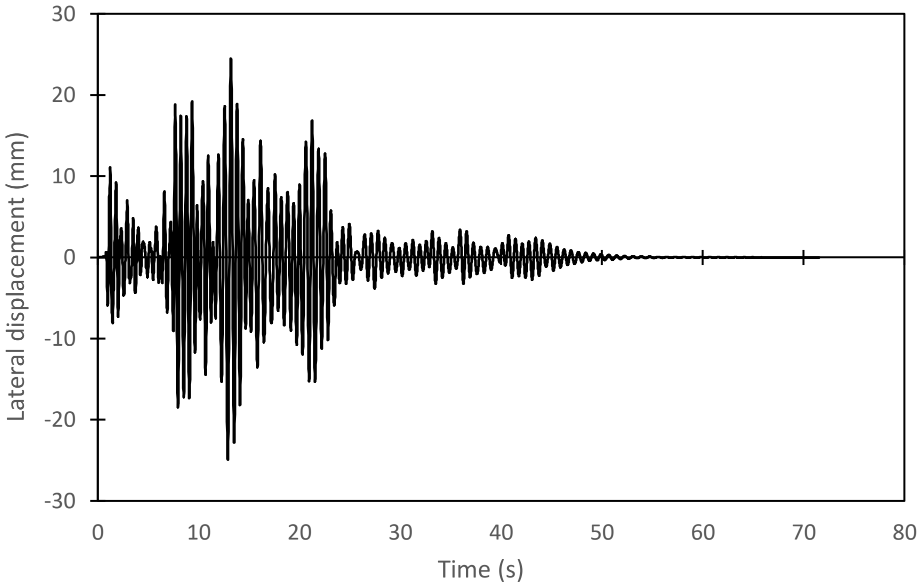
Lateral displacement (mm)
Time (s)
30
20
10
0
-10
-20
-30
0
10
20
30
40
50
60
70
80

5. TR1-5

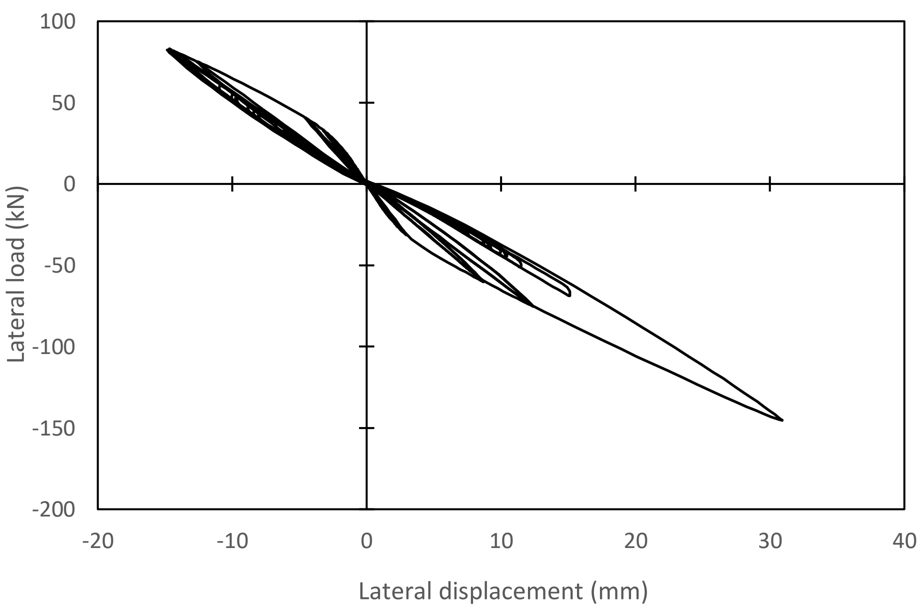
Lateral load (kN)
Lateral displacement (mm)
100
50
0
-50
-100
-150
-200
-20
-10
0
10
20
30
40

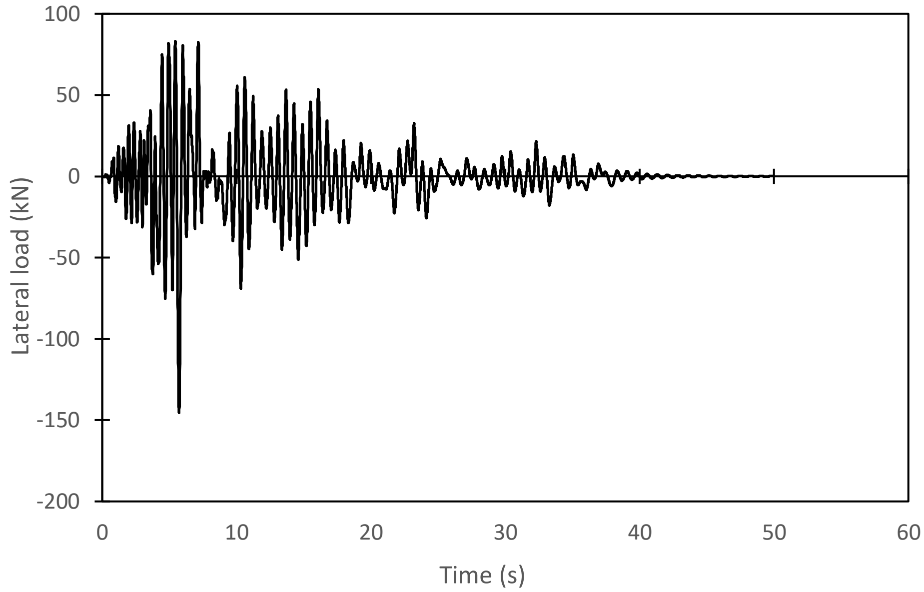

100
50
0
-50
-100
-150
-200
Lateral load (kN)
0
10
20
30
40
50
60
Time (s)

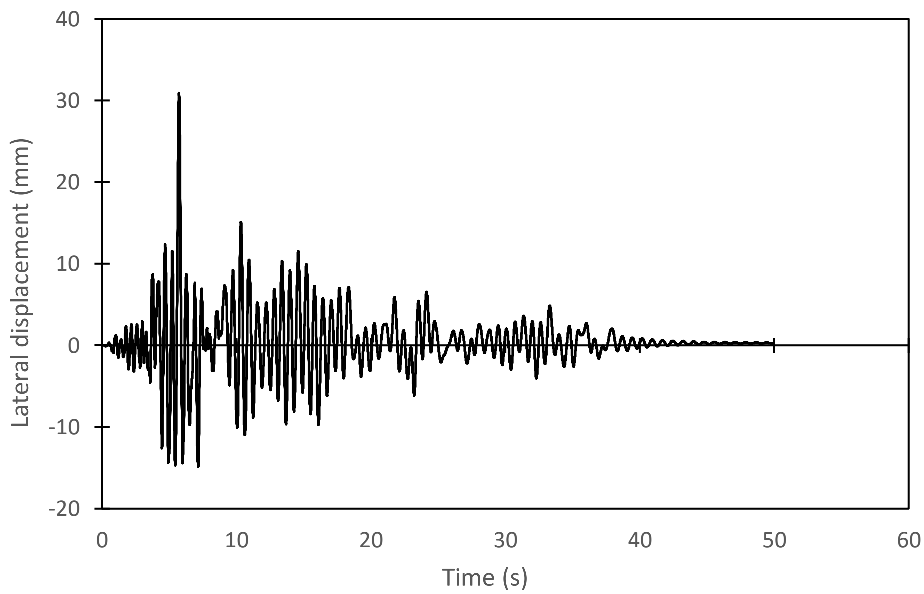

40
30
20
10
0
-10
-20
Lateral displacement (mm)
0
10
20
30
40
50
60
Time (s)

6. TR1-6

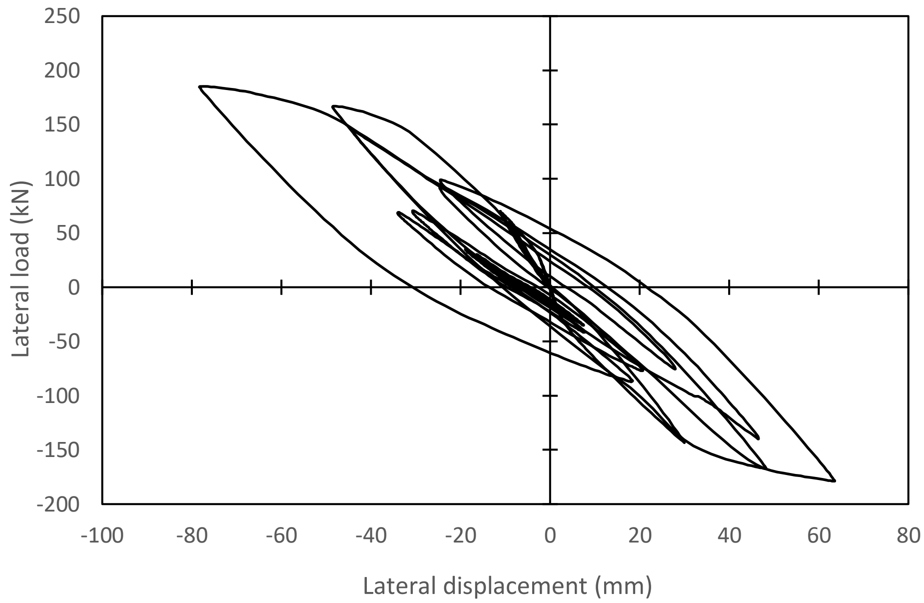
Lateral load (kN)
Lateral displacement (mm)
250
200
150
100
50
0
-50
-100
-150
-200
-100
-80
-60
-40
-20
0
20
40
60
80

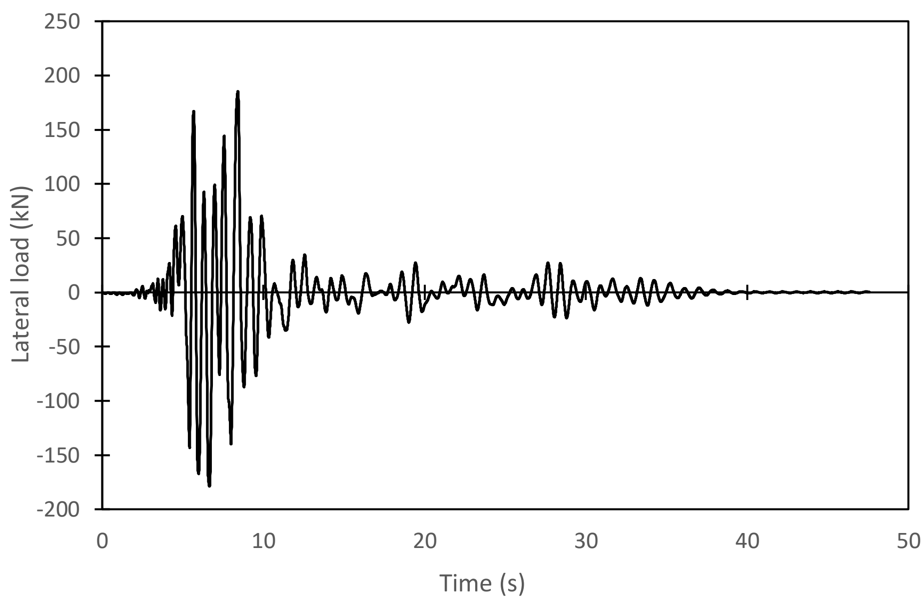
Lateral load (kN)
Time (s)
250
200
150
100
50
0
-50
-100
-150
-200
0
10
20
30
40
50

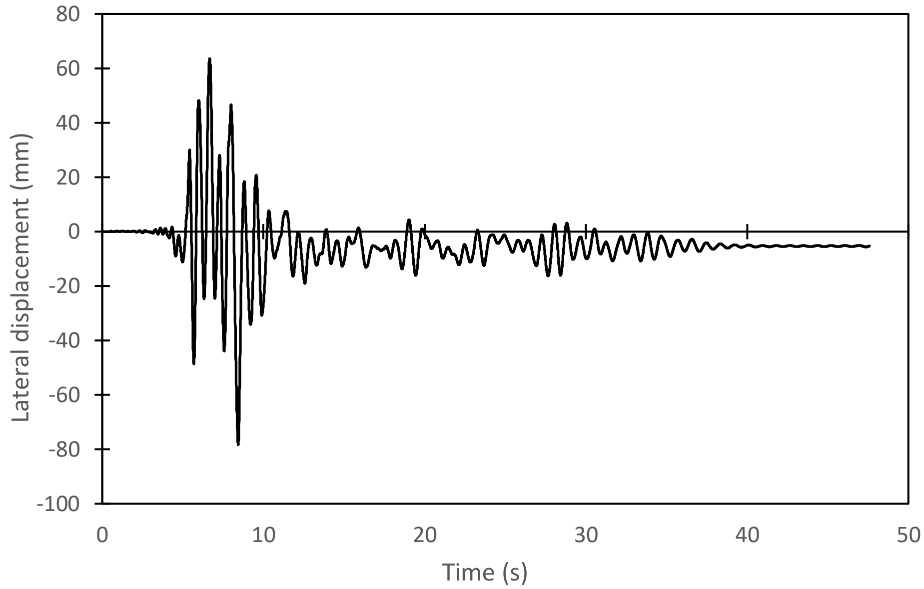

Lateral displacement (mm)
Time (s)
80
60
40
20
0
-20
-40
-60
-80
-100
0
10
20
30
40
50

7. TR2-1

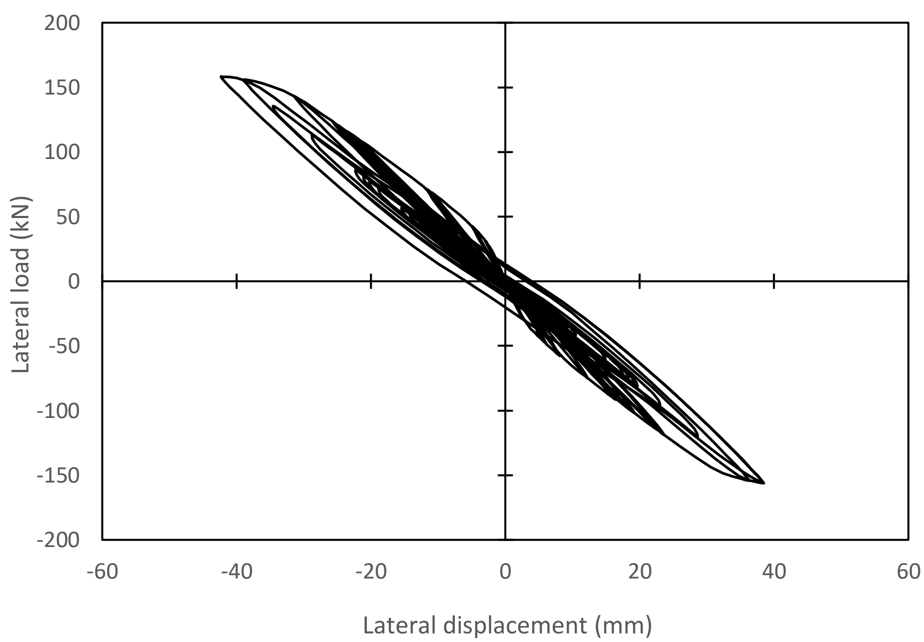

Lateral load (kN)
Lateral displacement (mm)
200
150
100
50
0
-50
-100
-150
-200
-60
-40
-20
0
20
40
60

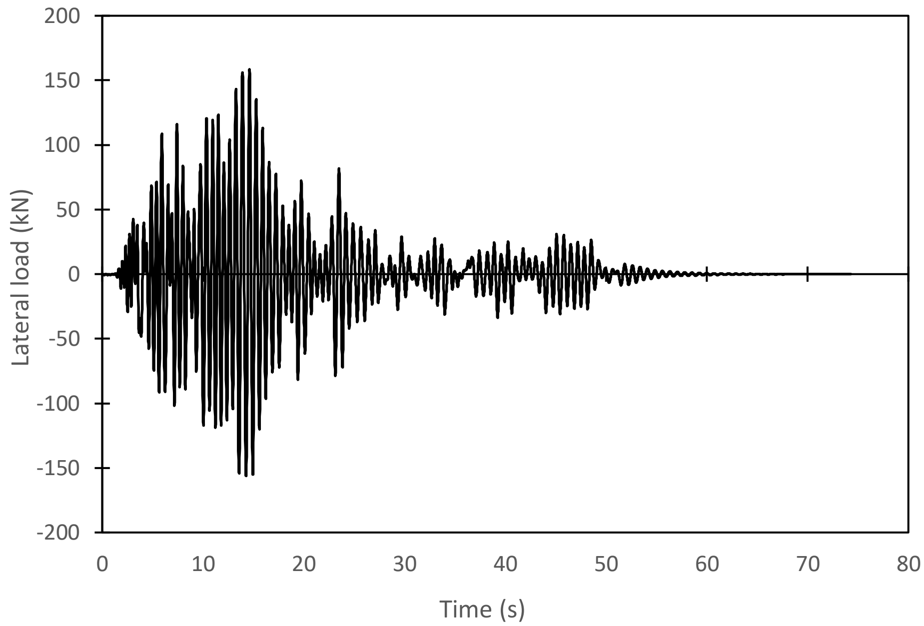
200
150
100
50
0
-50
-100
-150
-200
Lateral load (kN)
0
10
20
30
40
50
60
70
80
Time (s)

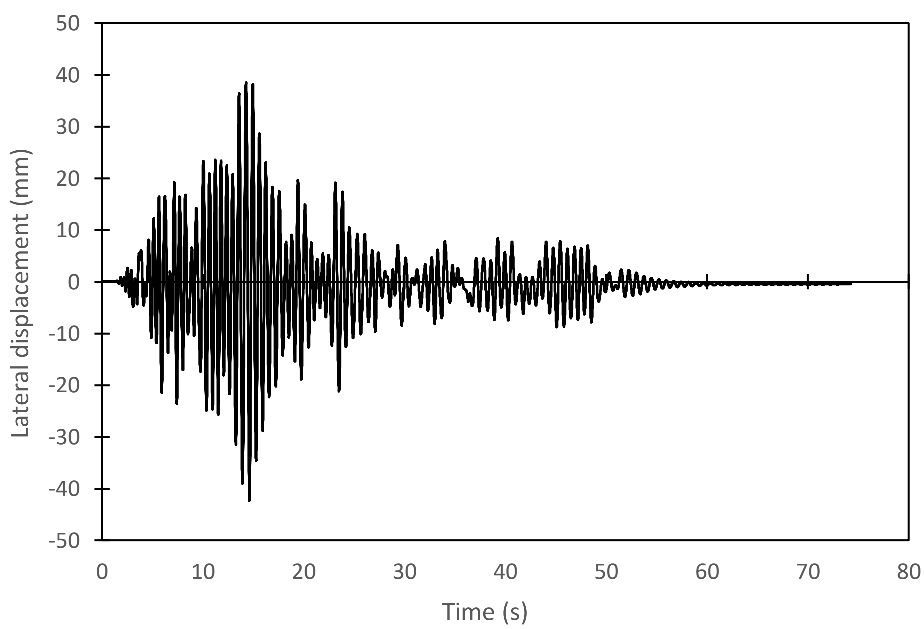
50
40
30
20
10
0
-10
-20
-30
-40
-50
Lateral displacement (mm)
0
10
20
30
40
50
60
70
80
Time (s)

8. TR2-2

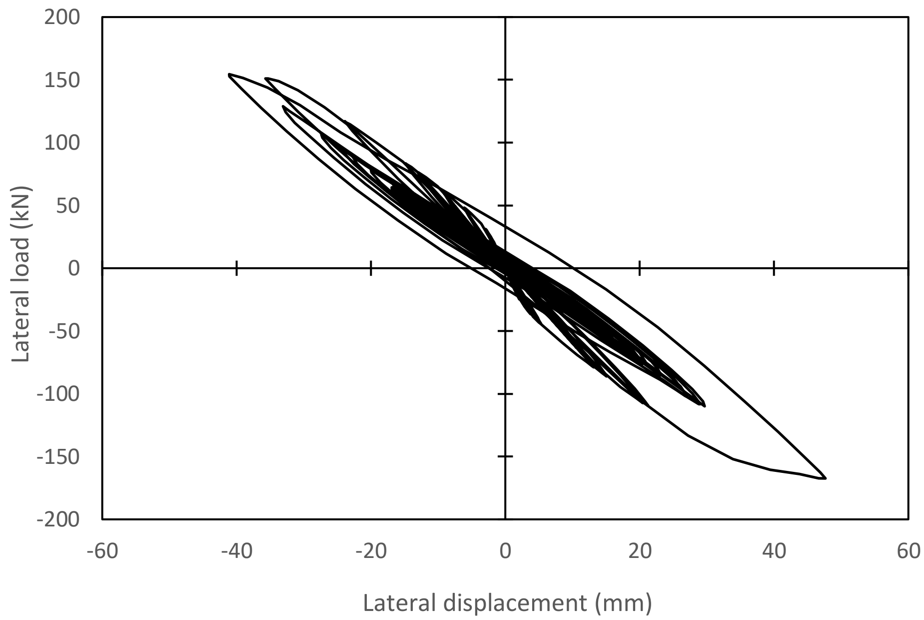

Lateral load (kN)
200
150
100
50
0
-50
-100
-150
-200
-60
-40
-20
0
20
40
60
Lateral displacement (mm)

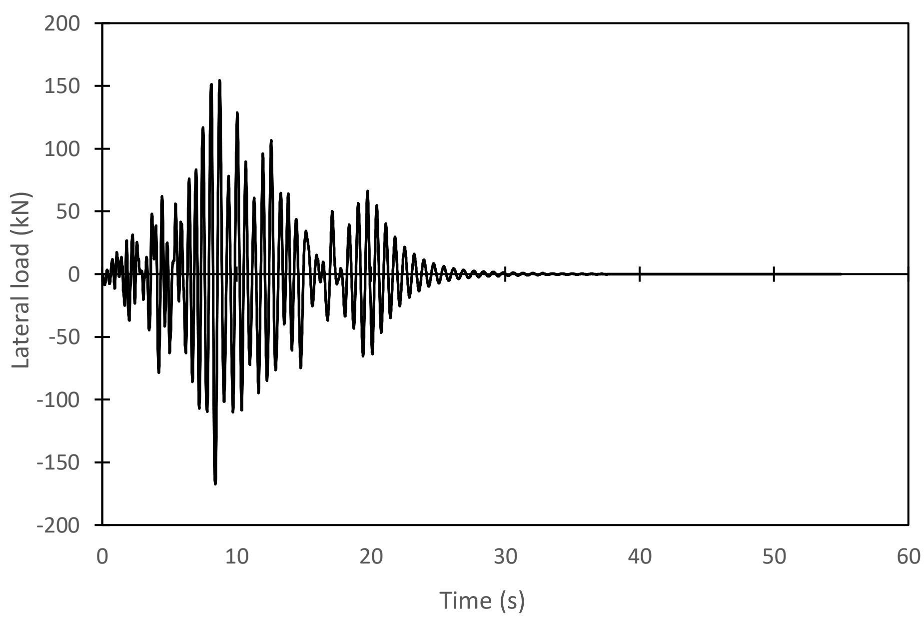

Lateral load (kN)
200
150
100
50
0
-50
-100
-150
-200
0
10
20
30
40
50
60
Time (s)

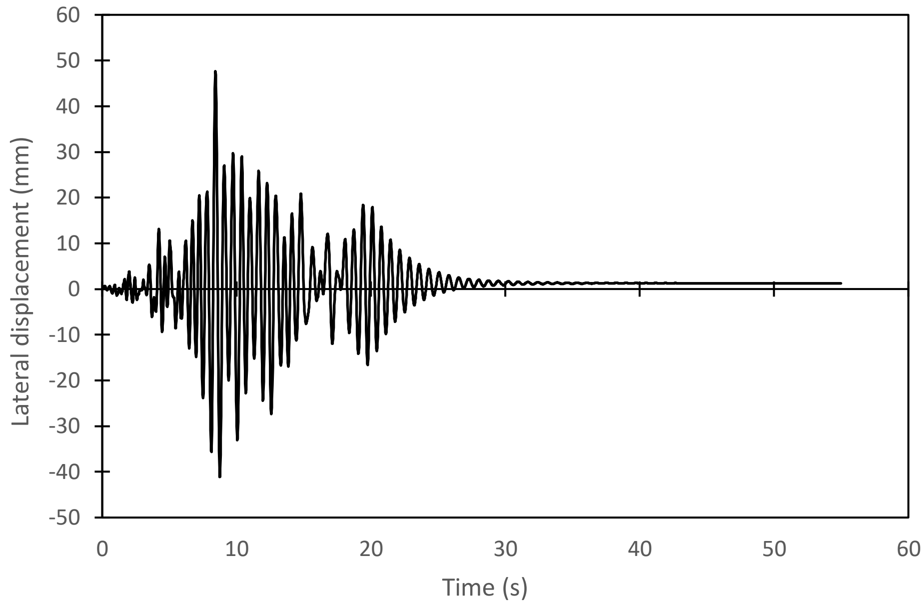

Lateral displacement (mm)
Time (s)
60
50
40
30
20
10
0
-10
-20
-30
-40
-50
0
10
20
30
40
50
60

9. TR2-3

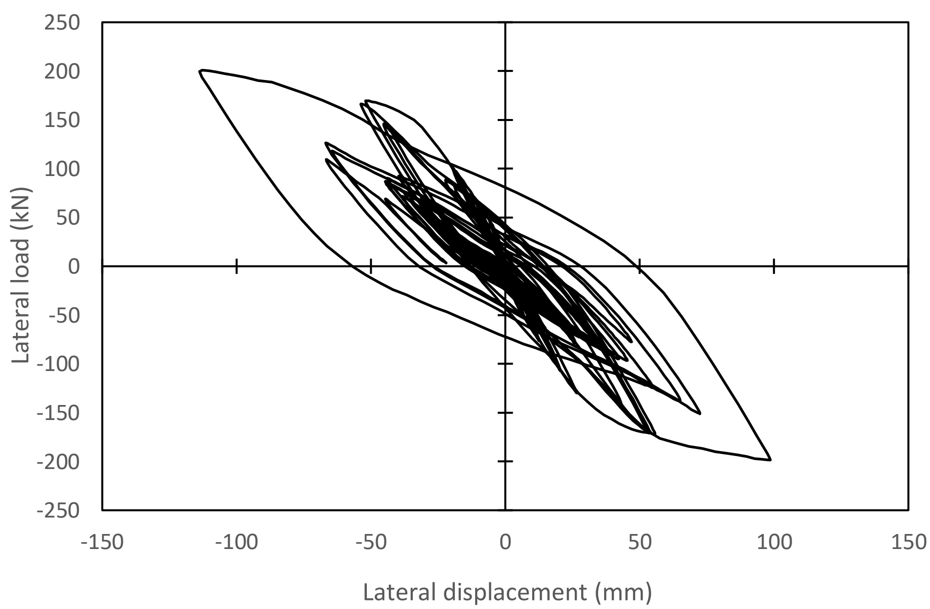

Lateral load (kN)
Lateral displacement (mm)
250
200
150
100
50
0
-50
-100
-150
-200
-250
-150
-100
-50
0
50
100
150

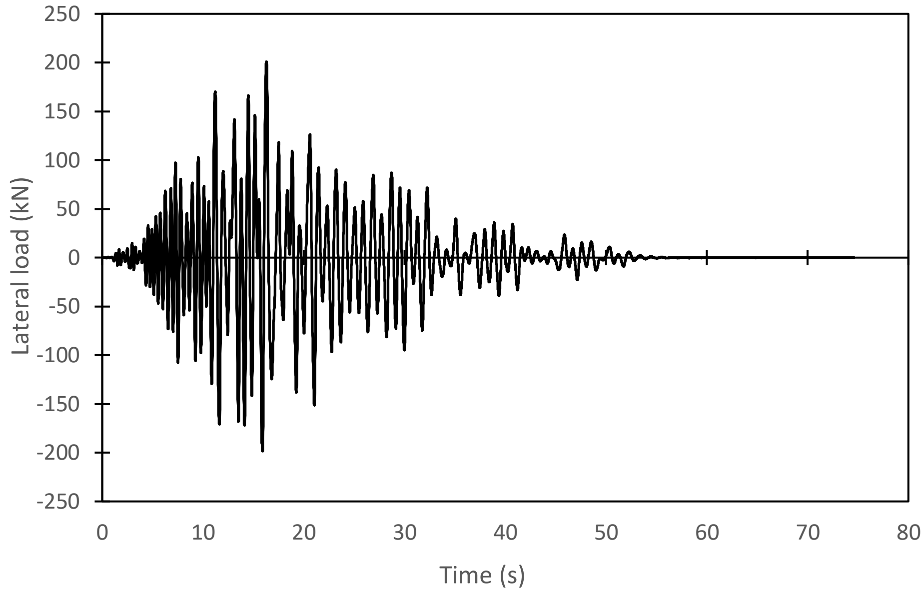
250
200
150
100
50
0
-50
-100
-150
-200
-250
Lateral load (kN)
0
10
20
30
40
50
60
70
80
Time (s)

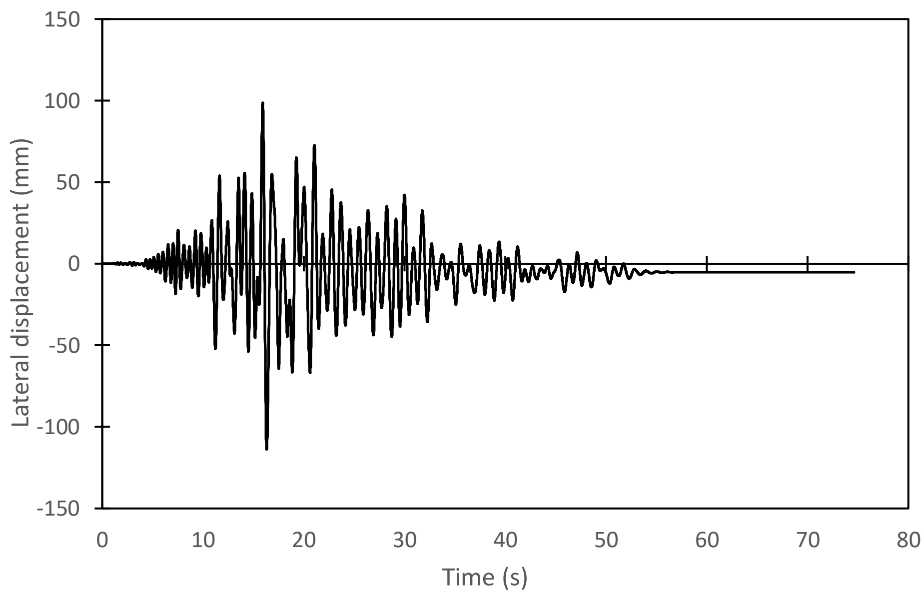
150
100
50
0
-50
-100
-150
Lateral displacement (mm)
0
10
20
30
40
50
60
70
80
Time (s)

10. TR2-4

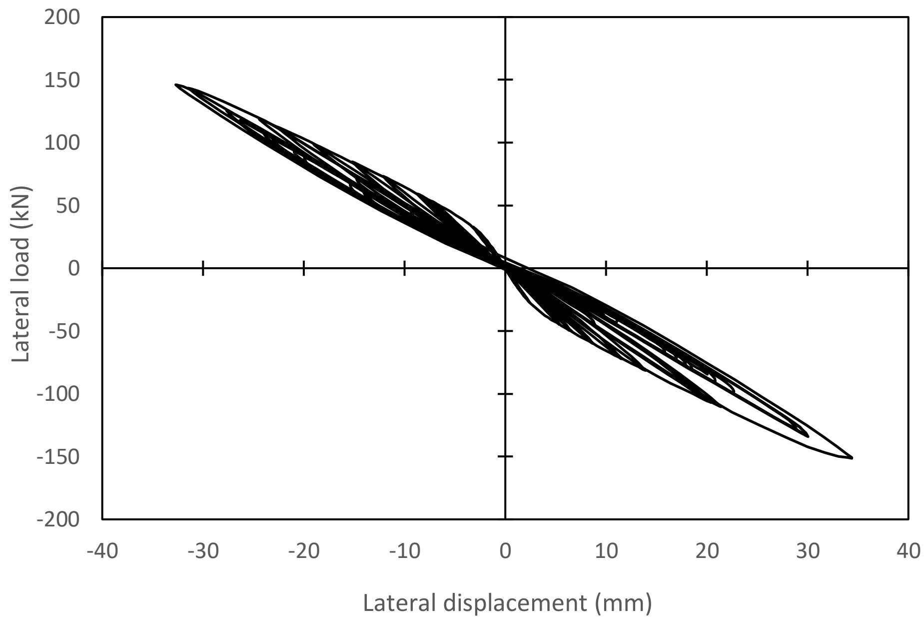

200
150
100
50
0
-50
-100
-150
-200
-40
-30
-20
-10
0
10
20
30
40
Lateral load (kN)
Lateral displacement (mm)

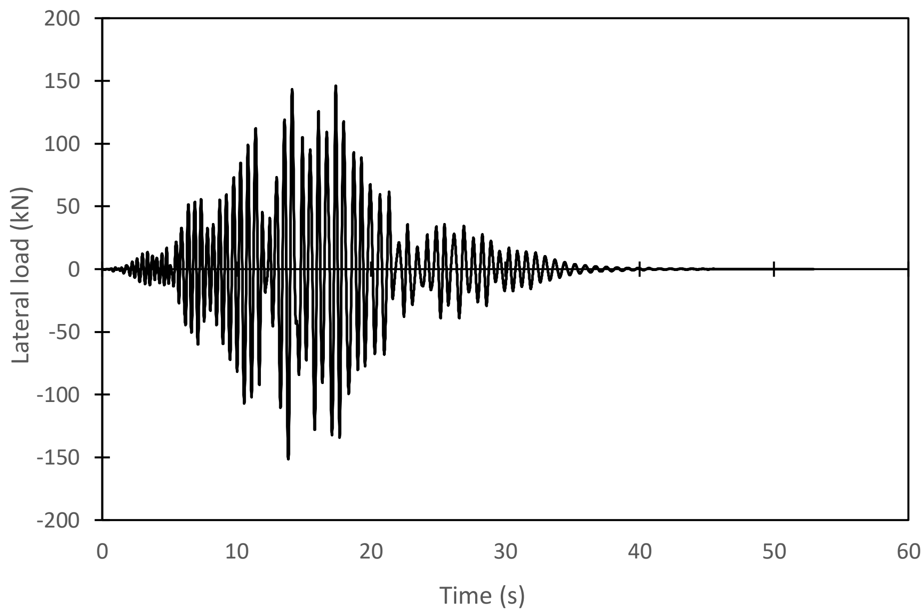

200
150
100
50
0
-50
-100
-150
-200
0
10
20
30
40
50
60
Lateral load (kN)
Time (s)

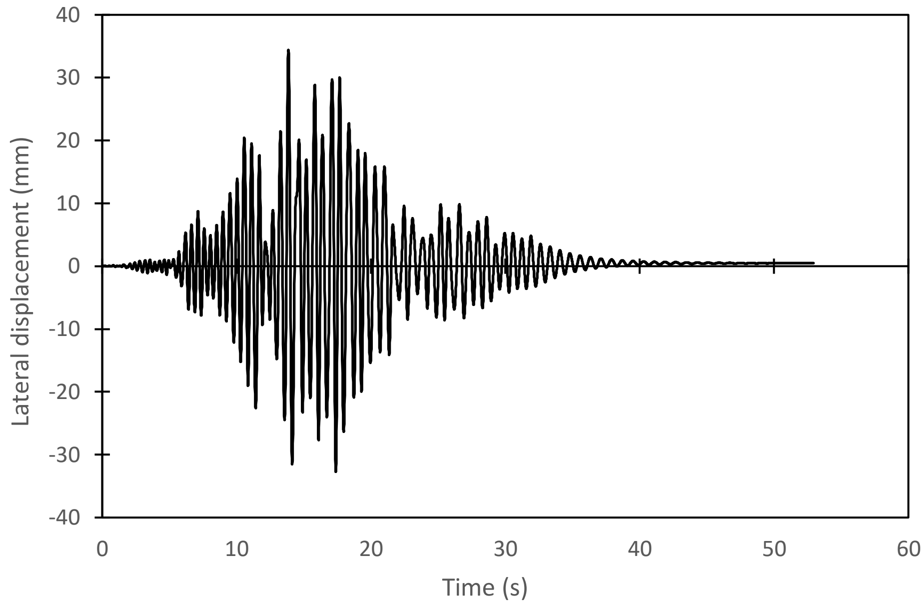
40
30
20
10
0
-10
-20
-30
-40
0
10
20
30
40
50
60
Lateral displacement (mm)
Time (s)

11. TR2-5

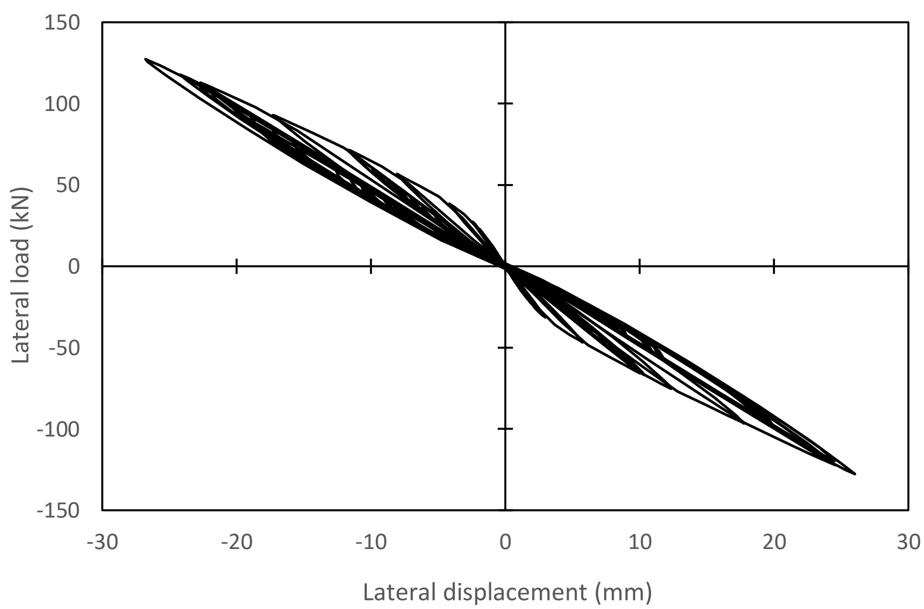
150
100
50
0
-50
-100
-150
-30
-20
-10
0
10
20
30
Lateral load (kN)
Lateral displacement (mm)

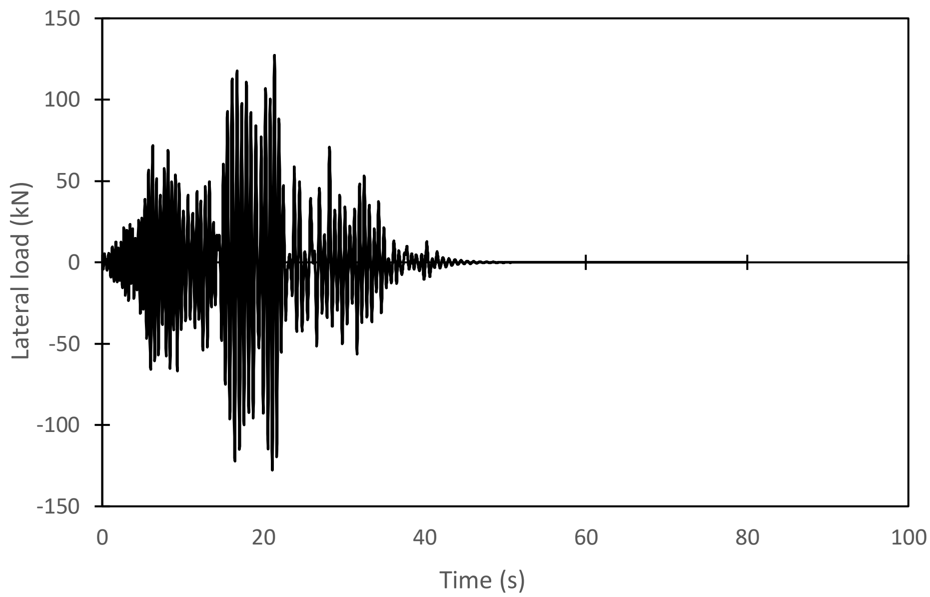
150
100
50
0
-50
-100
-150
Lateral load (kN)
0
20
40
60
80
100
Time (s)

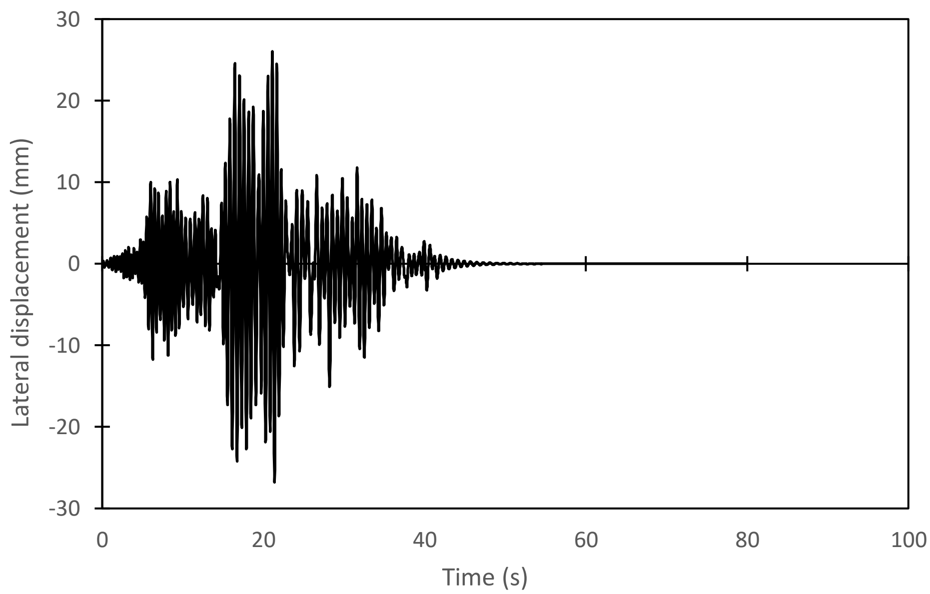
30
20
10
0
-10
-20
-30
Lateral displacement (mm)
0
20
40
60
80
100
Time (s)

B) Earthquake records Vancouver – BC

12. TR1-1

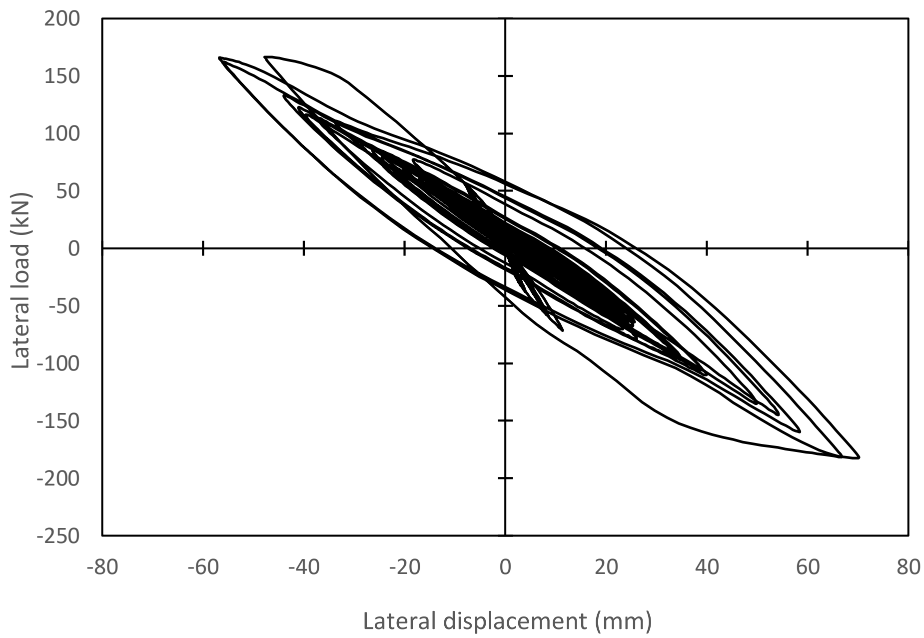

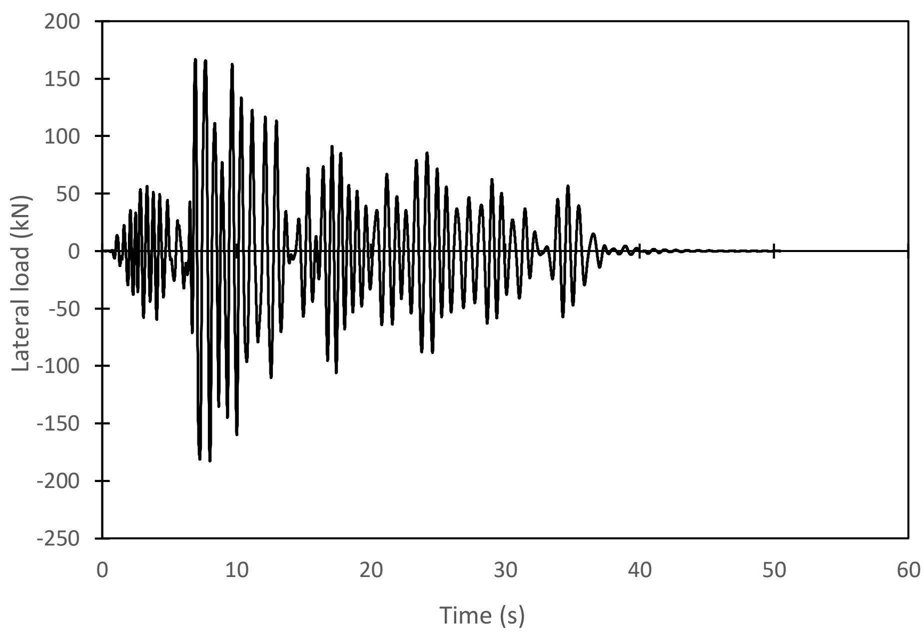

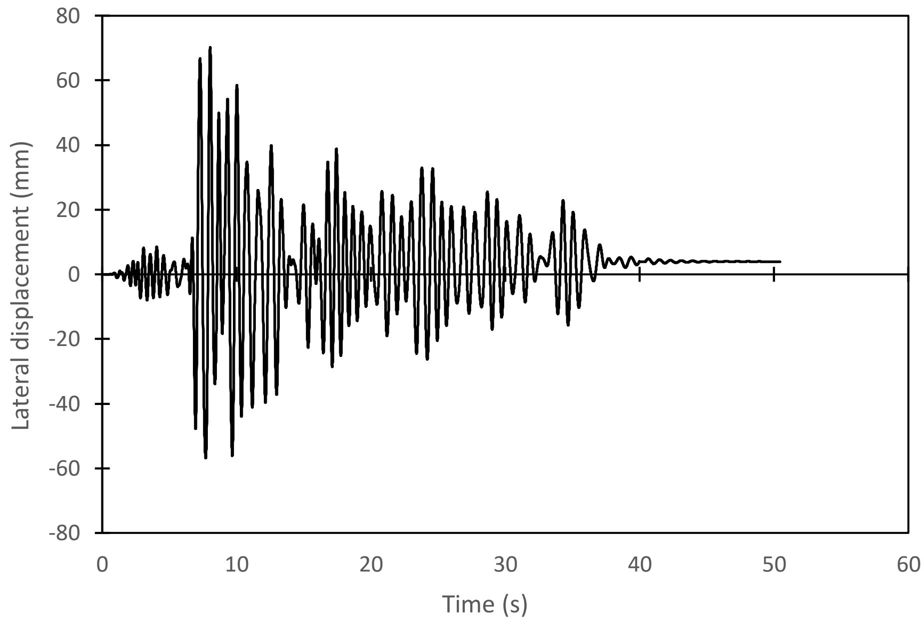
Lateral displacement (mm)
80
60
40
20
0
-20
-40
-60
-80
0
10
20
30
40
50
60
Time (s)

13. TR1-2

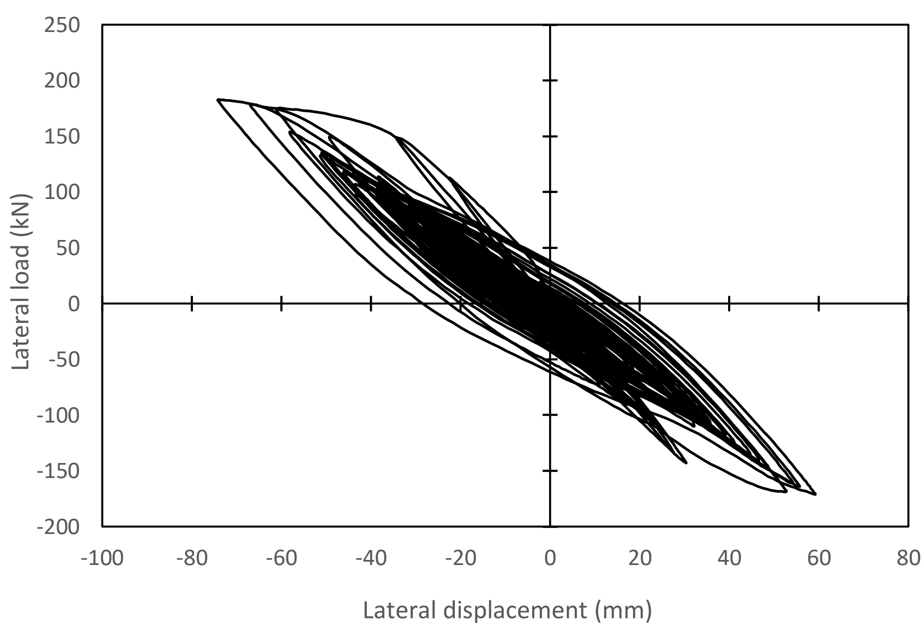
Lateral load (kN)
250
200
150
100
50
0
-50
-100
-150
-200
-100
-80
-60
-40
-20
0
20
40
60
80
Lateral displacement (mm)

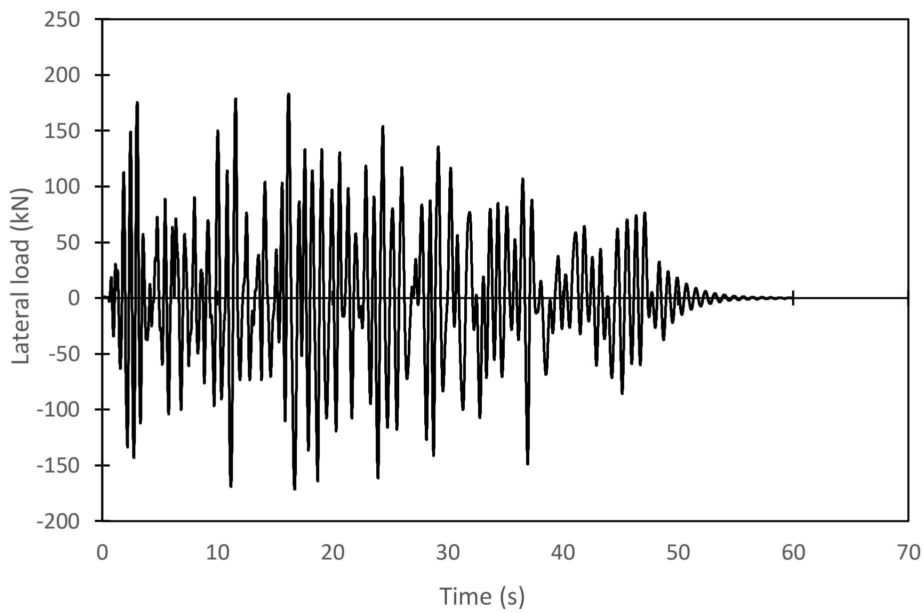
Lateral load (kN)
Time (s)
250
200
150
100
50
0
-50
-100
-150
-200
0
10
20
30
40
50
60
70

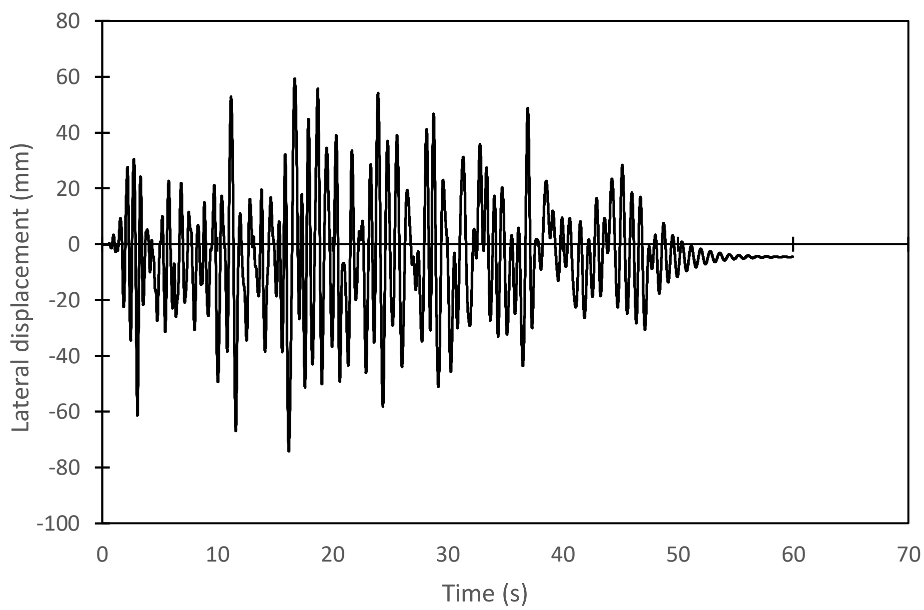
Lateral displacement (mm)
Time (s)
80
60
40
20
0
-20
-40
-60
-80
-100
0
10
20
30
40
50
60
70

14. TR1-3

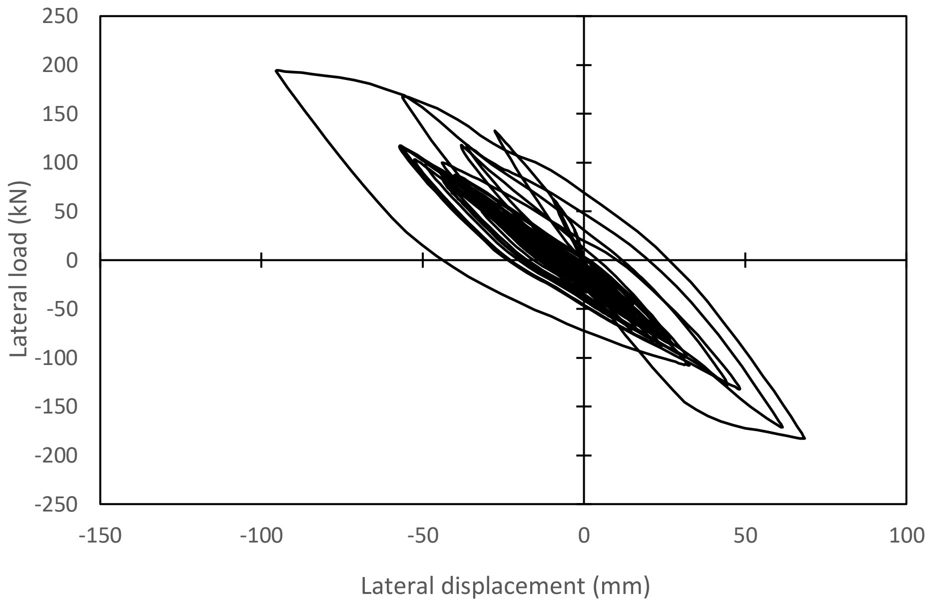
250
200
150
100
50
0
-50
-100
-150
-200
-250
Lateral load (kN)
-150
-100
-50
0
50
100
Lateral displacement (mm)

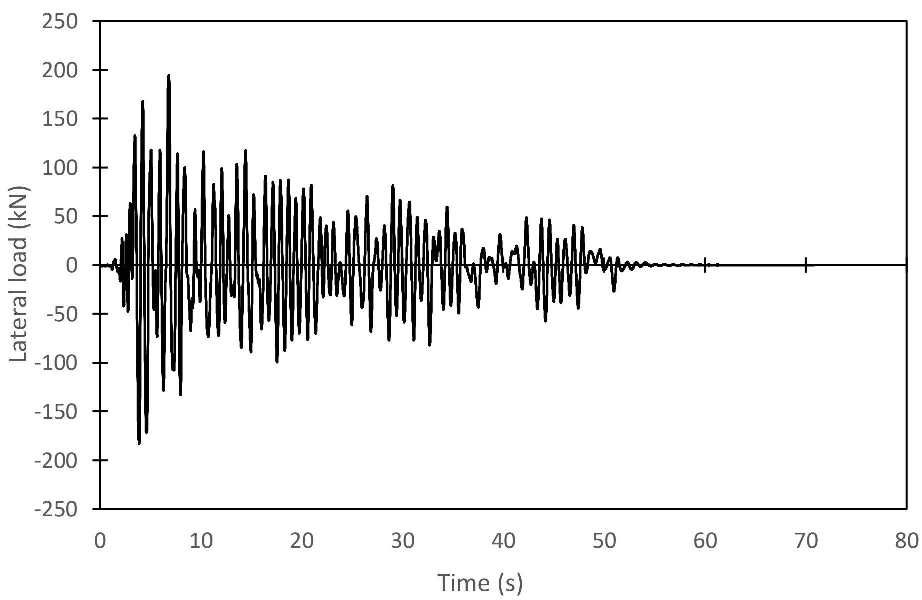
250
200
150
100
50
0
-50
-100
-150
-200
-250
Lateral load (kN)
0
10
20
30
40
50
60
70
80
Time (s)

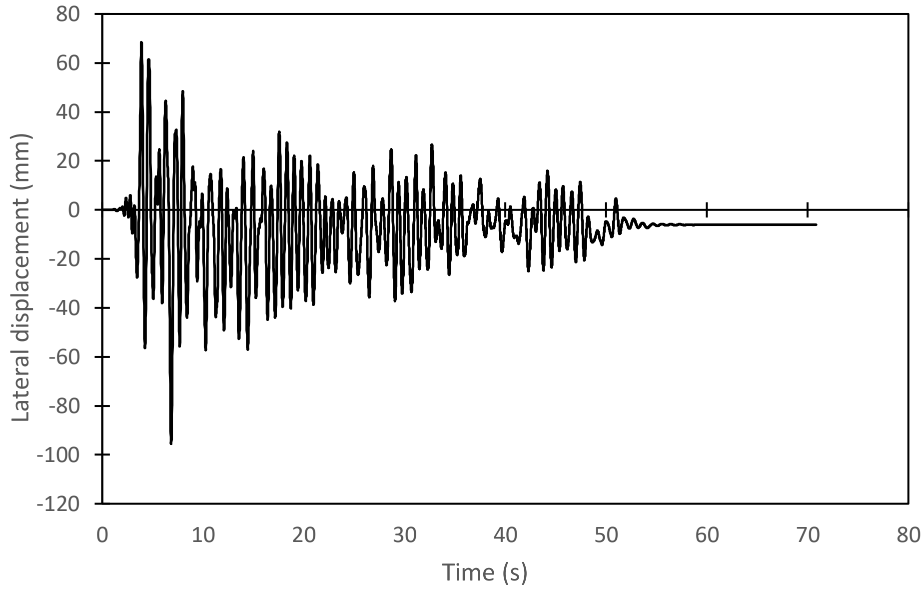
Lateral displacement (mm)
Time (s)
80
60
40
20
0
-20
-40
-60
-80
-100
-120
0
10
20
30
40
50
60
70
80

15. TR1-4

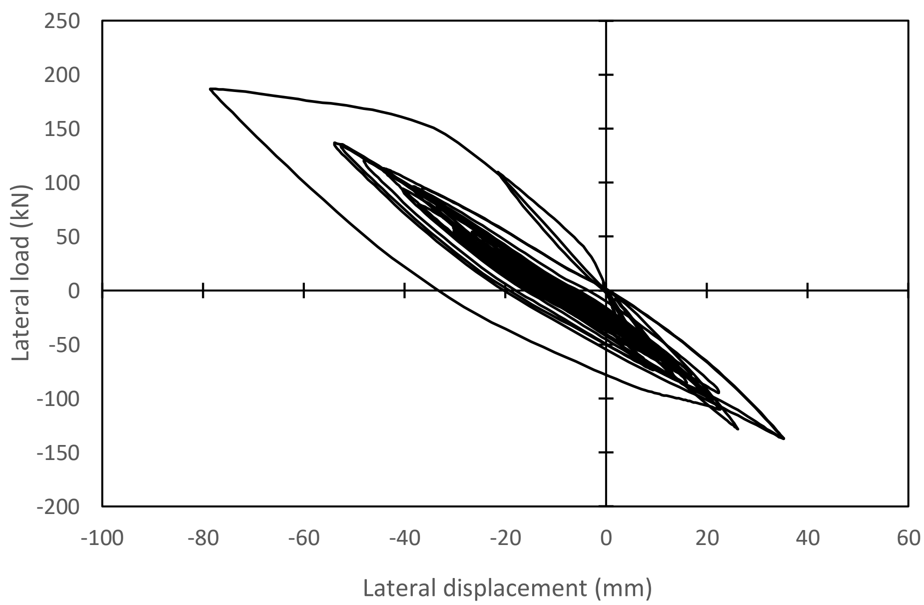
Lateral load (kN)
Lateral displacement (mm)
250
200
150
100
50
0
-50
-100
-150
-200
-100
-80
-60
-40
-20
0
20
40
60

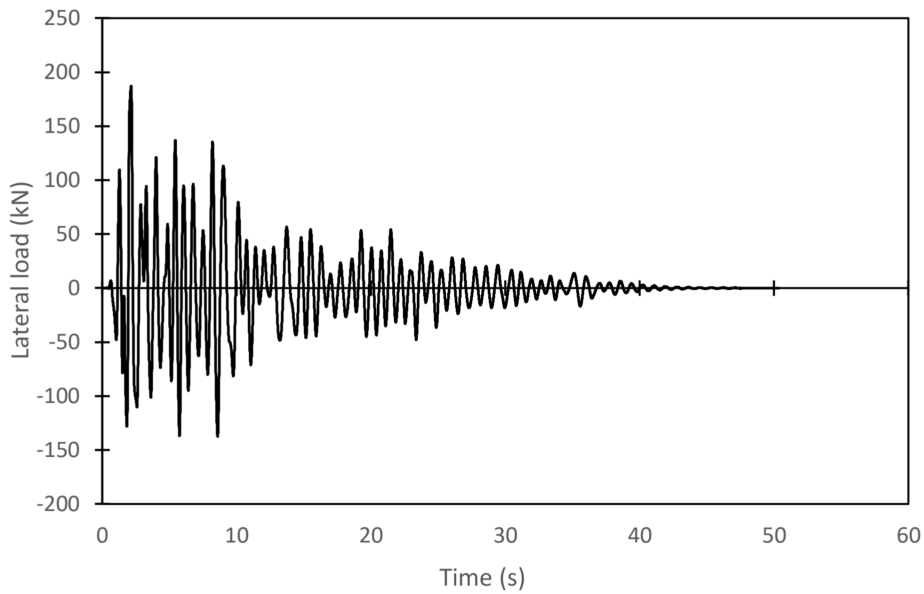
250
200
150
100
50
0
-50
-100
-150
-200
Lateral load (kN)
0
10
20
30
40
50
60
Time (s)

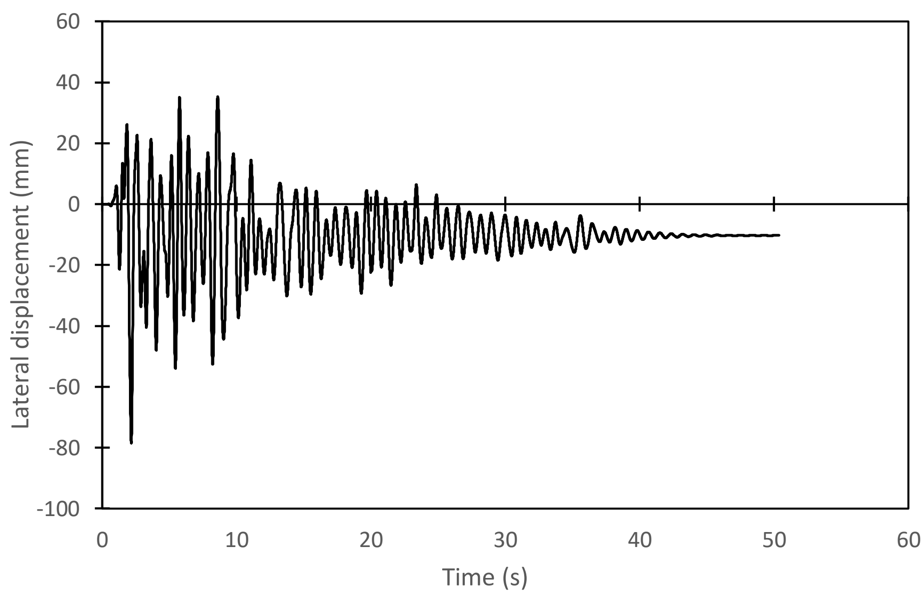
60
40
20
0
-20
-40
-60
-80
-100
Lateral displacement (mm)
0
10
20
30
40
50
60
Time (s)

16. TR2-1

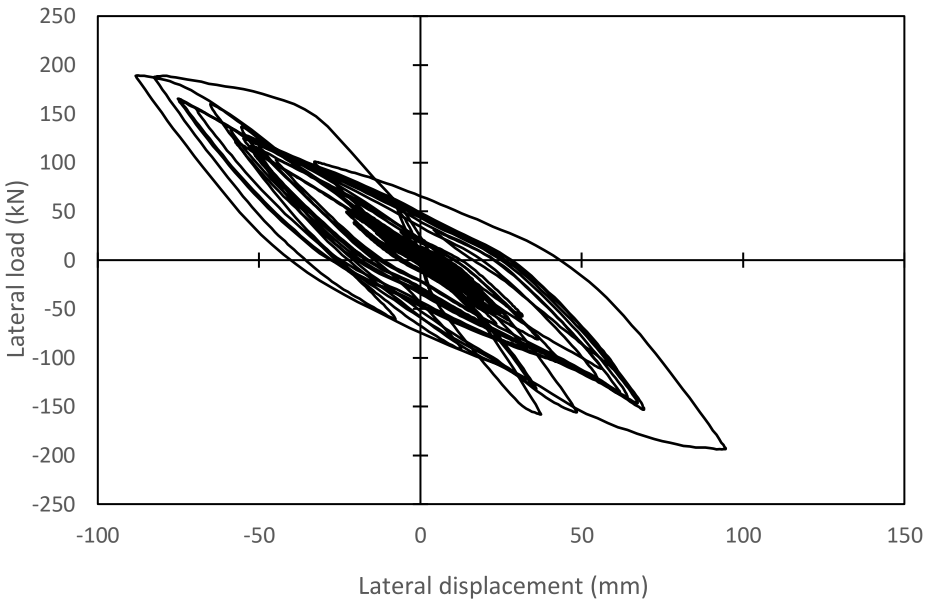
250
200
150
100
50
0
-50
-100
-150
-200
-250
Lateral load (kN)
-100
-50
0
50
100
150
Lateral displacement (mm)

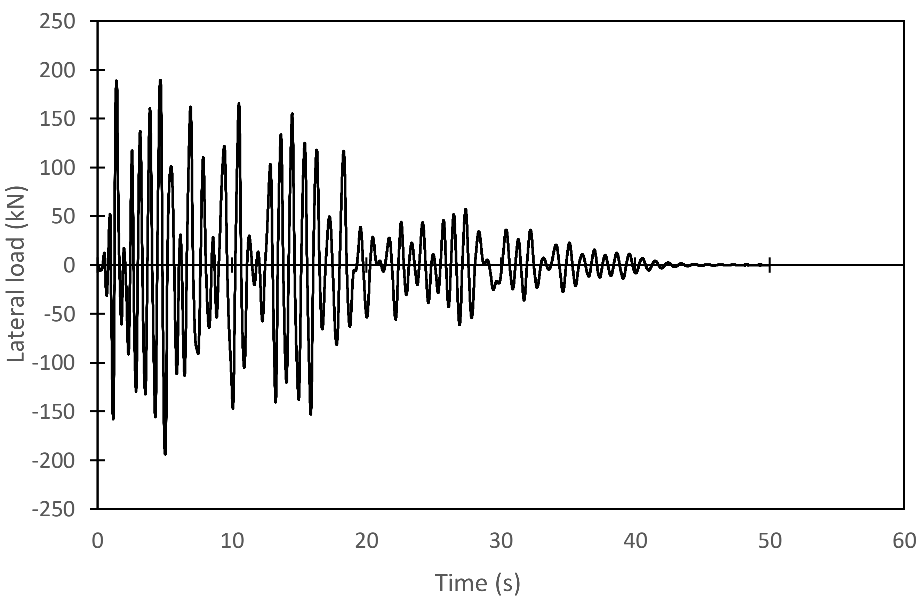
250
200
150
100
50
0
-50
-100
-150
-200
-250
Lateral load (kN)
0
10
20
30
40
50
60
Time (s)

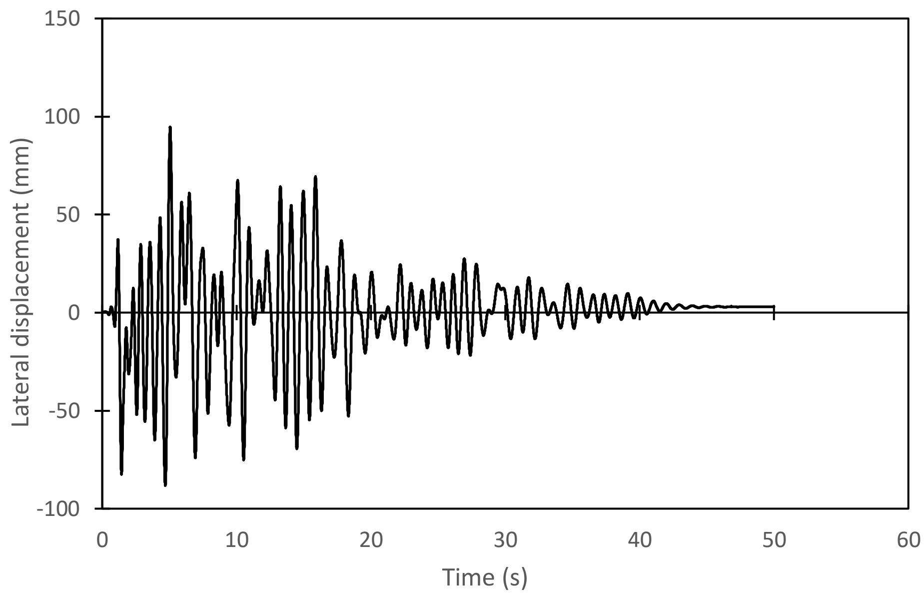
Lateral displacement (mm)
Time (s)
150
100
50
0
-50
-100
0
10
20
30
40
50
60

17. TR2-2

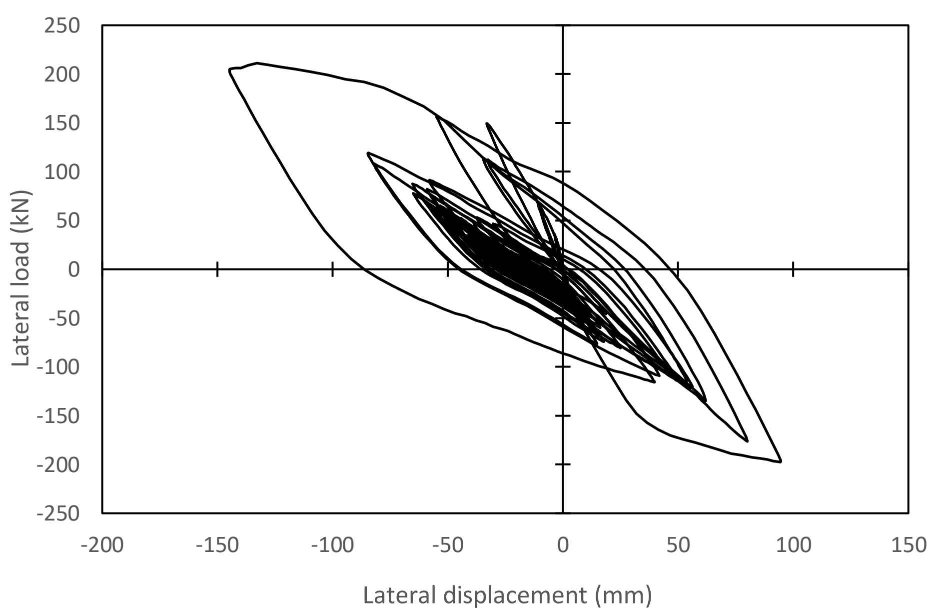
Lateral load (kN)
Lateral displacement (mm)
250
200
150
100
50
0
-50
-100
-150
-200
-250
-200
-150
-100
-50
0
50
100
150

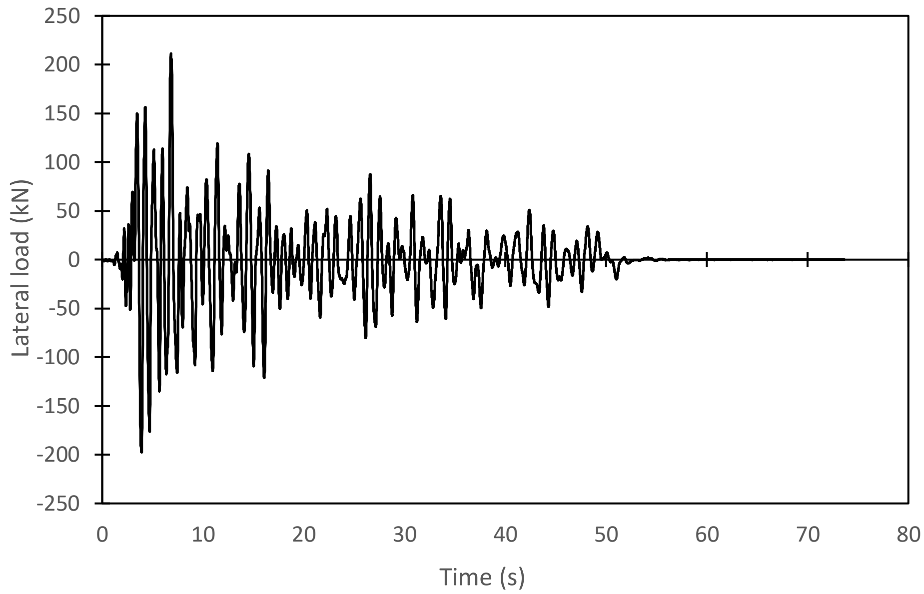
Lateral load (kN)
250
200
150
100
50
0
-50
-100
-150
-200
-250
0
10
20
30
40
50
60
70
80
Time (s)

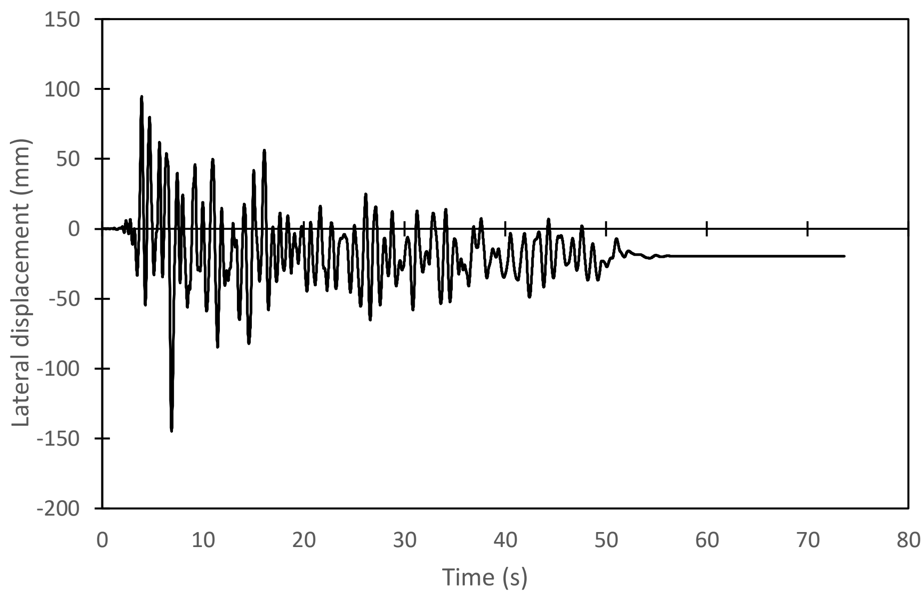
Lateral displacement (mm)
150
100
50
0
-50
-100
-150
-200
0
10
20
30
40
50
60
70
80
Time (s)

18. TR2-3

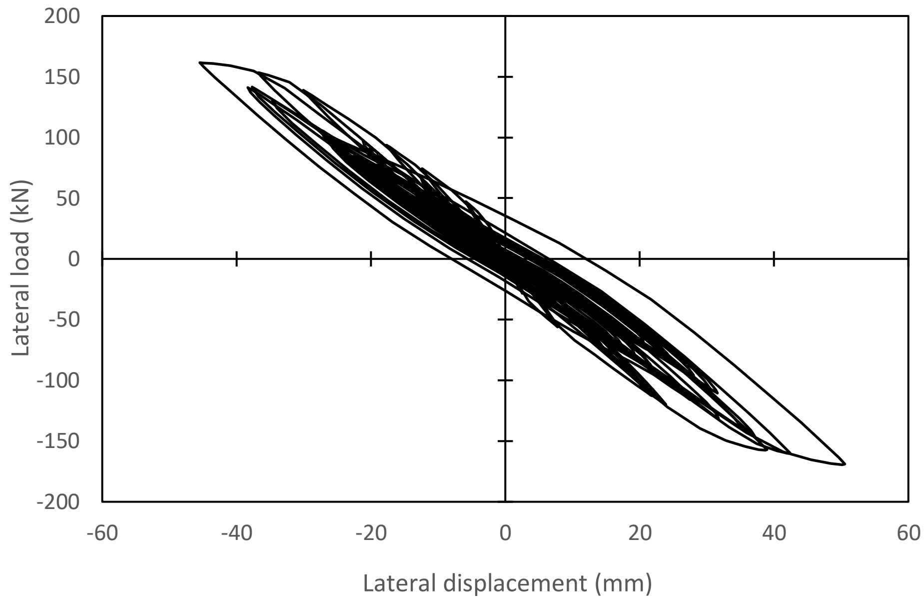
200
150
100
50
0
-50
-100
-150
-200
-60
-40
-20
0
20
40
60
Lateral load (kN)
Lateral displacement (mm)

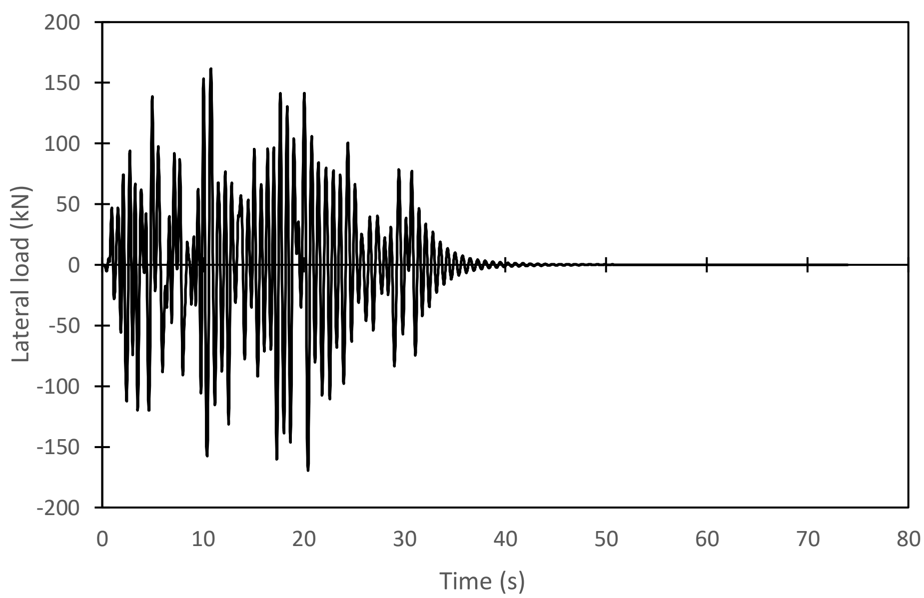
200
150
100
50
0
-50
-100
-150
-200
0
10
20
30
40
50
60
70
80
Lateral load (kN)
Time (s)

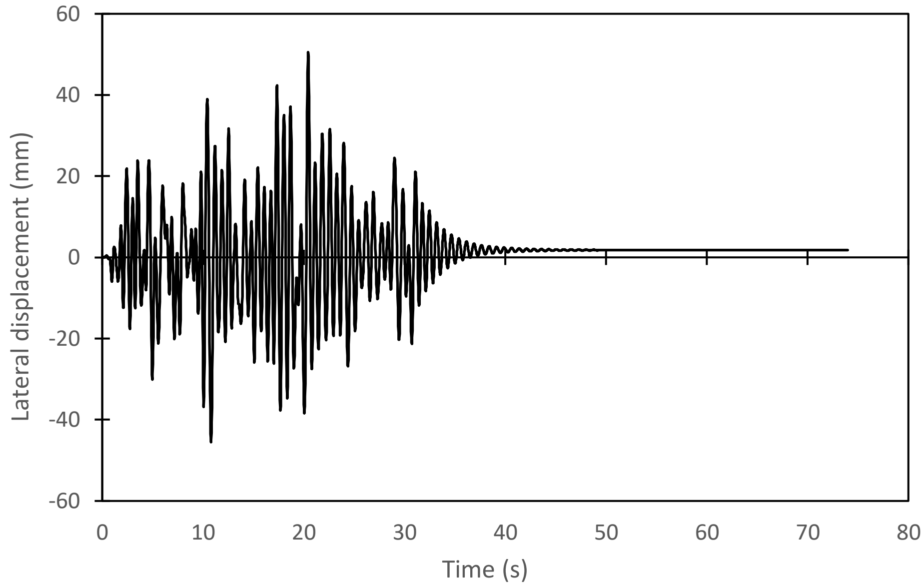
Lateral displacement (mm)
60
40
20
0
-20
-40
-60
0
10
20
30
40
50
60
70
80
Time (s)

19. TR3-1

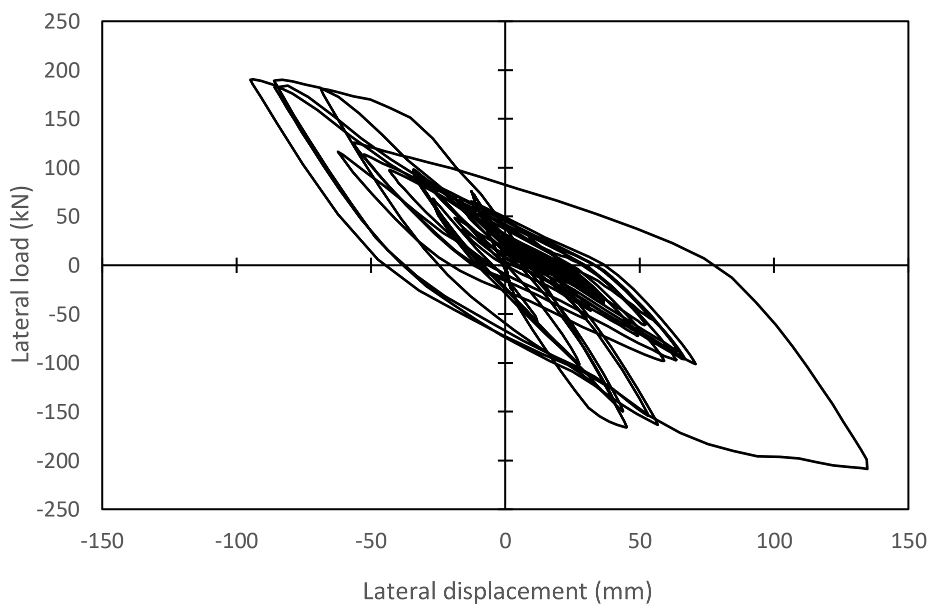
Lateral load (kN)
250
200
150
100
50
0
-50
-100
-150
-200
-250
-150
-100
-50
0
50
100
150
Lateral displacement (mm)

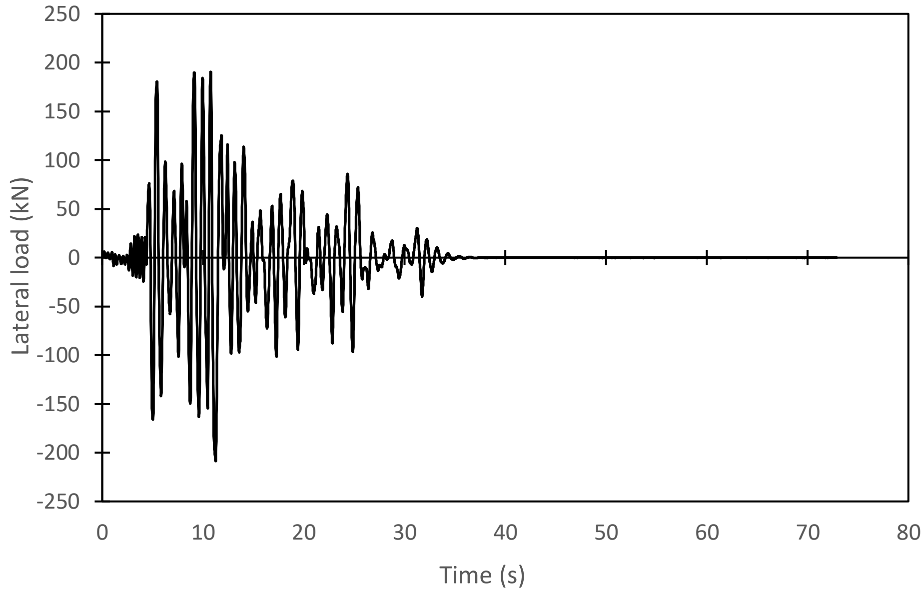

250
200
150
100
50
0
-50
-100
-150
-200
-250
Lateral load (kN)
0
10
20
30
40
50
60
70
80
Time (s)

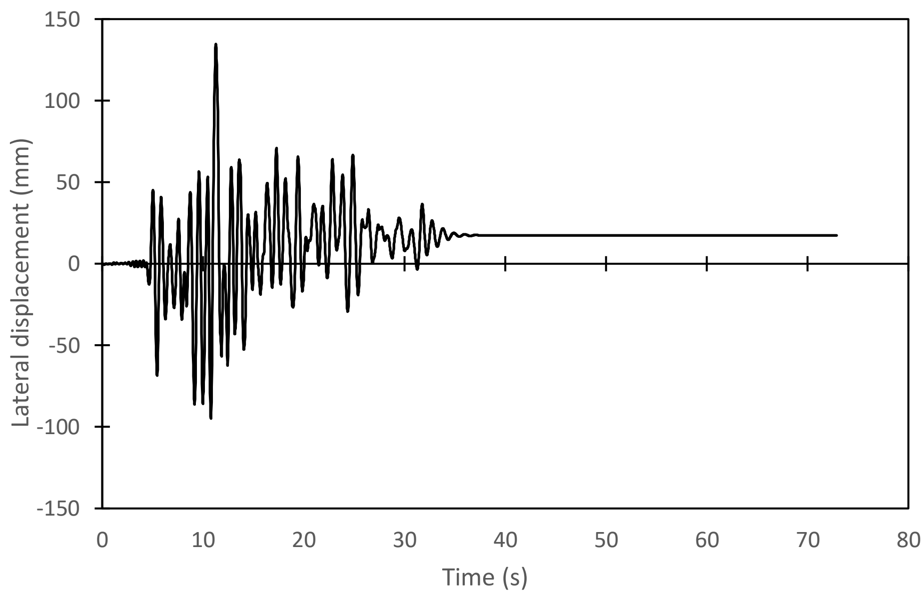

150
100
50
0
-50
-100
-150
Lateral displacement (mm)
0
10
20
30
40
50
60
70
80
Time (s)

20. TR3-2

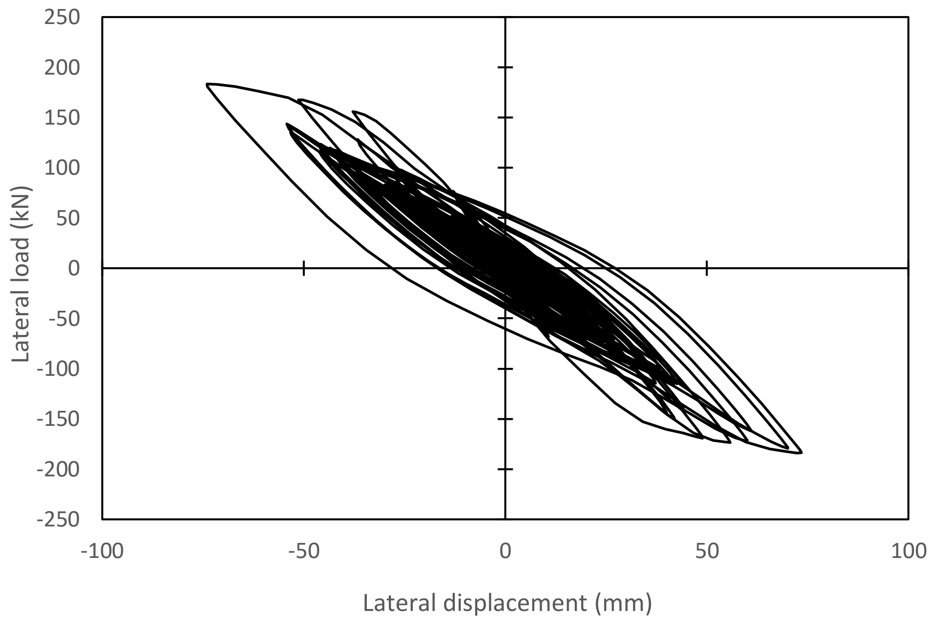
Lateral load (kN)
250
200
150
100
50
0
-50
-100
-150
-200
-250
-100
-50
0
50
100
Lateral displacement (mm)

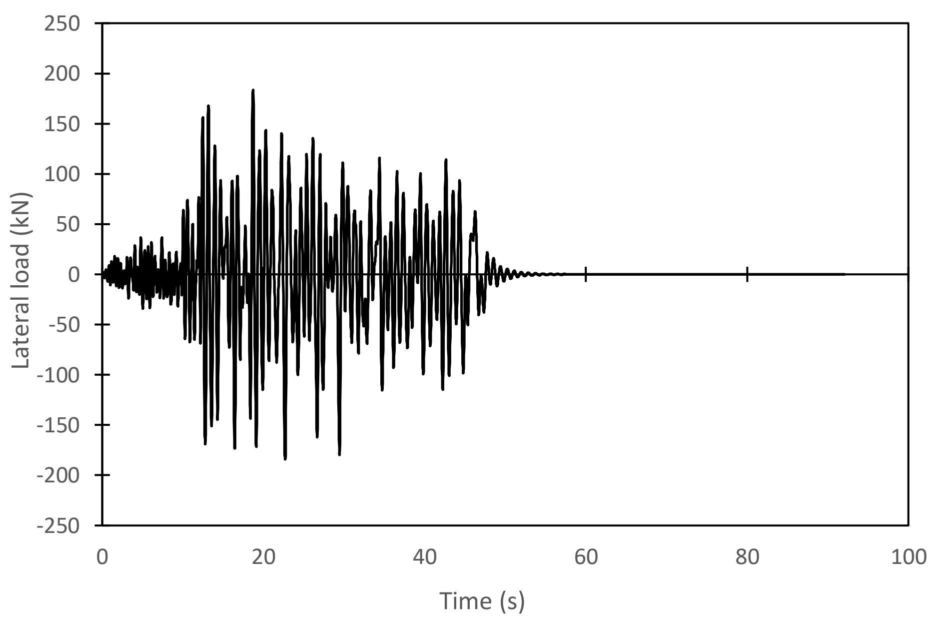
Lateral load (kN)
250
200
150
100
50
0
-50
-100
-150
-200
-250
0
20
40
60
80
100
Time (s)

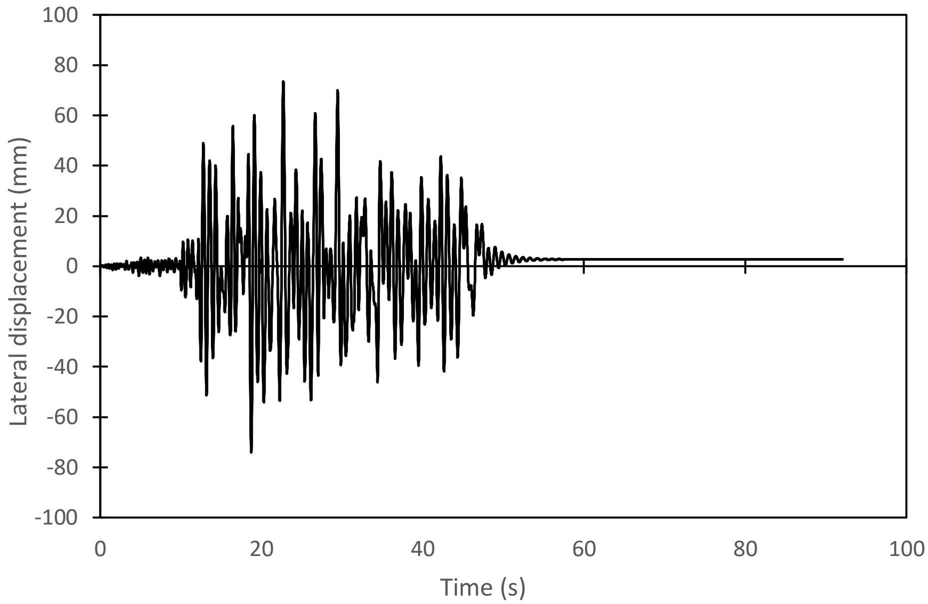
Lateral displacement (mm)
Time (s)
100
80
60
40
20
0
-20
-40
-60
-80
-100
0
20
40
60
80
100

21. TR3-3

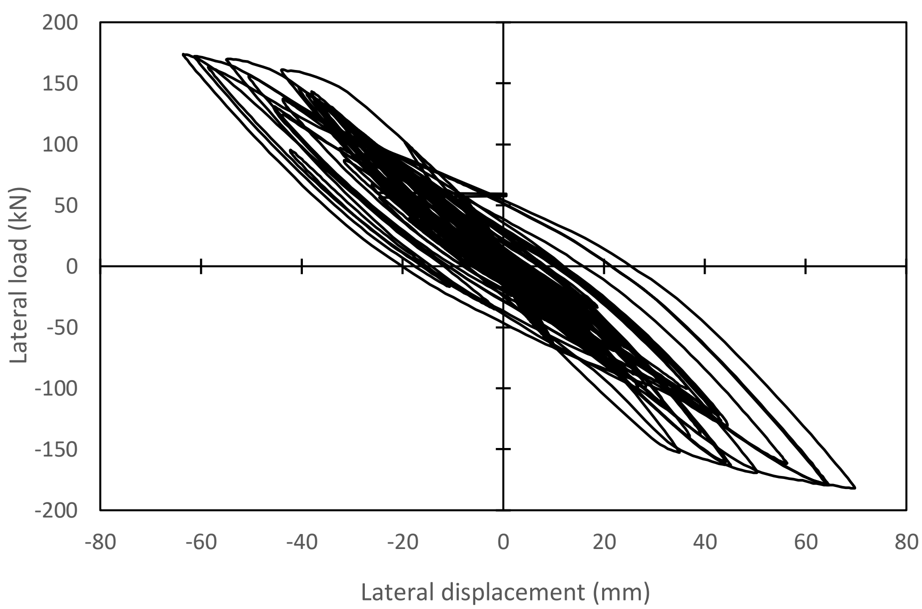
Lateral load (kN)
Lateral displacement (mm)
200
150
100
50
0
-50
-100
-150
-200
-80
-60
-40
-20
0
20
40
60
80

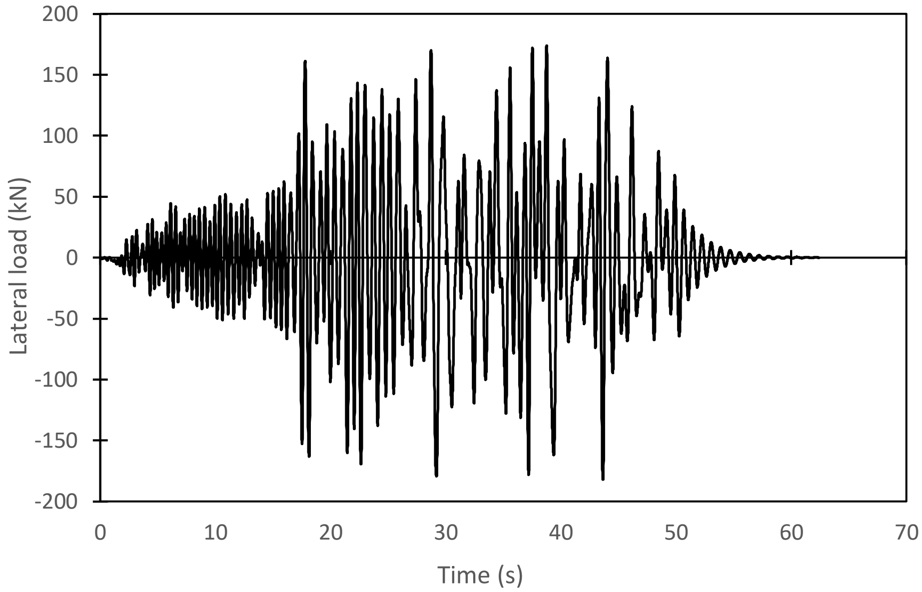
Lateral load (kN)
200
150
100
50
0
-50
-100
-150
-200
0
10
20
30
40
50
60
70
Time (s)

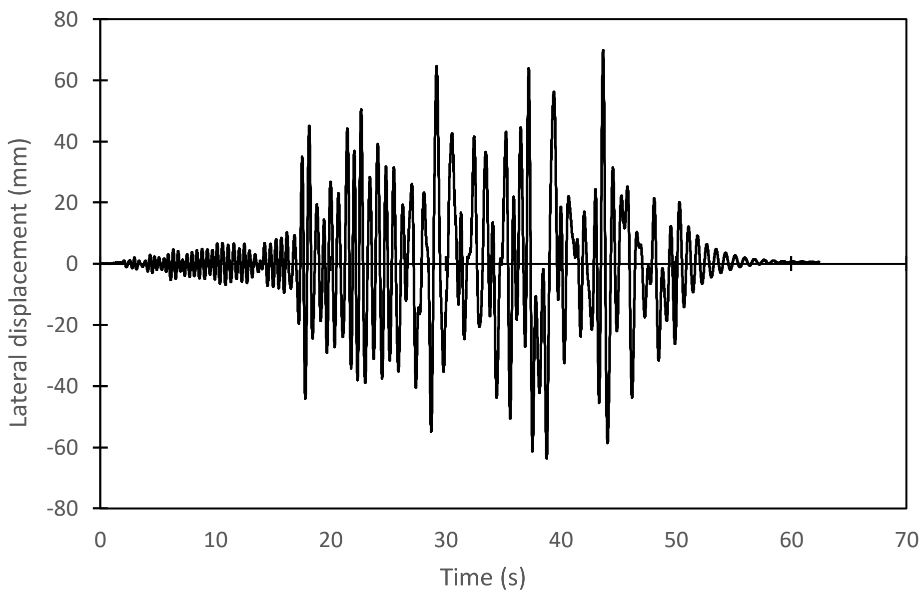
Lateral displacement (mm)
80
60
40
20
0
-20
-40
-60
-80
0
10
20
30
40
50
60
70
Time (s)

22. TR3-4

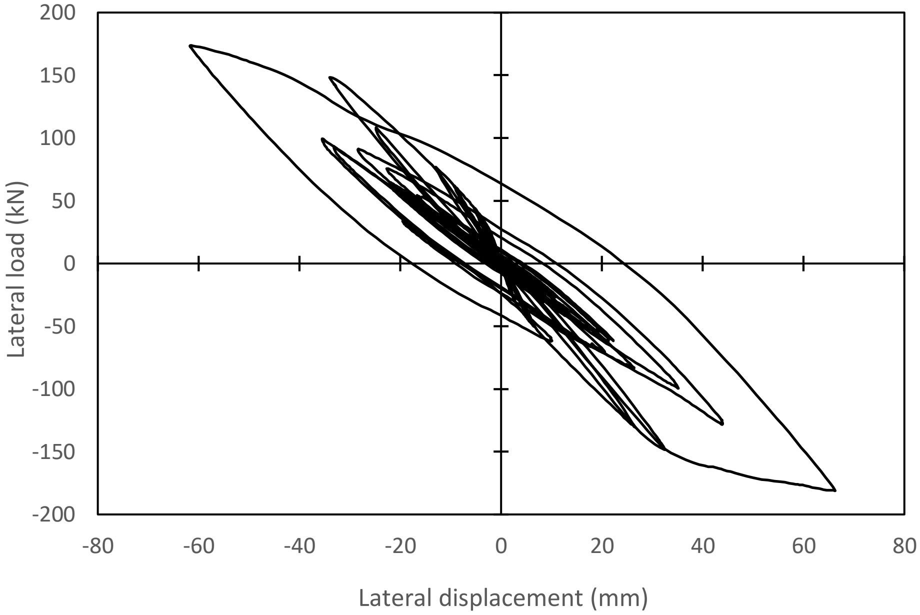
200
150
100
50
0
-50
-100
-150
-200
-80
-60
-40
-20
0
20
40
60
80
Lateral load (kN)
Lateral displacement (mm)

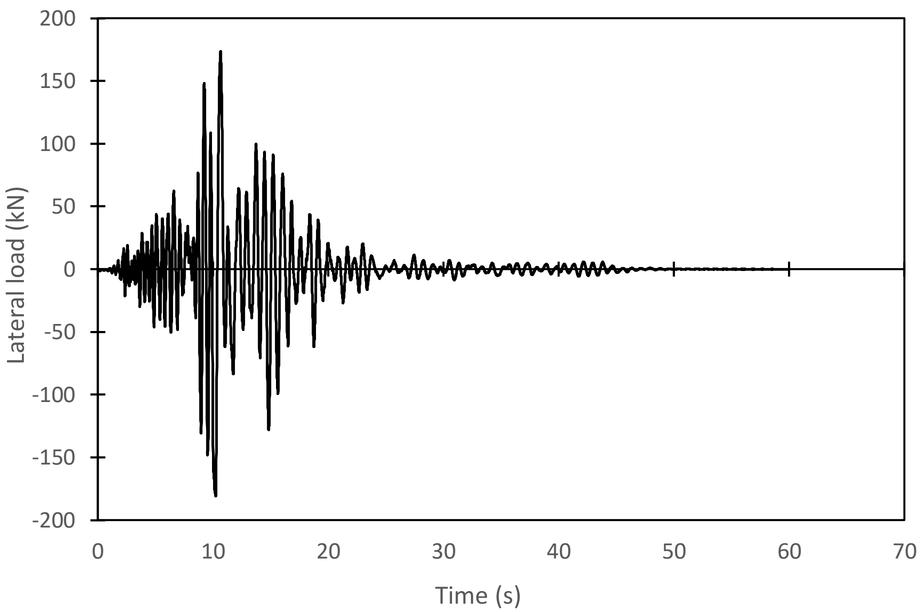
200
150
100
50
0
-50
-100
-150
-200
0
10
20
30
40
50
60
70
Lateral load (kN)
Time (s)

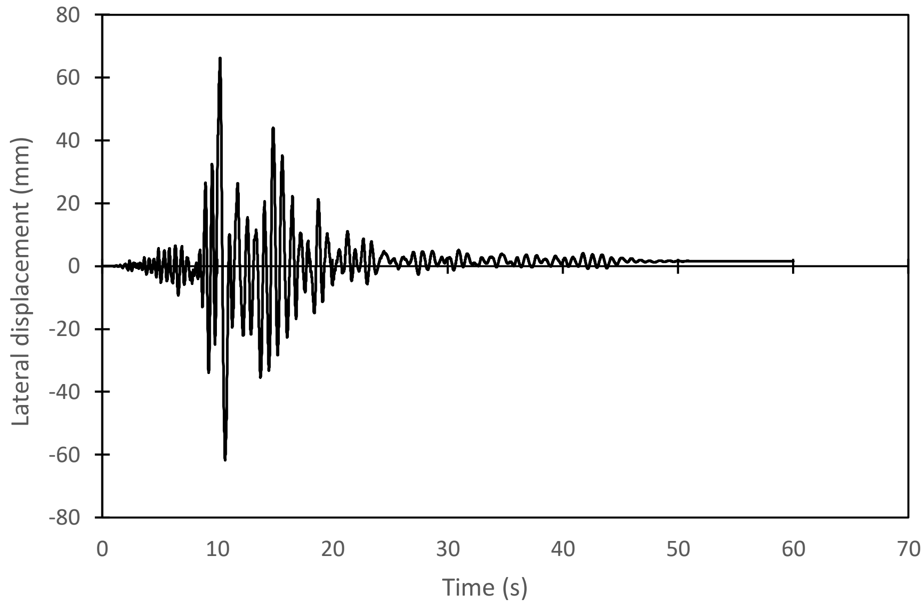

II. Dynamic response of the frame retrofitted with modified BRB incorporating SE-SMA core

A. Earthquake records Montreal – QC

23. TR1-1

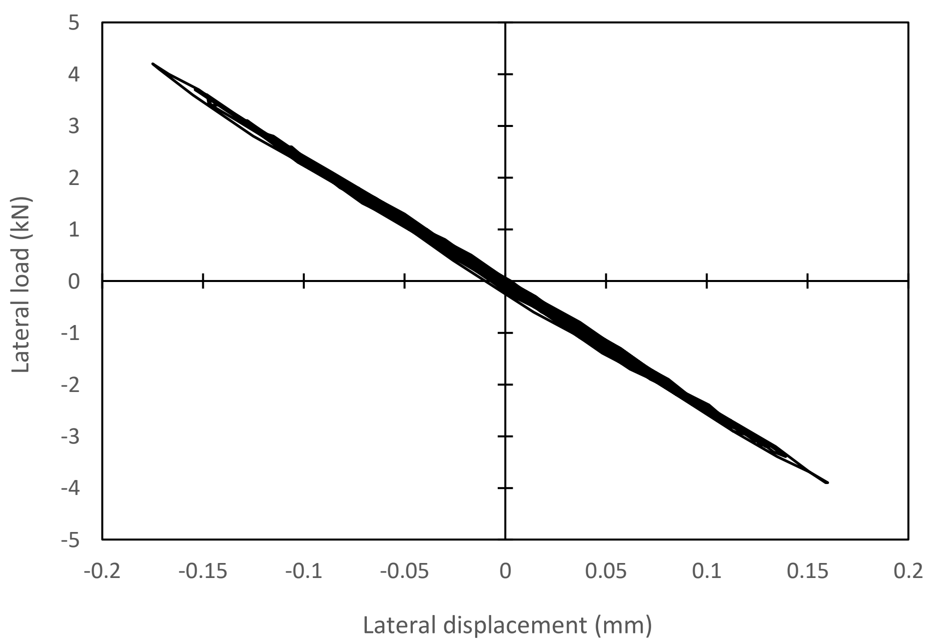

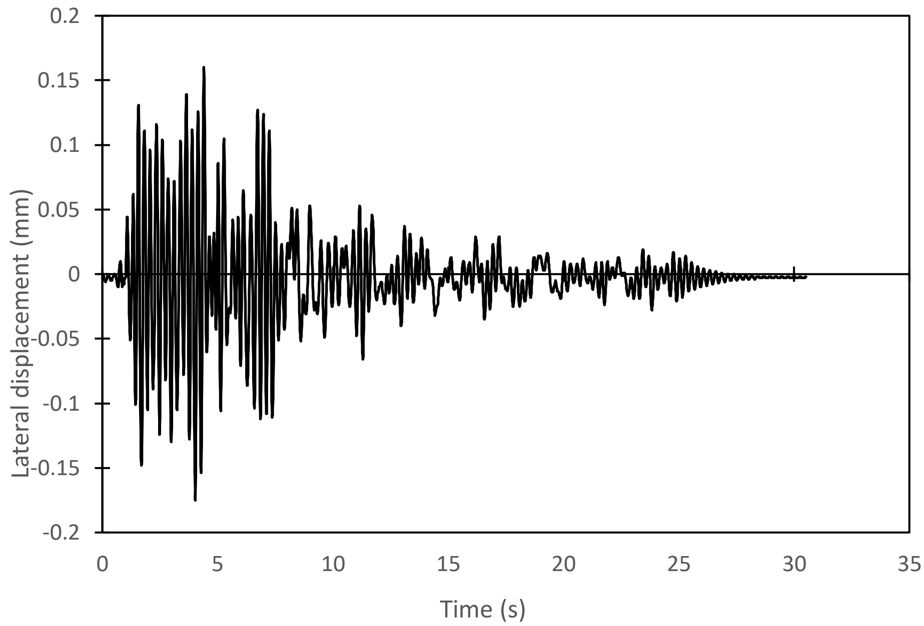
Lateral displacement (mm)
0.2
0.15
0.1
0.05
0
-0.05
-0.1
-0.15
-0.2
0
5
10
15
20
25
30
35
Time (s)

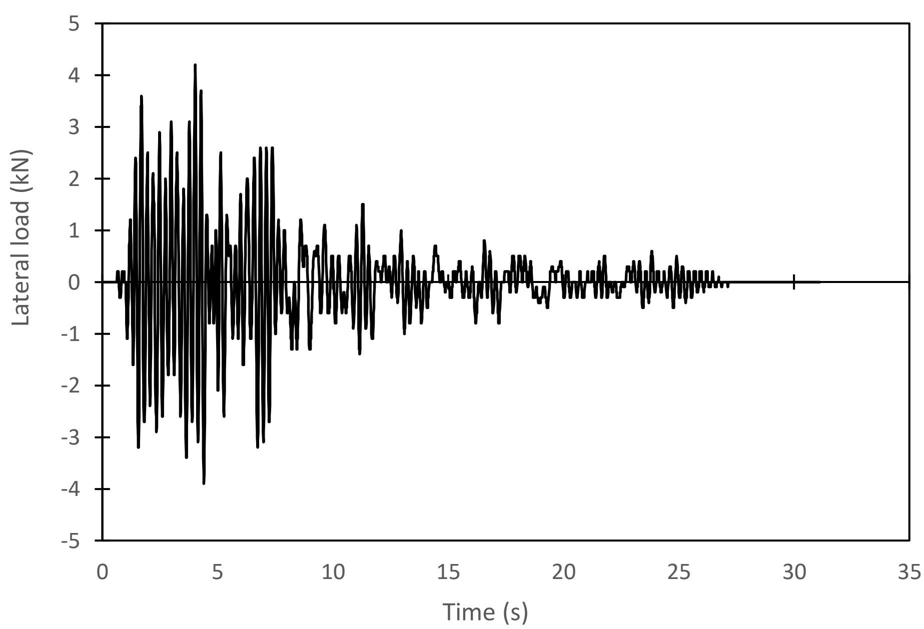
Lateral load (kN)
5
4
3
2
1
0
-1
-2
-3
-4
-5
0
5
10
15
20
25
30
35
Time (s)

24. TR1-2

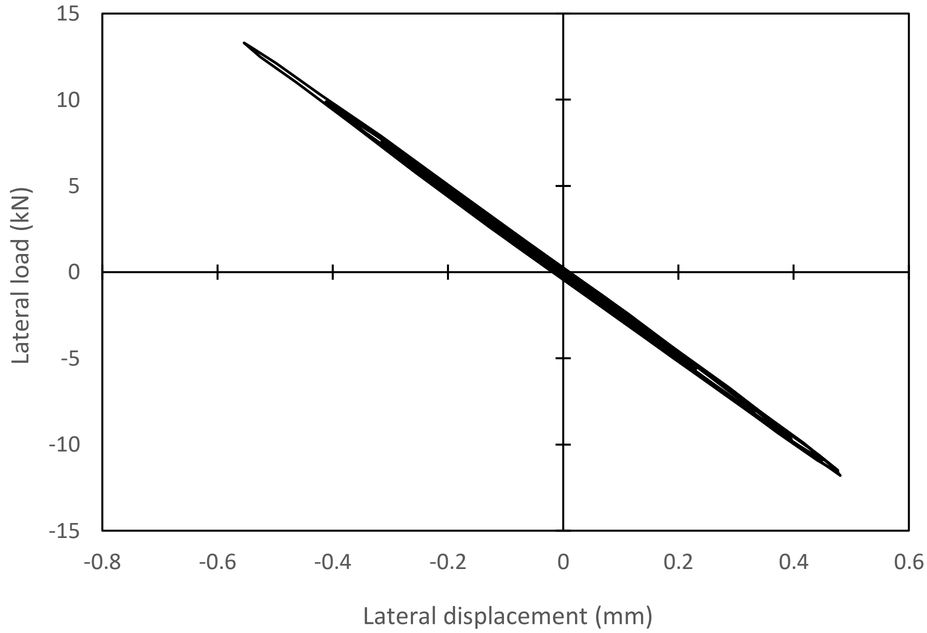
15
10
5
0
-5
-10
-15
-0.8
-0.6
-0.4
-0.2
0
0.2
0.4
0.6
Lateral load (kN)
Lateral displacement (mm)

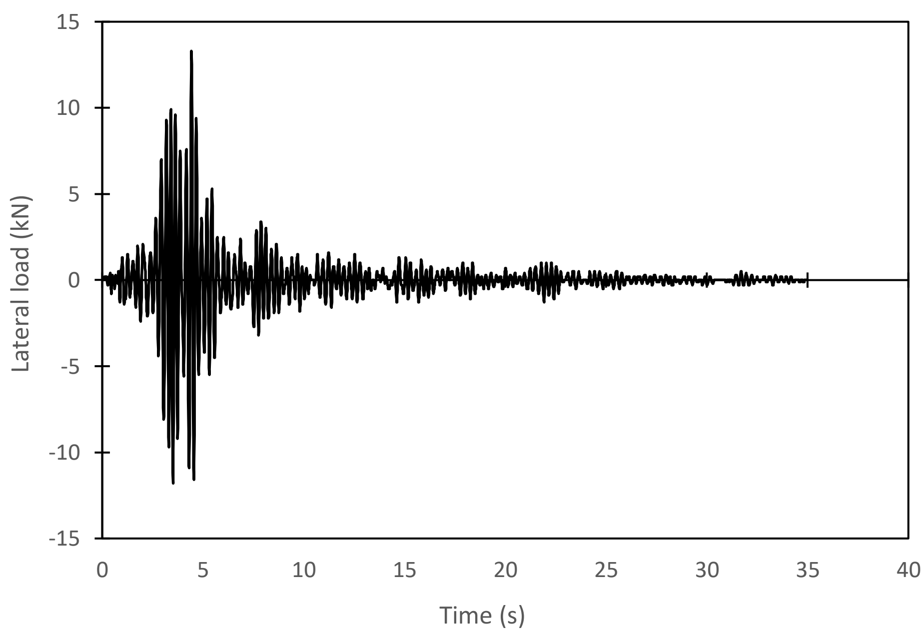
15
10
5
0
-5
-10
-15
0
5
10
15
20
25
30
35
40
Lateral load (kN)
Time (s)

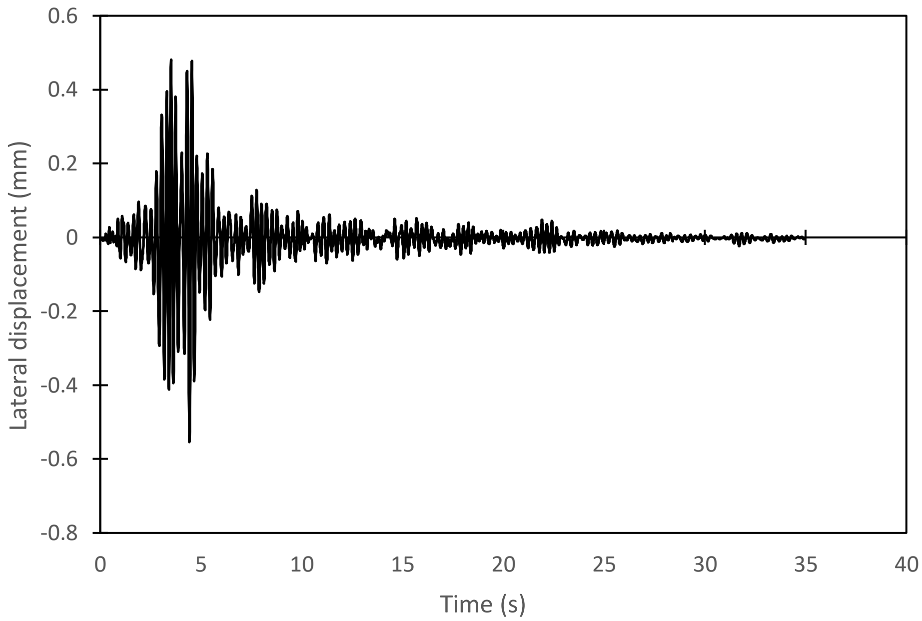
Lateral displacement (mm)
Time (s)
0.6
0.4
0.2
0
-0.2
-0.4
-0.6
-0.8
0
5
10
15
20
25
30
35
40

25. TR1-3

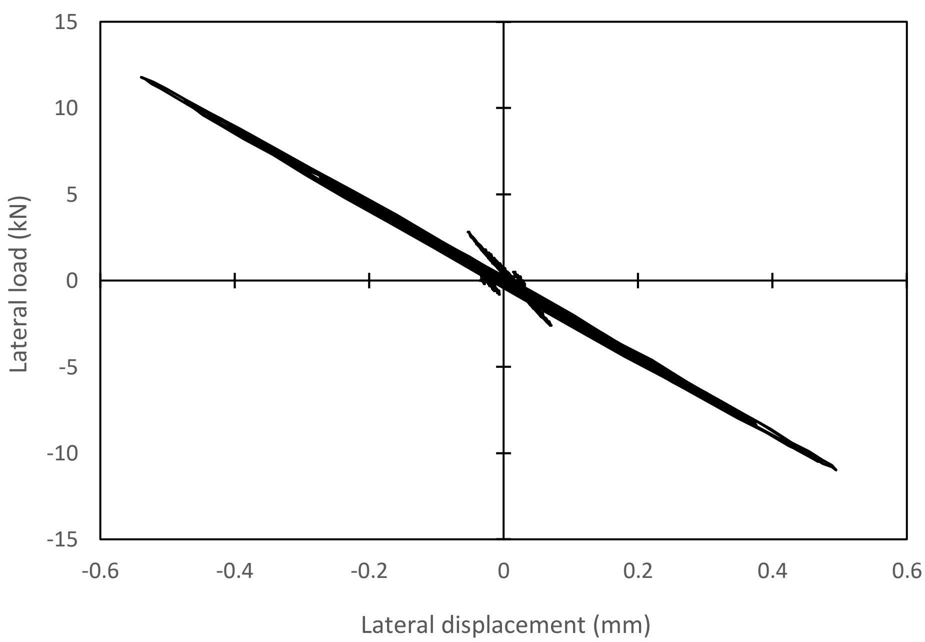
Lateral load (kN)
Lateral displacement (mm)
15
10
5
0
-5
-10
-15
-0.6
-0.4
-0.2
0
0.2
0.4
0.6

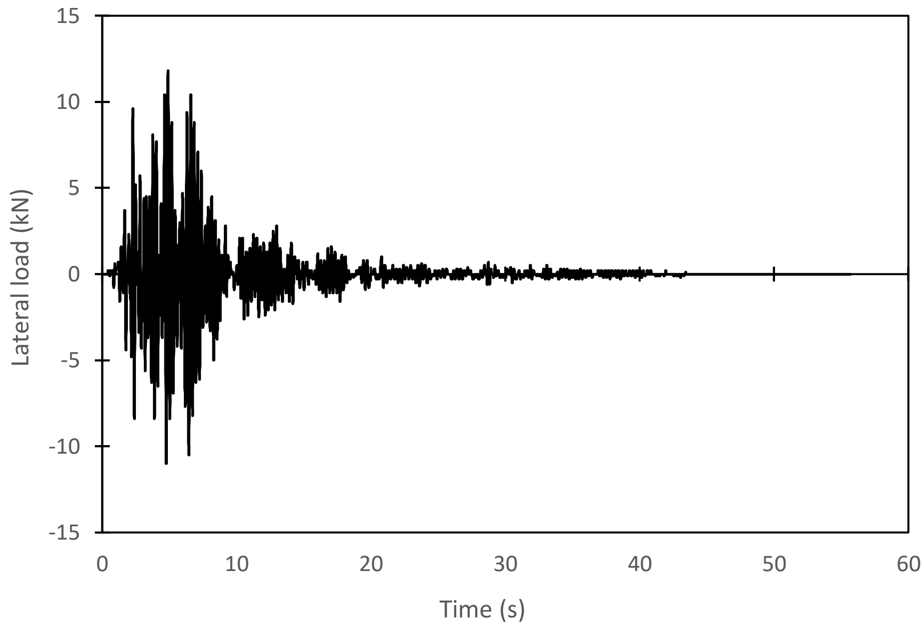

15
10
5
0
-5
-10
-15
Lateral load (kN)
0
10
20
30
40
50
60
Time (s)

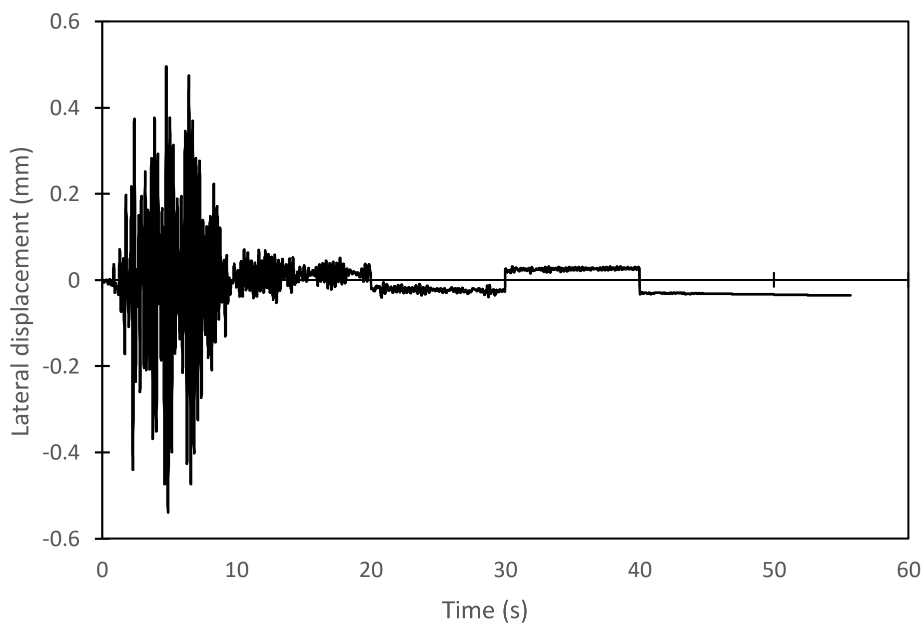

0.6
0.4
0.2
0
-0.2
-0.4
-0.6
Lateral displacement (mm)
0
10
20
30
40
50
60
Time (s)

26. TR1-4

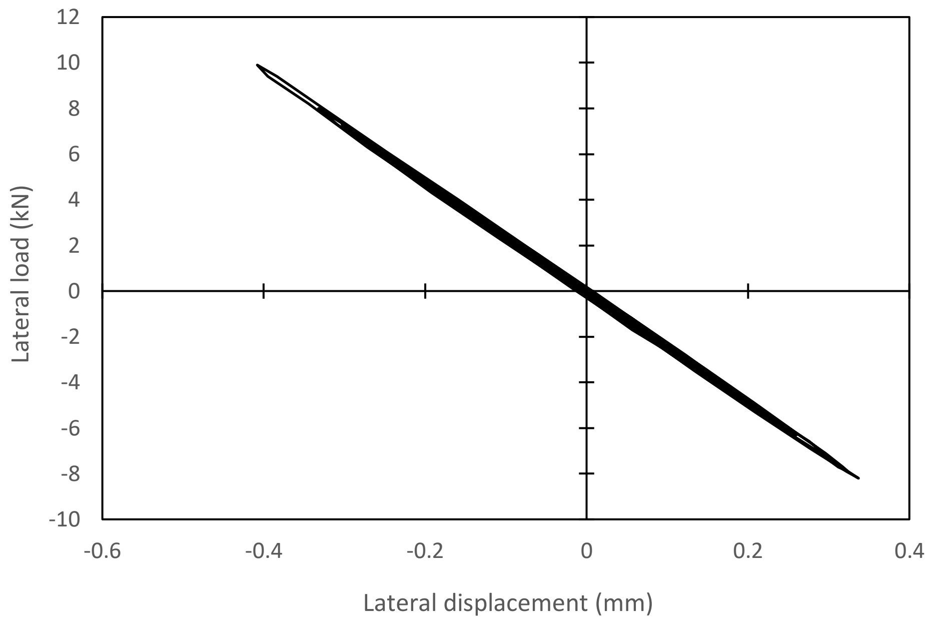

Lateral load (kN)
12
10
8
6
4
2
0
-2
-4
-6
-8
-10
-0.6
-0.4
-0.2
0
0.2
0.4
Lateral displacement (mm)

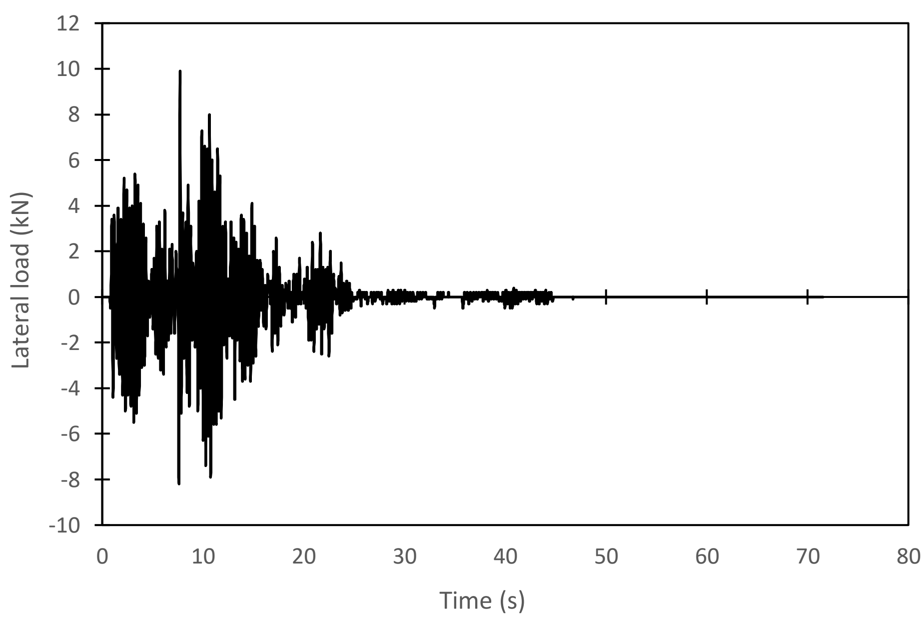

Lateral load (kN)
12
10
8
6
4
2
0
-2
-4
-6
-8
-10
0
10
20
30
40
50
60
70
80
Time (s)

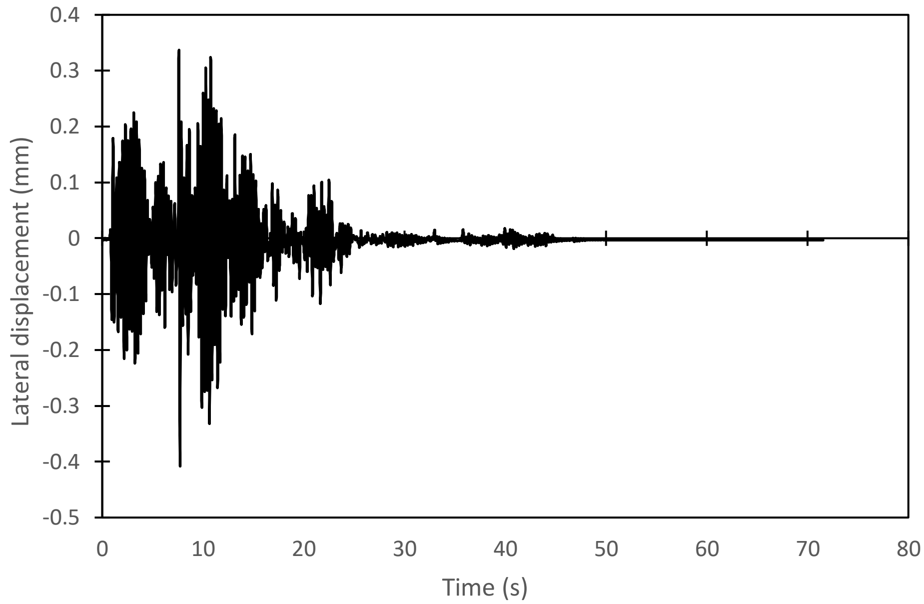

0.4
0.3
0.2
0.1
0
-0.1
-0.2
-0.3
-0.4
-0.5
Lateral displacement (mm)
0
10
20
30
40
50
60
70
80
Time (s)

27. TR1-5

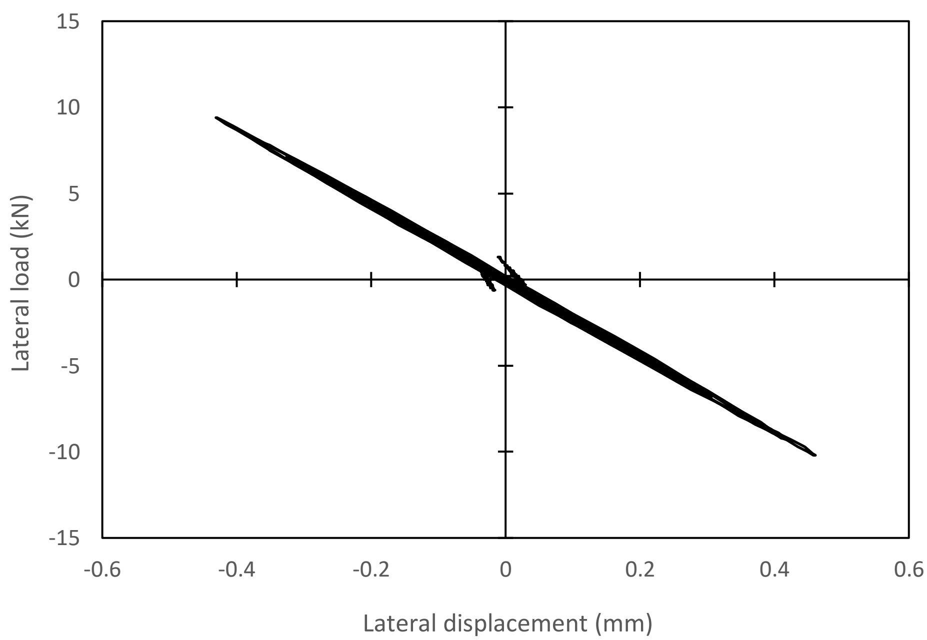

15
10
5
0
-5
-10
-15
Lateral load (kN)
-0.6
-0.4
-0.2
0
0.2
0.4
0.6
Lateral displacement (mm)

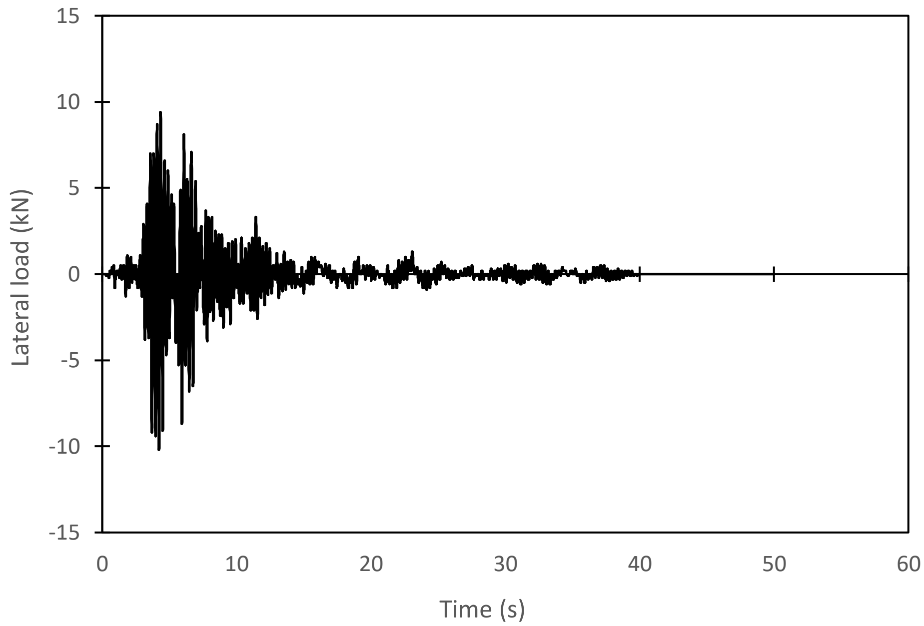
Lateral load (kN)
15
10
5
0
-5
-10
-15
0
10
20
30
40
50
60
Time (s)

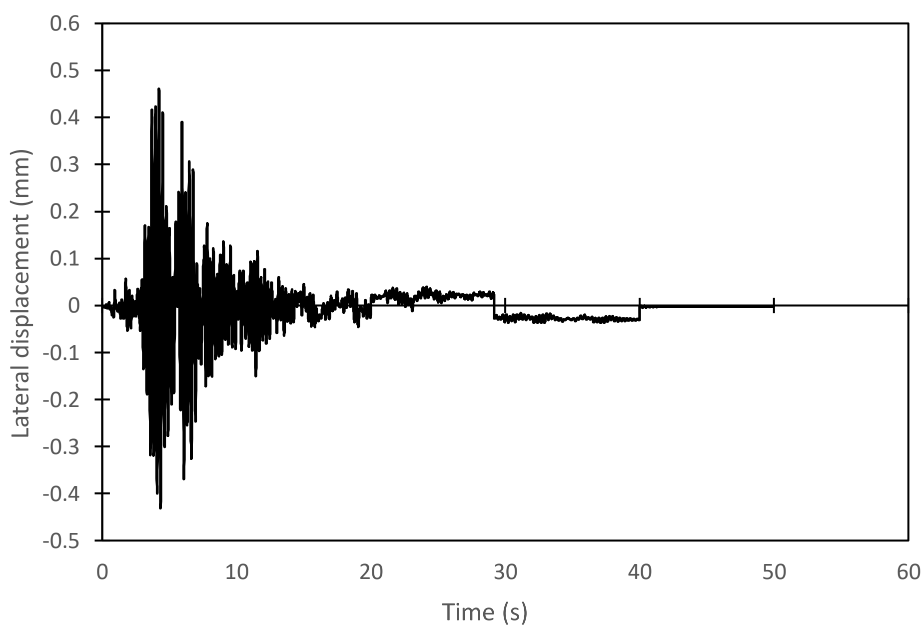
Lateral displacement (mm)
0.6
0.5
0.4
0.3
0.2
0.1
0
-0.1
-0.2
-0.3
-0.4
-0.5
0
10
20
30
40
50
60
Time (s)

28. TR1-6

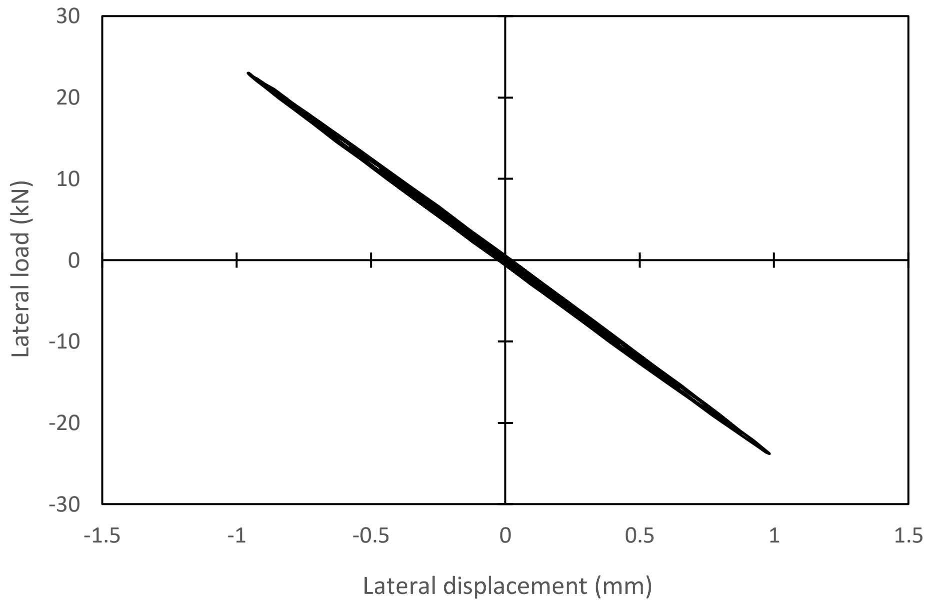
30
20
10
0
-10
-20
-30
-1.5
-1
-0.5
0
0.5
1
1.5
Lateral load (kN)
Lateral displacement (mm)

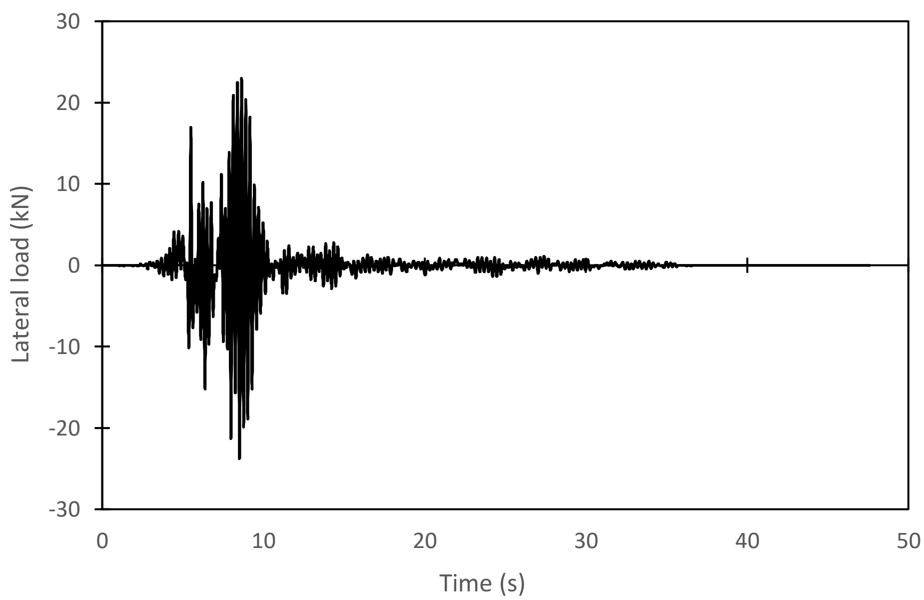
30
20
10
0
-10
-20
-30
0
10
20
30
40
50
Lateral load (kN)
Time (s)

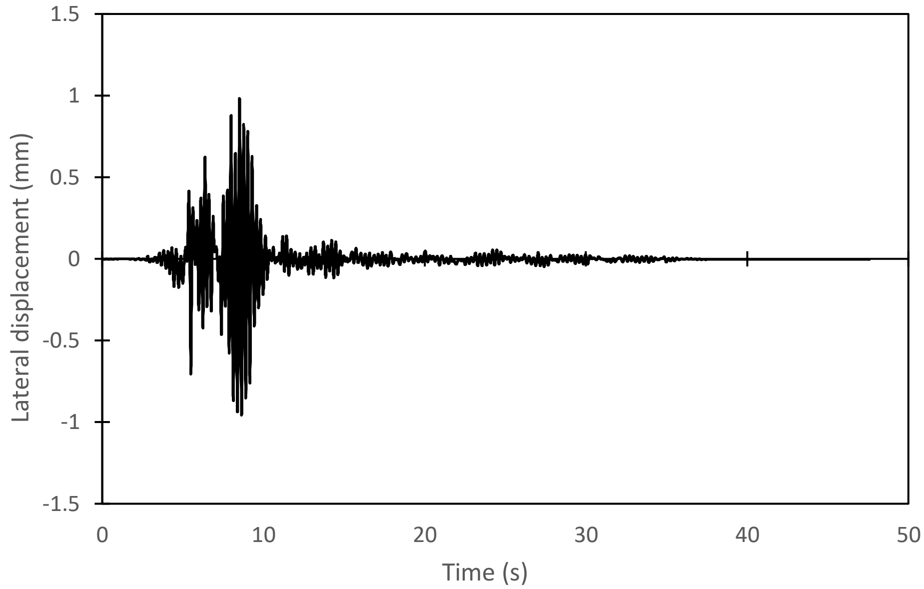
1.5
1
0.5
0
-0.5
-1
-1.5
Lateral displacement (mm)
0
10
20
30
40
50
Time (s)

29. TR2-1

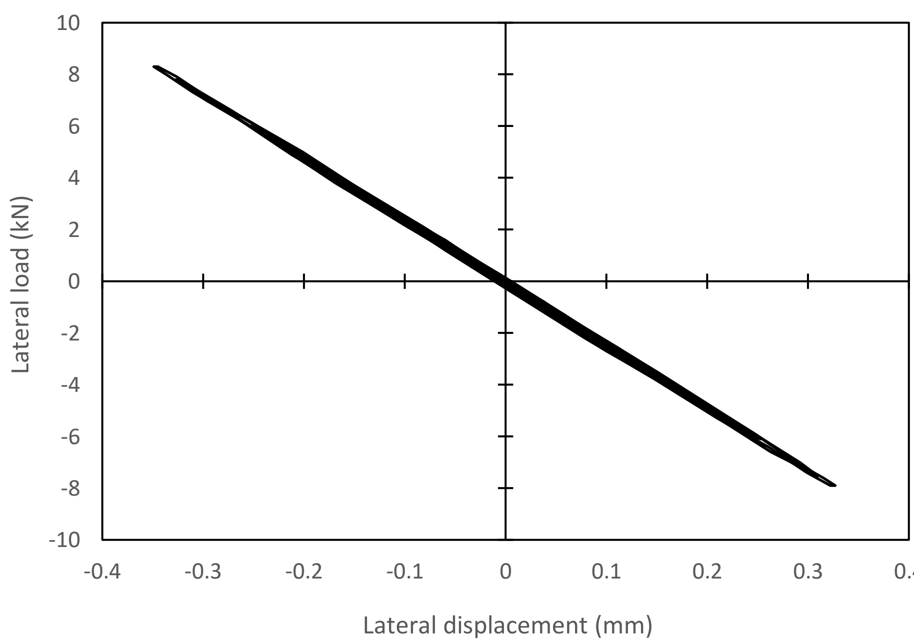
10
8
6
4
2
0
-2
-4
-6
-8
-10
Lateral load (kN)
-0.4
-0.3
-0.2
-0.1
0
0.1
0.2
0.3
0.4
Lateral displacement (mm)

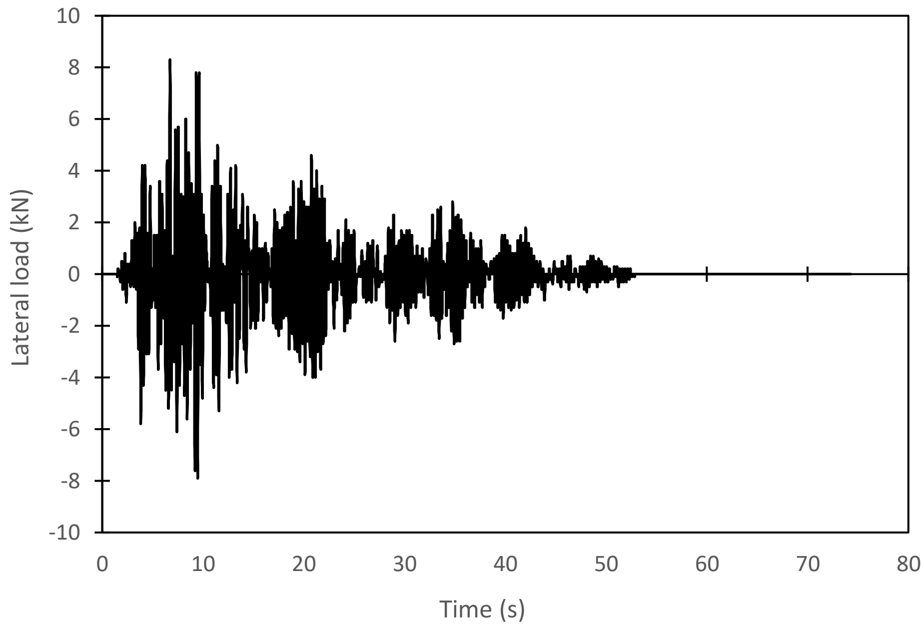
10
8
6
4
2
0
-2
-4
-6
-8
-10
Lateral load (kN)
0
10
20
30
40
50
60
70
80
Time (s)

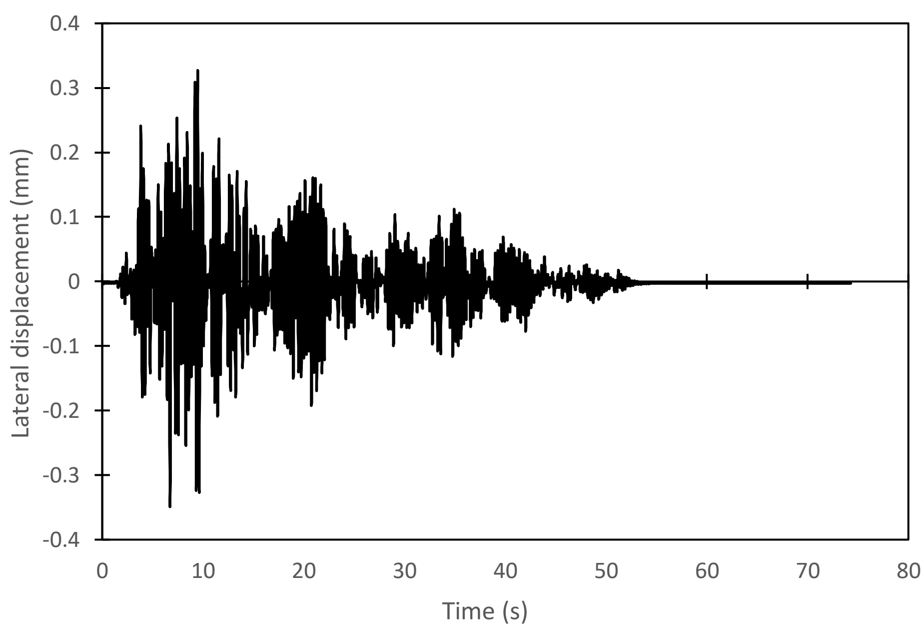
0.4
0.3
0.2
0.1
0
-0.1
-0.2
-0.3
-0.4
Lateral displacement (mm)
0
10
20
30
40
50
60
70
80
Time (s)

30. TR2-2

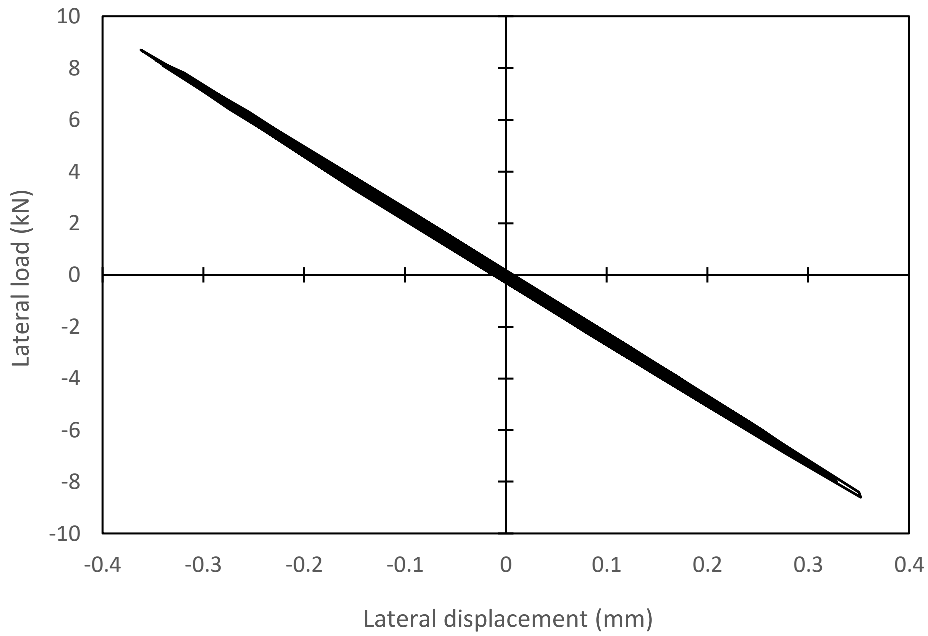
Lateral load (kN)
Lateral displacement (mm)
10
8
6
4
2
0
-2
-4
-6
-8
-10
-0.4
-0.3
-0.2
-0.1
0
0.1
0.2
0.3
0.4

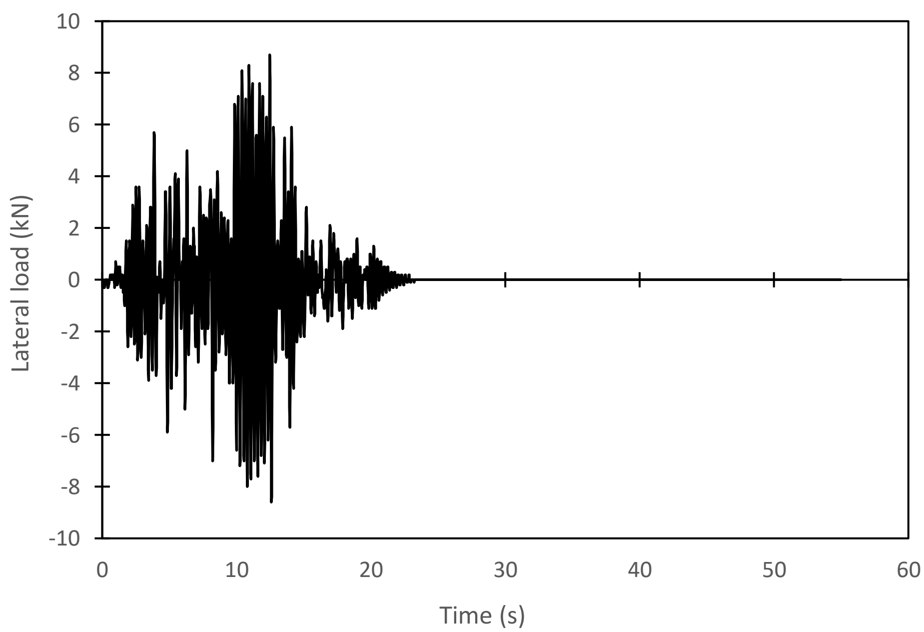
Lateral load (kN)
Time (s)
10
8
6
4
2
0
-2
-4
-6
-8
-10
0
10
20
30
40
50
60

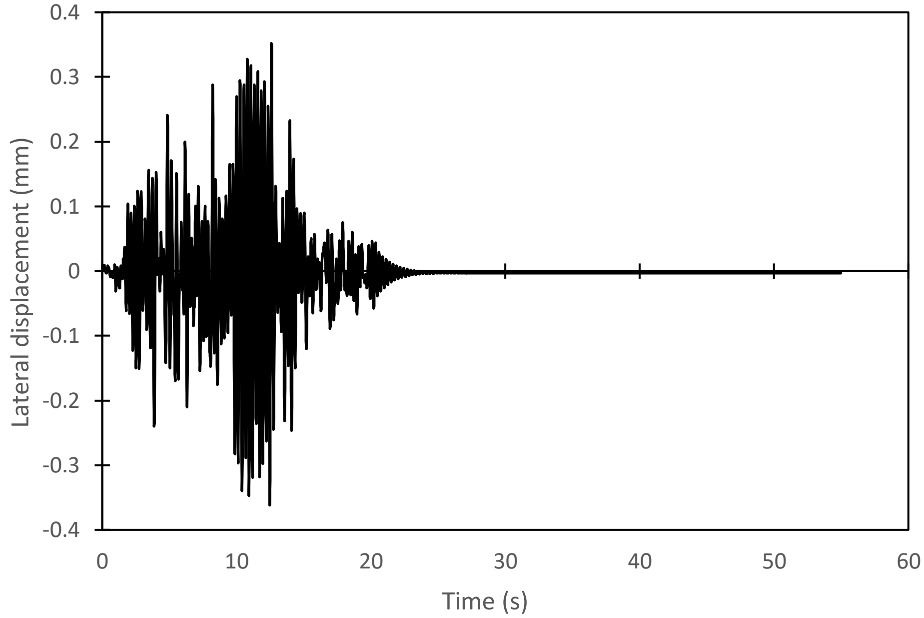

Lateral displacement (mm)
Time (s)
0.4
0.3
0.2
0.1
0
-0.1
-0.2
-0.3
-0.4
0
10
20
30
40
50
60

31. TR2-3

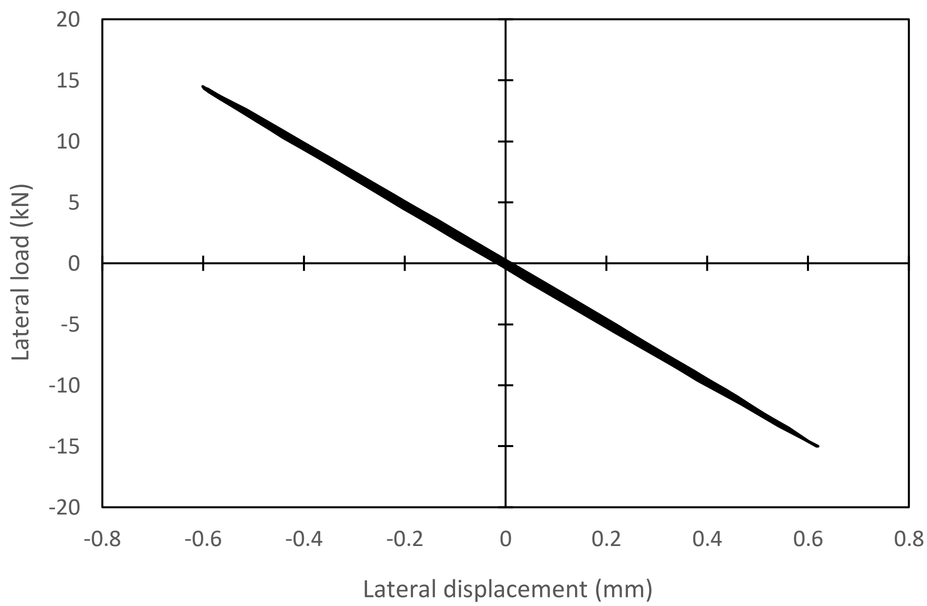

Lateral load (kN)
Lateral displacement (mm)
20
15
10
5
0
-5
-10
-15
-20
-0.8
-0.6
-0.4
-0.2
0
0.2
0.4
0.6
0.8

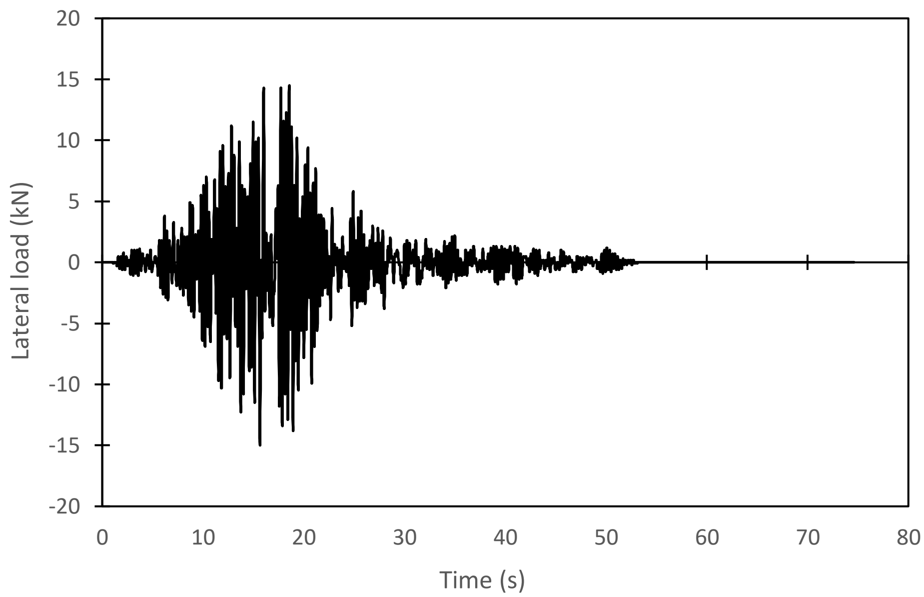
Lateral load (kN)
20
15
10
5
0
-5
-10
-15
-20
0
10
20
30
40
50
60
70
80
Time (s)

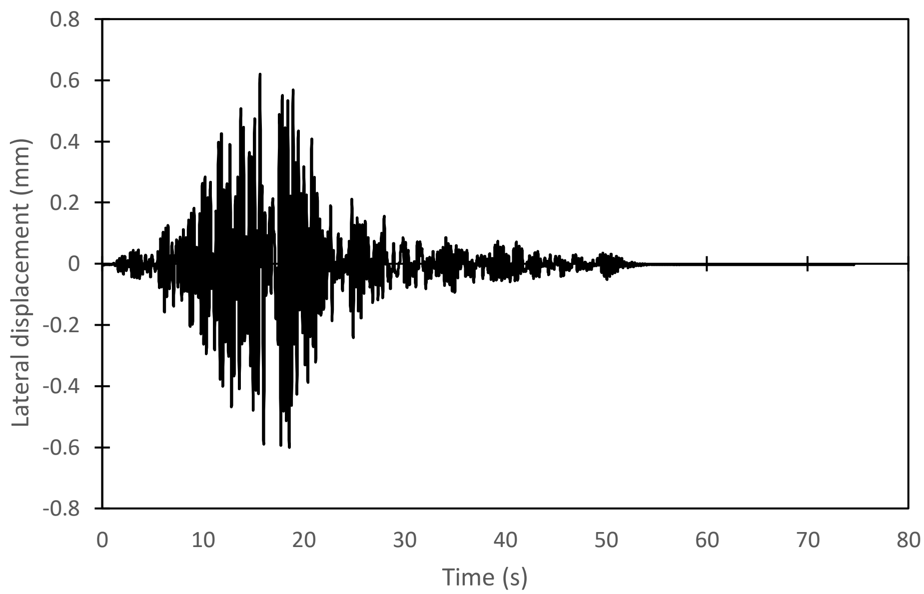
Lateral displacement (mm)
0.8
0.6
0.4
0.2
0
-0.2
-0.4
-0.6
-0.8
0
10
20
30
40
50
60
70
80
Time (s)

32. TR2-4

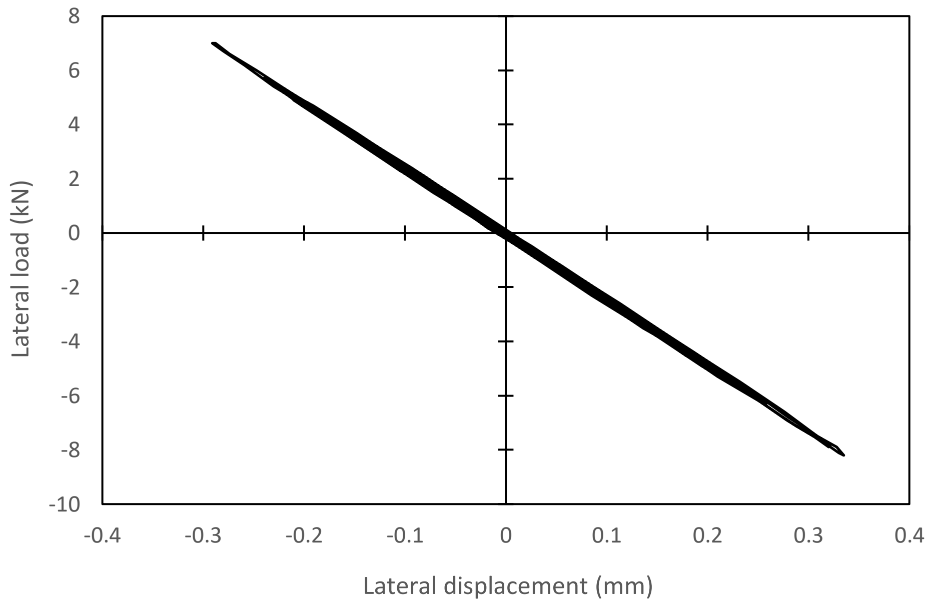

Lateral load (kN)
8
6
4
2
0
-2
-4
-6
-8
-10
-0.4
-0.3
-0.2
-0.1
0
0.1
0.2
0.3
0.4
Lateral displacement (mm)

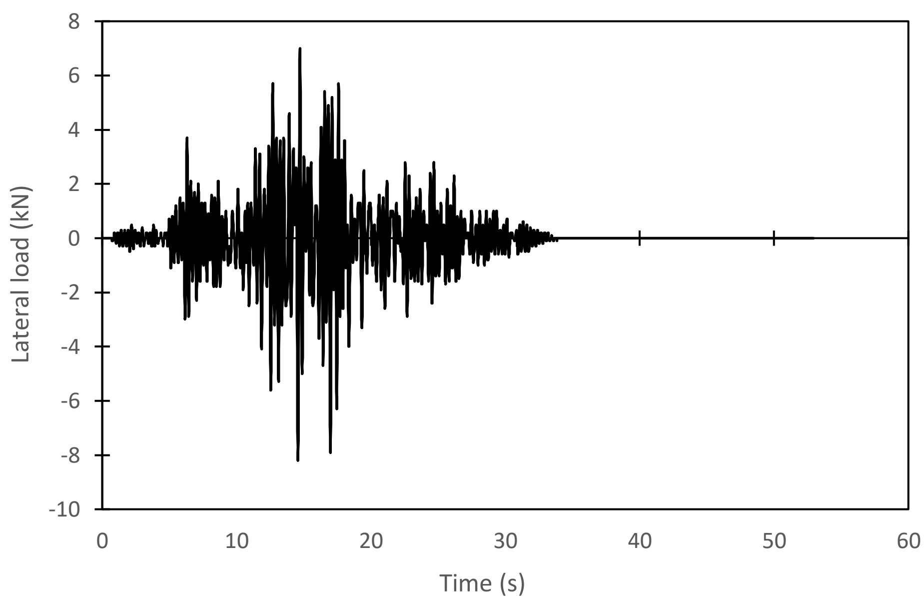

Lateral load (kN)
8
6
4
2
0
-2
-4
-6
-8
-10
0
10
20
30
40
50
60
Time (s)

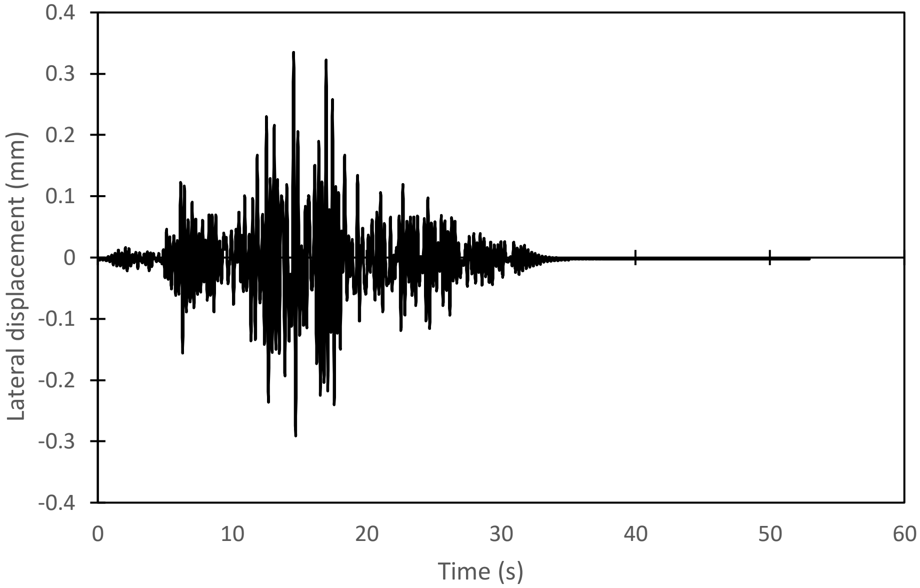
0.4
0.3
0.2
0.1
0
-0.1
-0.2
-0.3
-0.4
Lateral displacement (mm)
0
10
20
30
40
50
60
Time (s)

33. TR2-5

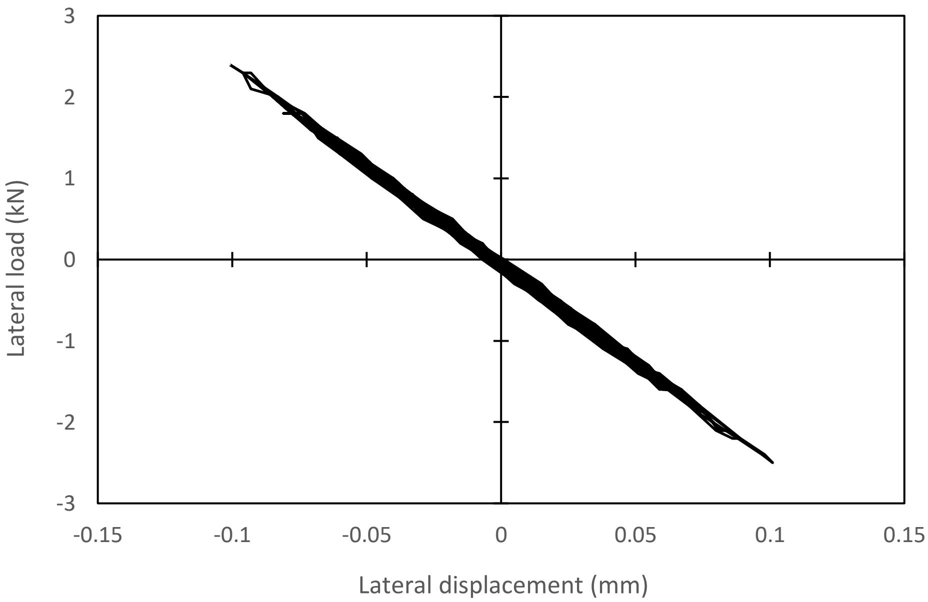
3
2
1
0
-1
-2
-3
Lateral load (kN)
-0.15
-0.1
-0.05
0
0.05
0.1
0.15
Lateral displacement (mm)

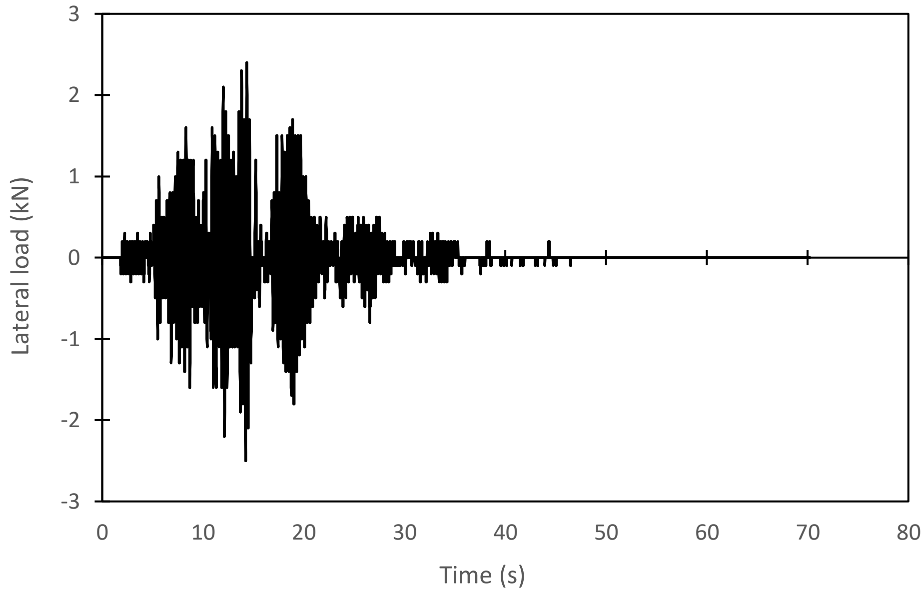

Lateral load (kN)
3
2
1
0
-1
-2
-3
0
10
20
30
40
50
60
70
80
Time (s)

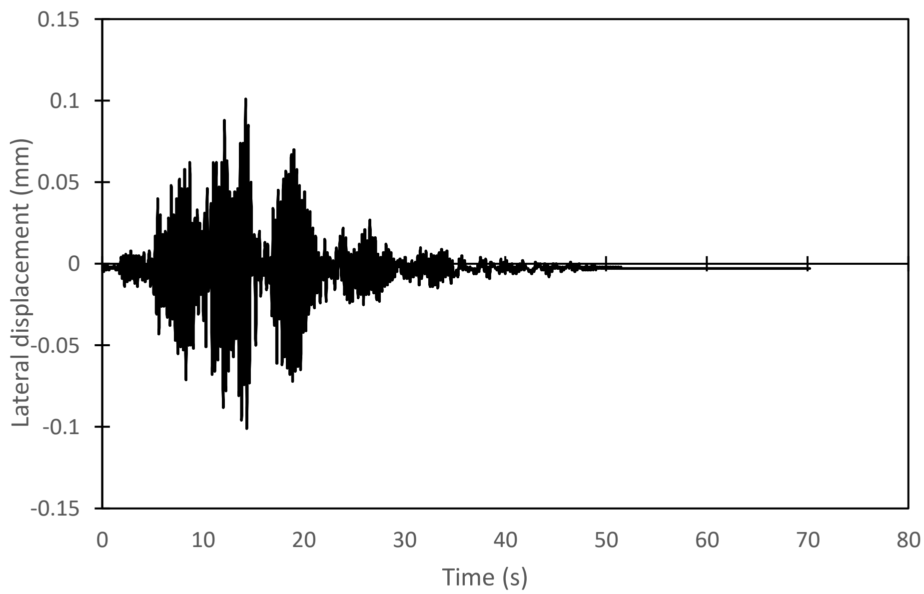

Lateral displacement (mm)
0.15
0.1
0.05
0
-0.05
-0.1
-0.15
0
10
20
30
40
50
60
70
80
Time (s)

B. Earthquake records Vancouver – BC

34. TR1-1

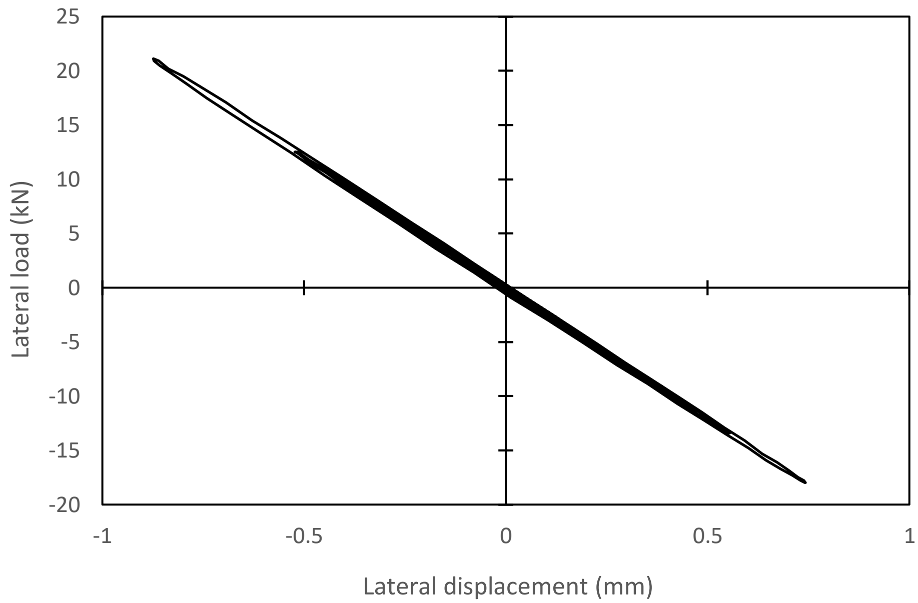

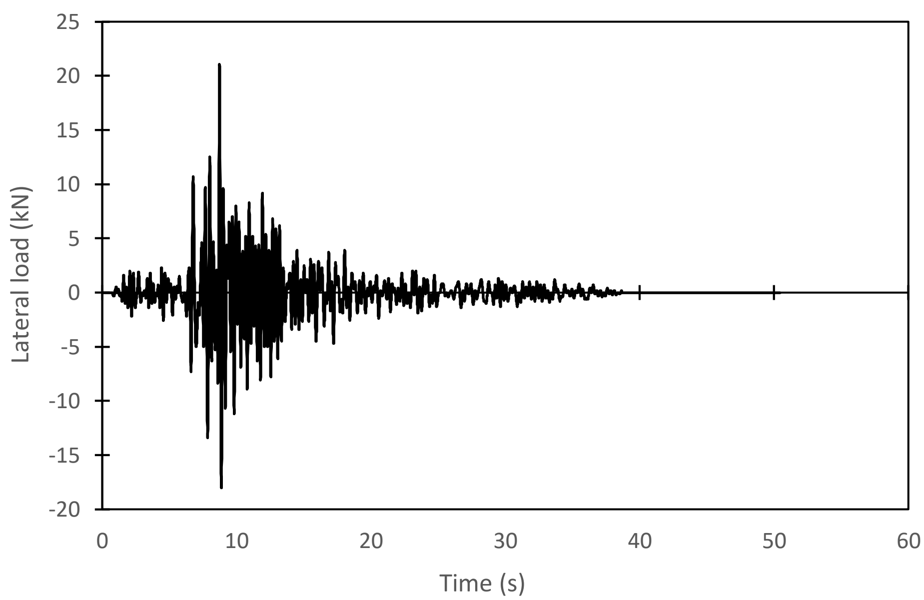

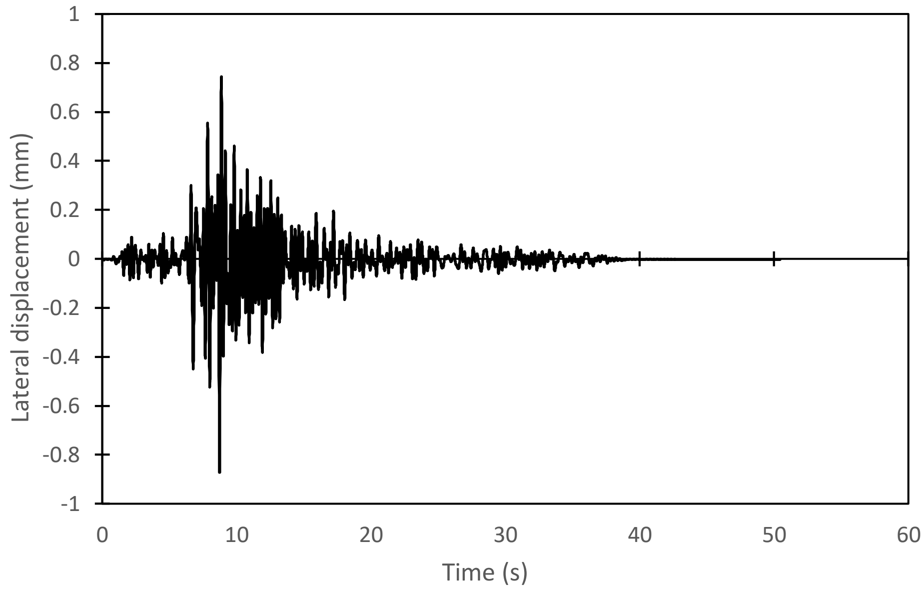
Lateral displacement (mm)
Time (s)
1
0.8
0.6
0.4
0.2
0
-0.2
-0.4
-0.6
-0.8
-1
0
10
20
30
40
50
60

35. TR1-2

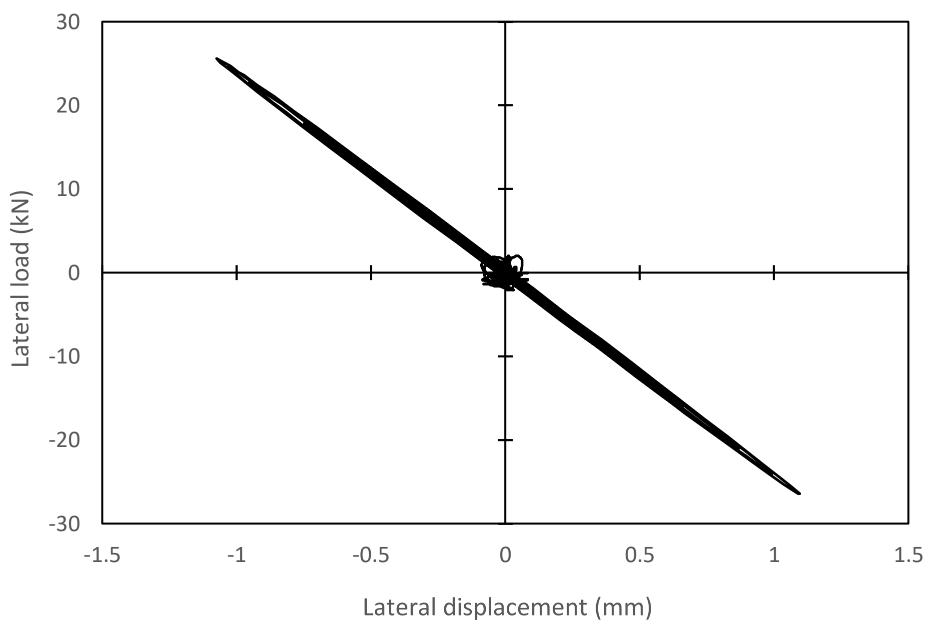
Lateral load (kN)
Lateral displacement (mm)
30
20
10
0
-10
-20
-30
-1.5
-1
-0.5
0
0.5
1
1.5

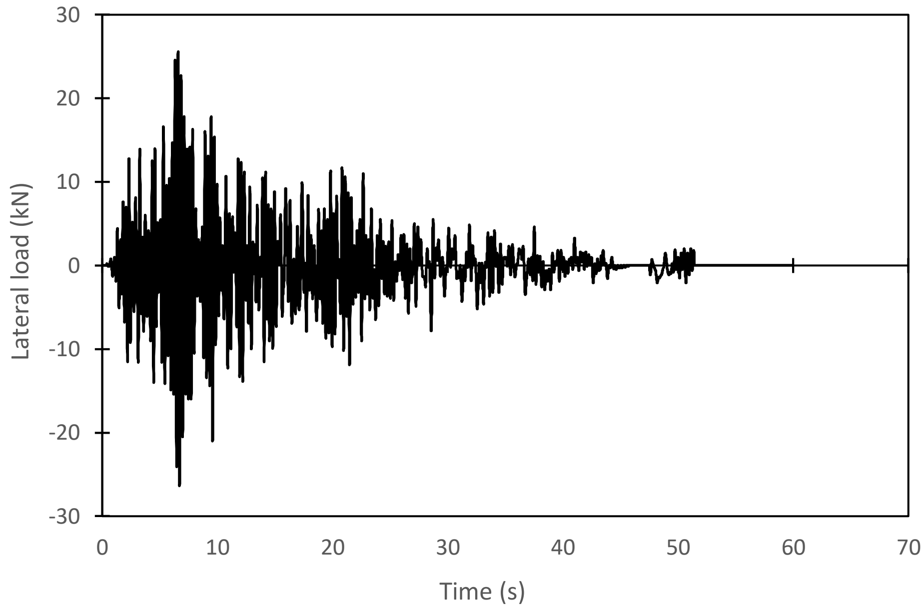

30
20
10
0
-10
-20
-30
Lateral load (kN)
0
10
20
30
40
50
60
70
Time (s)

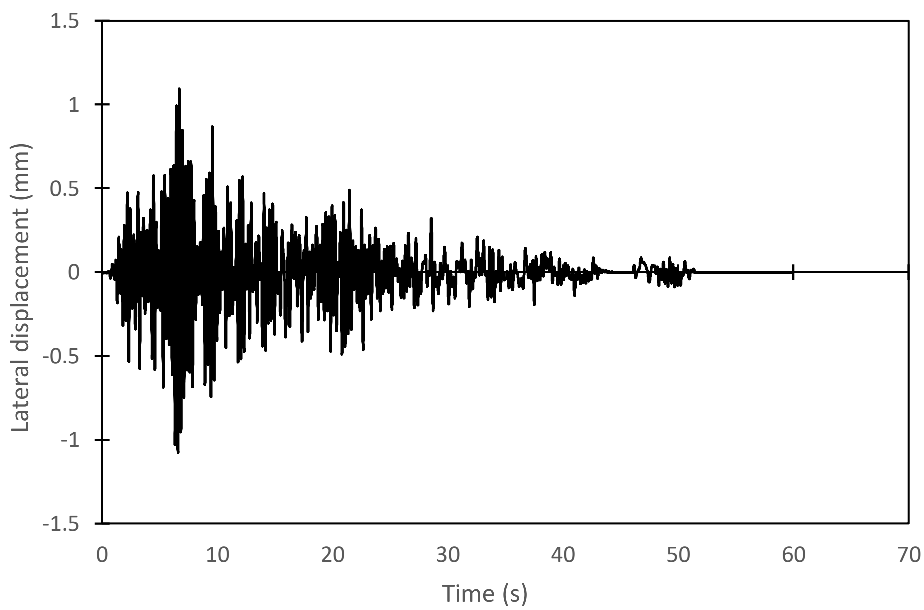

1.5
1
0.5
0
-0.5
-1
-1.5
Lateral displacement (mm)
0
10
20
30
40
50
60
70
Time (s)

36. TR1-3

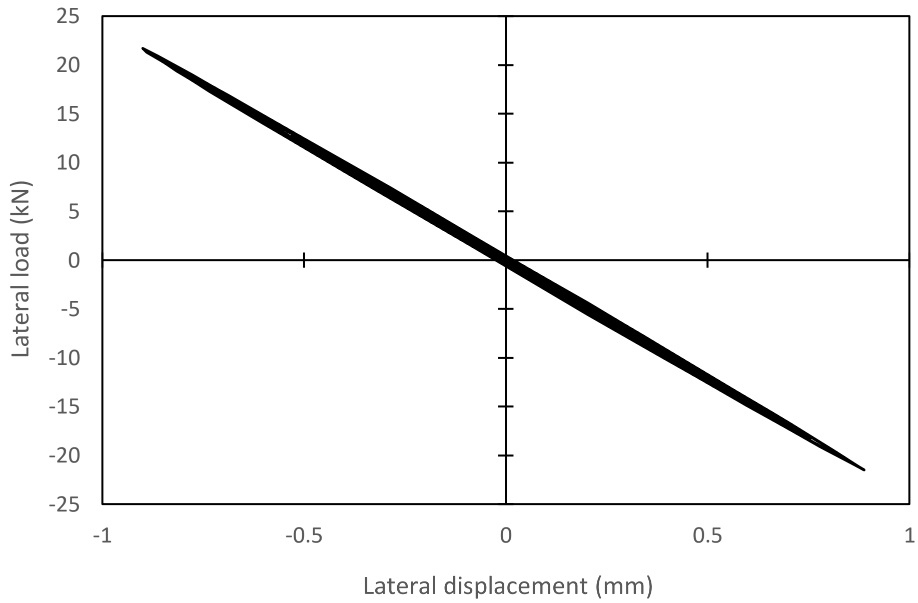

Lateral load (kN)
25
20
15
10
5
0
-5
-10
-15
-20
-25
-1
-0.5
0
0.5
1
Lateral displacement (mm)

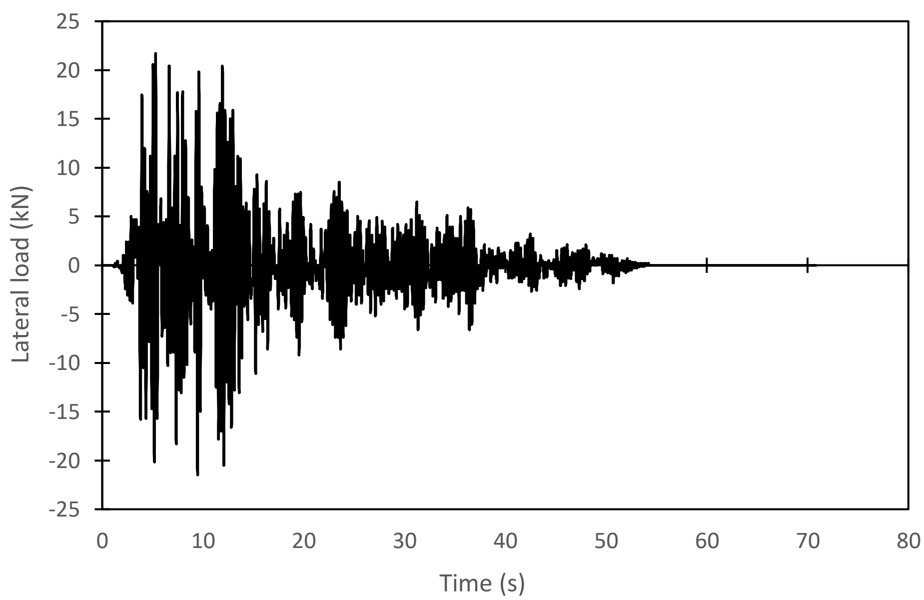

Lateral load (kN)
25
20
15
10
5
0
-5
-10
-15
-20
-25
0
10
20
30
40
50
60
70
80
Time (s)

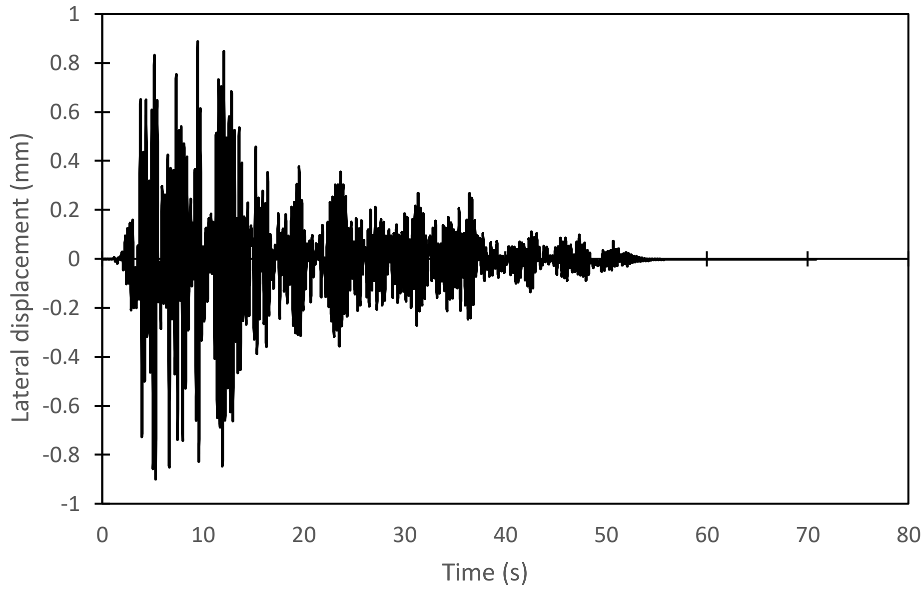
Lateral displacement (mm)
Time (s)
1
0.8
0.6
0.4
0.2
0
-0.2
-0.4
-0.6
-0.8
-1
0
10
20
30
40
50
60
70
80

37. TR1-4

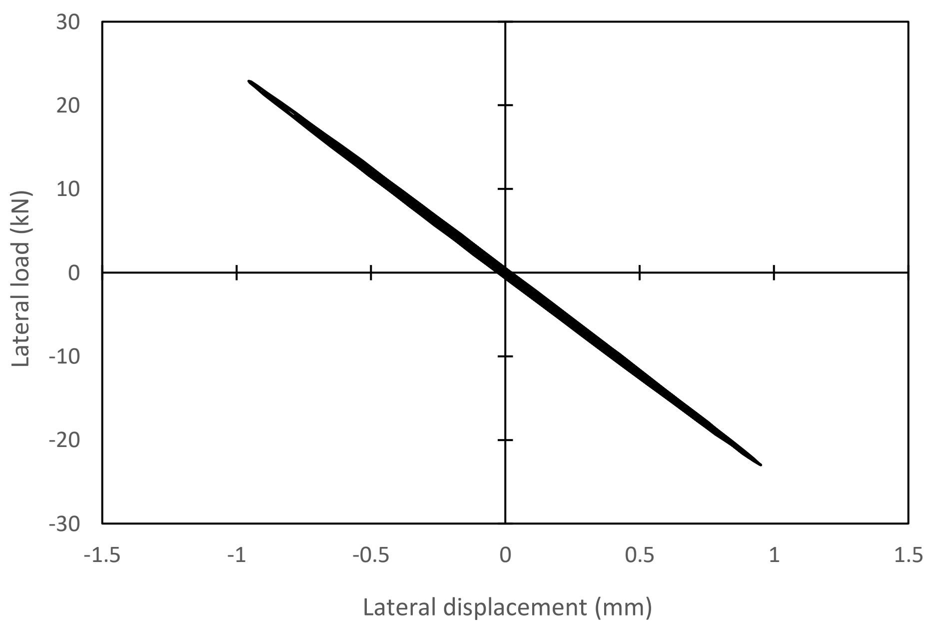
Lateral load (kN)
Lateral displacement (mm)
30
20
10
0
-10
-20
-30
-1.5
-1
-0.5
0
0.5
1
1.5

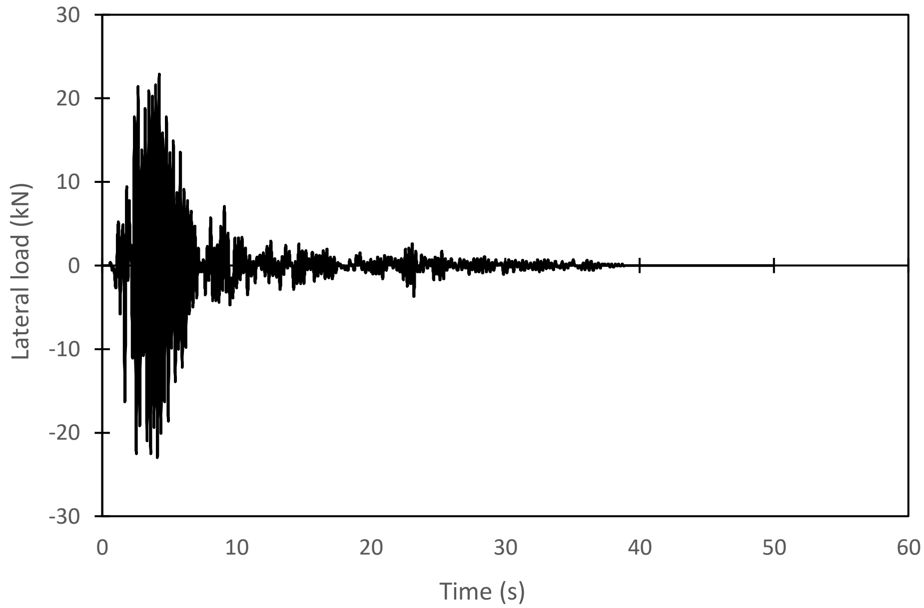

Lateral load (kN)
30
20
10
0
-10
-20
-30
0
10
20
30
40
50
60
Time (s)

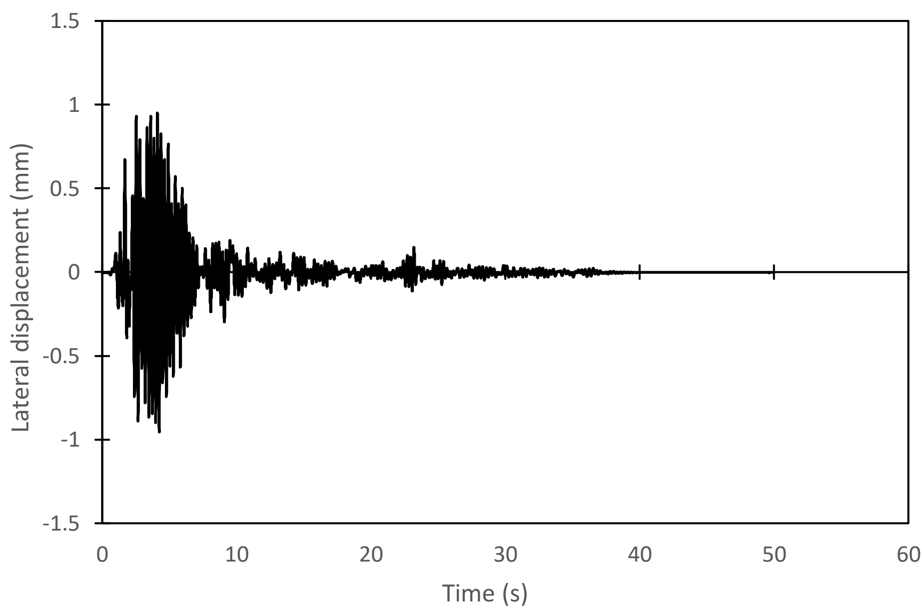

Lateral displacement (mm)
1.5
1
0.5
0
-0.5
-1
-1.5
0
10
20
30
40
50
60
Time (s)

38. TR2-1

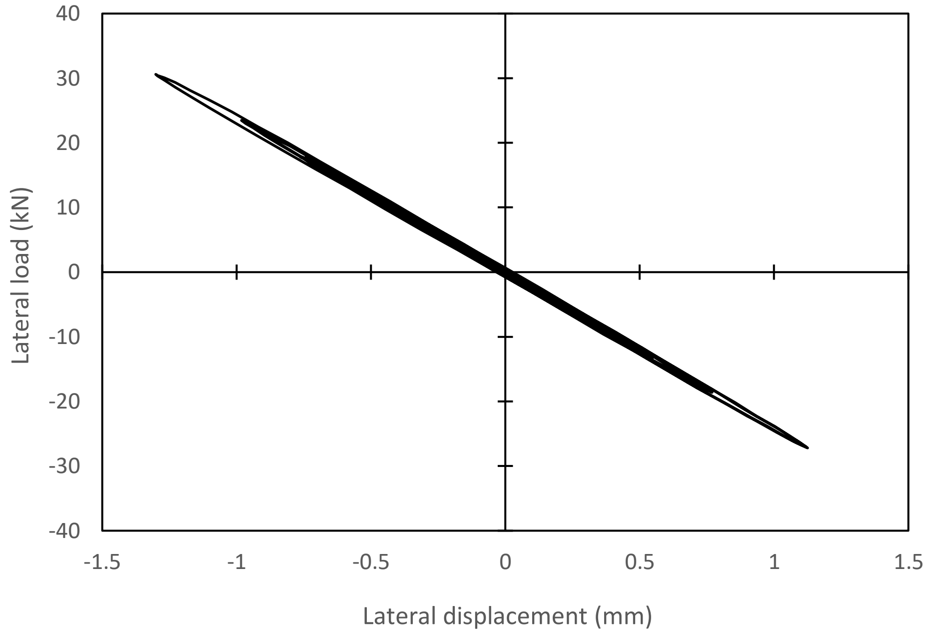
40
30
20
10
0
-10
-20
-30
-40
Lateral load (kN)
-1.5
-1
-0.5
0
0.5
1
1.5
Lateral displacement (mm)

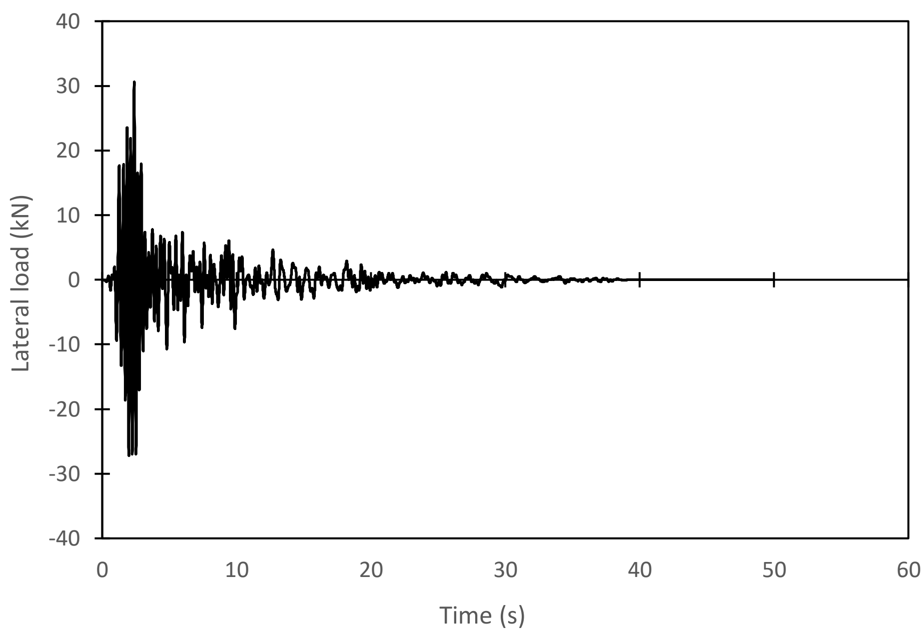
40
30
20
10
0
-10
-20
-30
-40
Lateral load (kN)
0
10
20
30
40
50
60
Time (s)

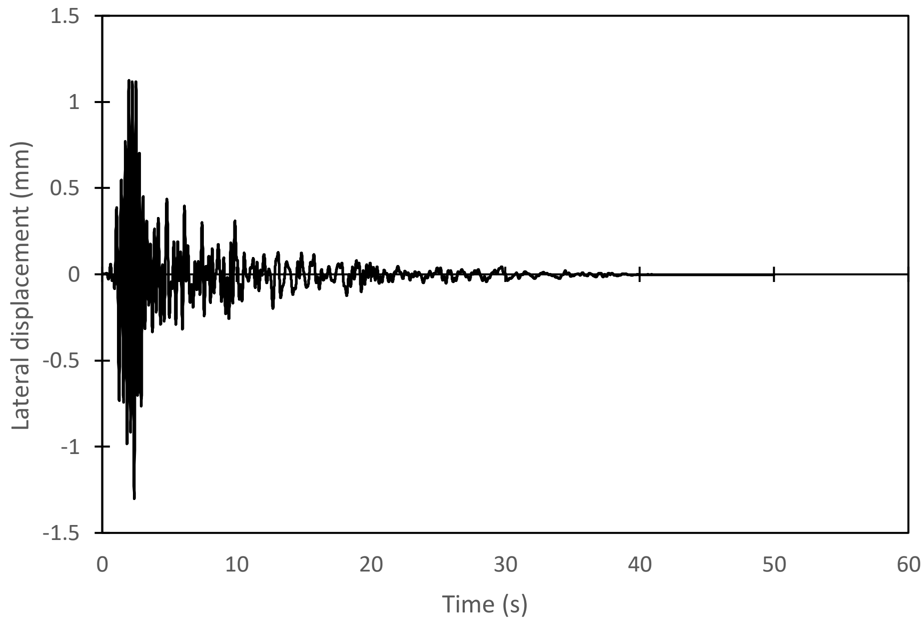
Lateral displacement (mm)
Time (s)
1.5
1
0.5
0
-0.5
-1
-1.5
0
10
20
30
40
50
60

39. TR2-2

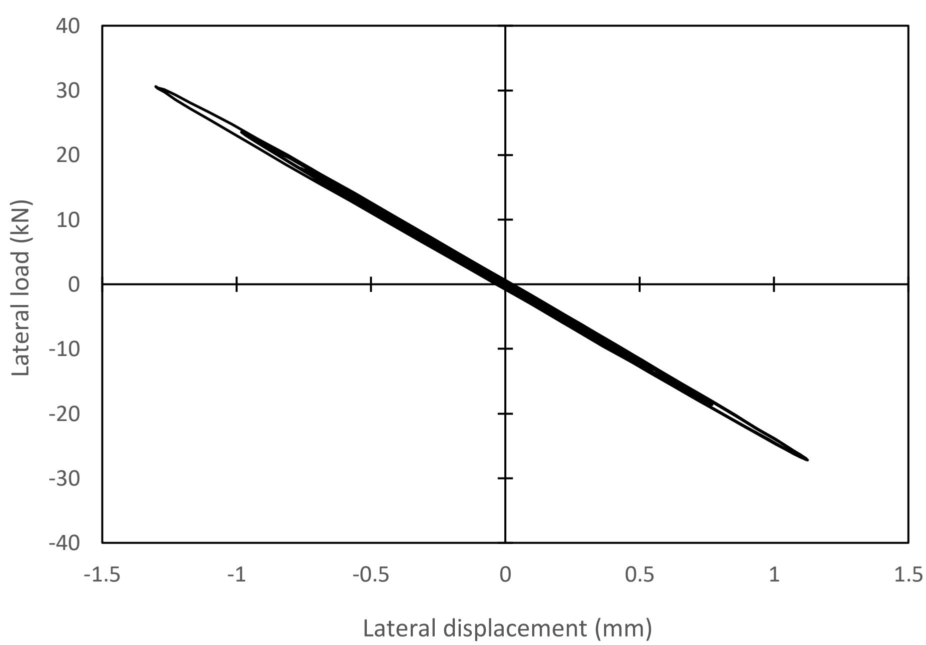
Lateral load (kN)
Lateral displacement (mm)
40
30
20
10
0
-10
-20
-30
-40
-1.5
-1
-0.5
0
0.5
1
1.5

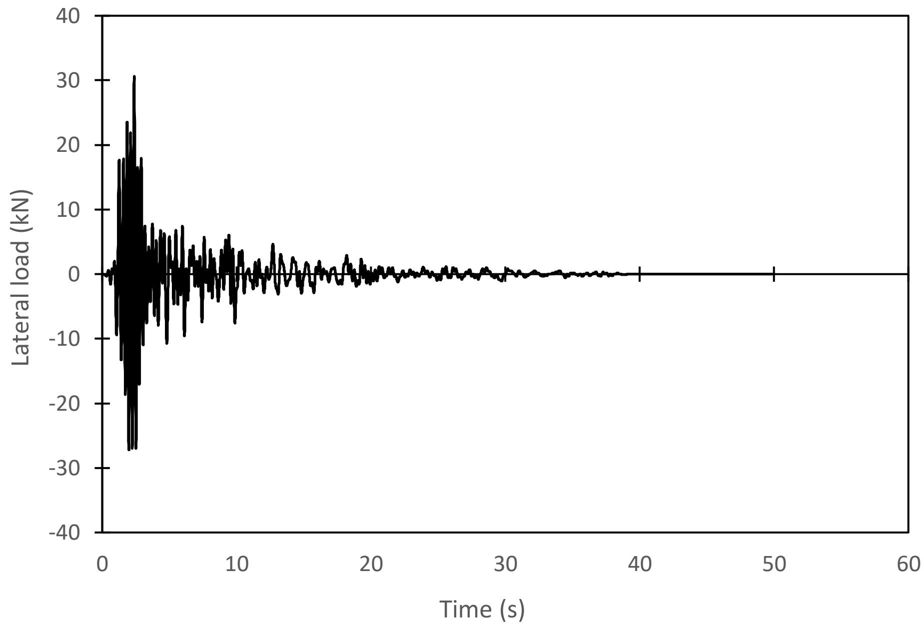

Lateral load (kN)
Time (s)
40
30
20
10
0
-10
-20
-30
-40
0
10
20
30
40
50
60

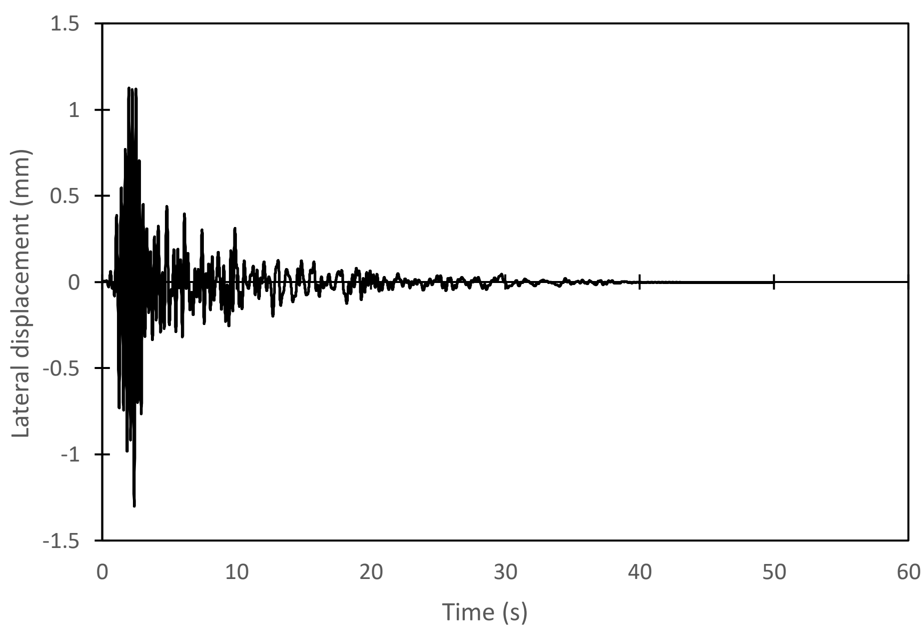

Lateral displacement (mm)
Time (s)
1.5
1
0.5
0
-0.5
-1
-1.5
0
10
20
30
40
50
60

40. TR2-3

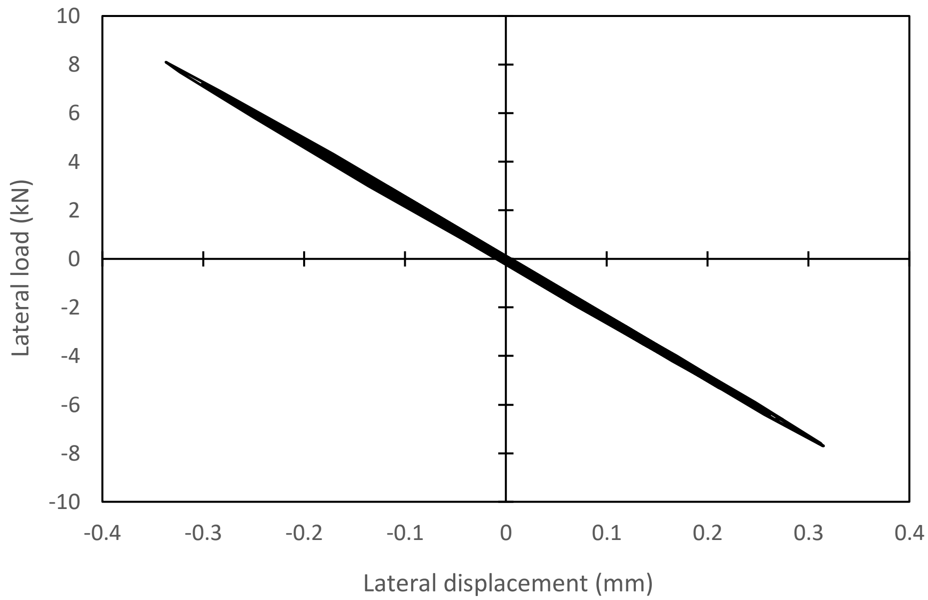

10
8
6
4
2
0
-2
-4
-6
-8
-10
Lateral load (kN)
-0.4
-0.3
-0.2
-0.1
0
0.1
0.2
0.3
0.4
Lateral displacement (mm)

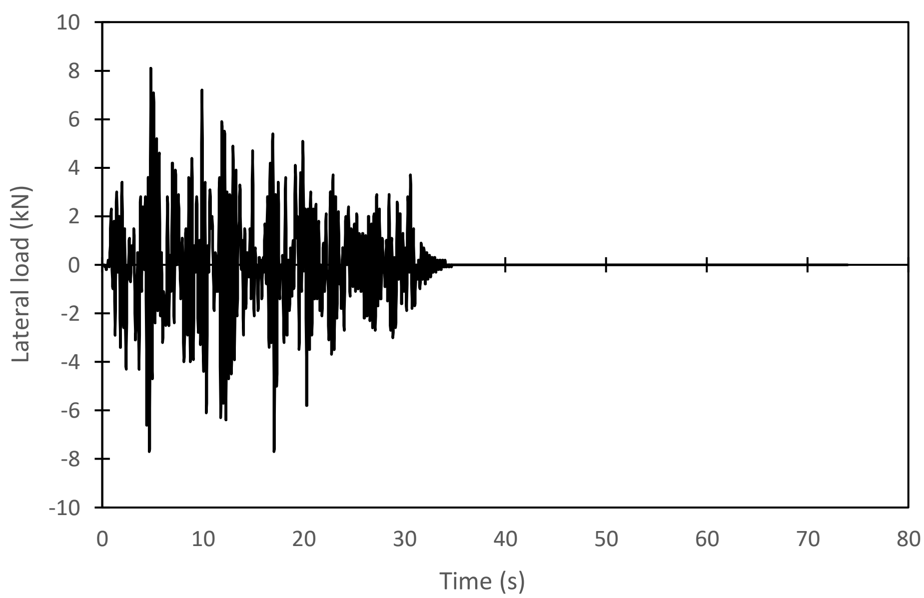

10
8
6
4
2
0
-2
-4
-6
-8
-10
Lateral load (kN)
0
10
20
30
40
50
60
70
80
Time (s)

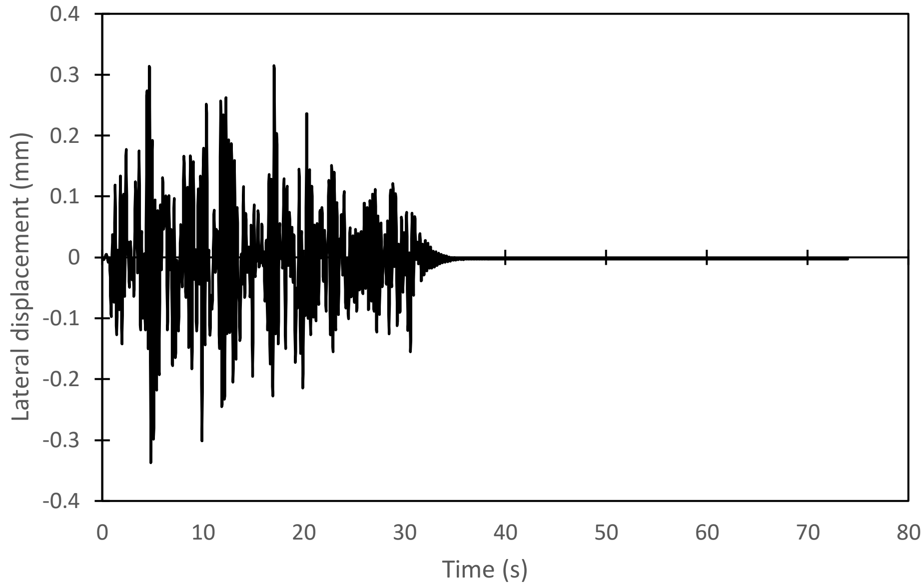
0.4
0.3
0.2
0.1
0
-0.1
-0.2
-0.3
-0.4
Lateral displacement (mm)
0
10
20
30
40
50
60
70
80
Time (s)

41. TR3-1

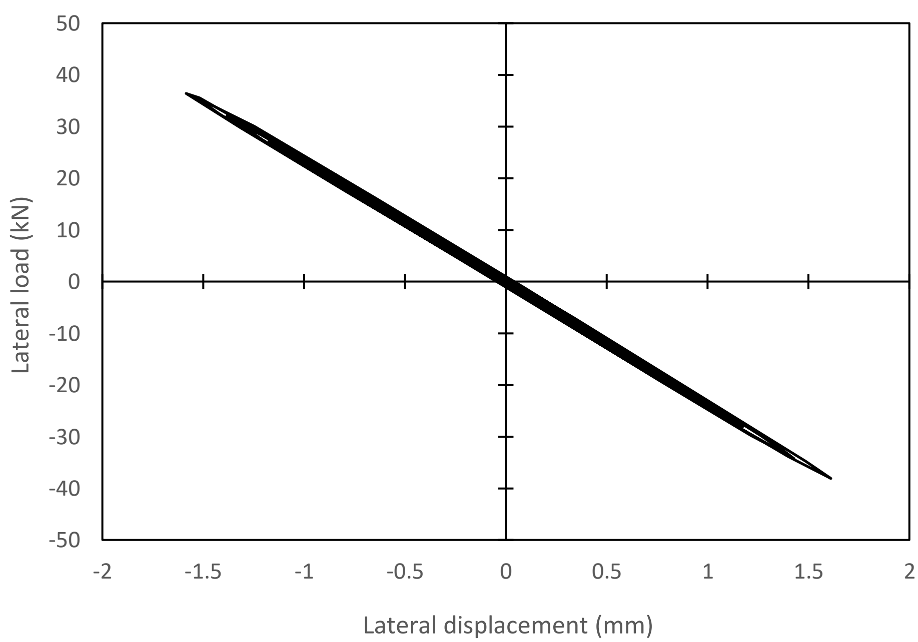
50
40
30
20
10
0
-10
-20
-30
-40
-50
Lateral load (kN)
-2
-1.5
-1
-0.5
0
0.5
1
1.5
2
Lateral displacement (mm)

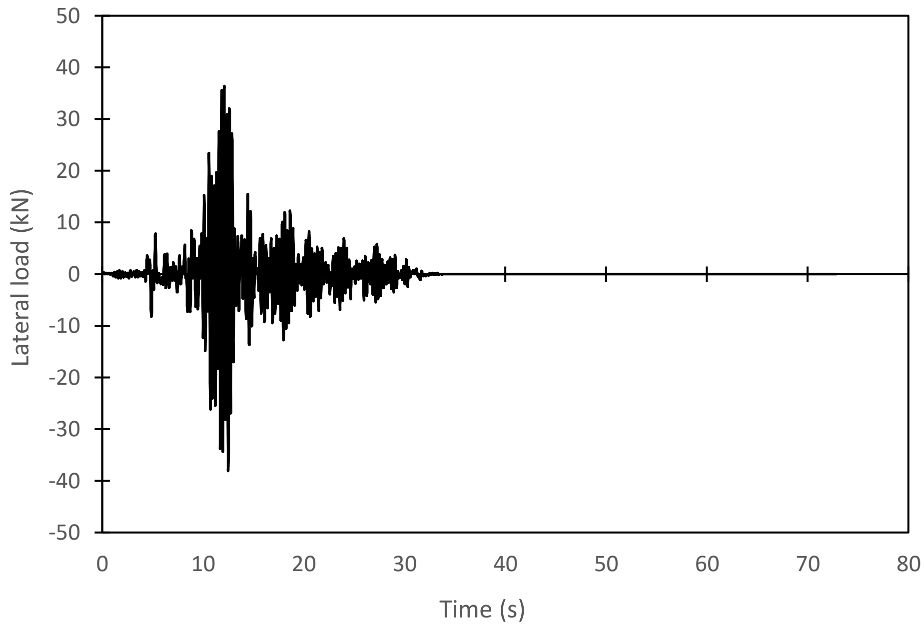
Lateral load (kN)
50
40
30
20
10
0
-10
-20
-30
-40
-50
0
10
20
30
40
50
60
70
80
Time (s)

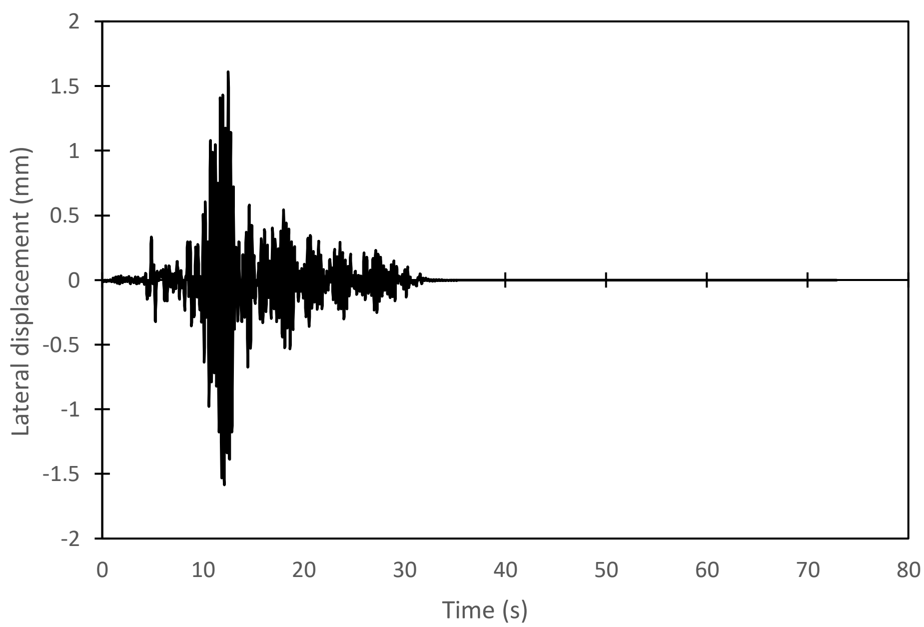
Lateral displacement (mm)
2
1.5
1
0.5
0
-0.5
-1
-1.5
-2
0
10
20
30
40
50
60
70
80
Time (s)

42. TR3-2

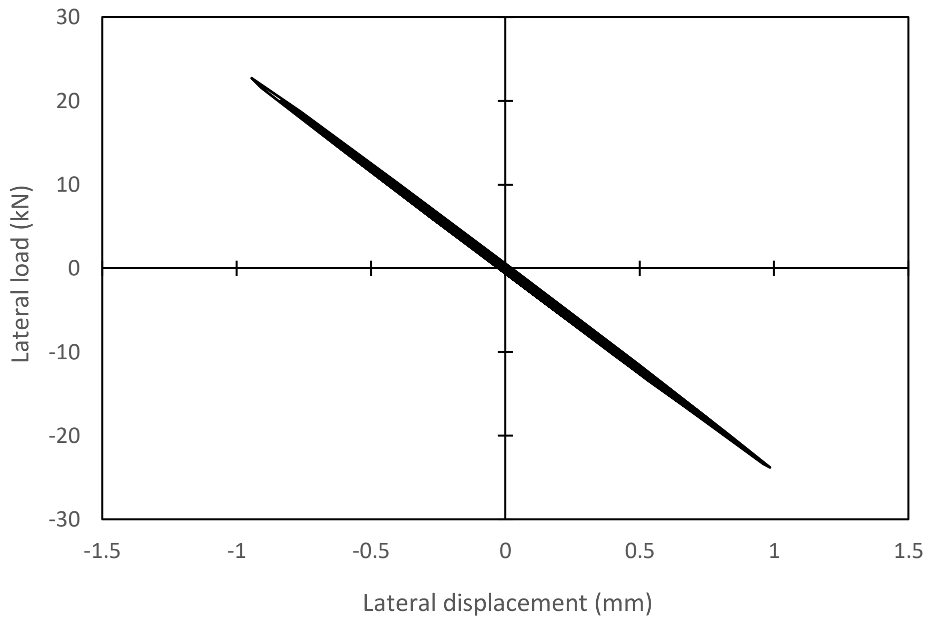

Lateral load (kN)
Lateral displacement (mm)
30
20
10
0
-10
-20
-30
-1.5
-1
-0.5
0
0.5
1
1.5

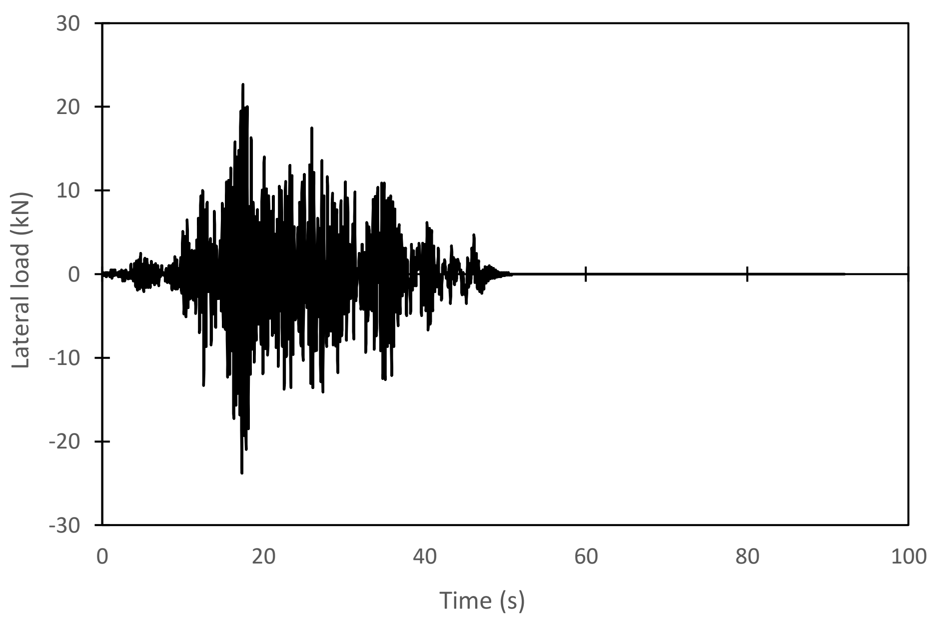

Lateral load (kN)
Time (s)
30
20
10
0
-10
-20
-30
0
20
40
60
80
100

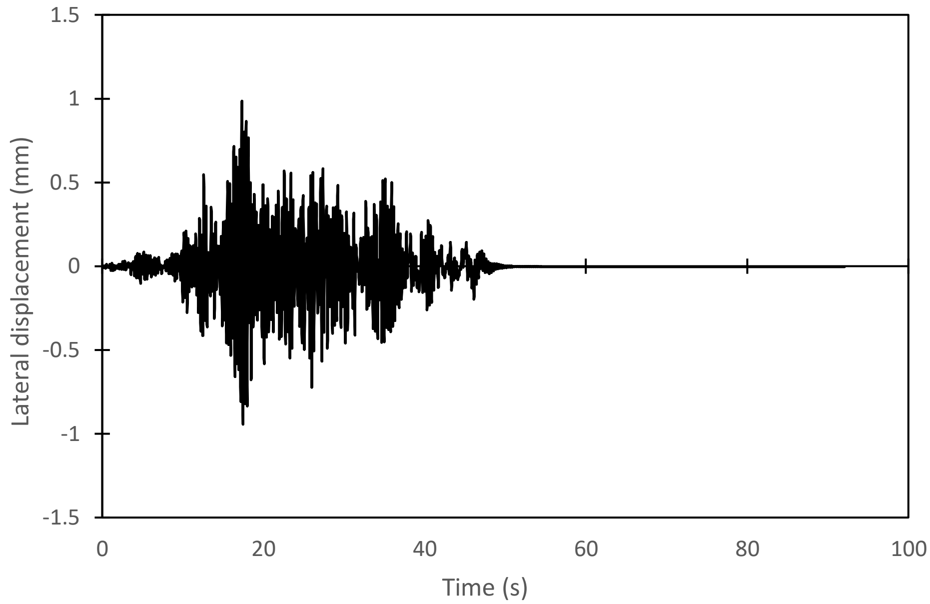
1.5
1
0.5
0
-0.5
-1
-1.5
0
20
40
60
80
100
Lateral displacement (mm)
Time (s)

43. TR3-3

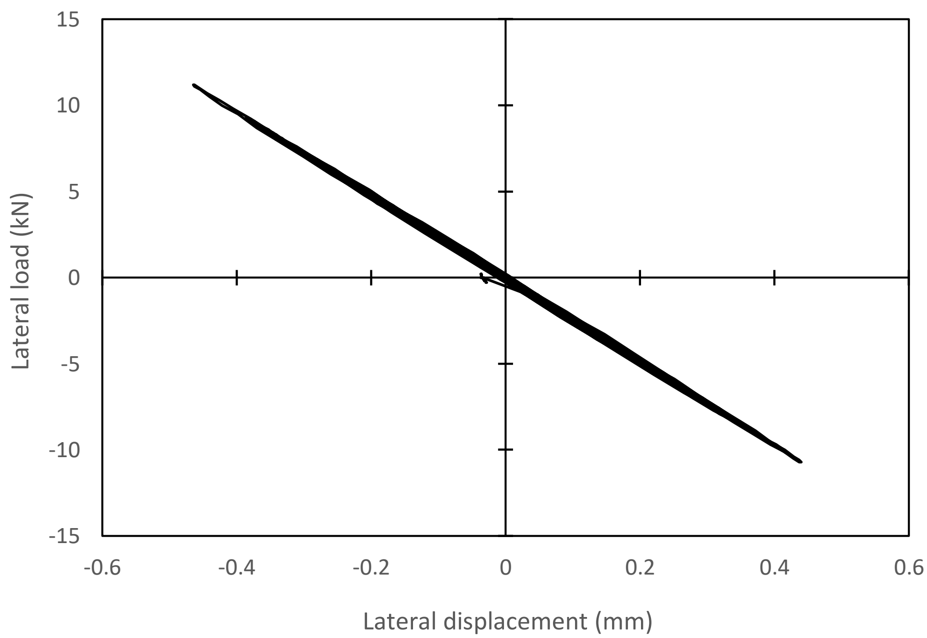
15
10
5
0
-5
-10
-15
-0.6
-0.4
-0.2
0
0.2
0.4
0.6
Lateral load (kN)
Lateral displacement (mm)

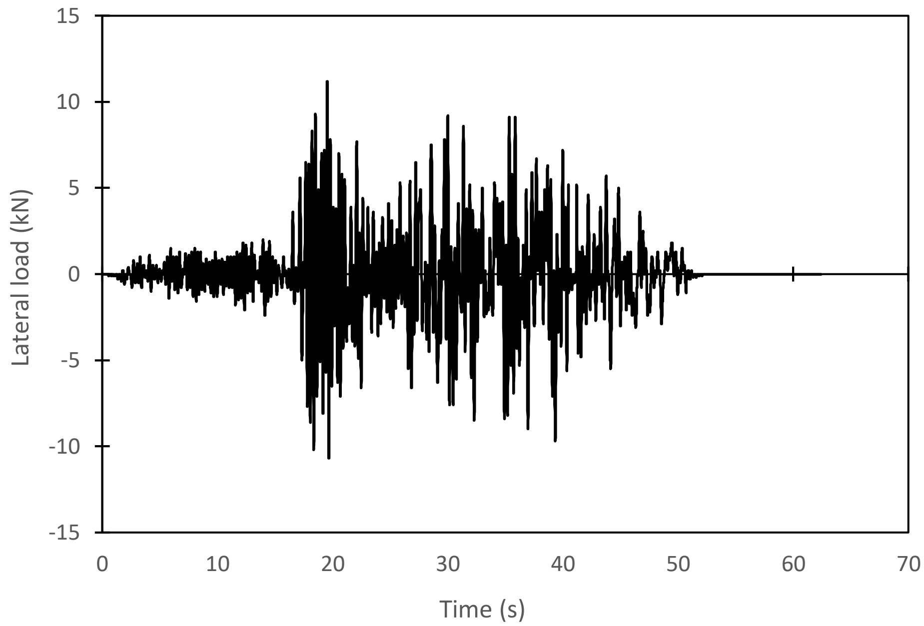
Lateral load (kN)
15
10
5
0
-5
-10
-15
0
10
20
30
40
50
60
70
Time (s)

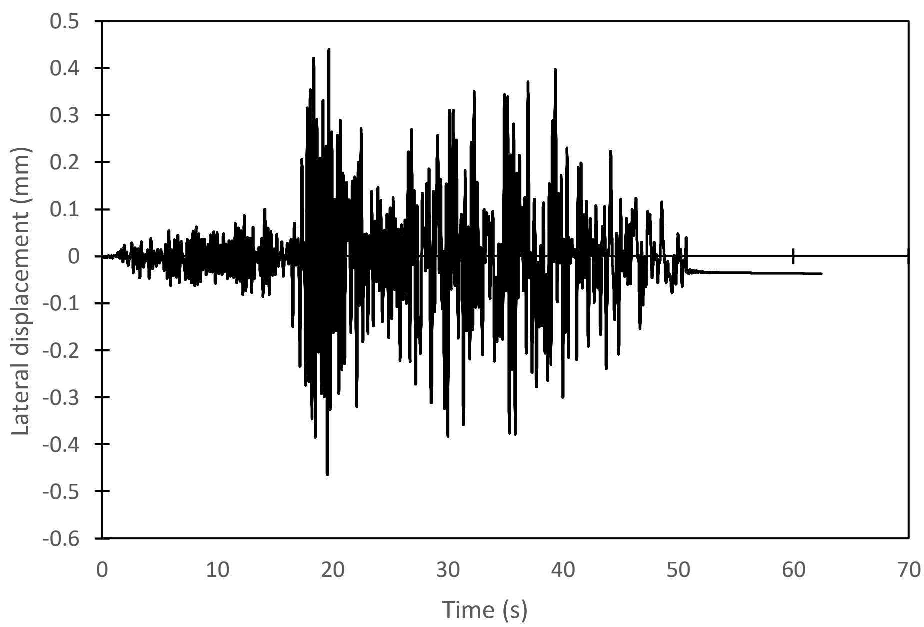
Lateral displacement (mm)
0.5
0.4
0.3
0.2
0.1
0
-0.1
-0.2
-0.3
-0.4
-0.5
-0.6
0
10
20
30
40
50
60
70
Time (s)

44. TR3-4

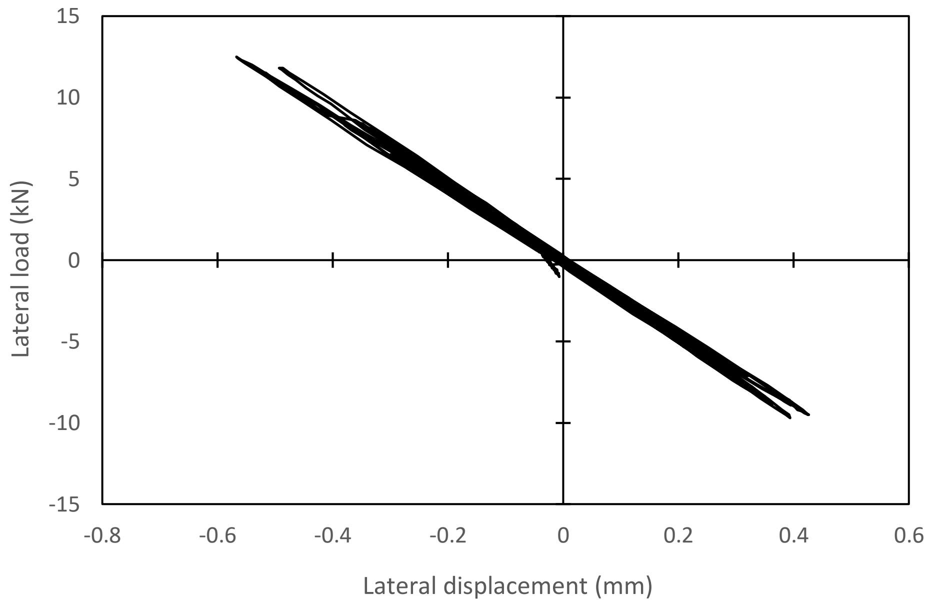
15
10
5
0
-5
-10
-15
Lateral load (kN)
-0.8
-0.6
-0.4
-0.2
0
0.2
0.4
0.6
Lateral displacement (mm)

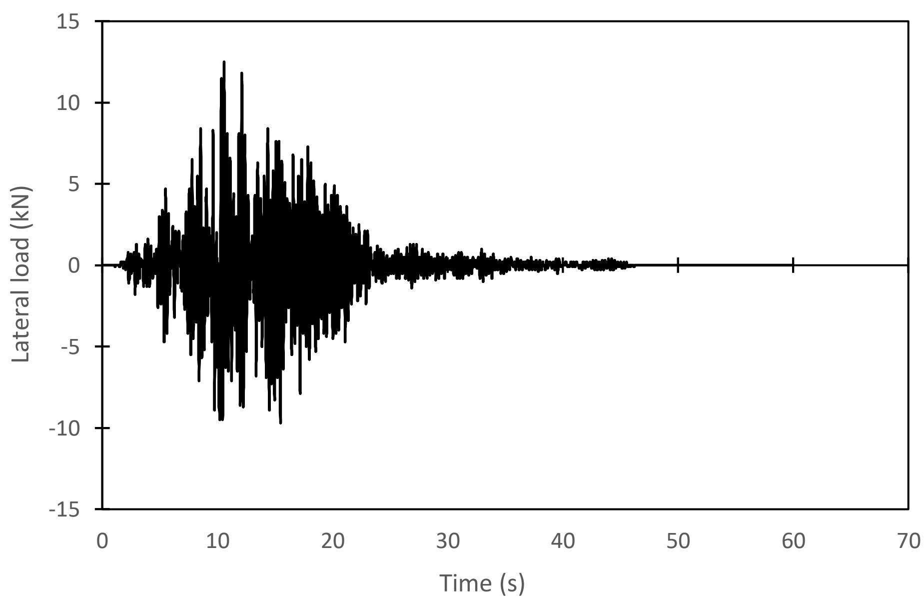
15
10
5
0
-5
-10
-15
Lateral load (kN)
0
10
20
30
40
50
60
70
Time (s)

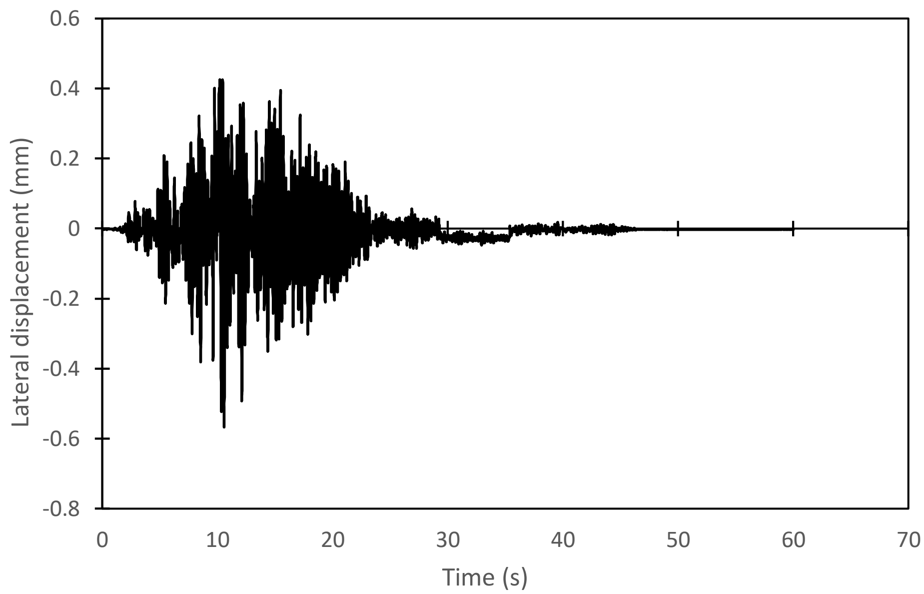
0.6
0.4
0.2
0
-0.2
-0.4
-0.6
-0.8
Lateral displacement (mm)
0
10
20
30
40
50
60
70
Time (s)